

Springer-Verlag Berlin Heidelberg GmbH

Physics and Astronomy

springeronline.com



Springer Series in SOLID-STATE SCIENCES

Series Editors:

M. Cardona P. Fulde K. von Klitzing R. Merlin H.-J. Queisser H. Störmer

The Springer Series in Solid-State Sciences consists of fundamental scientific books prepared by leading researchers in the field. They strive to communicate, in a systematic and comprehensive way, the basic principles as well as new developments in theoretical and experimental solid-state physics.

- | | |
|-------------------------------------------------------------------------------------------------------------------------------------------------------------------------------------------------|-------------------------------------------------------------------------------------------------------------------------------------------------------------|
| 126 Physical Properties of Quasicrystals
Editor: Z.M. Stadnik | 135 Electrodynamics
of Magnetoactive Media
By I. Vagner, B.I. Lembrikov,
and P. Wyder |
| 127 Positron Annihilation
in Semiconductors
Defect Studies
By R. Krause-Rehberg
and H.S. Leipner | 136 Nanoscale Phase Separation
and Colossal Magnetoresistance
The Physics of Manganites
and Related Compounds
By E. Dagotto |
| 128 Magneto-Optics
Editors: S. Sugano and N. Kojima | 137 Quantum Transport
in Submicron Devices
A Theoretical Introduction
By W. Magnus and W. Schoenmaker |
| 129 Computational Materials Science
From Ab Initio
to Monte Carlo Methods
By K. Ohno, K. Esfarjani,
and Y. Kawazoe | 138 Phase Separation
in Soft Matter Physics
Micellar Solutions, Microemulsions,
Critical Phenomena
By P.K. Khabibullaev and A.A. Saidov |
| 130 Contact, Adhesion and Rupture
of Elastic Solids
By D. Maugis | 139 Optical Response of Nanostructures
Microscopic Nonlocal Theory
By K. Cho |
| 131 Field Theories for Low-Dimensional
Condensed Matter Systems
Spin Systems
and Strongly Correlated Electrons
By G. Morandi, P. Sodano,
A. Tagliacozzo, and V. Tognetti | 140 Fractal Concepts
in Condensed Matter Physics
By T. Nakayama and K. Yakubo |
| 132 Vortices in Unconventional
Superconductors and Superfluids
Editors: R.P. Huebener, N. Schopohl,
and G.E. Volovik | 141 Excitons in Low-Dimensional
Semiconductors
Theory, Numerical Methods,
Applications
By S. Glutsch |
| 133 The Quantum Hall Effect
By D. Yoshioka | 142 Two-Dimensional Coulomb Liquids
and Solids
By Y. Monarkha and K. Kono |

Stephan Glutsch

Excitons in Low-Dimensional Semiconductors

Theory
Numerical Methods
Applications

With 41 Figures



Springer

Dr. Stephan Glutsch
Friedrich-Schiller-Universität
Institut für Festkörpertheorie
und Theoretische Optik
Max-Wien-Platz 1
07743 Jena, Germany
e-mail: stephan@ifto.physik.uni-jena.de

Series Editors:

Professor Dr., Dres. h. c. Manuel Cardona
Professor Dr., Dres. h. c. Peter Fulde*
Professor Dr., Dres. h. c. Klaus von Klitzing
Professor Dr., Dres. h. c. Hans-Joachim Queisser
Max-Planck-Institut für Festkörperforschung, Heisenbergstrasse 1, D-70569 Stuttgart, Germany
* Max-Planck-Institut für Physik komplexer Systeme, Nöthnitzer Strasse 38
D-01187 Dresden, Germany

Professor Dr. Roberto Merlin
Department of Physics, 5000 East University, University of Michigan
Ann Arbor, MI 48109-1120, USA

Professor Dr. Horst Störmer
Dept. Phys. and Dept. Appl. Physics, Columbia University, New York, NY 10027 and
Bell Labs., Lucent Technologies, Murray Hill, NJ 07974, USA

ISSN 0171-1873

ISBN 978-3-642-05781-6

Library of Congress Cataloging-in-Publication Data: Glutsch, S. (Stephan), 1964-. Excitons in low-dimensional semiconductors: theory, numerical methods, applications/ S. Glutsch. p. cm. - (springer series in solid-state sciences, ISSN 0171-1873; 141) Includes bibliographical references and index.

ISBN 978-3-642-05781-6 ISBN 978-3-662-07150-2 (eBook)
DOI 10.1007/978-3-662-07150-2

1. Exciton theory. 2. Low-dimensional semiconductors. I. Title. II. Series. QC176.8.E9G58 2003 530.4'16-dc22 2003060466

This work is subject to copyright. All rights are reserved, whether the whole or part of the material is concerned, specifically the rights of translation, reprinting, reuse of illustrations, recitation, broadcasting, reproduction on microfilm or in any other way, and storage in data banks. Duplication of this publication or parts thereof is permitted only under the provisions of the German Copyright Law of September 9, 1965, in its current version, and permission for use must always be obtained from Springer-Verlag Berlin Heidelberg GmbH. Violations are liable for prosecution under the German Copyright Law.

springeronline.com

© Springer-Verlag Berlin Heidelberg 2004
Originally published by Springer-Verlag Berlin Heidelberg New York in 2004
Softcover reprint of the hardcover 1st edition 2004

The use of general descriptive names, registered names, trademarks, etc. in this publication does not imply, even in the absence of a specific statement, that such names are exempt from the relevant protective laws and regulations and therefore free for general use.

Typesetting by the author using a Springer L^AT_EXmacropackage
Final layout: Frank Herweg, Leutershausen
Cover concept: eStudio Calamar Steinen
Cover production: *design & production* GmbH, Heidelberg

Printed on acid-free paper SPIN: 10938829 57/3141/ba - 5 4 3 2 1 0

Preface

Low-dimensional semiconductors are a vital part of today's semiconductor physics. Excitons in low-dimensional semiconductors are ideal objects for bringing textbook quantum mechanics to life. This quantum mechanics is the basis for a large number of phenomena related to discrete states, continua, and resonances; dimensionality transitions, depending on the geometric parameters, external fields, and the spectral range, can be observed. Apart from their fundamental theoretical interest, an understanding of low-dimensional semiconductors is important for experiments and device applications. Even though research on such semiconductors has been done for about thirty years, several breakthroughs (literally!) have been achieved only recently, and there are certainly more to come.

The present book is the result of more than one decade of theoretical research on excitons in low-dimensional semiconductors, much of it in co-operation with experimentalists. The goal is to give a comprehensive review on linear optical properties of low-dimensional semiconductors, with a brief introduction to related topics and references for further reading. The work is clearly methods-oriented with a strong focus on foundation, formalism, and numerical solutions; nevertheless, it contains several new results, which were first obtained by the author and have not been surpassed since. Whenever possible, the theory is compared with experimental results. I emphasize the general aspects but, at the same time, provide enough details for the reader, try to avoid superficiality and do not fight shy of difficult questions. The book is intended for scientists working in the field of semiconductor physics or optoelectronics, theorists and experimentalists, starting at graduate level. Only a basic knowledge of quantum mechanics and solid-state physics is required.

The four chapters are essentially self-contained, each with its own introduction, summary, and bibliography, so that they can be read separately. At the beginning of each chapter, I make specific recommendations for textbooks, which I consider of exceptional quality (i.e., which I would have bought myself). The general theory is always illustrated by a number of examples. Small-printed passages within the text are used for marginal notes and comments to provide some more details or to place a subject in a wider context, and also for technical proofs. The use of symbols is widely consistent within each chapter and, whenever possible, I tried to comply with conventions in

the literature. Important notations, conventions, and definitions are summarized in the appendix, together with further mathematical and physical supplements and computer programs.

The first chapter gives an introduction to the theory of optical transitions in semiconductors. Starting from the Bloch theorem, the effective-mass theory, which is the natural description of electrons and holes in semiconductors, is developed for the general case of band degeneracy, heterojunctions, and external fields. The optical transition rules are deduced from symmetry arguments and the optical density of states is introduced in order to characterize the dimensionality of a semiconductor. Finally, the Coulomb interaction is included in the theory and the Elliott formula is derived for the general case. Explicit results are given for a number of low-dimensional semiconductors.

Numerical calculations are essential for the theory of low-dimensional semiconductors. For many, the second chapter, which is somewhat technical, will be the most demanding one. I start with a classification scheme for the numerical complexity and point out the limitations of traditional methods. The rest of the chapter is devoted to the solution as an initial-value problem, which is split up into two parts, the discretization in real space, which is explained in the framework of Hilbert spaces, and the time-propagation scheme. Five problems, specified at the beginning of the chapter, are used to explain each step of the theory.

Fano resonances are a typical feature of absorption spectra of low-dimensional semiconductors, and are more the rule than the exception. This will be demonstrated in the third chapter. First, I present a solution of the Fano model in terms of Green's functions, commonly used in solid-state physics. Then the general theory of Fano resonances in low-dimensional semiconductors is developed in analogy to multi-channel scattering theory, known from atomic or nuclear physics. Finally, I give an overview of theoretical and experimental results on Fano resonances in low-dimensional semiconductors. I demonstrate the build-up of Fano resonances for two typical examples and compare the numerical results with experimental data.

Zener tunneling in superlattices is the topic of the fourth chapter. After a historical introduction, the theory of Wannier–Stark ladders and Kane functions is explained in detail. It is then shown by numerical calculations that this picture breaks down at high, but attainable fields. The results for the optical density of states and the optical absorption are in excellent agreement with recent measurements on superlattices. This chapter ends with the calculation of the tunneling rate, which also reveals an inconsistency of the Houston–Kane formalism. The calculated tunneling rate agrees very well with the linewidth observed in optical experiments.

At this point, I wish to thank those who have contributed to the success of this project for cooperation, ideas, discussions, suggestions, questions, critique, communication of unpublished material, technical assistance, proofreading, encouragement, or other kinds of support. An incomplete list in-

cludes: A. Ahland, S. Bar-Ad, F. Bechstedt, V. Bellani, D. S. Chemla, R. Enderlein, M. Fiedler, P. M. Goorian, P. H. Hahn, K. Hannewald, M. Helm, C. P. Holfeld, A. B. Hummel, A. Knorr, W. Langbein, K. Leo, H.-G. Leopold, F. Löser, D. Meinhold, D. Michaelis, K. Mittmann, P. Oswald, T. Pertsch, U. Peschel, B. Rosam, K. Rönnburg, H. G. Roskos, W. G. Schmidt, R. P. Seisyan, U. Siegner, P. E. Simmonds, M. S. Skolnick, S. M. Stepanow, R. G. Ulbrich, P. Vogl, J.-M. Wagner, R. Winkler, C. H. Ziener, and R. Zimmermann. Furthermore, I acknowledge financial support from the Deutsche Forschungsgemeinschaft and the Freistaat Thüringen, and computing resources from the John von Neumann Center for Computing, Forschungszentrum Jülich.

Jena, August 2003

Stephan Glutsch

Contents

1	Optical Transitions in Semiconductors	1
1.1	Effective-Mass Theory	2
1.1.1	Electron in a Periodic Potential	3
1.1.2	$\mathbf{k} \cdot \mathbf{p}$ Perturbation Theory	7
1.1.3	Low-Dimensional Structures	13
1.2	Electron–Light Interaction	17
1.2.1	Transition Matrix Elements	18
1.2.2	The Optical Density of States	20
1.2.3	Examples	23
1.3	Excitons	29
1.3.1	The Semiconductor Bloch Equations	31
1.3.2	The Elliott Formula	35
1.3.3	Examples	39
1.4	Summary and Conclusions	44
2	Numerical Calculation	47
2.1	Preliminaries	48
2.1.1	Formulation of the Problem	49
2.1.2	Overview	54
2.2	Approximation in Space	60
2.2.1	Orthonormal Base Functions	61
2.2.2	Non-Orthonormal Base Functions	69
2.2.3	Finite Differences	76
2.3	Solution of the Initial-Value Problem	83
2.3.1	The Time-Propagation Scheme	84
2.3.2	Two Examples	89
2.3.3	Absorbing Boundary Conditions	93
2.4	Summary and Conclusions	99
3	Fano Resonances	101
3.1	The Fano Model	102
3.1.1	One Resonance and One Continuum	103
3.1.2	The General Case	107
3.2	Fano Resonances as a General Feature	114
3.2.1	The Channel Picture	114

3.2.2	The Subband Picture	119
3.3	Examples	122
3.3.1	Overview	122
3.3.2	Bulk Semiconductor in a Magnetic Field	126
3.3.3	Quantum Well	136
3.4	Summary and Conclusions	142
4	Zener Breakdown in Superlattices	145
4.1	Bloch Electron in One Dimension	149
4.1.1	General Properties	150
4.1.2	Tightly Bound and Nearly Free Electrons	151
4.1.3	Two Samples	154
4.2	Bloch Electron in an Electric Field	158
4.2.1	Discrete Model and Tight-Binding Approximation	158
4.2.2	Kane Functions	162
4.2.3	Breakdown of Wannier–Stark Ladders	169
4.3	The Optical Spectrum	172
4.3.1	Optical Density of States	173
4.3.2	Optical Absorption	181
4.3.3	Optical Absorption in a Perpendicular Magnetic Field	188
4.4	The Tunneling Rate	191
4.4.1	Semiclassical Approach	192
4.4.2	Perturbation Theory	196
4.4.3	Discussion	203
4.5	Summary and Conclusions	206
A	Mathematical Supplement	209
A.1	Basic Definitions and Relations	209
A.2	Special Functions of Mathematical Physics	215
A.3	Miscellaneous Relations	217
B	Physical Supplement	223
B.1	Physical Constants and Material Parameters	223
B.2	Dimensionless Quantities	225
B.3	Crystal Symmetry	227
C	Essentials of Quantum Mechanics	231
C.1	The Quantum-Mechanical Eigenvalue Problem	231
C.1.1	The Spectrum of Schrödinger Operators	231
C.1.2	Selected Eigenvalue Problems	234
C.2	Angular Momentum in Quantum Mechanics	244
C.2.1	The Eigenvalue Problem	245
C.2.2	Orthogonal Transformations	247
C.2.3	Addition of Angular Momenta	248
C.2.4	Time Reversal	249

C.3 Perturbation Theory	250
C.3.1 Degenerate Time-Independent Perturbation Theory ..	250
C.3.2 Time-Dependent Perturbation Theory	251
D Computer Programs	255
D.1 Cartesian Coordinates	255
D.2 Polar Coordinates	260
D.3 Time-Reversal Symmetry	264
D.4 Absorbing Boundary Conditions	265
D.5 Cylindrical Coordinates	268
References	273
Index	289

1 Optical Transitions in Semiconductors

The purpose of this chapter is to give an introduction to the theory of optical transitions in semiconductors, to provide the “theoretical minimum” for the understanding of the next chapters. We aim to present the reasoning as clearly and straightforwardly as possible, avoiding both shallowness and unnecessary attention to details.

We try to make a compromise between keeping the notation consistent throughout the chapter and, at the same time, using the symbols that are familiar from the literature. Particular emphasis is put on formalism. We believe that the natural description for Wannier excitons in low-dimensional semiconductors is the formulation in real space by envelope functions, also known as Wannier representation. Our approach is essentially non-historical and the references are selected according to their comprehensiveness, clarity, elegance, in brief: usefulness.

At this point, we give some references for general reading. For the quantum-mechanical background, we recommend the world-classic Landau–Lifshitz [1]. “Quantum Mechanics” by Merzbacher is a carefully structured graduate-level textbook with a good selection of problems and examples [2]. A practical approach to quantum mechanics, with applications to atoms, is found in Friedrich’s “Theoretical Atomic Physics” [3]. Ziman’s book [4] is a brief, readable introduction to the quantum theory of the solid state. A comprehensive review on electronic states and optical transitions in semiconductors was published by Bassani and Pastori Parravicini in 1975 [5]. There is a number of recent books, which combine experimental, theoretical, and technical aspects and also pay attention to low-dimensional semiconductors. The work by Yu and Cardona [6] provides a good overview, is easy-to-read, balanced, with excellent typography. The clearly written textbook by Klingshirn on optics in semiconductors [7] is also a valuable resource. A more technical approach is Chuang’s “Physics of Optoelectronic Devices” [8], a workbook with many formulas, tables, and diagrams. For further reading on low-dimensional semiconductors, we recommend the book by Weisbuch and Vinter from 1991 [9], which gives a good overview and, in many respects, has not been surpassed by later publications. The experimental and technological side of low-dimensional semiconductors is examined in detail by Kelly [10]. For theoretical aspects, the recent work by Davies [11] is highly

recommended; it is an intermediate-level textbook, easy to read, with good illustrations and many worked-out examples. For a short introduction into the physics of two-dimensional structures, the booklet by Shik is helpful [12].

1.1 Effective-Mass Theory

The motion of electrons in periodic fields has been studied ever since the early years of quantum mechanics [13]. The symmetry of the crystal has consequences for the eigenvalues and eigenfunctions. Due to the invariance of the Hamiltonian under lattice translations, the eigenfunctions are Bloch waves and the spectrum consists of energy bands, separated by forbidden gaps. The band degeneracy at symmetric points can be classified according to the irreducible representations of the point group of the crystal [14]. To some point, electronic states in crystals are similar to atomic orbitals, for example, the crystal eigenfunctions may be s- or p-like.

The effective-mass approximation allows us to treat Bloch electrons like free particles with effective mass, momentum, etc., similar to the Drude model, where a metal is looked upon as a gas of free electrons. For a nondegenerate band, the dispersion near the Γ point is parabolic with an effective mass different from the free electron mass. A missing valence electron with negative mass and negative charge is interpreted as a hole with positive mass and positive charge. For degenerate bands, the energies and eigenfunctions near the degeneracy point follow from the eigenvalue problem of an effective Hamiltonian, which is determined by $\mathbf{k} \cdot \mathbf{p}$ perturbation theory [15]. The method of invariants allows the construction of the effective Hamiltonian solely from the transformation properties [16]. The wavefunctions are spinors, which transform according to the irreducible representations of the crystal point group. Then the natural definition of a hole is that of a time-reversed electron. In the presence of external fields, the eigenfunctions can be approximated by products of slowly varying envelope functions and rapidly varying lattice-periodic functions and the envelope functions obey a Schrödinger equation which contains the electric and magnetic field. In semiconductor heterostructures, the modulations of the band edges appear as additional potentials in the effective Hamiltonian [17].

This section presents a review on basic properties of electrons in crystals. We give a classification of the band degeneracy at the Γ point for zincblende semiconductors in terms of irreducible representations of the point group. The $\mathbf{k} \cdot \mathbf{p}$ perturbation theory and the method of invariants is briefly reviewed. Finally, we generalize the effective-mass theory to external potentials and semiconductor heterostructures.

There are numerous textbooks on the application of group representation theory in physics. The book by Inui, Tanabe, and Onodera [18] pays special attention to electronic states in crystals. Streitwolf's book [19] on group theory in solid-state physics is very helpful. The classification of bands by

means of irreducible representations is also explained in the recommended textbooks [5–7]. Yu and Cardona [6] give an easy-to-read introduction into group representation theory. The $\mathbf{k} \cdot \mathbf{p}$ theory of band structure is explained in a review article by Kane [20], in textbooks by Bassani and Pastori Parravicini [5] as well as by Tsidilkovski [21], who give a comprehensive review on band structure of semiconductors, and by Zeiger and Pratt [22], who focus on the magnetic field. The book by Bir and Pikus is considered the standard work on the method of invariants [23]. For further reading on effective-mass theory in semiconductor heterostructures we recommend a review article by Altarelli [17], a monograph by Bastard [24], and a textbook by Ivchenko and Pikus [25]. Chuang focuses more on applications and summarizes important formulas and material parameters [8].

1.1.1 Electron in a Periodic Potential

The Hamiltonian of an electron with spin in a lattice-periodic potential W , subjected to external electric and magnetic fields is given by [5, 8, 21, 22, 26]

$$\begin{aligned}\hat{H} = & \frac{1}{2m_0} \left[\frac{\hbar}{i} \nabla + e\mathbf{A}(\mathbf{r}) \right]^2 + W(\mathbf{r}) - eU(\mathbf{r}) \\ & + \frac{g\mu_B}{\hbar\mu_0} \mathbf{B} \cdot \mathbf{S} + \frac{1}{2m_0^2 c_0^2} [\mathbf{S} \times \nabla W(\mathbf{r})] \cdot [\frac{\hbar}{i} \nabla + e\mathbf{A}(\mathbf{r})],\end{aligned}\quad (1.1)$$

where U and \mathbf{A} are the scalar and vector potential of the electric and magnetic field, respectively, $\mathbf{B} = \nabla \times \mathbf{A}$ is the magnetic field, $e > 0$ is the elementary charge, and $\mathbf{S} = \frac{\hbar}{2} \boldsymbol{\sigma}$ is the spin operator. For the meanings of symbols and numerical values of physical constants, see App. B.1.

In reality, the semiconductor is a many-particle system and it takes several approximations to obtain a single-particle problem of the form (1.1). The potential W is an effective potential, which depends on all occupied electronic states. In older works on band structure, W is often derived by means of the Hartree or Hartree–Fock approximation. Today, a common methodology of reducing the many-particle to a single-particle problem is the density-functional theory (DFT). As we are only interested in the general properties of the eigenstates, we shall merely assume that a single-particle potential W exists and has the symmetry of the crystal.

The eigenfunctions of the Hamiltonian, $\varphi(\mathbf{r}) = (\varphi(\mathbf{r}, \uparrow), \varphi(\mathbf{r}, \downarrow))^T$, are two-component spinors. We first neglect the external fields. Due to the periodicity of the crystal potential, $W(\mathbf{r} + \mathbf{R}) = W(\mathbf{r})$ for arbitrary lattice vectors \mathbf{R} , the eigenfunctions can be represented as Bloch waves,

$$\varphi_{j\mathbf{k}}(\mathbf{r}) = \frac{1}{\sqrt{\Omega}} e^{i\mathbf{k} \cdot \mathbf{r}} \mathbf{u}_{j\mathbf{k}}(\mathbf{r}); \quad \mathbf{u}_{j\mathbf{k}}(\mathbf{r} + \mathbf{R}) = \mathbf{u}_{j\mathbf{k}}(\mathbf{r}), \quad (1.2)$$

where Ω is the normalization volume of the Born–von Kármán cyclic boundary conditions (App. C.1.2). The normalization of the Bloch functions

$$\langle j, \mathbf{k} | j', \mathbf{k}' \rangle = \sum_{m_s} \int d^3r \varphi_{j\mathbf{k}}^*(\mathbf{r}, m_s) \varphi_{j'\mathbf{k}'}(\mathbf{r}, m_s) = \delta_{jj'} \delta_{\mathbf{k}\mathbf{k}'} \quad (1.3)$$

entails a normalization of the lattice-periodic functions for equal \mathbf{k} on the Wigner–Seitz cell Ω_0 :

$$\langle j, \mathbf{k} | j', \mathbf{k} \rangle = \sum_{m_s} \frac{1}{\Omega_0} \int_{\Omega_0} d^3r u_{j\mathbf{k}}^*(\mathbf{r}, m_s) u_{j'\mathbf{k}}(\mathbf{r}, m_s) = \delta_{jj'} . \quad (1.4)$$

The Hamiltonian (1.1) without magnetic field fulfills time-reversal symmetry (App. C.2). If $\varphi_{j\mathbf{k}}$ is an eigenfunction of \hat{H} , then $\hat{K}\varphi_{j\mathbf{k}} \simeq \varphi_{j', -\mathbf{k}}$ is also an eigenfunction of \hat{H} . Consequently, it holds that $E_j(\mathbf{k}) = E_{j'}(-\mathbf{k})$.

Besides lattice translations, the Hamiltonian (1.1) is also invariant under the operations of the space group of the crystal (App. B.3). We shall first neglect spin-orbit interaction. This is equivalent to treating the electron as a spinless particle. The application of a space-group element $\{\alpha, \mathbf{a}\}$ on an eigenfunction $\varphi_{j\mathbf{k}}$ yields

$$\begin{aligned} \varphi'_{j\mathbf{k}}(\mathbf{r}) &= \varphi_{j\mathbf{k}}(\{\alpha, \mathbf{a}\}\mathbf{r}) = \varphi_{j\mathbf{k}}(\alpha\mathbf{r} + \mathbf{a}) \\ &= e^{i\mathbf{k}\cdot\mathbf{a}} \frac{1}{\sqrt{\Omega}} e^{i\alpha^{-1}\mathbf{k}\cdot\mathbf{r}} u_{j\mathbf{k}}(\alpha\mathbf{r} + \mathbf{a}) . \end{aligned} \quad (1.5)$$

The transformed function $\varphi'_{j\mathbf{k}}$ must be an eigenfunction of \hat{H} with the same eigenvalue $E_j(\mathbf{k})$. On the other hand, the characteristic wavevector of $\varphi'_{j\mathbf{k}}$ is $\alpha^{-1}\mathbf{k}$. Therefore, we have

$$\varphi'_{j\mathbf{k}} \simeq \varphi_{j', \alpha^{-1}\mathbf{k}} ; \quad E_j(\mathbf{k}) = E_{j'}(\alpha^{-1}\mathbf{k}) , \quad (1.6)$$

which is called star degeneracy. The above relation is particularly interesting for symmetric points, where $\alpha\mathbf{k} = \mathbf{k}$ for all $\alpha \in G_{0\mathbf{k}}$. The group $G_{0\mathbf{k}}$ is called the point group of the vector \mathbf{k} . If $j' \neq j$, then one speaks of band degeneracy. Let $E_j(\mathbf{k})$ be an M -fold degenerate band at the symmetric point \mathbf{k} and the degenerate eigenfunctions $\varphi_{\nu 1\mathbf{k}}, \dots, \varphi_{\nu M\mathbf{k}}$ be orthonormal. Then any eigenfunction $\varphi_{j\mathbf{k}}$ is a linear combination of the degenerate eigenfunctions:

$$\varphi_{j\mathbf{k}} = \sum_{m=1}^M f_m \varphi_{\nu m\mathbf{k}} . \quad (1.7)$$

The transformed eigenfunction $\varphi'_{j\mathbf{k}}(\mathbf{r})$ is also a linear combination of $\varphi_{\nu 1\mathbf{k}}, \dots, \varphi_{\nu M\mathbf{k}}$ with coefficients

$$f'_m = \sum_{m'=1}^M A_{mm'} f_{m'} . \quad (1.8)$$

The unitary matrices $A(\alpha)$ constitute an irreducible representation of the point group $G_{0\mathbf{k}}$. Therefore, band degeneracies can be classified according to the irreducible representations of the point group [6, 7, 14, 18, 19, 26].

In view of optical transitions, we consider the Γ point. The point group of $\mathbf{k} = 0$ is identical with the point group G_0 of the crystal (App. B.3). For zincblende crystals, $G_0 = T_d$ and the 24 elements of the point group consist of permutations of the Cartesian axes x , y , and z , where either none or two of the axes may change their sign. There are five irreducible representations of T_d , labelled $\Gamma_1, \dots, \Gamma_5$.¹ Besides this Koster notation, the Bouckaert–Smoluchowski–Wigner (BSW) notation $(\Gamma_1, \Gamma_2, \Gamma_{12}, \Gamma_{15}, \Gamma_{25})$ is also very common.

Table 1.1 shows representation, degeneracy, and transformation behavior of the eigenfunctions for the valence (v) and conduction (c) band of important zincblende semiconductors at the Γ point. The threefold degenerate valence band is made up of p orbitals of the individual atoms and, therefore, the eigenfunctions transform like p orbitals. The conduction band, which results from antibonding s orbitals, is nondegenerate, and the eigenfunction essentially behaves like an s orbital.

Table 1.1. Degeneracy of valence and conduction band without spin for zincblende semiconductors at the Γ point

Band	Representation	Degeneracy	Base functions
v	$\Gamma_4 = \Gamma_{15}$	3	$ 1, +1\rangle, 1, 0\rangle, 1, -1\rangle$ or $ X\rangle, Y\rangle, Z\rangle$
c	Γ_1	1	$ s\rangle$

If the spin–orbit interaction is negligible, as in GaP, the above scheme can be used for the classification of the energy bands. In most cases, however, the spin–orbit interaction is important. For an electron with spin, the space-group operations simultaneously affect the position and the spin coordinate (App. B.3). Then, instead of (1.5), we need to write

$$\varphi'_{j\mathbf{k}}(\mathbf{r}) = D^{(1/2)}(\alpha) \varphi_{j\mathbf{k}}(\alpha \mathbf{r} + \mathbf{a}). \quad (1.9)$$

The Hamiltonian (1.1) including spin–orbit interaction is invariant under the operations of the double space group (1.9).² Therefore, the relations (1.6–1.8) remain valid for spin–orbit interaction. Because the representation $D^{(1/2)}$ of O(3) is double-valued, the representations of the point group have to be double-valued, which means that the degenerate eigenfunctions transform according to the extra representation of the double point group.

¹ The meaning of Γ_4 and Γ_5 is not consistent in the literature. We use the notations $\Gamma_4 = \Gamma_{15}$ and $\Gamma_5 = \Gamma_{25}$.

² The proof follows from relations (C.80,C.83).

The double-valued representations of the point group of zincblende structures are labelled Γ_6 , Γ_7 , and Γ_8 . The band degeneracy at the Γ point in zincblende semiconductors including spin-orbit interaction and the relations to the spinless case are listed in Table 1.2. The sixfold degenerate valence band without spin-orbit interaction splits into a twofold degenerate split-off band (so) and a fourfold degenerate valence band. The effect of spin-orbit interaction is qualitatively the same as for atomic p and s orbitals. Fivefold degenerate d states cannot be observed in cubic crystals, because they do not correspond to irreducible representations of T_d .

Table 1.2. Degeneracy of valence and conduction band with spin-orbit interaction for zincblende semiconductors at the Γ point, and relation to the spinless case

Band	Representation	Degeneracy	Base functions
so	Γ_7	2	$ \frac{1}{2}, +\frac{1}{2}\rangle, \frac{1}{2}, -\frac{1}{2}\rangle$
v	Γ_8	4	$ \frac{3}{2}, +\frac{3}{2}\rangle, \frac{3}{2}, +\frac{1}{2}\rangle, \frac{3}{2}, -\frac{1}{2}\rangle, \frac{3}{2}, -\frac{3}{2}\rangle$
c	Γ_6	2	$ \uparrow\rangle, \downarrow\rangle$

$$\Gamma_4 \otimes D^{(1/2)} = \Gamma_7 \oplus \Gamma_8; \Gamma_1 \otimes D^{(1/2)} = \Gamma_6$$

A schematic drawing of the valence and conduction band of zincblende semiconductors near the Γ point is shown in Fig. 1.1. The band dispersions $E_j(\mathbf{k})$ are plotted versus Bloch wavevector \mathbf{k} for one direction. The Γ_8 valence band is fourfold degenerate only at $\mathbf{k} = 0$ and splits into the twofold degenerate heavy-hole (hh) and light-hole (lh) bands for $\mathbf{k} \neq 0$. In molecular physics and quantum chemistry, the analogs of conduction and valence band are called lowest unoccupied molecular orbital (LUMO) and highest occupied molecular orbital (HOMO), respectively.

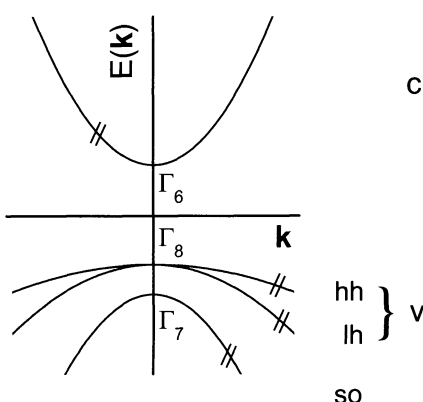


Fig. 1.1. Schematic drawing of the conduction, valence, and split-off band for a zincblende semiconductor near the Γ point. The symbol // means twofold degeneracy

We have seen that the eigenstates of electrons at the conduction and valence band edges are characterized by vector and spinor representations. Therefore, the Γ_8 valence electron essentially behaves like a particle with spin $\frac{3}{2}$, the Γ_1 conduction electron like a spinless particle etc. This analogy is widely used in the effective-mass theory.

The point group of diamond crystals O_h has 48 elements. Due to the relation $O_h = +T_d \cup -T_d$, the point group O_h has twice as much representations as T_d . In the Koster notation, a superscript \pm indicates the parity. In the BSW notation, unprimed and primed symbols are used, not directly related to the parity. Due to simultaneous time-reversal and inversion symmetry, each band is twofold degenerate (Kramers pair).

1.1.2 $\mathbf{k} \cdot \mathbf{p}$ Perturbation Theory

The behavior of the eigenvalues and eigenfunctions near a critical point can be studied by $\mathbf{k} \cdot \mathbf{p}$ perturbation theory [15, 20]. We will apply this method to determine the band structure near the Γ point.

We first neglect spin-orbit interaction and external fields. The lattice-periodic functions (1.2) obey the equation

$$\left[-\frac{\hbar^2}{2m_0} \Delta + \frac{\hbar}{m_0} \mathbf{k} \cdot \frac{\hbar}{i} \nabla + \frac{\hbar^2 k^2}{2m_0} + W(\mathbf{r}) \right] u_{j\mathbf{k}}(\mathbf{r}) = E_j(\mathbf{k}) u_{j\mathbf{k}}(\mathbf{r}) . \quad (1.10)$$

The term in square brackets can be considered as a Hamiltonian depending on an external parameter \mathbf{k} . In order to apply perturbation theory, we use the following decomposition:

$$\begin{aligned} \hat{H}(\mathbf{k}) &= \hat{H}^{(0)} + \hat{H}^{(i)}(\mathbf{k}) + \frac{\hbar^2 k^2}{2m_0} \\ \hat{H}^{(0)} &= -\frac{\hbar^2}{2m_0} \Delta + W(\mathbf{r}) ; \quad \hat{H}^{(i)}(\mathbf{k}) = \frac{\hbar}{m_0} \mathbf{k} \cdot \frac{\hbar}{i} \nabla . \end{aligned} \quad (1.11)$$

The term $\hbar^2 k^2 / (2m_0)$ is a scalar and does not affect the eigenfunctions. The eigenvalues and eigenfunctions in a neighborhood of $\mathbf{k} = 0$ can be calculated from the unperturbed eigenvalues and eigenfunctions, $E_j = E_j(\mathbf{k}=0)$ and $u_j = u_{j,\mathbf{k}=0}$.³ The matrix elements of the perturbation are

$$(j | \hat{H}^{(i)}(\mathbf{k}) | j') = \frac{\hbar}{m_0} \mathbf{k} \cdot \mathbf{p}_{jj'} ; \quad \mathbf{p}_{jj'} = \frac{1}{\Omega_0} \int_{\Omega_0} d^3 \mathbf{r} u_j(\mathbf{r}) \frac{\hbar}{i} \nabla u_{j'}(\mathbf{r}) , \quad (1.12)$$

which is the reason for the name “ $\mathbf{k} \cdot \mathbf{p}$ perturbation theory.”

In order to determine the eigenvalues and eigenfunctions of a degenerate band ν near $\mathbf{k} = 0$, we identify the degenerate eigenstates $j = \nu, m$ with

³ The orthonormal and complete functions $\left\{ e^{i\mathbf{k}\cdot\mathbf{r}} u_{j,\mathbf{k}=0}(\mathbf{r}) / \sqrt{\Omega} \right\}$ are called Luttinger-Kohn functions [27].

Löwdin's class A and all other eigenstates $j' \neq \nu, m$ with class B. For full cubic (O_h) symmetry, the momentum matrix elements between two p orbitals of the valence band are zero. The effective Hamiltonian (App. C.3) takes the form [15, 27]

$$H_{\text{eff}}(\mathbf{k}) = E_\nu + H_{\text{kin}}(\mathbf{k}) ; \quad H_{\nu \text{ kin } mm'}(\mathbf{k}) = \sum_{\alpha\alpha'} k_\alpha D_{\nu mm'}^{\alpha\alpha'} k_{\alpha'} , \quad (1.13)$$

where

$$D_{\nu mm'}^{\alpha\alpha'} = \frac{\hbar^2}{2m_0} \delta_{\alpha\alpha'} \delta_{mm'} + \left(\frac{\hbar}{m_0} \right)^2 \sum_{j'}' \frac{p_{\nu m, j'}^\alpha p_{j', \nu m'}^{\alpha'}}{E_\nu - E_{j'}} . \quad (1.14)$$

In the definition of D , the sum runs only over the class-B components. Because of the analogy with free particles, we use the subscript "kin" for the contribution quadratic in \mathbf{k} . The eigenvalues $E_{\nu l}(\mathbf{k})$, second order in the small parameter \mathbf{k} , follow from the eigenvalue problem

$$\sum_{m'} H_{\nu \text{ eff } mm'}(\mathbf{k}) c_{\nu l; \nu m'}(\mathbf{k}) = E_{\nu l}(\mathbf{k}) c_{\nu l; \nu m}(\mathbf{k}) \quad (1.15)$$

and the Bloch functions in first-order perturbation theory are

$$\varphi_{\nu l \mathbf{k}}(\mathbf{r}) = \frac{1}{\sqrt{\Omega}} e^{i\mathbf{k} \cdot \mathbf{r}} \left[\sum_m c_{\nu l; \nu m}(\mathbf{k}) u_{\nu m}(\mathbf{r}) + \sum_{j'}' c_{\nu l; j'}(\mathbf{k}) u_{j'}(\mathbf{r}) \right]$$

$$c_{\nu l; j'}(\mathbf{k}) = \sum_m \frac{\frac{\hbar}{m_0} \mathbf{k} \cdot \mathbf{p}_{j', \nu m}}{E_\nu - E_{j'}} c_{\nu l; \nu m}(\mathbf{k}) ; \quad j' \in B . \quad (1.16)$$

The class-B components of the eigenfunctions are often neglected in effective-mass theory, even though they may not be small.

As an example, we consider the threefold degenerate valence band of a zincblende semiconductor in the basis of the Cartesian p orbitals $|X\rangle$, $|Y\rangle$, $|Z\rangle$ (App. C.2). As result of the cubic symmetry, H_{kin} contains only three independent parameters, namely,

$$L = D_{XX}^{xx} ; \quad M = D_{YY}^{xx} ; \quad N = D_{XY}^{xy} + D_{XY}^{yx} . \quad (1.17)$$

It is worthwhile to note that contributions of the form $D_{XY}^{xy} - D_{XY}^{yx}$ are generally nonzero, but do not appear in the quadratic form (1.13).⁴ The explicit form of the kinetic Hamiltonian is [15, 21, 26, 27]

$$H_{\nu \text{ kin}}(\mathbf{k}) = \begin{pmatrix} Lk_x^2 + M(k_y^2 + k_z^2) & Nk_x k_y & Nk_x k_z \\ Nk_x k_y & Lk_y^2 + M(k_x^2 + k_z^2) & Nk_x k_y \\ Nk_x k_z & Nk_y k_z & Lk_z^2 + M(k_x^2 + k_y^2) \end{pmatrix} . \quad (1.18)$$

⁴ For this reason, the definition (1.14) is often given in symmetrized form.

For $\mathbf{k} \neq 0$, the threefold degenerate valence band Γ_4 splits up into three different bands.

In the presence of spin-orbit interaction, the operator $\hat{\mathbf{p}} = (\hbar/i)\nabla$ has to be replaced by $\hat{\pi} = (\hbar/i)\nabla + \mathbf{S} \times \nabla W(\mathbf{r})/(2m_0c_0^2)$, which leads to $\mathbf{k} \cdot \boldsymbol{\pi}$ perturbation theory [21, 22]. Alternatively, the effective Hamiltonian for the Γ_8 valence band can be derived expanding the $j = \frac{3}{2}$ base functions into p orbitals by means of Clebsch-Gordan coefficients [6, 26]. There is, however, a much easier way to find the effective Hamiltonian, which is the method of invariants.

The effective-mass theory can be generalized to external fields when the potentials U and \mathbf{A} in (1.1) are slowly varying functions. We call a function f slowly varying, if

$$\frac{1}{\Omega_0} \int_{\Omega_0} d^3\mathbf{r}' u^*(\mathbf{r}+\mathbf{r}') f(\mathbf{r}+\mathbf{r}') v(\mathbf{r}+\mathbf{r}') = (u | v) f(\mathbf{r}), \quad (1.19)$$

with the scalar product $(. | .)$ defined in (1.4), is approximately fulfilled for arbitrary lattice-periodic functions u, v . In other words, the variation of f within the Wigner-Seitz cell is negligible.

To find the eigenvalues and eigenfunctions of the Hamiltonian (1.1) in the presence of external fields, we start with the ansatz

$$\varphi(\mathbf{r}) = \sum_j \varphi_j(\mathbf{r}) u_j(\mathbf{r}), \quad (1.20)$$

where φ_j are slowly-varying functions, so-called envelope functions. Application of the Hamiltonian (1.1) to the functions (1.20) yields

$$\begin{aligned} (\hat{H}\varphi)(\mathbf{r}) &= \sum_j \left[E_j + \frac{\hbar^2 \hat{k}^2}{2m_0} + \frac{\hbar}{m_0} \hat{\mathbf{k}} \cdot \frac{\hbar}{i} \nabla_u - eU(\mathbf{r}) \right] \varphi_j(\mathbf{r}) u_j(\mathbf{r}) \\ \hat{\mathbf{k}} &= \frac{1}{i} \nabla_\varphi + \frac{e}{\hbar} \mathbf{A}(\mathbf{r}), \end{aligned} \quad (1.21)$$

where the subscripts u and φ at the Nabla operator indicate derivatives of the lattice-periodic functions and the envelope functions, respectively. The approximation (1.19) allows us to establish an eigenvalue equation solely for the envelope functions:

$$\sum_{j'} \left\{ \left[E_j + \frac{\hbar^2 \hat{k}^2}{2m_0} - eU(\mathbf{r}) \right] \delta_{jj'} + \frac{\hbar}{m_0} \hat{\mathbf{k}} \cdot \mathbf{p}_{jj'} \right\} \varphi_{j'}(\mathbf{r}) = E \varphi_j(\mathbf{r}). \quad (1.22)$$

With this formulation of the problem, the rest of the derivation goes alongside the same lines as in the case without external potentials. The eigenvalues and the class-A envelope functions follow from the equation [27]

$$\begin{aligned}\sum_{m'} \hat{H}_{\nu \text{ eff } mm'} \varphi_{\nu \lambda; \nu m'}(\mathbf{r}) &= E_{\nu \lambda} \varphi_{\nu \lambda; \nu m}(\mathbf{r}) \\ \hat{H}_{\nu \text{ eff } mm'} &= \sum_{\alpha \alpha'} \hat{k}_\alpha D_{\nu mm'}^{\alpha \alpha'} \hat{k}_{\alpha'} + [E_\nu - eU(\mathbf{r})] \delta_{mm'}\end{aligned}\quad (1.23)$$

and the eigenfunctions, including the class-B components, are

$$\begin{aligned}\varphi_{\nu \lambda}(\mathbf{r}) &= \sum_m \varphi_{\nu \lambda; \nu m}(\mathbf{r}) u_{\nu m}(\mathbf{r}) + \sum_{j'}' \varphi_{\nu \lambda; j'}(\mathbf{r}) u_{j'}(\mathbf{r}) \\ \varphi_{\nu \lambda; j'}(\mathbf{r}) &= \sum_{m=1}^M \frac{\frac{\hbar}{m_0} \hat{\mathbf{k}} \cdot \mathbf{p}_{j', \nu m}}{E_\nu - E_{j'}} \varphi_{\nu \lambda; \nu m}(\mathbf{r}) ; \quad j' \in B .\end{aligned}\quad (1.24)$$

In the second equation, the differential operator $\hat{\mathbf{k}}$ has to be *applied* to the space coordinate of the class-A envelope functions.

As a quantitative measure for the variation of the envelope functions in the presence of external fields we use the characteristic lengths $\lambda_{\text{mag}} = (\hbar/|eB|)^{1/2}$ and $\lambda_{\text{el}} = \hbar^{2/3}/|2meF|^{1/3}$. They have to be compared with the lattice constant a_0 . For the heavy hole in GaAs with $m = 0.5 m_0$ and field strengths $B = 12$ T and $F = 120$ kV/cm, we obtain $\lambda_{\text{mag}} = 74$ Å and $\lambda_{\text{el}} = 18.5$ Å, which is much larger than the lattice constant $a_0 = 5.65$ Å. Thus the effective-mass approximation is applicable even for large external fields.

Roughly spoken, the effective-mass approximation is generalized to external fields by changing $\hbar \mathbf{k}$ to $\frac{\hbar}{i} \nabla + e\mathbf{A}$. In the presence of a magnetic field, the components of $\hat{\mathbf{k}}$ do not commute with each other and it holds that $[\hat{k}_\alpha, \hat{k}_{\alpha+2}] = -ieB_{\alpha+2}/\hbar$. Then the antisymmetric components of D (1.13) give rise to contributions linear in \mathbf{B} . Their physical origin is the Zeeman splitting of the underlying atomic orbitals [26]. A systematic way to include the Zeeman effect is the method of invariants, which we discuss in the rest of this subsection.

We have found that the structure of $H_{\text{eff}}(\mathbf{k})$ is largely determined by the symmetry properties of the orbitals. The method of invariants [16, 23] is a powerful tool for constructing effective Hamiltonians exclusively from the transformation properties of the wavefunctions. Here we demonstrate the method of invariants for those representations, which are identical to vector or spinor representations of $O(3)$. We start with the eigenvalue problem for the class-A components (1.15) and the structure of the eigenfunctions (1.16). Application of the space-group operation $\{\alpha, \mathbf{a}\}$ to the eigenfunctions leads to the eigenvalue problem for the equivalent Bloch vector $\alpha^{-1}\mathbf{k}$. Because the class-A coefficients transform like (1.8), the transformation law for the effective Hamiltonian is

$$H_{\text{eff}}(\alpha^{-1}\mathbf{k}) = A(\alpha) H_{\text{eff}}(\mathbf{k}) A^{-1}(\alpha) . \quad (1.25)$$

Suppose that H_{kin} is a power series in \mathbf{k} and the angular-momentum matrices \mathbf{J} (App. C.2). From the fundamental relation for the angular-momentum matrices (C.80, C.83) it follows that

$$H_{\text{kin}}[\alpha^{-1}\mathbf{k}, \det(\alpha^{-1})\alpha^{-1}\mathbf{J}] = H_{\text{kin}}(\mathbf{k}, \mathbf{J}). \quad (1.26)$$

This identity is fulfilled only for those compounds of the polar vector \mathbf{k} and the axial vector \mathbf{J} which are invariant under the operations of the point group. Up to second order in \mathbf{k} these are k^2 , $J^2 \propto 1$, $(\mathbf{J} \cdot \mathbf{k})^2$, and $J_x^2 k_x^2 + J_y^2 k_y^2 + J_z^2 k_z^2$. The first three expressions are invariant under the full orthogonal group $O(3)$, while the last expression is only invariant under the operations of O_h .

For the fourfold degenerate Γ_8 valence band, the angular-momentum matrices are the J matrices (C.73) and the kinetic Hamiltonian, up to terms second order in \mathbf{k} , takes the form [16, 21]

$$\begin{aligned} H_{v \text{ kin}}(\mathbf{k}) = -\frac{\hbar^2}{2m_0} & \left[(\gamma_1 + \frac{5}{2}\gamma_2) k^2 - 2\gamma_3 (\mathbf{J} \cdot \mathbf{k})^2 \right. \\ & \left. + 2(\gamma_3 - \gamma_2) (J_x^2 k_x^2 + J_y^2 k_y^2 + J_z^2 k_z^2) \right]. \end{aligned} \quad (1.27)$$

This expression is known as the Luttinger (or Luttinger–Kohn) Hamiltonian and the real parameters $\gamma_1, \gamma_2, \gamma_3$ are called the Luttinger parameters. They have been determined for various materials from experiments and semi-empirical or ab-initio calculations.

The explicit expression of the eigenvalues of the Γ_8 valence band in the neighborhood of the Γ point is [6, 15, 21, 26]:

$$\begin{aligned} E_h^{(\mp)}(\mathbf{k}) = -E_v + \frac{\hbar^2}{2m_0} & \left[A k^2 \mp \sqrt{B^2 k^4 + C^2 (k_y^2 k_z^2 + k_x^2 k_z^2 + k_x^2 k_y^2)} \right] \\ = -E_v^{(\pm)}(\mathbf{k}); \quad A = \gamma_1; \quad B = 2\gamma_2; \quad C^2 = 12(\gamma_3^2 - \gamma_2^2). \end{aligned} \quad (1.28)$$

The topology of the Γ_8 valence bands imposes some inequalities between the coefficients A, B, C [21].

In (1.28) the subscript “h” refers to “hole,” which can be thought of as a missing electron. A rigorous definition will be given in the next subsection. The twofold degenerate hole eigenstates with energies $E_h^{(-)}(\mathbf{k}) = E_{hh}(\mathbf{k})$ and $E_h^{(+)}(\mathbf{k}) = E_{lh}(\mathbf{k})$ are called the heavy- and light-hole band. They are often identified with $|\frac{3}{2}, \pm\frac{3}{2}\rangle$ and $|\frac{3}{2}, \pm\frac{1}{2}\rangle$, which is true only for $\mathbf{k} \perp (001)$. The function (1.28) is nonanalytic at $\mathbf{k} = 0$ and the effective masses depend on the direction of \mathbf{k} (band warping), which signifies that the symmetry is lower than $O(3)$. For $\mathbf{k} \perp (100)$ and equivalent directions, the masses of heavy and light hole are $m_{hh, lh} = m_0/(\gamma_1 \mp 2\gamma_2)$. To treat the hole dispersions as isotropic, a variety of averaged hole masses have been defined. The decomposition of the Luttinger Hamiltonian (1.27) into spherical tensors leads to spherically averaged hole masses $m_{hh, lh} = m_0/[\gamma_1(1 \mp \mu)]$ with $\mu = (6\gamma_3 + 4\gamma_2)/5\gamma_1$ [28].

The expression (1.27) also applies to the vector or spinor representations Γ_4, Γ_6 , and Γ_1 , when \mathbf{J} is replaced by \mathbf{I} (C.79), $\frac{1}{2}\boldsymbol{\sigma}$ (C.71), and 0, respectively. For the Γ_4 band, there are also three independent parameters, which can be

identified with L, M, N in (1.18). The kinetic Hamiltonian for the Γ_6 band has only one parameter, because $\sigma_\alpha \sigma_{\alpha'} + \sigma_{\alpha'} \sigma_\alpha = 2 \delta_{\alpha\alpha'}$. The same is true for the identity representation Γ_1 .

In the presence of a magnetic field, the kinetic part of the Hamiltonian has to be symmetrized in the components of $\hat{\mathbf{k}}$, i.e., products $\hat{k}_\alpha \hat{k}_{\alpha'}$ are replaced by $\{ \hat{k}_\alpha \hat{k}_{\alpha'} \} = \frac{1}{2} (\hat{k}_\alpha \hat{k}_{\alpha'} + \hat{k}_{\alpha'} \hat{k}_\alpha)$. The additional contributions, called magnetic Hamiltonian, are found by constructing invariant expressions from the axial vectors \mathbf{B} and \mathbf{J} . The result for the Γ_8 band is [16]:

$$\begin{aligned}\hat{H}_{v\text{ kin}} &= -\frac{\hbar^2}{2m_0} \left[(\gamma_1 + \frac{5}{2}\gamma_2) \hat{k}^2 - 2\gamma_2 (J_x^2 \hat{k}_x^2 + J_y^2 \hat{k}_y^2 + J_z^2 \hat{k}_z^2) \right. \\ &\quad \left. - 4\gamma_3 \left(\{J_x J_y\} \{\hat{k}_x \hat{k}_y\} + \{J_y J_z\} \{\hat{k}_y \hat{k}_z\} + \{J_z J_x\} \{\hat{k}_z \hat{k}_x\} \right) \right] \\ \hat{H}_{v\text{ mag}} &= -\frac{e\hbar}{m_0} \left[\kappa \mathbf{J} \cdot \mathbf{B} + q \sum_\alpha J_\alpha^3 B_\alpha \right].\end{aligned}\quad (1.29)$$

The magnetic contribution contains two additional parameters, κ and q . Usually, it holds that $q \ll \kappa$ and the nonlinear (in \mathbf{J}) Zeeman effect is negligible, compared to the linear Zeeman effect. The effective Hamiltonian is a Hermitian differential operator and it holds that

$$H_{\text{eff}}^T(-\nabla) = H_{\text{eff}}^*(\nabla), \quad (1.30)$$

which can also be seen from the explicit expression (1.29).

For the Γ_6 conduction band, there is only one additional parameter and the contributions to the effective Hamiltonian can be written as

$$\hat{H}_{c\text{ kin}} = \frac{1}{2m_e} \left[\frac{\hbar}{i} \nabla + e \mathbf{A}(\mathbf{r}) \right]^2; \quad \hat{H}_{c\text{ mag}} = \frac{g_e \mu_B}{\mu_0} \mathbf{B} \cdot \frac{\boldsymbol{\sigma}}{2}. \quad (1.31)$$

They have exactly the same structure as for a free electron in a magnetic field, except that the effective mass and the Landé factor are different from the values for the free electron, m_0 and 2. If the spin-orbit interaction is negligible, like in Si, it holds that $g_e \approx 2$. If spin-orbit interaction is important, g_e is very different from 2 and can even be negative, like in GaAs. In magnetic semiconductors, the effective g -factor can be huge, in the order of 100. The expression for $\hat{H}_{c\text{ kin}}$ (1.31), which results from inserting the operator $-i\nabla + e\mathbf{A}/\hbar$ in the band dispersion, is called the Peierls-Onsager Hamiltonian [29, 30]. Because $I_\alpha^3 \propto I_\alpha$, the Γ_4 band, which is build upon p orbitals, shows only a linear Zeeman effect. The Γ_1 band, which results from a spinless s orbital does not show a Zeeman effect.

Because the effective mass of the electron is much smaller than the effective mass of the hole, corrections beyond second-order perturbation theory are more important for the conduction band than for the valence bands and it might be

necessary for a quantitative description to take into account conduction-band non-parabolicity. The conduction-band dispersion up to fourth order in \mathbf{k} , neglecting the small spin splitting, can be written as [31]

$$E_c(\mathbf{k}) = E_c + \frac{\hbar^2 k^2}{2m_e} + \alpha k^4 + \beta (k_x^2 k_y^2 + k_y^2 k_z^2 + k_z^2 k_x^2).$$

In this form, the approximation is of little practical use, because $\alpha, \beta < 0$ and $E_c(\mathbf{k}) \rightarrow -\infty$ for $k \rightarrow \infty$. Rössler improved the above formula by introducing \mathbf{k} -dependent parameters $\alpha(k) = \alpha_0 + \alpha_1 k$; $\beta(k) = \beta_0 + \beta_1 k$ with $\alpha_1, \beta_1 > 0$ and also gave numerical values for GaAs [32].

The method of invariants can also be used to take into account mechanical strain [8, 23]. In the lowest order, the invariant expressions have the same form as the contributions to H_{kin} in (1.29), when the symmetrized products $\{\hat{k}_\alpha \hat{k}_{\alpha'}\}$ are replaced by components of the symmetric deformation tensor $\varepsilon_{\alpha\alpha'}$. For the Γ_8 band, this leads to three additional terms with three parameters. As the deformation has the same effect as a nonzero wavevector, the hh-lh splitting at $\mathbf{k} = 0$ is removed. For the Γ_6 conduction band, we have one additional term and the energy shift is proportional to the trace of the deformation tensor, i.e., the volume deformation.

So far we treated zincblende crystals as if they had full cubic symmetry. In the case without spin-orbit interaction, the momentum-matrix elements between the degenerate valence-band states at $\mathbf{k} = 0$ are zero, because the valence-band eigenfunctions can be chosen to be real. For spin-orbit interaction, additional linear contributions appear in the effective Hamiltonian and the twofold degeneracy is split for general directions. The effects are rather small [20].

1.1.3 Low-Dimensional Structures

Semiconductor heterostructures have been known for about thirty years [33]. The modulation of the band edges leads to quantum confinement of carriers [34]. Important parameters for the design of heterostructures are the band alignments and the lattice constant. The band alignment can be nested (type I), staggered (type II) or misaligned (type III). In the case of equal lattice constants, the growth is pseudomorphic with no built-in strain. An important example is the material combination GaAs/(Ga,Al)As. For small lattice mismatch, the growth can be free of dislocations, but the layers are strained. An introduction is given in the textbooks [6, 9–11, 26] and in a book chapter by Sham [35].

A rigorous justification of the effective-mass approximation in semiconductor heterostructures is very difficult and can be given only under limiting assumptions. On the other hand, the results from effective-mass theory are often found in very good quantitative agreement with experiment. If the effective-mass approximation is justified, there is basically only one possibility for the structure of the effective Hamiltonian.

Heterostructures may consist of semiconductors and semiconductor alloys, which are not crystals by a rigorous definition. In the virtual-crystal approximation (VCA), an alloy is treated as an ideal semiconductor by averaging the atomic-core potential over all unit cells. Then the band edges and

effective-mass parameters of a ternary alloy $A_{1-x}B_xC$ can be interpolated between the parameters of the pure semiconductors AB and AC.

Let us assume that a heterostructure is composed of two materials a and b (pure semiconductors or alloys). The valence and conduction bands of both materials shall be of the same type, according to the classification in Tab. 1.1 or 1.2, with effective Hamiltonians $\hat{H}_{\nu \text{eff}}^{(a)}$ and $\hat{H}_{\nu \text{eff}}^{(b)}$. An important example is the system GaAs/Ga_{1-x}Al_xAs for about $x \leq 0.4$. We describe the changes of the material by interpreting the effective Hamiltonian and the band edge as functions of the coordinate: $\hat{H}_{\nu \text{eff}}(\mathbf{r}) = \hat{H}_{\nu \text{eff}}^{(a)}$ for material a and $\hat{H}_{\nu \text{eff}}(\mathbf{r}) = \hat{H}_{\nu \text{eff}}^{(b)}$ for material b. Then the effective Hamiltonian for the heterostructure takes the form

$$\hat{H}_{\nu \text{eff}} = \hat{H}_{\nu \text{kin}}(\mathbf{r}) + E_{\nu}(\mathbf{r}) - eU(\mathbf{r}) + \hat{H}_{\nu \text{mag}}(\mathbf{r}) . \quad (1.32)$$

In the kinetic part, defined in (1.29), the Luttinger parameters, which in general depend on the space coordinate, have to be placed between the components of $\hat{\mathbf{k}}$. Expression (1.32) is derived in [17] and it is shown that the class-A components of the envelope functions fulfill continuity of the density and current density at the interface. Since the boundary conditions should be fulfilled for the exact eigenfunctions, the zone-center Bloch functions should be approximately equal in each layer.

In the effective-mass equation (1.32), the effect of the geometric structure is captured in additional “potentials” $E_{\nu}(\mathbf{r})$ and it is often irrelevant whether quantum confinement is the result of the geometry, external fields, or both. Therefore, we will generally speak of low-dimensional semiconductors, which includes quantum confinement due to the geometric structure or external fields. A detailed classification will be given in Sect. 1.2 and in Chap. 3.

The eigenfunctions $\varphi_{\nu \lambda}$ of $\hat{H}_{\nu \text{eff}}$ (1.32) are orthonormal and complete:

$$\begin{aligned} \sum_m \int d^3\mathbf{r} \varphi_{\nu \lambda; \nu m}^*(\mathbf{r}) \varphi_{\nu \lambda'; \nu m}(\mathbf{r}) &= \delta_{\lambda \lambda'} \\ \sum_{\lambda} \varphi_{\nu \lambda; \nu m}(\mathbf{r}_1) \varphi_{\nu \lambda'; \nu m'}^*(\mathbf{r}_2) &= \delta_{mm'} \delta(\mathbf{r}_1 - \mathbf{r}_2) . \end{aligned} \quad (1.33)$$

Here, the quantum number λ denotes both discrete and continuum states (App. C.1). The function $\delta(\mathbf{r}_1 - \mathbf{r}_2)$ is not slowly varying, and is merely a symbolic notation for the completeness of the eigenfunctions.

The transition of valence electrons to the conduction band can be interpreted as the creation of electron–hole pairs and it is convenient to introduce effective Hamiltonians for electron and hole. For the conduction electron, the effective Hamiltonian (1.32) remains unchanged, except that we change the index “c” to “e” (for electron) and interpret the modulation of the conduction band edge as electron confinement potential $W_e(\mathbf{r}) = E_c(\mathbf{r})$. Then the electron eigenvalues and eigenfunctions $E_{e\lambda}$ and $\varphi_{e\lambda}$ are the same as for the

conduction band, namely, $E_{c\lambda}$ and $\varphi_{c\lambda}$. For the hole, denoted by the index “h,” we have the following correspondence [36]:

$$\hat{H}_{h\text{ eff}} = -\hat{K} \hat{H}_{v\text{ eff}} \hat{K}^{-1}; \quad \varphi_{h\lambda} = \hat{K} \varphi_{v\lambda}; \quad E_{h\lambda} = -E_{v\lambda}, \quad (1.34)$$

where \hat{K} is the time-reversal operator (App. C.2). The explicit expression

$$\begin{aligned} \hat{H}_{h\text{ eff}}(\mathbf{k}) &= -\hat{H}_{v\text{ kin}}(\hat{\mathbf{k}}_h) + W_h(\mathbf{r}) + eU(\mathbf{r}) + \hat{H}_{h\text{ mag}} \\ (1.35) \end{aligned}$$

$$\hat{\mathbf{k}}_h = \frac{1}{i} \nabla - \frac{e}{\hbar} \mathbf{A}(\mathbf{r}); \quad W_h(\mathbf{r}) = -E_v(\mathbf{r}); \quad \hat{H}_{h\text{ mag}} = \hat{H}_{v\text{ mag}}$$

follows from (1.29) and the transformation of the angular-momentum matrices under time reversal (App. C.2). Outwardly, the magnetic Hamiltonian of the hole is the same as for the valence electron, but it has to be noted that the angular momenta of valence electron and hole have opposite directions. The same holds true for the momentum: a momentum $\hbar \mathbf{k}$ of the valence electron corresponds to a momentum $-\hbar \mathbf{k}$ of the hole.

We shall now illustrate the mechanism of quantum confinement for the hole states in a quantum well (QW). We consider a GaAs/Ga_{1-x}Al_xAs quantum well with no external fields, with the [001] direction (or equivalent directions) being the growth direction. The Luttinger parameters are assumed to be the same for the active layer and for the barriers. Furthermore, the valence band edge of GaAs is used as the zero of the energy scale. The hole confinement potential,

$$W_h(z) = \begin{cases} 0 & \text{for } z \leq \frac{d}{2} \\ -\Delta E_v & \text{elsewhere,} \end{cases} \quad (1.36)$$

is determined by the valence-band offset $\Delta E_v < 0$.

Due to the translational symmetry in the xy plane, the in-plane parts of the eigenfunction are of the form $A^{-1/2} \exp(i\mathbf{k}_\parallel \cdot \mathbf{r}_\parallel)$ with the normalization area A and the in-plane vectors $\mathbf{r}_\parallel = (x, y)^T$ and $\mathbf{k}_\parallel = (k_x, k_y)^T$. The eigenfunctions in z direction parametrically depend on the in-plane wavevector \mathbf{k}_\parallel . For $\mathbf{k}_\parallel = 0$, m_j is a good quantum number and the components of the eigenfunction obey

$$\begin{aligned} \left[-\frac{\hbar^2}{2m_0} (\gamma_1 - 2\gamma_2) \frac{d^2}{dz^2} + W_h(z) \right] \varphi_{\pm \frac{3}{2} n}(z) &= E_{\pm \frac{3}{2} n} \varphi_{\pm \frac{3}{2} n}(z) \\ \left[-\frac{\hbar^2}{2m_0} (\gamma_1 + 2\gamma_2) \frac{d^2}{dz^2} + W_h(z) \right] \varphi_{\pm \frac{1}{2} n}(z) &= E_{\pm \frac{1}{2} n} \varphi_{\pm \frac{1}{2} n}(z). \end{aligned} \quad (1.37)$$

The resulting eigenvalues are twofold degenerate, and the effective masses for $m_j = \pm \frac{3}{2}$ and $m_j = \pm \frac{1}{2}$ are identical with the heavy- and light-hole masses in the [001] direction. The eigenvalue problem (1.37) is the same as

for a particle in a square well. The number of below-barrier bound states is finite and depends on the parameters of the confinement, with a minimum of one confined state for each hole species. For energies above $-\Delta E_v > 0$, the spectrum becomes continuous. For general \mathbf{k}_{\parallel} , the confined states give rise to twofold degenerate subbands $E_{\pm\frac{3}{2}n}(\mathbf{k}_{\parallel})$ and $E_{\pm\frac{1}{2}n}(\mathbf{k}_{\parallel})$ which, in general are not pure $m_j = \pm\frac{3}{2}$ or $m_j = \pm\frac{1}{2}$ eigenstates (valence-band mixing). As a consequence of symmetry, the in-plane dispersion is isotropic in the limit $k_{\parallel} \rightarrow 0$.

For the numerical calculation we assume a well thickness $d = 5$ nm and an Al mole fraction $x = 0.3$. The band offset and the Luttinger parameters are found in App. B.1. The results are shown in Fig. 1.2. The left graph shows the confinement potential (*thick solid line*), the confinement energies E_{m_jn} (*horizontal lines*), and the probability densities $|\varphi_{m_jn}|^2$ (*gray areas*) for $k_{\parallel} = 0$. There are two confined states for the heavy hole and one for the light hole, each of them being twofold degenerate. The leakage of the eigenfunctions through the barriers is larger for the light hole than for the heavy hole and increases with increasing quantum number for each hole species. The right graph of Fig. 1.2 shows the dispersions of the first three subbands, $E_{m_jn}(\mathbf{k}_{\parallel})$ for $\mathbf{k}_{\parallel} \perp (100)$ (*solid line*) and $\mathbf{k}_{\parallel} \perp (110)$ (*dashed line*). For small k_{\parallel} , the dispersions are isotropic, but become anisotropic and nonparabolic for larger k_{\parallel} . An anticrossing between first heavy- and light-hole subband is observed at $k_{\parallel} \approx 0.3$ nm $^{-1}$.

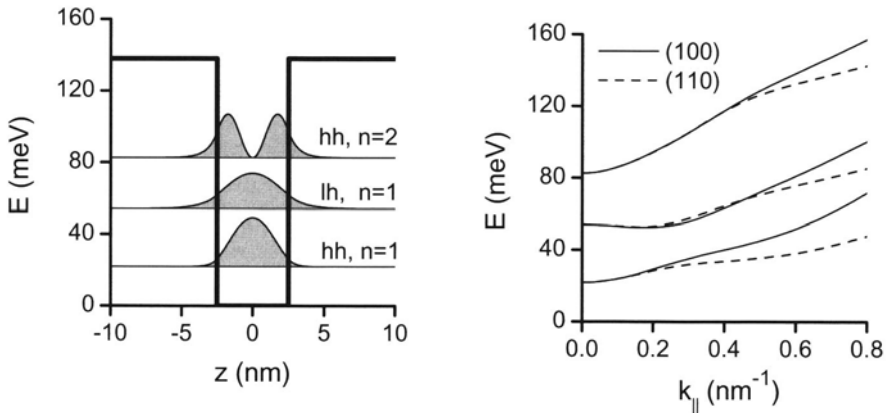


Fig. 1.2. Hole eigenstates in a GaAs/Ga_{1-x}Al_xAs quantum well for $x = 0.3$ and $d = 5$ nm. Left: Hole confinement potential, eigenstates and probability densities for $k_{\parallel} = 0$. Right: Subbands for $\mathbf{k}_{\parallel} \perp (100)$ (*solid line*) and $\mathbf{k}_{\parallel} \perp (110)$ (*dashed line*)

In optical spectra, the valence-band degeneracy leads to two series of transitions, but, as heavy and light hole are not independent particles, it is some-

times impossible to address an optical transition solely to one hole species. It is often desirable to neglect valence-band mixing and assume parabolic in-plane dispersions. First-order perturbation theory in the parameter \mathbf{k}_{\parallel} yields isotropic in-plane masses $m_0/(\gamma_1 \pm \gamma_2)$ for heavy and light hole, which is known in the literature as mass reversal [6, 11]. This approximation is unrealistic, even for narrow wells, as can be seen in the right part of Fig. 1.2: the in-plane masses for the first and second heavy-hole band are different, although they should be equal, and the in-plane mass of the light-hole band is negative, although it should be positive. Furthermore, the optical properties are determined also by larger in-plane wavevectors, where the hole dispersions are neither parabolic nor isotropic and the curvature is very different from the curvature near $\mathbf{k}_{\parallel} = 0$. Fortunately, the light-hole transitions are often negligible. In this case, reasonable agreement with the experiment is achieved in the two-band model with an in-plane heavy-hole mass given by the cyclotron mass (B.2). If the light hole is important, there is no way around the Luttinger Hamiltonian. Working with two independent hole species will only lead to spurious results.

For the electron, in the approximation (1.31), the subbands are parabolic with an effective mass m_e . However, especially for excited states ($n > 1$), nonparabolicity becomes important. Then the subband edges have lower energies than in the parabolic approximation. The subband dispersions near $k_{\parallel} = 0$ are still parabolic, but the in-plane mass $m_{e\ell} > m_e$ depends on the subband index n , which is known as the energy-dependent mass [37, 38].

1.2 Electron–Light Interaction

If the Coulomb interaction between the crystal electrons is neglected, the optical absorption is determined by the one-particle eigenstates. For bulk semiconductors, the transition matrix element is proportional to the momentum matrix element between the Bloch states. In the general case of a low-dimensional semiconductor, the transition matrix element is determined by the momentum matrix element of the zone-center Bloch functions and the overlap integral of conduction- and valence-band envelope functions. The optical transition of an electron from the valence to the conduction band can be interpreted as the creation of an electron–hole pair by annihilation of a photon.

The optical transitions in semiconductors are characterized by the optical (combined, joint) density of states. The functional form of the density of states at the absorption edge determines the dimensionality of the semiconductor, which can be different from the geometric dimension.

A review on band structure and optical transitions in semiconductors is given in an article by Bassani [39] and in the book by Bassani and Pastori Parravicini [5]. Also, in the book by Chuang [8] one chapter is devoted to optical transitions in semiconductors. Single-particle eigenstates and densities

of states for many low-dimensional semiconductors are found in the book by Davies [11].

In this section, we specify the operator of the electron–light interaction and the momentum matrix elements for the interband transitions in zincblende semiconductors. We derive the optical absorption for non-interacting electrons by means of Fermi’s golden rule and define the optical density of states. The result is reformulated in the electron–hole picture. Finally, we give analytic results for the optical density of states for a number of three-, two-, and one-dimensional semiconductors in the two-band model with perfect confinement.

1.2.1 Transition Matrix Elements

If propagation effects are neglected, the electromagnetic field inside the crystal is a plane wave, characterized by potentials

$$\begin{aligned} U(\mathbf{r}, t) &= 0 ; \quad \mathbf{A}(\mathbf{r}, t) = \underline{\mathbf{A}}(\mathbf{r}, t) + \text{c.c.} \\ \underline{\mathbf{A}}(\mathbf{r}, t) &= \underline{\mathbf{A}}_0 e^{+i\mathbf{q}\cdot\mathbf{r}-i\omega t} ; \quad \underline{\mathbf{A}}_0 = \underline{\mathbf{A}}_0 \boldsymbol{\xi} ; \quad |\boldsymbol{\xi}| = 1 . \end{aligned} \tag{1.38}$$

This vector-potential gauge is equivalent to the Coulomb gauge in the absence of sources. To describe optical pulses, we will allow the amplitude $\underline{\mathbf{A}}$ to be slowly varying with time. Because of $\nabla \cdot \mathbf{A} = 0$, the polarization vector $\boldsymbol{\xi}$ must be perpendicular to \mathbf{q} . Without loss of generality, we assume propagation in z direction, i.e., $\mathbf{q} = q \mathbf{e}_z$. Then, linear polarization is characterized by $\boldsymbol{\xi} = \mathbf{e}_x, \mathbf{e}_y$, while right- or left-circular polarization corresponds to polarization vectors $\boldsymbol{\xi} = \mathbf{e}_\pm = (\mathbf{e}_x \pm i\mathbf{e}_y)/\sqrt{2}$. The propagation vector \mathbf{q} is related to the frequency ω by $|\mathbf{q}| = \omega/c$, where $c = c_0/\sqrt{\epsilon_s}$ is the speed of light in the medium and ϵ_s is the static dielectric constant. In the optical limit, the photon wavenumber $q = |\mathbf{q}|$ is much smaller than the extension of the Brillouin zone, or, equivalently, the wavelength $\lambda = 2\pi/q$ is much larger than the size of the Wigner–Seitz cell. For example, if GaAs is excited near the absorption edge, $E_g = 1.519$ eV, the wavelength in the medium is $\lambda = 2\pi\hbar c_0/\sqrt{\epsilon_s} E_g = 225$ nm, which is much larger than the lattice constant $a_0 = 0.565$ nm.

The interaction of the crystal electrons with the classical light is described by inserting the time-dependent vector potential (1.38) into the Hamiltonian (1.1). In the optical limit, the spatial variation of \mathbf{A} can be neglected so that \mathbf{A} and $\hat{\mathbf{p}}$ commute. Furthermore, the term proportional to $A^2(t)$ is a scalar and can be removed by a unitary transform of the operators and wavefunctions [40]. The interaction operator then takes the form:⁵

$$\hat{H}^{(i)}(t) = \hat{H}^{(i)}(t) + \hat{H}^{(i)\dagger}(t) ; \quad \hat{H}^{(i)}(t) = \frac{e}{m_0} \underline{\mathbf{A}}(t) \cdot \hat{\mathbf{p}} . \tag{1.39}$$

⁵ Strictly, for spin–orbit interaction, $\hat{\mathbf{p}}$ has to be replaced by $\hat{\boldsymbol{\pi}}$ (p. 9) [36]. This does not change the results qualitatively, because all transition matrix elements depend on a single parameter, which can be determined from experiment.

In the rotating-wave approximation (RWA) (App. C.3), we replace the interband matrix elements of $\hat{H}^{(i)}$ by the matrix elements of the non-Hermitian operator $\underline{\hat{H}}^{(i)}$ so that $\langle c | \hat{H}^{(i)} | v \rangle \approx \langle c | \underline{\hat{H}}^{(i)} | v \rangle$ and $\langle v | \hat{H}^{(i)} | c \rangle \approx \langle v | \underline{\hat{H}}^{(i)\dagger} | c \rangle$.

We shall now specify the interband momentum matrix elements between valence- and conduction-band eigenfunctions of zincblende semiconductors at the Γ point. Without spin–orbit interaction, the conduction band is represented by an s orbital and the degenerate valence band is made up of p orbitals (Table 1.1). The only nonzero matrix elements are

$$P = \langle s | \hat{p}_x | X \rangle = \langle s | \hat{p}_y | Y \rangle = \langle s | \hat{p}_z | Z \rangle. \quad (1.40)$$

Table 1.3 shows the momentum matrix elements for the valence-to-conduction-band transitions for zincblende semiconductors without spin orbit interaction. Cartesian p orbitals correspond to linear polarization, while spherical harmonics correspond to circular polarization. For example, the transition $|X\rangle \rightarrow |s\rangle$ is excited by a polarization $\xi = e_x$ and the transition $|1, -1\rangle \rightarrow |s\rangle$ is excited by $\xi = e_+$ (the reciprocal vector of e_-).

Table 1.3. Momentum matrix elements for the $\Gamma_{4v} \rightarrow \Gamma_{1c}$ transition in zincblende semiconductors without spin–orbit interaction

\hat{p}/P	$ X\rangle$	$ Y\rangle$	$ Z\rangle$	$ 1, +1\rangle$	$ 1, \pm 0\rangle$	$ 1, -1\rangle$
$\langle s $	e_x	e_y	e_z	$-e_+$	e_z	$+e_-$

For spin–orbit interaction, the base functions of the valence and split-off band are related to the spherical harmonics $|1, m\rangle$ by the Clebsch–Gordan coefficients (Table C.1) and all momentum matrix elements can be again expressed in terms of P . The momentum matrix elements for the valence-to-conduction-band transition for zincblende semiconductors with spin–orbit interaction are summarized in Table 1.4.

Table 1.4. Momentum matrix elements in units of P for the $\Gamma_{8v} \rightarrow \Gamma_{6c}$ transition in zincblende semiconductors with spin–orbit interaction

\hat{p}/P	$ \frac{3}{2}, +\frac{3}{2}\rangle$	$ \frac{3}{2}, +\frac{1}{2}\rangle$	$ \frac{3}{2}, -\frac{1}{2}\rangle$	$ \frac{3}{2}, -\frac{3}{2}\rangle$
$\langle \uparrow $	$-e_+$	$\sqrt{\frac{2}{3}} e_z$	$+\sqrt{\frac{1}{3}} e_-$	0
$\langle \downarrow $	0	$-\sqrt{\frac{1}{3}} e_+$	$\sqrt{\frac{2}{3}} e_z$	$+e_-$

In atomic systems, the electron–light interaction is often written in terms of a dipole operator. The momentum and dipole matrix element between

initial (a) and final (b) state are defined as:

$$\begin{aligned}\langle b | \hat{\mathbf{p}} | a \rangle &= \int d^3r \varphi_b^*(\mathbf{r}) \frac{\hbar}{i} \nabla \varphi_a(\mathbf{r}) \\ \langle b | \hat{\boldsymbol{\mu}} | a \rangle &= \int d^3r \varphi_b^*(\mathbf{r}) (-e \mathbf{r}) \varphi_a(\mathbf{r}) .\end{aligned}\quad (1.41)$$

Suppose the Hamiltonian is of the form $\hat{H} = \hat{p}^2/2m_0 + W(\mathbf{r})$, and $|b\rangle$ and $|a\rangle$ are bound states with $\hat{H}|b\rangle = E_b|b\rangle$ and $\hat{H}|a\rangle = E_a|a\rangle$. Then the momentum operator can be expressed as $\hat{\mathbf{p}} = (im_0/\hbar)[\hat{H}, \mathbf{r}]$ and the relation between momentum and dipole matrix element is given by

$$\langle b | \hat{\mathbf{p}} | a \rangle = -\frac{im_0}{e\hbar} (E_b - E_a) \langle b | \hat{\boldsymbol{\mu}} | a \rangle . \quad (1.42)$$

For resonant excitation, $\hbar\omega \approx E_b - E_a$, the matrix element of the interaction operator (1.39) is

$$\frac{e}{m_0} \underline{\mathbf{A}} \cdot \langle b | \hat{\mathbf{p}} | a \rangle = -\underline{\mathbf{E}} \cdot \langle b | \hat{\boldsymbol{\mu}} | a \rangle . \quad (1.43)$$

In crystals, a linear potential $e \underline{\mathbf{E}} \cdot \mathbf{r}$ is not compatible with the cyclic boundary conditions and the relation between dipole and vector-potential coupling is more difficult (see also Chap. 4). As the optical excitation is nearly resonant, $\hbar\omega \approx E_g$, we formally replace the interaction operator (1.39) by

$$\hat{H}^{(i)}(t) = -\hat{\boldsymbol{\mu}} \cdot \underline{\mathbf{E}}(t) , \quad (1.44)$$

where the dipole matrix element

$$\langle c | \hat{\boldsymbol{\mu}} | v \rangle = \frac{-e\hbar}{im_0 E_g} \langle c | \hat{\mathbf{p}} | v \rangle \quad (1.45)$$

is merely a transcription of the momentum matrix element and has the symmetry of the momentum matrix element.

1.2.2 The Optical Density of States

The density of states is an important quantity in statistical physics. For a q -dimensional gas of free electrons, it holds that $\rho(E) \propto \Theta(E) E^{(q-2)/2}$. In time-dependent perturbation theory (App. C.3), the concept is generalized to the joint density of states, which involves initial states, final states, and the transition matrix element. We shall call a semiconductor q -dimensional if the optical density of states near the absorption edge behaves like the density of states for a q -dimensional electron gas. If the confinement is purely geometric, the density-of-states dimension q is equal to the geometric dimension d of the

low-dimensional structure. In case that the quantization is due to external fields, q can be smaller than d .

The optical absorption of non-interacting crystal electrons follows from Fermi's golden rule. We assume excitation near the fundamental gap, i.e., $|\hbar\omega - E_g| \ll E_g$, which is a precondition for the effective-mass approximation, the rotating-wave approximation, and the equivalence of vector-potential and dipole coupling. The matrix element of the interaction operator (1.39) between Bloch states $|\text{c}, l, \mathbf{k}\rangle$ and $|\text{v}, l', \mathbf{k}'\rangle$ is nonzero only for equal Bloch vectors $\mathbf{k} = \mathbf{k}'$, which is a consequence of neglecting the finite photon wavevector (“vertical transitions”).

We assume that the semiconductor is in its ground state, i.e., that the valence band is occupied and the conduction band is empty. The amount of energy absorbed per unit time is the sum of the transition rates for all processes $E_{\text{vl}'}(\mathbf{k}) \rightarrow E_{\text{cl}}(\mathbf{k})$, multiplied by the energy difference $E_{\text{cl}}(\mathbf{k}) - E_{\text{vl}'}(\mathbf{k})$. From Fermi's golden rule (App. C.3) it follows that

$$\begin{aligned} \frac{dE}{dt} &= \frac{2\pi}{\hbar} \sum_{\mathbf{k}} \sum_{ll'} |\langle \text{c}, l, \mathbf{k} | \frac{e}{m_0} \mathbf{A}_0 \cdot \hat{\mathbf{p}} | \text{v}, l', \mathbf{k} \rangle|^2 \\ &\quad \times \delta [E_{\text{cl}}(\mathbf{k}) - E_{\text{vl}'}(\mathbf{k}) - \hbar\omega] \hbar\omega . \end{aligned} \quad (1.46)$$

The intensity of the incident light (1.38) is the time average of the absolute magnitude of the Poynting vector, and is equal to

$$S = \lim_{T \rightarrow \infty} \frac{1}{T} \int_{-T/2}^{+T/2} dt |\mathbf{E}(t) \times \mathbf{H}(t)| = \frac{2 |A_0|^2 \omega^2}{\mu_0 c} = \frac{2 |E_0|^2}{\mu_0 c} . \quad (1.47)$$

The absorption coefficient is the total absorbed power (1.46), divided by the normalization volume Ω and the intensity S (1.47). The result is [5, 36, 39]

$$\alpha(\omega) = \frac{\omega}{c_0 n} D(\omega) \quad (1.48)$$

$$D(\omega) = \frac{1}{\Omega} \frac{1}{\varepsilon_0} \sum_{\mathbf{k}} \sum_{ll'} |\langle \text{c}, l, \mathbf{k} | \hat{\mathbf{p}} \cdot \boldsymbol{\xi} | \text{v}, l', \mathbf{k} \rangle|^2 \pi \delta [E_{\text{cl}}(\mathbf{k}) - E_{\text{vl}'}(\mathbf{k}) - \hbar\omega] .$$

The absorption coefficient for interaction-free electrons is proportional to the optical density of states $D(\omega)$. The delta function stands for energy conservation: the energy of the photon is equal to the difference between conduction- and valence-band energies. In cubic semiconductors without external fields, $D(\omega)$ as a quadratic form in $\boldsymbol{\xi}$ is independent of the direction and polarization of the incident light.

Having derived the absorption coefficient for interaction-free electrons in bulk semiconductors, we now generalize the definition of the optical density of states for low-dimensional semiconductors. In analogy to (1.48), we define

$$D(\omega) = \frac{1}{\Omega^{(d)}} \frac{1}{\varepsilon_0} \sum_{\lambda\lambda'} |\langle c, \lambda | \hat{\mu} \cdot \boldsymbol{\xi} | v, \lambda' \rangle|^2 \pi \delta(E_{c\lambda} - E_{v\lambda'} - \hbar\omega). \quad (1.49)$$

For the calculation of the dipole matrix elements we approximate the eigenfunctions by their class-A components. Due to the separation of slowly and rapidly varying parts, the momentum operator acts only on the lattice-periodic functions. Then the dipole matrix elements

$$\mu_{c\lambda,v\lambda'} = \langle c, \lambda | \hat{\mu} | v, \lambda' \rangle = \sum_{mm'} \mu_{cm,vm'} \int d^3r \varphi_{c\lambda;cm}^*(\mathbf{r}) \varphi_{v\lambda';vm'}(\mathbf{r}) \quad (1.50)$$

consist of the product of the dipole matrix elements of the zone-center Bloch functions and the overlap integrals of the conduction and valence-band envelope functions, which are the eigenfunctions of the effective Hamiltonian (1.32).

The normalization “volume” depends on the geometric dimension of the semiconductor: $\Omega^{(3)} = \Omega$ for bulk semiconductors or superlattices, $\Omega^{(2)} = A$ (normalization area) for quantum wells, $\Omega^{(1)} = L$ (normalization length) for quantum wires, and $\Omega^{(0)} = 1$ for quantum dots. For $d < 3$, there is no meaningful definition of an absorption coefficient. Nevertheless, the optical density of states is proportional to measured absorption or photoluminescence excitation (PLE) spectra. Sometimes, periodic arrays of low-dimensional semiconductors are treated as effective three-dimensional materials. Optical response functions can also be defined for single low-dimensional objects, which is useful for the description of near-field optical experiments.

In the electron–hole picture introduced in the last section, optical excitation of electrons from the valence into the conduction band can be interpreted as the creation of electron–hole pairs by annihilation of photons. Using the correspondence (1.34), the optical density of states can be written as

$$D(\omega) = \frac{1}{\varepsilon_0} \sum_{\lambda\lambda'} |F_{\lambda\lambda'}|^2 \pi \delta(E_{e\lambda} + E_{h\lambda'} - \hbar\omega); \quad F_{\lambda\lambda'} = \frac{\langle \boldsymbol{\xi} \cdot \mathbf{M} | \lambda\lambda' \rangle}{\sqrt{\Omega^{(d)}}}$$

$$\langle \boldsymbol{\xi} \cdot \mathbf{M} | \lambda\lambda' \rangle = \sum_{mm'} \boldsymbol{\xi} \cdot \mathbf{M}_{mm'}^* \int d^3r \varphi_{e\lambda;m}(\mathbf{r}) \varphi_{h\lambda';m'}(\mathbf{r}) \quad (1.51)$$

$$\mathbf{M}_{mm'} = \sum_{m''} T_{m'm''} \mu_{cm,vm''}.$$

Here, the transition energy is equal to the sum of the electron and hole energies. The oscillator strength $|F_{\lambda\lambda'}|^2$ follows from the electron–hole pair eigenfunction, which, in the approximation of interaction-free particles, is equal to the product of electron and hole eigenfunctions. The sum in (1.51) runs over all electron and hole eigenstates λ and λ' . Therefore, we may depart from the prescription (1.34), which gives a one-to-one correspondence between valence electron and hole quantum number. For example, for a hole

with eigenfunction $\propto \exp(+i\mathbf{k}\cdot\mathbf{r})$ one would rather use the quantum number $+k$ instead of the wavevector of the valence electron $-k$.

1.2.3 Examples

In the last section we have seen that the eigenvalue problem of the hole is fairly complicated and analytical solutions can be found only in special cases. On the other hand, the principal effects of quantum confinement can be understood on the basis of a two-band model. Even quantitative agreement is found for three- and two-dimensional structures.

In the two-band model, conduction and valence band are nondegenerate with isotropic and parabolic dispersions

$$E_c(\mathbf{k}) = E_c + \frac{\hbar^2 k^2}{2m_e} ; \quad E_v(\mathbf{k}) = E_v - \frac{\hbar^2 k^2}{2m_h} ; \quad m_e, m_h > 0 \quad (1.52)$$

and the scalar electron–light interaction is given by

$$\hat{H}^{(i)} = -\hat{\mu} \underline{E}(t) ; \quad \langle c, \mathbf{k} | \hat{\mu} | v, \mathbf{k}' \rangle = \mu \delta_{\mathbf{k}\mathbf{k}'} . \quad (1.53)$$

This model approximately describes the optical transition $\Gamma_{4v} \rightarrow \Gamma_{1c}$ or one of the transitions $\Gamma_{8v} \rightarrow \Gamma_{6c}$ (heavy hole or light hole) in the spherical approximation. For general low-dimensional semiconductors, the effective Hamiltonians for electron and hole in the two-band model are

$$\hat{H}_{e,h,\text{eff}} = \frac{1}{2m_{e,h}} \left[\frac{\hbar}{i} \nabla \pm e \mathbf{A}(\mathbf{r}) \right]^2 \mp eU(\mathbf{r}) + W_{e,h}(\mathbf{r}) \quad (1.54)$$

and the pair creation amplitude is equal to

$$\langle M | \lambda, \lambda' \rangle = \mu^* \int d^3 r \varphi_{e\lambda}(\mathbf{r}) \varphi_{h\lambda'}(\mathbf{r}) . \quad (1.55)$$

First, we consider the bulk semiconductor. In the two-band model, the calculation of the optical density of states of a bulk semiconductor (1.48) is straightforward and yields:

$$\begin{aligned} D(\omega) &= \frac{|\mu|^2}{\varepsilon_0} \frac{1}{\Omega} \sum_{\mathbf{k}} \pi \delta \left(E_g + \frac{\hbar^2 k^2}{2m} - \hbar\omega \right) \\ &= \frac{|\mu|^2}{\varepsilon_0} \frac{1}{(2\pi)^3} \int_0^\infty dk 4\pi k^2 \pi \delta \left(E_g + \frac{\hbar^2 k^2}{2m} - \hbar\omega \right) \\ &= \frac{|\mu|^2 m^{3/2}}{\sqrt{2} \varepsilon_0 \pi \hbar^3} \sqrt{\hbar\omega - E_g} \Theta(\hbar\omega - E_g) . \end{aligned} \quad (1.56)$$

The transition rate is zero for photon energies $\hbar\omega$ below the band gap E_g and has the same form as the density of states of a three-dimensional electron gas. As a consequence of the spatial homogeneity, $D(\omega)$ depends only on the reduced mass $m = m_e m_h / (m_e + m_h)$. As the electron mass is much smaller than the hole mass (GaAs: $m_e \approx \frac{1}{7} m_h$), the details of the hole dispersion are less important. Therefore, the two-band model gives also reasonable quantitative agreement with the experiment.

Now we turn to geometrically low-dimensional semiconductors. For simplicity, we assume perfect confinement, i.e., infinite barriers, which corresponds to the quantum-mechanical problem of a “particle in a box.” It is convenient to define the electron and hole energies relatively to the band edges of the active layer. Then, in the final expression for the optical density of states, the gap of the active layer, E_g , is subtracted from the photon energy $\hbar\omega$.

For a quantum well with active layer $0 \leq z \leq d$, the eigenfunctions and eigenvalues for electron and hole are

$$\begin{aligned}\varphi_{e,h\,n\,\mathbf{k}_\parallel}(\mathbf{r}) &= \frac{1}{\sqrt{A}} e^{i\mathbf{k}_\parallel \cdot \mathbf{r}_\parallel} \sqrt{\frac{2}{d}} \sin\left(\frac{n\pi z}{d}\right) \\ E_{e,h\,n}(\mathbf{k}_\parallel) &= \frac{\hbar^2 k_\parallel^2}{2m_{e,h}} + \frac{\hbar^2 \pi^2 n^2}{2m_{e,h} d^2}; \quad n \in \mathbb{N}\end{aligned}\tag{1.57}$$

and the pair creation amplitude is equal to

$$\langle M | n, \mathbf{k}_\parallel; n, \mathbf{k}'_\parallel \rangle = \mu^* \delta_{nn'} \delta_{\mathbf{k}_\parallel, -\mathbf{k}'_\parallel}. \tag{1.58}$$

The two-dimensional optical density of states

$$D(\omega) = \frac{|\mu|^2 m}{2 \varepsilon_0 \hbar^2} \sum_{n=1}^{\infty} \Theta\left(\hbar\omega - E_g - \frac{\hbar^2 \pi^2 n^2}{2md^2}\right) \tag{1.59}$$

is a series of step functions, as characteristic for a two-dimensional semiconductor. In realistic structures, electron–hole symmetry for the wavefunction is not fulfilled and so-called weakly allowed transitions with $n \neq n'$ and $n - n' \bmod 2 = 0$ contribute to the optical density of states (see also the discussion in Sect. 3.3). In the limit $d \rightarrow \infty$, the two-dimensional optical density of states (1.59), divided by the sample thickness d , goes over into the three-dimensional optical density of states (1.56).

For strong confinement, i.e., infinite barriers and $d \rightarrow 0$, the energetic distance of the subbands increases and the optical density of states near the e1–h1 transition goes over into

$$D(\omega) = \frac{|\mu|^2 m}{2 \varepsilon_0 \hbar^2} \Theta\left(\hbar\omega - E_g^{(2)}\right); \quad E_g^{(2)} = E_g + \frac{\hbar^2 \pi^2}{2md^2}, \tag{1.60}$$

which is the optical density of states for an ideal two-dimensional semiconductor with band gap $E_g^{(2)}$. The two-dimensional semiconductor is defined in complete analogy to the three-dimensional semiconductor (1.52–1.55), except that one coordinate (here: z) is absent.

An application for the two-dimensional model semiconductor is the quantum-well wire in the case that the well thickness d is much smaller than the wire width b . Here, electron and hole are confined in the interval $0 \leq y \leq b$, but can freely move in the x direction. The calculation, which is as easy as for the quantum well, yields the optical density of states

$$D(\omega) = \frac{|\mu|^2 m^{1/2}}{\sqrt{2} \varepsilon_0 \hbar} \sum_{n=1}^{\infty} \frac{\Theta(\hbar\omega - E_g^{(2)} - \frac{\hbar^2 \pi^2 n^2}{2mb^2})}{\sqrt{\hbar\omega - E_g^{(2)} - \frac{\hbar^2 \pi^2 n^2}{2mb^2}}} . \quad (1.61)$$

This function shows the typical $1/\sqrt{\omega}$ singularities known from the one-dimensional electron gas.

In the limit $b \rightarrow \infty$, the above function, divided by b , goes over into the ideal two-dimensional optical density of states (1.60). In the opposite case, $b \rightarrow 0$, we obtain an ideal one-dimensional semiconductor, where

$$D(\omega) = \frac{|\mu|^2 m^{1/2}}{\sqrt{2} \varepsilon_0 \hbar} \frac{\Theta(\hbar\omega - E_g^{(1)})}{\sqrt{\hbar\omega - E_g^{(1)}}} \quad (1.62)$$

and $E_g^{(1)}$ is defined in analogy to the two-dimensional case (1.60).

A one-dimensional semiconductor can also be realized by applying a magnetic field to a bulk semiconductor. For the choice of the vector potential $\mathbf{A}(\mathbf{r}) = (0, Bx, 0)$ (Landau gauge), the eigenfunctions and eigenvalues are [1]:

$$\begin{aligned} \varphi_{e,h,n,k_y,k_z}(\mathbf{r}) &= \frac{1}{\sqrt{L_z}} e^{ik_z z} \frac{1}{\sqrt{L_y}} e^{ik_y y} \chi_n \left(x \pm \frac{\hbar k_y}{eB} \right) \\ \chi_n(x) &= \frac{1}{\sqrt{2^n n! \sqrt{\pi} \lambda_{\text{mag}}}} e^{-x^2/2\lambda_{\text{mag}}^2} H_n \left(\frac{x}{\lambda_{\text{mag}}} \right) \\ E_{e,h,n}(k_y, k_z) &= \hbar\omega_{c,e,h} \left(n + \frac{1}{2} \right) + \frac{\hbar^2 k_z^2}{2m_{e,h}} ; \quad n \in \mathbb{N}_0 , \end{aligned} \quad (1.63)$$

where $\lambda_{\text{mag}} = \sqrt{\hbar/|eB|}$ is the magnetic length and $\omega_{c,e,h} = |eB|/m_{e,h}$ are the cyclotron frequencies of the electron and hole, respectively. The eigenfunctions give rise to a pair-creation amplitude

$$\langle M | n, k_y, k_z; n', k'_y, k'_z \rangle = \mu^* \delta_{nn'} \delta_{k_y, -k'_y} \delta_{k_z, -k'_z} , \quad (1.64)$$

Because the magnetic length is independent of the effective mass, the harmonic-oscillator eigenfunctions $\chi_n(x)$ are the same for electron and hole and

optical transitions are possible only between the same Landau quantum numbers. For the the optical density of states we obtain

$$D(\omega) = \frac{1}{2\pi\varepsilon_0 L_x} \int dk_y \sum_{n=0}^{\infty} \frac{|\mu|^2}{2\pi} \int_{-\infty}^{+\infty} dk_z \pi \delta \left[E_g + \hbar\omega_c(n+\frac{1}{2}) + \frac{\hbar^2 k_z^2}{2m} - \hbar\omega \right], \quad (1.65)$$

where $\omega_c = \omega_{ce} + \omega_{ch} = |eB|/m$. A problem arises from the fact that the electron and hole energies are independent of the wavenumber k_y . Therefore, in the above expression, the integral over k_y runs empty. Together with the infinite normalization length L_y , this gives a limit of the form ∞/∞ . From the form of the eigenfunctions (1.63) we notice that a final normalization length L_x is equivalent to the restriction $-|eB|L_x/(2\hbar) \leq k_y \leq +|eB|L_x/(2\hbar)$. Therefore, we replace

$$\frac{1}{2\pi L_x} \int dk_y = \frac{|eB|}{2\pi\hbar} \quad (1.66)$$

and the final result is

$$D(\omega) = \frac{|eB|}{2\pi\varepsilon_0\hbar} \frac{|\mu|^2 m^{1/2}}{\sqrt{2}\hbar} \sum_{n=0}^{\infty} \frac{\Theta[\hbar\omega - E_g - \hbar\omega_c(n+\frac{1}{2})]}{\sqrt{\hbar\omega - E_g - \hbar\omega_c(n+\frac{1}{2})}}. \quad (1.67)$$

As a consequence of the translational symmetry, the optical density of states depends only on the reduced mass m . However, this translational symmetry is not obvious, because, even though the magnetic field \mathbf{B} is constant, the vector potential \mathbf{A} depends on the coordinates. For large B , the last expression goes over into the optical density of states of an ideal one-dimensional semiconductor (1.62), divided by $2\pi\hbar/|eB|$, which has the dimension of an area, so that $[D(\omega)] = 1$.

If a quantum well is subjected to a perpendicular magnetic field, the eigenvalue spectra for electron and hole are entirely discrete. For the ideal two-dimensional semiconductor in a perpendicular magnetic field, the calculation of the optical density of states goes alongside the same lines as for the bulk semiconductor in a magnetic field (1.63–1.67), except that we drop the z direction. The result is

$$D(\omega) = \frac{|\mu|^2 |eB|}{2\pi\varepsilon_0\hbar} \sum_{n=0}^{\infty} \pi \delta \left[\hbar\omega - E_g^{(2)} - \hbar\omega_c(n+\frac{1}{2}) \right]. \quad (1.68)$$

The series of delta functions indicates that the system is zero-dimensional.

It is worthwhile to note that a magnetic field does not always reduce the dimension by two. A paradox is observed for quantum-well wires in a perpendicular magnetic field. For a finite wire width, the semiconductor is one-dimensional, but becomes zero-dimensional if the width goes towards infinity[41]. External electric fields can also reduce the dimension of a semiconductor. This will be the topic of Chap. 4.

For quantum dots, the optical density of states is also a sum over δ functions, like (1.68), but the spacing of the absorption lines is fairly irregular.

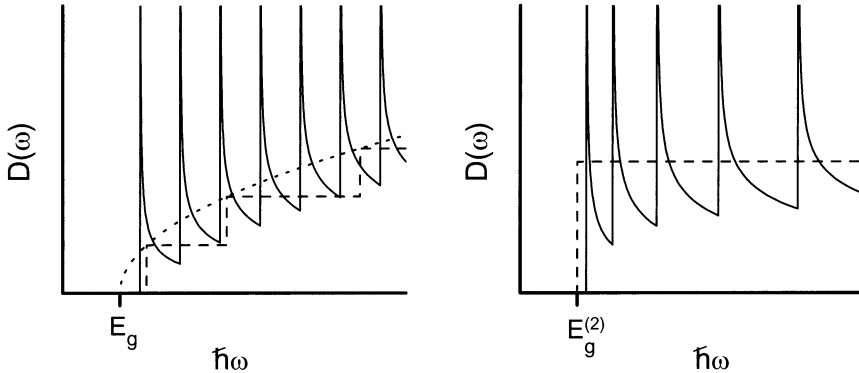


Fig. 1.3. Schematic plot of the optical density of states. Left: Bulk semiconductor (dotted line), quantum well (dashed line), and bulk semiconductor in a magnetic field (solid line). Right: Ideal two-dimensional semiconductor (dashed line) and ideal quantum-well wire (solid line)

The results for three-, two-, and one-dimensional semiconductors are shown schematically in Fig. 1.3. The left plot shows $D(\omega)$ for a bulk semiconductor, a quantum well, and a bulk semiconductor in a magnetic field. In these systems, the physical dimension is $p = 3$, i.e., they have a finite extension in three space directions. Therefore, the envelope of the optical density of states is proportional to $(\hbar\omega - E_g)^{1/2}$. The optical density of states for the ideal two-dimensional semiconductor and the quantum-well wire, modeled on the basis of an ideal two-dimensional semiconductor, is shown in the right part of Fig. 1.3. These idealized systems have a physical dimension $p = 2$ and the envelope of $D(\omega)$ goes like $\Theta(\hbar\omega - E_g^{(2)})$.

Finally, we consider a semiconductor in a static electric field. We start from the formulation (1.51) with the simplifications of the two-band model (1.54–1.55), where $\mathbf{A} = 0$, $U(\mathbf{r}) = eFz$, and, without loss of generality, $F > 0$. As in the case of the quantum well, we can separate the motion in the xy plane with energy $E_{||} = \hbar^2 k_{||}^2 / (2m)$. Carrying out the integration over $d^2 \mathbf{k}_{||}$, the density of states is equal to

$$D(\omega) = \frac{|\mu|^2 m}{2\varepsilon_0 \hbar^2} \sum_{\lambda' \lambda''} \frac{1}{L_z} \left| \int_{-L_z/2}^{+L_z/2} dz \varphi_{e\lambda'}(z) \varphi_{h\lambda''}(z) \right|^2 \Theta(\hbar\omega - E_g - E_{e\lambda'} - E_{h\lambda''}), \quad (1.69)$$

where $\varphi_{e\lambda'}$ and $\varphi_{h\lambda''}$ are the eigenfunctions of the electron and hole in potentials $\pm eFz$. These functions are known analytically and the z integral could be carried out explicitly. A trick, which will later be explored more systematically, is to introduce a pair eigenfunction $\Phi_A(Z, z) = \varphi_{e\lambda}(z_e) \varphi_{h\lambda'}(z_h)$, where $Z = (m_e z_e + m_h z_h)/M$, $z = z_e - z_h$, and $M = m_e + m_h$. The eigenvalue problem

$$\left[-\frac{\hbar^2}{2M} \frac{d^2}{dZ^2} - \frac{\hbar^2}{2m} \frac{d^2}{dz^2} + eFz \right] \Phi_A(Z, z) = E_A \Phi_A(Z, z) \quad (1.70)$$

can be separated into center-of-mass and relative motion such that $E_A = \hbar^2 K_z^2 / (2M) + E_\lambda$ and $\Phi_A(Z, z) = L_z^{-1/2} e^{iK_z Z} \varphi_\lambda(z)$, where, as long as L_z is finite, the normalization domain for $\varphi_\lambda(z)$ still depends on Z . Inserting Φ_A and E_A into expression (1.69) results in

$$D(\omega) = \frac{|\mu|^2 m}{2\varepsilon_0 \hbar^2} \sum_\lambda |\varphi_\lambda(0)|^2 \Theta(\hbar\omega - E_g - E_\lambda), \quad (1.71)$$

and only solutions with wavenumber $K_z = 0$ contribute to the optical density of states. Now, we carry out the limit $L_z \rightarrow \infty$, where the z domain goes over into $(-\infty, +\infty)$ so that the spectrum of the relative motion, E , is equal to the real axis. The eigenfunctions $\varphi_E(z)$ are given by the Airy function (C.46). According to (C.11), the energy normalization of the eigenfunctions changes the sum over λ into an integral over dE and we finally obtain

$$D(\omega) = \frac{|\mu|^2 m}{2\varepsilon_0 \hbar^2} \int_{-\infty}^{\hbar\omega - E_g} dE |\varphi_E(0)|^2. \quad (1.72)$$

As in the case of a constant magnetic field (1.67), the optical absorption depends only on the relative motion of the electron–hole pair, which is a consequence of the translational symmetry.

Also of some interest is the one-dimensional semiconductor in an electric field, where we restrict ourselves to the ideal one-dimensional case. The calculation goes alongside the three-dimensional case, except that we drop the integration over $d^2\mathbf{k}$. The result

$$D(\omega) = \frac{|\mu|^2}{\varepsilon_0} |\varphi_E(0)|^2; \quad E = \hbar\omega - E_g^{(1)} \quad (1.73)$$

is, roughly spoken, the derivative of expression (1.72).

The function $D(\omega)$ is shown in Fig. 1.4 for a bulk semiconductor (left) and an ideal one-dimensional semiconductor (right), for two field strengths F_1 and F_2 , where $|F_2| > |F_1|$. The electric field leads to a modulation of the optical spectrum, which is known as Franz–Keldysh effect [42–44]. In the one-dimensional case, the absorption even goes to zero between the maxima.

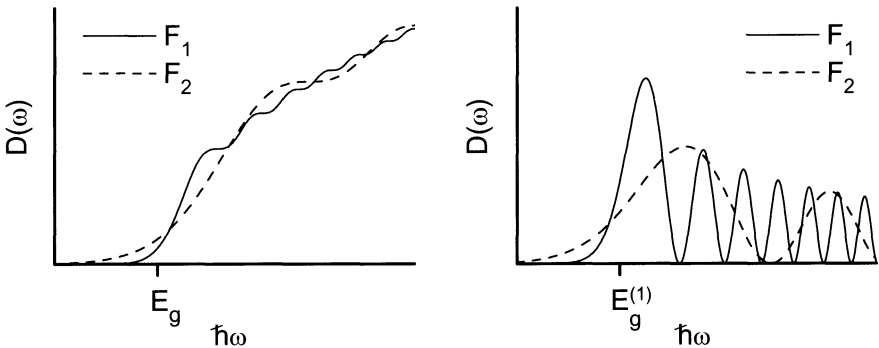


Fig. 1.4. Optical density of states for a three-dimensional (left) and one-dimensional (right) semiconductor in an electric field, where $|F_2| > |F_1|$

The modulation is nonperiodic and scales with $|F|^{2/3}$, as can be seen from the eigenfunction φ_E (C.46). The absorption is nonzero even below the gap, which is a consequence of the unbounded energy spectrum for the electron and the hole, and the decrease is exponential, which follows from the asymptotics of the Airy function (C.45). In the limit $F \rightarrow 0$, the optical density of states approaches the solution for the field-free case, (1.56) and (1.62), where in the latter case the convergence is not pointwise.

1.3 Excitons

In the previous section we have seen that the optical excitation of a semiconductor leads to the creation of electron–hole pairs and the absorption coefficient is proportional to the overlap integral of the electron and hole eigenfunctions. In reality, an electron–hole pair is subjected to Coulomb interaction, which leads to bound states and scattering states. This analog to the Hydrogen atom is called exciton. For bound states, the total energy of the electron–hole pair is smaller than the sum of the energies of the individual particles. Therefore, the threshold for the optical absorption is below the band gap E_g . For scattering states with an energy above the band gap, we expect an increase of the absorption, compared to interaction-free particles, because the attractive Coulomb interaction tends to increase the probability of finding electron and hole in the same place. The theory of excitons has been developed already in the thirties [45]. We distinguish two categories of excitons: Wannier–Mott excitons, with an effective extension (Bohr radius) much larger than the lattice constant, and Frenkel excitons, where electron and hole are concentrated in one unit cell. The wavefunction of a Wannier exciton can be represented as a product of functions strongly localized on the Wigner–Seitz cell, so-called Wannier functions, and a slowly varying amplitude. In a pioneering work, Elliott derived a relation between the absorption

coefficient and the eigenstates of the electron–hole pairs [46]. This Elliott formula explains very well the experimental findings. Some years later, this result was generalized for ideal two-dimensional semiconductors by Shinada and Sugano [47], which qualitatively explains the absorption of quantum wells.

The early theory of excitons has been refined in several directions. In the presence of band degeneracy the excitonic states are multiplets, subjected to a finestructure splitting [48]. Some of these states are dipole allowed, others are dipole forbidden (bright and dark excitons). The finite light wavevector causes anticrossing between the exciton and photon dispersions and the resulting elementary excitation is called a polariton [7, 49–51]. Polaritons are particularly important in structures with optical confinement. Highly excited semiconductors are characterized by a macroscopic electron and hole density, which significantly changes the dynamics due to many-particle effects. The theory of highly excited semiconductors is important for the operation of semiconductor lasers. A number of interesting phenomena is observed in low-dimensional semiconductors due to the interplay of Coulomb interaction, structural confinement, and external fields, some of them being discussed in the next chapters.

There is plenty of literature on the theory of excitons. We recommend the classics by Knox [52], by Dexter and Knox [50], and a monograph “Polarons and Excitons,” edited by Kuper and Whitfield, with contributions by Elliott and Haken [53]. Bassani et al. [5, 39] and Dimmock [36] put special emphasis on the optical absorption of excitons. More recent books by Stahl and Balslev [54] and by Zimmermann [55] deal with excitons in low-dimensional semiconductors and in highly excited semiconductors. Also, in the recommended textbooks [6–8, 56] a large portion is devoted to excitons.

The absorption coefficient can be derived in several ways. The simplest method, which was used in the early papers, is a heuristic generalization of the free-particle result. In the formulation (1.51), we need to replace $\varphi_\lambda(\mathbf{r}_e)\varphi_{\lambda'}(\mathbf{r}_h)$ by $\Phi_\Lambda(\mathbf{r}_e, \mathbf{r}_h)$ and $E_{e\lambda} + E_{h\lambda'}$ by \mathcal{E}_Λ , where Φ_Λ and \mathcal{E}_Λ are the eigenvalues and eigenfunctions of the electron–hole Hamiltonian $\hat{\mathcal{H}} = \hat{H}_{e\text{eff}}(\mathbf{r}_e, \frac{\hbar}{i}\nabla_e) + \hat{H}_{h\text{eff}}(\mathbf{r}_h, \frac{\hbar}{i}\nabla_h) - e^2/(4\pi\varepsilon_0\varepsilon|\mathbf{r}_e - \mathbf{r}_h|)$ with an effective dielectric constant ε to take into account the screening of the semiconductor. More rigorously, the two-particle Schrödinger equation and the absorption coefficient can also be derived from the Hartree–Fock approximation for the many-electron state with one electron being excited above the ground state [36, 57]. In many-particle physics, the polarization functions obeys a Bethe–Salpeter equation and the Elliott formula follows from the statically screened ladder approximation [58, 59]. This method can in principle be generalized to take into account many-particle effects, i.e., interaction beyond the Hartree–Fock approximation. A more recent development is the semiconductor Bloch equations, which is the equation of motion for the one-particle density matrix

in statically screened Hartree–Fock approximation. The optical absorption follows from linearizing the equations in the optical field.

In this section we follow the latter path and calculate the optical absorption from the semiconductor Bloch equations. We first specify the semiconductor Bloch equations for bulk semiconductors in Bloch representation and for low-dimensional semiconductors in real-space (Wannier representation) and summarize important facts about screening. Then we calculate the linear optical susceptibility by solving the semiconductor Bloch equations in first order in the optical field. Finally, we discuss the effects of Coulomb interaction for the analytically solvable ideal three- and two-dimensional semiconductor.

1.3.1 The Semiconductor Bloch Equations

The semiconductor Bloch equations describe the time evolution of the density matrix in the presence of electron–light interaction and play the same role as the optical Bloch equations for two-level systems [60]. Here, we shall specify the semiconductor Bloch equations for the two-band model of a bulk semiconductor and for the general case of a low-dimensional semiconductor with degenerate bands. We try to motivate the origin of the Coulomb interaction, but cannot give a rigorous derivation. This would require some “deep diving” into many-particle physics, which is beyond the scope of our work.

First, we consider a bulk semiconductor in the two-band model (Sect. 1.2). The density matrix in Bloch representation is defined as

$$\langle \hat{a}_{j_2 \mathbf{k}_2}^\dagger(t) \hat{a}_{j_1 \mathbf{k}_1}(t) \rangle = \delta_{\mathbf{k}_1 \mathbf{k}_2} n_{j_1 j_2}(\mathbf{k}_1, t), \quad (1.74)$$

where \hat{a}_{jk}^\dagger and \hat{a}_{jk} are creation and annihilation operators of an electron in the state $|j, \mathbf{k}\rangle$. As a consequence of the crystal symmetry, the density matrix is diagonal in the wavevectors $\mathbf{k}_1, \mathbf{k}_2$. The four functions (1.74) can be written as a matrix

$$N(\mathbf{k}) = \begin{pmatrix} f_c(\mathbf{k}) & \psi(\mathbf{k}) \\ \psi^*(\mathbf{k}) & f_v(\mathbf{k}) \end{pmatrix}, \quad (1.75)$$

where the diagonal matrix elements $f_c = n_{cc}$; $f_v = n_{vv}$ are the occupation numbers of conduction and valence band and $\psi = n_{cv} = n_{vc}^*$ is the microscopic polarization. In the electron–hole picture, $f_e = f_c$ and $f_h = 1 - f_v$ are interpreted as occupation numbers of electrons and holes, and ψ is called the electron–hole pair amplitude. Charge neutrality requires electron and hole densities to be equal,

$$n = n_e = n_h; \quad n_{e,h} = \frac{2}{\Omega} \sum_{\mathbf{k}} f_{e,h}(\mathbf{k}), \quad (1.76)$$

and n is called electron–hole pair density.⁶ The optical polarization P is equal to the dipole density and takes the form

⁶ A factor 2 is introduced to account for the spin degeneracy.

$$P(t) = \mu^* \frac{1}{\Omega} \sum_{\mathbf{k}} \psi(\mathbf{k}, t) + \text{c.c.} \quad (1.77)$$

We consider optical interaction with a pulse of the form $\mathbf{E}(t) = \underline{\mathbf{E}}(t) + \text{c.c.}$ near the band gap. The Fourier transforms $\underline{\mathbf{E}}(\omega)$ and $\underline{\mathbf{E}}^*(-\omega)$ of $\underline{\mathbf{E}}(t)$ and $\underline{\mathbf{E}}^*(t)$ are spectrally narrow near $\hbar\omega = +E_g$ and $\hbar\omega = -E_g$, respectively. The equation of motion for the density matrix in rotating-wave approximation is given by the semiconductor Bloch equations [56, 61, 62]:

$$i\hbar \frac{\partial}{\partial t} N(\mathbf{k}, t) = [H(\mathbf{k}, t), N(\mathbf{k}, t)] \quad (1.78)$$

with the effective Hamiltonian

$$H(\mathbf{k}, t) = \begin{pmatrix} E_c(\mathbf{k}) & -\mu \underline{E}(t) \\ -\mu^* \underline{E}^*(t) & E_v(\mathbf{k}) \end{pmatrix} - \frac{1}{\Omega} \sum_{\mathbf{k}'} V_s(\mathbf{k}-\mathbf{k}') [N(\mathbf{k}', t) - N^{(0)}(\mathbf{k}')] \quad (1.79)$$

$$N^{(0)}(\mathbf{k}) \equiv \text{diag}(0, 1).$$

In the absence of Coulomb interaction ($V_s = 0$), equation (1.78) is identical to the von Neumann equation for the time evolution of the statistical operator. The polarization (1.77) can be written as

$$P(t) = \underline{P}(t) + \text{c.c.}; \quad \underline{P}(t) = \mu^* \frac{1}{\Omega} \sum_{\mathbf{k}} \psi(\mathbf{k}, t), \quad (1.80)$$

where in the rotating-wave approximation, $\psi(t)$ and \underline{P} have only positive-frequency components.

The second term in the effective Hamiltonian (1.79) is the exchange contribution from time-dependent Hartree–Fock (mean-field, effective-field) theory, where the bare Coulomb potential has been replaced by a statically screened Coulomb potential V_s . The Hartree contribution vanishes because of local charge neutrality for the envelope functions. A more rigorous derivation of the semiconductor Bloch equation is possible by the method of Green's functions, with a selfenergy in static V_s approximation. It is important to know that the screened Hartree–Fock or linear V_s approximation is only applied to the excited electron–hole pairs, i.e., to the proportion of the density matrix, which departs from the ground state.

The semiconductor Bloch equations provide the theoretical framework for studying optically excited semiconductors and can explain a variety of phenomena in linear and nonlinear spectroscopy on semiconductors such as Coulomb enhancement, polarization interference, and photon echoes. The Coulomb effects can be drastic and, in many cases, it is impossible to even give a qualitative description without taking into account Coulomb interaction. As the screening is static, memory effects cannot be described by the equations (1.78–1.79). In recent years, several attempts have been made to go beyond

the semiconductor Bloch equations. Two directions are noticeable: dynamic screening due to electron–phonon and electron–electron interaction [63, 64] and equations of motion for hierarchies of density matrices [65].

In the case of low-dimensional semiconductors, the semiconductor Bloch equations are often represented in the basis of the electron and hole eigenfunctions (for a review, see [66]). Alternatively, we can use the Wannier representation (1.20) with the variables ν, m, \mathbf{r} .⁷ Then the semiconductor Bloch equations and the interband polarization take the simple form [54, 67]:

$$\begin{aligned} i\hbar \frac{\partial}{\partial t} N(\mathbf{r}_1, \mathbf{r}_2, t) &= [H(t), N(t)](\mathbf{r}_1, \mathbf{r}_2) \\ H(\mathbf{r}_1, \mathbf{r}_2, t) &= \left(\begin{array}{c|c} \hat{H}_{\text{c eff}}(\mathbf{r}_1, \frac{\hbar}{i}\nabla_1) & -\boldsymbol{\mu}_{\text{cv}} \cdot \underline{\mathbf{E}}(t) \\ \hline -\boldsymbol{\mu}_{\text{vc}} \cdot \underline{\mathbf{E}}^*(t) & \hat{H}_{\text{v eff}}(\mathbf{r}_1, \frac{\hbar}{i}\nabla_1) \end{array} \right) \delta(\mathbf{r}_1 - \mathbf{r}_2) \\ &\quad - V_s(\mathbf{r}_1, \mathbf{r}_2) [N(\mathbf{r}_1, \mathbf{r}_2, t) - N^{(0)}(\mathbf{r}_1, \mathbf{r}_2)] \quad (1.81) \\ N^{(0)}(\mathbf{r}_1, \mathbf{r}_2) &= \text{diag}(0, 1) \delta(\mathbf{r}_1 - \mathbf{r}_2) \\ \underline{\mathbf{P}}(t) &= \frac{1}{\Omega} \sum_{m_1 m_2} \int d^3 \mathbf{r} \boldsymbol{\mu}_{\nu m_2, cm_1} n_{cm_1, \nu m_2}(\mathbf{r}, \mathbf{r}, t). \end{aligned}$$

The commutator is defined with the usual matrix product for integral operators and the symbol $\boldsymbol{\mu}_{\nu_1 \nu_2}$ is a compact notation for the matrix $\boldsymbol{\mu}_{\nu_1 m_1, \nu_2 m_2}$. Equations (1.81) describe the general case, where the density matrix depends on six coordinates. However, the problem radically simplifies in the presence of symmetries. Evidently, the semiconductor Bloch equations for bulk semiconductors (1.78–1.79) are a special case of (1.81).

The Coulomb interaction between electrons and holes, which appears in the semiconductor Bloch equations, is subjected to screening from the electronic background, the ionic lattice, and the electron–hole plasma. Here, we briefly summarize important facts for bulk semiconductors; for further reading, we refer to the textbooks and review articles [4, 7, 55, 56, 59].

The screened Coulomb potential is equal to $V_s(\mathbf{k}, \omega) = v(\mathbf{k})/\epsilon(\mathbf{k}, \omega)$, where $v(\mathbf{k}) = e^2/(\epsilon_0 k^2)$ is the bare Coulomb potential and $\epsilon(\mathbf{k}, \omega)$ is the longitudinal dielectric function. If the semiconductor is in the ground state, no intraband transitions are possible and the off-resonant interband transitions give rise to a constant background screening $\epsilon(\infty)$. In polar semiconductors, the ionic lattice contributes

⁷ The variables ν, m, \mathbf{r} are not quantum numbers. The true Wannier representation uses quantum numbers ν, m, \mathbf{R} , where the lattice vector \mathbf{R} is the location of the Wannier function. As the envelope functions are slowly varying, the difference equation for the exciton wavefunction can be approximated as a differential equation [45].

to the screening because of electron–phonon interaction. The oscillator model yields a frequency-dependent dielectric function of the form

$$\varepsilon(\omega) = \varepsilon(\infty) \frac{\omega_{\text{LO}}^2 - (\omega + i\epsilon)^2}{\omega_{\text{TO}}^2 - (\omega + i\epsilon)^2} ; \quad \epsilon = +0 ; \quad |\hbar\omega| \ll E_g ,$$

where ω_{LO} and ω_{TO} are the frequencies of the longitudinal and transversal optical phonons, respectively. The static dielectric constant $\varepsilon(0) = \varepsilon_s$ is related to the background dielectric constant $\varepsilon(\infty) = \varepsilon_\infty$ by the Lyddane–Sachs–Teller relation

$$\frac{\varepsilon(0)}{\varepsilon(\infty)} = \frac{\omega_{\text{LO}}^2}{\omega_{\text{TO}}^2} > 1 .$$

If the above function $\varepsilon(\omega)$ is replaced by a constant ε , we obtain the statically screened Coulomb potential

$$V(\mathbf{k}) = \frac{e^2}{\varepsilon_0 \varepsilon k^2} ; \quad V(\mathbf{r}) = \frac{e^2}{4\pi \varepsilon_0 \varepsilon r} .$$

The frequency dependence of the dielectric function can be neglected if the LO phonon energy $\hbar\omega_{\text{LO}}$ is much smaller or much larger than the exciton binding energy E_B^* . For $E_B^* \ll \hbar\omega_{\text{LO}}$ or $E_B^* \gg \hbar\omega_{\text{LO}}$, the dielectric constant ε is equal to $\varepsilon(0)$ or $\varepsilon(\infty)$, respectively. For GaAs we have $E_B^* = 4.7$ meV and $\hbar\omega_{\text{LO}} = 36$ meV; thus we can assume that $\varepsilon \approx \varepsilon(0)$. The Haken potential [7, 52, 53] interpolates between these limits.

In the presence of electron–hole pairs, the dielectric function is given by the Lindhard formula, which corresponds to the random-phase approximation (RPA) for the polarization function. The asymptotic expression for $\omega = 0$ and $k \rightarrow 0$ is

$$\varepsilon(\mathbf{k}) = \varepsilon \frac{k_s^2 + k^2}{k^2}$$

with the screening wavenumber

$$k_s^2 = -\frac{e^2}{4\pi \varepsilon_0 \varepsilon} \sum_{\nu=c,v} \frac{2}{\Omega} \sum_{\mathbf{k}} \frac{df_\nu(k)}{dE_\nu(k)} .$$

Special cases are the Thomas–Fermi screening for zero carrier temperature and the Debye–Hückel screening for high temperature. The statically screened Coulomb potential

$$V_s(\mathbf{k}) = \frac{e^2}{\varepsilon_0 \varepsilon (k^2 + k_s^2)} ; \quad V_s(\mathbf{r}) = \frac{e^2}{4\pi \varepsilon_0 \varepsilon r} e^{-k_s r}$$

is called Thomas–Fermi, Debye, or Yukawa potential. Because V_s is short-ranged, it has only a finite number of bound states [3]. The spectrum becomes entirely continuous for

$$k_s a_B^* > 1.19 ,$$

where a_B^* is the Bohr radius of the exciton. The latter equation is known as Mott criterion and the unbinding of excitons due to screening is called Mott transition.

An important consequence of the exchange–correlation interaction [second term in (1.79)] is the dependence of the band gap on the carrier density. The band renormalization

$$\begin{aligned}\Delta E_g(\mathbf{k}) = & -\frac{1}{\Omega} \sum_{\mathbf{k}'} V_s(\mathbf{k} - \mathbf{k}') \left[n_{cc}(\mathbf{k}) + 1 - n_{vv}(\mathbf{k}) \right] \\ & - \frac{1}{\Omega} \sum_{\mathbf{k}'} \left[V(\mathbf{k} - \mathbf{k}') - V_s(\mathbf{k} - \mathbf{k}') \right]\end{aligned}$$

consists of two parts, the screened exchange (SX) contribution and the Coulomb hole (CH) contribution [56, 59]. Both effects lead to a shrinkage of the gap energy with increasing carrier density. At the same time, the reduction of the binding energy with increasing k_s tends to compensate the gap shrinkage [59].

In low-dimensional semiconductors, the treatment of screening is generally difficult. The occupation numbers for the different subbands, which enter the formula for the dielectric function, have to be determined from a kinetic equation. Even the treatment of the background screening can be complicated, if the dielectric constants are different for different layers. For simple geometries, V can be found by the method of image charges [68, 69]. The effect of dielectric mismatch has been studied quantitatively for GaAs/(Ga,Al)As quantum wells [38]. Furthermore, in low-dimensional semiconductors, in the absence of spatial homogeneity, the Hartree contribution to the effective Hamiltonian is nonzero [70]. This term is neglected in most calculations.

1.3.2 The Elliott Formula

The optical absorption can be traced back to the solution of an eigenvalue problem of an electron–hole pair, subjected to Coulomb interaction [46]. In this subsection we derive the Elliott formula from the semiconductor Bloch equations by means of linear response theory.

The linear optical susceptibility is defined as

$$\chi_{\alpha\beta}(\omega) = \frac{1}{\varepsilon_0} \frac{\partial P_\alpha(\omega)}{\partial E_\beta(\omega)}. \quad (1.82)$$

From $\mathbf{D}(\omega) = \varepsilon_0 \mathbf{E}(\omega) + \mathbf{P}(\omega) = \varepsilon_0 \varepsilon(\omega) \mathbf{E}(\omega)$ it follows that $\varepsilon_{\alpha\beta}(\omega) = \delta_{\alpha\beta} + \chi_{\alpha\beta}(\omega)$, where $\varepsilon(\omega)$ is called the optical function. Because $\mathbf{P}(t)$ and $\mathbf{E}(t)$ are real quantities, the components of χ fulfill $\chi_{\alpha\beta}(\omega) = \chi_{\alpha\beta}^*(-\omega)$. Furthermore, as a consequence of causality, the exact optical susceptibility obeys the Kramers–Kronig relations (A.14).

To determine the optical absorption, we assume a small optical field of the form $\mathbf{E}(t) = \underline{\mathbf{E}}(t) + \text{c.c.}; \underline{\mathbf{E}}(t) = \underline{\mathbf{E}}_0 \boldsymbol{\xi} e^{-i\omega t}; \omega > 0$. The polarization, linear in the optical field, is $\mathbf{P}(t) = \underline{\mathbf{P}}_0 e^{-i\omega t} + \text{c.c.}$, where $\underline{\mathbf{P}}_0 = \varepsilon_0 \chi(\omega) \underline{\mathbf{E}}_0$. For bulk semiconductors, the absorbed energy per volume and time is equal to

$$\frac{dw}{dt} = \lim_{T \rightarrow \infty} \frac{1}{T} \int_{-\frac{T}{2}}^{+\frac{T}{2}} dt \frac{d\mathbf{P}(t)}{dt} \cdot \mathbf{E}(t), \quad (1.83)$$

where $d\mathbf{P}(t)/dt$ is the current density of the polarization charges. Dividing the expression (1.83) by the intensity S (1.47) yields the absorption coefficient

$$\alpha(\omega) = \frac{\omega}{c_0 n} \operatorname{Im} [\boldsymbol{\xi}^* \cdot \chi(\omega) \boldsymbol{\xi}] . \quad (1.84)$$

Alternatively, the optical absorption can be calculated by solving the wave equation with a complex refractive index $n = \sqrt{\varepsilon(\omega)}$, where the absorption coefficient is related to the imaginary part of the complex wavevector [7]. For cubic semiconductors without external field it holds that $\chi_{\alpha\beta} = \delta_{\alpha\beta} \chi$ and the absorption is independent of the polarization of the incident light.

The linear optical susceptibility due to interband transitions can be obtained from solving the semiconductor Bloch equations (1.81) in linear order in the optical field. We assume that the semiconductor is in the ground state, where $N_{cc}(\mathbf{r}_1, \mathbf{r}_2, t) \equiv 0$, $N_{vv}(\mathbf{r}_1, \mathbf{r}_2, t) \equiv \delta(\mathbf{r}_1 - \mathbf{r}_2)$, and $V_s = V$. The nondiagonal element of the density matrix obeys the differential equation

$$\begin{aligned} i\hbar \frac{\partial}{\partial t} N_{cm_1,vm_2}(\mathbf{r}_1, \mathbf{r}_2, t) &= \sum_{m'_1} \hat{H}_{c\text{ eff}} m_1 m'_1 (\hat{\mathbf{k}}_1, \mathbf{r}_1) N_{cm'_1,vm_2}(\mathbf{r}_1, \mathbf{r}_2, t) \\ &\quad - \sum_{m'_2} \left[\hat{H}_{v\text{ eff}} m_2 m'_2 (\hat{\mathbf{k}}_2, \mathbf{r}_2) \right]^* N_{cm_1,vm'_2}(\mathbf{r}_1, \mathbf{r}_2, t) \\ &\quad - \boldsymbol{\mu}_{cm_1,vm_2} \cdot \underline{\mathbf{E}}(t) \delta(\mathbf{r}_1 - \mathbf{r}_2) \\ &\quad - V(\mathbf{r}_1 - \mathbf{r}_2) N_{cm_1,vm_2}(\mathbf{r}_1, \mathbf{r}_2, t) . \end{aligned} \quad (1.85)$$

The complex conjugate of $\hat{H}_{v\text{ eff}}$ results from overrolling the Nabla operator, which changes $\hat{\mathbf{k}}$ to $\hat{\mathbf{k}}^*$, and from the Hermiticity of $\hat{H}_{v\text{ eff}}$ (1.30). We notice that $\hat{H}_{v\text{ eff}}^*$ is closely related to the effective hole Hamiltonian $\hat{H}_{h\text{ eff}}$ (1.34). To change to the electron–hole picture, we introduce the electron–hole pair amplitude,

$$\Psi_{m_1 m_2} = \sum_{m'_2} T_{m_2 m'_2} N_{cm_1,vm'_2} , \quad (1.86)$$

which is a second-rank spinor. For the $\Gamma_{8v} \rightarrow \Gamma_{6c}$ transition, Ψ has $4 \times 2 = 8$ components, for the two-band semiconductor, Ψ is a scalar, etc. With this definition of the electron–hole creation amplitude \mathbf{M} (1.51), the equation of motion (1.85) goes over into

$$\begin{aligned} i\hbar \frac{\partial}{\partial t} \Psi_{m_e m_h}(\mathbf{r}_e, \mathbf{r}_h, t) &= \sum_{m'_e m'_h} \hat{\mathcal{H}}_{m_e m_h, m'_e m'_h} \Psi_{m'_e m'_h}(\mathbf{r}_e, \mathbf{r}_h, t) \\ &\quad - \mathbf{M}_{m_e m_h} \cdot \underline{\mathbf{E}}(t) \delta(\mathbf{r}_e - \mathbf{r}_h) \end{aligned} \quad (1.87)$$

with the electron–hole Hamiltonian

$$\begin{aligned} \hat{\mathcal{H}}_{m_e m_h, m'_e m'_h} &= \hat{H}_{e\text{ eff}} m_e m'_e (\mathbf{r}_e, \frac{\hbar}{i} \nabla_e) \delta_{m_h m'_h} + \delta_{m_e m'_e} \hat{H}_{h\text{ eff}} m_h m'_h (\mathbf{r}_h, \frac{\hbar}{i} \nabla_h) \\ &\quad - V(\mathbf{r}_e - \mathbf{r}_h) \delta_{m_e m'_e} \delta_{m_h m'_h} . \end{aligned} \quad (1.88)$$

The Coulomb interaction between electron and hole stems from the exchange–correlation part of the selfenergy. Equation (1.87) is an inhomogeneous Schrödinger equation with a source term given by the optical field and the electron–hole creation amplitude. The optical polarization (1.81), expressed in terms of Ψ and \mathbf{M} , is

$$\underline{\mathbf{P}}(t) = \frac{1}{\Omega^{(d)}} \sum_{m_e m_h} \mathbf{M}_{m_e m_h}^* \int d^3r \Psi_{m_e m_h}(\mathbf{r}, \mathbf{r}, t). \quad (1.89)$$

The linear optical response of a semiconductor can now be interpreted as follows. The optical field $\mathbf{E}(t)$ creates a wavepacket at equal electron and hole coordinates $\mathbf{r}_e = \mathbf{r}_h$. This wavepacket propagates under the influence of the Hamiltonian $\hat{\mathcal{H}}$. The polarization $\underline{\mathbf{P}}(t)$ is probed also at $\mathbf{r}_e = \mathbf{r}_h$. The electron–hole-pair Hamiltonian (1.88) was already derived in Wannier's paper from 1937 on the basis of Wannier functions [45]. The Nabla operator stems from approximating the difference equation by a differential equation, see footnote 7 on p. 33.

To simplify the notation, we consider $\hat{\mathcal{H}}_{m_e m_h, m'_e m'_h} \delta(\mathbf{r}_e - \mathbf{r}'_e) \delta(\mathbf{r}_h - \mathbf{r}'_h)$, $\Psi_{m_e m_h}(\mathbf{r}_e, \mathbf{r}_h)$, and $\mathbf{M}_{m_e m_h} \delta(\mathbf{r}_e - \mathbf{r}_h)$ as representations of the operator $\hat{\mathcal{H}}$ and the Dirac vectors $|\Psi\rangle$ and $|\mathbf{M}\rangle$ in the basis $\{|\mathbf{r}_e, m_e; \mathbf{r}_h, m_h\rangle\}$. Then (1.87) and (1.89) write as

$$i\hbar \frac{d}{dt} |\Psi(t)\rangle - \hat{\mathcal{H}} |\Psi(t)\rangle = -\underline{\mathbf{E}}(t) \cdot |\mathbf{M}\rangle \quad (1.90)$$

and

$$\underline{\mathbf{P}}(t) = \frac{1}{\Omega^{(d)}} \langle \mathbf{M} | \Psi(t) \rangle. \quad (1.91)$$

By means of Fourier transform, the differential equation (1.90) goes over into an algebraic equation, and the retarded solution (App. A.1) is

$$|\Psi(\omega)\rangle = [\hat{\mathcal{H}} - \hbar(\omega + i\epsilon)]^{-1} |\mathbf{M}\rangle \cdot \underline{\mathbf{E}}(\omega). \quad (1.92)$$

Using the orthonormality and completeness of the eigenstates of $\hat{\mathcal{H}}$,

$$\hat{\mathcal{H}} |\Phi_\Lambda\rangle = \mathcal{E}_\Lambda |\Phi_\Lambda\rangle; \quad \langle \Phi_\Lambda | \Phi_{\Lambda'} \rangle = \delta_{\Lambda\Lambda'}; \quad \sum_\Lambda |\Phi_\Lambda\rangle \langle \Phi_\Lambda| = 1, \quad (1.93)$$

where the quantum number Λ stands for discrete and continuous states, the inverse operator can be given in explicit form and the electron–hole pair amplitude becomes

$$|\Psi(\omega)\rangle = \sum_\Lambda |\Phi_\Lambda\rangle \frac{1}{\mathcal{E}_\Lambda - \hbar(\omega + i\epsilon)} \langle \Phi_\Lambda | \mathbf{M} \rangle \cdot \underline{\mathbf{E}}(\omega). \quad (1.94)$$

Having found the solution for the electron–hole-pair amplitude in linear order in the optical field, we readily calculate the optical susceptibility. From the definition (1.82) and the equations (1.91) and (1.94) it follows that

$$\underline{\chi}_{\alpha\beta}(\omega) = \frac{P_\alpha(\omega)}{\varepsilon_0 \underline{E}_\beta(\omega)} = \frac{1}{\varepsilon_0} \frac{1}{\Omega^{(d)}} \sum_A \frac{\langle M_\alpha | \Phi_A \rangle \langle \Phi_A | M_\beta \rangle}{\mathcal{E}_A - \hbar(\omega + i\epsilon)}. \quad (1.95)$$

As an artifact of the rotating-wave approximation, the above function does not fulfill $\underline{\chi}_{\alpha\beta}(\omega) = \underline{\chi}_{\alpha\beta}^*(-\omega)$. In reality, N_{cv} and N_{vc} contain both positive- and negative-frequency components. In order to account for the nonresonant contributions, we have to replace \underline{E} by E in (1.94). The exact optical susceptibility is $\chi_{\alpha\beta}(\omega) = [P_\alpha(\omega) + P_\alpha^*(-\omega)]/[\varepsilon_0 E_\beta(\omega)] = \underline{\chi}_{\alpha\beta}(\omega) + \underline{\chi}_{\alpha\beta}^*(-\omega)$. We mention that, in the effective-mass approximation, the real part of $\chi_{\alpha\beta}$ is often divergent and the Kramers–Kronig relations are not fulfilled. Anyway, the refractive index cannot be calculated just from the transition between valence and conduction band.

The imaginary part of the optical susceptibility (1.95) follows from Dirac's identity (A.12) and the final result for the absorption coefficient (1.84) is [36, 46, 53]

$$\alpha(\omega) = \frac{E_g}{\hbar c_0 n \varepsilon_0} \sum_A |F_A|^2 \pi \delta(\mathcal{E}_A - \hbar\omega) \quad (1.96)$$

$$F_A = \frac{1}{\sqrt{\Omega^{(d)}}} \langle \boldsymbol{\xi} \cdot \mathbf{M} | \Phi_A \rangle = \frac{1}{\sqrt{\Omega^{(d)}}} \sum_{m_e m_h} \boldsymbol{\xi} \cdot \mathbf{M}_{m_e m_h}^* \int d^3r \Phi_{A; m_e m_h}(\mathbf{r}, \mathbf{r}, t),$$

known as the Elliott formula.

The delta function indicates that optical transitions occur only if the photon energy $\hbar\omega$ is equal to an eigenvalue \mathcal{E}_A of the two-particle Hamiltonian $\hat{\mathcal{H}}$. The prefactor $|F_A|^2$ is called the oscillator strength of the transition. For bound states the spectrum is discrete, while scattering states give rise to an absorption continuum. For some geometries or external-field configurations, the spectrum may also exhibit resonances, that is solutions between bound and scattering states. Examples for resonances will be discussed in the next chapters.

Because only positive frequencies are considered in (1.96), the rotating-wave approximation does not affect the absorption coefficient. The optical susceptibility generalizes the optical density of states, introduced in Sect. 1.2, and the special case $\text{Im}[\boldsymbol{\xi}^* \cdot \chi(\omega) \boldsymbol{\xi}] = D(\omega)$ is obtained for $V = 0$, $\mathcal{E}_A = E_{e\lambda} + E_{h\lambda'}$, and $\Phi_A(\mathbf{r}_e, \mathbf{r}_h) = \varphi_{e\lambda}(\mathbf{r}_e) \varphi_{h\lambda'}(\mathbf{r}_h)$.

In reality, the positive infinitesimal ϵ is a finite quantity and the optical transitions are homogeneously broadened. There are different theoretical approaches to homogeneous line broadening and a detailed discussion would be beyond the scope of this work. The simplest model is that of a stochastic resonance, where the interaction with an external reservoir is described by a transition energy fluctuating

in time [71, 72]. In the fast-modulation limit, the lineshape is Lorentzian and the decay of the polarization is exponential, which is observed in many experiments. There are other cases, where the line broadening is non-Lorentzian. For example, the electron–phonon interaction in polar semiconductors at room temperatures leads to an exponential decline of the absorption line, known as Urbach tail [50, 56]. In the following, homogeneous broadening is taken into account by a phenomenological constant $\epsilon > 0$.

The dependence of the Coulomb interaction on the electron and hole “spin projections” m_e, m_h has been neglected by averaging over the Wigner–Seitz cell. We shall qualitatively discuss this electron–hole exchange interaction [7, 48]. For bulk semiconductors with zincblende structure, the eigenfunctions of the electron–hole Hamiltonian (1.88) transform according to $\Gamma_8 \otimes \Gamma_7 = \Gamma_3 \oplus \Gamma_4 \oplus \Gamma_5$. An additional short-range interaction proportional to $\sigma_e \cdot J_h$ leads to a splitting between the dipole-allowed Γ_4 states ($f = j - s = 1$, singlet exciton) and the dipole-forbidden Γ_3 and Γ_5 states ($f = j + s = 2$, triplet exciton). An additional long-range interaction, which depends on the light wavevector \mathbf{q} , leads to a splitting of the Γ_4 exciton into an optically forbidden longitudinal ($\Gamma_{4L}; m_f = 0$) and an optically allowed transversal exciton ($\Gamma_{4T}; m_f \pm 1$). This interaction term is nonanalytic and the L–T splitting persists for $\mathbf{q} \rightarrow 0$.

Besides the spin variables, selection rules also apply for the dependence on the space coordinate [7, 36, 52]. From the definition of the oscillator strength (1.89, 1.96) it follows that the eigenfunctions of the optically allowed transitions transform like the unit representation. Therefore, in the presence of symmetries (translation, rotation), the eigenvalue problem can be drastically simplified and only the eigenvalues and eigenfunctions of a reduced Hamiltonian appear in the Elliott formula. This will be exemplified in the next subsection.

1.3.3 Examples

In the general case, the eigenvalue problem (1.93) cannot be solved exactly. Analytical solutions are known only for a few simplified models. These models are useful to approximately describe realistic semiconductors, to qualitatively study the structure of the optical spectrum, and to explain basic concepts, such as binding energy, oscillator strength, or Coulomb enhancement. In this subsection we will discuss the optical absorption of the three-dimensional and the ideal two-dimensional semiconductor in the two-band model. The three-dimensional case was treated in 1957 in the original paper by Elliott [46]. A couple of years later Shinada and Sugano derived an explicit expression for the ideal two-dimensional semiconductor [47]. The formulas for three and two dimensions are summarized in the textbook by Chuang [8].

In the two-band model (Sect. 1.2), the dipole matrix element, the exciton wavefunctions, and the optical susceptibility are scalars. The electron–hole Hamiltonian

$$\hat{\mathcal{H}} = E_g - \frac{\hbar^2}{2m_e} \Delta_e - \frac{\hbar^2}{2m_h} \Delta_h - \frac{e^2}{4\pi\epsilon_0\epsilon|\mathbf{r}_e - \mathbf{r}_h|} \quad (1.97)$$

is known from the three-dimensional Hydrogen problem and its eigenvalues and eigenfunctions are known exactly [1, 8]. We first perform a separation into center-of-mass and relative coordinates:

$$\begin{aligned} \mathbf{R} &= \frac{m_e \mathbf{r}_e + m_h \mathbf{r}_h}{M}; \quad \mathbf{r} = \mathbf{r}_e - \mathbf{r}_h \\ M &= m_e + m_h; \quad \frac{1}{m} = \frac{1}{m_e} + \frac{1}{m_h}. \end{aligned} \quad (1.98)$$

Then, the electron–hole Hamiltonian goes over into

$$\begin{aligned} \hat{\mathcal{H}} &= \hat{\mathcal{H}}_{\text{c.m.}} + \hat{\mathcal{H}}_{\text{rel}}; \quad \hat{\mathcal{H}}_{\text{c.m.}} = -\frac{\hbar^2}{2M} \Delta_{\mathbf{R}} \\ \hat{\mathcal{H}}_{\text{rel}} &= E_g - \frac{\hbar^2}{2M} \Delta_{\mathbf{r}} - \frac{e^2}{4\pi\epsilon_0\varepsilon r}. \end{aligned} \quad (1.99)$$

The eigenfunctions of the center-of-mass Hamiltonian are plane waves and the eigenfunctions and eigenvalues of $\hat{\mathcal{H}}$ can be written as

$$\Lambda = \mathbf{K}, \lambda; \quad \Phi_{\Lambda}(\mathbf{R}, \mathbf{r}) = \frac{1}{\sqrt{\Omega}} e^{i\mathbf{K}\cdot\mathbf{R}} \varphi_{\lambda}(\mathbf{r}); \quad \mathcal{E}_{\Lambda} = \frac{\hbar^2 K^2}{2M} + E_{\lambda}, \quad (1.100)$$

where E_{λ} and φ_{λ} are the eigenfunctions of $\hat{\mathcal{H}}_{\text{rel}}$. For the oscillator strength (1.96) it follows that

$$|F_{\Lambda}|^2 = |\mu|^2 \left| \frac{1}{\sqrt{\Omega}} \int d^3 \mathbf{R} \Phi_{\Lambda}(\mathbf{R}, \mathbf{r}=0) \right|^2 = |\mu|^2 \delta_{\mathbf{K}, \mathbf{0}} |\varphi_{\lambda}(\mathbf{r}=0)|^2. \quad (1.101)$$

Because the light wavevector was neglected (optical limit), only electron–hole pairs with zero total momentum are created and the center-of-mass motion does not affect the absorption spectrum. Thus the oscillator strength is determined by the eigenfunctions of the relative Hamiltonian $\hat{\mathcal{H}}_{\text{rel}}$, taken at $\mathbf{r} = 0$, which means that only spherically symmetric (s) states contribute to the optical absorption. They follow from a reduced Hamiltonian

$$\hat{\mathcal{H}}_{\text{red}} = E_g - \frac{\hbar^2}{2m} \frac{1}{r^2} \frac{d}{dr} (r^2 \frac{d}{dr}) - \frac{e^2}{4\pi\epsilon_0\varepsilon r}. \quad (1.102)$$

The bound states φ_{ns} with energies $E_n < E_g$ and the scattering states φ_{Es} with $E \geq E_g$ are normalized according to

$$\int_0^{\infty} dr 4\pi r^2 \begin{Bmatrix} \varphi_{ns}^*(r) \varphi_{n's}(r) \\ \varphi_{ns}^*(r) \varphi_{E's}(r) \\ \varphi_{Es}^*(r) \varphi_{E's}(r) \end{Bmatrix} = \begin{Bmatrix} \delta_{nn'} \\ 0 \\ \delta(E-E') \end{Bmatrix}. \quad (1.103)$$

Due to this “energy normalization” we replace the sum over the scattering states in the Elliott formula (1.96) by an integral over the energy (C.11) and the absorption becomes:

$$\alpha(\omega) = \frac{E_g}{\hbar c_0 n \varepsilon_0} |\mu|^2 \left\{ \sum_{n=1}^{\infty} |\varphi_{ns}(0)|^2 \pi \delta(\hbar\omega - E_n) + \Theta(\hbar\omega - E_g) \pi |\varphi_{\hbar\omega,s}(0)|^2 \right\}. \quad (1.104)$$

For $\hbar\omega < E_g$, the spectrum is made up of discrete lines, but becomes entirely continuous for $\hbar\omega \geq E_g$.

For the discussion below, we introduce dimensionless units $\hbar = m = e^2/4\pi\varepsilon_0\varepsilon = 1$ (excitonic Hartree units, see App. B.2), define the photon energy relative to the fundamental gap E_g , and set the prefactors in (1.104) equal to unity. In these units, the eigenfunctions at $r = 0$ and eigenvalues of (1.102) are (App. C.1.2)

$$\begin{aligned} |\varphi_{ns}(0)|^2 &= \frac{1}{\pi n^3}; \quad E_n = -\frac{1}{2n^2} \\ |\varphi_{Es}(0)|^2 &= \frac{1}{\pi} \frac{1}{1 - e^{-\frac{2\pi}{\sqrt{2E}}}}; \quad E \geq 0, \end{aligned} \quad (1.105)$$

leading to an absorption coefficient

$$\alpha(\omega) = \sum_{n=1}^{\infty} \frac{1}{n^3} \delta(\omega + \frac{1}{2n^2}) + \Theta(\omega) \frac{1}{1 - e^{-\frac{2\pi}{\sqrt{2\omega}}}}. \quad (1.106)$$

This is the famous Elliott formula for the optical absorption of a direct semiconductor, as it was presented in the original paper [46].

The bound states of the reduced Hamiltonian (1.102) result in a Rydberg series of sharp absorption lines, while the scattering states give rise to an absorption continuum. The peak largest in magnitude is located at $E_g - 1 \text{ Ry}^*$, where 1 Ry^* is the exciton binding energy (or exciton Rydberg, see App. B.2). The absorption coefficient $\alpha(\omega)$ is nonzero at $\omega = 0$, in contrast to the free-particle absorption. This is because the attractive Coulomb interaction increases the probability of finding the electron and hole at the same place. The discrete spectrum has a limit point at $\omega = 0$ and it holds that

$$\lim_{n \rightarrow \infty} \frac{|\varphi_{ns}(0)|^2}{E_{n+1} - E_n} = |\varphi_{E=0,s}(0)|^2, \quad (1.107)$$

which means that the discrete spectrum smoothly merges into the continuous spectrum [3].

For high energies, one would expect the absorption coefficient to be the same as for free particles. However, the asymptotic behavior of α for $\omega \rightarrow \infty$ is

$$\alpha(\omega) \sim \frac{\sqrt{2\omega}}{2\pi} + \frac{1}{2}, \quad (1.108)$$

which is equal to the free-particle absorption (1.56) plus a constant. The ratio between the absorption coefficient including Coulomb interaction and the free-particle absorption,

$$S(\omega) = \frac{2\pi}{\sqrt{2\omega} \left(1 - e^{-\frac{2\pi}{\sqrt{2\omega}}} \right)}, \quad (1.109)$$

known as Sommerfeld factor, goes to infinity for $\omega \rightarrow +0$ and to unity for $\omega \rightarrow \infty$.

In practice, due to homogeneous broadening, the lines of the discrete spectrum have a finite broadening. For a constant homogeneous broadening $\epsilon > 0$, the lineshape of the discrete transitions will be Lorentzian and the continuous absorption follows from the convolution of the continuous part in (1.106) with a Lorentzian distribution $\epsilon/[\pi(\omega^2+\epsilon^2)]$. This integral can easily be calculated numerically or analytically in terms of higher transcendental functions [73].

The same procedure can be applied to the ideal two-dimensional semiconductor [8, 47], which is used as a model to approximately describe excitons in quantum wells. With the eigenvalues and eigenfunctions of the two-dimensional Hydrogen atom (App. C.1.2), the dimensionless absorption coefficient becomes:

$$\alpha(\omega) = \sum_{n=1}^{\infty} \frac{1}{(n-\frac{1}{2})^3} \delta\left[\omega + \frac{1}{2(n-\frac{1}{2})^2}\right] + \Theta(\omega) \frac{1}{1 + e^{-\frac{2\pi}{\sqrt{2\omega}}}}. \quad (1.110)$$

Here, we have defined the photon energy $\hbar\omega$ relative to the gap of the two-dimensional semiconductor $E_g^{(2)}$. Equation (1.110) is the Elliott formula for the ideal two-dimensional semiconductor. Again, for $\omega < 0$ we have a Rydberg series of discrete lines, while the absorption spectrum for $\omega \geq 0$ is continuous. The absorption coefficient is nonzero for $\omega = +0$. Because the free-particle absorption (1.60) is also nonzero in this limit, the Sommerfeld factor remains finite, namely $S(0) = 2$. In the opposite limit, $\omega \rightarrow \infty$, the Sommerfeld factor goes to unity and, this time, the absorption including Coulomb interaction approaches the free-particle absorption.

Figure 1.5 shows the absorption coefficient for the three-dimensional semiconductor (left) and the ideal two-dimensional semiconductor (right). The absorption including Coulomb interaction (*solid line*) is compared with the free-particle absorption (*dotted line*). A homogeneous broadening $\epsilon = 0.1$ was introduced. Only the ground-state exciton is resolved, while the higher bound states give rise to a quasi-continuum, which smoothly merges into the continuum of scattering states. The continuous absorption near the band gap is drastically enhanced by the Coulomb interaction. The binding energy of the two-dimensional exciton is by a factor of 4 larger than for the three-dimensional exciton and the oscillator strength of the ground-state exciton, relative to the continuous spectrum, is 8 times larger.

The theoretical values for the two-dimensional exciton binding energy and oscillator strength are never reached in practice. The reason is that the extension of the eigenfunctions in growth direction cannot be made arbitrarily

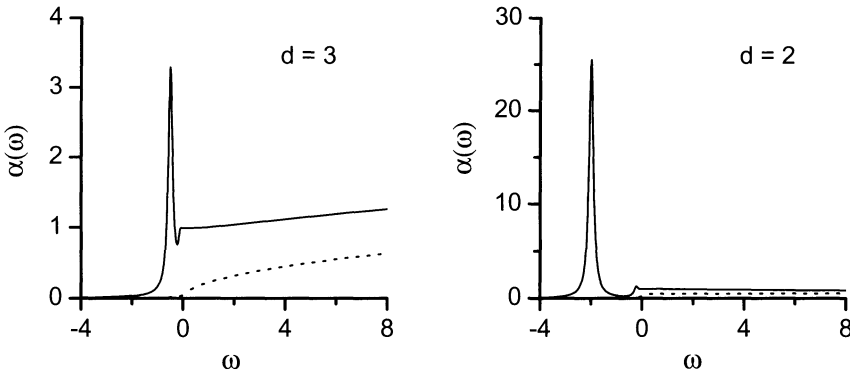


Fig. 1.5. Absorption coefficient versus frequency ω in excitonic Hartree units in three dimensions (left) and two dimensions (right). The absorption with Coulomb interaction (*solid line*) is compared with the free-particle absorption (*dotted line*)

small because of the finite barriers [7, 9–11, 38, 74]. Even for infinite barriers, the binding energy rapidly decreases with increasing well width [75].

The three- and two-dimensional exciton are special cases for the exciton in the d -dimensional space. Solutions can also be found for non-integer dimensions $d > 1$, which provide analytical approximations for the optical absorption of realistic low-dimensional semiconductors near the absorption edge[76]. For example, realistic two-dimensional semiconductors would have an effective dimension $2 < d < 3$ and realistic one-dimensional semiconductors a dimension between 1 and 2 [77]. The binding energy of the one-dimensional exciton is divergent, because the singularity of the Coulomb potential $1/|x|$ is not integrable. Sometimes, one-dimensional model potentials with integrable singularities are used for the description of excitons in quantum wires [78, 79]. In this case, the Sommerfeld factor is zero at the absorption edge.

Finally, we specify the ground-states wavefunction for the three-dimensional exciton in real units (s. App. C.1.2):

$$\varphi_{1s}(r) = \frac{1}{\sqrt{\pi a_B^{*3}}} e^{-r/a_B^*} . \quad (1.111)$$

The characteristic extension of φ_{1s} is the exciton Bohr radius a_B^* . Therefore, the effective-mass approximation is justified if

$$a_B^* \gg a_0 , \quad (1.112)$$

which is fulfilled for Wannier–Mott excitons. For GaAs it holds that $a_B^* = 120 \text{ \AA}$, which is much larger than the lattice constant $a_0 = 5.65 \text{ \AA}$.

1.4 Summary and Conclusions

In the first chapter we gave an overview of the band structure and optical transitions in bulk and low-dimensional semiconductors. The formalism introduced will be the basis for the understanding of the following chapters.

The effective-mass approximation is an intuitive method for the description of electrons in crystals. This theory can be generalized for external fields and heterostructures. Then the eigenfunctions are given by products of lattice-periodic functions and slowly varying envelope functions. In heterostructures, the modulations of the band edge act as additional potentials for electrons and holes. In low-dimensional semiconductors, which can be realized by geometric confinement or external fields, the motion of electrons and holes is restricted to less than three dimensions.

The interaction between light and matter is mediated by the momentum matrix elements between valence- and conduction-band states. Formally, the momentum matrix element can be rewritten as a dipole matrix element so that the interaction Hamiltonian takes the same form as for atomic systems. For interaction-free electrons, the optical absorption follows from Fermi's golden rule, leading to the optical density of states. The transition of an electron from the valence to the conduction band can be interpreted as the creation of an electron-hole pair. The optical density of states determines the dimensionality of a semiconductor.

If Coulomb interaction between electrons and holes is taken into account, the optical absorption is given by the Elliott formula, which relates the transition energies and oscillator strength to an eigenvalue problem of an electron-hole pair. The Elliott formula can be obtained by heuristic generalization of the interaction-free result, the method of Green's functions, or by linearization of the semiconductor Bloch equations, in the limit of a small optical field. For simple geometries, the electron-hole eigenvalue problem can be solved analytically. Exciton bound states are manifested in the optical absorption spectrum by sharp lines below the continuum edge. The continuum absorption, which results from scattering states of the exciton, is strongly enhanced, in comparison to the interaction-free result. Besides bound and scattering states, quantum resonances may be observed in the optical spectrum.

Table 1.5. Characteristic units for energy, length, time, electric field, and magnetic field for the Hydrogen atom and the GaAs exciton ($1 \text{ as} = 10^{-18} \text{ s}$)

Unit	[E]	[a]	[t]	[F]	[B]
Hydrogen atom	27.2 eV	0.529 Å	24.2 as	$5.14 \times 10^9 \text{ V/cm}$	$2.35 \times 10^5 \text{ T}$
GaAs Exciton	9.37 meV	117 Å	70.3 fs	$7.98 \times 10^3 \text{ V/cm}$	4.78 T

The exciton can be considered as an analog to the Hydrogen atom. However, the characteristic values for energy, length, time, electric and magnetic field for the hydrogen atom and the exciton differ by orders of magnitude. Therefore, one speaks also of mesoscopic systems. Several quantum phenomena, which cannot be observed in atomic systems, can be studied on excitons and vice versa. In Table 1.5, the characteristic values for energy, length, time, electric and magnetic field are compared for the hydrogen atom (microscopic scale) and the exciton in GaAs (mesoscopic scale). For the definition of dimensionless quantities, see App. B.2.

2 Numerical Calculation of the Optical Absorption in Low-Dimensional Semiconductors

In the last chapter we have seen that the optical absorption of a semiconductor is related to an effective Hamiltonian of an electron–hole pair, subjected to Coulomb interaction, geometric confinement, and external fields. Analytical solutions are available only for idealized cases such as the three-dimensional semiconductor [1], the two-dimensional semiconductor [2], a one-dimensional model semiconductor [3], or a d -dimensional semiconductor, where $d \in (1, \infty)$ [4]. A number of approximate analytical or numerical solutions have been derived for more complicated cases; some are in excellent agreement with today’s full numerical solutions. Such examples include the doped semiconductor, where the Coulomb potential is modified by Thomas–Fermi screening [5], and the bulk semiconductor in an electric field [6, 7].

The invention of semiconductor heterostructures [8] opened up the possibility to study quantum confinement in semiconductors. A number of new phenomena was observed, including dimensionality transitions, the quantum-confined Stark effect, Wannier–Stark ladders, motional narrowing, Fano interference, or Zener tunneling. For a theoretical understanding, it is crucial to perform accurate numerical calculations, because simplifying assumptions may result in a loss of important physical content. In fact, for many of those effects it is impossible even to estimate the order of magnitude without a numerical calculation.

Since the middle of the eighties, a number of low-dimensional semiconductors has been studied theoretically: quantum wells, superlattices, quantum wires, rough interfaces, both with and without external fields. The discretization of the Hamiltonian was performed using the eigenfunctions of the interaction-free electron–hole pair, cubic splines, finite elements, and finite differences; the optical absorption was calculated by standard matrix algebra, iterative methods, the equation-of-motion method, or the scattering approach.

In this chapter we give a systematic review on numerical methods for the calculation of the optical absorption in low-dimensional semiconductors. We shall introduce a highly efficient method, which is based upon the discretization of the Hamiltonian in real space and the solution of the initial-value problem in real time. Even though we limit ourselves to the linear absorption coefficient of a semiconductor in the thermodynamic ground state, the basic

computational techniques are very general and will be useful also for treating highly excited semiconductors, nonlinear optical response, electron–phonon interaction, or the calculation of the luminescence signal.

This chapter is organized as follows. In Sect. 2.1 we introduce the basic notations, give an overview of the literature, discuss various strategies based on exact or iterative methods, give an approximate classification scheme for the complexity of the problem, and specify five examples, which will be used as benchmark problems to test the capability of various numerical methods. Section 2.2 is devoted to the discretization of the operator by means of orthonormal base functions, nonorthonormal base functions, and finite differences. In Sect. 2.3 we describe the solution of the initial-value problem and the technique of absorbing boundary conditions. The numerical realization is explained in detail and demonstration programs are found in App. D. Summary and conclusions are given in Sect. 2.4.

Currently, there is no textbook which would approximately match the scope of this chapter. Detailed references will be given on the beginning of each section. For general reading on numerical mathematics we recommend the textbook by Schwarz, which covers a wide range of numerical methods [9], and the “Numerical Recipes,” a practical approach, which also comes with many program examples in Fortran or C [10]. The LAPACK (CLAPACK), available on the Internet, is a collection of Fortran (C) subroutines for numerical linear algebra, including the solution of linear sets of equations and eigenvalue problems.

2.1 Preliminaries

Using appropriate coordinates, the optical susceptibility in effective-mass approximation can be reduced to a handful quantities: the reduced electron–hole Hamiltonian, the dipole matrix element, the domain, and the boundary conditions. The complexity of the problem depends on the dimension of the partial differential equation and the number of scattering directions. One can roughly distinguish between three categories: one dimensional problems (class I), multi-dimensional problems with one scattering coordinate (class II), and multi-dimensional problems with more than one scattering coordinate (class III). We shall specify five examples belonging to these classes. They will be used in the next sections to test various numerical methods.

A straightforward method of calculating the optical absorption is the conversion of the effective Hamiltonian into a matrix and the solution of an algebraic eigenvalue problem or a set of equations by standard methods. We analyze the numerical effort and storage for different matrix patterns resulting from the discretization of the Hamiltonian. In principle, all problems of class I and class II can be dealt with by standard matrix algebra. Several nonstandard approaches (iterative methods, reformulation of the problem) have been proposed in the literature. Most of them are superior to standard

matrix algebra for specific structures, but cannot solve the general class-III problem. The solution of the initial-value problem is presently the most prospective method for the solution of class-III problems.

In this section we introduce the basic notations, specify the problem, and review the literature in the field. We give an overview of the numerical complexity for the solution by standard matrix algebra and discuss the potential of nonstandard approaches.

There is no shortage in books on numerical matrix algebra. Besides the textbook by Schwarz [9], we recommend the works by Jennings and McKeown [11], by Parlett [12], and by Golub and Van Loan [13]. A review on iterative methods for the solution of linear sets of equations is given in [14].

2.1.1 Formulation of the Problem

Throughout this chapter, we assume a two-band semiconductor and use dimensionless units $\hbar = m = e^2/(4\pi\varepsilon_0\varepsilon) = e = 1$ (App. B.2). The major advantage is that in a numerical calculation all quantities will be in the order of unity, instead of, for instance, 10^{-34} SI units. Furthermore, dimensionless units allow us to easily estimate whether a parameter is small, intermediate, or large. For example, a quantum well thickness $d = 0.25$ is considered small, which means that we are in the limit of strong confinement. A magnetic field $B = 3$ is considered large, as the cyclotron frequency $\omega_c = B$ is much larger than the binding energy of the three-dimensional exciton, which is equal to $\frac{1}{2}$. We shall also ignore the prefactors in the expression of the optical susceptibility (1.95) and the absorption coefficient (1.96). In these units the absorption coefficient is equal to the imaginary part of the optical susceptibility:

$$\alpha(\omega) = \text{Im } \chi(\omega) . \quad (2.1)$$

The generalization to degenerate bands is straightforward and the real units can easily be restored from the dimensionless expressions.

In the last chapter, we have seen that the optical susceptibility (1.95) can be determined from the eigenvalues and eigenstates of an electron-hole Hamiltonian by means of the Elliott formula:

$$\chi(\omega) = \sum_{\Lambda} \frac{|\langle \mu | \Phi_{\Lambda} \rangle|^2}{E_{\Lambda} - (\omega + i\epsilon)} \quad (2.2)$$

$$\hat{H} |\Phi_{\Lambda}\rangle = E_{\Lambda} |\Phi_{\Lambda}\rangle ; \quad \langle \Phi_{\Lambda} | \Phi_{\Lambda'} \rangle = \delta_{\Lambda\Lambda'} ; \quad \sum_{\Lambda} |\Phi_{\Lambda}\rangle \langle \Phi_{\Lambda}| = 1 .$$

Here, ϵ is a positive quantity, which takes into account the homogeneous line broadening. In this chapter we will generally consider discrete eigenstates, because the numerical calculations will always be done on a finite domain. Previously, the electron-hole amplitude in Fourier representation was expressed in terms of an inverse operator (1.92):

$$\chi(\omega) = \langle \mu | [\hat{H} - (\omega + i\epsilon)]^{-1} | \mu \rangle . \quad (2.3)$$

By Fourier transform, this expression is equal to:

$$\chi(\omega) = i \int_0^\infty dt e^{i(\omega+i\epsilon)t} \langle \mu | e^{-iHt} | \mu \rangle . \quad (2.4)$$

The latter formulation corresponds to the solution of the inhomogeneous Schrödinger equation for the electron-hole amplitude (1.90), which, for $E(t) \propto \delta(t)$ goes over in an initial-value problem of the homogeneous Schrödinger equation. All three equations (2.2–2.4) are equivalent and can be used as a basis for the numerical calculation of the optical absorption.

Expressions of the form (2.2) or (2.3) are also encountered in the description of light-matter interaction and of scattering processes in atomic and nuclear physics. Therefore, it is of general interest to have an efficient method for their numerical evaluation.

The number of coordinates and, therefore, the complexity of the problem, can often be reduced by exploiting the symmetry of the problem. It is sufficient to consider the projection of the Hamiltonian onto the smallest invariant subspace, which contains the dipole matrix element (see Sect. 1.3). To take into account the symmetries of the problem, we introduce curvilinear coordinates:

$$u = (u_1, \dots, u_l) \in G ; \quad g(u_1, \dots, u_l) > 0 \text{ a.e.} \quad (2.5)$$

$$\langle \Phi | \Psi \rangle = \int_G \underline{du} \Phi^*(u) \Psi(u) ; \quad \underline{du} = du_1 \cdots du_l g(u)$$

A set of functions $\{f_\alpha\}_{\alpha=1}^\infty$ is called an orthonormal base, if the relations

$$\begin{aligned} \int \underline{du} f_\alpha^*(u) f_\beta(u) &= \delta_{\alpha\beta} \\ \sum_{\alpha=1}^\infty f_\alpha(u) f_\alpha^*(u') &= \underline{\delta}(u, u') = \frac{\delta(u - u')}{\sqrt{g(u) g(u')}} , \end{aligned} \quad (2.6)$$

known as orthonormality and closure relation, are fulfilled. Of particular importance are products of one-dimensional coordinates, where the domain, the weight function, and the weighted delta function have the structure

$$\begin{aligned} G &= G_1 \times \cdots \times G_l ; \quad g(u) = g_1(u_1) \cdots g_l(u_l) \\ \underline{\delta}(u, u') &= \underline{\delta}_1(u_1, u'_1) \cdots \underline{\delta}_l(u_l, u'_l) . \end{aligned} \quad (2.7)$$

Examples are Cartesian, polar, cylindrical, and spherical coordinates. For these coordinates, the base functions can be chosen to be products of base functions for the individual coordinates:

$$f_\alpha(u) = f_{1\alpha_1}(u_1) \cdots f_{l\alpha_l}(u_l) . \quad (2.8)$$

In general coordinates the above expressions (2.2–2.4) for the optical susceptibility go over into ordinary or partial differential equations. Equation (2.2) is equivalent to an eigenvalue problem for a differential operator:

$$\begin{aligned} \chi(\omega) &= \sum_A \frac{|F_A|^2}{E_A - (\omega + i\epsilon)} ; \quad F_A = \int \underline{d}u \mu^*(u) \Phi_A(u) \\ \hat{H} \Phi_A(u) &= E_A \Phi_A(u) \\ \int \underline{d}u \Phi_A^*(u) \Phi_{A'}(u) &= \delta_{AA'} ; \quad \sum_A \Phi_A(u) \Phi_A(u') = \underline{\delta}(u, u') . \end{aligned} \quad (2.9)$$

The operator \hat{H} is Hermitian with respect to the scalar product (2.5). Once the eigenvalues and eigenfunctions are determined, the optical susceptibility can be calculated from the oscillator strengths $|F_A|^2$ for all ω . The representation of $\chi(\omega)$ in terms of an inverse operator (2.3) is equivalent to solving a boundary-value problem for a differential operator:

$$\chi(\omega) = \int \underline{d}u \mu^*(u) \Psi(u, \omega) ; \quad [\hat{H} - (\omega + i\epsilon)] \Psi(u, \omega) = \mu(u) , \quad (2.10)$$

where the operator $\hat{H} - (\omega + i\epsilon)$ is regular but non-Hermitian. This time, the equation has to be solved for each ω . Finally, the exponential of an operator (2.4) is calculated by solving an initial-boundary-value problem of a Schrödinger equation:

$$\begin{aligned} \chi(\omega) &= \lim_{T \rightarrow \infty} \int_0^T dt e^{i\omega t} P(t) ; \quad P(t) = e^{-\epsilon t} \int \underline{d}u \mu^*(u) \Psi(u, t) \\ i \frac{\partial}{\partial t} \Psi(u, t) &= \hat{H} \Psi(u, t) ; \quad \Psi(u, 0) = i \mu(u) . \end{aligned} \quad (2.11)$$

The function $P(t)$ plays the role of the polarization (1.91), when the optical field (1.90) is of the form $E(t) = \delta(t)$. The upper integration limit T has to be much larger than the inverse homogeneous broadening $1/\epsilon$; practically it is sufficient to terminate the integration at a value between $5/\epsilon$ and $8/\epsilon$. The equation of motion has to be solved only once and the optical spectrum is obtained by Fourier transform.

Equations (2.9–2.11) are very general and cover also representations in quasi-momentum (\mathbf{k}) space. In this case, the Hamiltonian \hat{H} is an integral operator. As the numerical solution of integral equations is less efficient than the solution of

the corresponding differential equation, we shall concentrate on the real-space (or Wannier) representation.

Before we give a number of examples for reduced problems, we show how the general case of a semiconductor structure with spatial variations of the band edge and external fields is reproduced. The Hamiltonian, domain, weight function, and dipole matrix element are identified with the expressions

$$\begin{aligned}\hat{H} = & \frac{1}{2m_e} \left[\frac{1}{i} \nabla_e + \mathbf{A}(\mathbf{r}_e) \right]^2 + \frac{1}{2m_h} \left[\frac{1}{i} \nabla_h - \mathbf{A}(\mathbf{r}_h) \right]^2 \\ & + W_e(\mathbf{r}_e) + W_h(\mathbf{r}_h) + \mathbf{F} \cdot (\mathbf{r}_e - \mathbf{r}_h) - \frac{1}{|\mathbf{r}_e - \mathbf{r}_h|} \\ G = & \Omega \times \Omega ; \quad g(\mathbf{r}_e, \mathbf{r}_h) \equiv 1 ; \quad \mu(\mathbf{r}_e, \mathbf{r}_h) = \frac{\delta(\mathbf{r}_e - \mathbf{r}_h)}{\sqrt{\Omega^{(d)}}} .\end{aligned}\quad (2.12)$$

This Hamiltonian is a special case of (1.88) for the two-band model. The domain is the three-dimensional normalization volume Ω for both coordinates \mathbf{r}_e and \mathbf{r}_h , so the mathematical dimension is $l = 6$. A factor $1/\sqrt{\Omega^{(d)}}$ is included in the definition of the dipole matrix element, in order to reproduce the prefactor $1/\Omega^{(d)}$ in (1.95) and (1.96). The effective electron and hole masses $m_{e,h}$ are given in units of the reduced mass. The dimension¹ m of the unbound motion depends on the external fields \mathbf{A}, \mathbf{F} and the potentials $W_{e,h}$.

The reduction of the six-dimensional problem (2.12) to fewer coordinates is straightforward in most cases (see Sect. 1.3). In the presence of a homogeneous magnetic field, the separation of center-of-mass and relative motion is somewhat more involved (App. C.1.2). In the following we give five examples, which will be used as benchmark problems to study various numerical methods.

A. Ideal two-dimensional semiconductor in a perpendicular magnetic field

The reduced eigenvalue problem (see App. C.1.2) is mathematically one-dimensional ($l = 1$) and the eigenfunctions depend only on the radial coordinate of the relative motion:

$$\begin{aligned}\hat{H} = & -\frac{1}{2} \frac{1}{\varrho} \frac{\partial}{\partial \varrho} \left(\varrho \frac{\partial}{\partial \varrho} \right) - \frac{1}{\varrho} + \frac{1}{8} B^2 \varrho^2 \\ G = & [0, \infty) ; \quad g(\varrho) = 2\pi\varrho ; \quad \mu(\varrho) = \frac{\delta(\varrho)}{2\pi\varrho} .\end{aligned}\quad (2.13)$$

In dimensionless units, the cyclotron frequency ω_c is equal to the magnetic field strength. For $B = 0$, the motion is unbound ($m = 1$) and we observe

¹ Here $m \in \mathbb{N}_0$ is not to be confused with the reduced mass, which was set to 1 by the introduction of dimensionless quantities.

a Rydberg series of discrete eigenvalues and a one-parametric continuum. In contrast, for $B \neq 0$, the motion is confined ($m = 0$) and the spectrum is completely discrete. Analytical solutions are known for zero magnetic field (1.110) and for the case that the Coulomb interaction is neglected (1.68), but not in-between these limiting cases.

B. Ideal quantum well with finite thickness

The eigenvalue problem is three-dimensional ($l = 3$) with the radial coordinate for the in-plane motion and the electron and hole coordinates in growth direction:

$$\hat{H} = -\frac{1}{2} \frac{1}{\varrho} \frac{\partial}{\partial \varrho} \left(\varrho \frac{\partial}{\partial \varrho} \right) - \frac{1}{2m_e} \frac{\partial^2}{\partial z_e^2} - \frac{1}{2m_h} \frac{\partial^2}{\partial z_h^2} - \frac{1}{\sqrt{\varrho^2 + (z_e - z_h)^2}} - \frac{\pi^2}{2d^2}$$

$$G = G_\varrho \times G_{z_e} \times G_{z_h}; \quad G_\varrho = [0, \infty); \quad G_{z_e} = G_{z_h} = [\![0, d]\!] \quad (2.14)$$

$$g(\varrho, z_e, z_h) = 2\pi\varrho; \quad \mu(\varrho, z_e, z_h) = \frac{\delta(\varrho)}{2\pi\varrho} \delta(z_e - z_h).$$

Here, we have assumed isotropic electron and hole masses and m_e and m_h in the above equation are dimensionless quantities, given in units of the reduced mass. The infinite barriers are modeled by finite intervals for the motion in the z direction and vanishing boundary conditions $\![0, d]\!$. The two-dimensional continuum edge $\pi^2/(2d^2)$ was subtracted from the Hamiltonian. The spectrum of \hat{H} for $F \geq 0$ is a one-parametric continuum ($m = 1$). The solution is trivial if the Coulomb interaction is neglected (1.59). In the presence of Coulomb interaction, no analytical solution is available, except in the limit $d \rightarrow 0$, which gives the ideal two-dimensional semiconductor (1.110).

C. Ideal two-dimensional semiconductor in Cartesian coordinates

The optical susceptibility follows from:

$$\hat{H} = -\frac{1}{2} \left(\frac{\partial^2}{\partial x^2} + \frac{\partial^2}{\partial y^2} \right) - \frac{1}{\sqrt{x^2 + y^2}} \quad (2.15)$$

$$G = \mathbb{R}^2; \quad g(x, y) \equiv 1; \quad \mu(x, y) = \delta(x) \delta(y).$$

This is not truly a reduced problem and the separation in polar coordinates would lead to Example A for $B = 0$. Nevertheless, we shall perform a numerical calculation in Cartesian coordinates as an example for a two-dimensional problem ($l = 2$) with a two-parametric continuum ($m = 2$). Analytical solutions are available with Coulomb interaction (1.110) and without Coulomb interaction (1.60).

D. Exciton in a stochastic potential

If the internal motion of the exciton is neglected, the optical susceptibility is determined by the center-of-mass motion of an exciton in a stochastic potential:

$$\hat{H} = -\frac{1}{2}\left(\frac{\partial^2}{\partial x^2} + \frac{\partial^2}{\partial y^2}\right) + W(x, y) \quad (2.16)$$

$$G = \left[-\frac{L_x}{2}, +\frac{L_x}{2}\right] \times \left[-\frac{L_y}{2}, +\frac{L_y}{2}\right] ; \quad g(x, y) \equiv 1 ; \quad \mu(x, y) = \frac{1}{\sqrt{L_x L_y}} .$$

This time, the total exciton mass $M = m_e + m_h$ is set to unity for the definition of the dimensionless units. The system is macroscopically homogeneous and isotropic, which means that the autocorrelation function of the stochastic potential $\langle\langle W(x, y) W(x', y') \rangle\rangle$ depends only on $\sqrt{(x-x')^2 + (y-y')^2}$. We make use of cyclic boundary conditions [., .[to model the infinite domain, because they are compatible with the transition matrix element μ and the stochastic potential W . Like Example C, the problem is two-dimensional ($l = 2$) with unbound motion in both directions ($m = 2$).

E. Bulk semiconductor in an electric field

In cylindrical coordinates, when the direction of the electric field \mathbf{F} is identified with the z direction, the eigenvalue problem

$$\begin{aligned} \hat{H} &= -\frac{1}{2} \frac{1}{\varrho} \frac{\partial}{\partial \varrho} \left(\varrho \frac{\partial}{\partial \varrho} \right) - \frac{1}{2} \frac{\partial^2}{\partial z^2} - \frac{1}{\sqrt{\varrho^2 + z^2}} + Fz \\ G &= G_\varrho \times G_z ; \quad G_\varrho = [0, \infty) ; \quad G_z = (-\infty, +\infty) \end{aligned} \quad (2.17)$$

$$g(\varrho, z) = 2\pi\varrho ; \quad \mu(\varrho, z) = \frac{\delta(\varrho)}{2\pi\varrho} \delta(z) .$$

is two-dimensional ($l = 2$). For $F \neq 0$, the spectrum of the operator is entirely continuous and is identical to the real axis. The continuum is two-parametric ($m = 2$) both for $F = 0$ and for $F \neq 0$ because of the contributions both from the ϱ and from the z motion. Analytical solutions are known for $F = 0$ (1.106) and for $F \neq 0$ without Coulomb interaction (1.72). An approximate numerical solution has been presented thirty years ago by Blossey [6].

2.1.2 Overview

In this subsection we give an overview about methods of calculating the optical susceptibility of low-dimensional semiconductors. The numerical solution

has many facets: formulation, preparation, numerical effort, storage, implementation, flexibility. Although the main focus is on low numerical effort and storage, we favor methods that are straightforward, conceptually simple, and easy to use.

To model realistic systems, one may need to take into account band mixing, anisotropy, nonparabolicity, finite barriers, and dielectric mismatch. Even though these details result in much extra work, they do not fundamentally change the complexity. From the point of view of the numerical complexity, very approximately, we distinguish between the following three categories.

Class I. The problem is mathematically one-dimensional ($l = 1$). In this case, both the eigenvalue problem and the boundary-value problem are ordinary differential equations. Very few idealized models like Example A belong to class I. A large number of numerical methods is capable of treating class-I problems.

Class II. The problem has more than one dimension ($l > 1$). The continuum is either one-parametric ($m = 1$), or there is one pronounced scattering direction. The main characteristics of this class is that the boundary-value problem of a partial differential equation can be converted to a set of ordinary differential equations, which is the basis for several numerical methods. The majority of problems found in the literature belongs to this class, a typical representative is Example B.

Class III. The problem has many scattering directions $m > 1$. Examples C–E belong to this category. In some cases, reformulation as a class-II problem may be possible. Otherwise, very few numerical methods can handle class-III problems.

Important examples for the classes I, II, and III with references are shown in Table 2.1. The references are selected from the numerical point of view and do not cover analytical or partially analytical results.

We mention that the class of complexity may depend on the approximations made in the numerical modeling. A prominent example is the Kane approximation for the single-particle eigenstates of a superlattice in a perpendicular electric field, which reduces a class-III problem to a problem of class II. In this approximation, the spectrum is continuous only for the in-plane motion, while in reality the spectrum is continuous for all space directions. We shall discuss the physical consequences in Chap. 4.

Somewhat distinct from the above categories are quantum dots. They have usually a low symmetry and the mathematical dimension can be as high as six. The two-band model is often a too coarse approximation so that all eight components of the exciton wavefunction have to be considered. What simplifies the problem considerably is the fact that the optical spectrum is entirely discrete and only a few (say, twenty) lowest eigenstates are of interest. A discussion of various strategies can be found in [50]. An efficient method for calculating the ground state was developed by the present author [51], which could also be generalized to calculate the lowest excited states.

Table 2.1. Classification scheme for the numerical complexity, examples, and references

Class	l	m	Examples	References
I	1	0	ideal two-dim. semiconductor + \mathbf{B}_\perp	[15]
	1	1	ideal d -dimensional semiconductor	[16]
	1	1	stochastic potential in one dimension	[17, 18]
II	2	1	bulk semiconductor + \mathbf{B}	[19]
	3	1	superlattice + \mathbf{B}_\perp	[20–22]
	3	1	superlattice + \mathbf{F}_\perp (approx.)	[21, 23–26]
	3	1	superlattice + $\mathbf{F}_\perp + \mathbf{B}_\perp$ (exact)	[27]
	3	1	quantum well	[28–34]
	3	1	quantum well + \mathbf{F}_\perp (approx.)	[29, 35–37]
	3	1	quantum-well wire	[38, 39]
	3	1	quantum-well wire + \mathbf{B}_\perp	[40]
III	2	2	stochastic potential in two dimensions	[41–43]
	2	2	bulk semiconductor + \mathbf{F}_\perp	[44]
	3	2	superlattice	[21–24, 41, 45–47]
	3	2	superlattice, quantum well + \mathbf{F}_\perp	[27, 44, 48]
	4	2	superlattice + $\mathbf{F}_\perp + \mathbf{B}_\parallel$ (approx.)	[49]

The solution by standard matrix algebra has a number of advantages. First, there is a well-defined interface between physics and numerics. Second, standard methods are usually easy to use, software is readily available, and there exist efficient implementations, some of them being optimized for supercomputers. Basically all class-I and -II problems can be solved by standard methods. The solution of eigenvalue problems or boundary-value problems of differential operators by exact methods consists of two stages: the discretization of the differential operator and the solution of an algebraic problem. The discretization can be performed using orthonormal base functions, finite elements, finite differences, or a combination of the three methods. The resulting matrix has $N \times N$ elements and can be fully occupied, banded, tridiagonal, or irregularly sparse. We define the bandwidth as the smallest number B with

$$H_{ij} = 0 \quad \text{for } |i - j| > B . \quad (2.18)$$

Since we are primarily interested in the order of magnitude, the following figures for the storage and computational effort are independent of the specific definition of B . Orthonormal base functions lead to fully occupied matrices. Band matrices result from the discretization of multi-dimensional problems by means of finite differences and finite elements, or a combination of these methods with one-particle or general-purpose base functions. For the solution of class-II problems, it is important to achieve a small bandwidth $B \ll N$. Tridiagonal matrices are obtained from the discretization of mathematically one-dimensional problems by first-order finite elements or finite differences;

the discretization of those problems by finite elements or finite differences of higher order results in band matrices, where the bandwidth is small, typically $B \leq 3$. For class-I problems, cubic splines lead to band matrices with an effective bandwidth $B \leq 10$, which means that the other matrix elements are vanishingly small and can be neglected.

Table 2.2 summarizes the storage necessary for various matrix patterns resulting from the discretization of the differential operator. The storage of the full matrix is practicable only for class-I problems and some class-II problems. For class-III problems, N is huge, typically in the order of 10^6 , and such problems can be treated only by methods for general sparse matrices.

Table 2.2. Matrix patterns and memory for the discretization of the differential operators for problems of class I, II, and III

Matrix pattern	Base functions	Memory		
		Class I	Class II	Class III
full	orthonormal	$O(N^2)$	$[O(N^2)]$	∞
banded	finite elements, finite differences, combination	$O(NB)$ $B \leq 3$	$O(NB)$	∞
tridiagonal	finite elements, finite differences	$O(N)$	—	—
irregularly sparse	finite elements, finite differences	—	$O(N)$	$O(N)$

Having discretized the partial differential operator, the optical susceptibility can be calculated by solving an algebraic ordinary or generalized eigenvalue problem, or a linear set of equations. Although diagonalization of full, banded, or tridiagonal matrices is in principle an iterative method, we shall employ the term “exact diagonalization,” because these methods behave like exact methods. The number of eigenvalues L required for the calculation of $\chi(\omega)$ by (2.9) can be as low as 10, like in Example A for $B \neq 0$, or in the same order as N , if continuum states are involved. In order to numerically solve (2.10), the linear set of equations has to be solved for W frequencies, with W being in the order of 1000, independent of the problem.

Table 2.3 summarizes the numerical effort for calculating $\chi(\omega)$ by means of an algebraic eigenvalue problem or a linear set of equations for different matrices resulting from the discretization of the differential operator. For full matrices, solving the eigenvalue problem is faster than solving a linear set of equations for each ω and there is no major difference if some or all eigenvalues are calculated. For band matrices, solving the boundary-value

problem is preferred. For tridiagonal matrices, the numerical effort is usually not an important issue. There is no efficient way of treating irregularly sparse matrices by exact methods. The limitations arise both from storage and from computational effort.

Table 2.3. Numerical effort for solving the eigenvalue and boundary-value problem by exact methods

Class	Matrix pattern	Numerical effort	
		Eigenvalue problem	Boundary-value problem
I, [II]	full	$O(N^3)$	$O(WN^3)$
I, II	banded	$O(N^2B) + O(LNB^2)$	$O(WNB^2)$
I	tridiagonal	$O(LN)$	$O(WN)$
III	irreg. sparse	∞	∞

Exact methods have been extensively used in the last 15 years to calculate the optical absorption of low-dimensional semiconductors and still have some importance today. Traditionally, the eigenfunctions of the interaction-free electron–hole pair, the “unperturbed problem,” are used to transform the eigenvalue or the boundary-value problem into an algebraic problem. This method has been applied to quantum wells and superlattices, without and with external fields [15, 25, 28, 29, 31, 33, 35, 37]. Unless the matrix elements are known analytically, which is the case only for idealized systems [15, 32], they have to be evaluated by numerical integration [25, 28, 29, 33, 35, 37]. For the directions of free motion, the eigenfunctions are plane waves and the Coulomb potential goes over into an integral operator. The Coulomb integral has been discretized by quadrature methods [25, 31, 33, 35, 37] or by nonorthonormal base functions [28, 29]. The above methods result in full matrices and the spectrum is calculated by exact solution of an ordinary eigenvalue problem [15, 25, 31, 33, 35, 37], a generalized eigenvalue problem [28, 29], or a linear set of equations [35]. The largest matrix dimension N reported is in the order of a few thousand [33]. The limitation of this method is obvious: the number of numerical eigenvalues, which contribute to the spectrum, cannot be larger than N , and N is severely restricted by storage and by computing time. Therefore, only a one-parametric continuum can be treated in a limited energy region. In some cases, like highly excited semiconductors, the electron–hole Hamiltonian is non-Hermitian and absorption, gain, or luminescence spectra need to be calculated by solving a set of equations with a full matrix [52–54]. The method of solving a boundary-value problem with band matrices has been used by the author for the bulk semiconductor in a magnetic field, quantum wells, and quantum-well wires [19, 55], where the base functions in the confinement directions were one-particle base functions in the case of strong confinement or cubic splines. Due to band storage, the total number of

base functions can be considerably higher than for full matrices, in the order of 100 000. Therefore, most class-II two problems can be treated by band matrices and the continuous absorption can be studied in a larger region. On the other hand, to achieve a small bandwidth, the number of base functions has to be small with the exception of one continuum direction. For tridiagonal matrices, a few million base functions or grid points could be easily handled, but this is usually not necessary for one-dimensional problems. The exciton in a stochastic potential in one dimension has been treated with $N = 2^{17}$ base functions [17].

We have seen that standard methods are not suitable for large-scale problems, in particular for those of category III. Several alternatives have been proposed: the scattering approach, iterative methods, and the solution of a time-dependent Schrödinger equation. Here, we shall examine these methods with respect to their usefulness to solve class-III problems.

The scattering approach, an established method in nuclear, atomic, and molecular physics, can be used to solve the boundary-value problem [16, 24] or the eigenvalue problem [34, 40]. The method is based upon rewriting the partial differential equation as a set of ordinary differential equations for one scattering coordinate and is therefore a typical class-II method, very likely the most efficient one. Several techniques like hyperspherical coordinates, the adiabatic approximation, and the R -matrix method have been developed over decades, which allow the treatment of difficult problems with a high numerical accuracy. A major advantage of the scattering approach is that the homogeneous broadening can be made very small, which is favorable for studying natural lineshapes [21, 24, 30, 34, 39, 40].

Iterative diagonalization usually gives only a few reliable eigenpairs and has difficulties with degenerate or closely spaces eigenvalues. Therefore, in the original form, it is useful only for quantum dots, where the spectrum is fully discrete and only a few tens of eigenstates are required. In 1980, Haydock proposed a method of evaluating expressions of the form (2.10) for large-scale quantum systems on the basis of the Lanczos algorithm [56, 57]. This recursion method was adapted by Chang and coworkers to calculate optical spectra for quantum wells and superlattices, including staggered band alignment [20, 36, 45, 46]. As the discretization of the Hamiltonian was done in \mathbf{k} space, these calculations did not yet exploit the full potential of the method. In fact, a number of similar problems were treated by standard matrix algebra [31, 33]. Recently, Di Stefano et al. combined Lanczos recursion with discretization in real space to simulate the near-field optical response of rough interfaces in one [18] and two dimensions [43]. The latter problem belongs to class III. Lanczos recursion has also been successfully applied to electron–phonon interaction [58], which has a complexity comparable to class III.

There is a couple of iterative methods for the numerical solution of sets of equations with large sparse matrices, which result from discretizing par-

tial differential equations. A review is given in [14]. So far, only a very few iterative methods have been successfully applied to the calculation of optical spectra. Recently, Ahland et al. solved some class-III problems, including bulk semiconductors and superlattices in an electric field, using a variant of the conjugate-gradient method [44]. At present, there is not sufficient evidence that the general class-III problem can be solved by iterative methods.

In the last decade, solution of time-dependent Schrödinger equations has been used to calculate densities of states and various response functions. It was predicted already in 1984 by MacKinnon that this method could be more efficient than Lanczos recursion [59]. In a review article, Kosloff compared various time-dependent and stationary methods for molecular dynamics [60]. In material science, this equation-of-motion method is used to calculate the densities of states and linear and nonlinear optical susceptibilities for nanocrystals and amorphous solids [61–64].

In 1996, the author described a method of calculating the optical susceptibility of low-dimensional semiconductors in effective-mass approximation by solving the initial-value problem (2.11). Due to discretization of the differential operator in real space and the explicit time-propagation scheme, memory and numerical effort scale like $O(N)$ [41]. In the last years, a number of time-dependent calculations have been reported, including quantum wells, quantum-well wires, type-I and type-II superlattices, superlattices in electric fields, excitons in stochastic potentials in two dimensions, quantum dots, and the quantum-confined Stark effect [22, 26, 32, 42, 47, 48, 65, 66]. A major progress is the introduction of absorbing boundary conditions, which leads to a significant reduction of both memory and numerical effort [67]. This allowed us to calculate the optical absorption of a superlattice in the regime of the Zener breakdown [27]. Very recently, absorbing boundary conditions were used to treat the superlattice in the Voigt geometry [49]. Even under the assumption of Wannier–Stark ladders, this is the most complicated problem listed in Table 2.1 with $l = 4$ and $m = 2$.

Time-dependent calculations have also been successfully applied to calculate optical spectra for electron–phonon interaction [68, 69] and for indirect semiconductors in the Bloch representation [70]. As a conceptually simple, highly efficient, and very flexible method, the equation-of-motion method is worthwhile to be explored in detail. This will be done in Sect. 2.3.

2.2 Approximation in Space

The solution of the eigenvalue, boundary-value, or initial-value problem requires the conversion of the operator into a matrix. One method is the approximation of functions by orthonormal or nonorthonormal base functions. The approximation of functions automatically entails approximations of operators, the scalar product, and the delta function. The procedure can be considered as projection onto a finite-dimensional subspace of the Hilbert

space. Of particular interest are general-purpose base functions like splines or base functions with a finite support. The latter functions lead to sparse matrices, which drastically reduces the storage and numerical effort.

Another possibility are finite differences. Here the philosophy is to approximate the differential operator. Finite differences are generally faster and easier to implement than finite elements. On the other hand, they also require more theoretical preparations. Special care needs to be taken for the scalar product, the delta function, the preservation of Hermiticity, and singular potentials.

In this section we explain the discretization of the differential operator by means of orthonormal base functions, nonorthonormal base functions, and finite differences. We discuss a strategy to reduce the bandwidth, which will allow us to solve the general class-II problem. We also give estimates for the length of the interval and the number of base functions necessary to model continuum states by a quasi-continuum of discrete resonances.

For general reading on finite differences we recommend the standard work of Richtmyer and Morton [71] and the books by Strikwerda [72] and by Ames [73]. The book by Celia and Gray [74] covers both finite differences and finite elements.

2.2.1 Orthonormal Base Functions

The eigenvalue problem (2.9) can be rewritten as a variational problem (App. C.1):

$$\begin{aligned} E[\Phi] &= \langle \Phi | \hat{H} | \Phi \rangle = \int \underline{d}u \Phi^*(u) \hat{H} \Phi(u) = \text{extr} \\ I[\Phi] &= \|\Phi\|^2 = \langle \Phi | \Phi \rangle = \int \underline{d}u |\Phi(u)|^2 = 1 . \end{aligned} \quad (2.19)$$

To solve (2.19) approximately for the first L eigenvalues and eigenfunctions, we expand Φ into a finite number of orthonormal base functions (2.6) according to

$$\Phi(u) = \sum_{\alpha=0}^{N-1} \Phi_\alpha f_\alpha(u) ; \quad L \leq N < \infty . \quad (2.20)$$

Then the functionals E and I are then functions of the coefficients Φ_α :

$$E[\Phi] = \Phi_\alpha^* H_{\alpha\beta} \Phi_\beta ; \quad H_{\alpha\beta} = \langle f_\alpha | \hat{H} | f_\beta \rangle ; \quad I[\Phi] = \Phi_\alpha^* \Phi_\alpha . \quad (2.21)$$

Here and in the following, we adopt the sum convention over double indices, i.e.,

$$\cdots \alpha \cdots \alpha = \sum_{\alpha=0}^{N-1} \cdots \alpha \cdots \alpha . \quad (2.22)$$

A necessary condition for an extremum of E under the constraint $I = 1$ is

$$\frac{\partial E}{\partial \Phi_\alpha^*} - \lambda \frac{\partial I}{\partial \Phi_\alpha^*} = 0 \quad (2.23)$$

with the Lagrange multiplier λ . Carrying out the partial derivatives and comparison with (2.19) yields the approximate eigenfunctions and eigenvalues

$$\begin{aligned} \Phi_A &= \Phi_{A;\alpha} f_\alpha(u) ; \quad H_{\alpha\beta} \Phi_{A;\beta} = E_A \Phi_{A;\alpha} \\ \Phi_{A;\alpha} \Phi_{A';\alpha} &= \delta_{AA'} ; \quad E_A = E[\Phi_A] \end{aligned} \quad (2.24)$$

for $A = 1, \dots, L$. Then the optical susceptibility (2.2) is approximately equal to

$$\chi(\omega) = \sum_{A=1}^L \frac{|F_A|^2}{E_A - (\omega + i\epsilon)} ; \quad F_A = \mu_\alpha^* \Phi_{A;\alpha} ; \quad \mu_\alpha = \langle f_\alpha | \mu \rangle . \quad (2.25)$$

The eigenvalue problem of the $N \times N$ matrix needs to be solved once and then the optical susceptibility is calculated for each frequency ω .

It is worthwhile to discuss some properties of the approximation (2.25). For $\epsilon > 0$ and $\omega < \omega_{\max}$, ω_{\max} fixed, the imaginary part of $\chi(\omega)$ converges towards the exact solution for $L, N \rightarrow \infty$. As the sum is finite, the Kramers–Kronig relations (A.14) are always fulfilled, which, as an artifact of the effective-mass approximation, may not be the case for the exact solution, because the real part becomes divergent. Even then, the divergence of $\text{Re } \chi(\omega)$ for $L \rightarrow \infty$ is only logarithmical and does not lead to numerical problems. To achieve a high accuracy of the first L eigenpairs, the number of base functions N has to be much larger than L . On the other hand, the remaining $N - L$ eigenvalues lie far outside the frequency range under consideration and it makes no difference if N is used instead of L for the upper limit of the sum (2.25). In practical calculations, the sum can also be terminated at some cutoff energy.

The boundary-value problem (2.10) can also be derived from a variational principle. In a strong formulation, the residual

$$R(u, \omega) = \mu(u) - [\hat{H} - (\omega + i\epsilon)] \Psi(u, \omega) \quad (2.26)$$

is to be minimized as function of N unknown variables $\Psi_0(\omega), \dots, \Psi_{N-1}(\omega)$, which are the expansion coefficients for the solution

$$\Psi(u, \omega) = \Psi_\alpha(\omega) f_\alpha(u) . \quad (2.27)$$

However, if $|\mu\rangle$ is not normalizable, then $\|R\|$ is also infinite. A weaker formulation is the method of weighted residuals [73, 74], which requests that

$$\langle w_\alpha | R(\omega) \rangle = 0 \quad (2.28)$$

for N weight functions w_0, \dots, w_{N-1} , which are N conditions for the N unknown Ψ_α . There are different methods for the choice of the weight functions. The best known is the method of Bubnov–Galerkin [73, 74], which uses the base functions f_α as weight functions. This is equivalent to the condition that the residual $|R\rangle$ lies outside the subspace spanned by the base elements $|f_1\rangle, \dots, |f_{N-1}\rangle$. Then (2.26–2.28) result in a set of N equations

$$[H_{\alpha\beta} - (\omega + i\epsilon) \delta_{\alpha\beta}] \Psi_\beta(\omega) = \mu_\alpha \quad (2.29)$$

and the optical susceptibility (2.3) becomes

$$\chi(\omega) = \mu_\alpha^* \Psi_\alpha(\omega) . \quad (2.30)$$

The algebraic equations (2.29–2.30) are equivalent to (2.24–2.25) for $L = N$. The numerical solution requires the solution of a set of equations for each ω .

The initial-value problem (2.11) is reduced to a set of differential equations by discretizing the space coordinates (method of lines). The projection onto the N -dimensional subspace of the $\{f_\alpha\}$ results in the following equations:

$$P(t) = e^{-\epsilon t} \mu_\alpha^* \Psi_\alpha(t) ; \quad i \frac{d}{dt} \Psi_\alpha(t) = H_{\alpha\beta} \Psi_\beta(t) ; \quad \Psi_\alpha(0) = i \mu_\alpha . \quad (2.31)$$

By Fourier transform, this is equivalent to (2.29–2.30). The initial-value problem for a set of N coupled differential equations needs to be solved once. Then the spectrum is calculated by means of fast Fourier transform (FFT).

The matrix eigenvalue problem (2.24–2.25) and the set of equations (2.29–2.30) are equivalent and give the same result within machine precision. For the initial-value problem (2.31), which is a linear set of differential equations, a very small error is introduced by the time-propagation, the discrete Fourier transform, and the truncation of the integration. Otherwise, the result is identical to the solution of the eigenvalue or the boundary-value problem.

Orthonormal base functions can be obtained from the analytic solution of the eigenproblem of some unperturbed operator $\hat{H}^{(0)}$, for example the operator of the interaction-free electron–hole pair or the operator of the kinetic energy. The spectrum of $\hat{H}^{(0)}$ has to be entirely discrete, in order to yield an orthonormal and complete set of normalizable eigenfunctions. A discrete spectrum is found only for the $l - m$ confinement directions. For the n directions of unbound motion, artificial boundary conditions have to be introduced to discretize the spectrum. Estimates for the size of the normalization domain will be given in the next subsection.

We shall now demonstrate the use of orthonormal base functions in the case of Example A. To many, the natural choice of base functions are the eigenfunctions of the interaction-free part of the Hamiltonian

$$\hat{H}^{(0)} = -\frac{1}{2} \Delta_\varrho + \frac{B^2 \varrho^2}{8} . \quad (2.32)$$

They can be given in explicit form in terms of Laguerre functions (App. C.1.2):

$$f_n(\varrho) = \Phi_n^{(0)}(\varrho) = \sqrt{\frac{B}{2\pi}} e^{-\frac{B\varrho^2}{4}} L_n\left(\frac{B\varrho^2}{2}\right)$$

$$E_n^{(0)} = B(n + \frac{1}{2}) ; \quad n \in \mathbb{N}_0 , \quad (2.33)$$

where we assumed that $B > 0$. If we insert these approximate eigenvalues and eigenfunctions into (2.9), we immediately obtain the optical density of states of a two-dimensional semiconductor in a magnetic field (1.68).

Another variant is to declare the operator of the kinetic energy

$$\hat{H}^{(0)} = \hat{H}_{\text{kin}} = -\frac{1}{2} \Delta_{\varrho} = -\frac{1}{2} \frac{1}{\varrho} \frac{d}{d\varrho} (\varrho \frac{d}{d\varrho}) . \quad (2.34)$$

to be the Hamiltonian of the unperturbed problem. For semi-vanishing boundary conditions $[0, R]$, the spectrum is a pure point spectrum. In the numerical calculation, the domain radius R depends on the spectral range under consideration and the magnetic field. The normalized eigenfunctions and eigenvalues are (App. C.1.2)

$$f_n(\varrho) = \frac{1}{\sqrt{\pi} R |J'_0(x_n)|} J_0\left(\frac{x_n \varrho}{R}\right) ; \quad E_n^{(0)} = \frac{1}{2} \left(\frac{x_n}{R}\right)^2 ; \quad n \in \mathbb{N} . \quad (2.35)$$

An alternative to the eigenfunctions of a Hermitian operator are general-purpose base functions. Important examples are orthogonal polynomials, wavelets, B-splines or cubic splines. In the case of superlattices, Wannier or Kane functions play an important role (Chap. 4).

We shall consider cubic splines in more detail [9, 10, 75]. Given an interval $[a, b]$, a sequence of nodes $a = u_0 < u_1 < \dots < u_{N-1} < u_N = b$, and a real-valued function Φ . A cubic spline approximation s of the function Φ is a polynomial of degree 3 on each sub-interval $[u_{j-1}, u_j]$ with the property that $s(u_i) = \Phi(u_i)$ for $i = 0, \dots, N$ and that s , s' and s'' are continuous in $[a, b]$. Natural splines are characterized by the condition $s''(a) = s''(b) = 0$. Let us now consider the splines s_0, \dots, s_N with the property $s_i(u_j) = \delta_{ij}$ and natural boundary conditions. Because $c_0 s_0 + \dots + c_N s_N = 0$ if and only if $c_0 = \dots = c_N = 0$, these functions are linearly independent, which is another word for base functions.

The left part of Fig. 2.1 shows base splines for an interval $[0, 5]$ with nodes at $\varrho = 0, 1, 2, 3, 4, 5$ and natural boundary conditions. Because of the vanishing boundary condition at $\varrho = 5$, we have 5 base functions s_0, \dots, s_4 . We see that the base functions are strongly localized.

In theory, any set of linearly independent functions $\{s_j\}_{j=1}^N$ can be orthonormalized. For this purpose, we determine the matrix

$$G_{ij} = \int_a^b du g(u) s_i(u) s_j(u) , \quad (2.36)$$

known as Gram's matrix. Without loss of generality, we assume that the s_j are real so that G is real. Because G is symmetric and positive definite, there exists a matrix B with the property

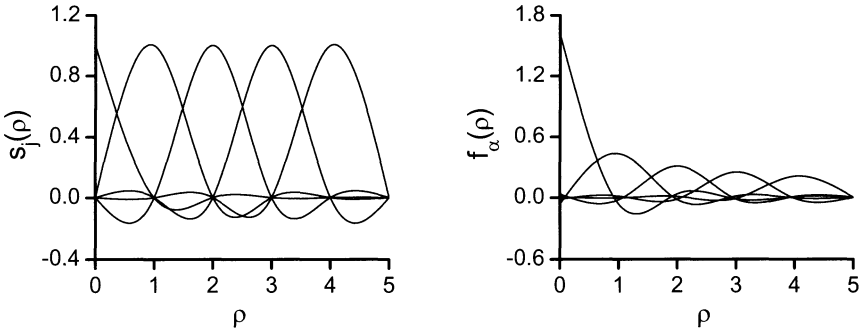


Fig. 2.1. Left: Cubic splines on the interval $[0, 5]$ with nodes at $\rho = 0, \dots, 5$ and natural boundary conditions on both ends. Right: Löwdin-orthonormalized base functions

$$B^T G B = 1 . \quad (2.37)$$

Then the functions

$$f_\alpha(u) = \sum_{j=1}^N s_j B_{j\alpha} ; \quad \alpha = 1, \dots, N \quad (2.38)$$

are orthonormal. The matrix B is not unique. The Hilbert–Schmidt (or Gram–Schmidt) orthonormalization of the functions s_j corresponds to a triangular matrix B (Cholesky decomposition). We favor the Löwdin orthonormalization [76], which treats all original functions s_j equal and preserves certain symmetries of the original base functions [77]. Let

$$G = T \operatorname{diag}(g_1, \dots, g_N) T^T ; \quad T^T T = 1 . \quad (2.39)$$

Then, a solution for the matrix B is given by

$$B = B^T = G^{-1/2} = T \operatorname{diag}\left(\frac{1}{\sqrt{g_1}}, \dots, \frac{1}{\sqrt{g_N}}\right) T^T . \quad (2.40)$$

We Löwdin-orthonormalized the splines from the left part of Fig. 2.1. As weight function, we assumed $g(\rho) = 2\pi\rho$ from the radial part of polar coordinates. The result is shown on the right side of Fig. 2.1. To some degree, the orthonormal base functions resemble the original functions. Both the original splines and the orthonormalized splines are strongly localized. This feature can be used to produce an approximate band matrix from the discretization of the Hamiltonian.

A question, which naturally arises, is: can we orthonormalize everything? In practice, the answer is negative. The numerical orthonormalization requires the original functions to be “almost orthonormal,” which means that the condition

number of G , defined as $\text{cond } G = \|G\| \|G^{-1}\| = \max(g_0, \dots, g_N) / \min(g_0, \dots, g_N)$ has to be moderate, say, lower than 1000. Otherwise the result will be inaccurate or the orthonormalization may even fail, because the lowest eigenvalues of G become numerically negative.

We shall now numerically solve Example A using different base functions. We start with the Laguerre functions (2.33). This has been done in 1990 by Stafford et al. [15]. The matrix elements of the Coulomb potential can be calculated analytically and it holds that [78]

$$\begin{aligned} V_{nn'} &= 2\pi \int_0^\infty d\varrho f_n^*(\varrho) f_{n'}(\varrho) = \sqrt{\frac{B}{2}} \int_0^\infty dx \frac{1}{\sqrt{x}} e^{-x} L_n(x) L_{n'}(x) \\ &= \sqrt{\frac{B}{2}} \frac{\Gamma(n+\frac{1}{2})}{\Gamma(n+1)} {}_3F_2(-n', \frac{1}{2}, \frac{1}{2}; 1, \frac{1}{2}-n; 1), \end{aligned} \quad (2.41)$$

where ${}_pF_q$ is the generalized hypergeometric series (App. A.2). The approximate eigenvalues and oscillator strengths (2.25) are determined from the matrix eigenvalue problem:

$$\begin{aligned} \sum_{n'=0}^{N-1} [(n+\frac{1}{2})B \delta_{nn'} - V_{nn'}] \Phi_{A;n'} &= E_A \Phi_{A;n} \\ F_A &= \sum_{n=0}^{N-1} \Phi_{A;n} f_n(0) = \sqrt{\frac{B}{2\pi}} \sum_{n=0}^{N-1} \Phi_{A;n}. \end{aligned} \quad (2.42)$$

It is important to note that the evaluation of the generalized hypergeometric series takes $\min(n, n')$ floating-point operations, which means that the numerical effort to calculate all matrix elements is comparable to the numerical effort for the diagonalization, namely $O(N^3)$, and a faster diagonalization routine would not significantly reduce the computation time.

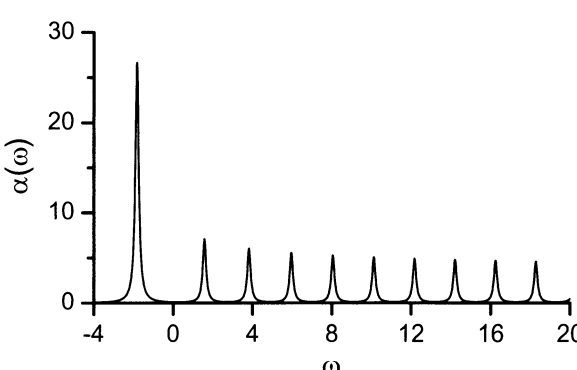


Fig. 2.2. Optical absorption of an ideal two-dimensional semiconductor in a perpendicular magnetic field $B = 2$, calculated with $N = 2000$ Laguerre functions

The resulting optical absorption $\text{Im } \chi(\omega)$ for a magnetic field $B = 2$ and a homogeneous broadening $\epsilon = 0.1$, calculated with 2000 base functions, is shown in Fig. 2.2. The one-parametric continuum from the field-free case (Fig. 1.5) is fully discretized due to the Landau quantization. With the exception of the lowest peak, the spectrum resembles the optical density of states (1.68): the absorption lines are about equally spaced and have roughly the same oscillator strength. For the frequency range under consideration, 10 eigenstates contribute to the optical spectrum. The energetic position and oscillator strength of the ground state ($\Lambda = 0$) are very close to the values for $B = 0$ (Fig. 1.5) and the correction of the ground-state energy proportional to B^2 is called diamagnetic shift.

Next, we use the eigenfunctions of \hat{H}_{kin} on a finite interval with $[0, R]$, given by (2.35). The matrix elements of the potentials

$$U_{nn'} = 2\pi \int_0^R d\varrho \varrho f_n^*(\varrho) \frac{B^2 \varrho^2}{8} f_{n'}(\varrho); \quad V_{nn'} = 2\pi \int_0^R d\varrho f_n^*(\varrho) f_{n'}(\varrho) \quad (2.43)$$

are determined by numerical integration and the transition energies and oscillator strength are found from solving the matrix eigenvalue problem

$$\sum_{n'=1}^N \left[\frac{1}{2} \left(\frac{x_n}{R} \right)^2 \delta_{nn'} + U_{nn'} - V_{nn'} \right] \Phi_{\Lambda;n'} = E_{\Lambda} \Phi_{\Lambda;n} \quad (2.44)$$

$$F_{\Lambda} = \sum_{n=1}^N \Phi_{\Lambda;n} f_n(0) = \sum_{n=1}^N \frac{\Phi_{\Lambda;n}}{\sqrt{\pi} R |J'_0(x_n)|}.$$

The normalization radius R is estimated by the classical point of return $\sqrt{8E_{\Lambda}/B}$ plus three times the magnetic length $1/\sqrt{B}$. For $E_{\Lambda} \leq \omega_{\max} = 20$ and $B = 2$, a domain radius $R = 9$ is sufficient. This time, neither the magnetic field nor the Coulomb potential is contained in $\hat{H}^{(0)}$ and the accuracy can be tested for the limiting cases $V_{nn'} = 0$ and $U_{nn'} = 0$, where the solution is known analytically. We found that 200 base functions are sufficient to achieve the same accuracy as in the previous calculation. The calculation of one matrix element takes $O(N)$ operations in the average, with a large prefactor. Therefore, the occupation of the matrix takes much longer than the diagonalization.

Why does the second set of base functions gives a much faster convergence than the first set? Taking the effective extension of the 2000th base function (2.33), as given by the classical point of return, it becomes clear that the in the first method about 90% of the interval was wasted.

Can the number of base functions and, therefore, the numerical effort, be further reduced? We notice that both the first and the second method suffer from another problem: the first derivatives of the base functions (2.33) and (2.35) at $\varrho = 0$ are equal to zero, in contrast to the exact eigenfunctions.²

² The behavior of the eigenfunctions of \hat{H} (2.13) at the origin is $\Phi'_{\Lambda}(0) = -2\Phi_{\Lambda}(0)$.

Therefore, the convergence should improve by using orthonormalized splines with natural boundary conditions at $\varrho = 0$ and $\varrho = R$. The matrix elements for the kinetic energy, the parabolic potential, and the Coulomb potential,

$$H_{\text{kin } nn'} = \pi \int_0^R d\varrho \varrho f'_n(\varrho) f'_{n'}(\varrho) \quad (2.45)$$

$$U_{nn'} = 2\pi \int_0^R d\varrho \varrho f_n(\varrho) \frac{B^2 \varrho^2}{8} f_{n'}(\varrho) ; \quad V_{nn'} = 2\pi \int_0^R d\varrho f_n(\varrho) f_{n'}(\varrho) ,$$

are calculated numerically. In principle, they can be determined analytically from the polynomial coefficients of the f_n in the sub-intervals. The diagonalization of the matrix $H + U - V$ gives the transition energies and oscillator strength:

$$\sum_{n'=0}^{N-1} [H_{\text{kin } nn'} + U_{nn'} - V_{nn'}] \Phi_{A;n'} = E_A \Phi_{A;n} \quad (2.46)$$

$$F_A = \sum_{n=0}^{N-1} \Phi_{A;n} f_n(0) .$$

Again, for these general-purpose base functions, we can check the accuracy by reproducing the analytical results in the limiting cases $U = 0$ and $V = 0$. For the interval $[0, R]$ with $R = 9$, we were able to reproduce the spectrum with only 45 base functions. Because the base functions are strongly localized, the result does not change if all matrix elements with $|n - n'| > 10$ are set to zero. Then the matrix is sparse and the calculation of all matrix elements takes $O(N)$ operations. This feature can be used for large-scale computations.

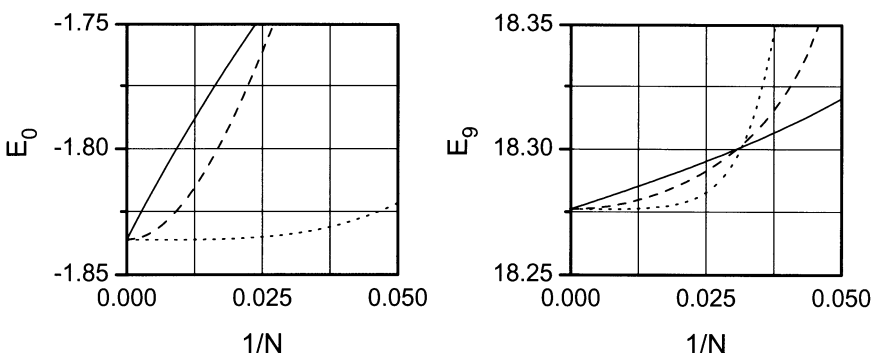


Fig. 2.3. Numerical eigenvalues E_0 (left) and E_9 (right) as function of $1/N$, calculated with Laguerre functions (*solid line*), Bessel functions (*dashed line*), and orthonormalized cubic splines (*dotted line*)

It is worthwhile to compare the accuracy of the approximation by Laguerre functions, Bessel functions, and cubic splines. In Fig. 2.3, the zeroth and ninth numerical eigenvalues E_0 and E_9 are shown as functions of the parameter $1/N$. For both eigenvalues, the convergence of the approximation by Laguerre functions is only linear, while the other base functions show a convergence that scales like $1/N^2$ and $1/N^4$, respectively. For the ground state, the spline approximation is much more accurate than the other methods already for $N = 20$. For $N \geq 40$, the spline approximation is more accurate than the other approximations for all 10 lowest eigenvalues.

We have seen that the numerical efficiency depends crucially on the choice of the base functions. The result of the numerical experiment is counter-intuitive: the Laguerre functions, which were “closest to the physics,” gave the worst performance, while the cubic splines, which have nothing to do with the physical problem, gave the best performance. If we wish to treat problems in many dimensions ($l > 1$), the Laguerre functions cannot be chosen as base functions, because for one dimension we are already close the the limit of the computational resources. In the case of Bessel functions, we would be able to use about 10 more base functions for the other directions, which would allow us to handle a quantum well of finite thickness in a perpendicular magnetic field, a problem which falls in the class “quantum dots” (p. 55). For the cubic splines, we can add another 50 base functions for full matrices or 1000 base functions for band matrices, which would allow us to treat a bulk semiconductor in a magnetic field, which is a class-II problem [19]. There are other systems with strong confinement, like quantum wells or quantum wires, where an expansion into single-particle eigenfunctions shows rapid convergence. Nevertheless, the general class-II or class-III problem cannot be efficiently treated by orthonormal base functions. In the next subsection, we shall demonstrate the solution of a class-II problem by nonorthonormal base functions.

2.2.2 Non-Orthonormal Base Functions

In the last subsection, we have seen how orthonormal base functions can be constructed from nonorthonormal linearly independent functions. However, in many cases there is no need to explicitly orthonormalize the base functions and is easier and numerically more efficient to directly work with nonorthonormal base functions.

Consider a set of linearly independent functions $\{f_j\}_{j=0}^{N-1}$ which is a subset of a complete set of functions. We assume that the functions are real. For the formulation of the problem we introduce upper and lower indices and adopt a sum convention

$$\dots_j \dots^j = \sum_{j=0}^{N-1} \dots_j \dots^j . \quad (2.47)$$

In this notation, the Gram's matrix G (2.36) and its inverse G^{-1} write as

$$\begin{aligned} G &= (G_{ij}) ; \quad G_{ij} = \langle f_i | f_j \rangle \\ G^{-1} &= (G^{ij}) ; \quad G^{ij} G_{jk} = G_{kj} G^{ji} = \delta_k^i . \end{aligned} \tag{2.48}$$

As a general rule, upper and lower index are connected by

$$\dots_i = G_{ij} \dots^j ; \quad \dots^i = G^{ij} \dots_j . \tag{2.49}$$

After these preparations, we turn to the numerical calculation of the optical susceptibility. We start with the eigenvalue problem (2.9). With the ansatz

$$\Phi(u) = \Phi^i f_i(u) , \tag{2.50}$$

the functionals

$$E[\Phi] = \Phi^{i*} H_{ij} \Phi^j ; \quad I[\Phi] = \Phi^{i*} G_{ij} \Phi^j \tag{2.51}$$

become functions of the coefficients Φ^i . Then we proceed as in the last subsection. The main difference between (2.21) and (2.51) is the positive definite matrix G , which is in general not equal to the unity matrix. As a consequence, the solution leads to a generalized eigenvalue problem. The eigenvalues and oscillator strength are given by

$$H_{ij} \Phi_{\Lambda; }^j = E_{\Lambda} G_{ij} \Phi_{\Lambda; }^j \tag{2.52}$$

$$F_{\Lambda} = \mu_j^* \Phi_{\Lambda; }^j ; \quad \Phi_{\Lambda; }^{i*} G_{ij} \Phi_{\Lambda'; }^j = \delta_{\Lambda \Lambda'} ; \quad \mu_j = \langle f_j | \mu \rangle .$$

The generalized eigenvalue problem $H\Phi = EG\Phi$; $G > 0$ is a standard problem in physics and quantum chemistry, and computational routines are readily available. The numerical solution is based upon factorization of G and subsequent solution of an ordinary eigenvalue problem.

Now we solve the boundary-value problem (2.10) by means of the Galerkin method. As in the previous subsection, we identify the weight functions w_j (2.28) with the base functions f_j . This leads us immediately to the following set of equations

$$[H_{ij} - (\omega + i\epsilon) G_{ij}] \Psi^j(\omega) = \mu_i ; \quad \chi(\omega) = \mu_i^* \Psi^i(\omega) . \tag{2.53}$$

From the point of view of the numerical complexity, there is no difference to (2.29): a set of N equations has to be solved for each frequency ω . Usually, the matrices H and G , which result from the discretization by finite elements, have the same pattern and the overall bandwidth is not increased by subtracting $(\omega + i\epsilon) G$ from H .

The solution of the initial-value problem (2.11) is performed by projection onto the N -dimensional subspace defined by the linear combinations of the f_0, \dots, f_{N-1} . This results in a set of N coupled differential equations

$$\begin{aligned} P(t) &= e^{-\epsilon t} \mu_j^* \Psi^j(t) \\ i \frac{d}{dt} \Psi^j(t) &= G^{jk} H_{kl} \Psi^l(t); \quad \Psi^j(0) = i \mu^j = i G^{jk} \mu_k. \end{aligned} \tag{2.54}$$

The difference to the case of orthonormal base functions (2.31) is the occurrence of the G^{ij} in the differential equation for Ψ^i .

Although we do not explicitly orthonormalize the base functions $\{f_j\}_{j=0}^{N-1}$, the condition of G needs to be moderate. An ill-conditioned matrix G leads to inaccuracy or failure in the numerical solution of (2.52), (2.53), or (2.54).

In the derivation of (2.52) we have seen that the nonorthonormality of the base functions entails a new definition of a scalar product. For $\Phi(u) = \Phi^i f_i(u)$; $\Psi(u) = \Psi^i f_i(u)$ we have

$$\langle \Phi | \Psi \rangle = \Phi^\dagger G \Psi = \langle \Phi, \Psi \rangle, \tag{2.55}$$

where $\Phi = (\Phi^0, \dots, \Phi^{N-1})^T$ and $\Psi = (\Psi^0, \dots, \Psi^{N-1})^T$. The norm $\|\Phi\| = \langle \Phi, \Phi \rangle$ is called a weighted or energy norm. A matrix A is called G -Hermitian if $\langle A\Phi, \Psi \rangle = \langle \Phi, A\Psi \rangle$ for all Φ, Ψ . This is equivalent to $A^\dagger G = GA$, or, in other words, that GA is a Hermitian matrix by the usual definition. Obviously, the matrix $G^{-1}H$, which appears in the Schrödinger equation (2.54) is G -Hermitian. The definition of unitarity goes alongside the same lines: a matrix U is G -unitary if $\langle U\Phi, U\Psi \rangle = \langle \Phi, \Psi \rangle$ for all Φ, Ψ . This is equivalent to $U^\dagger G U = G$. The time-evolution matrix $\exp(-iG^{-1}Ht)$ is G -unitary.

An important example for nonorthonormal base functions are base functions with a finite support, also known as finite elements. They lead to sparse matrices with $O(N)$ nonzero matrix elements. We first discuss the the solution of the eigenvalue and the boundary-value problem by exact methods for band matrices. We assume that the coordinates are products of one-dimensional coordinates (2.7) and that the base functions $\{f_i\}_{i=1}^{N-1}$ are products of base functions $\{f_{i_1}\}_{i_1=0}^{N_1-1}, \dots, \{f_{i_l}\}_{i_l=0}^{N_l-1}$ for the individual directions. The bandwidth of the base functions $\{f_{i_k}\}_{i_k=0}^{N_k-1}$ is defined as the smallest number B_k with the property $f_{i_k}(u_k) f_{j_k}(u_k) = 0$ a.e. for $|i_k - j_k| > B_k$. For the one-dimensional case ($l = 1$), the bandwidth B of the matrix (2.18) is equal to B_1 . For the multi-dimensional case, the bandwidth depends on the arrangement of the indices. For

$$\begin{aligned} j &= j_1 N_2 \cdots N_l + j_2 N_3 \cdots N_l + \cdots + j_{l-1} N_l + j_l \\ j &= 0, \dots, N-1; \quad N = N_1 \cdots N_l \end{aligned} \tag{2.56}$$

$$G_{ij} = G_{i_1 j_1} \cdots G_{i_l j_l}; \quad H_{ij} = H_{i_1 \cdots i_l, j_1 \cdots j_l}$$

the overall bandwidth B of the matrices G and H is

$$\begin{aligned} B &= B_1 N_2 \cdots N_l + B_2 N_3 \cdots N_l + \cdots + B_{l-1} N_l + B_l \\ &\quad B_1 N_2 \cdots N_l < B < (B_1 + 1) N_2 \cdots N_l . \end{aligned} \tag{2.57}$$

The number B depends crucially on the outer bandwidth B_1 , but is virtually independent on the inner bandwidths B_2, \dots, B_l . Therefore, the optimal strategy for obtaining a small bandwidth is to use finite elements with a small bandwidth for the outer direction j_1 and optimized base functions for the inner directions j_2, \dots, j_m . It is also obvious that the conversion to a band matrix is practicable only for class-II problems, because a large number of base functions (i.e., in the order of 1000) is allowed only for one direction.

For the initial-value problem (2.54) we assume that we have to apply the matrix $G^{-1}H$ at each time step. The matrix H has not to be stored at once and the different contributions to the Hamiltonian (kinetic energy, confinement potentials, Coulomb potential) can be applied separately. Usually, the numerical effort for the multiplication with H is negligible compared to the multiplication with G^{-1} which corresponds to a solution of a set of equations. Because of the structure of G (2.56), the matrix elements of G^{-1} are

$$G^{ij} = G^{i_1 j_1} \cdots G^{i_l j_l} ; \quad G^{i_l j_l} G_{j_l k_l} = \delta_{k_l}^{i_l} . \tag{2.58}$$

This means that the solution of a set of equations can be done for each of the l directions separately, while the other $l-1$ indices play the role of parameters. For a high numerical efficiency, the bandwidth has to be kept small for each direction. Then the application of G^{-1} by means of the decomposition (2.58) is an $O(N)$ method. This is also the basic idea of the alternating direction implicit (ADI) method (see Sect. 2.3). It may be efficient to work with orthonormal base functions for some of the directions with strong confinement. For these coordinates, the contribution to G is a unit matrix and no set of equations has to be solved. On the other hand, the numerical effort for the multiplication with H increases.

So far we did not discuss the case of cyclic boundary conditions. There exists an efficient algorithm for the solution of sets of equations with a cyclic tridiagonal matrix [10]. This is interesting for the solution of the boundary-value problem in one dimension and for the solution of the initial-value problem in multidimensions.

An important example for finite elements are piecewise linear functions. Given an interval $[a, b]$ and a set of nodes $a = x_0 < x_1 < \cdots < x_{N-1} < x_N = b$, the i -th base function f_i is equal to unity at $x = x_i$ and equal to zero at all other nodes. Furthermore, f_i is continuous, and is a linear function in the sub-intervals between the nodes. For vanishing boundary conditions on both ends $\llbracket a, b \rrbracket$ the index i runs from 1 to $N-1$, for vanishing boundary conditions on one end $[a, b]$ or periodic boundary conditions $[a, b[, i$ runs from 0 to $N-1$. Piecewise linear base functions are shown in Fig. 2.4 for the interval $[0, 10]$, with nodes $x_0 = 0, x_1 = 1, \dots, x_9 = 9$. The nodes do

not need to be equidistant and the definition can be generalized to piecewise quadratic, cubic, etc. polynomials, called B-splines [75].

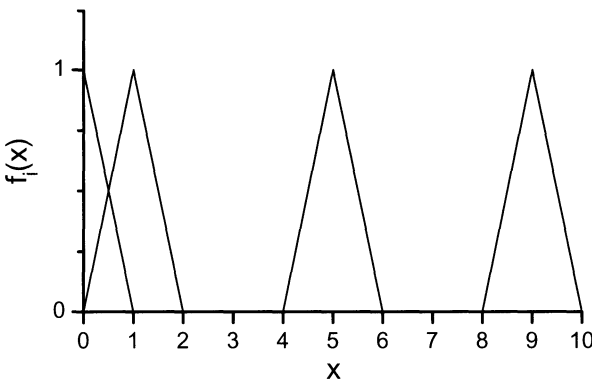


Fig. 2.4. Piecewise linear base function for an interval $[0, 10]$ with nodes $x_0 = 0$, $x_1 = 1, \dots, x_9 = 9$. The base functions f_i are shown for $i = 0, 1, 5$, and 9

Let us now come back to the problem of artificial boundary conditions. A common methodology in quantum mechanics for the treatment of continuum states is to introduce a finite normalization volume and, at the end of the calculation, let the size go to infinity. Obviously, this is not possible in a numerical calculation. Here, the domain has to be sufficiently large so that the ensemble of discrete lines appears as continuum. Consider a free electron in one dimension on a domain with length L . The eigenvalues are given by

$$E_n = \frac{n^2\pi^2}{2L^2} ; \quad n \in \mathbb{N}. \quad (2.59)$$

The spacing of eigenvalues increases linearly with quantum number n . A necessary condition is that the spacing of subsequent eigenvalues is smaller than the homogeneous broadening ϵ for all $E_n \leq \omega_{\max}$. For the length of the domain and the number of base functions N in Cartesian coordinates it follows that

$$L \geq \frac{\sqrt{2\omega_{\max}}\pi}{\epsilon} ; \quad N \geq \frac{2\omega_{\max}}{\epsilon}. \quad (2.60)$$

For example, for $\omega_{\max} = 20$ and $\epsilon = 0.1$ we have $L \geq 200$ and $N \geq 400$, i.e., we would need a domain $[-100, +100]$ and at least 400 sine functions. For finite elements or finite differences, the number of base functions follows from the step size, which is determined by the accuracy.

For the radial direction of polar coordinates, we arrive at the same estimate for the normalization radius R and the number of base functions, which follows from the asymptotic behavior of the solutions (2.35) for large n (App. A.2). For Cartesian coordinates with periodic boundary conditions, the normalization length and the number of base functions are in the same

order. It is recommended to check the influence of boundary effects by performing calculations without Coulomb interaction or for individual directions and comparison with the analytical result.

We see that the avoidance of boundary effect may drastically enhance the size of the normalization domain and, therefore, the numerical effort. For some problems, the size of the normalization domain can be prohibitive for a numerical solution. On the other hand, the flat continuum near ω_{\max} provides little or no physical information (cf. Fig. 1.5). A very efficient method to deal with the asymptotically free motion are absorbing boundary conditions, which will be discussed in the next section.

Finally, we demonstrate the numerical calculation of the optical absorption for Example B by means of nonorthonormal base functions. For the ϱ direction we use piecewise linear functions f_i (cf. Fig. 2.4). For the confinement (z) directions we use products of one-particle eigenfunctions for electron and hole. Then the total base functions are:

$$f_{i_1 i_2 i_3}(\varrho, z_e, z_h) = f_{i_1}(\varrho) \sqrt{\frac{2}{d}} \sin\left(\frac{i_2 \pi z_e}{d}\right) \sqrt{\frac{2}{d}} \sin\left(\frac{i_3 \pi z_h}{d}\right). \quad (2.61)$$

The optical susceptibility is calculated according to (2.53). The matrix elements of G and H are

$$G_{i_1 i_2 i_3, j_1 j_2 j_3} = G_{i_1 j_1} \delta_{i_2 j_2} \delta_{i_3 j_3}; \quad G_{i_1 j_1} = 2\pi \int_0^R d\varrho \varrho f_{i_1}^*(\varrho) f_{j_1}(\varrho) \quad (2.62)$$

and

$$\begin{aligned} H_{i_1 i_2 i_3, j_1 j_2 j_3} &= H_{\text{kin } \varrho i_1 j_1} \delta_{i_2 j_2} \delta_{i_3 j_3} + G_{i_1 j_1} \left(\frac{i_2^2 \pi^2}{2m_e d^2} + \frac{i_3^2 \pi^2}{2m_h d^2} \right) \delta_{i_2 j_2} \delta_{i_3 j_3} \\ &\quad - V_{i_1 i_2 i_3, j_1 j_2 j_3} \end{aligned} \quad (2.63)$$

$$H_{\text{kin } \varrho i_1 j_1} = \pi \int_0^R d\varrho \varrho f_{i_1}^*(\varrho) f'_{j_1}(\varrho)$$

$$V_{i_1 i_2 i_3, j_1 j_2 j_3} = 2\pi \int_0^R d\varrho \varrho \int_0^d dz_e \int_0^d dz_h \frac{f_{i_1 i_2 i_3}^*(\varrho, z_e, z_h) f_{j_1 j_2 j_3}(\varrho, z_e, z_h)}{\sqrt{\varrho^2 + (z_e - z_h)^2}}.$$

For the transition matrix elements we find

$$\mu_{i_1 i_2 i_3} = f_{i_1}(0) \delta_{i_2 i_3} = \delta_{i_1, 0} \delta_{i_2 i_3}. \quad (2.64)$$

The Kronecker symbol $\delta_{i_2 i_3}$ in the last expression is a consequence of the perfect confinement, where electrons and holes have the same eigenfunctions.

We mention that the eigenfunctions $f_{i_1}(\varrho)$ do not need to have continuous derivatives of second order. Only the functional

$$E_{\text{kin}}[\Phi] = 2\pi \int_0^R d\varrho \varrho |\Phi'(\varrho)|^2 \quad (2.65)$$

must approach the exact eigenvalue of $\hat{H}_{\text{kin},\varrho}$ on the domain $[0, R]$ when Φ approaches the exact eigenfunction. This is the case already if Φ is an approximation by piecewise linear functions.

For the actual calculation we considered a well width $d = 1$ and used the GaAs effective-mass ratio so that the effective masses in units of the reduced mass are $m_e = 1.136$ and $m_h = 8.328$. Because $m = m_e m_h / (m_e + m_h) = 1$, the absorption coefficient in dimensionless units depends only on m_h/m_e . The homogeneous line broadening was assumed to be $\epsilon = 0.1$. For the functions f_{j_1} we used equidistant nodes with a spacing $h = \frac{1}{16}$ and a domain radius $R = 200$. For the z directions, we took into account the lowest eight subband transitions $(j_2, j_3) = (1, 1), (1, 3), (1, 5), (2, 2), (2, 4), (1, 7), (2, 6)$, and $(3, 1)$. Thus the energy cutoff was 39.5, which is the onset of the subband pair $(3, 3)$. The dimension of the matrix was $N = 200 \times 16 \times 8 = 25\,600$ with a bandwidth of $B = 1 \times 8 + 7 = 15$.

With these numerical parameters, we achieved full convergence in the energy region $\omega \leq 20$. The number of base elements for the radial direction is 3200, which by far exceeds the estimate for N from (2.60). This is because the maximum step size h is determined by the accuracy for reproducing the exciton ground state. In the next subsection we shall develop a method of discretizing the Coulomb potential which exactly reproduces the ground state and allows us to moderately increase the step size.

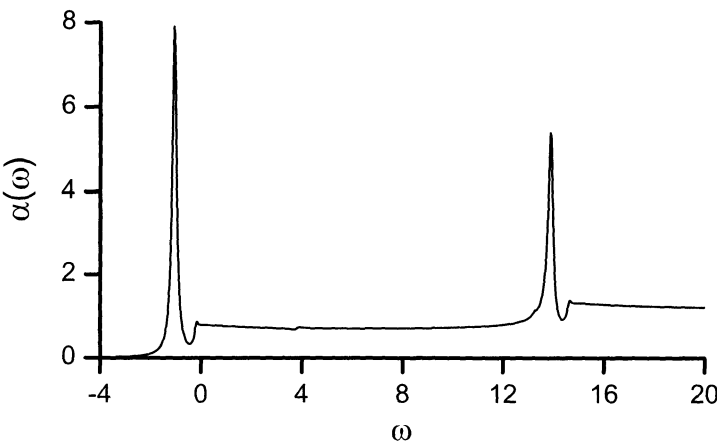


Fig. 2.5. Optical absorption for Example B, calculated using a combination of piecewise linear polynomials and one-particle eigenfunctions

The result of the numerical calculation is shown in Fig. 2.5, where the absorption coefficient $\alpha(\omega) = \text{Im } \chi(\omega)$ is plotted versus the frequency ω . The main peaks stem from the ground-state excitons of the $(1,1)$ and $(2,2)$ subband transitions. Their position is virtually independent of the mass ratio.

Although we introduced a Lorentzian broadening, the 1s exciton of the (2,2) transition shows a slightly asymmetric lineshape. Two additional lines with a very small oscillator strength can be observed at about $\omega = 4$ and $\omega = 13.5$. These transitions correspond to the (1,3) and (1,5) transitions, which, according to (2.64) should be forbidden. We postpone the discussion of the lineshapes and the weakly allowed transitions to the next chapter. Furthermore, it can be seen that because of the finite width the binding energy is smaller than 2 and the ratio between the oscillator strengths of the ground-state exciton and the continuum is significantly smaller than for the ideal two-dimensional semiconductor (cf. Fig. 1.5).

The above example shows how, in principle, most class-II problems can be solved by a combination of finite elements for the scattering directions and optimal base functions for the confinement directions. Another example is the bulk semiconductor in a magnetic field, which was treated by 1500 third-order B-splines for the field direction and 15 cubic splines for the radial direction perpendicular to the magnetic field, leading to a matrix dimension of $N = 22\,500$ and a bandwidth of $B = 44$ [19].

Although the method introduced in this subsection is straightforward, it has also several drawbacks. We have to convert an array with $2l$ indices to a matrix in band storage. Another problem is the calculation of the multi-dimensional Coulomb integrals (2.63). Some authors suggest to use computer algebra to determine the Coulomb integrals [44]. Unless the single-particle eigenfunctions and eigenvalues are known analytically, they have to be calculated numerically in a separate program. In the next subsection we will get to know a method which considerably simplifies the discretization of the space variables. The programming effort will be further reduced by solving the initial-value problem (Sect. 2.3), because the matrix H does not need to be stored as a whole or to be converted into sparse-matrix storage. In Chap. 3, we shall calculate the absorption of a quantum well, similar to the last example, by solving the initial-value problem, using a combination of single-particle eigenfunctions and finite differences.

2.2.3 Finite Differences

The method of finite elements was based upon approximation of functions. Once the functions were approximated, we automatically obtained formulas for the approximation of operators, the scalar product, and the delta function. In contrast, the method of finite differences is based upon approximation of operators. But we also need approximations for the scalar product, the delta function, and singular potentials. Finite differences are often more efficient than finite elements and the programming effort is much lower, but they are also theoretically more demanding.

We start with the general theory. Later, we shall give explicit expressions for Cartesian and polar coordinates. We consider a one-dimensional domain with a grid of sample points $\{u_i\}_{i=0}^{N-1}$. We shall also assume that

the grid is regular, i.e., that $u_{i+1} - u_i = h$ for all i . The expressions can be immediately generalized for l -dimensional coordinates which are products of one-dimensional coordinates. The function values $\Phi(u_i)$ at the grid points form an N -dimensional vector $\Phi = (\Phi_0, \dots, \Phi_{N-1})^T$. The scalar product of two elements Φ, Ψ of the Hilbert space is approximated by a quadrature formula:

$$\langle \Phi | \Psi \rangle = \sum_{j=0}^{N-1} g_j \Phi_j^* \Psi_j = \langle \Phi, \Psi \rangle = \Phi^\dagger G \Psi ; \quad \|\Phi\| = \sqrt{\langle \Phi, \Phi \rangle}$$

$$G = \text{diag}(g_0, \dots, g_{N-1}) ; \quad g_i > 0 . \quad (2.66)$$

In the finite-dimensional vector space, defined by the function values at the grid points, the equation $\Psi(u) = \hat{H}\Phi(u)$ is approximated by

$$\Psi_i = \sum_j H_{ij} \Phi_j ; \quad \Psi = H\Phi . \quad (2.67)$$

For one-dimensional problems, the matrix H is usually a band matrix, while in many dimensions H is irregularly sparse. The approximation (2.67) is consistent if

$$\lim_{h \rightarrow 0} \Psi_i = (\hat{H}\Phi)(u_i) \quad (2.68)$$

for all i , in other words, if with reduction of the step sizes $h = (h_1, \dots, h_l)$ the approximate result approaches the exact result. Another important issue for Schrödinger equations is the question of Hermiticity. As the operator \hat{H} is Hermitian, i.e., $\langle \hat{H}\Phi | \Psi \rangle = \langle \Phi | \hat{H}\Psi \rangle$ for all Φ, Ψ , its discretization must also be Hermitian, i.e., $\langle H\Phi, \Psi \rangle = \langle \Phi, H\Psi \rangle$, which means that the matrix GH must be Hermitian according to the usual definition.

In order to find an approximation of the weighted delta function (2.6), we consider the equation

$$\int du' g(u') \underline{\delta}(u, u') \Phi(u') = \Phi(u) . \quad (2.69)$$

In the finite-difference approximation, this equation translates into

$$\sum_{j=0}^{N-1} g_j \underline{\delta}_{ij} \Phi_j = \Phi_i \quad (2.70)$$

and it follows that the discretization of the function $\underline{\delta}$ is

$$\underline{\delta}_{ij} = \frac{\delta_{ij}}{g_i} . \quad (2.71)$$

Now we write the three formulations for the optical susceptibility in the finite-difference approximation. We start with the eigenvalue problem (2.9). The optical susceptibility is:

$$\chi(\omega) = \sum_A \frac{|F_A|^2}{E_A - (\omega + i\epsilon)} ; \quad F_A = \langle \boldsymbol{\mu}, \boldsymbol{\Phi}_A \rangle \quad (2.72)$$

$$H \boldsymbol{\Phi}_A = E_A \boldsymbol{\Phi}_A ; \quad \langle \boldsymbol{\Phi}_A, \boldsymbol{\Phi}_{A'} \rangle = \delta_{AA'} .$$

In this formulation, H is not Hermitian as matrix in the general case. Multiplication from the left with the matrix G (2.66) yields

$$GH \boldsymbol{\Phi}_A = E_A G \boldsymbol{\Phi}_A ; \quad \boldsymbol{\Phi}_A G \boldsymbol{\Phi}_{A'} = \delta_{AA'} , \quad (2.73)$$

which is a Hermitian generalized eigenvalue problem. However, as G is a diagonal matrix, the latter equation can explicitly converted into a Hermitian ordinary eigenvalue problem. Multiplication with the diagonal matrix $B = G^{-1/2}$ leads to the equation

$$B^{-1} H B \boldsymbol{\Psi}_A = E_A \boldsymbol{\Psi}_A ; \quad \boldsymbol{\Psi}_A^\dagger \boldsymbol{\Psi}_{A'} = \delta_{AA'} , \quad (2.74)$$

where $B^{-1} H B$ is a Hermitian matrix and $\boldsymbol{\Psi}_A = B^{-1} \boldsymbol{\Phi}_A$.

In the finite-difference approximation, the boundary-value problem (2.10) takes the form

$$\chi(\omega) = \langle \boldsymbol{\mu}, \boldsymbol{\Psi}(\omega) \rangle ; \quad [H - (\omega + i\epsilon) G] \boldsymbol{\Psi}(\omega) = \boldsymbol{\mu} . \quad (2.75)$$

In this case the complexity is not fundamentally different from the case of orthonormal or nonorthonormal base functions.

For the initial-value problem (2.11) we find

$$\begin{aligned} \chi(\omega) &= \int_0^T dt e^{+i\omega t} P(t) ; \quad P(t) = e^{-\epsilon t} \langle \boldsymbol{\mu}, \boldsymbol{\Psi}(t) \rangle \\ i \frac{d}{dt} \boldsymbol{\Psi}(t) &= H \boldsymbol{\Psi}(t) ; \quad \boldsymbol{\Psi}(0) = i \boldsymbol{\mu} . \end{aligned} \quad (2.76)$$

In contrast to the discretization by finite elements (2.54), this time no application of G^{-1} is necessary and the time-evolution matrix $\exp(-iHt)$ is G -unitary. Provided the solution of the differential equation (2.76) can be found only by application of the matrix H at each time step, (2.76) gives rise to a highly efficient method which takes fully into account the sparsity of H .

Next we derive explicit expressions for Cartesian coordinates. We consider the finite interval $[a, b]$ with mesh points $x_j = a + jh$; $h = (b - a)/N$. The scalar product of two functions is approximated as

$$\begin{aligned} \langle \boldsymbol{\Phi} | \boldsymbol{\Psi} \rangle &= \int_a^b dx \boldsymbol{\Phi}^*(x) \boldsymbol{\Psi}(x) = h \sum_i \boldsymbol{\Phi}_i^* \boldsymbol{\Psi}_i = \langle \boldsymbol{\Phi}, \boldsymbol{\Psi} \rangle = \boldsymbol{\Phi}^\dagger G \boldsymbol{\Psi} \\ G &= h . \end{aligned} \quad (2.77)$$

For vanishing boundary conditions $\llbracket a, b \rrbracket$ the sum runs from $i = 1$ to $N - 1$ and for periodic boundary conditions $[a, b[$ the sum runs from $i = 0$ to $N - 1$. In each case, the integrand $\Phi^*(x)\Psi(x)$ can be considered as a periodic function and the accuracy of the quadrature (2.77) is higher than in the case where the integrand is an arbitrary function. With the above definition of the scalar product, the function $\underline{\delta}(x, x') = \delta(x - x')$ is discretized as

$$\underline{\delta}_{ij} = \frac{\delta_{ij}}{h}. \quad (2.78)$$

A general method of generating finite-difference schemes for differential operators is the expansion of the function in a Taylor series. From

$$\Phi(x \pm h) = \Phi(x) \pm \Phi'(x)h + \frac{1}{2}\Phi''(x)h^2 \pm \frac{1}{6}\Phi'''(x)h^3 + O(h^4) \quad (2.79)$$

it follows that

$$\begin{aligned} \Phi'(x) &= \frac{\Phi(x+h) - \Phi(x-h)}{2h} + O(h^2) \\ \Phi''(x) &= \frac{\Phi(x+h) - 2\Phi(x) + \Phi(x-h)}{h^2} + O(h^2). \end{aligned} \quad (2.80)$$

The expression for the second derivative can also be obtained by applying the formula for the first derivative twice with step size $\frac{h}{2}$. The next order is given by [79]

$$\Phi''(x) = \frac{-\Phi(x+2h) + 16\Phi(x+h) - 30\Phi(x) + 16\Phi(x-h) - \Phi(x-2h)}{12h^2}, \quad (2.81)$$

which is accurate up to terms $O(h^4)$. In both cases, (2.80) and (2.81), the discretized operator $\Delta_x = \partial^2/\partial x^2$ is Hermitian, i.e.,

$$\langle \Delta_x \Phi, \Psi \rangle = \langle \Phi, \Delta_x \Psi \rangle. \quad (2.82)$$

An alternative to approximating differential operators by finite differences is the Fourier method [60, 80, 81], which can be used with Cartesian coordinates and periodic boundary conditions. In Fourier (quasi-momentum) domain the operator $-\Delta$ is local, and is identical to k^2 . The transformation between direct and Fourier space can be performed efficiently by the fast Fourier transform (FFT) algorithm. For systems with spherical symmetry the three-dimensional Fourier transform reduces to a one-dimensional Fourier-sine transform, but special care has to be taken for the origin $r = 0$. For the calculation of linear optical spectra, there are more efficient methods than the Fourier method. However, the Fourier method is an alternative for solving the nonlinear semiconductor Bloch equations (Sect. 1.3), which involves convolutions [82].

Now we turn to polar coordinates. For the radial part, we assume boundary conditions $[0, R]$ and a mesh size $h = R/N$. The mesh points are then $\varrho_j = jh; j = 0, \dots, N - 1$. The scalar product is approximated by

$$\begin{aligned} \langle \Phi | \Psi \rangle &= 2\pi \int_0^R d\varrho \varrho \Phi^*(\varrho) \Psi(\varrho) \\ &= \sum_{j=0}^{N-1} g_j \Phi_j^* \Psi_j = \langle \Phi, \Psi \rangle = \Phi^\dagger G \Psi . \end{aligned} \quad (2.83)$$

For the matrix elements of $G = \text{diag}(g_0, \dots, g_{N-1})$ we use

$$g_0 = 2\pi \int_0^{h/2} d\varrho \varrho = \frac{\pi}{4} h^2 ; \quad g_j = 2\pi \int_{(j-1/2)h}^{(j+1/2)h} d\varrho \varrho = 2\pi h^2 j \quad \text{for } j \geq 1 . \quad (2.84)$$

Although this choice is plausible, it is not clear whether the g_i are unique. The discretization of the weighted delta function $\underline{\delta}$ is done by formula (2.71). An important role plays the point $\varrho = 0$, because in many cases, such as Examples A, B, E, the dipole matrix element is proportional to $\underline{\delta}(\varrho) = \delta(\varrho)/(2\pi\varrho)$. In this case we obtain

$$\underline{\delta}_{i0} = \frac{4}{\pi h^2} \delta_{i0} . \quad (2.85)$$

To generate a finite-difference scheme for the radial Laplacian Δ_ϱ , we start with the expression

$$\Delta_\varrho \Phi(\varrho) = \Phi''(\varrho) + \frac{1}{\varrho} \Phi'(\varrho) . \quad (2.86)$$

Replacing Φ'' and Φ' by their first-order finite-difference approximations (2.80), we find for $j > 0$:

$$\begin{aligned} (\Delta_\varrho \Phi)_j &= \frac{1}{\varrho_j} \frac{\varrho_{j+1/2} \Phi_{j+1} - 2\varrho_j \Phi_j + \varrho_{j-1/2} \Phi_{j-1}}{h^2} + O(h^2) \\ \varrho_{j \pm 1/2} &= (j \pm \frac{1}{2})h . \end{aligned} \quad (2.87)$$

The point $\varrho = 0$ needs special attention. We assume that the function Φ is analytic as function of the coordinates x and y . Then the first derivative is zero at $\varrho = 0$ and the second term in the expression (2.86) is of the form $0/0$. From the Taylor expansion

$$\Phi(\varrho) = \Phi(0) + \frac{1}{2} \varrho^2 \Phi''(0) + O(\varrho^3) \quad (2.88)$$

it follows that

$$\lim_{\varrho \rightarrow 0} \frac{\Phi'(\varrho)}{\varrho} = \Phi''(0) . \quad (2.89)$$

Therefore, the Laplacian at the origin is

$$(\Delta_\varrho \Phi)_0 = 2\Phi''(0) = \frac{4\Phi_1 - 4\Phi_0}{h^2} + O(h^2). \quad (2.90)$$

The latter formula can also be obtained from the discretization of the Laplacian in two-dimensional Cartesian coordinates. As Φ depends only on the radius, the points $(0, 0)$, $(+h, 0)$, $(-h, 0)$, $(0, +h)$, and $(0, -h)$ in the xy plane are equivalent. The Hermiticity of $\Delta_{\varrho jj'}$ is obvious for $j, j' \geq 1$ (2.87). By miracle, it holds that $g_0 \Delta_{\varrho 01} = g_1 \Delta_{\varrho 10}$ and, therefore,

$$\langle \Delta_\varrho \Phi, \Psi \rangle = \langle \Phi, \Delta_\varrho \Psi \rangle. \quad (2.91)$$

for all Φ, Ψ . We mention that for the fourth-order finite-difference approximation of Δ_ϱ analogously to (2.81), Hermiticity is not fulfilled. The existence of higher-order finite-difference approximations, which are compatible with the approximation of the scalar product (2.83–2.84), remains an open question.

For the solution of the initial-value problem it will be necessary to know the norm of the discretized Hamiltonian H . In most cases, the norm of H is determined by the discretization of the operator of the kinetic energy. Generally, the a norm of a matrix A can be introduced as

$$\|A\| = \max_{\Phi} \frac{\langle \Phi, A \Phi \rangle}{\|\Phi\|^2}. \quad (2.92)$$

For Hermitian matrices, which result from the discretization of Hermitian differential operators, the norm defined above is equal to the largest eigenvalue in magnitude. The norm of the discretized operator $\Delta_x = \partial^2/\partial x^2$ can be determined explicitly for periodic or vanishing boundary conditions. As the expressions are asymptotically equal for a large number of grid points, we limit ourself to periodic boundary conditions. The eigenfunctions of the discretized operator Δ_x are $\Phi_k(x_j) = \exp(-ikx_j)/\sqrt{L_x}$ with $k \in [-\frac{\pi}{h}, +\frac{\pi}{h}]$. The variable k is also discretized so that the functions $\Phi_k(x_j)$ fulfill the boundary conditions. For the second-order difference formula (2.80) the eigenvalues are $E(k) = -4 \sin^2(\frac{hk}{2})/h^2$. The largest eigenvalue in magnitude is found for $k = \pm \frac{\pi}{h}$ and the norm becomes

$$\|\Delta_x\| = \frac{4}{h^2}. \quad (2.93)$$

The expression for vanishing boundary conditions can be found in [83]. For the fourth-order formula (2.81), the largest eigenvalue in magnitude is also found at $k = \pm \pi/h$. From the eigenfunction $\Psi_{\pm \pi/h}(x_j) \propto (-1)^j$ it follows that

$$\|\Delta_x\| = \left| \frac{1}{h^2} \left(-\frac{1}{12} - \frac{16}{12} - \frac{30}{12} - \frac{16}{12} - \frac{1}{12} \right) \right| = \frac{16}{3h^2}. \quad (2.94)$$

For the discretization of Δ_ϱ (2.87, 2.90), the eigenfunctions are not known analytically. The numerical solution of the eigenvalue problem for boundary conditions $[0, R=Nh]$ yields

$$\|\Delta_\varrho\| = \frac{a}{h^2}; \quad a = 4.84194\dots \quad (2.95)$$

in the limit $N \rightarrow \infty$. This limit is practically reached for $N \geq 10$.

Besides differential operators, the Hamiltonian often contains potentials. For smooth potentials W , the discretization is as simple as

$$(W\Phi)_i = W_i \Phi_i; \quad W_i = W(u_i). \quad (2.96)$$

Apparently, the above formula is not applicable for potentials that contain singularities, even if the singularities are integrable. On the other hand, omission of the singular point is not recommended, because the oscillator strengths $|F_A|^2$ are determined by the amplitudes of the eigenfunctions exactly at the point of the Coulomb singularity. Here, we propose a very easy method for the discretization of the Coulomb potential. The ground-state energy $E_{\text{g.s.}}$ and wavefunction $\Phi_{\text{g.s.}}$ of the Coulomb potential in two and three dimensions is known analytically (App. C.1.2). From the discretized eigenvalue problem

$$-\frac{1}{2} \sum_{j'} \Delta_{jj'} \Phi_{\text{g.s.};j'} - V_j \Phi_{\text{g.s.};j} = E_{\text{g.s.}} \Phi_{\text{g.s.};j} \quad (2.97)$$

we obtain an explicit expression for the unknown coefficients V_j :

$$-V_j = E_{\text{g.s.}} + \frac{1}{2} \frac{\sum_{j'} \Delta_{jj'} \Phi_{\text{g.s.};j'}}{\Phi_{\text{g.s.};j}}. \quad (2.98)$$

This formula exactly reproduces the ground state. Excited states are less crucial, because they are less localized at the origin.

So far, it is not clear if the above discretization gives accurate results if the potential is different from V or the operator of the kinetic energy is different from $-\frac{1}{2}\Delta$. To demonstrate the robustness of the discretization of V we treat two examples. First, we calculate the ground state E_0 for Example A as function of the cyclotron frequency ω_c . Second, we calculate the ground state of the operator

$$\hat{H} = -\frac{1}{2m} \Delta_\varrho - \frac{1}{\varrho} \quad (2.99)$$

with variable mass m . In both cases, the discretization of the Coulomb potential is performed with the ground-state energy $E_{\text{g.s.}} = -2$ and the ground-state wavefunction (C.61). The ground-state energy of the operator (2.99) is analytically known to be equal to $-2m$. The result of the numerical calculation is shown in Fig. 2.6. For a mesh size $h = \frac{1}{10}$ the results are virtually undistinguishable from the exact results, but even for $h = \frac{1}{5}$ the accuracy is reasonable. These values are much larger than the step size in the last example, which was $h = \frac{1}{16}$. Even though the method (2.98) cannot be rigorously justified, the practical results are even better than for finite elements and the programming effort is much smaller. The ground-state-adapted discretization of the Coulomb potential has been successfully used by other authors [84].

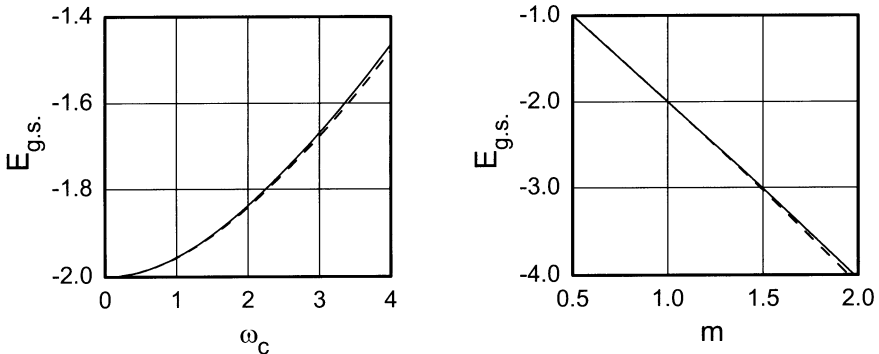


Fig. 2.6. Left: Ground-state energy $E_{g.s.}$ for Example A as function of the cyclotron frequency ω_c . Right: Ground-state energy of the operator (2.99) as function of the reduced mass m . The mesh sizes are $h = \frac{1}{10}$ (solid line) and $h = \frac{1}{5}$ (dashed line)

As the discretization of the potentials results in a diagonal matrix, the calculation of the norm is very easy. The norm is identical to the largest matrix element in magnitude.

Having treated the same examples by means of orthonormal base functions, finite elements, and finite differences, it is time to compare the three methods. The scope for the application of orthonormal base functions is very limited. Their only application are the confinement directions for some systems of strong confinement. In principle, almost all problems that can be solved using finite elements can also be solved using finite difference and vice versa. On the other hand, from the point of view of the programming effort, finite elements are much more costly than the finite differences. A particularly tedious procedure is the calculation of the Coulomb matrix elements. In contrast, in the framework of finite difference we have a very simple formula (2.98), which yields a diagonal matrix for the Coulomb potential. Also, the computing time is larger for finite elements, compared to finite differences with the same node spacing. In order to increase the accuracy, we recommend to reduce the mesh size in the finite-difference approximation, or to increase the order of the approximation in the case of Cartesian coordinates. Higher-order B-splines may be useful for the treatment of the radial part of polar or spherical coordinates, because of the difficulties of finding a higher-order finite-difference approximation which is consistent with the approximation of the scalar product.

2.3 Solution of the Initial-Value Problem

The solution of the eigenvalue and the boundary-value problem as algebraic eigenvalue problem or linear set of equations does not fully take into account

the sparsity of the matrix. In the last section, we have demonstrated that, by minimizing the bandwidth, all class-II problems can in principle be solved as boundary-value problems. This strategy cannot be applied to class-III problems, because they involve multiple continua. Consider a system with a two-parametric continuum like Example C, D, or E. If the Hamiltonian is discretized on a mesh with 1000×1000 points, then the resulting matrix has a dimension of $N = 1\,000\,000$ with an overall bandwidth of $B \approx 1000$. Neither the storage nor the numerical effort would allow the solution as a matrix eigenvalue problem or as a set of equations by exact methods (cf. Tabs. 2.2 and 2.3). At present, there is also no convincing evidence that the task can be fulfilled by iterative methods.

In this section we demonstrate that the solution of the initial-value problem in combination with sparse matrices, which result from the discretization by finite differences, can be used as an efficient method for the calculation of the optical susceptibility, generally applicable to class-III problems, with a numerical effort and storage scaling like $O(N)$. We also show how, in some cases, storage and computational effort can be considerably reduced by the introduction of absorbing boundary conditions [67].

Until now, the time-dependent Schrödinger equation lives in the shadows of the mainstream mathematical literature, but is intensively studied in quantum chemistry and computational physics. An excellent review on the numerical solution of the time-dependent Schrödinger equation is given in an article by Kosloff [60].

2.3.1 The Time-Propagation Scheme

We wish to solve the initial-value problem

$$i \frac{d}{dt} \Psi(t) = H \Psi(t) ; \quad \Psi(0) = i \mu . \quad (2.100)$$

The above notation applies for the discretization by means of orthonormal base functions or finite differences. For finite elements, the matrix H has to be replaced by $G^{-1}H$ (2.54).

The eigenvalues of H (2.100) play an important role for the stability of a discretization scheme. We suppose that the eigenvalues are ordered according to

$$E_0 \leq \dots \leq E_{N-1} . \quad (2.101)$$

The norm of H is given by $\|H\| = \max(|E_0|, |E_{N-1}|)$; without loss of generality we assume $E_{N-1} > 0$ and $\|H\| = E_{N-1}$.

First we shall demonstrate what happens if we solve the above equation the naive way, namely

$$\Psi(t+\Delta t) = (1 - i\Delta t H) \Psi(t) . \quad (2.102)$$

This discretization in time domain is known as the Euler method. In order to analyze the accuracy and stability, we perform a decomposition into eigenmodes according to

$$\Psi(t) = \sum_{\Lambda=1}^{N-1} c_\Lambda(t) \Phi_\Lambda ; \quad c_\Lambda(0) = \langle \Phi_\Lambda, i\mu \rangle . \quad (2.103)$$

Then the eigenmodes at $t_q = q\Delta t$ are

$$c_\Lambda(t_q) = (1 - i\Delta t E_\Lambda)^q c_\Lambda(0) = \left(1 - i\frac{E_\Lambda T}{p}\right)^q c_\Lambda(0) , \quad (2.104)$$

where $p = T/\Delta t$ is the number of time steps in the interval $[0, T]$. In order to closely approximate the exact solution for $E_\Lambda \leq \omega_{\max}$ in the interval $t \in [0, T]$ we have to choose $\Delta t \ll 1/\omega_{\max}$. However, for this choice of Δt , the modes with large energy $E_\Lambda \gg \omega_{\max}$ would rapidly explode. From

$$|c_{N-1}(t_q)|^2 = \left(1 + \frac{E_{N-1}^2 T^2}{p^2}\right)^q |c_{N-1}(0)|^2 \quad (2.105)$$

it follows that the time step needs to be much smaller, namely $\Delta t \approx 1/(\|H\|^2 T)$. The discretization scheme (2.102) for the Schrödinger equation is said to be unstable, because for any step size Δt , the norm $\|\Psi\| = \sqrt{|c_1|^2 + \dots + |c_{N-1}|^2}$ goes to infinity as $t \rightarrow \infty$.

We mention that for the diffusion equation

$$\frac{d}{dt} \Psi(t) = \Delta \Psi(t) \quad (2.106)$$

the Euler scheme is conditionally stable. By the same analysis as above it is easy to show that the time step has to be

$$\Delta t < \frac{2}{\|\Delta\|} , \quad (2.107)$$

where $\|\Delta\|$ is the norm of the discretized Laplacian.

Several alternatives have been proposed for the solution of the time-dependent Schrödinger equation. A review is given in an article by Kosloff [60] and by Taha and Ablowitz [85].

In the Crank–Nicolson scheme [10, 85, 86]

$$\Psi(t+\Delta t) = \left(1 + \frac{1}{2}i\Delta t H\right)^{-1} \left(1 - \frac{1}{2}i\Delta t H\right) \Psi(t) , \quad (2.108)$$

also known as explicit–implicit method, a set of equations has to be solved at each time step. As the approximation of the exponential is G -unitary, this method is unconditionally stable (i.e., for each Δt), but is efficient only for one space dimension ($m = 1$), where H is a band matrix and the application of the inverse operator takes only $O(N)$ operations. This is not of practical interest

since for class I the optical susceptibility can be conveniently calculated by solving an eigenvalue or boundary-value problem.

The operator-splitting method starts with an expression for the Hamiltonian of the form $\hat{H} = \hat{H}_{\text{kin}} + \hat{H}_{\text{pot}}$. The time evolution is approximated as [60, 62, 80, 87]

$$\Psi(t+\Delta t) = e^{-\frac{1}{2}i\Delta t H_{\text{kin}}} e^{-i\Delta t H_{\text{pot}}} e^{-\frac{1}{2}i\Delta t H_{\text{kin}}} \Psi(t). \quad (2.109)$$

A variant is the Fourier method, where the exponential of $H_{\text{kin}} = \frac{1}{2}\hat{k}^2$ is calculated in (quasi-)momentum space [60, 80, 87]. The transition from real to momentum space by fast Fourier transform (FFT) takes in the order of $N \ln N$ operations.

A generalization of the Crank–Nicolson method for multidimensions is called alternating direction implicit (ADI) method [10, 71, 72]. Here the solution of a tridiagonal set of equations is performed separately for each direction, so the numerical effort for each time step is still $O(N)$. An example is the propagation scheme

$$\begin{aligned} \Psi(t+\Delta t) &= \left(1 + \frac{1}{2}i\Delta t H_{\text{kin}}^{(1)}\right)^{-1} \left(1 + \frac{1}{2}i\Delta t H_{\text{kin}}^{(2)}\right)^{-1} e^{-i\Delta t H_{\text{pot}}} \\ &\quad \times \left(1 - \frac{1}{2}i\Delta t H_{\text{kin}}^{(2)}\right) \left(1 - \frac{1}{2}i\Delta t H_{\text{kin}}^{(1)}\right) \Psi(t), \end{aligned} \quad (2.110)$$

with $\hat{H}_{\text{kin}}^{(1)}$ and $\hat{H}_{\text{kin}}^{(2)}$ being the components of the kinetic-energy operator for different space directions.

Even though the schemes (2.109) and (2.110) are unconditionally stable, they have one major drawback, since the errors result from the noncommutativity of the operators \hat{H}_{kin} and \hat{H}_{pot} . This error is particularly large near the origin of the Coulomb potential. On the other hand, the oscillator strength is taken exactly at this point. This means that a very small step size must be used to achieve convergence for the optical spectrum. Other disadvantages are the high numerical costs for the FFT or the solution of a tridiagonal set of equations, compared to the multiplication with a sparse matrix, and the fact that the Fourier method is limited virtually to Cartesian coordinates with periodic boundary conditions. Therefore, these methods are not the first choice for the numerical solution of the time-dependent Schrödinger equation.

Global propagators like the Chebychev and the Lanczos scheme are based upon polynomial approximations of the time-evolution operator $\exp(-iHt)$ [60]. While these methods are very efficient to calculate the solution for one large value of t , they do not yield the intermediate values for $t_q = q \Delta t$, which are required for the calculation of the optical spectrum.

For our scope of problems, the method of choice is the central-difference or leapfrog scheme [59, 60, 81, 85, 86, 88]:

$$i \frac{\Psi(t+\Delta t) - \Psi(t-\Delta t)}{2\Delta t} = H \Psi(t) \quad (2.111)$$

It is an explicit method, because $\Psi(t+\Delta t)$ is calculated explicitly from $\Psi(t)$ and $\Psi(t-\Delta t)$:

$$\Psi(t+\Delta t) = \Psi(t-\Delta t) - 2i\Delta t H \Psi(t). \quad (2.112)$$

The stability of the leapfrog method can be studied by means of von Neumann stability analysis, calculating the growth factors [60, 86, 88]. Alternatively, the equation of motion for the individual modes can be solved exactly. We start from (2.111) and replace H by E_A and Φ by c_A . Then the difference equation is solved by the ansatz $c_A(t_q) = \alpha^q$, which gives rise to two solutions α^\pm . In the case of degeneracy, when $\alpha^+ = \alpha^- = \alpha$, a linearly independent solution is given by $c_A(t_q) = q\alpha^q$. Then we find [41, 59]

$$c_A^\pm(t_q) = \begin{cases} [-iE_A\Delta t \pm \sqrt{1 - (E_A\Delta t)^2}]^q & \text{for } E_A\Delta t \neq 1 \\ (1 \pm q)(-i)^q & \text{for } E_A\Delta t = 1. \end{cases} \quad (2.113)$$

If the stability criterion

$$\Delta t < 1/\|H\| \quad (2.114)$$

is fulfilled, then $|c_A^\pm(t_q)| = 1$ for each A . For $\Delta t > 1/\|H\|$, some modes will grow exponentially. Thus the leapfrog scheme is conditionally stable. The time step (2.114) is by a factor $\|H\|T$ larger than for the crude Euler method (2.102). This factor can be as large as a few hundred.

Now we turn to the question of accuracy. The three-level recursion (2.112) needs two initial values $\Psi(0)$ and $\Psi(\Delta t)$. To calculate $\Psi(\Delta t)$ from $\Psi(0)$ we use the second-order approximation of the exponential

$$\Psi(\Delta t) = [1 - i\Delta t H - \frac{1}{2}(\Delta t H)^2] \Psi(0). \quad (2.115)$$

With this initial conditions the solution for the eigenmodes is

$$c_A(t_q) = c_0 (a_A^+ e^{-i\omega_A^+ t_q} + a_A^- e^{-i\omega_A^- t_q})$$

$$a_A^+ = \frac{1 - \frac{1}{2}(E_A\Delta t)^2 + \sqrt{1 - (E_A\Delta t)^2}}{2\sqrt{1 - (E_A\Delta t)^2}}; \quad a_A^- = 1 - a_A^+ \quad (2.116)$$

$$\omega_A^+ = \frac{\arcsin(E_A\Delta t)}{\Delta t}; \quad \omega_A^- = \pm \frac{\pi}{\Delta t} - \omega_A^-.$$

The deviation of c_A^+ from 1 is $\frac{1}{16}(E_A\Delta t)^4 + O[(E_A\Delta t)^6]$. In Examples C–E it holds that $\omega_{\max} < \frac{1}{7}\|H\|$, so that the error for the amplitudes is smaller than 10^{-4} . The relative deviation of the frequencies ω_A^+ from the eigenvalues E_A is $\frac{1}{6}(E_A\Delta t)^2 + O[(E_A\Delta t)^4]$, which for $E_A \leq \omega_{\max}$ is smaller than 10^{-2} . The frequencies ω_A^+ are located in the interval $(-\pi/2\Delta t, +\pi/2\Delta t)$, while the ghost states ω_A^- are found outside this interval.

From the time-evolution of the eigenmodes we see that that the time evolution by the leapfrog method is almost a unitary transform. It can be shown that the quantities $\text{Re} \langle \Psi(t_{q+1}), \Psi(t_q) \rangle$ and $\text{Re} \langle H\Psi(t_{q+1}), H\Psi(t_q) \rangle$ are conserved [81].

The norm of the matrix H , which governs the step size Δt , can be estimated from the individual components, i.e., kinetic energy, confinement, external fields, and Coulomb potential. Furthermore, the critical step size Δt can be determined experimentally: if Δt is too large, the calculation will explode quickly.

As an explicit method, the leapfrog scheme is very flexible and can be used with finite differences, finite elements, orthonormal base functions or with the Fourier method [81]. In combination with finite differences the application is straightforward and the numerical implementation is highly efficient, especially on vector machines. The numerical effort of calculating one spectrum is equal to

$$n_{\text{op}} = ckN\|H\|/\epsilon = ckN \text{cond}[H - (\omega + i\epsilon)] ; \quad 5 \leq c \leq 8 , \quad (2.117)$$

where the upper integration limit is assumed to be $5/\epsilon \leq T \leq 8/\epsilon$ and kN is the number of floating-point operations necessary for one time step (2.112), which is basically the multiplication of a vector with the sparse matrix H .

In some cases, the numerical effort can be reduced by a factor of 2 [89]. From (2.4) and (2.11) it follows that

$$\langle \Psi(0) | \Psi(t) \rangle = \langle \Psi(-t/2) | \Psi(+t/2) \rangle . \quad (2.118)$$

If the dipole matrix element $\mu(u)$ and the differential operator \hat{H} are real, then it holds that $\Psi(u, -t/2) = -\Psi^*(u, +t/2)$ and, therefore

$$P(2t) = -i \langle \Psi^*(t) | \Psi(t) \rangle , \quad (2.119)$$

which means that in order to calculate $P(t)$ for $0 \leq t \leq T$ we need to solve the initial-value problem only for the interval $0 \leq t \leq T/2$. The realization in the computer program is demonstrated in App. D.3. The generalization to the case of time-reversal symmetry is straightforward.

We mention that the leapfrog scheme combined with finite elements is also an $O(N)$ method, provided the coordinates are products of one-dimensional coordinates (2.7). Then, using the idea of the ADI method, the application of G^{-1} at each time step (2.54) is done separately for each direction, according to (2.58). Finite differences and finite elements can also be combined with orthonormal base functions for some directions [27] or the Fourier method [49]. Recently, the equation-of-motion method was used for the calculation of the excitonic absorption of bulk Silicon and Silicon surfaces, using a Bloch basis [70].

2.3.2 Two Examples

The calculation of the optical susceptibility by solving the initial-value problem is a highly efficient and can be applied for class-III problems. In this subsection we shall demonstrate the application of this method for Examples C and D from Sect. 2.1.

We start with Example C (2.15). For the numerical calculation we use a finite domain with vanishing boundary conditions

$$G = \left[-\frac{L_x}{2}, +\frac{L_x}{2} \right] \times \left[-\frac{L_y}{2}, +\frac{L_y}{2} \right] \quad (2.120)$$

and a regular mesh

$$\begin{aligned} x_j &= -\frac{L_x}{2} + j h_x ; \quad j = 1, \dots, N_x ; \quad h_x = \frac{L_x}{N_x+1} ; \quad N_x \text{ odd} \\ y_l &= -\frac{L_y}{2} + l h_y ; \quad l = 1, \dots, N_y ; \quad h_y = \frac{L_y}{N_y+1} ; \quad N_y \text{ odd} . \end{aligned} \quad (2.121)$$

For the discretization of the Laplacian we use the second- and fourth-order finite-difference formulas (2.80) and (2.81). The vanishing boundary conditions (2.120) are equivalent to an antiperiodic continuation of the function Ψ . Therefore, it holds that

$$\begin{aligned} \Psi\left(\pm\frac{L_x}{2} + h_x, y, t\right) &= -\Psi\left(\pm\frac{L_x}{2} - h_x, y, t\right) \\ \Psi\left(x, \pm\frac{L_y}{2} + h_y, t\right) &= -\Psi\left(x, \pm\frac{L_y}{2} - h_y, t\right) . \end{aligned} \quad (2.122)$$

These relations are important for the application of the fourth-order formula (2.81) for arguments near the domain boundaries. The discretization of the Coulomb potential is performed by means of the ground-state method (2.98), where $\Delta_{jj'}$ is the discretization of the Laplacian by second- or fourth-order finite differences, respectively.

In order to apply the leapfrog scheme, we need an upper estimate for the norm of the discretized Hamiltonian. The effect of the Coulomb potential on the norm is negligible and $\|H\|$ is determined by the discretization of the Laplacian. From (2.93) and (2.94) it follows that

$$\|H\| \leq 2 \left(\frac{1}{h_x^2} + \frac{1}{h_y^2} \right) \quad (2.123)$$

for the second-order discretization and

$$\|H\| \leq \frac{8}{3} \left(\frac{1}{h_x^2} + \frac{1}{h_y^2} \right) \quad (2.124)$$

for the fourth-order discretization.

The homogeneous linewidth ϵ was chosen to be 0.1. The estimates for the normalization length in one dimension (Sect. 2.2) do not exactly apply for two dimensions. We found that normalization lengths $L_x = L_y = 150$ were sufficient for a smooth continuum in the frequency range $\omega \leq 20$. The number of mesh points was $N_x = N_y = 999$ resulting in step sizes $h_x = h_y = 0.15$. The total dimension of the problem was $N = N_x N_y \approx 1\,000\,000$.

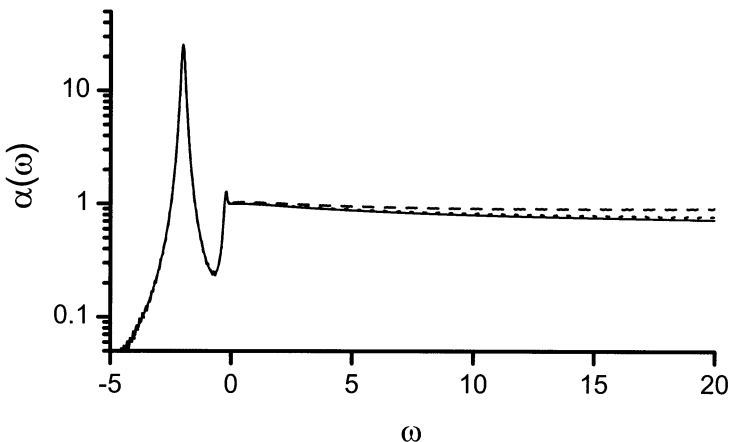


Fig. 2.7. Optical absorption for the ideal two-dimensional semiconductor. *Solid line:* analytical result (right of Fig. 1.5), *dashed line:* numerical result using second-order finite differences, *dotted line:* numerical result using fourth-order finite differences

The result of the calculation is shown in Fig. 2.7. The absorption coefficient α is shown as function of the frequency ω , using a logarithmic scale. The analytical result (*solid line*) is compared with the numerical result using second-order finite differences (*dashed line*) and fourth-order finite differences (*dotted line*). The result of the second-order finite differencing already shows the correct qualitative behavior. The continuum absorption is slightly enhanced, compared to the exact solution. For fourth-order finite differences, the numerical result is nearly undistinguishable from the analytical result. The programs by which Fig. 2.7 was obtained are listed in App. D.1.

Before we turn to the numerical calculation of the optical absorption for Example D we shall introduce a method of generating a Gaussian stochastic potential for a given autocorrelation function [17]. We assume a d -dimensional domain $\Omega^{(d)}$ with Born–von Kármán boundary conditions and consider the function

$$W(\mathbf{r}) = \frac{1}{\sqrt{\Omega^{(d)}}} \sum_{\mathbf{k}}' e^{i\mathbf{k} \cdot \mathbf{r}} C(\mathbf{k}) s(\mathbf{k}) ; \quad s(\mathbf{k}) = s(k) \geq 0 . \quad (2.125)$$

The prime at the sum means that the point $\mathbf{k} = 0$ is excluded from the summation. The quantities $C(\mathbf{k})$ are complex stochastic variables, equally distributed on the unit circle. They are independent for different \mathbf{k} except for the restriction

$$C(\mathbf{k}) = C^*(-\mathbf{k}). \quad (2.126)$$

The function W is real. From $\langle\langle C(\mathbf{k}_1) C(\mathbf{k}_2) \rangle\rangle = \delta_{\mathbf{k}_1, -\mathbf{k}_2}$ it follows that

$$\begin{aligned} \langle\langle W(\mathbf{r}_1) W(\mathbf{r}_2) \rangle\rangle &= A(\mathbf{r}_1 - \mathbf{r}_2) \\ A(\mathbf{r}) = A(r) &= \frac{1}{(2\pi)^d} \int d^d \mathbf{k} e^{i\mathbf{k}\cdot\mathbf{r}} s^2(\mathbf{k}), \end{aligned} \quad (2.127)$$

in the limit $\Omega^d \rightarrow \infty$. Here $\langle\langle \dots \rangle\rangle$ means the ensemble average. The function A is called the autocorrelation function of the stochastic potential. Higher correlation functions reduce to products of pair correlation functions, for example,

$$\begin{aligned} \langle\langle W(\mathbf{r}_1) W(\mathbf{r}_2) W(\mathbf{r}_3) W(\mathbf{r}_4) \rangle\rangle &= A(\mathbf{r}_1 - \mathbf{r}_2) A(\mathbf{r}_3 - \mathbf{r}_4) \\ &\quad + A(\mathbf{r}_1 - \mathbf{r}_3) A(\mathbf{r}_2 - \mathbf{r}_4) \quad (2.128) \\ &\quad + A(\mathbf{r}_1 - \mathbf{r}_4) A(\mathbf{r}_2 - \mathbf{r}_3). \end{aligned}$$

The ensemble-averaged product of an odd number of potentials is zero. In the limit $\Omega^{(d)} \rightarrow \infty$, the ensemble average can be replaced by the average over the normalization volume:

$$\langle\langle W(\mathbf{r}_1) \cdots W(\mathbf{r}_l) \rangle\rangle = \frac{1}{\Omega^{(d)}} \int d^d \mathbf{r} W(\mathbf{r}_1 + \mathbf{r}) \cdots W(\mathbf{r}_l + \mathbf{r}). \quad (2.129)$$

From

$$\langle\langle W^l(\mathbf{r}) \rangle\rangle = \begin{cases} A^{l/2}(0) (l-1)!! & \text{for } l \text{ even} \\ 0 & \text{for } l \text{ odd} \end{cases} \quad (2.130)$$

it follows that $W(\mathbf{r})$ for fixed \mathbf{r} is a Gaussian random variable and the probability density is

$$p(w) = \langle\langle \delta[w - W(\mathbf{r})] \rangle\rangle = \frac{1}{\sqrt{2\pi\sigma^2}} e^{-\frac{w^2}{2\sigma^2}}; \quad \sigma^2 = A(0). \quad (2.131)$$

The above method of generating a Gaussian stochastic potential (2.125) is widely used to model the effect of interface roughness in low-dimensional semiconductors [18, 43, 90–92].

As example we assume an autocorrelation function

$$A(x, y) = \sigma^2 \exp\left(-\frac{x^2 + y^2}{2\lambda^2}\right). \quad (2.132)$$

A realization for W is shown in Fig. 2.8 for a potential strength $\sigma = 0.5$ and a correlation length $\lambda = 1$. The coordinate ξ means an arbitrary direction in the xy plane.

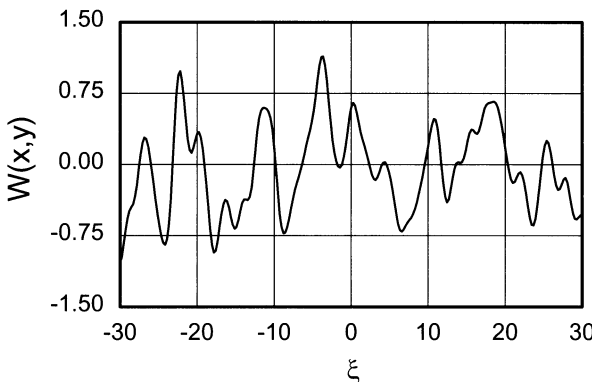


Fig. 2.8. One realization of the stochastic potential (2.125) with an autocorrelation function (2.132) for parameters $\sigma = 0.5$ and $\lambda = 1$

Now we numerically calculate the optical absorption for Example D with a stochastic potential generated by means of formula (2.125), characterized by an autocorrelation function (2.132). As the stochastic potential W and the dipole matrix element μ are periodic functions with the periodicity domain $[-L_x/2, +L_x/2] \times [-L_y/2, +L_y/2]$, we use periodic boundary conditions. The mesh is given by

$$\begin{aligned} x_j &= -\frac{L_x}{2} + j h_x ; \quad j = 1, \dots, N_x ; \quad h_x = \frac{L_x}{N_x} ; \quad N_x \text{ even} \\ y_l &= -\frac{L_y}{2} + l h_y ; \quad l = 1, \dots, N_y ; \quad h_y = \frac{L_y}{N_y} ; \quad N_y \text{ even} . \end{aligned} \quad (2.133)$$

Due to the periodic boundary conditions, x is equivalent to $x - L_x$ and y is equivalent to $y - L_y$. This relation is important for the discretization of the Laplacian near the domain boundaries by means of the formulas (2.80) and (2.81). The discretization of the smooth potential W was performed by means of the simple rule (2.96). As in the numerical treatment of Example C, the norm of H is mainly determined by the the Laplacian. For safety reasons, we use the estimate

$$\|H\| \leq \|-\frac{1}{2}\Delta\| + 5\sigma . \quad (2.134)$$

For the actual calculations we use normalization lengths $L_x = L_y = 500$, a number of mesh points $N_x = N_y = 1024$, and a homogeneous linewidth $\epsilon = 0.1$. The result is shown in Fig. 2.9. The optical absorption α is plotted versus frequency for a potential strength $\sigma = 0.5$ and different correlation lengths $\lambda = 0.5, 1.0$, and 2.0 . For comparison, the classical result ($\lambda \rightarrow \infty$), which results from the convolution of the probability density (2.131) with

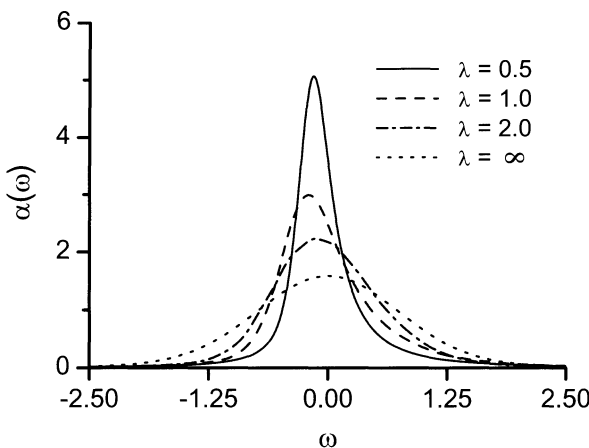


Fig. 2.9. Optical absorption α vs. frequency ω for Example D using a Gaussian stochastic potential with an autocorrelation function (2.132). The parameters are $\epsilon = 0.1$, $\sigma = 0.5$, and $\lambda = 0.5$ (solid line), 1.0 (dashed line), and 2.0 (dash-dotted line). For comparison, the classical result is shown (dotted line)

the Lorentzian $\epsilon/(\omega^2 + \epsilon^2)$, is shown. The numerical result is fully converged, and is the same for the discretization of the Laplacian by the second-order and by the fourth-order formula. The absorption spectrum is a deterministic quantity and is independent of the specific realization of W . For a small correlation length, we observe a strong departure from the classical result. The maximum is shifted to lower frequencies, the linewidth (FWHM) is much smaller than the classical linewidth (motional narrowing), and the absorption spectrum is asymmetric with a slowly dropping shoulder at the high-energy side [93]. With increasing correlation length λ , the quantum-mechanical result approaches the classical result.

2.3.3 Absorbing Boundary Conditions

The solution of the initial-value problem with finite differences is a highly efficient method for calculating the optical absorption, where the numerical effort and storage scale like $O(N)$. A weak point so far is the huge number of grid points (typically in the order of 1000) for each continuum direction. In some cases, the number of base functions and, therefore, numerical effort and storage, can be drastically reduced by the application of absorbing boundary conditions. Absorbing (transmitting, open) boundary conditions are used in quantum-mechanical and electromagnetic calculations to simulate open systems [94–97]. In 1999, Ahland et al. have demonstrated the usefulness of absorbing boundary conditions for the calculation of the optical absorption in the presence of continuum states [67]. A discussion of various methods is found in a recent publication by Zambrano and Arce on the quantum confined Stark effect [48].

The purpose of absorbing boundary conditions is to simulate wave propagation in an infinite domain by suppressing reflection of the wavepackets at the boundaries. Candidates for absorbing boundary conditions are those

directions where (i) the initial wavepacket is localized near the origin, (ii) the polarization Ψ is of interest only in a small region around the origin and (iii) the potential approaches a constant far from the origin so that the time evolution of Ψ is the same as for a free particle. Conditions (i) and (ii) are fulfilled if the dipole matrix element is localized, which is almost always the case. Asymptotic free motion is given for those directions which are not subjected to geometric confinement or the action of external potentials. Representatives are Example A in the case $B = 0$, the ϱ direction of Example B, the x and y directions of Example C, and the ϱ direction of Example E.

In order to derive the formulation for absorbing boundary conditions, we consider a very simple model of a free particle in one dimension:

$$i \frac{\partial}{\partial t} \Psi(x, t) = \hat{H} \Psi(x, t); \quad \hat{H} = -\frac{1}{2} \frac{\partial^2}{\partial x^2}; \quad \Phi(x, 0) = i \mu(x). \quad (2.135)$$

We assume that the function $\mu(x)$ is localized near the origin. The solution of (2.135) on an infinite domain can be written in the following form:

$$\begin{aligned} \Psi(x, t) &= \Psi^+(x, t) + \Psi^-(x, t) \\ \Psi^\pm(x, t) &= \frac{1}{2\pi} \int_{-\infty}^{+\infty} dk \Theta(\pm k) e^{+ikx - i\frac{k^2}{2}t} i \tilde{\mu}(k), \end{aligned} \quad (2.136)$$

where $\tilde{\mu}(k)$ is the Fourier transform of $\mu(x)$. The functions Ψ^\pm represent wavepackets travelling in positive and negative x direction. This can be seen from calculating the speed of the wavepackets:

$$\begin{aligned} X^\pm(t) &= \int_{-\infty}^{+\infty} dx x |\Psi^\pm(x, t)|^2 \\ \frac{d}{dt} X^\pm(t) &= \frac{1}{2\pi} \int_{-\infty}^{+\infty} dk \Theta(\pm k) k |\tilde{\mu}(k)|^2 \gtrless 0. \end{aligned} \quad (2.137)$$

Now we consider vanishing boundary conditions at $x = +L_1/2 > 0$. This will mainly affect the wavepacket Ψ^+ traveling in positive x direction. To fulfill the boundary conditions, this function needs to be replaced by

$$\begin{aligned} \Psi^+(x, t) &= \int_0^{+\infty} dk [e^{ikx} + R(k) e^{-ikx}] e^{-i\frac{k^2}{2}t} i \tilde{\mu}(k) \\ R(k) &= -e^{+ikL_1}. \end{aligned} \quad (2.138)$$

The quantity $|R(k)|^2$ is interpreted as reflection coefficient and it holds that $|R(k)|^2 = 1$. The reflection at the boundaries is responsible for the occurrence of discrete resonances in the absorption instead of a flat continuum.

The idea of absorbing boundary conditions is to modify the Hamiltonian or the boundary conditions such that $R(k) = 0$ for all $k > 0$. In this case, the system will behave like an open system for $x \leq +L_1/2$. This can be done by modifying the potential [94] or the operator of the kinetic energy [67]. We follow the latter path and introduce an absorption layer $[+L_1/2, +L_2/2]$ with boundary condition $\Psi(+L_2/2, t) = 0$. Inside the absorption layer we modify the Hamiltonian in such a way that the eigenfunctions $\Phi_k(x)$, which belong to the eigenvalue $\frac{1}{2}k^2$ for positive k , fulfill

$$\Phi_k(x) = e^{ikx} \text{ for } x \leq +\frac{L_1}{2}; \quad \Phi_k(x) \rightarrow 0 \text{ for } x \rightarrow +\frac{L_2}{2}. \quad (2.139)$$

For the eigenfunctions we make the ansatz [67]

$$\Phi_k(x) = e^{ik\xi(x)}; \quad \xi'(x) \text{ continuous} \quad (2.140)$$

$$\xi(x) = x \text{ for } x \leq +\frac{L_1}{2}; \quad \xi(x) \rightarrow |\infty| e^{i\beta} \text{ for } x \rightarrow +\frac{L_2}{2}; \quad 0 < \beta < \frac{\pi}{2}.$$

The functions (2.140) are eigenfunctions of the modified Hamiltonian [67]

$$\hat{H} = -\frac{1}{2} \frac{1}{s(x)} \frac{\partial}{\partial x} \frac{1}{s(x)} \frac{\partial}{\partial x}; \quad s(x) = \frac{d\xi}{dx}. \quad (2.141)$$

The effect of the stretching factor $s(x)$ is twofold. The real part $\operatorname{Re} s(x) > 1$ makes the interval artificially longer, while the imaginary part $\operatorname{Im} s(x) > 0$ leads to damping of the outgoing wave. Theoretically, the reflection coefficient is zero for all $k > 0$. In the numerical calculation, reflection-free propagation is fulfilled only for a finite set of wavenumbers, because of a finite number of mesh points in the absorption layer.

It is worthwhile to examine the effect of the absorbing boundary conditions on bound states. For a negative eigenvalue E_A , the asymptotic behavior of the eigenfunction for large x is $\Phi_A(x) \sim \exp(-\sqrt{-2E_A}x)$. As in the case of scattering states, the coordinate transform (2.140) leads to $\Phi_A(+L_2/2) = 0$.

The treatment of the negative x direction is in complete analogy to the treatment of the positive x direction. In this case, an absorption layer needs to be introduced in order to prevent reflection of the wavepacket Ψ^- . For a symmetric domain we end up with the expression (2.141) for the modified Hamiltonian, where the function s fulfills $s(x) = s(-x)$.

It is more convenient to approximate the Hamiltonian (2.141) as

$$\hat{H} = -\frac{\partial}{\partial x} \frac{1}{2m(x)} \frac{\partial}{\partial x} \quad (2.142)$$

$$m(x) = 1 \text{ for } |x| \leq \frac{L_1}{2}; \quad m(x) \rightarrow |\infty| e^{i\alpha} \text{ for } x \rightarrow \pm \frac{L_2}{2}; \quad 0 < \alpha < \pi,$$

where $m(x)$ takes the role of $s^2(x)$. The expression (2.142) is the typical form of a Hamiltonian when the mass of the particle depends on the coordinate. In this notation, the numerical discretization of the operator (2.142)

and the generalization to curvilinear coordinates is straightforward. The fact that the mass $m(x)$ is complex leads to non-Hermitian contributions to the Hamiltonian:

$$\begin{aligned}\hat{H} &= \hat{H}^{(I)} + \hat{H}^{(II)} \\ \hat{H}^{(I)} &= \frac{\partial}{\partial x} \operatorname{Re} \frac{-1}{2m(x)} \frac{\partial}{\partial x}; \quad \hat{H}^{(II)} = i \frac{\partial}{\partial x} \operatorname{Im} \frac{-1}{2m(x)} \frac{\partial}{\partial x}.\end{aligned}\tag{2.143}$$

The Hermitian part $\hat{H}^{(I)}$ corresponds to a Schrödinger equation of a particle where the mass increases towards infinity as the particle approaches the outer boundaries $\pm L_2/2$. The anti-Hermitian part $\hat{H}^{(II)}$, which is nonzero only in the absorption layer, gives rise to diffusion with a diffusion coefficient $-\frac{1}{2} \operatorname{Im} m^{-1}(x) \geq 0$. As the amplitude of the wavepacket is zero in the average, the diffusion leads to a destruction of the polarization inside the absorption layer. This process is more effective for larger wavenumbers k and, therefore, for higher frequencies.

The generalization of (2.142) for the radial part of polar coordinates with an absorption layer $[R_1, R_2]$ is

$$\hat{H} = -\frac{1}{\varrho} \frac{\partial}{\partial \varrho} \frac{\varrho}{2m(\varrho)} \frac{\partial}{\partial \varrho}\tag{2.144}$$

$$m(\varrho) = 1 \text{ for } \varrho \leq R_1; \quad m(\varrho) \rightarrow |\infty| e^{i\alpha} \text{ for } \varrho \rightarrow R_2; \quad 0 < \alpha < \pi.$$

Hermitian and anti-Hermitian part are obtained by replacing $m^{-1}(\varrho)$ by $\operatorname{Re} m^{-1}(\varrho)$ and $i \operatorname{Im} m^{-1}(\varrho)$, respectively.

The discretization of the differential operators (2.142) and (2.144) by second-order finite differences is

$$\begin{aligned}(\hat{H} \Psi)_j &= -\frac{1}{2} \frac{m_{j+1/2}^{-1} \Psi_{j+1} - [m_{j+1/2}^{-1} + m_{j-1/2}^{-1}] \Psi_j + m_{j-1/2}^{-1} \Psi_{j-1}}{h^2} \\ m_{j \pm 1/2} &= m(x_j \pm \frac{h}{2})\end{aligned}\tag{2.145}$$

and

$$\begin{aligned}(\hat{H} \Psi)_j &= -\frac{1}{2} \frac{\frac{\varrho_{j+1/2}}{m_{j+1/2}} \Psi_{j+1} - [\frac{\varrho_{j+1/2}}{m_{j+1/2}} + \frac{\varrho_{j-1/2}}{m_{j-1/2}}] \Psi_j + \frac{\varrho_{j-1/2}}{m_{j-1/2}} \Psi_{j-1}}{h^2} \text{ for } j > 0 \\ (\hat{H} \Psi)_0 &= -\frac{1}{2} \frac{m_{1/2}^{-1} (4\Psi_1 - 4\Psi_0)}{h^2}.\end{aligned}\tag{2.146}$$

in analogy to (2.80) and (2.87, 2.90). The discretization of the Hermitian and anti-Hermitian part follows from the real and imaginary part and the resulting matrices $H^{(I)} = \operatorname{Re} H$ and $H^{(II)} = i \operatorname{Im} H$ are Hermitian and anti-Hermitian with respect to the scalar product $\langle \cdot, \cdot \rangle$ (2.66).

As the equation of motion is a combination of a Schrödinger and a diffusion equation, the leapfrog scheme is no longer stable. Instead, Hermitian and anti-Hermitian part need to be treated separately by leapfrog and Euler steps. Then the time propagation is:

$$\begin{aligned}\Psi'(x, t+\Delta t) &= \Psi(x, t-\Delta t) - 2i\Delta t H^{(I)} \Psi(x, t) \\ \Psi(x, t+\Delta t) &= [1 - i\Delta t H^{(II)}] \Psi'(x, t+\Delta t).\end{aligned}\tag{2.147}$$

The stability criteria for the leapfrog and Euler step, according to (2.114) and (2.107), are $\Delta t < 1 / \|H^{(I)}\|$ and $\Delta t < 2 / \|H^{(II)}\|$. The complex mass can be chosen such that $\operatorname{Re} m^{-1}(\varrho) \leq 1$ and $\operatorname{Im} m^{-1}(\varrho) \leq 2$. In this case, the introduction of absorption layers does not lead to a reduction of the step size.

Even though the derivation of absorbing boundary conditions was somewhat heuristic, using simplifying assumptions, the method works very well in practice. In the rest of this subsection we shall demonstrate the use of absorbing boundary conditions for Example A with $B = 0$ and for Example E.

In Example A for $B = 0$, the continuum is one-parametric. Asymptotically, the motion of the wavepacket for large ϱ is the same as for a free particle. Absorbing boundary conditions have been tested for this case also by Ahland et al. [67].

To introduce absorbing boundary conditions, we modify the kinetic part of the effective Hamiltonian according to (2.144), with a complex effective mass

$$m(\varrho) = \begin{cases} 1 & \text{for } \varrho \leq R_1 \\ 1 + i \left[\sec \left(\frac{\pi}{2} \frac{\varrho - R_1}{R_2 - R_1} \right) - 1 \right] & \text{for } R_1 < \varrho < R_2 \end{cases}\tag{2.148}$$

and apply vanishing boundary conditions at the outer radius $\varrho = R_2$. Hermitian and anti-Hermitian part of the Hamiltonian are given by

$$\begin{aligned}H^{(I)} &= -\frac{1}{2} \frac{1}{\varrho} \frac{\partial}{\partial \varrho} \operatorname{Re} \frac{1}{m(\varrho)} \frac{\partial}{\partial \varrho} - \frac{1}{\varrho} \\ H^{(II)} &= -\frac{1}{2} \frac{1}{\varrho} \frac{\partial}{\partial \varrho} i \operatorname{Im} \frac{1}{m(\varrho)} \frac{\partial}{\partial \varrho}.\end{aligned}\tag{2.149}$$

The discretization in space and time was performed according to (2.146) and (2.147) and the ground-state method (2.98) was used for the two-dimensional Coulomb potential. The parameters of the calculations are: $\epsilon = 0.1$, $R_1 = 15$, $R_2 = 20$, and $h = \frac{1}{10}$. The time step was determined by the estimate $\Delta t < 1 / \|-\frac{1}{2} \Delta_\varrho\|$ with $\|-\frac{1}{2} \Delta_\varrho\|$ given by (2.95).

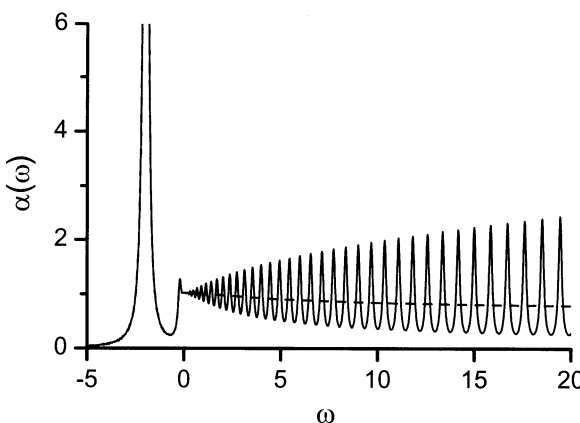


Fig. 2.10. Optical absorption for the ideal two-dimensional semiconductor (Example A with $B = 0$). *Solid line:* no absorbing boundary conditions. *Dashed line:* absorbing boundary conditions. In both cases, the outer domain radius is $R_2 = 20$

The result of the calculation is seen in Fig. 2.10. The absorption coefficient α is plotted versus frequency ω . The *solid line* shows the result in the absence of absorbing boundary conditions, which is obtained for $m(\varrho) \equiv 1$. Due to reflection at $\varrho = R_2$, the spectrum is entirely discrete. The result for absorbing boundary conditions is shown as a *dashed curve*. This time, we observe a continuous spectrum in the whole frequency range. It was found that the spectrum is practically independent of the specific form of the complex effective mass $m(\varrho)$ and identical results were obtained using other functions than (2.148), which obey the conditions (2.144). The spectrum for absorbing boundary conditions is undistinguishable from the result of a calculation with no absorbing boundary conditions and a domain $[0, R=200]$. The demonstration program is listed in App. D.4.

Now we turn to Example E. Asymptotically free motion is fulfilled for the ϱ direction. In z direction, the motion is also unbound and the resulting spectrum is continuous, but the behavior is not the same as for a free particle, since the potential does not approach a constant. For this reason, we shall apply absorbing boundary conditions only for the ϱ direction. The domain, the absorber, the effective mass, and the step size for the ϱ direction are the same as used for Example A. For the z direction we use second-order finite differences, a domain $[-L_z/2, +L_z/2]$ with $L_z = 300$, and a step size $h_z = 0.075$. The norm of H was estimated as $\|H\| \leq \|-\frac{1}{2}\Delta_\varrho\| + \|-\frac{1}{2}\Delta_z\| + \frac{1}{2}|F|L_z$.

In Fig. 2.11, the absorption spectrum of a bulk semiconductor in an electric field F is shown for different values of the field $F = 0, 0.5, 1.0$, and 2.0 . For $F = 0$, the spectrum consists of a Rydberg series of s excitons for $\omega < 0$ and a continuous part for $\omega \geq 0$. Because of the homogeneous linewidth of $\epsilon = 0.1$, only the 1s exciton can be distinguished. For any $F \neq 0$, the spectrum is entirely continuous and the continuum is two-parametric due to the unbound motion in ϱ and z direction. The Franz–Keldysh oscillations, which are also seen in the optical density of states (Fig. 1.4), result from the os-

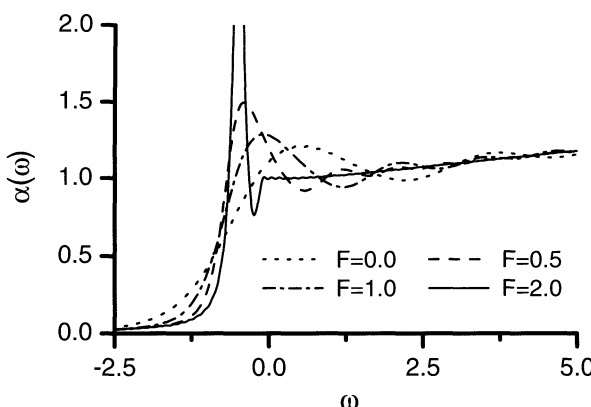


Fig. 2.11. Optical absorption versus frequency for a bulk semiconductor in an electric field (Example E). The field strength is $F = 0$ (solid line), $F = 0.5$ (dashed line), $F = 1.0$ (dash-dotted line), and $F = 2$ (dotted line)

cillating behavior of the Airy function. This effect will be discussed in more detail in Chap. 4. The Coulomb interaction leads to an enhancement of the the amplitude near $\omega = 0$ and the numerical result is in good agreement with a semi-numerical solution by Blossey [6, 7]. The results from absorbing boundary conditions are the same as obtained for vanishing boundary conditions and a domain for the ϱ direction of $[0, R=200]$. The absorbing boundary conditions lead to a reduction in memory of about a factor of 10 and in computing time of about a factor of 6.

2.4 Summary and Conclusions

The interplay of geometric confinement, external field, and Coulomb interaction gives rise to a number of interesting phenomena in the optical spectrum. As analytical solutions are available only for a few simplified models, which are not of particular interest, it is vital to have an efficient numerical method to calculate the optical absorption.

There are three equivalent formulations for the calculation of the optical susceptibility: the eigenvalue problem (Elliott formula), the boundary-value problem, and the initial-value problem, which can be solved either exactly, using standard matrix algebra, or iteratively. From the point of complexity, one can distinguish between one-dimensional problems (class I), multi-dimensional problems with one scattering direction (class II), multi-dimensional problems with many scattering directions (class III), and problems with entirely discrete spectrum (quantum dots). The state of art is the treatment of class-II problems by the scattering approach or by Lanczos recursion. However, as we demonstrated in this chapter, the class-II problem can also be solved by standard matrix algebra. Some problems of class III were treated approximately as class-II problems. For a long time, no efficient method was available for solving the general class-III problem.

The solution of the initial-value problem in combination with the discretization in real space by finite differences is a very efficient method to calculate the optical absorption in low-dimensional semiconductors, and is capable of treating class-III problems. The elements of the sparse matrix H follow directly from the discretization of the differential operator \hat{H} and no evaluation of integrals or calculation of single-particle eigenfunctions is required. The implementation is straightforward, because only the multiplication with a sparse matrix is required at each time step. The method is also very flexible: it takes very little programming effort to add or remove confinement potentials, external fields, or coordinates.

Both the numerical effort and the storage scale linearly with the number of grid points, independent on the dimensionality or the number of continuum directions. The algorithm is very efficient on vector machines, because the multiplication with H can be expressed entirely in terms of vector operations. For directions of asymptotically free motion, numerical effort and storage can be drastically reduced by absorbing boundary conditions, without loosing accuracy. At present, the solution of the initial-value problem with absorbing boundary condition is the fastest method available.

Because of its conceptual simplicity, the described algorithm should be the preferred method also for the general class-II problem. The equation-of-motion method can be combined with orthonormal base functions, finite elements, the Fourier method, or mixed representations. In recent years, a number of difficult geometries have been treated for the first time, including quantum wires, stochastic potentials in two dimensions, and type-II superlattices. In the next two chapters, we will use the described method to study two important phenomena: Fano resonances and the Zener breakdown in superlattices.

3 Fano Resonances in the Optical Absorption of Low-Dimensional Semiconductors

Fano interference is known as the quantum-mechanical interaction between discrete and continuous states [1]. This effect is often observed in atomic physics, when discrete transitions are degenerate with the autoionization continuum, and the characteristic lineshapes are called Fano (or Fano–Beutler) resonances [2, 3]. A review on Fano resonances in atoms is found in the textbook by Friedrich [4].

Because the basic ingredients – discrete states, continuum states, and quantum-mechanical coupling – are found in many situations, Fano interference is a universal phenomenon, and is observed in many fields of physics. In nuclear physics, the same phenomenon is called Breit–Wigner or Feshbach resonances [5–7]. Bhatia and Temkin unified the approaches by Fano and Feshbach and gave a derivation of the Fano lineshape by means of Feshbach’s projection-operator formalism [8]. In solid-state physics, several mechanisms have been found to produce Fano resonances in the absorption spectra of semiconductors, solid rare gases, and insulators: exciton–phonon interaction [9, 10], excitons from different critical points [11, 12], doping [13], and impurities [14]. Furthermore, Fano interference is observed in Raman spectroscopy [15–17] and nonlinear spectroscopy on biexcitons in semiconductors [18].

Fano resonances in the optical spectra of low-dimensional semiconductors have been systematically studied during the last decade. In these structures the degeneracy of discrete and continuum states stems from bound excitons and scattering states, which belong to different subbands and the quantum-mechanical coupling is mediated by the Coulomb interaction. Examples are superlattices [19–34], quantum wells [19, 35–53], bulk semiconductors and superlattices in a magnetic field [23, 26, 47, 48, 54–64], and quantum wires [45, 65–69]. The removal of the valence-band degeneracy due to confinement or external stress can give rise to Fano interference between heavy- and light-hole transitions [70–73].

The interference between the zero-phonon and one-phonon exciton transitions may cause Fano resonances in the optical absorption, as has been shown in one-dimensional model calculations [74]. Besides interband transitions, Fano resonances have been found also in intersubband transitions [75–77] and in the transport properties [78–81] of low-dimensional semiconductors. Flo-

quet states, which are solutions of the Schrödinger equation in time-periodic potentials, are discussed as a source for Fano interference [82, 83].

In this chapter we demonstrate that Fano interference is a general feature in the optical spectra of low-dimensional semiconductors, and is more the rule than the exception. In Sect. 3.1 we review the Fano model and give a derivation of the absorption profile. In Sect. 3.2 we explain the general mechanism for Fano interference in low-dimensional semiconductors, identify candidates for Fano interference, and compare the predictions with theoretical and experimental results from the literature. Two examples are discussed in Sect. 3.3 and a summary is given in Sect. 3.4.

3.1 The Fano Model

In his pioneering work, Fano assumed a model Hamiltonian, where a discrete line is coupled to an energetically degenerate continuum. The situation is drawn schematically in the left part of Fig. 3.1. Assume the system is in the ground state $|0\rangle$. Excitation can take place either into a discrete state $|E_0\rangle$ or into a continuum $|E\rangle$, which is energetically degenerate with the discrete state. Furthermore, there is a quantum-mechanical interaction ν between the discrete state and the continuum. The absorption profile, as function of the normalized energy, is shown in the right part of Fig. 3.1. The normalization of the energy and the parameter q depend on the oscillator strengths of both the discrete state and the continuum and on the quantum-mechanical coupling. Despite the simplifying assumptions, the Fano formula reproduces the experimental lineshapes in great detail. The particular strength of the model is its simplicity and the situation shown in Fig. 3.1 is very general and is not limited to optical spectroscopy.

In the original paper [1], Fano gives analytical solutions for one resonance interacting with one continuum, one resonance interacting with many continua, and many resonances interacting with one continuum. While the basic idea is simple, the development of the theory, which is based upon solving the eigenvalue problem, is intricate. There are very few alternatives, and most of them are either no less complicated or do not go as far as Fano's paper. The textbook of Cohen-Tannoudji, Dupont-Roc, and Grynberg [84] gives a somewhat simpler derivation for the case of one discrete resonance and one continuum. Mies [85], Starace [86], and others [87–89] reproduce Fano's result and also treat the case of many resonances interacting with many continua. Starace gives an expression of the total cross section as a sum over partial cross sections, each one having the form of Fano's result for many discrete states interacting with one continuum [86]. However, the use of specific methods of scattering theory is contrary to the universality of the subject. For example, Bloch states can cause Fano interference, but do not behave like free particles for large distances. Davis and Feldkamp treat the case of many resonances without the use of scattering theory [90]. Their

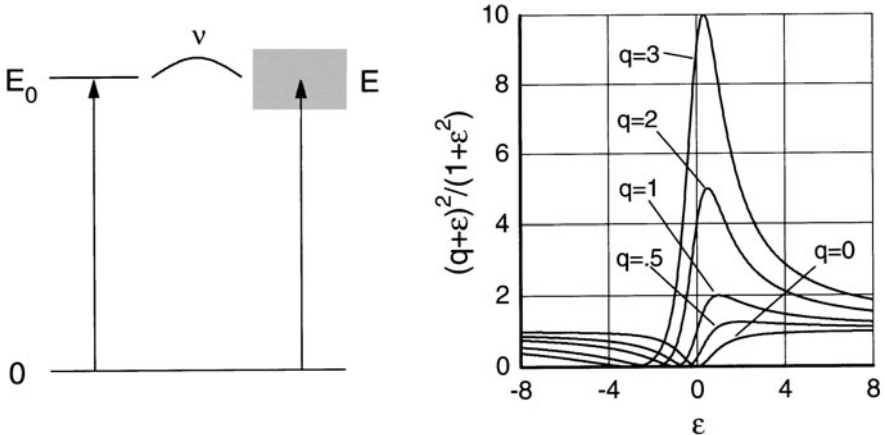


Fig. 3.1. Left: Schematic drawing of the Fano model. Right: Absorption profile as function of the normalized energy for different values of the asymmetry parameter $q = 0, 0.5, 1, 2$, and 3 . Reverse the scale of the abscissa for negative q

approach is based upon solving an eigenvalue problem, similar to the original work by Fano [1]. In solid-state physics, it is common to express the optical absorption in terms of an inverse operator (Green's function). This has been done by several authors [69, 91–93], but those papers are all restricted to the simplest case of one resonance and one continuum. Very recently, the general results for many resonances and many continua has been derived by the present author, based on the calculation of the Green's function [94].

In this section, we derive a formula for the optical absorption of the Fano model. First, we give a brief derivation for the simplest case of one resonance interacting with one continuum. This result will be generalized to many resonances interacting with many continua. We reproduce the explicit expressions by Fano for many resonances interacting with one continuum and by Starace for many resonances interacting with many continua. The calculation is entirely based upon simple matrix algebra, for which we summarize important formulas in App. A.3.

3.1.1 One Resonance and One Continuum

We consider the following model Hamiltonian and transition matrix elements

$$H = \begin{pmatrix} E_0 & V_1 & V_2 & V_3 & \cdots \\ V_1^* & E_1 & 0 & 0 & \cdots \\ V_2^* & 0 & E_2 & 0 & \cdots \\ V_3^* & 0 & 0 & E_3 & \cdots \\ \vdots & \vdots & \vdots & \vdots & \ddots \end{pmatrix}; \quad |M\rangle = \begin{pmatrix} M_0 \\ M_1 \\ M_2 \\ M_3 \\ \vdots \end{pmatrix}. \quad (3.1)$$

Here, E_0 is the energy of the discrete state. The continuum is modeled by closely spaced resonances E_j ($j > 0$). Discrete state and continuum are coupled by matrix elements V_j . The transition matrix elements to the discrete state and the continuum are M_0 and M_j ($j > 0$) respectively. We consider the case that all elements of H and $|M\rangle$ are real, which is the situation treated in the Fano paper [1]. The result is invariant against the phase transformation $\arg(\tilde{V}_j \tilde{M}_j / \tilde{M}_0) = \arg(V_j M_j / M_0)$. However, for general complex Hermitian H and complex $|M\rangle$, the absorption profile will not have the typical Fano lineshape.

To facilitate the transition to the continuous limit, we introduce the density of states $D(E_j) = 1/(E_{j+1} - E_j)$ ($j > 0$). The quantities V_j and M_j ($j > 0$) are then expressed as

$$V_j = \frac{\nu(E_j)}{\sqrt{D(E_j)}} ; \quad M_j = \frac{\mu(E_j)}{\sqrt{D(E_j)}}, \quad (3.2)$$

where μ and ν are continuous functions of the energy. For $D(E_j) \rightarrow \infty$, the summation is replaced by integration according to

$$\sum_j' \frac{f[\sqrt{D(E_j)} V_j, \sqrt{D(E_j)} M_j]}{D(E_j)} = \int dE f[\nu(E), \mu(E)]. \quad (3.3)$$

The prime at the sum means that the index $j = 0$ of the discrete state is excluded from the summation.

To calculate the optical absorption, we follow the procedures in Sect. 2.1. In dimensionless units, the optical susceptibility is equal to

$$\chi(\omega) = \sum_j \frac{|\langle M | \Phi_j \rangle|^2}{\mathcal{E}_j - (\omega + i\epsilon)}, \quad (3.4)$$

where \mathcal{E}_j and $|\Phi_j\rangle$ are the eigenvalues and normalized eigenvectors of H , and $\epsilon = +0$ is a positive infinitesimal. This time, no finite broadening is assumed. As explained in the previous chapter, formula (3.4) is equivalent to

$$\chi(\omega) = \langle M | R(\omega + i\epsilon) | M \rangle ; \quad R(z) = (H - z)^{-1}. \quad (3.5)$$

The function $R(z)$ is called the resolvent and its matrix elements are known as the Green's function. The absorption coefficient α is equal to the imaginary part of the optical susceptibility:

$$\alpha(\omega) = \text{Im } \chi(\omega). \quad (3.6)$$

It is convenient to calculate the absorption coefficient on the basis of the representation (3.5). The sparsity of H allows us to give the matrix elements of $R(z)$ in explicit form. With Lemma 2 (App. A.3) it follows that

$$\begin{aligned}
R_{00}(z) &= \left[H_0 - z - \sum_j' \frac{V_j^2}{E_j - z} \right]^{-1} \\
R_{j0}(z) &= - \frac{V_j R_{00}(z)}{E_j - z}; \quad R_{0k}(z) = - \frac{R_{00}(z) V_k}{E_k - z}; \quad j, k > 0 \quad (3.7) \\
R_{jk}(z) &= \frac{\delta_{jk}}{E_j - z} + \frac{V_j R_{00}(z) V_k}{(E_j - z)(E_k - z)}; \quad j, k > 0.
\end{aligned}$$

The optical susceptibility, which follows from the elements of R , is equal to [69, 91–93]:

$$\begin{aligned}
\chi(\omega) &= \left[M_0 - \sum_j' \frac{M_j V_j}{E_j - (\omega + i\epsilon)} \right] R_{00}(\omega + i\epsilon) \left[M_0 - \sum_k' \frac{V_k M_k}{E_k - (\omega + i\epsilon)} \right] \\
&+ \sum_j' \frac{M_j^2}{E_j - (\omega + i\epsilon)}. \quad (3.8)
\end{aligned}$$

To perform the continuous limit, we replace the summation by integration (3.3). In the evaluation of expression (3.8), we encounter the following integrals:

$$\begin{aligned}
\int dE \frac{\nu^2(E)}{E - (\omega + i\epsilon)} &= F + \frac{1}{2} i \Gamma \\
\int dE \frac{\nu(E) \mu(E)}{E - (\omega + i\epsilon)} &= G + \frac{1}{2} i \Delta \quad (3.9) \\
\int dE \frac{\mu^2(E)}{E - (\omega + i\epsilon)} &= K + \frac{1}{2} i \Lambda,
\end{aligned}$$

where F, G, K, Γ, Δ , and Λ are real numbers. We shall neglect their frequency dependence near the resonance. By virtue of Dirac's identity (A.12) F, G , and K can be written as principal-value integrals and for Γ, Δ , and Λ we have

$$\Gamma = 2\pi \nu^2; \quad \Delta = 2\pi \nu \mu; \quad \Lambda = 2\pi \mu^2 \quad (3.10)$$

and

$$\Delta^2 = \Gamma \Lambda. \quad (3.11)$$

With the above definitions, the optical susceptibility becomes

$$\chi(\omega) = \frac{(M_0 - G - \frac{1}{2}\Delta)^2}{E_0 - F - (\omega + i\epsilon) - \frac{1}{2}i\Gamma} + K + \frac{1}{2}\Lambda. \quad (3.12)$$

In the limit $\omega \rightarrow \pm\infty$ (practically: far away from the resonance $E_0 - F$), the absorption goes over into the absorption of the continuous background

$$\alpha(\infty) = \text{Im } \chi(\infty) = \frac{1}{2} \Lambda , \quad (3.13)$$

which is equal to $\pi\mu^2$. We assume the nontrivial case $\Gamma > 0$, which means that the coupling matrix element ν is different from zero. Otherwise, we would observe a sum of a discrete resonance and a continuous background. Then the function (3.12) is analytic near the real axis and we may replace $\omega + i\epsilon$ by ω . We use the relation (3.11) to eliminate the parameter Γ in (3.12). After some algebra, the absorption, normalized to $\alpha(\infty)$, becomes

$$\frac{\alpha(\omega)}{\alpha(\infty)} = \frac{\text{Im } \chi(\omega)}{\alpha(\infty)} = \frac{[E_0 - F - \omega - (M_0 - G)\Delta/\Lambda]^2}{(E_0 - F - \omega)^2 + \frac{1}{4}\Delta^4/\Lambda^2} . \quad (3.14)$$

Introducing the dimensionless parameters

$$\varepsilon = \frac{\omega - E_0 - F}{\frac{1}{2}\Gamma} ; \quad q = \frac{M_0 - G}{\frac{1}{2}\Delta} , \quad (3.15)$$

we obtain the famous result [1]

$$\frac{\alpha(\omega)}{\alpha(\infty)} = \frac{(q + \varepsilon)^2}{1 + \varepsilon^2} , \quad (3.16)$$

which was shown in the right part of Fig. 3.1.

The function (3.16) is semi-positive with one zero at $\varepsilon = -q$. For finite q , the absorption profile is asymmetric, with a slow rise on one side and a dip below the continuum level on the other side. For $q = 0$, the profile is symmetric and does not have a maximum, while for $q \rightarrow \pm\infty$, the function approaches a Lorentzian. Furthermore, it holds that $\alpha(\varepsilon; q) = \alpha(-\varepsilon; -q)$, which means that the energy scale is reversed if q changes sign.

The lineshape parameters q and Γ determine the form and the width of the resonance. The asymmetry parameter q depends on the oscillator strength of the discrete state, the oscillator strength of the continuum states, and the coupling parameter ν . The quantity $\frac{1}{2}\Gamma = \pi\nu^2$ is a natural linewidth, because we have introduced no additional broadening. The position of the resonance E_0 is shifted by the amount F through coupling to the continuum (Dirac shift). In similar manner, the oscillator strength of the discrete resonance M_0 is modified by admixture of continuum states. Thus, if $G \neq 0$, a maximum appears in the absorption even if $M_0 = 0$. The principal-value integrals F and G may be nonzero also for nonresonant interaction, when the discrete state is not degenerate with the continuum and Γ and Δ are zero.

To discuss the limiting cases, we need to consider the effect of M_0 , μ , and ν on both lineshape parameters q and Γ (3.15). To avoid divergencies, we start from expression (3.12). For vanishing coupling ν between discrete resonance and continuum we have $q \rightarrow \pm\infty$ and $\Gamma \rightarrow 0$. Then the function (3.16) goes over into a delta function plus a constant background. If the discrete state is not optically active, i.e., $M_0 - G = 0$, we observe a Fano resonance

with $q = 0$, which is manifested as a dip of width $\frac{1}{2}\Gamma$ in the continuum at the shifted position of the discrete resonance (window resonance [4]). If the transition matrix element of the continuum goes to zero, then we are in the limit $q \rightarrow \infty$, $\alpha(\infty) \rightarrow 0$ and the absorption is a Lorentzian of width $\frac{1}{2}\Gamma$. The latter situation corresponds to exponential dephasing, known as Fano decay [93]. The decay constant is equal to $\pi\nu^2$, which is the golden-rule result (App. C.3).

The general complex case, when H and $|M\rangle$ cannot be transformed into real quantities, is hardly ever discussed. In the last chapter, where we assumed a two-band model, the reduced Hamiltonians and the dipole matrix elements were always real. One should expect complex Fano interference in heterostructures in tilted magnetic fields. To some extent, complex Fano interference should also play a role when valence-band degeneracy is taken into account [38, 44, 53].

3.1.2 The General Case

Now we consider a number of discrete states, interacting with a continuous background. Only if the spacing of the discrete lines is much larger than the natural line broadening, each of the resonances can be treated individually. Otherwise, we need to generalize the model from the last subsection to take into account many resonances.

In the case of m discrete resonances, the model Hamiltonian and the vector of transition matrix elements take the form:

$$H = \left(\begin{array}{c|cccc} H_0 & V_1 & V_2 & V_3 & \cdots \\ \hline V_1^T & E_1 & 0 & 0 & \cdots \\ V_2^T & 0 & E_2 & 0 & \cdots \\ V_3^T & 0 & 0 & E_3 & \cdots \\ \vdots & \vdots & \vdots & \vdots & \ddots \end{array} \right) ; \quad |M\rangle = \begin{pmatrix} M_0 \\ M_1 \\ M_2 \\ M_3 \\ \vdots \end{pmatrix}. \quad (3.17)$$

This time, H_0 is a real symmetric $m \times m$ matrix, M_j and the V_j are real m -dimensional column vectors, and the transposes V_j^T are real m -dimensional row vectors. We can go further and assume that these m resonances interact with n continua. Then $E_\beta, E_{n+\beta}, E_{2n+\beta}, \dots$ belong to the β -th continuum, where β runs from 1 to n . Now, the r.h.s. of (3.3) needs to be modified to include the summation over β :

$$\sum_j \frac{f(\sqrt{D(E_j)}V_j, \sqrt{D(E_j)}M_j)}{D(E_j)} = \sum_{\beta=1}^n \int dE f[\nu^{(\beta)}(E), \mu^{(\beta)}(E)]. \quad (3.18)$$

The real m -dimensional row vector $\nu^{(\beta)}$ contains the coupling strengths of the discrete resonances to the β -th continuum and the real number $\mu^{(\beta)}$ is the transition amplitude of the β -th continuum.

After these preparations, the generalization of (3.12) is merely a formality. Using the block version of Lemma 2 (App. A.3), the Green's function becomes:

$$\begin{aligned} R_{00}(\omega) &= \left[H_0 - (\omega + i\epsilon) - \sum_j' \frac{V_j V_j^T}{E_j - (\omega + i\epsilon)} \right]^{-1} \\ R_{j0}(\omega) &= - \frac{V_j^T R_{00}(\omega)}{E_j - (\omega + i\epsilon)} ; \quad R_{0k}(\omega) = - \frac{R_{00}(\omega) V_k}{E_k - (\omega + i\epsilon)} ; \quad j, k > 0 \\ R_{jk}(\omega) &= \frac{\delta_{jk}}{E_j - (\omega + i\epsilon)} + \frac{V_j^T R_{00}(\omega) V_k}{[E_j - (\omega + i\epsilon)][E_k - (\omega + i\epsilon)]} ; \quad j, k > 0 . \end{aligned} \quad (3.19)$$

This leads us to the optical susceptibility

$$\begin{aligned} \chi(\omega) &= \left[M_0^T - \sum_j' \frac{M_j V_j^T}{E_j - (\omega + i\epsilon)} \right] R_{00}(\omega) \left[M_0 - \sum_k' \frac{V_k M_k}{E_k - (\omega + i\epsilon)} \right] \\ &\quad + \sum_j' \frac{M_j^2}{E_j - (\omega + i\epsilon)} . \end{aligned} \quad (3.20)$$

In analogy to (3.9) we define

$$\begin{aligned} \sum_{\beta=1}^n \int dE \frac{\nu^{(\beta)}(E) \nu^{(\beta)T}(E)}{E - (\omega + i\epsilon)} &= F + \frac{1}{2} i \Gamma \\ \sum_{\beta=1}^n \int dE \frac{\nu^{(\beta)}(E) \mu^{(\beta)}(E)}{E - (\omega + i\epsilon)} &= G + \frac{1}{2} i \Delta \\ \sum_{\beta=1}^n \int dE \frac{\mu^{(\beta)2}(E)}{E - (\omega + i\epsilon)} &= K + \frac{1}{2} i \Lambda . \end{aligned} \quad (3.21)$$

This time F and Γ are real symmetric $m \times m$ matrices, G and Δ are real m -dimensional column vectors, and K and Λ are real numbers. The explicit expressions for Γ , Δ , and Λ are

$$\begin{aligned} \Gamma &= \sum_{\beta=1}^n \Gamma^{(\beta)} ; & \Delta &= \sum_{\beta=1}^n \Delta^{(\beta)} ; & \Lambda &= \sum_{\beta=1}^n \Lambda^{(\beta)} \end{aligned} \quad (3.22)$$

$$\Gamma^{(\beta)} = 2\pi \nu^{(\beta)} \nu^{(\beta)T} ; \quad \Delta^{(\beta)} = 2\pi \nu^{(\beta)} \mu^{(\beta)} ; \quad \Lambda^{(\beta)} = 2\pi \mu^{(\beta)2} .$$

Finally, the optical susceptibility becomes

$$\begin{aligned} \chi(\omega) = & (M_0 - G - \frac{1}{2} i \Delta)^T [H_0 - F - (\omega + i\epsilon) - \frac{1}{2} i \Gamma]^{-1} (M_0 - G - \frac{1}{2} i \Delta) \\ & + K + \frac{1}{2} i \Lambda . \end{aligned} \quad (3.23)$$

The matrix F leads not only to a shift of the discrete states, but also to a coupling of different resonances.

With formula (3.23) we have found a compact formulation for the optical susceptibility for the general case of many resonances interacting with many continua. The dimension of the vector space is equal to the number of discrete resonances, independent of the number of continua. Although the formulation (3.23) can easily be used for a numerical calculation of the spectrum, it does not allow to draw qualitative conclusions for the behavior of the absorption profile. Therefore, we shall further simplify (3.23) for a single resonance, interacting with one or many continua, many resonances interacting with one continuum, and many resonances interacting with many continua.

A. Single resonance and many continua

In the case of one resonance, interacting with many continua, the vector space in (3.23) is one-dimensional, Γ , Λ , and Δ are scalars, and the optical susceptibility reduces to (3.12). On the other hand, for general n we can no longer assume (3.11) to hold true, which means that Γ cannot be eliminated in (3.23). Then, instead of (3.16), the normalized absorption becomes

$$\frac{\alpha(\omega)}{\alpha(\infty)} = \frac{\Delta^2}{\Gamma \Lambda} \frac{(q + \varepsilon)^2}{1 + \varepsilon^2} + 1 - \frac{\Delta^2}{\Gamma \Lambda} \quad (3.24)$$

with ε and q from definition (3.15). Because of the Cauchy–Schwarz inequality,

$$\Delta^2 \leq \Gamma \Lambda , \quad (3.25)$$

formula (3.24) describes a Fano resonance plus a constant background [1]. This qualitative result can also be found without an explicit calculation. By linear combination of the different continua we can remove the coupling to $n - 1$ continua. Then the absorption is equal to the absorption of one discrete state, coupled to one continuum, plus the absorption of the $n - 1$ continua, which are not involved in the Fano interference.

The principal result (3.23) is not limited to one-parametric continua. Let us assume an m -parametric continuum ($m > 1$), characterized by a continuous variable $k = (k_1, \dots, k_m)$. Then, in (3.21), the integration over dE has to be replaced by an integration over dk . Instead of (3.22), the quantities Γ , Δ , and Λ are given by $m-1$ -dimensional surface integrals (App. C.1)

$$\left\{ \begin{array}{c} \Gamma \\ \Delta \\ \Lambda \end{array} \right\} = 2\pi \int_{E(k)=\omega} \frac{ds}{|\nabla E(k)|} \left\{ \begin{array}{c} \nu(k) \nu^T(k) \\ \nu(k) \mu(k) \\ \mu(k) \mu(k) \end{array} \right\} . \quad (3.26)$$

For one resonance, we end up with (3.25) and the spectrum will be a Fano resonance plus a continuous background. Introducing quantum numbers on the surface, the integrals (3.26) go over into expressions like (3.22), where the index set is infinite. Thus a multi-parametric continuum is equivalent to one continuum with an infinite multiplicity.

B. Many resonances and one continuum

Now we turn to the case that m resonances interact with a single continuum. Then we can establish a relation between Γ , Δ , and Λ of the form

$$\Lambda \Gamma = \Delta \Delta^T. \quad (3.27)$$

To simplify the notation, we replace $M_0 - G$ by M_0 , $H_0 - F$ by H_0 and ignore the real constant K , which does not contribute to the absorption coefficient. First, we consider $\Lambda \neq 0$. The limit $\Lambda \rightarrow 0$ will be taken in the final expression. With (3.27), the optical susceptibility (3.23), normalized to $\alpha(\infty)$, becomes

$$\frac{\chi(\omega)}{\alpha(\infty)} = (M_0 - \frac{1}{2}i\Delta)^T \left\{ \frac{1}{2}\Lambda [H_0 - (\omega + i\epsilon)] - \frac{1}{4}i\Delta\Delta^T \right\}^{-1} (M_0 - \frac{1}{2}i\Delta) + i. \quad (3.28)$$

The real symmetric matrix H_0 has m real eigenvalues. In the eigensystem of H_0 we have $\tilde{H}_0 = \text{diag}(\tilde{E}_{0,1}, \dots, \tilde{E}_{0,m})$ and $\tilde{\Delta} = (\tilde{\Delta}_1, \dots, \tilde{\Delta}_m)^T$. The irreducible case, where all resonances are coupled to the continuum, is given by $\tilde{E}_{0,1} < \tilde{E}_{0,2} < \dots < \tilde{E}_{0,m}$ and $\tilde{\Delta}_k \neq 0$ for $k = 1, \dots, m$.

In order to take the limit $\epsilon \rightarrow 0$, we have to study the analyticity of the function near the real axis. From Lemma 3 (App. A.3) it follows that

$$\det \left[\frac{1}{2}\Lambda(H_0 - z) - \frac{1}{4}i\Delta\Delta^T \right] = \left(\frac{\Lambda}{2} \right)^m \prod_{j=1}^m (\tilde{E}_{0,j} - z) \left[1 - \frac{1}{2}i \sum_{k=1}^m \frac{\tilde{\Delta}_k^2/\Lambda}{\tilde{E}_{0,k} - z} \right]. \quad (3.29)$$

In the irreducible case, this function has no zeros on the real axis. Consequently, in (3.28) we can replace $\omega + i\epsilon$ by ω .

So far, the generalization of (3.12) for many resonances was straightforward. The nontrivial part is the generalization of the expression (3.14). It is hopeless to repeat the explicit calculations from the last subsections for vectors and matrices. If there is a generalization to the m -dimensional case, the result should be of the form:

$$\frac{\alpha(\omega)}{\alpha(\infty)} = \left| \frac{\det(H_0 - \omega - M_0 \Delta^T / \Lambda)}{\det(H_0 - \omega - \frac{1}{2}i\Delta\Delta^T / \Lambda)} \right|^2. \quad (3.30)$$

The proof of (3.30) follows from Lemma 4 (App. A.3).

We have already given an explicit expression for the denominator of (3.30). With the analogous expansion for the numerator, the normalized absorption becomes

$$\frac{\alpha(\omega)}{\alpha(\infty)} = \frac{\left[1 - \sum_{k=1}^m \frac{\tilde{M}_{0,k}\tilde{\Delta}_k/\Lambda}{\tilde{E}_{0,k}-\omega}\right]^2}{1 + \frac{1}{4}\left[\sum_{k=1}^m \frac{\tilde{\Delta}_k^2/\Lambda}{\tilde{E}_{0,k}-\omega}\right]^2} = \cos^2 \varphi \left[1 - \sum_{k=1}^m q_k \tan \varphi_k\right]^2, \quad (3.31)$$

where

$$\begin{aligned} \tan \varphi_k &= \frac{1}{2} \frac{\tilde{\Delta}_k^2/\Lambda}{\tilde{E}_{0,k}-\omega} = \frac{\pi \tilde{\nu}_k^2}{\tilde{E}_{0,k}-\omega} \\ \tan \varphi &= \sum_{k=0}^m \tan \varphi_k; \quad q_k = \frac{2\tilde{M}_{0,k}}{\tilde{\Delta}_k} = \frac{\tilde{M}_{0,k}}{\pi \mu \tilde{\nu}_k}. \end{aligned} \quad (3.32)$$

The latter expression is identical to the results by Fano and others [1, 85, 88–90]. As the denominator is nonzero on the whole real axis, the zeros of the absorption profile are governed by the numerator. A sufficient condition for m zeros is that either $\tilde{M}_{0,k}\tilde{\Delta}_k > 0$ for all k or $\tilde{M}_{0,k}\tilde{\Delta}_k < 0$ for all k , in other words, that the individual q -parameters $q_k = \tilde{M}_{0,k}/\tilde{\Delta}_k$ are nonzero and have the same sign. The zeros occur between two subsequent resonances $\tilde{E}_{0,k}$ and $\tilde{E}_{0,k+1}$ and either between $-\infty$ and $\tilde{E}_{0,1}$ or between $\tilde{E}_{0,m}$ and $+\infty$.

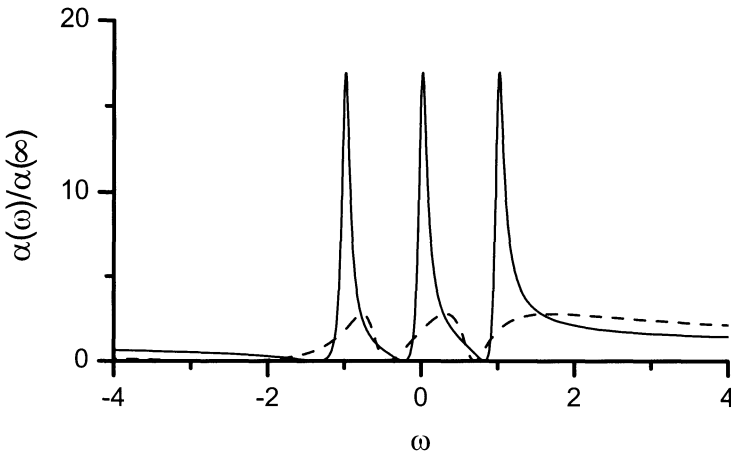


Fig. 3.2. Normalized optical absorption for three resonances, interacting with one continuum. The parameters in (3.30) are: $H_0 = \text{diag}(-1, 0, +1)$, $\Lambda = 1$, $M_0 = (1, 1, 1)^T$. Solid line: $\Delta = (0.5, 0.5, 0.5)^T$. Dashed line: $\Delta = (1.5, 1.5, 1.5)^T$

In Fig. 3.2, the normalized absorption is shown for three resonances interacting with one continuum. The parameters are $H_0 = \text{diag}(-1, 0, +1)$, $\Lambda = 1$, and $M_0 = (1, 1, 1)^T$. For the parameter Δ we consider two cases:

$\Delta = (0.5, 0.5, 0.5)^T$ (*solid line*) and $\Delta = (1.5, 1.5, 1.5)^T$ (*dashed line*). In the first case, the individual linewidths and q -parameters are $\frac{1}{2}\Gamma_{kk} = 0.125$ and $q_k = 2$ ($k = 1, 2, 3$). The individual lineshapes are not affected by the spacing of the resonances and are similar to a Fano profile for $q = 2$ (cf. Fig. 3.1). The maxima are close to the positions of the resonances $\omega = -1, 0$, and $+1$. In the second case, we have $\frac{1}{2}\Gamma_{kk} = 1.125$ and $q_k = 0.667$. This time, the natural linewidths are larger than the spacing of the resonances. Nevertheless, the absorption drops to zero three times. The lineshape is very different from the Fano profile (right of Fig. 3.1), the maxima are not located at the positions of the discrete states, and the actual linewidth, which is limited by the spacing of the resonances, is smaller than $\frac{1}{2}\Gamma_{kk}$. Other examples for fixed q -parameters and varying linewidths are shown in the paper by Mies [85]. The case that q changes its sign inside a Rydberg series (q reversal) is also observed [89]. Then $\alpha(\omega)$ may not go to zero between two resonances.

Now we consider the case that the transition probability of the continuum is zero, which means that $\mu = 0$, $\Lambda = 0$, and $\Delta = 0$. Here, the irreducible case is characterized by $\tilde{\nu}_k \neq 0$ for all k . Furthermore, we assume $M_0 \neq 0$, otherwise the absorption coefficient vanishes identically. From (3.31), in the limit $\Lambda \rightarrow 0$, we obtain

$$\alpha(\omega) = \frac{\left[\sum_{k=1}^m \frac{\tilde{M}_{0,k} \sqrt{\pi} \tilde{\nu}_k}{\tilde{E}_{0,k} - \omega} \right]^2}{1 + \left[\sum_{k=1}^m \frac{\pi \tilde{\nu}_k^2}{\tilde{E}_{0,k} - \omega} \right]^2}. \quad (3.33)$$

The function $\alpha(\omega)$ approaches zero for $\omega \rightarrow \pm\infty$. If all $\tilde{M}_{0,k} \tilde{\nu}_k$ are nonzero and have the same sign, then the absorption coefficient has $m - 1$ zeros between the resonances $\tilde{E}_{0,k}$. Writing the latter expression in general coordinates and using Lemma 3 (App. A.3) we find that

$$\alpha(\omega) = \left| \frac{\det(H_0 - \omega) - \det(H_0 - \omega - M_0^T \sqrt{\pi} \nu^T)}{\det(H_0 - \omega - i\sqrt{\pi} \nu \sqrt{\pi} \nu^T)} \right|^2. \quad (3.34)$$

C. Many resonances and many continua

For many resonances and many continua, the optical absorption can be written as a sum over all continua. From the definitions (3.22), the expression (3.23), and the proof of Lemma 4 it follows that

$$\alpha(\omega) = \text{Im } \chi(\omega) = \frac{1}{2} \sum_{\beta=1}^n \Lambda^{(\beta)} \left| 1 - (M_0 - \frac{1}{2}i\Delta)^T (H_0 - \omega - \frac{1}{2}i\Gamma)^{-1} \frac{\Delta^{(\beta)}}{\Lambda^{(\beta)}} \right|^2. \quad (3.35)$$

Again, for notational convenience, we dropped F , G , and K .

As each term under the sum depends on all continua via Δ and Γ , it cannot be brought into the form (3.31). To overcome this problem, we introduce the orthogonal transformation

$$\bar{\nu}^{(\beta)} = \sum_{\beta=1}^n U^{\beta'\beta} \nu^{(\beta')} ; \quad \bar{\mu}^{(\beta)} = \sum_{\beta=1}^n U^{\beta'\beta} \mu^{(\beta')} . \quad (3.36)$$

Then we define $\bar{\Gamma}^{(\beta)}$, $\bar{\Delta}^{(\beta)}$, and $\bar{\Lambda}^{(\beta)}$ in analogy to (3.22). Because $\bar{\Gamma} = \Gamma$, $\bar{\Delta} = \Delta$, and $\bar{\Lambda} = \Lambda$, the optical susceptibility is invariant under the transformation (3.36), which means that in (3.35) we can replace $\Delta^{(\beta)}$ by $\bar{\Delta}^{(\beta)}$ and $\Lambda^{(\beta)}$ by $\bar{\Lambda}^{(\beta)}$.

We now determine the $n \times n$ orthogonal matrix $U(\omega)$ such that

$$\bar{\nu}^{(\beta)\text{T}}(\omega) (H_0 - \omega)^{-1} \bar{\nu}^{(\beta')}(\omega) = \bar{z}^{(\beta)}(\omega) \delta^{\beta\beta'} . \quad (3.37)$$

While some of the $\bar{z}^{(\beta)}(\omega)$ have single poles when ω crosses an eigenvalue of H_0 , the quantities $\bar{\Gamma}^{(\beta)}$, $\bar{\Delta}^{(\beta)}$, and $\bar{\Lambda}^{(\beta)}$ can be chosen to be continuous functions of ω .

From the series expansion

$$(H_0 - \omega - \frac{1}{2} i \Gamma)^{-1} = (H_0 - \omega)^{-1} + (H_0 - \omega)^{-1} \frac{1}{2} i \Gamma (H_0 - \omega)^{-1} + \dots \quad (3.38)$$

and the relation $\bar{\Gamma}^{(\beta)} = \bar{\Delta}^{(\beta)} \bar{\Delta}^{(\beta)\text{T}} / \bar{\Lambda}^{(\beta)}$ it follows that

$$\bar{\Delta}^{(\beta)\text{T}}(H_0 - \omega - \frac{1}{2} i \Gamma)^{-1} \bar{\Delta}^{(\beta')} = \delta^{\beta\beta'} \bar{\Delta}^{(\beta)} (H_0 - \omega - \frac{1}{2} i \bar{\Gamma}^{(\beta)})^{-1} \bar{\Delta}^{(\beta')} . \quad (3.39)$$

Going over to the transformed quantities and using the relation (3.39), expression (3.35) goes over into

$$\begin{aligned} \alpha(\omega) &= \frac{1}{2} \sum_{\beta=1}^n \bar{\Lambda}^{(\beta)} \left| 1 - (M_0 - \frac{1}{2} i \bar{\Delta}^{(\beta)})^{\text{T}} (H_0 - \omega - \frac{1}{2} i \bar{\Gamma}^{(\beta)})^{-1} \frac{\bar{\Delta}^{(\beta)}}{\bar{\Lambda}^{(\beta)}} \right|^2 \\ &= \frac{1}{2} \sum_{\beta=1}^n \bar{\Lambda}^{(\beta)} \left| \frac{\det(H_0 - \omega - M_0 \bar{\Delta}^{(\beta)\text{T}} / \bar{\Lambda}^{(\beta)})}{\det(H_0 - \omega - \frac{1}{2} i \bar{\Delta}^{(\beta)} \bar{\Delta}^{(\beta)\text{T}} / \bar{\Lambda}^{(\beta)})} \right|^2 . \end{aligned} \quad (3.40)$$

In this expression each of the terms under the sum is of the form (3.31). The latter equation is identical to the formula by Starace, which expresses the total cross section as a sum of partial cross sections [86]. For two or more continua, the absorption (3.40) usually does not drop to zero, because the zeros of the n individual contributions will not be at the same positions. Furthermore, the partial cross sections may not have m zeros, because the transformed quantities $\bar{\Delta}^{(\beta)}$ and $\bar{\Lambda}^{(\beta)}$ are frequency-dependent. Therefore, formula (3.40) is of little use and nothing speaks against using expression (3.35) for numerical calculations.

3.2 Fano Resonances as a General Feature of the Optical Absorption in Low-Dimensional Semiconductors

In the first two chapters we have shown that the optical absorption can be traced back to an effective Hamiltonian governing the motion of an electron–hole pair. On the basis of this Hamiltonian we show that Fano resonances are a typical feature of the optical spectrum of low-dimensional semiconductors. We start with multichannel scattering theory familiar from atomic and nuclear physics. In this framework, Fano interference results from Coulomb coupling between confined and free motion. Then we take a more general view, employing the subband picture. This allows us to explain Fano interference also in systems which are not strictly low-dimensional, like superlattices.

3.2.1 The Channel Picture

The concept of channels is familiar from nuclear and atomic physics [4, 7, 95]. In recent years, this notion has also been used for excitons in confined systems [53, 67]. In this subsection we explain the mechanism of Fano interference in low-dimensional semiconductors in terms of the interaction of open and closed channels. This is appropriate for most low-dimensional semiconductors. A more general view will be taken in the next subsection.

For the following qualitative analysis we make very general assumptions. For notations and conventions we refer to Sect. 2.1. We consider an l -dimensional reduced problem with m dimensions of unbound motion, where $l > m > 1$. We assume the coordinates for unbound and bound motions, w and v , to be separable, i.e.,

$$\begin{aligned} u = (u_1, \dots, u_l) &= (v, w); \quad G_u = G_v \times G_w; \quad g_u(u) = g_v(v) g_w(w) \\ v = (v_1, \dots, v_m) &= (u_1, \dots, u_m) \\ w = (w_1, \dots, w_{l-m}) &= (u_{m+1}, \dots, u_l). \end{aligned} \tag{3.41}$$

The reduced Hamiltonian can be written in the form

$$\hat{H} = \hat{H}_{\text{kin } w} + W(w) + \hat{H}_{\text{kin } v} - V(w, v), \tag{3.42}$$

where $\hat{H}_{\text{kin } w}$ and $\hat{H}_{\text{kin } v}$ are the operators of the kinetic energy in the unbound and bound directions. The potentials W and $-V$, which describe the quantum confinement and the Coulomb interaction, have the asymptotic properties

$$W(w) \rightarrow +\infty \text{ for } |w| \rightarrow \infty; \quad -V(w, v) \sim -\frac{1}{|v|} \text{ for } |v| \rightarrow \infty, \tag{3.43}$$

where $|w|$ and $|v|$ are the lengths of w and v in Cartesian coordinates. Furthermore, $-V$ is not separable and the singularity of V at the origin $\mathbf{r}_e = \mathbf{r}_h$

is integrable. A schematic drawing of the potentials W and V for $l = 2$ and $m = 1$ is shown in Fig. 3.3. This shape of the potential is typical for Fano interference [78].

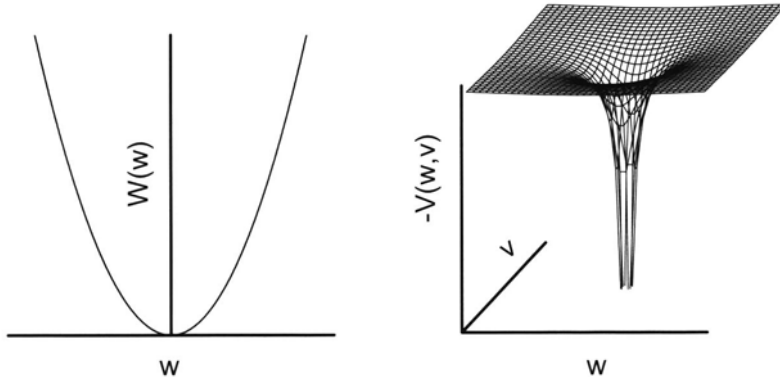


Fig. 3.3. Schematic drawing of the potentials $W(w)$ and $-V(w, v)$

Due to the asymptotic properties of W , the spectrum of the operator $\hat{H}_{\text{kin } w} + W(w)$ is entirely discrete. The eigenvalue problem for the confined directions is

$$\left[\hat{H}_{\text{kin } w} + W(w) \right] \varphi_n(w) = E_n \varphi_n(w) . \quad (3.44)$$

Each eigenstate $|n\rangle$ of the confined motion gives rise to a channel in which the electron-hole pairs can move in the directions of free motions v . For a given photon energy ω , a channel n is said to be open, if $\omega \geq E_n$, and closed, if $\omega < E_n$. The discrete spectrum for the confined directions can also be the result of vanishing boundary conditions, as we have used previously for perfect confinement (Sects. 1.2 and 2.1).

First, we totally neglect Coulomb interaction, i.e., we assume $V = 0$. Then the eigenfunctions and eigenvalues of the unperturbed Hamiltonian are of the form

$$\begin{aligned} \Phi_A(u) &= \varphi_{nk}(u) = \varphi_n(w) \psi_k(v) ; \quad k = (k_1, \dots, k_m) \\ \mathcal{E}_A &= \varepsilon_{nk}(u) = E_n + \varepsilon(k) ; \quad \varepsilon(k) \in [0, \infty) , \end{aligned} \quad (3.45)$$

where $\psi_k(v)$ are the eigenfunctions of $\hat{H}_{\text{kin } v}$ with the continuous spectrum $\varepsilon(k)$. The energies $\varepsilon_n(k)$ with the lower edges E_n are called subbands. The optical absorption, which results from the approximation (3.45), is equal to the optical density of states (Sect. 1.2).

In order to include Coulomb interaction, we expand the eigenfunctions of \hat{H} into the normalized eigenfunctions of the confined motion φ_n according to

$$\Phi_A(u) = \sum_n \varphi_n(w) \Phi_{A;n}(v) . \quad (3.46)$$

Then the components $\Phi_{A;n}$ obey the coupled channel equations:

$$\left[E_n + \hat{H}_{\text{kin } v} - V_{nn}(v) \right] \Phi_{A;n}(v) - \sum_{n'}' V_{nn'}(v) \Phi_{A;n'}(v) = \mathcal{E}_A \Phi_{A;n}(v) , \quad (3.47)$$

where

$$V_{nn'}(v) = \int \underline{d}w \varphi_n^*(w) V(w, v) \varphi_{n'}(w) . \quad (3.48)$$

The diagonal elements $-V_{nn}$ govern the Coulomb interaction within the channels, while the nondiagonal elements $-V_{nn'}$ with $n \neq n'$ are responsible for the coupling between different channels. The optical absorption, expressed in terms of the eigenvalues \mathcal{E}_A and the normalized eigenfunctions Φ_A , is

$$\alpha(\omega) = \sum_A |F_A|^2 \pi \delta(\omega - \mathcal{E}_A) ; \quad F_A = \sum_n \int \underline{d}v \mu_n^*(v) \Phi_{A;n}(v) , \quad (3.49)$$

where

$$\mu_n(v) = \int \underline{d}w \varphi_n^*(w) \mu(w, v) \quad (3.50)$$

are the projections of the dipole matrix element onto the n -th channel. The sum over A includes discrete and continuous states. The set of equations (3.47) is used by many authors to numerically calculate the optical absorption [43, 53, 66, 67].

An approximation of (3.47), which takes into account only the Coulomb interaction within each channel, are the single-channel equations:

$$\begin{aligned} \left[E_n + \hat{H}_{\text{kin } v} - V_{nn}(v) \right] \psi_{n\lambda}(v) &= E_{n\lambda} \psi_{n\lambda}(v) \\ \left[E_n + \hat{H}_{\text{kin } v} - V_{nn}(v) \right] \psi_{nq}(v) &= E_n(q) \psi_{nq}(v) . \end{aligned} \quad (3.51)$$

Here, the coupling of different channels is neglected and n plays the role of a parameter. Because the Coulomb potential is long-ranged, the number of bound states $E_{n\lambda} < E_n$ (excitons) is infinite [4]. Furthermore, there is an m -parametric continuum of scattering states $E_n(q) \geq E_n$, $q = (q_1, \dots, q_m)$. In this approximation, the eigenfunctions of \hat{H} ,

$$\Phi_A(u) = \varphi_n(w) \begin{Bmatrix} \psi_{n\lambda}(v) \\ \psi_{nq}(v) \end{Bmatrix} , \quad (3.52)$$

are products of the confined eigenfunctions φ_n and the eigenfunctions of the single-channel equations for the discrete and continuous eigenvalues. Assuming standard normalization of the discrete and continuous eigenfunctions (3.52), the optical absorption takes the form

$$\alpha(\omega) = \sum_n \left\{ \sum_{\lambda} |F_{n\lambda}|^2 \pi \delta(\omega - E_{n\lambda}) + \int dq |F_n(q)|^2 \pi \delta[\omega - E_n(q)] \right\}$$

$$F_{n\lambda} = \int dv \mu_n^*(v) \psi_{n\lambda}(v); \quad F_n(q) = \int dv \mu_n^*(v) \psi_{nq}(v). \quad (3.53)$$

Equation (3.53) describes a superposition of absorption spectra for the individual channels n . The contribution of each individual channel is an absorption spectrum of an m -dimensional semiconductor, with a discrete spectrum below the subband edge E_n and a continuous spectrum above E_n .

Now we qualitatively discuss the effect of channel coupling on the absorption spectrum. Theoretically, instead of solving the coupled channel equations (3.47), one can use the functions $\varphi_n(w) \psi_{n\lambda}(v)$ and $\varphi_n(w) \psi_{nq}(v)$ as base functions. In the formulation (3.5), the optical absorption is

$$\alpha(\omega) = \text{Im} \langle \mu | [\hat{H} - (\omega + i\epsilon)]^{-1} | \mu \rangle. \quad (3.54)$$

The components of \hat{H} and $|\mu\rangle$ in the basis $|n, \lambda\rangle$ and $|n, q\rangle$ are

$$\begin{aligned} \langle n, \lambda | \hat{H} | n', \lambda' \rangle &= \delta_{nn'} \delta_{\lambda\lambda'} E_{n\lambda} - (1 - \delta_{nn'}) \int dv \psi_{n\lambda}^*(v) V_{nn'}(v) \psi_{n'\lambda'}(v) \\ \langle n, \lambda | \hat{H} | n', q' \rangle &= -(1 - \delta_{nn'}) \int dv \psi_{n\lambda}^*(v) V_{nn'}(v) \psi_{n'q'}(v) \\ \langle n, q | \hat{H} | n', q' \rangle &= \delta_{nn'} \underline{\delta}(q, q') E_n(q) - (1 - \delta_{nn'}) \int dv \psi_{nq}^*(v) V_{nn'}(v) \psi_{n'q'}(v) \end{aligned} \quad (3.55)$$

and

$$\langle n, \lambda | \mu \rangle = F_{n\lambda}^*; \quad \langle n, q | \mu \rangle = F_n^*(q). \quad (3.56)$$

Fano interference takes place if a discrete state from a higher channel is degenerate with the continuum from a lower channel and the nondiagonal Coulomb matrix element [second line of (3.55)] is different from zero:

$$E_{n\lambda} = E_{n'}(q'); \quad -\langle n, \lambda | V | n', q' \rangle \neq 0. \quad (3.57)$$

The structure of the Hamiltonian (3.55) is shown in Fig. 3.4 for two interacting channels and a one-parametric continuum ($m = 1$). The energy, which is used as parameter, increases with the matrix index. On the diagonal, the excitons and continuum states are represented by points and lines, respectively. On the onset of the second continuum, the line becomes thicker, indicating that there is another continuum underneath. The excitons of the first channel remain bound states and manifest in the optical absorption as a Rydberg series of discrete lines. The excitons of the second channel interact with the continuum of the first channel and, therefore, turn into Fano resonances. Graphically, the Fano interference is shown by vertical and horizontal lines, crossing the diagonal.

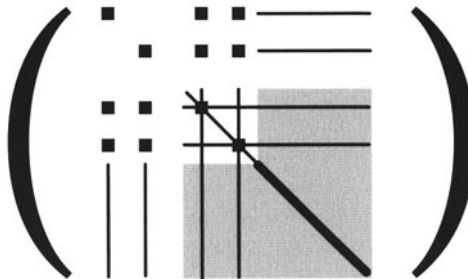


Fig. 3.4. Structure of the Hamiltonian (3.55). A one-parametric continuum is assumed and only the first two channels $n = 1$ and $n = 2$ are shown

In contrast to the simple Fano model (Sect. 3.1), we have also interaction among discrete states of different channels (off-diagonal points), continuum states of different channels (gray areas), and nonresonant interaction between discrete lines and continua belonging to different channels (vertical and horizontal lines which do not cross the diagonal). These nonresonant couplings do not change the situation qualitatively. On the other hand, the quantitative changes can be significant, especially for weak confinement, so that the direct calculation of the line parameters from the single-channel eigenfunctions (3.51) is not advised. In some cases the Dirac shift may cause an exciton, which is degenerate with a continuum, to be shifted below the continuum edge and to remain a bound state. In any case, a complete numerical calculation of the absorption spectrum is recommended, which can be done by the methods discussed in Chap. 2.

For quantum confinement, which results from band discontinuities, the assumption of an infinitely high potential is an idealization. In reality, only a finite number of bound states are supported, while the above-barrier spectrum is continuous. Insofar, the dimension of a semiconductor may depend on the energy range under consideration. Nevertheless, the principal results remain valid also for a finite number of bound states. To observe Fano interference, it is sufficient to have interaction between one open and one closed channel. Formally, the completeness of the channel eigenfunctions φ_n can be maintained introducing a continuous channel index for the above-barrier states. The case of finite barriers can also be treated by the methods of the next subsection, where we take a more general view.

A final remark on the term “exciton” is in order. In our notion, an exciton can be either a bound state with a square-integrable eigenfunction or a resonance in the continuum, which originates from a bound state of the Coulomb potential. Besides Fano resonances, other examples for resonances are excitons in electric fields (Example E from Chap. 2), saddle-point excitons [24], or excitons on rough interfaces (Example D from Chap. 2). Another repre-

sentative are Wannier–Stark resonances, which we will discuss in the next chapter.

3.2.2 The Subband Picture

The picture from the last subsection (Fig. 3.3) is very intuitive, but not every occurrence of Fano interference can be explained in terms of Coulomb coupling between bound and free motion. Sometimes, the situation is more complicated, as we will show in the following example. Imagine a one-dimensional superlattice, characterized by an electron–hole Hamiltonian

$$\hat{H} = -\frac{1}{m_e} \frac{\partial^2}{\partial z_e^2} - \frac{1}{m_h} \frac{\partial^2}{\partial z_h^2} + W_e(z_e) + W_h(z_h) - V(z_e - z_h)$$

$$\mu(z_e, z_h) = \delta(z_e - z_h), \quad (3.58)$$

where W_e and W_h are periodic potentials with the same period a and V is an effective one-dimensional Coulomb potential with integrable singularity at $z_e = z_h$. The individual potentials W_e and W_h have no bound states, which could give rise to channels. The problem is that, although the number of coordinates cannot be smaller than two, \hat{H} is not truly a reduced Hamiltonian. If we change over to center-of-mass and relative coordinates $Z = (m_e z_e + m_h z_h)/(m_e + m_h)$ and $z = z_e - z_h$, then the solutions, which contribute to the absorption, are periodic in Z , which can be interpreted as confined motion. On the other hand, the Coulomb potential depends only on the relative coordinate z and does not couple bound and unbound motion. Nevertheless, in the above configuration we can have Fano interference on the account of Coulomb interaction. Such situation arises when a superlattice is subjected to a magnetic field in growth direction [24, 26, 34, 64]. Excitons in superlattices show a number of interesting phenomena, so we will postpone the discussion of the superlattice eigenvalue problem to Chap. 4.

The subband picture is more general than the channel picture, but also more qualitative. While every channel can be considered as a subband, the opposite is not true. Discrete and continuous quantum numbers are not necessarily associated with directions of bound and asymptotically free motion. Apart from this difference, the development of the theory essentially follows the same lines as in the last subsection. First, the Hamiltonian is expanded into the eigenstates of the interaction-free Hamiltonian, which have the form of subbands. Then Fano interference is a result of Coulomb interaction between different subbands.

As in the last subsection, we consider a reduced Hamiltonian

$$\hat{H} = \hat{H}_{\text{kin}}(u, v) + W(u) - V(u), \quad (3.59)$$

defined on an l -dimensional manifold $u = (u_1, \dots, u_l)$. This time, we do not suppose the interaction-free Hamiltonian $\hat{H}_{\text{kin}}(u, v) + W(u)$ to be separable. A

weaker assumption is that the eigenvalues of the interaction-free Hamiltonian have the form of subbands:

$$\Phi_A(u) = \varphi_{nk}(u); \quad \mathcal{E}_A = \varepsilon_n(k); \quad k = (k_1, \dots, k_m). \quad (3.60)$$

The continuum dimension m may depend on the subband index l . Thus the eigenfunctions (3.60) are orthonormal and complete also for a finite number of subbands and we do not need a continuous channel index, as it was the case in the last subsection. The interaction-free absorption, which is identical to the optical density of states, is equal to

$$\begin{aligned} \alpha(\omega) &= \sum_n \int \underline{d}k |\mu_n(k)|^2 \pi \delta[\varepsilon_n(k) - \omega] \\ \mu_n(k) &= \int \underline{d}u \varphi_{nk}^*(u) \mu(u). \end{aligned} \quad (3.61)$$

In the next step, we include the Coulomb effects within the subbands. For this purpose, we expand the Coulomb potential into the unperturbed subband eigenfunctions:

$$V_{nn'}(k, k') = \int \underline{d}u \varphi_{nk}^*(u) V(u) \varphi_{n'k'}(u). \quad (3.62)$$

For the eigenfunctions of \hat{H} we make the ansatz

$$\Phi_A(u) = \int \underline{d}k \varphi_{nk}(u) \begin{Bmatrix} \psi_{n\lambda}(k) \\ \psi_{nq}(k) \end{Bmatrix}. \quad (3.63)$$

In this diagonal approximation, the discrete and continuous eigenfunctions obey the eigenvalue problem

$$\begin{aligned} \int \underline{d}k' [\varepsilon_n(k) \underline{\delta}(k, k') - V_{nn'}(k, k')] \psi_{n\lambda}(k') &= E_{n\lambda} \psi_{n\lambda}(k) \\ \int \underline{d}k' [\varepsilon_n(k) \underline{\delta}(k, k') - V_{nn'}(k, k')] \psi_{nq}(k') &= E_n(q) \psi_{nq}(k) \quad (3.64) \\ q &= (q_1, \dots, q_m) \end{aligned}$$

and the absorption spectrum, which corresponds to the approximation (3.64), is given by

$$\alpha(\omega) = \sum_n \left\{ \sum_\lambda |F_{n\lambda}|^2 \pi \delta(\omega - E_{n\lambda}) + \int \underline{dq} |F_n(q)|^2 \pi \delta[\omega - E_n(q)] \right\}$$

$$F_{n\lambda} = \int \underline{dk} \mu_n^*(k) \psi_{n\lambda}(k); \quad F_{nq} = \int \underline{dk} \mu_n^*(k) \psi_{nq}(k). \quad (3.65)$$

Equation (3.65) describes a superposition of discrete lines and continua from different subbands, where the discrete lines are not coupled to the continuum, because we have neglected the nondiagonal Coulomb matrix elements.

To take into account Coulomb interaction between the subbands, (3.65) can be extended to coupled subband equations, in analogy to the coupled channel equations (3.47). For a long time, the expansion into subband eigenfunctions (3.60) has been the standard approach for the numerical calculation of the optical absorption [24, 25, 38, 43, 44, 53, 66, 67, 69].

As we wish to identify Fano resonances, we use the solutions of the eigenproblem (3.64) as base functions. Then only the nondiagonal Coulomb matrix elements ($n \neq n'$) have to be considered. In this basis, the matrix elements of the Hamiltonian are

$$\begin{aligned} \langle n, \lambda | \hat{H} | n', \lambda' \rangle &= \delta_{nn'} \delta_{\lambda\lambda'} E_{n\lambda} \\ &\quad - (1 - \delta_{nn'}) \iint \underline{d}k \underline{d}k' \psi_{n\lambda}^*(k) V_{nn'}(k, k') \psi_{n'\lambda'}(k') \\ \langle n, \lambda | \hat{H} | n', q' \rangle &= -(1 - \delta_{nn'}) \iint \underline{d}k \underline{d}k' \psi_{n\lambda}^*(k) V_{nn'}(k, k') \psi_{n'q'}(k') \\ \langle n, q | \hat{H} | n', q' \rangle &= \delta_{nn'} \underline{\delta}(q, q') E_n(k) \\ &\quad - (1 - \delta_{nn'}) \iint \underline{d}k \underline{d}k' \psi_{nq}^*(k) V_{nn'}(k, k') \psi_{n'q'}(k'), \end{aligned} \quad (3.66)$$

in complete analogy to (3.55). The optical absorption, the components of the dipole matrix element, and the condition for Fano interference are the same as in the last subsection, Eqs. (3.54), (3.56), and (3.57).

The subband picture adopted in this subsection is more general than the channel picture and allows us to treat more complicated systems like superlattices, superlattices in electric fields (Wannier–Stark ladders), or structures with nonparabolic electron and hole dispersions. On the other hand, some rules on the properties of Schrödinger operators in real space do no longer apply. Although $-V_{nn}(k, k')$ is negatively semidefinite as integral operator, it is not guaranteed that each subband has excitons. The upper subband edges can be finite and, in some cases, the density of states (3.61) reveals spectral gaps. In the optical absorption, discrete lines can appear energetically above continuous transitions if excitons of excited subbands fall into spectral gaps. Depending on the curvature of the $\varepsilon_n(k)$, the intra-subband Coulomb interaction can lead to saddle-point excitons, which are degenerate with continuum states of the same subband. The mechanism is similar to Fano interference and leads to an enhancement of the continuous absorption below the saddle points [24].

3.3 Examples

Fano interference is a challenging task both for theorists and experimentalists. The eigenvalue problem of the reduced Hamiltonian is a partial differential equation requiring a numerical solution of a class-II or class-III problem (see Chap. 2) with high resolution. In the last decade, such numerical methods have been developed. In particular, Lanczos recursion, the formulation as scattering problem, and the equation-of-motion method, described in the last chapter, allows to calculate the optical absorption for virtually all geometries. On the experimental side, the samples have to be of very high quality so that the homogeneous and inhomogeneous broadening due to sample imperfections are smaller than the natural linewidth of the Fano resonance. For this reason, the experiment is still somewhat behind theory, especially for quantum wires. In some cases, experimental spectra of high quality have been published in the past, but the asymmetric lineshapes were not interpreted as Fano resonances. Examples are bulk semiconductors in a magnetic field [54–56], quantum wells and superlattices in a perpendicular electric field [20, 21, 36], or the (e2, hh2) transition in quantum wells [42].

Fano resonances in low-dimensional semiconductors can be treated on different levels: qualitative or “philosophical” studies, which predict Fano interference for some geometries, model calculations, estimates of the line-shape parameters, and calculations of whole absorption spectra in different approximations. Some experimental papers present direct evidence for Fano interference, while in other works only the interpretation is based on Fano interference. In this section, we will mainly quote quantitative theoretical studies and direct experimental evidence of Fano interference. We first give an overview about theoretical and experimental results on Fano resonances in low-dimensional semiconductors. Then we present numerical results for two examples, a bulk semiconductor in magnetic field and a quantum well, and make a comparison with experimental data.

3.3.1 Overview

In the last two chapters, we have come to know several definitions of the dimension of a semiconductor. First, a semiconductor has a physical dimension p , which means that its volume – finite or infinite – has the unit cm^p . For all realistic structures, this physical dimension is $p = 3$. In idealized models, p can be lower. For example, quantum-well wires can be modeled on the basis of an ideal two-dimensional systems so that $p = 2$. The dimension p determines the envelope of the optical density of states for large frequencies, which behaves like $(\omega - E_g^{(p)})^{(p-2)/2}$. The geometric dimension d is the number of Cartesian directions in which the structure is translationally invariant or periodic. This is also the dimension of the normalization volume $\Omega^{(d)}$ in the expressions for the optical density of states (1.51) or the optical susceptibility (1.95). For bulk semiconductors and superlattices it holds that $d = 3$, for

quantum wells and wires we have $d = 2$ and $d = 1$, respectively, independent of external fields. Most important is the density-of-states dimension q , which means that the onset of the free absorption behaves like the absorption of a q -dimensional electron-hole system, $D(\omega) \propto (\omega - E_g^{(q)})^{(q-2)/2}$ for $q > 0$, where $E_g^{(q)}$ is the continuum onset. For $q = 0$, the spectrum is entirely discrete. We will call a semiconductor q -dimensional if its density-of-states dimension is equal to q . If the confinement is purely geometric, it holds that $q = d$; if part of the quantization is due to external fields, then $q < d$. Generally, we have the relation

$$3 \geq p \geq d \geq q \geq 1 \quad (3.67)$$

between p , d , and q . The last condition, $q \geq 1$, is necessary for Fano interference, because the spectrum of zero-dimensional semiconductors is entirely discrete.

The mathematical dimensions l and m from the last chapter determine the numerical complexity. In the last section we have learned that

$$l > m \geq 1 \quad (3.68)$$

is necessary for Fano interference. If the channel picture (Sect. 3.2) is applicable, then the volume element $\mathrm{d}v$ has the dimension cm^q . For the two-band model with isotropic dispersions it holds that $m \leq q$.

Zero-dimensional semiconductors like quantum dots or quantum wells in a perpendicular magnetic field do not show Fano resonances because their optical spectrum is entirely discrete. In the two-band model, the bulk semiconductor and the ideal two-dimensional semiconductor lead to a one-dimensional ($m = 1$) problem, and there is no mixing between discrete and continuum states.

Table 3.1 summarizes examples of three-, two-, and one-dimensional semiconductors for which Fano resonances in the interband absorption are either predicted theoretically or measured experimentally. Here, we have restricted ourselves to Fano interference on the account of Coulomb interaction, which can be explained in the two-band model. The dimensions l and m refer to the two-band model with isotropic effective masses. This table shows that Fano interference can occur in all dimensions $q = 3, 2$, and 1 . Thus, a semiconductor does not need to be “low-dimensional” according to our definition. The term “quantum structures” is more appropriate.

Superlattices are sometimes referred to as low-dimensional semiconductors. However, they are geometrically three-dimensional because of the periodicity along the growth axis, which is also reflected by the factor $1/\Omega$ in the optical density of states (1.49) and the optical absorption (1.96). Furthermore, the optical density of states shows the typical $\sqrt{\omega}$ edge [96], indicating that $q = 3$. Nevertheless, we can have Fano interference when an exciton of a higher miniband is degenerate with the in-plane and perpendicular-plane continua of lower minibands [31]. In this case, the absorption will not drop

Table 3.1. Examples for Fano resonances in the optical absorption of three-, two-, and one-dimensional semiconductors, type of the confinement, and references.

$d \ q \ l \ m$	System	Confinement	Theory	Experiment
3 3 3 2	superlattice	geometric	[26, 28, 31, 32]	[19, 27]
3 2 3 1	superlattice + \mathbf{F}_\perp	field	[22–25, 30, 32, 34]	[20, 21, 29, 33, 34]
2 2 3 1	quantum well*	geometric	[38, 40, 43–45, 49, 50, 53]	[19, 35, 37, 41, 42, 47, 48, 51, 52]
2 2 3 1	quantum well* + \mathbf{F}_\perp	geometric	[39, 46]	[36]
2 2 3 2	quantum-wire array	geometric	[68]	
3 1 2 1	bulk + \mathbf{B}	field	[58–60]	[47, 48, 54–58, 61–63]
3 1 3 1	superlattice + \mathbf{B}_\perp	geom. + field	[24, 26, 34]	[64]
1 1 3 1	quantum wire	geometric	[45, 65, 66, 68, 69]	
1 1 3 1	quantum wire + \mathbf{B}_\perp	geometric	[67]	

* incl. MQW

to zero, even if there is no homogeneous broadening. In Table 3.1, superlattices are the only system with $m > 1$ where the numerical solution leads to a class-III problem. This explains why there have been little specific efforts to search for Fano resonances in these systems. So far, Fano interference between transitions to the Γ and X points of the conduction band in superlattices has been studied qualitatively [97]. We mention that $q = 2$ and $m = 1$ for the superlattice in a perpendicular electric field is an approximation and the Fano resonances may disappear at high fields (see next Chapter). Often, periodic arrays are fabricated merely for technological reasons, but the coupling of different layers is negligible. Then, the lower minibands are practically dispersionless and the superlattice behaves like an ensemble of independent quantum wells (multiple quantum well, MQW). It is sometimes difficult to clearly distinguish between superlattice and MQW. For quantum wells, which are class-II problems with strong confinement, Fano resonances have been predicted already in 1989 [38].

Experimentally, Fano resonances have been detected in bulk material or layered structures, which can be fabricated by epitaxial growth so that the interface roughness and, therefore, the inhomogeneous broadening can be kept very small. Good agreement between theory and experiment is found for superlattices in electric fields [29, 34, 39] and for quantum wells [44]. The bulk semiconductor in a magnetic field is an ideal object for the observation of Fano resonances. Not only is the quality of bulk semiconductors significantly higher than of quantum wells or superlattices, but the confinement, which is purely field-induced, is free of fluctuations on a microscopic scale. In this system, asymmetric lineshapes have been observed in absorption spectra as early as in 1973, but were not interpreted as Fano resonances [54]. We shall

study the bulk semiconductor in a magnetic field and the quantum well in detail in the next subsection.

If a magnetic field is applied in the growth direction of a superlattice, then the in-plane electron–hole motion is subjected to Landau quantization. The only direction of continuous motion is the growth direction, which means that the continuum is one-parametric. Fano interference can arise from coupling of different Landau levels [23, 64], as observed in bulk semiconductors in a magnetic field, as well as from coupling of different minibands within the same Landau level [26]. The latter case can be approximately described by the one-dimensional model from the last subsection (3.58). Moreover, excitons of higher minibands or Landau levels can fall into absorption gaps. Then the spectrum of excited optical transitions is a mixture of discrete lines, Fano resonances, and flat continuum [26].

The Landau quantization can reduce the dimension by 2, in case that the magnetic field is applied perpendicular to a plane of free motion. This was already observed for an ideal two-dimensional semiconductor in a perpendicular magnetic field (Sects. 1.2 and 2.2). However, the dimension is not reduced for arbitrary direction of the magnetic field. For example, a quantum-well wire in a perpendicular magnetic field is still a one-dimensional semiconductor [67, 98]. A paradox is observed for wide quantum-well wires in a perpendicular magnetic field: if for fixed magnetic field the wire width goes to infinity, the dimensionality changes from $q = 1$ to $q = 0$.

The spectrum of a superlattice in the Voigt geometry (electric field in growth direction, magnetic field parallel to the layers) is not at all understood. It is observed that the Fano resonances at $B = 0$ disappear for $B \neq 0$, the linewidth increases, and the lineshape becomes irregular [21]. Very recently, the experimental findings were reproduced in numerical calculations by Stepanow [99]. This work shows the evolution of the spectrum with electric and magnetic field. As the electron–hole Hamiltonian cannot be reduced to a real differential operator, this system is a candidate for Fano interference with complex parameters (see Sect. 3.1).

Fano resonances are also predicted for quantum wires. The mathematical dimension $l = 3$ refers to the approximation where a quantum well wire is modeled as a physically two-dimensional ($p = 2$) structure. In the simplest approximation of parabolic confinement and electron–hole symmetry, center-of-mass and relative motion can be separated so that l can be reduced to 2. This has been used in the first calculation of Fano resonances in quantum wires [45]. If the finite thickness is taken into account, we would have $l = 5$ for quantum-well wires or V-shaped quantum wires and $l = 4$ for cylindrical quantum wires. Numerical calculations for V-shaped quantum wires, which have been published so far, do not have the quality to discern Fano resonances [100]. Quantum-wire arrays are the two-dimensional pendant of superlattices [68]. If the coupling between the individual wires is important, then the continuum is two-parametric.

Experimentally, the lateral structuration process results in large fluctuations of the wire width and, therefore, in a large inhomogeneous broadening. For many years, no specific features in the optical spectrum were detected which could be attributed to effects of lateral quantization. Brunner et al. used laser-induced interdiffusion for the preparation of quantum-well wires [101]. The luminescence spectrum reveals signatures of center-of-mass and size quantization. The experiments by Vouilloz et al. and Martinet et al. already allow to classify individual subband transitions, but the broadening is still too large to reveal Fano lineshapes [102, 103]. So it will be a challenge in the future to measure the first Fano resonance in a quantum wire.

In the remaining part of this section we demonstrate Fano interference in the optical absorption for two examples of low-dimensional semiconductors: the bulk semiconductor in a magnetic field and the quantum well. These systems are relatively easy to treat numerically and there are also experimental data which can be compared with the theoretical results.

3.3.2 Bulk Semiconductor in a Magnetic Field

The bulk semiconductor in a magnetic field is the simplest example for Fano interference. In the two-band model with isotropic effective masses, the Hamiltonian is defined on a two-dimensional manifold. The separation between center-of-mass and relative motion is demonstrated in App. C.1.2. In excitonic Hartree units (App. B.2), the expressions for the reduced Hamiltonian and the dipole matrix element are

$$\hat{H} = -\frac{1}{2} \frac{1}{\varrho} \frac{\partial}{\partial \varrho} \varrho \frac{\partial}{\partial \varrho} + \frac{B^2 \varrho^2}{8} - \frac{1}{2} \frac{\partial^2}{\partial z^2} - \frac{1}{\sqrt{\varrho^2 + z^2}}$$

$$G = G_\varrho \times G_z ; \quad G_\varrho = [0, \infty) ; \quad G_z = (-\infty, +\infty) \quad (3.69)$$

$$g(\varrho, z) = 2\pi\varrho ; \quad \mu(\varrho, z) = \frac{\delta(\varrho)}{2\pi\varrho} \delta(z) .$$

The main difference to Example A from Chap. 2 is the additional coordinate z , in which the motion is unbound. The dimensions of the semiconductor are $d = 3$, $q = 1$, $l = 2$, and $m = 1$. The solutions of (3.69) have been analyzed qualitatively by Seisyan and Zakharchenya in a review on interband magneto-optics [104]. The class-II problem (3.69) has been solved numerically by the author in 1994, at that time as boundary-value problem. These were the first calculated magnetoexciton spectra which show Fano resonances [58]. Later the calculations were performed for a larger range of parameters, using the equation-of-motion method [59]. Today, nine years later, these results are still unsurpassed.

Because of the dimensionless variables, the Hamiltonian (3.69) is the same as for a Hydrogen atom in a magnetic field, but the characteristic value of

the magnetic field is smaller by several orders of magnitude (cf. Table 1.5). This allows to observe the diamagnetic shift, which is practically impossible for the Hydrogen atom. An interesting fact is that the classical motion of an atom in a magnetic field is chaotic [4].

The problem (3.69) fits into the channel picture of Sect. 3.2 if we identify:

$$w = \varrho ; \quad v = z ; \quad \underline{d}w = d\varrho \, 2\pi\varrho ; \quad \underline{d}v = dz$$

$$\begin{aligned} \hat{H}_{\text{kin } \varrho} &= -\frac{1}{2} \Delta_{\varrho} ; \quad \hat{H}_{\text{kin } z} = -\frac{1}{2} \frac{\partial^2}{\partial z^2} \\ W(\varrho) &= \frac{B^2 \varrho^2}{8} ; \quad V(\varrho, z) = \frac{1}{\sqrt{\varrho^2 + z^2}} . \end{aligned} \quad (3.70)$$

The potentials W and $-V$ qualitatively behave as shown in Fig. 3.3.

After these preparations, we proceed as in Sect. 3.2. First, we solve the eigenvalue problem of $\hat{H}_{\text{kin } \varrho} + W(\varrho)$ for the confined direction:

$$\left(-\frac{1}{2} \Delta_{\varrho} + \frac{B^2 \varrho^2}{8} \right) \varphi_n(\varrho) = E_n \varphi_n(\varrho) . \quad (3.71)$$

We assume that $B > 0$. Then the eigenvalues (Landau levels) are $E_n = (n + \frac{1}{2}) \omega_c = (n + \frac{1}{2}) B$; $n \in \mathbb{N}_0$. The explicit expressions for the eigenfunctions were given in the last chapter, equation (2.33). With these eigenfunctions, the projections of the dipole matrix element μ and the matrix elements of the Coulomb potential V are

$$\mu_n(z) = \int_0^\infty d\varrho 2\pi\varrho \varphi_n^*(z) \mu(\varrho, z) = \sqrt{\frac{B}{2\pi}} \delta(z) \quad (3.72)$$

and

$$V_{nn'}(z) = \int_0^\infty d\varrho 2\pi\varrho \varphi_n^*(\varrho) V(\varrho, z) \varphi_{n'}(\varrho) . \quad (3.73)$$

As the potentials $V_{nn'}(z)$ will be further used in finite-difference calculations, we determine their discretizations by the ground-state method. Then, instead of (3.73), we use

$$V_{nn'j} = \lim_{h_\varrho \rightarrow 0} \sum_i g_{\varrho i} \varphi_n^*(\varrho_i) V_{ij} \varphi_{n'}(\varrho_i) , \quad (3.74)$$

where ϱ_i and z_j are the mesh points of the coordinates ϱ and z with mesh sizes h_ϱ and h_z , respectively, V_{ij} is the discretization of $V(\varrho_i, z_j)$ by means of the ground-state method (2.98), and the $g_{\varrho i}$ are the weights for the ϱ integration, defined in (2.84).

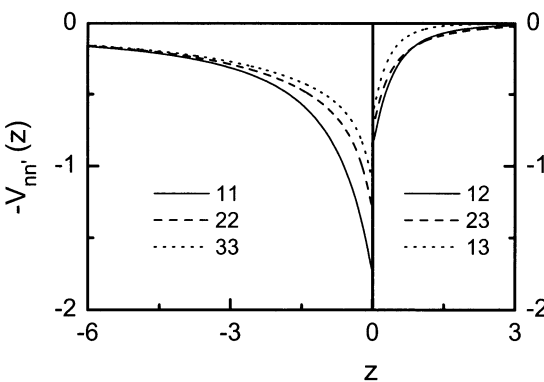


Fig. 3.5. Coulomb matrix elements $-V_{nn'}(z) = -V_{nn'}(-z)$ for $n = n'$ (left) and $n \neq n'$ (right). The magnetic field is $B = 2$

The diagonal ($n = n'$) and nondiagonal ($n \neq n'$) Coulomb matrix elements $-V_{nn'}(z)$ for the phase choice (2.33) are shown in Fig. 3.5. The diagonal matrix elements, which govern the electron–hole interaction within the channels, behave like $-V_{nn}(z) \sim -1/|z|$ for $|z| \rightarrow \infty$. In contrast, the nondiagonal matrix elements show a faster decay, $V_{nn'}(z) = O(|z|^{-3})$ for $|z| \rightarrow \infty$. For $z = 0$, the potentials are finite and are identical to the matrix elements of the two-dimensional Coulomb potential (2.41). Therefore, the discretized potentials $V_{nn'}{}_j$ go over into the exact expressions $V_{nn'}(z_j)$ (3.73) in the limit $h_z \rightarrow 0$.

With the expressions for μ_n and $V_{nn'}$ (3.72–3.73), the optical susceptibility becomes

$$\chi(\omega) = \sum_{\Lambda} \frac{|F_{\Lambda}|^2}{\mathcal{E}_{\Lambda} - (\omega + i\epsilon)} ; \quad F_{\Lambda} = \sqrt{\frac{B}{2\pi}} \sum_{n=0}^{\infty} \Phi_{\Lambda;n}(0) , \quad (3.75)$$

where the eigenvalues \mathcal{E}_{Λ} and eigenfunctions Φ_{Λ} are the solution of the coupled channel equations:

$$\sum_{n'=0}^{\infty} \left\{ \left[(n+\frac{1}{2})B - \frac{1}{2} \frac{\partial^2}{\partial z^2} \right] \delta_{nn'} - V_{nn'}(z) \right\} \Phi_{\Lambda;n'}(z) = \mathcal{E}_{\Lambda} \Phi_{\Lambda;n}(z) . \quad (3.76)$$

The single-channel equations, which take into account Coulomb interaction only within each Landau level, follow from (3.76) by setting the nondiagonal ($n \neq n'$) Coulomb matrix elements equal to zero.

The numerical calculation of the optical absorption $\alpha(\omega) = \text{Im } \chi(\omega)$ can be conveniently done by rewriting the equations (3.75–3.76) as an initial-value problem (2.4). The number of Landau levels needs to be truncated at some finite value. This is an example for a mixed representation, mentioned in the last chapter, where some directions are expanded into an orthonormal and complete set, while others are discretized in real space. In order to analyze the lineshape, we use a very small homogeneous broadening $\epsilon = 0.01$. For

the discretization of the z direction we use parameters $G_z = [-L/2, +L/2]$ with $L = 2000$ and $h_z = 0.1$. The large normalization length L is necessary in order to achieve a sufficiently dense spacing of eigenvalues in the quasi-continuum, according to the estimate (2.60). For comparison, we shall also perform a solution of (3.69) completely in real space, which automatically takes into account coupling of all Landau levels. For the discretization of the additional ϱ direction, we use parameters $G_\varrho = [0, R]$, $R = 9/B + 5/\sqrt{B}$, and $h_\varrho = 0.1/\sqrt{B}$, where we estimated the extension of the wavefunction by the classical point of return.

Figure 3.6 shows the calculated optical absorption in different approximations. The magnetic field is fixed at $B = 2$. Curve (a) shows the optical absorption in case that the Coulomb interaction of electrons and holes is totally neglected. This function is identical to the optical density of states, and is a sum over one-dimensional densities of states, starting at the Landau levels $E_n = (n + \frac{1}{2})\omega_c$. The absorption remains finite at the edges E_n because of the homogeneous broadening introduced. The first three Landau levels $n = 0, 1, 2$ fall into the frequency range under consideration.

In the next step (b), we take into account only the diagonal Coulomb matrix elements $V_{nn}(z)$. In this single-channel approximation, the optical absorption is still a sum over absorptions spectra for the individual Landau levels. In contrast to the free-particle case, the absorption of each Landau level n consist of a Rydberg series of discrete lines with energies $E_{n\lambda} < E_n$ and a continuum for $E \geq E_n$. The number of discrete lines is infinite, because the Coulomb matrix elements $-V_{nn}(z)$ are long-ranged, but only three peaks are resolved because of the finite homogeneous broadening. The exciton binding energies become smaller with increasing Landau-level number, because the attractive potentials become weaker (cf. Fig. 3.5). The absorption does not have a singularity at the Landau-level edges as in the interaction-free case, but the continuum is completely flat, similarly to three- and two-dimensional semiconductors (cf. Fig. 1.5). Thus the Sommerfeld factor is zero at the absorption edge. This was noticed in one of the early papers on the optical absorption of one-dimensional semiconductors [105]. The continuous absorption steps up when a new Landau level comes into play. Bound and continuum states of different Landau levels coexist because we have neglected the non-diagonal Coulomb matrix elements.

If we take into account the coupling between the lowest three Landau levels (c), the excitons of the higher Landau levels ($n = 1, 2$) turn into Fano resonances because of the degeneracy with continuum states of the lower Landau levels. For these excitons, the natural linewidths are much larger than the homogeneous broadening so that the profiles observed are very close to the natural line profiles for $\epsilon = +0$. The excitons which belong to the zeroth Landau level remain bound states and lead to discrete (Lorentzian) lines, because they are not degenerate with continuum states. The absorption almost drops to zero on the high-energy side of the lowest exciton from the

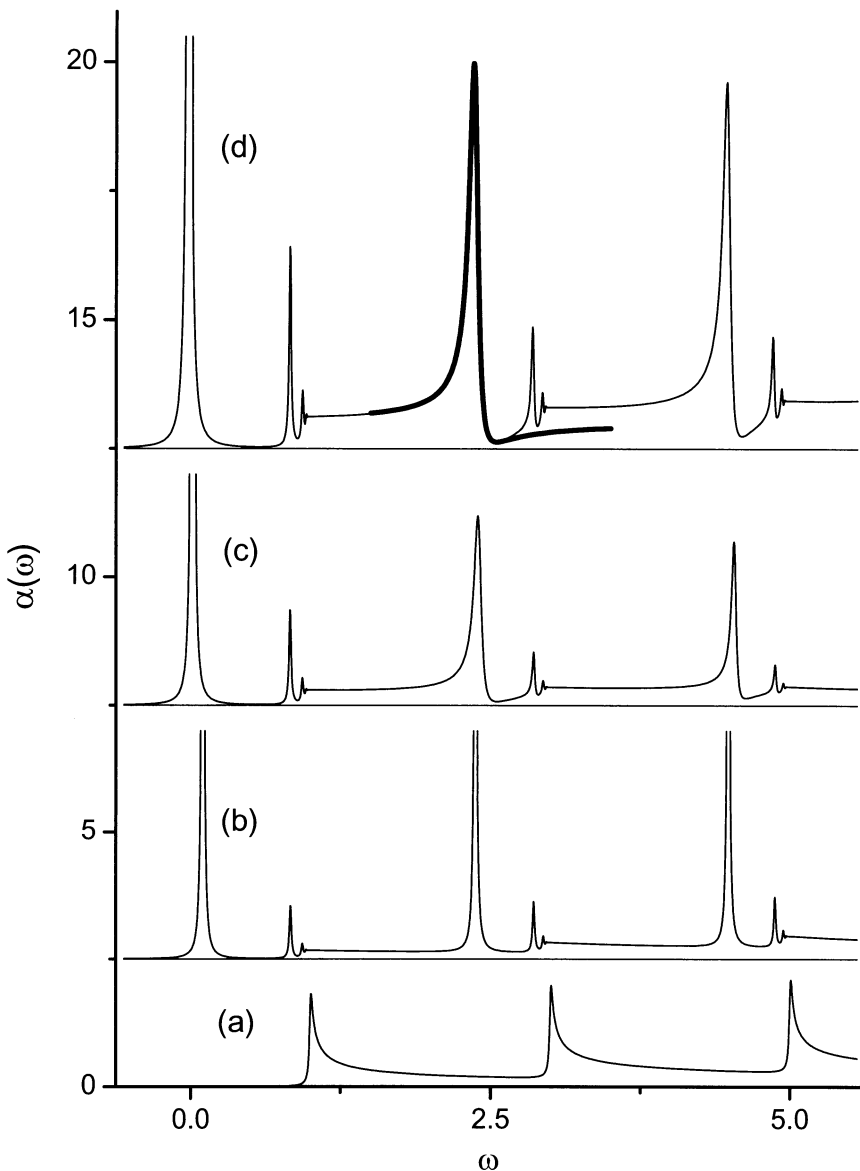


Fig. 3.6. Optical absorption of a bulk semiconductor for $B = 2$ in different approximations: a) interaction-free particles, b) Coulomb interaction only within the channels, c) coupling of the lowest three channels, and d) complete numerical solution of (3.69). The homogeneous broadening is $\epsilon = 0.01$. Thick solid line: fit to a Fano profile with $q = -4.27$ and $\frac{1}{2}\Gamma = 4.31 \times 10^{-2}$

first ($n = 1$) Landau level. For $\epsilon = +0$ (no homogeneous broadening), the absorption would exactly go to zero, according to the results of Sect. 3.1. This is no longer true for the next Landau level ($n = 2$), because the exciton is degenerate with two continua. The excited states of the Rydberg series are not well resolved, because their natural linewidth is comparable to or lower than the homogeneous broadening. In the case of a Rydberg series, degenerate with a continuum, the original Fano paper predicts equally sharp resonances, similar in shape [1].

The result of the full solution (d) is very similar to the result for three Landau levels (c). The main difference is the absolute magnitude of the absorption, which is increased by about a factor of two. Furthermore, the positions of the excitons change with the total number of channels taken into account. This stresses the importance of the nonresonant contributions for a quantitative description, while all qualitative features are already found in the approximation (c) (see also the discussion of the Hamiltonian, Fig. 3.4). From Sect. 2.2 we know that in order to reproduce the full solution by the coupled channel equations we would need to take into account more than thousand Landau levels, which is close to impossible. Thus, the present system is a good example for the superiority of the real-space method from the last chapter.

The lineshapes of the resonances are perfectly described by the Fano profile. This is demonstrated for the first ($n = 1$) Landau level (*thick solid line*). From the numerical fit we obtained the parameters $q = -4.27$ and $\frac{1}{2}\Gamma = 4.31 \times 10^{-2}$. In the presence of a constant homogeneous broadening, the lineshape is given by convolution of the Fano profile with a Lorentzian. The resulting function is a Fano profile plus a constant. The asymmetry parameter q remains unchanged, but the natural linewidth $\frac{1}{2}\Gamma$ is increased by the homogeneous broadening ϵ . Therefore, in the present case, the actual natural linewidth is 3.31×10^{-2} , which is still much larger than the homogeneous broadening. The lineshape parameters for solution (c) and (d) are different, which once more shows the importance of the nonresonant contributions.

Next, we study the evolution of the spectrum with the magnetic field. For the calculation, we use parameters $B = 0.25 \dots 4$ and a realistic homogeneous broadening $\epsilon = 0.05$. For GaAs parameters, $m_e = 0.067 m_0$, $m_h = 0.50 m_0$, $\epsilon = 13.1$, the units of energy and magnetic field are $[E] = 9.37$ meV and $[B] = 4.78$ T, respectively. Thus, the magnetic field ranges from 1.16 T to 19.12 T and the homogeneous broadening is equal to 0.468 meV, which corresponds to realistic experimental situations. The cyclotron energy of the relative motion, as function of the magnetic field, is given by $\hbar\omega_c/\text{meV} = 1.96 B/\text{T}$. The zero of the energy scale is the gap energy at zero temperature $E_g(0\text{K}) = 1.519$ eV. For the numerical grid we use the same parameters as for Fig. 3.6 (d), except that the normalization length in z direction is only $L = 400$, because the homogeneous broadening is larger. A corresponding computer program, which

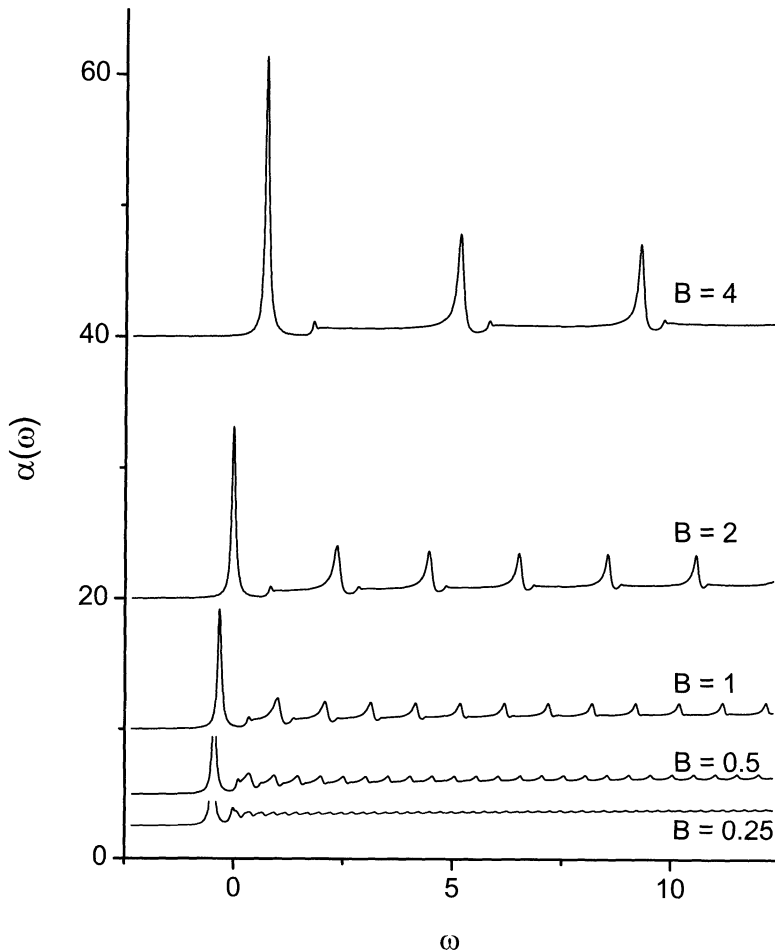


Fig. 3.7. Calculated optical absorption for different magnetic fields $B = 0.25, 0.5, 1, 2$, and 4 . The homogeneous broadening is $\epsilon = 0.05$

also demonstrates the method of absorbing boundary conditions, is shown in App. D.5.

The results are shown in Fig. 3.7. Below the continuum onset $\frac{1}{2}\omega_c = \frac{1}{2}B$, we have a series of discrete lines. Only the 1s exciton is resolved because of the finite homogeneous broadening. For small magnetic field, $B \ll 1$, the absorption resembles the absorption without magnetic field (cf. Fig. 1.5), with a small modulation of nearly equidistant peaks, which stems from the Landau quantization. The lineshapes of these resonances cannot be clearly identified.

With increasing field, clear and distinct Fano resonances emerge. Their positions nearly scale as $(n + \frac{1}{2})B$ for $n \geq 1$. For fixed Landau index $n \geq 1$, the heights of the Fano resonances increase about linearly with field, which can be expected from the form of the μ_n (3.72). As the spacing of the resonances is also linear in B , the averaged absorption for $\omega \geq 0$ is independent of the magnetic field.

In contrast to the Fano resonances, the shift of the ground state is quadratic in the field. First-order perturbation theory (App. C.3) with the 1s wavefunction (C.53) gives a diamagnetic shift

$$\Delta E_{1s} \sim \int d^3r |\varphi_{1s}(\mathbf{r})|^2 \frac{B^2(x^2+y^2)}{8} = \frac{B^2}{4} \text{ for } B \rightarrow 0. \quad (3.77)$$

Only for large magnetic fields, the shift of the ground state becomes linear with field, as the continuum onset shifts linearly with B , but the increase of the binding energy with magnetic field is sublinear.

In the high-field limit, $B \gg 1$, the Fano–Rydberg series of different Landau levels are well separated by continua, for which the absorption is nearly constant or slightly decreases as the energy increases. The energetic spacing of the Landau levels, which is equal to the cyclotron frequency, is much larger than the natural linewidth. The binding energy of the lowest exciton at $B = 4$ has increased by about a factor of 2.6, compared to the case of $B = 0$. The ratio between the oscillator strength of the 1s exciton and the continuum has also drastically increased. These are signatures of a transition to a lower dimension [106], in this case from $q = 3$ to $q = 1$.

Dimensionality transitions can also be observed in wide quantum wells or quantum wires, where the geometric dimensionality changes from $d = 3$ to $d = 2$ or from $d = 2$ to $d = 1$ [65]. For geometric confinement, when the spatial extension is increased far above the Bohr radius of the exciton, one observes center-of-mass quantization, which is manifested by a series of discrete lines below the continuum onset. This feature is absent in Fig. 3.7, because the dimensionality transition takes place only in the space of the relative coordinates, as can be seen from the Hamiltonian (3.69).

Fano resonances in magnetoabsorption spectra of bulk GaAs have been identified first by Siegner et al. [57]. Absorption spectra from these experiments are shown in Fig. 3.8 for left-circular (σ^-) polarization and different magnetic fields $B = 0, 2, 6$ and 12 T [58]. The spectra have been individually normalized. The experimental results qualitatively agree with the calculations (Fig. 3.7). We observe discrete (Lorentzian) lines below the continuum onset. Their positions show a weak dependence on the magnetic field. For $B > 0$, structures appear in the continuum, which turn out as Fano resonances with a negative q -parameter.

The major difference between experiment and theory is the valence-band mixing, which is not considered in the two-band model. For $B = 0$, two discrete lines are observed, which can be attributed to the 1s excitons of

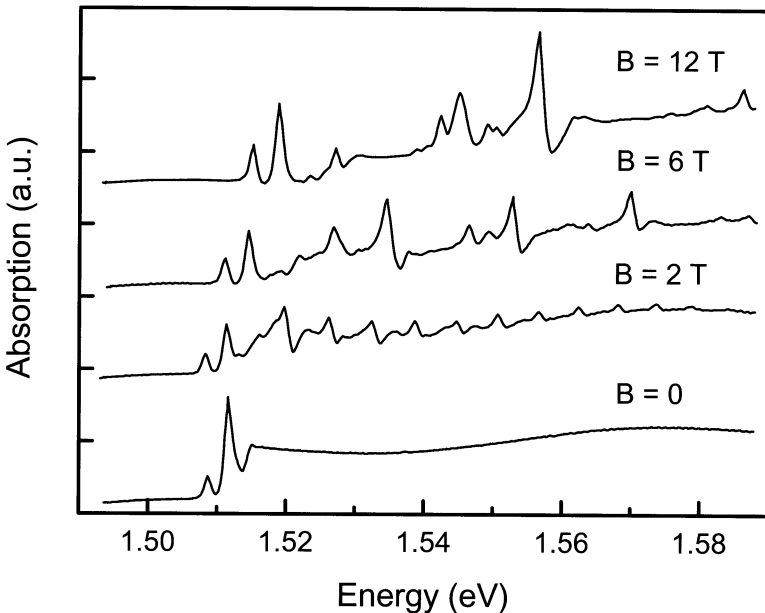


Fig. 3.8. Measured absorption spectra of GaAs for different values of the magnetic field: $B = 0, 2 \text{ T}, 6 \text{ T}$ and 12 T (from [58])

the transitions $|\frac{3}{2}, +\frac{3}{2}\rangle \rightarrow |\uparrow\rangle$ and $|\frac{3}{2}, +\frac{1}{2}\rangle \rightarrow |\downarrow\rangle$, usually referred to as heavy- and light-hole transition (see also the discussion in Sect. 1.1). The valence-band degeneracy is lifted due to mechanical strain in the sample and the light-hole exciton appears below the heavy-hole exciton. Both transitions give rise to a Landau fan for nonzero magnetic field. The hole masses, deduced from the fan charts, are in the order of the theoretical in-plane masses $m_{\text{hh} \parallel} = m_0/(\gamma_1+\gamma_2)$ and $m_{\text{lh} \parallel} = m_0/(\gamma_1-\gamma_2)$ (mass reversal).

We notice that the experimental q -parameters are smaller than in the calculations, which means that the Fano effect is stronger. The reason is that, in contrast to the simplified model (3.69), two continua (hh and lh) contribute to the Fano interference.

Magnetoexciton spectra are generally very sensitive to the details of the band structure (valence-band degeneracy, conduction-band nonparabolicity, Zeeman splitting) [58, 64, 107], while without magnetic field a reasonable quantitative agreement is often observed already for the two-band model [33, 34]. It would be very interesting to make a comparison with calculations based on an 8×8 effective Hamiltonian, which could also help to find improved values for the band-structure parameters. Such calculation is in principle possible by the methods of Chap. 2, but has not been done so far.

The lineshape parameter q shows a weak field dependence, both in theory and in experiment. According to (3.15), q is determined by both the

quantum-mechanical coupling and the oscillator strength of the continuum. For the bulk semiconductor in a magnetic field, the Coulomb matrix elements, which are responsible for the quantum-mechanical coupling, increase with field, while the continuum absorption decreases with field, which tends to compensate the first effect. The situation is different for superlattices in an electric field, studied theoretically by Whittaker [22–24] and experimentally by Holfeld et al. [29]. Here, the Coulomb matrix elements remain constant at high F , while the continuum absorption strongly decreases with increasing field. This leads to a strong dependence of q on the electric field.

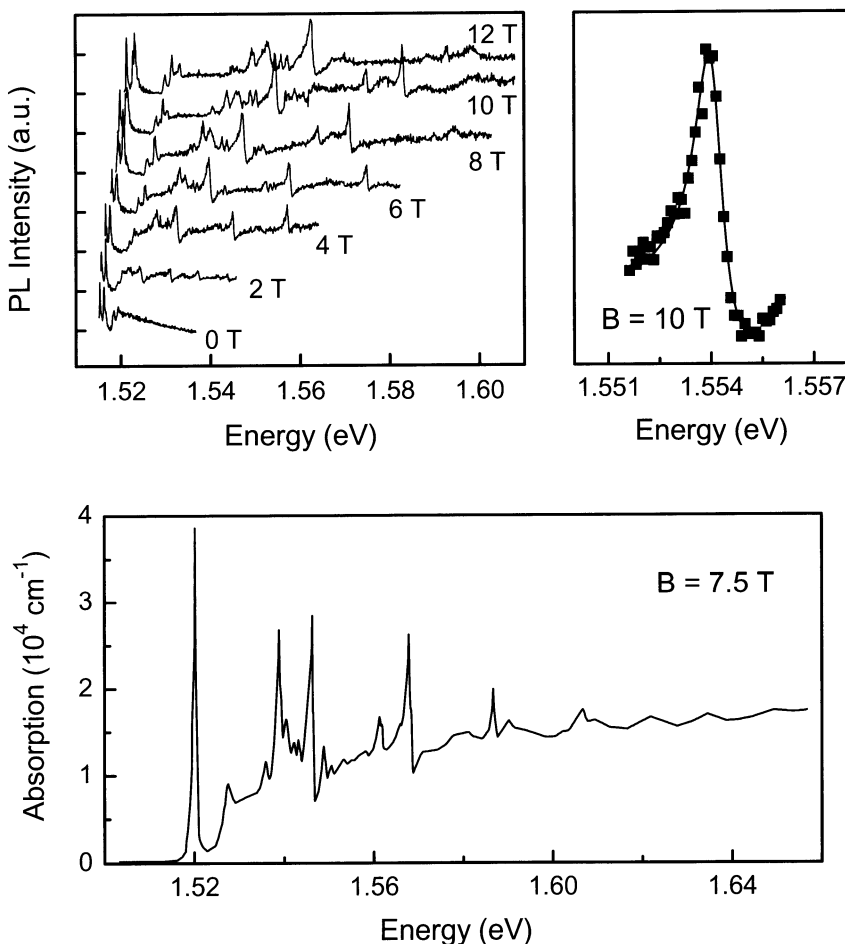


Fig. 3.9. Experimental results on Fano resonances in GaAs magnetoexciton spectra. Top: Bellani et al. 1996 [47]. Bottom: Vasilenko and Seisyan 1999 [63]. Used by permission

Finally, in Fig. 3.9 we show a selection of results by other authors. In 1996, Bellani et al. published PLE spectra of GaAs in a magnetic field [47, 48] (top left). As in Fig. 3.8, one can clearly identify the Landau levels for the heavy- and light-hole transitions, which, except for the ground state, show a linear shift with field strength. The well-resolved lineshapes are described by the Fano formula (3.16). This is demonstrated for the first ($n = 1$) heavy-hole transition at $B = 10$ T (top right). The lineshape parameter given by these authors is $q = -2.9$, which, in the limits of accuracy, is exactly the same as the value found by Siegner, $q = -2.86$ [58]. Absorption spectra by Vasilenko et al. from 1999 (bottom left) also show clear and distinct Fano resonances [63]. For GaAs in a magnetic field, the characteristic lineshapes were seen in experiments already before they were identified as Fano resonances and the physical mechanism was uncovered. We know of a paper by Becker et al. from 1987 [55] and an unpublished thesis by Lage from 1989 [56]. Possibly, the earliest occurrence of asymmetric lineshapes in GaAs magnetoexciton spectra is in a paper by Seisyan et al. from 1973 [54].

3.3.3 Quantum Well

The second example is the quantum well. In the two-band model, the reduced Hamiltonian, the domain, the volume element, and the dipole matrix element are given by

$$\begin{aligned} \hat{H} = & -\frac{1}{2m_e} \frac{\partial^2}{\partial z_e^2} - \frac{1}{2m_{hz}} \frac{\partial^2}{\partial z_h^2} + U_e(z_e) + U_h(z_h) \\ & - \frac{1}{2m_e} \frac{1}{\varrho} \frac{\partial}{\partial \varrho} \varrho \frac{\partial}{\partial \varrho} - \frac{1}{\sqrt{\varrho^2 + (z_e - z_h)^2}} \end{aligned} \quad (3.78)$$

$$G = G_{z_e} \times G_{z_h} \times G_\varrho ; \quad G_{z_e} = G_{z_h} = (-\infty, +\infty) ; \quad G_\varrho = [0, \infty)$$

$$g(z_e, z_h, \varrho) = 2\pi\varrho ; \quad \mu(z_e, z_h, \varrho) = \delta(z_e - z_h) \frac{\delta(\varrho)}{2\pi\varrho} .$$

Here, we have introduced dimensionless units $\hbar = m = e^2/(4\pi\varepsilon_0\varepsilon) = 1$, where $m = m_e m_h / (m_e + m_h)$ is an averaged reduced mass, calculated from the averaged hole mass m_h . We shall allow for different hole masses m_{hz} and $m_{h\varrho}$ for the perpendicular and parallel direction, respectively. The reduced in-plane mass is $m_\varrho = m_e m_{h\varrho} / (m_e + m_{h\varrho})$. The confinement of electron and hole is modeled by rectangular potentials

$$U_{e,h}(z) = \begin{cases} 0 & \text{for } |z| \leq \frac{d}{2} \\ \pm \Delta E_{c,v} & \text{for } |z| > \frac{d}{2} . \end{cases} \quad (3.79)$$

For type-I confinement, which we will assume here, the barrier heights $\pm E_{c,v}$ are positive.

In order to apply the channel picture from Sect. 3.2, we identify

$$\begin{aligned} w &= (z_e, z_h) ; \quad \hat{H}_{\text{kin } w} = -\frac{1}{2m_e} \frac{\partial^2}{\partial z_e^2} - \frac{1}{2m_{h_z}} \frac{\partial^2}{\partial z_h^2} ; \quad W(w) = U_e(z_e) + U_h(z_h) \\ v &= \varrho ; \quad \hat{H}_{\text{kin } v} = -\frac{1}{2m_\varrho} \frac{1}{\varrho} \frac{\partial}{\partial \varrho} \varrho \frac{\partial}{\partial \varrho} ; \quad V(w, v) = \frac{1}{\sqrt{\varrho^2 + (z_e - z_h)^2}} . \end{aligned} \quad (3.80)$$

According to the classification at the beginning of this section, the dimensionality of the problem is $d = q = 2$; $l = 3$; $m = 1$.

The eigenvalues and normalized eigenfunctions for the bound states of electron and hole in the potentials $U_{e,h}$ follow from the eigenvalue problem

$$\left[-\frac{1}{2m_{e,h_z}} \frac{d^2}{dz^2} + U_{e,h}(z) \right] \varphi_{e,h,n}(z) = E_{e,h,n} \varphi_{e,h,n}(z) . \quad (3.81)$$

The number of bound states for electron and hole is finite. Above the thresholds $H_{e,h}$ the eigenvalues become continuous with a multiplicity of 2 and the dimensionality goes over to $d = q = 3$. We shall consider only the bound states. They have either even or odd parity. The ground state, $n = 1$, has even parity, the first excited state $n = 2$ has odd parity, and so on. The discrete eigenvalues and eigenfunctions of the operator $\hat{H}_w = \hat{H}_{\text{kin } w} + W(w)$ are $E_{en_e} + E_{hn_h}$ and $\varphi_{en_e}(z_e) \varphi_{hn_h}(z_h)$.

If the Coulomb interaction is neglected, then the eigenvalue problem of the Hamiltonian is separable, the eigenvalues and eigenfunctions are $E_{en_e} + E_{hn_h} + k^2/(2m_\varrho)$ and $\varphi_{en_e}(z_e) \varphi_{hn_h}(z_h) J_0(k\varrho)/(2\pi)$ (App. C.1.2), and the optical absorption, which is equal to the optical density of states, is

$$D(\omega) = \sum'_{n_e n_h} \left| \int_{-\infty}^{+\infty} dz \varphi_{en_e}(z) \varphi_{hn_h}(z) \right|^2 \frac{m_\varrho}{2} \Theta(\omega - E_{en_e} - E_{hn_h}) . \quad (3.82)$$

Because the quantum well is symmetric, the oscillator strengths are zero for odd-parity (i.e., forbidden) transitions with $(n_e - n_h) \bmod 2 \neq 0$, and the prime at the sum means that only pairs with even parity, $(n_e - n_h) \bmod 2 = 0$, are taken into account. In contrast to Example B in Sect. 1.2, the eigenfunctions of electron and hole, $\{\varphi_{en_e}\}$ and $\{\varphi_{hn_h}\}$, are different due to the finite barriers and, besides the allowed transitions $n_e = n_h$, weakly allowed transitions with $n_e \neq n_h$ and $(n_e - n_h) \bmod 2 = 0$ contribute to the optical density of states.

In order to numerically calculate the optical susceptibility, including Coulomb interaction, we expand the Coulomb potential $V(\varrho, z_e, z_h)$ into the single-particle eigenfunctions:

$$V_{n_e n_h, n'_e n'_h}(\varrho) = \int_{-\infty}^{+\infty} dz_e \int_{-\infty}^{+\infty} dz_h \frac{\varphi_{en_e}^*(z_e) \varphi_{hn_h}^*(z_h) \varphi_{en'_e}(z_e) \varphi_{hn'_h}(z_h)}{\sqrt{\varrho^2 + (z_e - z_h)^2}} . \quad (3.83)$$

These matrix elements are zero if $(n_e + n_h + n'_e + n'_h) \bmod 2 \neq 0$, which means that even-parity transitions are coupled only to even-parity transitions and odd-parity transitions are coupled only to odd-parity transitions. The non-vanishing matrix elements $V_{n_e n_h, n'_e n'_h}(\varrho)$ have a logarithmic singularity at $\varrho = 0$, in contrast to the previous example; the behavior for $\varrho \rightarrow \infty$ is $V_{n_e n_h, n'_e n'_h}(\varrho) \sim \varrho^{-1}$ for $(n_e, n_h) = (n'_e, n'_h)$ and $V_{n_e n_h, n'_e n'_h}(\varrho) = O(\varrho^{-3})$ otherwise.

The optical susceptibility is given by

$$\chi(\omega) = \sum_A \frac{\left| \sum_{n_e n_h}' \Phi_{A; n_e n_h}(0) \int_{-\infty}^{+\infty} dz \varphi_{e n_e}(z) \varphi_{h n_h}(z) \right|^2}{E_A - (\omega + i\epsilon)}, \quad (3.84)$$

where the Φ_A are the normalized eigenfunctions of the coupled channel equations

$$\begin{aligned} \sum_{n'_e n'_h}' \left[(E_{e n_e} + E_{h n_h}) \delta_{n_e n'_e} \delta_{n_h n'_h} - \frac{1}{2m_\varrho} \frac{1}{\varrho} \frac{d}{d\varrho} \varrho \frac{d}{d\varrho} - V_{n_e n_h, n'_e n'_h}(\varrho) \right] \Phi_{A; n'_e n'_h}(\varrho) \\ = E_A \Phi_{A; n_e n_h}(\varrho). \end{aligned} \quad (3.85)$$

The equation for the odd-parity eigenfunctions $(n_e - n_h) \bmod 2 \neq 0$ has exactly the same appearance as (3.85), but these states do not contribute to the linear (one-photon) absorption.

For the numerical solution, we again rewrite the equations (3.84–3.85) as an initial-value problem. The singular potentials (3.83) are discretized by the ground-state method, as explained in the last subsection. The parameters of the calculation are $m_e = 0.067 m_0$, $m_{hz} = 0.377 m_0$, $m_{h\varrho} = 0.491 m_0$, $m_h = 0.5 m_0$, $d = 20 \text{ nm}$, $E_g = 1.519 \text{ eV}$, $\Delta E_c = 0.3 \times 790 \text{ meV}$, and $-\Delta E_v = 0.3 \times 460 \text{ meV}$, which corresponds to a 200 \AA GaAs/Ga_{0.7}Al_{0.3}As quantum well. The homogeneous broadening is chosen to be $\epsilon = 0.1 \text{ meV}$.

The solutions of the single-particle equations (3.81) give five below-barrier states for the electron and eight below-barrier states for the hole. The electron and hole eigenstates with $n_e \leq 2$ and $n_h \leq 4$ can be considered as strongly confined and the optical spectrum for $\hbar\omega \leq E_g + E_{e2} + E_{h4}$ will resemble the spectrum of an ideal quantum well. In this energy region the expansion (3.85) was found to be fully converged.

The numerical result of (3.84) is shown in Fig. 3.10 for different approximations. The optical absorption $\alpha(\omega) \propto \text{Im } \chi(\omega)$ is shown as function of the photon energy $\hbar\omega$. The lowest spectrum (a) shows the optical absorption in the absence of Coulomb interaction, i.e., when all Coulomb matrix elements $V_{n_e n_h, n'_e n'_h}(\varrho)$ are set to zero. This function is identical to the optical density of states (3.82), when the function $\Theta(\omega)$ is replaced by $\frac{1}{\pi} \arctan \frac{\omega}{\epsilon} + \frac{1}{2}$. The overlap integral between φ_{e1} and φ_{h3} is nonzero, but vanishingly small, so that the (1,3) transition cannot be resolved in the optical density of states.

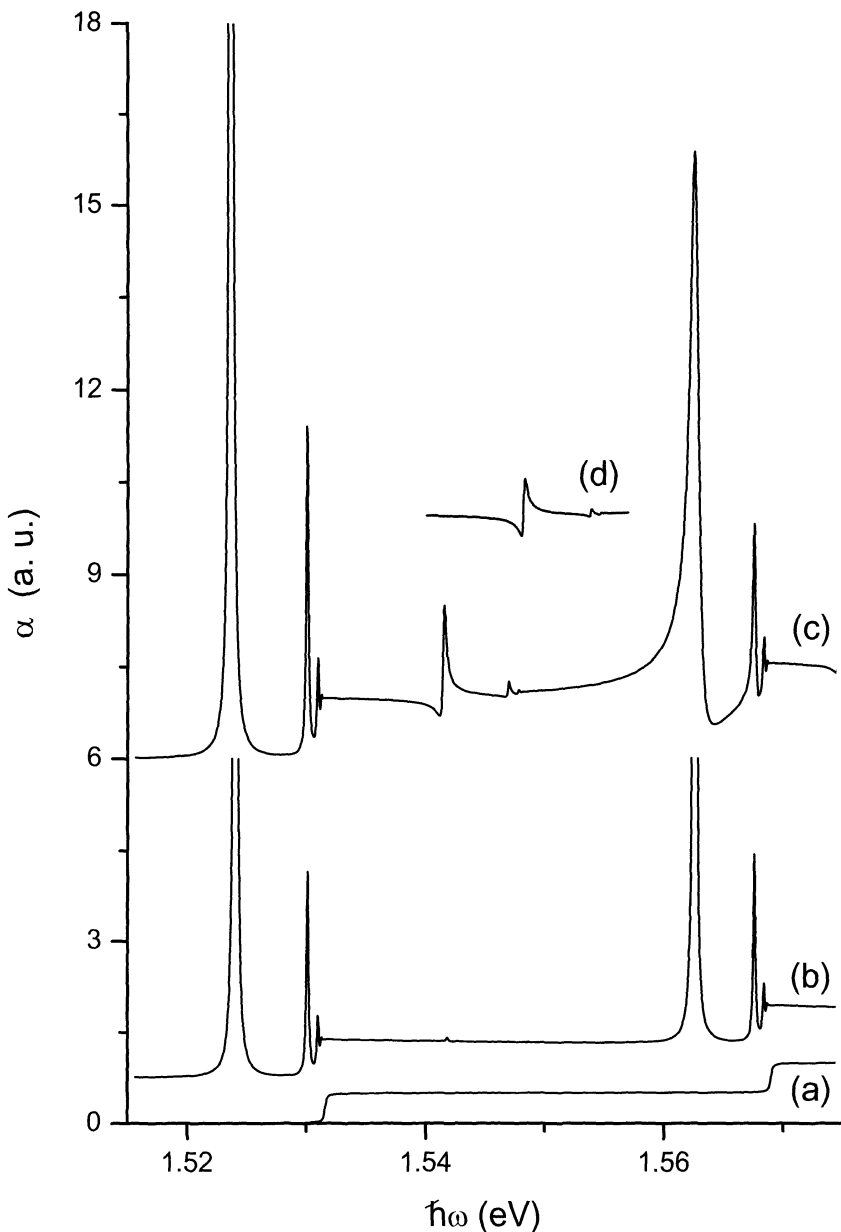


Fig. 3.10. Calculated optical absorption of a 200 Å GaAs/Ga_{0.7}Al_{0.3}As single quantum well in different approximations: a) no Coulomb interaction; b) diagonal Coulomb interaction; c) diagonal and nondiagonal Coulomb interaction; and d) same as (c) for infinite barriers

The middle spectrum (b) is the optical absorption in the diagonal approximation, i.e., $V_{n_e n_h, n'_e n'_h}(\varrho)$ is set to zero for $(n_e, n_h) \neq (n'_e, n'_h)$. We observe two Rydberg series belonging to the (1,1) and (2,2) transitions and flat continua above the thresholds $E_g + E_{e1} + E_{h1}$ and $E_g + E_{e2} + E_{h2}$, respectively. There is a very small peak at about $\hbar\omega = 1.542$ eV, which belongs to the lowest exciton of the (1,3) transition.

The upper spectrum (c) shows the result when all Coulomb matrix elements are taken into account. The Coulomb interaction of the different subbands leads to an increase of the oscillator strengths for all transitions. The excitons of the (2,2) transition are energetically degenerate with the continua of the (1,1) and (1,3) transitions and the discrete lines turn into Fano resonances with negative q -parameter, as observed for the bulk semiconductor in a magnetic field (cf. Fig. 3.6). We also observe a Fano resonance for the 1s exciton of the (1,3) transition, which is degenerate with the continuum of the (1,1) transition. This time the q -parameter is negative and smaller in magnitude than for the (2,2) transition. As the eigenfunctions of the discrete and continuum states, which are involved in the Fano interference, are not known analytically, it is difficult to forecast the values or even the sign of the parameter q . An additional complication is the nonresonant Coulomb interaction (see the discussion of Fig. 3.4 and the remarks below). A crude approximation gives the following rule:

$$q < 0 \text{ for } (n_e - n_h) \bmod 4 = 0 ; \quad q > 0 \text{ for } (n_e - n_h) \bmod 4 = 2 , \quad (3.86)$$

which is consistent with empirical findings on quantum wells and quantum wires [43, 45, 65, 66].

The spectrum (b), where Coulomb interaction between different subband pairs was neglected, shows that the probability for the (1,3) transition is extremely small. This should result in a Fano resonance with very small lineshape parameter q (window resonance). However, the q -parameter in the upper curve (c) is not small at all, giving proof that the oscillator strength of the (1,3) exciton is significant. The reason for this is that Coulomb coupling between allowed and weakly allowed transitions increases the oscillator strength of the weakly allowed transitions (the term G in Eq. 3.15). It is interesting to make a comparison with the spectrum of an ideal quantum well ($\pm \Delta E_{c,v} \rightarrow +\infty$), which is shown as curve (d). We see that the oscillator strength and the lineshape parameters are of the same order of magnitude as for finite barriers, although for infinite barriers the transition matrix element between the single-particle eigenstates is exactly zero. This comparison shows that, contrary to a popular view, weakly allowed transitions are not the result of finite barriers. The enhancement of the weakly allowed transition by the Fano effect was discussed already in an early paper by Masselink et al. [19]. This view was also expressed by Willcox and Whittaker [43]. Chu and Chang found that valence-band mixing increases the oscillator strength of the weakly allowed transitions [38], but in the present example, which is treated in the two-band approximation, this effect plays no role.

In contrast to the bulk semiconductor in a magnetic field, a quantum well is a system of strong confinement and the expansion into subbands rapidly converges. High-resolution spectra have been published more than a decade ago. It was already in 1989 that a Fano resonance has been predicted by Chu and Chang for the (1,3) heavy-hole transition [38]. Calculations by Willcox and Whittaker from 1994 show Fano resonances for all excited subband transitions [43]. The most advanced calculations so far, based upon an 8×8 Hamiltonian, were published by Winkler [44].

Experimental evidence for Fano resonances in quantum wells has been presented by several authors. A spectrum published by Viña et al. in 1990 shows Fano resonances for the (1,3) and (2,2) heavy-hole transitions [37]. In 1994, Oberli et al. observed a Fano lineshape for the (1,3) transition in an asymmetric double quantum well [41]. Shortly afterwards, Simmonds and coworkers identified a Fano resonance at the (1,3) transition in a shallow quantum well [42]. The (2,2) transition also has an asymmetric profile, which was not emphasized by these authors. A detailed analysis of Fano lineshapes in quantum wells was published in 1996 by Bellani et al. [47,48]. The asymmetry and natural line broadening for the (1,1) and (1,3) heavy-hole transitions are also seen in older publications, before Fano resonances were known to be a general property of quantum-well spectra. Examples are found in a series of papers by Miller, Gossard, and coworkers from the eighties [35]. High-resolution spectra by Masselink et al. also show asymmetric broadenings for several transitions.

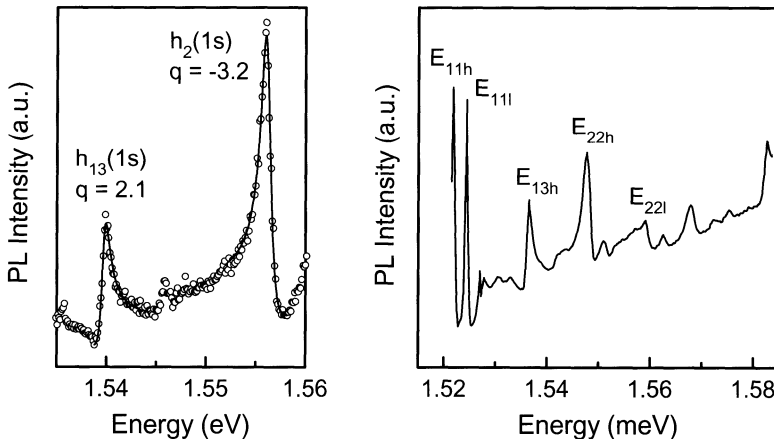


Fig. 3.11. Experimental results on Fano resonances in quantum wells. Left: Bellani et al. 1996 [48]. Right: Simmonds et al. 1994 [42]. Used by permission

Figure 3.11 shows experimental quantum-well spectra published by Bellani et al. [48] and by Simmonds et al. [42]. Bellani used a 200 Å wide

GaAs/Ga_{0.7}Al_{0.3}As quantum well. The sample and material parameters are the same as in our numerical calculation. The PLE spectrum qualitatively agrees with the above numerical result with respect to the arrangement of the peaks, the natural linewidths, and the q -parameters. The position of the (2,2) exciton resonance in the experiment appears about 4 meV below the theoretical value. This is likely an effect of the conduction-band nonparabolicity, which is not considered in our model. The same features are seen in Simmonds' data from a 200 Å GaAs/(Ga,Al)As quantum well with 4.5 % Al. The well thickness is the same as in Bellani's experiment, but the transitions are red-shifted because of the thinner and shallower barriers. Otherwise, we observe exactly the same constellation: the weakly allowed (1,3) with a small positive q is followed by the allowed (2,2) transition with a large negative q .

3.4 Summary and Conclusions

We have seen that Fano interference is a general phenomenon in the optical absorption of low-dimensional semiconductors. The origin of Fano interference is the Coulomb coupling between bound excitons of higher subbands (Landau levels, Wannier–Stark levels, minibands) and continuum states of lower subbands. For most structures, the Fano interference can be explained in the channel picture, where the motion of an electron–hole pair is asymptotically free in some directions and bound in other directions. The subband picture is more general than the channel picture and can also explain Fano interference in periodic structures.

For Fano interference, the dimension which is relevant for the optical density of states is typically $q = 1$ or $q = 2$. In some cases, like superlattices, the dimension is $d = 3$. For zero-dimensional ($d = 0$) systems, Fano interference is impossible, because the spectrum is entirely discrete. The mathematical dimensions of the partial differential equations have to be $l \geq m + 1$ and $m \geq 1$, i.e., there has to be at least one direction of bound motion and the continuum has to be at least one-parametric. The simplest example is the bulk semiconductor in a magnetic field ($l = 2, m = 1$), where the excitons of higher Landau levels are degenerate with the continuum of lower Landau levels and quantum-mechanical coupling takes place on the account of Coulomb interaction. Furthermore, Fano interference is typical for superlattices, quantum wells, and quantum wires.

In order to theoretically predict Fano resonances, it is essential to perform accurate numerical calculations, which take into account continuum states. Systems with Fano interference lead to class-II or class-III problems (see Chap. 2). Class-II problems can be treated by Lanczos recursion, the solution of a boundary-value problem, or reformulation as a scattering problem and Fano lineshapes have been calculated by all of these methods. Today, the general class-III problem can be dealt with as initial-value problem. Except

for some band-structure details, we are able to calculate the optical spectrum for almost all low-dimensional systems.

The quantum confinement, necessary for Fano interference, can result from the geometric structure, external fields, or both. A major advantage of external fields is that they do not possess any roughness on a microscopic scale so that the inhomogeneous broadening can be significantly smaller than in samples with geometric confinement. For this reason, the most beautiful Fano resonances have been observed in bulk semiconductors in a magnetic field, already in the 80s. For superlattices and quantum wells, the quality of structures has significantly improved in the last decade, and Fano resonances are commonly observed in these structures (see Table 3.1).

Although a pronounced Fano effect is also predicted for quantum-wire arrays and single quantum wires, the experimental observation should be difficult because of the large fluctuations of the wire width. More recent experimental developments are nonlinear spectroscopy on Fano resonances [29, 51, 108, 109], quantum confined Fano interference, where the Fano resonances are discretized due to additional geometric quantization [62], and tunable Fano resonances [29].

4 Zener Breakdown in Superlattices

The motion of a one-dimensional Bloch electron with mass m and charge $-e$ in an external field F is governed by the Hamiltonian

$$\hat{H} = -\frac{\hbar^2}{2m} \frac{d^2}{dz^2} + U(z) + eFz ; \quad U(z+a) = U(z) . \quad (4.1)$$

The eigenvalue problem of \hat{H} , known as the Wannier–Stark problem, has drawn the attention of generations of physicists.

The effective-mass theory, which began to develop in the twenties and thirties of the last century, treats crystal electrons like real electrons with an effective mass, different from the free-electron mass [1, 2]. In the effective-mass approximation, the spectrum of a Bloch electron in a constant electric field is entirely continuous. The oscillatory behavior of the electron and hole eigenfunctions in real space is manifested as oscillations in the absorption spectrum, known as Franz–Keldysh oscillations [3–5].¹

In a pioneering work from 1934, Zener studied tunneling between energy bands due to an electric field [6]. This work very successfully described the electric breakdown in semiconductors by means of semiclassical tunneling theory, using a heuristic “tilted-band picture.” Following a paper by Houston from 1940 [7], numerous activities in the fifties and sixties were devoted to a rigorous quantum-mechanical description of Bloch electrons in electric fields in the context of Zener tunneling [8–14]. The Houston functions as approximate solutions of the time-dependent Schrödinger equation describe a Bloch electron with time-dependent wavenumber $k(t) = k(0) - eFt/\hbar$, which oscillates in time with period $T_{BO} = 2\pi\hbar/|eFa|$, because the points k and $k + \frac{2\pi}{a}$ in reciprocal space are equivalent. In the crystal-momentum approximation, the approximate solutions of the time-independent Schrödinger equation are given by Kane functions and the spectrum of the operator consists of ladders of equally spaced eigenvalues $E_{jl} = E_{j0} + eFal$, known as Wannier–Stark ladders. It can be shown that the Houston functions and the crystal-momentum representation are equivalent [5, 15, 16].

A problem of the theory is that the operator eFz is not a small perturbation. The coupling of different bands by the electric field is responsible for the Zener tunneling, but its influence on the structure of the spectrum

¹ See also the discussion of Figs. 1.4 and 2.11.

remained unclear for a long time. At first sight, it seems plausible that the coupling of different bands leads to small quantitative changes of the energy levels, but the spectrum is still given by discrete Wannier–Stark levels. On the other hand, common wisdom tells us that a potential of the form $U(z) + eFz$ should not support bound states because the motion in the $-F$ direction is asymptotically unbound, a point which was already stressed in Wannier’s original work [13].

The usual way of answering such questions is to look for limiting cases and exactly solvable models. For a single quantum well with finite barriers in a perpendicular electric field, it can easily be seen that the spectrum is continuous, which is observed experimentally in the quantum-confined Stark effect [17]. It is unlikely to happen that in case of a multiple quantum well the spectrum turns into a discrete one. In the case of exactly solvable models, the results are conflicting. The discrete model [8, 18–22], which is closely related to the tight-binding approximation, leads to discrete Wannier–Stark ladders. An exactly solvable problem was presented which leads to a continuous spectrum [23], but the periodic potential employed was nonlocal, i.e., an integral operator, and it is not clear if this result can be generalized. No exact solutions are available for any realistic potential $U(z)$.

In the late sixties, the nature of the Wannier–Stark spectrum became a main focus of the theory. Wannier–Stark ladders and Bloch oscillations were challenged in a series of papers by Zak and Rabinovitch, pointing out inconsistencies in previous proofs [24–26]. The continuous nature of the spectrum was rigorously established in 1977 by Avron et al. [27] and in 1983 by Bentosela et al. under weaker assumptions for the potential [28]. The proofs are based upon functional-analytical methods and do not cover discontinuous potentials. A mathematically less rigorous treatment by Ao suggests that the spectrum is continuous if the gaps algebraically approach zero, which should be the case for all realistic potentials [29]. The Wannier–Stark controversy resurfaced again in the late eighties, when Emin and Hart proposed a decomposition of the potential such that the Kane functions would become the exact eigenfunctions [30].

Despite the fact that the spectrum of the Wannier–Stark Hamiltonian is entirely continuous, Wannier–Stark ladders are not ruled out. They live on as resonances, i.e., quasi-bound states with a long lifetime [31].² In the mathematical theory, resonances are defined as complex eigenvalues of an analytical continuation of \hat{H} , which correspond to complex poles of the resolvent [32–36]. The imaginary part, which is given by Fermi’s golden rule for constant perturbations [32, 37], governs the decay of wavepackets [38]. It is exponentially small with field [34, 35] and equals the Zener tunneling rate [39]. Thus for sufficiently small field, the width of the resonances is much smaller than the ladder spacing. Krieger and Iafrate estimated the Zener tunneling

² Other examples of resonances are the Stark effect of the exciton (Chap. 2) and Fano resonances (Chap. 3).

time from the valence to the conduction band of bulk GaAs at 100 kV/cm to be in the order of one year [16]. However, Zener tunneling is not the only decay mechanism and there has never been convincing experimental evidence for Wannier–Stark ladders or Bloch oscillations in natural crystals.

The situation changed after Esaki and Tsu invented the semiconductor superlattice, a prototype of an artificial crystal [40]. Here, the periodic potential is realized by periodic modulation of the band edges. In superlattices, the situation is much more favorable for Wannier–Stark ladders and Bloch oscillations than in natural crystals because of the larger lattice constant and the smaller miniband width. Optical experiments in the interband region are performed at low, ideally zero, electron–hole-pair density and the lifetime of quasiparticles is by orders of magnitude larger than for strongly correlated systems. Furthermore, the parameters of the potentials can be controlled by varying the layer thickness and the composition.

Numerous experimental and theoretical studies on superlattices have been performed in the last thirty years; here we concentrate on those works which are related to Wannier–Stark ladders, Bloch oscillations, and Zener tunneling. In the late eighties, Wannier–Stark ladders have been observed in photoluminescence, photocurrent, and electoreflection spectroscopy on superlattices [41–44]. At a closer look, the optical spectra show Franz–Keldysh oscillations [45] and Fano resonances [46]. The time-dependent pendant of Wannier–Stark ladders, Bloch oscillations, have been detected by various techniques of nonlinear optical spectroscopy [47–52]. These experiments have been explained theoretically in the picture of discrete Wannier–Stark ladders and closed minibands [45, 53–60] and the generally accepted view for at least one decade was that an electric field \mathbf{F} , applied parallel to the growth axis of a superlattice, leads to a two-dimensional quantization of the carriers; in the presence of a magnetic field $\mathbf{B} \parallel \mathbf{F}$, the spectrum should change from one- to zero-dimensional due to the influence of the electric field [61].

Little work has been done so far to study Zener tunneling in superlattices. This possibility was predicted already in 1989 by Leo and MacKinnon on the basis of a two-band model [62]. In contrast, a numerical study by Bouchard and Luban suggests that Zener tunneling is very small for a realistic superlattice and cannot hinder Bloch oscillations [63, 64], which is in line with experimental results by Dekorsy et al. [50]. Interaction of a finite number of Wannier–Stark ladders, which can be viewed as a precursor of Zener tunneling, has been studied experimentally by Schneider et al. [43] and by Till et al. [65]. Zener tunneling from the valence to the conduction band of a p-i-n diode with superlattice intrinsic layer was studied by Murayama et al. [66]. They found a the current-voltage characteristics showing Wannier–Stark resonances. In 1998, Sibille and coworkers discovered resonances in the interminiband transport, which they called “resonant Zener breakdown” [67]. Tunneling between Wannier–Stark ladders and continuum states in transport and infrared absorption experiments was observed in 1999 by Helm et al. [68].

In the same year, a Zener breakdown was predicted for the optical absorption of superlattices by the present author [69] and the experimental evidence was presented shortly afterwards by Rosam et al. [70–72]. The evolution of the linewidth with field follows Zener's formula, but there are also pronounced resonances from interaction of Wannier–Stark ladders [72]. An additional magnetic field perpendicular to the layers leads to Landau quantization of the in-plane motion and gives direct experimental evidence of the continuous spectrum [73].

Besides semiconductor superlattices, other types of artificial crystals have been studied in recent years. Periodic potentials can be created by standing waves of counterpropagating laser beams and an additional linear potential is mimicked by a frequency detuning increasing linearly with time. In 1996–1997, Bloch oscillations, Wannier–Stark ladders, and Zener tunneling have been observed on cold atoms in accelerating optical potentials [74, 75]. An optical analog is a periodic waveguide array with linear variation of the propagation constant where optical Bloch oscillations were predicted in 1998 [76] and measured in 1999 [77, 78].

Much progress has been reported in the last decade in the field of numerical simulations. Examples are the numerical simulation of transport in mesoscopic devices modeled by multichannel scattering theory [79], the calculation of Bloch oscillations and Zener tunneling in real time [63, 64, 80], the calculation of the optical absorption of superlattices with no restriction in the number of minibands [69, 72], and the numerical calculation of Wannier–Stark resonances by Floquet theory [81].

In this chapter, we study the Zener effect in the optical absorption of superlattices. We demonstrate that the nature of the Wannier–Stark spectrum, which is of fundamental theoretical interest, is also highly relevant for optical experiments on superlattices. The simple picture of Wannier–Stark ladders becomes invalid already at moderate fields and the optical spectrum shows a number of new features. At high but attainable fields, the Wannier–Stark ladders break down completely and the spectrum becomes entirely continuous, giving clear evidence that a superlattice in a perpendicular electric field is a three-dimensional semiconductor. Finally, we compare the line broadening observed in the experiment with the result of the Zener theory.

This chapter is organized as follows. In Sect. 4.1, we summarize important properties of the Bloch electron in one dimension. We also introduce the approximations of tightly bound and nearly free electrons. In Sect. 4.2, we review the most important approximations for the Bloch electron in an electric field: the discrete model, which is closely related to the tight-binding approximation, and the Kane functions. In order to demonstrate the breakdown of Wannier–Stark ladders, we also make a comparison with a full numerical calculation. In Sect. 4.3, we numerically calculate the optical density of states and the optical absorption, including Coulomb interaction. A comparison is made with the approximation by discrete Wannier–Stark ladders and with

experimental spectra. Finally, in Sect. 4.4, we derive a formula for the tunneling rate, which includes both resonant and nonresonant tunneling, and make a comparison with the linewidth measured in the experiment. We also point out inconsistencies in previous theories. A summary is given in Sect. 4.5.

There is no book or article which would cover the topic of this chapter. There are some publications with review character which are helpful for an introduction into Wannier–Stark ladders, Bloch oscillations, Zener tunneling, and the Wannier–Stark controversy. We recommend the papers by Krieger and Iafrate [16], Nenciu [82], Di Carlo et al. [79], Bouchard and Luban [64], and a book chapter by Döhler [83]. Where it is appropriate, we give recommendations for further reading at the beginning of each section.

4.1 Bloch Electron in One Dimension

Because the Wannier–Stark problem (4.1) has no analytical solutions for physically relevant cases, it is quite natural to split it up into an unperturbed problem of an electron in a periodic potential and a perturbation eFz . For the unperturbed problem we know several exact or approximate solutions, the numerical solution is fairly easy, and some analytical properties can be deduced from the differential equation. The one-dimensionality significantly reduces the complexity, both analytically and numerically, because the eigenvalue problem is an ordinary differential equation and there are only two possible directions of the electric field: the positive and the negative z axis. In this section we summarize some general properties for the one-dimensional Bloch electron, introduce important notations and conventions, and explain the most common approximations, the nearly free and the tightly bound electron.

There is plenty of literature on the Bloch electron. In their famous article from 1931, Kronig and Penney calculate the band structure of an electron in a periodic delta potential [84]. The Kronig–Penney model is discussed in many textbooks, but the more general case of a rectangular potential can also be found in the literature [37, 85, 86].³ A review by Sommerfeld and Bethe from 1933 discusses various aspects of electrons in periodic potentials, including general properties of the solution in three dimensions, effective-mass theory, the Kronig–Penney model, and the approximations of nearly free and tightly bound electrons [2]. Analytic properties of wavefunctions and energies for the one-dimensional Bloch electrons are discussed in articles by James [87] and Kohn [88] and, from a mathematical perspective, in the textbook by Reed and Simon [32]. A reprint collection of solvable one-dimensional problems with introduction and bibliography has been published by Lieb and Mattis [89].

³ Kronig and Penney [84] start with a rectangular potential, but derive explicit solutions only in the limiting case of delta barriers. Following a convention in the literature, the term “Kronig–Penney model” is used only for the periodic delta potential.

4.1.1 General Properties

The eigenvalue problem for a one-dimensional Bloch electron is

$$\left[-\frac{\hbar^2}{2m} \frac{d^2}{dz^2} + U(z) \right] \psi_{jk}(z) = E_j(k) \psi_{jk}(z); \quad U(z+a) + U(z). \quad (4.2)$$

and the eigenfunctions are Bloch functions

$$\begin{aligned} \psi_{jk}(z) &= \frac{1}{\sqrt{2\pi}} e^{ikz} u_{jk}(z); \quad u_{jk}(z) = u_{jk}(z-a) \\ j \in \mathbb{N}; \quad k \in (-\frac{\pi}{a}, +\frac{\pi}{a}) \end{aligned} \quad (4.3)$$

Inserting the Bloch functions (4.3) into (4.2) yields the eigenvalue problem for the lattice-periodic functions:

$$\left[-\frac{\hbar^2}{2m} \frac{d^2}{dz^2} + \frac{\hbar k}{2im} \frac{d}{dz} + \frac{\hbar^2 k^2}{2m} + U(z) \right] u_{jk}(z) = E_j(k) u_{jk}(z). \quad (4.4)$$

Because of the periodic boundary conditions, the spectrum of the reduced Hamiltonian for a fixed k is purely discrete. The latter equation is perfectly suitable for the numerical calculation of the energy bands and Bloch functions. We assume normalization of the lattice-periodic functions according to

$$(u_{jk} | u_{j'k'}) = \frac{1}{a} \int_{-\frac{\pi}{a}}^{+\frac{\pi}{a}} u_{jk}^*(z) u_{j'k'}(z) = \delta_{jj'} \cdot \quad (4.5)$$

Then the orthonormality and closure relations for the Bloch functions read

$$\int_{-\infty}^{+\infty} dz \varphi_{jk}^*(z) \varphi_{j'k'}(z) = \delta_{jj'} \delta(k - k'); \quad k, k' \in (-\frac{\pi}{a}, +\frac{\pi}{a}), \quad (4.6)$$

and

$$\sum_{j=1}^{\infty} \int_{-\frac{\pi}{a}}^{+\frac{\pi}{a}} dk \psi_{jk}(z) \psi_{jk}^*(z') = \delta(z - z'). \quad (4.7)$$

We briefly summarize important analytical properties of the solutions in case that U is piecewise continuous[32]. The spectrum is purely continuous with spectral gaps, more strictly, it holds that $E_{j \min} \leq E_j(k) \leq E_{j \max}$ and $E_{1 \min} < E_{1 \max} \leq E_{2 \min} < E_{2 \max} \leq \dots$. The energy bands $E_j(k)$ are symmetric around $k = 0$ and real analytic monotonous functions for $k \in (-\frac{\pi}{a}, 0)$ and $k \in (0, +\frac{\pi}{a})$. Thus in the one-dimensional case there is no band overlap, and band degeneracy is possible only at the symmetric points $k = 0$ and $k = \pm \frac{\pi}{a}$ if the gap is closed. The following statements

about the number of gaps have shown to be true. If no gaps are present, then $U(z) = \text{const}$. If the number of gaps is finite, then U is real analytic. The usual case is that all gaps are open.⁴ We shall assume the “usual case.” Then the bands $E_j(k)$ are analytic functions for $k \in (-\infty, +\infty)$ and it holds that $E_j(k + \frac{2\pi}{a}) = E_j(k)$ for all $k \in \mathbb{R}$. Therefore, it is common to replace the Brillouin zone $(-\frac{\pi}{a}, +\frac{\pi}{a}]$ by the “periodic interval” $[-\frac{\pi}{a}, +\frac{\pi}{a}[$, consisting of the open interval $(-\frac{\pi}{a}, +\frac{\pi}{a})$ and the common endpoint $\pm\frac{\pi}{a}$. Then, E_j with the above properties is said to be analytic on $[-\frac{\pi}{a}, +\frac{\pi}{a}[$. The definition of continuity, differentiability, etc., on periodic intervals is straightforward.

One may now wish to construct Bloch functions $\psi_{jk}(z)$ which are analytic with respect to k in $[-\frac{\pi}{a}, +\frac{\pi}{a}[$, i.e., analytic for $k \in (-\infty, +\infty)$ and periodic in k with period $\frac{2\pi}{a}$. We shall give a recipe for the important case that the potential is symmetric, i.e., $U(+z) = U(-z)$, which was studied in the original paper by Kohn [88]. To enforce analyticity in $[-\frac{\pi}{a}, +\frac{\pi}{a}]$, we determine lattice-periodic functions such that $\text{Re } u_{jk}$ and $\text{Im } u_{jk}$ have opposite parity and $u_{j,+k}(z) = u_{j,-k}^*(z)$. This limits the degrees of freedom to a factor ± 1 for each k , which is chosen such that $u_{jk}(z)$ is continuous in k . The Bloch functions fulfill $\psi_{j,+k}(z) = \psi_{j,-k}^*(z)$ and have the same properties as the u_{jk} regarding analyticity and parity. From $\psi_{j,+ \pi/a}(z) \simeq \psi_{j,- \pi/a}(z)$ it follows that $\psi_{j,\pm \pi/a}$ has a definite parity and that either $\psi_{j,+ \pi/a}(z) = \psi_{j,- \pi/a}(z) \in \mathbb{R}$ (Kohn’s case A) or $\psi_{j,+ \pi/a}(z) = -\psi_{j,- \pi/a}(z) \in i\mathbb{R}$ (Kohn’s case B). In the first case, $\psi_{jk}(z)$ is analytic in $[-\frac{\pi}{a}, +\frac{\pi}{a}[$. In the second case, we need to multiply the Bloch functions by a factor $e^{\pm ika/2}$. Alternatively, the second case can be reduced to the first one by shifting the origin of the z axis from 0 to $\pm\frac{a}{2}$. However, in the general case, it is not possible that all bands belong to case A. We shall always choose the origin such that the lowest miniband belongs to case A. For these special Bloch functions, we can extend the variables k, k' in (4.6) to the whole real axis. Then $\delta(k - k')$ is replaced by the periodic delta function $\underline{\delta}(k - k')$ (Table A.3) which is equivalent to the delta function on the periodic interval $[-\frac{\pi}{a}, +\frac{\pi}{a}[$.

4.1.2 Tightly Bound and Nearly Free Electrons

The approximation of tightly bound electrons starts from the eigenfunctions of the individual atoms and assumes weak coupling so that only interaction with a finite number of neighbors, usually the next neighbors, is taken into account. Here, we shall adopt this method for a superlattice to approximately solve the eigenvalue problem (4.2). Then the individual quantum wells play the role of atoms.

In a first step, we perform a decomposition of the lattice-periodic potential according to

⁴ This statement is a free transcription from [32].

$$U(z) = \sum_{n=-\infty}^{+\infty} [U_0(z-an) - h] + h, \quad (4.8)$$

where $U^{(0)}(z)$ is the potential of a single quantum well with barrier height h (right part of Fig. 4.1). Let $E^{(0)}$ and $w^{(0)}$ be the ground-state energy and normalized wavefunction of the single quantum well. Then for the eigenfunctions (4.2) we make the ansatz

$$\psi(z) = \sum_{n=-\infty}^{+\infty} \Psi_n w^{(0)}(z - an). \quad (4.9)$$

We assume that $w^{(0)}$ is symmetric, real, and strongly localized inside the well so that only coupling of next neighbors needs to be considered. Then, for the expansion coefficients Ψ_n we obtain the generalized eigenvalue problem:

$$A\Psi_n - (B - E^{(0)}S)(\Psi_{n+1} + \Psi_{n-1}) = E\Psi_n + ES(\Psi_{n+1} + \Psi_{n-1}), \quad (4.10)$$

where

$$\begin{aligned} A &= E^{(0)} + \int_{-\infty}^{+\infty} dz w^{(0)}(z) [U(z) - U^{(0)}(z)] w^{(0)}(z) \\ B &= - \int_{-\infty}^{+\infty} dz w^{(0)}(z) [U(z) - U^{(0)}(z)] w^{(0)}(z-a) \\ S &= \int_{-\infty}^{+\infty} dz w^{(0)}(z) w^{(0)}(z-a). \end{aligned} \quad (4.11)$$

The solutions of (4.10) are of the form $\Psi_n \propto e^{iqn}$; $q \in (-\pi, +\pi]$ and for the dispersion we obtain

$$\begin{aligned} E(q) &= \frac{A - 2(B - E^{(0)}S) \cos q}{1 + 2S \cos q} \\ &= A - 2B \cos q - 2(A - E^{(0)})S + O(S^2). \end{aligned} \quad (4.12)$$

As $(A - E^{(0)})S$ is a product of two small quantities, the eigenvalues first-order in the perturbation do not depend on S . However, this does not mean that S itself is negligible; instead, because $E \approx E^{(0)}$, the errors on the l.h.s. and r.h.s. of (4.10) approximately cancel each other. As result, the approximate eigenvalues and eigenfunctions of (4.2) are

$$E(k) = A - 2B \cos(ka)$$

$$\begin{aligned}\psi_k(z) &= \sqrt{\frac{a}{2\pi}} \sum_{n=-\infty}^{+\infty} e^{ikan} w^{(0)}(z-an) = \frac{1}{\sqrt{2\pi}} e^{ikz} u_k(z) \\ u_k(z) &= \sqrt{a} \sum_{n=-\infty}^{+\infty} e^{-ik(z-an)} w^{(0)}(z-an),\end{aligned}\quad (4.13)$$

where $k = q/a$ is the Bloch wavenumber. The tight-binding Bloch functions are analytic on $[-\frac{\pi}{a}, +\frac{\pi}{a}]$ and orthonormality (4.6) is fulfilled up to a factor $1 + 2S \cos(ka)$, which is usually ignored.

So far, we applied the tight-binding approximation only for the ground state of the quantum well. In principle, it can be applied for all below-barrier states, and every below-barrier state of the quantum well gives rise to one miniband. However, the tight-binding approximation will become increasingly inaccurate when the eigenvalues approach the barrier energy and will even fail for above-barrier states, because the single-well eigenfunctions are not normalizable.

In some sense, the approximation of nearly free electrons is the exact opposite of the tight-binding approximation. Here, the operator of the kinetic energy is the unperturbed Hamiltonian and the lattice-periodic potential U is considered a small perturbation. For this reason, we write the k -dependent Hamiltonian (4.4), which acts in the Hilbert space of the lattice-periodic functions, in the form

$$\begin{aligned}\hat{H}(k) &= \hat{H}^{(0)}(k) + \hat{H}^{(i)} \\ \hat{H}^{(0)}(k) &= \frac{1}{2m} \left(\frac{\hbar}{i} \frac{d}{dz} + ik \right)^2; \quad \hat{H}^{(i)} = U(z).\end{aligned}\quad (4.14)$$

The eigenvalues and eigenfunctions of $\hat{H}^{(0)}(k)$, which obey the periodicity condition, are

$$\begin{aligned}E_K^{(0)}(k) &= \frac{\hbar^2 |k+K|^2}{2m}; \quad u_K^{(0)}(z) = e^{iKz} \\ K &\in \frac{2\pi}{a} \mathbb{Z}; \quad k \in (-\frac{\pi}{a}, +\frac{\pi}{a}).\end{aligned}\quad (4.15)$$

The variable K is a member of the reciprocal lattice and plays the role of a band index. The eigenfunctions $u_K^{(0)}(z)$ do not depend on the variable k . They are orthonormal with respect to the scalar product (4.5). Obviously, (4.15) is nothing but the solution for the free electron (C.16), written in Blochian form. The functions $E_K^{(0)}(k)$ are called the “empty-lattice bands.”

In order to apply perturbation theory, we need the matrix elements of the perturbation with respect to the unperturbed lattice-periodic functions:

$$(u_K | \hat{H}^{(i)} | u_{K'}) = \frac{1}{a} \int_{-\frac{a}{2}}^{+\frac{a}{2}} dz e^{-i(K-K')z} U(z) = \tilde{U}_{K-K'} = \tilde{U}_{K'-K}^*. \quad (4.16)$$

They are independent of the parameter k , and are identical to the Fourier coefficients of the lattice-periodic potential. We assume that $U(z)$ is symmetric. Then all Fourier coefficients are real. We shall also assume that they are all different from zero.

First-order nondegenerate perturbation theory leads to a rigid shift of all empty-lattice bands by the diagonal matrix element $(u_K | \hat{H}^{(i)} | u_K) \equiv \tilde{U}_0$, which is equal to the spatial average over the periodic potential. However, in the case that the empty-lattice bands are degenerate, which takes place at the symmetric points $k_0 = 0$ and $k_0 = \pm \frac{\pi}{a}$, one has to apply degenerate perturbation theory (App. C.3). We consider the crossing point of two empty-lattice bands $E_K^{(0)}(k_0) = E_{K'}^{(0)}(k_0); K \neq K'$. Then the secular equation,

$$\begin{vmatrix} E_K^{(0)}(k_0) + \tilde{U}_0 - E(k) & \tilde{U}_{K-K'} \\ \tilde{U}_{K'-K} & E_{K'}^{(0)}(k_0) + \tilde{U}_0 - E(k) \end{vmatrix} = 0, \quad (4.17)$$

gives the approximate band dispersions in the neighborhood of k_0 :

$$\begin{aligned} E^{(\pm)}(k) &= \tilde{U}_0 + \frac{1}{2} [E_K^{(0)}(k) + E_{K'}^{(0)}(k)] \\ &\pm \frac{1}{2} \sqrt{[E_K^{(0)}(k) - E_{K'}^{(0)}(k)]^2 + 4|\tilde{U}_{K-K'}|^2}. \end{aligned} \quad (4.18)$$

Thus the periodic potential leads to a removal of the band degeneracy and a gap of approximately $\Delta E = 2|\tilde{U}_{K-K'}|$. This is also the asymptotic behavior of the gaps for a large class of potentials, including the periodic delta potential [85].

4.1.3 Two Samples

As example, we consider the electron minibands of a superlattice. We shall perform a numerical solution of the eigenvalue problem (4.4) and also make a comparison with the approximations of tightly bound and nearly free electrons.

We consider an infinite superlattice, where the active layers of thickness d are separated by barriers of thickness b . The electron confinement is modeled by a rectangular potential with barrier height h , which is equal to the difference of the band edges between barriers and active layers. A sketch of the periodic potential $U(z)$ is shown on the left side of Fig. 4.1. The single-well potential $U^{(0)}$, which is the starting point of the tight-binding approximation, is shown on the right side of Fig. 4.1. Both potentials are chosen to be

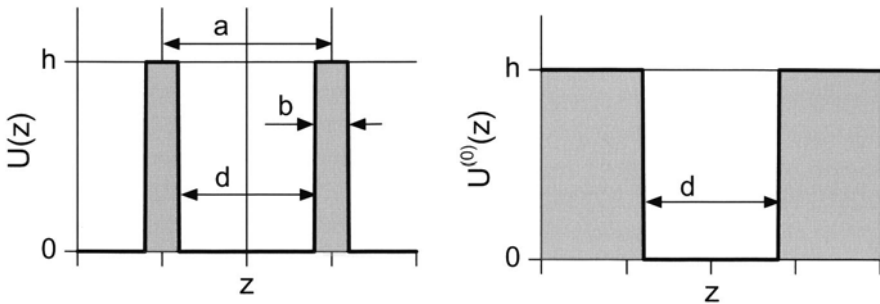


Fig. 4.1. Sketch of the electron confinement potential. Left: Superlattice potential $U(z)$. Right: Single-well potential $U^{(0)}(z)$

symmetric around $z = 0$ in order to employ the symmetry properties of the eigenfunctions.

We shall study two strongly coupled superlattices, a 111/17 Å wide GaAs/Ga_{0.7}Al_{0.3}As superlattice and a 76/39 Å GaAs/Ga_{0.92}Al_{0.08}As superlattice, henceforth to be called Sample 1 and Sample 2, respectively. The parameters for the potential $U(z)$ (Fig. 4.1) are summarized in Table 4.1. The superlattice period is about the same for both samples. In Sample 1, the Al content in the barriers is relatively large, but the barrier width is very small. In Sample 2, the Al content is much smaller, but the barrier width is larger than in Sample 1. Such superlattices are called shallow superlattices. For the effective masses and the dielectric constant, which will be used in the calculation of the optical absorption, we use the parameters of the well material GaAs throughout: $m_e = 0.067 m_0$, $m_{hz} = 0.377 m_0$, $m_{h\parallel} = 0.491 m_0$, and $\epsilon = 13.1$ (App. B.1). This approximation may cause minor quantitative changes but will not change the results qualitatively. For the Wannier–Stark problem, the hole is uninteresting, because the lowest hole minibands are nearly dispersionless and can always be described in the strong-confinement limit.

Table 4.1. Effective-mass parameters for Samples 1 and 2.

Parameter	Sample 1	Sample 2
d	11.1 nm	7.6 nm
b	1.7 nm	3.9 nm
$a = d + b$	12.8 nm	11.5 nm
x_{Al}	30%	8%
$h_e = +\Delta E_c$	237 meV	63.2 meV
$h_h = -\Delta E_v$	138 meV	36.8 meV

We numerically solved the eigenvalue problem for the lattice-periodic functions (4.4), where m was identified with the effective mass m_e and the potential $U(z)$ is the same as shown in Fig. 4.1 with the parameters from Table 4.1 and $h = h_e$. As base functions, we used N quadratic B-splines with periodic boundary conditions, where N was 256 for Sample 1 and 230 for Sample 2.

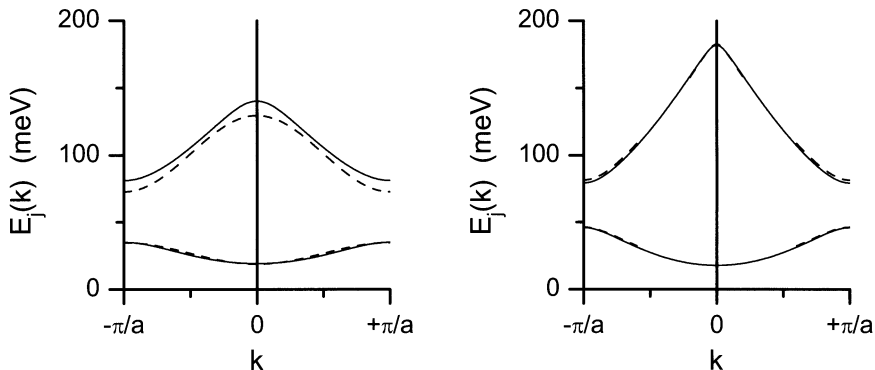


Fig. 4.2. Left: First two electron minibands for Sample 1 (*solid line*) and comparison with the tight-binding approximation (*dashed line*). Right: First two electron minibands for Sample 2 (*solid line*) and comparison with the approximation of nearly free electrons (*dashed line*)

The first two electron minibands are shown in Fig. 4.2 for Sample 1 (left) and Sample 2 (right). The numerical results are compared with the tight-binding approximation for Sample 1 and the approximation of nearly free electrons for Sample 2. The exact dispersions $E_j(k)$ (*solid line*) are analytic functions and symmetric around $k = 0$ and $k = \pm \frac{\pi}{a}$. In the case of Sample 1, there are two minibands below the barriers $h_e = 237$ meV. For the lowest miniband ($j = 1$), the tight-binding approximation (*dashed line*) is very accurate. Thus the first miniband can be described in the tight-binding approximation. This approximation is not as good for the first excited miniband ($j = 2$), but gives still meaningful quantitative results. For Sample 2, only one miniband is below the barriers $h = 63.2$ meV. This time, the approximation of nearly free electrons (*dashed line*) is accurate already for the first miniband and, starting with the top of the second miniband, is virtually undistinguishable from the exact solution. Consequently, Sample 2 is close to the limit of nearly free electrons.

For the Bloch functions, we used the phase convention introduced on p. 151, where $\psi_{j,-k}(z) = \psi_{j,+k}^*(z)$, and $\text{Re } \psi_{jk}(z)$ and $\text{Im } \psi_{jk}(z)$ are of opposite parity. The results are shown in Fig. 4.3 for Sample 1 (left) and Sample 2 (right). The parameter of the curve is the Bloch wavenumber, which varies

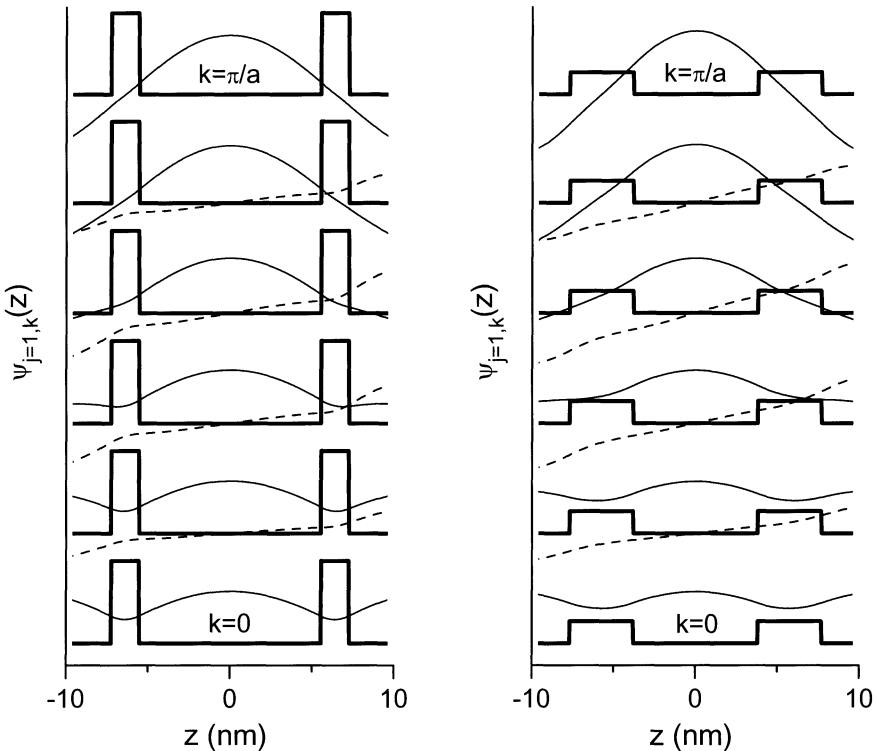


Fig. 4.3. Real (*solid line*) and imaginary part (*dashed line*) of the Bloch functions $\psi_{jk}(z)$ vs. z for Sample 1 (left) and Sample 2 (right) and different parameters $k = 0, 0.2\pi/a, 0.4\pi/a, 0.6\pi/a, 0.8\pi/a$, and π/a . The potential $U(z)$ is shown as *thick solid line*

between $k = 0$ and $k = \frac{\pi}{a}$. The superlattice potentials are sketched as *thick solid lines*. The real part of the eigenfunctions (*solid line*) is symmetric for all k and the imaginary part (*dashed line*) is antisymmetric for all k . For $k = 0$, the imaginary part is zero, the eigenfunction is symmetric and periodic in z with period a . This is also the total ground state of the superlattice. For $k = \frac{\pi}{a}$, the imaginary part is zero again and the eigenfunction is antiperiodic in z , i.e., $\psi_{1,k=\pi/a}(z) = -\psi_{1,k=\pi/a}(z+a)$. For negative values of k , the eigenfunctions are found by complex conjugation, i.e., the imaginary part changes sign. The Bloch functions fulfill $\psi_{1,\pm\pi/a}(z) = \psi_{1,-\pi/a}(z)$, which means they belong to Kohn's case A. This is expected for all below-barrier minibands from the tight-binding approximation, and is also confirmed for the second miniband of Sample 1. The qualitative behavior of the Bloch function for $j = 1$ is the same for both samples. However, the solution for Sample 1 is closer to the limit of strong confinement, in which $\text{Re } \psi_{jk}(z)$ is independent of k and $\text{Im } \psi_{jk}(z) = 0$ for $z \in [-\frac{a}{2}, +\frac{a}{2}]$. In contrast, the Bloch functions

for Sample 2 are close to the limit of nearly free electrons, where $\text{Im } \psi_{1k}(z)$ is nearly discontinuous at $k = \pm \frac{\pi}{a}$.

4.2 Bloch Electron in an Electric Field

In the case of zero electric field, especially for the one-dimensional case, the analytical properties of the energy bands and the Bloch functions are well known, there are even some analytical solutions, and the exact solution can be very well bracketed between the limits of tightly bound and nearly free electrons. Not so for $F \neq 0$: there are no analytical solutions for any realistic potential, the nature of the spectrum has been a matter of controversy for many years, and the analytical proof of the continuous spectrum can neither be understood by lesser mortals, nor is it helpful for practical calculations. Therefore, in the past people have relied on approximate solutions and continue to do so. Here, we discuss the most common approximations, the discrete model, which is closely related to the tight-binding approximation [8, 18–22, 64, 90], and the Kane functions [12, 14, 15, 91]. Especially the Kane functions have largely influenced the understanding of the Wannier–Stark problem. For some parameters, they are good qualitative and even quantitative approximations of the exact solutions, they are useful for numerical calculations, but ultimately lead to the wrong track concerning the nature of the spectrum. The failure of these approximations will be discussed at the end of this section and its consequences for the optical absorption will be the subject of Sect. 4.3.

4.2.1 Discrete Model and Tight-Binding Approximation

In order to get an idea about the structure of the solutions (4.1), a first step is to construct a discrete model, where an infinite-dimensional vector $\Phi = (\dots, \Phi_{-1}, \Phi_0, \Phi_1, \dots)^T$ takes the role of the wavefunction φ . The eigenvalue problem for Φ reads

$$\sum_{n'=-\infty}^{+\infty} H_{nn'} \Phi_{n'} = E \Phi_n$$

$$H_{nn'} = A \delta_{nn'} - B (\delta_{n,n'-1} + \delta_{n,n'+1}) + f n \delta_{nn'} \quad (4.19)$$

$$A, B, f \in \mathbb{R}; \quad B, f \neq 0.$$

This is the same equation as derived in the tight-binding approximation (Sect. 4.1) except for the additional linear term $f n$. We already know the solution for $f = 0$, which is

$$\Phi_{q;n} = \frac{1}{\sqrt{2\pi}} e^{iqn} ; \quad q \in [-\pi, +\pi[\quad (4.20)$$

$$E(q) = A - 2B \cos q = A - 2B + 4B \sin^2 \frac{q}{2} .$$

For $f \neq 0$, we proceed as follows. The components of Φ can be looked upon as the coefficients of a Fourier series:

$$\Phi_n = \frac{1}{2\pi} \int_{-\pi}^{+\pi} dq e^{+inq} \tilde{\Phi}(q) ; \quad \tilde{\Phi}(q) = \sum_{n=-\infty}^{+\infty} e^{-inq} \Phi_n . \quad (4.21)$$

In Fourier space, the original equation (4.19) translates into

$$(A - 2B \cos q + if \frac{d}{dq}) \tilde{\Phi}(q) = E \tilde{\Phi}(q) . \quad (4.22)$$

For fixed E , the above equation is a first-order differential equation in the variable q and the solution is

$$\begin{aligned} \tilde{\Phi}(q) &= c \exp \left[\frac{1}{if} \int_0^q dq' (E - A + 2B \cos q') \right] \\ &= c \exp \left(\frac{E - A}{if} + \frac{2B \sin q}{if} \right) . \end{aligned} \quad (4.23)$$

According to the ansatz (4.21), the solutions $\tilde{\Phi}(q)$ need to be periodic with period 2π . This restricts the the possible eigenvalues to

$$E_l = \langle E \rangle + fl ; \quad l \in \mathbb{Z} ; \quad \langle E \rangle = \frac{1}{2\pi} \int_{-\pi}^{+\pi} dq E(q) = A . \quad (4.24)$$

The corresponding eigenvectors are

$$\Phi_{l;n} = \frac{c}{2\pi} \int_{-\pi}^{+\pi} dq e^{+iq(n-l)} e^{\frac{2B}{if} \sin q} = c J_{n-l} \left(\frac{2B}{f} \right) = c J_{l-n} \left(-\frac{2B}{f} \right) , \quad (4.25)$$

where J_n is the Bessel function of first kind (App. A.2). The scalar product of two eigenvectors is

$$\langle \Phi_l, \Phi_{l'} \rangle = \sum_{n=-\infty}^{+\infty} \Phi_{l;n}^* \Phi_{l';n} = \frac{1}{2\pi} \int_{-\pi}^{+\pi} dq \tilde{\Phi}_l^*(q) \tilde{\Phi}_{l'}(q) = |c|^2 \delta_{ll'} . \quad (4.26)$$

We set $c = 1$ so that the eigenvectors (4.25) are orthonormal and real. Because the components $\Phi_{l;n}$ depend only on the difference $l - n$, the above equation also yields the closure relation.

The result for $f \neq 0$ can be summarized as follows. The eigenvalues are discrete and the eigenvectors are normalizable in the conventional sense, in contrast to the case $f = 0$. The solutions fulfill the ladder property, i.e., a shift of an eigenvector by l lattice sites results in a shift of the eigenvalue by fl . The origin of the ladder is E_0 is equal to the averaged band energy $\langle E \rangle$.

So far, the normalizability of the eigenvectors was plugged in by the ansatz (4.21). Alternatively, one can start with the general solution of the second-order difference equation (4.19), which is [8, 18, 19, 21, 22, 64]

$$\Phi_n = c J_{\pm n \pm \frac{A-E}{f}} (\pm \frac{2B}{f}) + d Y_{\pm n \pm \frac{A-E}{f}} (\pm \frac{2B}{f}), \quad (4.27)$$

where Y_ν is the Bessel function of second kind (Weber's or Neumann's function). From the asymptotic behavior of J_ν and Y_ν ,

$$\begin{aligned} \lim_{n \rightarrow -\infty} |J_{n+\nu}(x)| &= \infty \text{ for } x > 0; \quad \nu \notin \mathbb{Z} \\ \lim_{n \rightarrow +\infty} |Y_{n+\nu}(x)| &= \infty \text{ for } x > 0; \quad \nu \in \mathbb{R}, \end{aligned} \quad (4.28)$$

which can be derived from the integral representations [92, 93], it follows that $d = 0$ and $(A - E)/f \in \mathbb{Z}$. For a finite length with boundary conditions, the coefficient d is nonzero and the eigenvalues are not Wannier–Stark ladders, but as the normalization domain goes to infinity, the coefficient d approaches zero and the spectrum goes over into the Wannier–Stark ladder.

Let us consider the extension σ of the eigenfunctions, which is defined as

$$\sigma^2[n] = \langle n^2 \rangle - \langle n \rangle^2 = \sum_{n=-\infty}^{+\infty} |\Phi_{l;n}|^2 n^2 - \left[\sum_{n=-\infty}^{+\infty} |\Phi_{l;n}|^2 n \right]^2. \quad (4.29)$$

Due to the ladder property, this quantity is independent of l , so we choose $l = 0$. From

$$\begin{aligned} \sum_{n=-\infty}^{+\infty} |\Phi_{0;n}|^2 n^2 &= \frac{1}{2\pi} \int_{-\pi}^{+\pi} dq \left| i \frac{d}{dq} \tilde{\Phi}_{0;n}(q) \right|^2 = \frac{1}{2\pi} \int_{-\pi}^{+\pi} dq \left(\frac{2B \cos q}{f} \right)^2 = \frac{2B^2}{f^2} \\ \sum_{n=-\infty}^{+\infty} |\Phi_{0;n}|^2 n &= \frac{1}{2\pi} \int_{-\pi}^{+\pi} dq \tilde{\Phi}_{0;n}^*(q) i \frac{d}{dq} \tilde{\Phi}_{0;n}(q) = \frac{1}{2\pi} \int_{-\pi}^{+\pi} dq \frac{2B \cos q}{f} = 0 \end{aligned} \quad (4.30)$$

it follows that

$$\sigma^2[n] = \frac{2B^2}{f^2} = \frac{\sigma^2[E]}{f^2}, \quad (4.31)$$

with the mean square variance of the energy dispersion (4.20), defined as

$$\sigma^2[E] = \langle E^2 \rangle - \langle E \rangle^2 = \frac{1}{2\pi} \int_{-\pi}^{+\pi} dq E^2(q) - \left[\frac{1}{2\pi} \int_{-\pi}^{+\pi} dq E(q) \right]^2. \quad (4.32)$$

Thus the localization of the eigenfunctions increases as the field increases. Their extension $\sigma[n]$ is proportional to $1/|f|$ [90]. In the limit $f \rightarrow \pm\infty$, the eigenfunctions are completely localized and the components of the eigenvectors are $\Phi_{l;m} = \delta_{lm}$.

We mention that, by similar methods as above, one can also exactly solve the eigenvalue problem of a two-dimensional lattice in an electric field. Localization is observed when the direction of the electric field does not coincide with a crystallographic direction [22, 94].

The solution of the Wannier–Stark problem (4.1) in the tight-binding approximation, from which the discrete model was deduced, is

$$E_l = A + eFa l; \quad \varphi_l(z) = \sum_{n=-\infty}^{+\infty} J_{n-l}\left(\frac{2B}{eFa}\right) w^{(0)}(z-an) = \varphi_0(z-al), \quad (4.33)$$

where A and B are given by the expressions (4.11) and the parameter f from the discrete model is replaced by eFa . It is a common practice to tacitly neglect the overlap integral S (4.11), even though there is no rigorous justification as in the case $F = 0$. As far as we are only interested in the qualitative behavior of the solution, this negligence may be justified. We mention that an exact solution is also possible for $S \neq 0$ and still leads to a Wannier–Stark ladder [20].

It is interesting to see the connection between the discrete model and the problem of an electron in an electric field (C.40), which is the same as the Wannier–Stark problem (4.1) for $U(z) \equiv 0$ and $F \neq 0$. The finite-difference scheme (see Chap. 2) with $z_n = n \Delta z$, $n \in \mathbb{Z}$ is

$$-\frac{\hbar^2}{2m} \frac{\psi(z_{n-1}) - 2\psi(z_n) + \psi(z_{n+1})}{(\Delta z)^2} + eFz_n \psi(z_n) = E \psi(z_n).$$

This equation is equivalent to problem (4.19) if we identify

$$\Phi_n = \sqrt{\Delta z} \psi(z_n); \quad A = \frac{\hbar^2}{m(\Delta z)^2}; \quad B = \frac{\hbar^2}{2m(\Delta z)^2}; \quad f = eF\Delta z.$$

The factor $\sqrt{\Delta z}$ is introduced because of the weighted scalar product (2.66) with $g_n = \Delta z$. According to (4.24) and (4.25), the finite-difference solution is

$$E_l = \frac{\hbar^2}{meF(\Delta z)^2} + eFl\Delta z; \quad \psi_l(z_n) = \frac{1}{\sqrt{\Delta z}} J_{n-l}\left(\frac{\hbar^2}{m(\Delta z)^3 eF}\right).$$

Now we perform the limit $\Delta z \rightarrow 0$, while E_l and z_n remain finite quantities. Without loss of generality, we assume $eF > 0$. From Debye's asymptotic expression [92, 93]

$$J_n(x) \sim \left(\frac{x}{2}\right)^{-1/3} \text{Ai}\left[\left(\frac{x}{2}\right)^{-1/3}(n-x)\right] \quad \text{for } x > 0; \quad |n-x| \rightarrow \infty; \quad n-x = O\left(x^{1/3}\right)$$

we find

$$\psi_l(z_n) \sim \sqrt{\Delta z} \left(\frac{2meF}{\hbar^2} \right)^{1/3} \text{Ai} \left[\left(\frac{2meF}{\hbar^2} \right)^{1/3} \left(z_n - \frac{E_l}{eF} \right) \right].$$

The factor $\sqrt{\Delta z}$ shows that the result is not normalizable in the limit $\Delta z \rightarrow 0$. On the other hand, in this limit, the density of the eigenvalues $D(E_l) = 1/(E_{l+1} - E_l) = 1/(eF\Delta z)$ goes to zero, which means that the spectrum becomes continuous. To go over to energy normalization (App. C.1), we have to multiply the above function with $\sqrt{D(E_l)}$, which leads to the known result (C.46).

The continuum limit of (4.25) also applies for finite A and B when $f \rightarrow 0$. Then the solution has the form (C.46), but the effective mass is determined by the curvature of the band dispersion at $k = 0$ or $k = \pm \frac{\pi}{a}$. This effect is observed as Franz–Keldysh oscillations in the spectra of superlattices at small electric fields [45].

4.2.2 Kane Functions

While the qualitative character of the tight-binding approximation is obvious, the Kane functions, developed in the context of tunneling theory, were believed to be virtually exact for a long time. There were even claims that Kane functions can be constructed which would be exact solutions of the Wannier–Stark problem.

An attempt to solve (4.1) is to use the solution for $F = 0$, the Bloch functions, as base functions. Then, for the eigenfunctions of the Wannier–Stark problem we make the ansatz

$$\varphi(z) = \sum_j \sqrt{\frac{a}{2\pi}} \int_{-\frac{\pi}{a}}^{+\frac{\pi}{a}} dk \tilde{\varphi}_j(k) \psi_{jk}(z). \quad (4.34)$$

With the normalization of the Bloch functions (4.6), the integration over the modulus square of the eigenfunction (4.34) gives:

$$\int_{-\infty}^{+\infty} dz |\varphi(z)|^2 = \sum_j \frac{a}{2\pi} \int_{-\frac{\pi}{a}}^{+\frac{\pi}{a}} dk |\tilde{\varphi}_j(k)|^2. \quad (4.35)$$

The ansatz (4.34) is in principle correct, if the sum runs over all energy bands $j = 1, \dots, \infty$. However, in practice, it is necessary to truncate the sum at a finite number n . In this case, the solution (4.35) is normalizable and the spectrum is discrete. In turn, if the spectrum of the Wannier Stark problem (4.1) is continuous and the eigenfunctions are not square integrable, the sum is divergent and the Hamiltonian (4.1) does not possess subspaces, which consist of a finite number of bands. We shall come back to this problem in the next subsection.

We assume that $\psi_{jk}(z)$ is continuous and has piecewise continuous derivatives with respect to k in the periodic interval $[-\frac{\pi}{a}, +\frac{\pi}{a}]$. For $F = 0$, the

Hamiltonian (4.1) is diagonal in the Bloch functions $\{\psi_{jk}\}$ and its matrix elements are $E_j(k) \delta_{jj'} \underline{\delta}(k - k')$. To calculate the matrix element of the perturbation we use the explicit form of the Bloch functions (4.3) and apply the product rule:

$$\begin{aligned}
& \int_{-\infty}^{+\infty} dz \psi_{jk}^*(z) eFz \psi_{j'k'}(z) = \frac{1}{2\pi} \int_{-\infty}^{+\infty} dz eFz e^{-i(k-k')z} u_{jk}^*(z) u_{j'k'}(z) \\
& = -ieF \frac{d}{dk'} \int_{-\infty}^{+\infty} dz \psi_{jk}^*(z) \psi_{j'k'}(z) \\
& + eF \frac{1}{2\pi} \int_{-\infty}^{+\infty} dz e^{-i(k-k')z} u_{jk}^*(z) i \frac{\partial u_{j'k'}(z)}{\partial k'} \\
& = ieF \delta_{jj'} \frac{d}{dk} \underline{\delta}(k - k') + eF \underline{\delta}(k - k') Z_{jj'}(k) ,
\end{aligned} \tag{4.36}$$

where

$$Z_{jj'}(k) = \frac{1}{a} \int_{-\frac{a}{2}}^{+\frac{a}{2}} dz u_{jk}^*(z) i \frac{\partial u_{j'k}(z)}{\partial k} ; \quad Z_{jj'}(k) = Z_{j'j}^*(k) . \tag{4.37}$$

The interband dipole matrix element $Z_{jj'}(k)$ ($j \neq j'$) can be expressed by the momentum matrix element $p_{jj'}(k)$ [9]. From

$$\begin{aligned}
\langle j, k | \hat{z} | j', k' \rangle &= \underline{\delta}(k - k') Z_{jj'}(k) \\
\langle j, k | \hat{p} | j', k' \rangle &= \underline{\delta}(k - k') p_{jj'}(k)
\end{aligned} \tag{4.38}$$

and

$$[\hat{H}, \hat{z}] = \frac{\hbar}{im} \hat{p} \tag{4.39}$$

with \hat{H} being the Hamiltonian in (4.2) it follows that

$$Z_{jj'}(k) = \frac{\hbar}{im [E_j(k) - E_{j'}(k)]} p_{jj'}(k) . \tag{4.40}$$

With the matrix elements (4.36) the eigenvalue problem for the functions $\tilde{\varphi}_j(k)$ reads:

$$\left[E_j(k) + ieF \frac{d}{dk} \right] \tilde{\varphi}_j(k) + eF \sum_{j'} Z_{jj'}(k) \tilde{\varphi}_{j'}(k) = E \tilde{\varphi}_j(k) . \tag{4.41}$$

If the matrix $Z(k)$ is uniformly bounded in $[-\frac{\pi}{a}, +\frac{\pi}{a}]$, which is always the case for a finite number of bands, then the functions $\tilde{\varphi}_j(k)$ are continuous in $[-\frac{\pi}{a}, +\frac{\pi}{a}]$. Furthermore, it is required that $\tilde{\varphi}_j(+\frac{\pi}{a}) = \tilde{\varphi}_j(-\frac{\pi}{a})$, otherwise the integral over the derivative of $\delta(k - k')$ (4.37) would be divergent for $k = \pm\frac{\pi}{a}$. This periodicity condition limits the possible eigenvalues E .

The common approximation is to neglect the nondiagonal elements of the matrix $Z(k)$ and thus to decompose (4.41) into independent differential equations, which can be solved explicitly. Then the eigenvalues and eigenfunctions, which fulfill the periodicity conditions for $\tilde{\varphi}_j$, are

$$E_{jl} = \frac{a}{2\pi} \int_{-\frac{\pi}{a}}^{+\frac{\pi}{a}} dk' [E_j(k') + eFZ_{jj}(k')] + eFal ; \quad l \in \mathbb{Z} \quad (4.42)$$

$$\tilde{\varphi}_{jl}(k) = \exp \left\{ \frac{1}{ieF} \int_0^k dk' [E_{jl} - E_j(k') - eFZ_{jj}(k')] \right\} .$$

The approximate eigenfunctions in real space,

$$\varphi_{jl}(z) = \sqrt{\frac{a}{2\pi}} \int_{-\frac{\pi}{a}}^{+\frac{\pi}{a}} dk \tilde{\varphi}_{jl}(k) \psi_{jk}(z) , \quad (4.43)$$

are known as Kane functions [12, 14, 15, 91].

The Kane functions are orthonormal, i.e.,

$$\int_{-\infty}^{+\infty} dz \varphi_{jl}^*(z) \varphi_{j'l'}(z) = \delta_{jj'} \delta_{ll'} , \quad (4.44)$$

and fulfill the ladder property

$$\varphi_{jl}(z) = \varphi_{j0}(z - al) . \quad (4.45)$$

The Bloch functions, expressed in terms of the Kane functions, are

$$\psi_{jk}(z) = \sqrt{\frac{a}{2\pi}} \sum_{l=-\infty}^{+\infty} \tilde{\varphi}_{jl}^*(k) \varphi_{jl}(z) . \quad (4.46)$$

This means that the Kane functions $\{\varphi_{jl}\}$ are complete in the subspace of the j -th band. In the approximation of decoupled bands, every energy band results in one Wannier–Stark ladder, while for the tight-binding approximation Wannier–Stark ladders are found only for below-barrier minibands.

Let us now briefly outline the solution of Eq. (4.41) for a finite number n of coupled bands. In compact notation, this equation reads

$$ieF \frac{d}{dk} \tilde{\varphi}(k) = [E - D(k)] \tilde{\varphi}(k); \quad \tilde{\varphi}(+\frac{\pi}{a}) = \tilde{\varphi}(-\frac{\pi}{a}), \quad (4.47)$$

where the n -dimensional vector $\tilde{\varphi}$ and the elements of the $n \times n$ matrix D are defined as

$$\tilde{\varphi}(k) = (\tilde{\varphi}_1(k), \dots, \tilde{\varphi}_n(k))^T; \quad D_{jj'}(k) = E_j(k) \delta_{jj'} + eF Z_{jj'}(k). \quad (4.48)$$

The solutions of (4.47) are

$$E_{\iota l} = E_{\iota 0} + eFa l; \quad \tilde{\varphi}_{\iota l}(k) = e^{\frac{E_{\iota l} k}{ieF}} S(k) \tilde{\varphi}_{\iota}; \quad \iota = 1, \dots, n; \quad l \in \mathbb{Z}, \quad (4.49)$$

where the ordered exponential S is defined as

$$S(k) = \sum_{p=0}^{\infty} \left(\frac{-1}{ieF} \right)^p \int_0^k dk_1 \int_0^{k_1} dk_2 \cdots \int_0^{k_{p-1}} dk_p D(k_1) \cdots D(k_p) \quad (4.50)$$

(the first term of the sum is 1) and the $E_{\iota 0}$ and $\tilde{\varphi}_{\iota}$ are the solution of the eigenvalue problem of a unitary matrix:

$$S(+\frac{\pi}{a}) S(-\frac{\pi}{a})^{-1} \tilde{\varphi}_{\iota} = e^{-\frac{2\pi}{a} \frac{E_{\iota 0}}{ieF}} \tilde{\varphi}_{\iota} \quad (4.51)$$

$$\tilde{\varphi}_{\iota}^* \cdot \tilde{\varphi}_{\iota'} = \delta_{\iota \iota'}; \quad -\frac{eFa}{2} \leq E_{\iota 0} < +\frac{eFa}{2}.$$

The eigenfunctions in real space fulfill the ladder property $\varphi_{\iota l}(z) = \varphi_{\iota 0}(z - al)$, are orthonormal with respect to the quantum numbers ι, l , and are complete in the subspace of the n Bloch bands. Thus, for coupling of a finite number of bands n , we observe n intermingled Wannier–Stark ladders and the result is not qualitatively different from the result for uncoupled bands. The case of a finite number of minibands is not of much interest. Model calculations have been published for two bands [22, 95].

The solutions of (4.41) are independent of the phase of the Bloch functions. If we go over to Bloch functions $\psi'_{jk}(z) = e^{+i\Phi_j(k)} \psi_{jk}(z)$, where $\Phi_j(k) \in \mathbb{R}$ and $\Phi_j(k + \frac{2\pi}{a}) = \Phi_j(k)$, then the matrix elements (4.37) transform according to $Z'_{jj'}(k) = e^{-i\Phi_j(k)} Z_{jj'}(k) e^{+i\Phi_{j'}(k)} - \delta_{jj'} d\Phi_j(k)/dk$ and the solutions of the differential equation (4.41) change to $\tilde{\varphi}'_j(k) = e^{-i\Phi_j(k)} \tilde{\varphi}_j(k)$ so that expression (4.34) remains invariant.

Now, we study the extension of the Kane functions. In analogy to (4.29), we define

$$\sigma^2[z] = \langle \varphi_{jl} | \hat{z}^2 | \varphi_{jl} \rangle - [\langle \varphi_{jl} | \hat{z} | \varphi_{jl} \rangle]^2 \quad (4.52)$$

$$= \int_{-\infty}^{+\infty} dz |\varphi_{jl}(z)|^2 z^2 - \left[\int_{-\infty}^{+\infty} dz |\varphi_{jl}(z)|^2 z \right]^2.$$

Of course, the extension $\sigma[z]$ is independent of the index l . The discrete model suggests that $\sigma[z] = \sigma[E]/|eF|$ (4.31), which is also the result of a semiclassical approximation [59, 96], valid for small F . For large fields, we expect deviations from this formula, because the localization of the Kane function will not be perfect and the extension will still be in the order of the well thickness, which can be seen from the tight-binding approximation (4.33).

We shall now evaluate expression (4.52) for a symmetric superlattice. We do this in the basis of the special Bloch functions (p. 151). Without loss of generality we assume case A so that for symmetry reasons the matrix element $Z_{jj}(k)$ vanishes identically. Because $\tilde{\varphi}_j(+k) = \tilde{\varphi}_j^*(-k)$ and $\psi_{j,+k}(z) = \psi_{j,-k}^*(z)$, the Kane functions (4.42–4.43) are real, which can be expected, because the original eigenvalue problem is a real differential equation. From integration by parts we find that

$$z \varphi_{jl}(z) = \sqrt{\frac{a}{2\pi}} \int_{-\frac{\pi}{a}}^{+\frac{\pi}{a}} dk \left[i \frac{d\tilde{\varphi}_{jl}(k)}{dk} \psi_{jk}(z) + \tilde{\varphi}_{jl}(k) \frac{1}{\sqrt{2\pi}} e^{ikz} i \frac{\partial u_{jk}(z)}{\partial z} \right] \quad (4.53)$$

and for the extension it follows from $Z_{jj}(k) \equiv 0$ that

$$\begin{aligned} \sigma^2[z] &= \frac{a}{2\pi} \int_{-\frac{\pi}{a}}^{+\frac{\pi}{a}} dk \left| \frac{d\tilde{\varphi}_{jl}(k)}{dk} \right|^2 - \left[\frac{a}{2\pi} \int_{-\frac{\pi}{a}}^{+\frac{\pi}{a}} dk \tilde{\varphi}_{jl}(k) i \frac{d\tilde{\varphi}_{jl}(k)}{dk} \right]^2 \\ &\quad + \frac{1}{2\pi} \int_{-\frac{\pi}{a}}^{+\frac{\pi}{a}} dk \int_{-\frac{a}{2}}^{+\frac{a}{2}} dz \left| \frac{\partial u_{jk}(z)}{\partial k} \right|^2 = \frac{\sigma^2[E]}{(eF)^2} + \text{const} , \end{aligned} \quad (4.54)$$

where $\sigma^2[E]$ is the mean square variance of the band dispersion $E_j(k)$, defined in analogy to (4.32).

Thus the result (4.54) is the same as for the discrete model (4.31), up to an additive constant, independent of F , which will be determined below. Because of the analyticity of $\psi_{jk}(z)$ for $k \in [-\frac{\pi}{a}, +\frac{\pi}{a}]$, the procedure (4.53–4.54) can be repeated for higher powers of z , which shows that all moments $\langle \varphi_{jl} | \hat{z}^n | \varphi_{jl} \rangle$; $n \in \mathbb{N}_0$ are finite and the Kane functions are rapidly decreasing.

A set of functions, similar to the Kane functions, but more general, are the Wannier functions, defined as

$$w_{jl}(z) = \sqrt{\frac{a}{2\pi}} \int_{-\frac{\pi}{a}}^{+\frac{\pi}{a}} dk e^{-ikal} \psi_{jk}(z) \quad (4.55)$$

for a given set of Bloch functions $\{\psi_{jk}\}$. The Wannier functions are orthonormal with respect to j and l and fulfill the ladder property. However, they are

not unique, because of the freedom of the phase in the definition of the Bloch functions. The Kane functions (4.43) are a special case of the Wannier functions. Of particular interest, especially for numerical calculations, are Wannier functions with a minimal spatial extension, defined by the variance (4.52). It is easy to see that this is the case if the Bloch functions in definition (4.55) are the special Bloch functions. The proof goes alongside the same lines as (4.53–4.54). These special Wannier functions⁵ are real, symmetric or antisymmetric around the lattice points $z = al$, depending on whether $\psi_{j,k=0}$ is symmetric or antisymmetric, and rapidly decreasing for $z \rightarrow \pm\infty$. From the explicit form of the coefficients $\tilde{\varphi}_{jl}(k)$ (4.42) we find that

$$\lim_{|eF| \rightarrow \infty} \varphi_{jl}(z) = w_{jl}(z). \quad (4.56)$$

The Kane functions go over into the Wannier functions also in the limit of dispersionless bands $E_j(k) = \text{const}$, which is fulfilled for deep levels. For the special Wannier functions, the first two terms in (4.54) are zero so that the remaining constant term is equal to the square variance of the Wannier functions [97].

It is interesting to see the relation between the Kane functions and the tight-binding approximation. The tight-binding Bloch functions (4.13) fulfill $\psi_k(z) = \psi_{k+2\pi/a}(z)$, i.e., they belong to Kohn's case A. If the band dispersion and the Bloch functions in tight-binding approximation (4.13) were inserted in (4.42–4.43), then the Wannier–Stark energies and Kane functions are identical to expression (4.33). The Wannier functions of the tight-binding model, which are equal to the Kane functions (4.33) in the limit $F \rightarrow \pm\infty$, are identical to the tight-binding orbitals $w^{(0)}(z - al)$. If the true Wannier functions $w_{jl}(z)$ for fixed j are used as base functions and no restriction is made with respect to the number of neighbors, then the eigenvectors (4.19) would contain the Fourier coefficients of the functions $\tilde{\varphi}_{jl}(k)$ (4.42).

Even though the introduction of the Houston functions was somewhat heuristic in the first place [7], it can be shown that they are fully equivalent to the Kane functions [5, 15, 16]. For fixed band index j , the Kane functions φ_{jl} are a complete system in the subspace of the j -th band. The expansion of a Bloch function with wavenumber k_0 in terms of Kane functions is

$$\psi_{jk_0}(z) = \sum_l \langle \varphi_{jl} | \psi_{jk_0} \rangle \varphi_{jl}(z) = \sqrt{\frac{a}{2\pi}} \sum_l \tilde{\varphi}_{jl}^*(k_0) \varphi_{jl}(z). \quad (4.57)$$

In the absence of tunneling, i.e., when the nondiagonal matrix elements $Z_{jj'}$ ($j \neq j'$) are neglected, the time dependence of the Kane functions is given by

$$\varphi_{jl}(z, t) = e^{\frac{E_{jl}t}{i\hbar}} \varphi_{jl}(z). \quad (4.58)$$

Then for the time dependence of the Bloch functions (4.57) it follows that

⁵ often simply called “Wannier functions”

$$\psi_{jk_0}(z, t) = \exp \left\{ \frac{1}{i\hbar} \int_0^t dt' \bar{E}[k(t')] \right\} \psi_{j,k(t)}(z) \quad (4.59)$$

with

$$\bar{E}_j(k) = E_j(k) - eFZ_{jj}(k); \quad k(t) = k_0 - eFt/\hbar. \quad (4.60)$$

The functions (4.59) are the Houston functions [7]. They oscillate with the Bloch period $T_{\text{BO}} = 2\pi\hbar/|eFa|$. The replacement of the $E_j(k)$ by $\bar{E}_j(k)$ was made later [5, 11, 98, 99].

At the end of this subsection, we numerically calculate the approximate eigenfunctions of a superlattice in an electric field. We do this for Sample 1 and Sample 2 with parameters given in Sect. 4.1. We compare the Kane functions (4.42–4.43) with the tight-binding approximation (4.33). To calculate the Kane functions, we solved the eigenvalue problem (4.4) as described in Sect. 4.1. The Brillouin zone $[-\frac{\pi}{a}, +\frac{\pi}{a}]$ was sampled with 200 points, which should give accurate results for the Kane functions (4.42–4.43) for $|z| \ll 100a$. According to the results for the band structure (Fig. 4.2), the tight-binding approximation should be fairly accurate for Sample 1, but in case of Sample 2 should only give the right trends.

The result of the calculation is shown in Fig. 4.4 for Sample 1 (left) and Sample 2 (right). The first Kane function $\varphi_{j=1,l=0}$ (*solid line*) is compared with the tight-binding approximation (*dashed line*). The field strength F is varied between 5 kV/cm and 40 kV/cm, and $F = \infty$ denotes the Wannier functions, which are the Kane functions in the limit $F \rightarrow \pm\infty$ (4.56). The effective potential $U(z) + eFa$ is shown as a *thick solid line*.

Both exact and approximate Kane functions are weakly localized for small fields and the spatial extension is roughly proportional $1/F$ (4.54). The extension is larger for Sample 2, because the dispersion of the first miniband is larger. From Fig. 4.2, one would expect roughly a factor of 2. For finite electric field, the Kane functions are nonsymmetric. In the negative field direction ($z < 0$), they always change sign near the points $a(n + \frac{1}{2})$. The agreement between exact and tight-binding Kane functions is fairly good for Sample 1. The differences between both functions are much larger for Sample 2, but there is still good qualitative agreement. The tight-binding approximation leads to about the same error in the whole field range, it does not become exact for $F \rightarrow 0$ or $F \rightarrow \pm\infty$; neither does it behave qualitatively different from the Kane function in one of these limits. This is because the same crucial assumption of decoupled minibands has been made for both approximations.

For large fields, the Kane function goes over into the special Wannier function w . In this sense, a field of 40 kV/cm can be considered large, because the Kane functions are already very close to Wannier functions. In the tight-binding approximation, the Wannier function is equal to the single-well eigenfunction $w^{(0)}$. For Sample 1, exact and approximate Wannier functions are strongly confined inside the well and the difference between $w(z)$ and $w^{(0)}(z)$ is very small. The exact solution goes below zero outside the well.

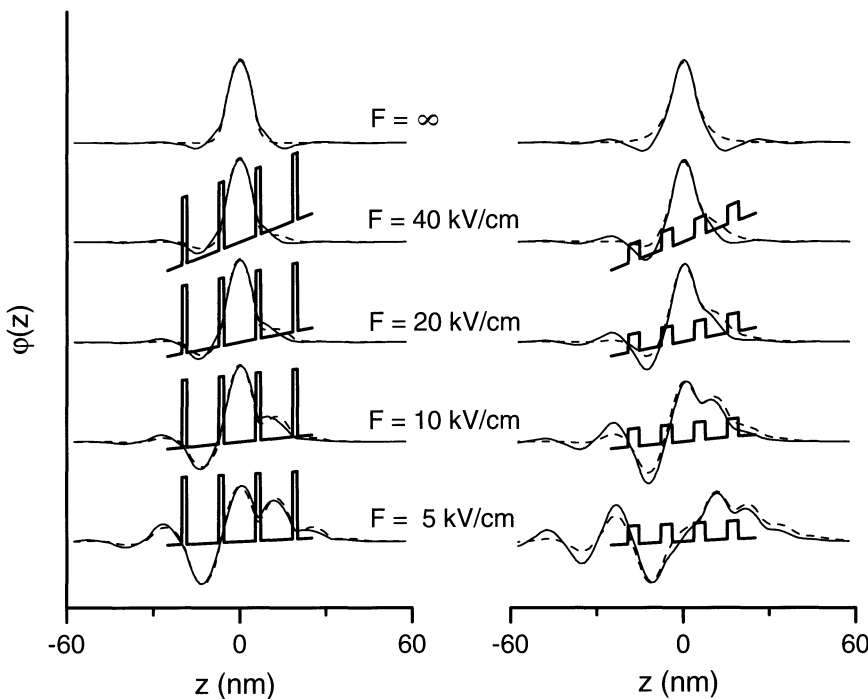


Fig. 4.4. Kane functions for different values of the electric field F for Sample 1 (left) and Sample 2 (right). The exact Kane function (*solid line*) is compared with the tight-binding approximation (*dashed line*). The case $F = \infty$ corresponds to the Wannier function. The potential $U(z) = eFz$ is shown as a *thick solid line*

This is necessary for the orthonormality of the functions $\{w(z-an)\}$. In contrast, the approximate Wannier function is always positive and approximate Wannier functions of neighboring wells are not orthogonal. The overlap integral S (4.11) for Sample 1 is equal to 0.043. For Sample 2, the confinement is much weaker, both exact and approximate Wannier function have a larger probability outside the active layer $[-\frac{d}{2}, +\frac{d}{2}]$, and the difference between w and $w^{(0)}$ is larger, especially outside the well. The overlap integral is larger than for Sample 1, namely $S = 0.289$.

4.2.3 Breakdown of Wannier–Stark Ladders

In the last subsection we have seen that the localization of the Kane function increases as the electric field increases (cf. Fig. 4.4). Furthermore, the Kane function remains square integrable for each field F . Intuitively, it is plausible that this cannot be true. Of course, the solution for $U = 0$ (C.46) also localizes with increasing F , but the eigenfunction is not square integrable.

For the Wannier–Stark problem (4.1), one would expect that in the limit $F \rightarrow \infty$ the influence of the periodic potential U becomes negligible and the eigenfunctions somehow approach the solution for $U = 0$ (C.46), which is not square integrable.

It is not trivial to numerically calculate the exact eigenfunctions of the Wannier–Stark problem. One might think of numerically solving (4.41) for a large number of minibands. As we have seen in the last subsection, this is in principle not possible, because any finite sum over minibands leads to square integrable eigenfunctions (4.35), while the exact solution is delta normalized. From the approximation of nearly free electrons (Sect. 4.1) and the relation (4.40) it follows that the coupling matrix elements $Z_{jj'}(k)$ between adjacent bands increase like $|K - K'| / |\tilde{U}_{K-K'}|$, which is superlinear, while the increase of the band width is linear. Therefore, with increasing number of minibands, the nondiagonal elements of the matrix D (4.48) are no longer small perturbations.⁶ Practically, it is observed that the solution is not convergent with respect to the number n of minibands taken into account. Therefore, it is also questionable if the coupling of any finite number of minibands better describes the reality than the Kane functions, which are based upon uncoupled minibands.

An alternative is a numerical solution in real space on a finite domain. This is often sufficient for practical purposes, but does not give the right asymptotics in the negative field direction; instead, the eigenfunctions depend on the boundary conditions. Tunneling of above-barrier states with a slowly decreasing tail has been observed in numerical calculations by Ritze et al. [100] and by the present author [101]. This is in contradiction to the Kane approximation, where there is no principal difference between below-barrier and above-barrier states.

For some applications, one wishes to directly calculate the width of the resonances. This has been done by Ritze and coworkers [100], using the heuristic concept of a generalized density of states. A more rigorous approach by Glück et al. is based upon analytic continuation [81]; unfortunately, this method is limited to analytic potentials.

To demonstrate the failure of the Kane approximation, we numerically calculate the eigenfunctions of the Wannier–Stark Hamiltonian (4.1) on the domain $[-L_z/2, +L_z/2]$. In one dimension, the eigenvalue problem can be solved with arbitrary accuracy. We use the conduction-band parameters of Sample 1 and a normalization length $L_z = 50a$. The Hamiltonian was discretized by second-order finite differences (2.80) with a step size of $a/128 = 1\text{\AA}$. At the points of discontinuity, the potential $U(z)$ (Fig. 4.1) was replaced by $[U(z+0) + U(z-0)] / 2$. The resulting tridiagonal matrix was diagonalized by bisection and inverse iteration, which takes $O(N)$ operations for the calculations of each eigenpair.

⁶ A similar example, which can be solved analytically, is the expansion of the free-electron Hamiltonian into the eigenfunctions of the harmonic oscillator.

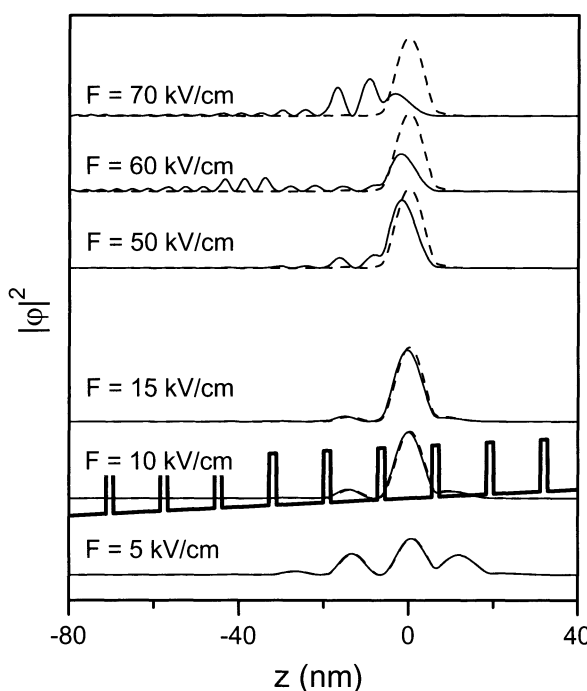


Fig. 4.5. Modulus square of the eigenfunctions of (4.1) for various fields F for Sample 1. The numerically exact solutions (*solid line*) are compared with the Kane approximation (*dashed line*). The effective potential $U(z) + eFz$ is shown as a *thick solid line*

The result of the calculation is shown in Fig. 4.5. The modulus square of the eigenfunction $|\varphi(z)|^2$ is plotted versus the coordinate z (*solid line*). For comparison, we also plot the solution of the Kane approximation (*dashed line*). The potential $U(z) + eFz$ is shown as a *thick solid line*. The domain shown in the plot is much smaller than the normalization domain of the numerical calculation.

For small fields, $F \leq 10 \text{ kV/cm}$, exact and approximate solution are virtually identical. Of course, the exact solution would be not normalizable, but the amplitude of the slowly decreasing tail is vanishingly small so that even the normalization on the large domain does not change the height near $z = 0$. For $F = 15 \text{ kV/cm}$, the maximum is slightly shifted to the left. This has to do with the quadratic Stark shift, which will be discussed in the next subsection. For large fields, $F \geq 50 \text{ kV/cm}$, the behavior of the Kane function and the exact solution is very different. The Kane function has already reached its high-field limit and is virtually identical to the Wannier function (cf. Fig. 4.4). In contrast, for the exact solution we observe tunneling through the barriers and the probability density outside the interval $[-\frac{a}{2}, +\frac{a}{2}]$ is comparable to or even larger than the probability density inside this interval. For $F = 70 \text{ kV/cm}$, one can no longer speak of localization in a certain well. In contrast to the Kane function, which is nearly symmetric, the exact solution is strongly asymmetric. The slowly decreasing tail qualitatively behaves like

the Airy function (cf. Fig. C.1), with the distance of consecutive zeros scaling like $1/\sqrt{-z}$. For a much larger electric field (not shown), the localization of the eigenfunction would increase again with an extension scaling as $|F|^{-1/3}$.

Due to the normalization on a finite domain, the amplitude of the exact solution is arbitrary. In contrast to the Kane functions, the exact solutions cannot be clearly associated with a certain miniband. Instead, they were hand-picked from 4 to 17 functions in the energy range $-eFa/2 < E \leq +eFa/2$ to closely resemble the Kane functions. There is a large (theoretically infinite) number of anticrossing between Wannier–Stark ladders of different minibands. The exact solution shown in Fig. 4.5 is one representative out of a continuum of states, which fulfills the boundary condition $\varphi(-L_z/2) = 0$. Therefore, it has no direct physical meaning. On the other hand, the numerical solution shown in Fig. 4.5 is a significant null-result and impressively shows the breakdown of the Kane approximation. If the exact solution was rapidly decaying like the Kane function, the influence of the finite domain would be negligible in the whole field range for a sufficiently large number of periods, as has been observed for the discrete model [21]. In the next subsection, we shall calculate the optical absorption, which can be measured experimentally, and for which the limit $L_z \rightarrow \infty$ is well-defined.

4.3 The Optical Spectrum

As the spectrum of the Wannier–Stark problem is entirely continuous, a single eigenfunction has no physical meaning. On the other hand, the whole ensemble of eigenfunctions enters measurable quantities like the optical density of states (Sect. 1.2) or the optical absorption (Sect. 1.3).

The optical density of states is based on single-particle eigenfunctions and neglects Coulomb interaction. The numerical calculation is easier than for the optical absorption. Therefore, it is quite natural to calculate the optical density of states first to have an orientation about the optical transitions. In the case of a superlattice in an electric field, this has been done by Schmidt et al. to study the interference between Wannier–Stark ladders and Franz–Keldysh oscillations [45]. However, these calculations were done in the basis of Kane functions and, therefore, cannot properly describe the continuous nature of the spectrum. An exact numerical solution is very easy, because the eigenvalue problem (4.1) is one-dimensional, but has not been published before 1999 [69]. These studies reveal a number of interesting phenomena, which are absent in the usual two-miniband model, and at large field strength, the Zener breakdown is observed, which is manifested as a disappearance of all discrete resonances.

In order to make a detailed comparison with the experiment, one needs to calculate the optical absorption including Coulomb interaction. This is difficult because of the three-dimensional nature of the problem and only very few authors succeeded. In 1990, Dignam and Sipe pointed out the difference

between single-particle and exciton Wannier–Stark ladders [54]. However, their analysis was limited to bound states, which is a coarse approximation, because the absorption spectrum is entirely continuous and bound and scattering states of different Wannier–Stark levels give rise to Fano interference. Linder et al. calculated absorption spectra including Coulomb interaction and continuum states, but the relatively large homogeneous broadening prevents a detailed study of the lineshape [56]. The first theoretical high-resolution spectra were published 1993 by Whittaker [57]. These spectra show Fano resonances, which were later found experimentally by Holfeld et al. [46].

So far, all these calculations relied on closed miniband eigenspaces and the base set was made up of Wannier functions [54, 57] or Kane functions [56], often calculated within the tight-binding approximation. It is nearly impossible to numerically model Stark-effect phenomena by expansion into single-particle eigenfunctions, because the eigenvalue spectra of electron and hole already becomes continuous. The real-space–real-time method, introduced in Chap. 2, does not rely on single-particle eigenstates and is therefore capable of treating difficult problems like the present one (see also Example E). This has also been demonstrated by Ahland et al. [102] and by Zambrano and Arce [103]. The superlattice in a perpendicular electric field has been treated by the present author and the spectra show a Zener breakdown at large but attainable fields [69, 72]. These predictions have been confirmed experimentally by Rosam, Meinhold, and coworkers [70–73]. A magnetic field applied in growth direction removes the in-plane continuum and, therefore, allows to directly observe the transition from discrete Wannier–Stark states to a continuum [72, 73].

In this section, we calculate the optical density of states, a forerunner of the optical absorption, the optical absorption including Coulomb interaction, and the optical absorption in the Faraday geometry, when an additional magnetic field is applied in the growth direction of the superlattice. A comparison is made with experimental results.

4.3.1 Optical Density of States

The one-dimensional optical density of states (see Sect. 1.2) is defined as

$$D(\omega) = \frac{|\mu|^2}{\varepsilon_0} \frac{1}{L_z} \sum_{\lambda_e \lambda_h} \left| \int_{-L_z/2}^{+L_z/2} dz \varphi_{e\lambda_e}(z) \varphi_{h\lambda_h}(z) \right|^2 \pi \delta(\omega - E_g - E_{e\lambda_e} - E_{h\lambda_h}). \quad (4.61)$$

The electron eigenvalues and eigenfunctions are the solution of (4.1). For the hole, we have to replace m_e , U_e , and $-e$ by m_{hz} , U_h , and $+e$. Both sets of eigenfunctions $\{\varphi_{e\lambda_e}\}$ and $\{\varphi_{h\lambda_h}\}$ are normalized on the finite domain $[-L_z/2, +L_z/2]$, where the limit $L_z \rightarrow \infty$ is assumed.

The three-dimensional optical density of states, which characterizes the optical absorption of a superlattice without Coulomb interaction, is proportional to the integral over the one-dimensional optical density of states. Of course, the optical absorption without Coulomb interaction is measurable only in theory. However, for the problem under consideration, i.e., the Zener breakdown, the Coulomb interaction is of minor importance, at least from the principal point of view. It is observed that for superlattices in a perpendicular electric field the one-dimensional optical density of states resembles the optical absorption of a three-dimensional superlattice, including excitonic effects [56, 101]. Later in this section, we shall also calculate the optical absorption, including Coulomb interaction.

For a numerical calculation of the optical density of states (4.61), one just needs to choose a sufficiently large normalization domain and apply some kind of boundary conditions. Nevertheless, the representation (4.61) does not take into account all symmetries and it is not obvious if the limit $L_z \rightarrow \infty$ exists and leads to a meaningful quantity. To eliminate the artificial boundary conditions, we go over to center-of-mass and relative coordinates, as we did before in the case of a bulk semiconductor in an electric field (Sect. 1.2). The pair eigenfunction, which replaces the product $\varphi_e(z_e)\varphi_h(z_h)$, obeys the eigenvalue problem

$$\left[-\frac{\hbar^2}{2M} \frac{\partial^2}{\partial Z^2} - \frac{\hbar^2}{2m} \frac{\partial^2}{\partial z^2} + U_e(Z + \frac{m_h}{M}) + U_h(Z - \frac{m_e}{M}) + eFz \right] \Phi(Z, z) = \mathcal{E} \Phi(Z, z) . \quad (4.62)$$

The oscillator strength in expression (4.61) now follows from integration over the center-of-mass coordinate Z , while the relative coordinate is taken at $z = 0$. The coordinate Z runs from $-L_z/2$ to $+L_z/2$ and the domain for z depends on Z . The area is the same as in the single-particle coordinates, namely L_z^2 . As we consider the limit $L_z \rightarrow \infty$, we can replace the domain by $[-L_z/2, +L_z/2] \times [-L_z/2, +L_z/2]$ and the result is independent of the type of boundary conditions.

The operator (4.62) is periodic in Z with period a . Using cyclic boundary conditions with $L_z = N a$; $N \in \mathbb{N}$, the eigenfunctions can be written in Bloch form $\Phi_\lambda(Z, z) = e^{iKZ} \Psi_{K\lambda}(Z, z)/\sqrt{N}$, where $\Psi_{K\lambda}(Z, z) = \Psi_{K\lambda}(Z+a, z)$. The integration over Z from $-L_z/2$ to $+L_z/2$ leads to the selection rule $K = 0$ and the integration can be restricted to the interval $[-\frac{a}{2}, +\frac{a}{2}]$. Then the optical density of states becomes

$$D(\omega) = \frac{|\mu|^2}{\varepsilon_0} \frac{1}{a} \sum_{\lambda} \left| \int_{-a/2}^{+a/2} dZ \Psi_{\lambda}(Z, z=0) \right|^2 \pi \delta(\hbar\omega - E_g - \mathcal{E}_{\lambda}) . \quad (4.63)$$

Here, we suppressed the index $K = 0$, and \mathcal{E}_λ and Ψ_λ are the eigenvalues and eigenfunctions of the operator (4.62) on the domain $[-\frac{a}{2}, +\frac{a}{2}] \times$

$[-L_z/2, +L_z/2]$, normalized to unity. Now, as the normalization length does no longer explicitly appear in (4.63), we can take the limit $L_z \rightarrow \infty$. Then, the quantum number λ goes over into E, J with $E \in (-\infty, +\infty)$ being the energy and J characterizing the infinite degeneracy due to the periodic boundary conditions for the Z direction. At the same time, we change from $\delta_{\lambda\lambda'}$ to energy normalization $\delta(E - E') \delta_{JJ'}$ and to integration over E (App. C.1). The integral eliminates the delta function and the final result is

$$D(\omega) = \frac{|\mu|^2}{\varepsilon_0} \frac{\pi}{a} \sum_J \left| \int_{-a/2}^{+a/2} dZ \Psi_{\hbar\omega-E_g,J}(Z, z=0) \right|^2, \quad (4.64)$$

which is free of any artificial normalization. For $U_e = U_h = 0$ it goes over into the known formula for the ideal one-dimensional semiconductor in an electric field (1.73).

We shall also consider the result of the Kane approximation. We limit ourselves to the lowest electron and hole miniband $j_e = j_h = 1$. Then, in expression (4.61), we have to replace the eigenfunctions by the Kane functions φ_{e1l_e} and φ_{h1l_h} , where l_e and l_h are the indices of the electron and hole Wannier–Stark ladders. The Kane functions of the hole are calculated from the hole Bloch functions in the same way as electron Kane functions from the electron Bloch functions (4.42–4.43), except that $-e$ has to be changed to $+e$. Therefore, the hole energies are $E_{h1l_h} = E_{h10} - eFa_l h$, where $E_{h10} = \langle E_{h1} \rangle$, and the oscillating part of the hole Kane function points in the direction of positive F .

The finite interval in (4.61) is incompatible with the ladder property of the Kane functions. Therefore, we have to explicitly take the limit $L_z \rightarrow \infty$. Ignoring boundary effects, we can fit N Kane functions into the interval $[-L_z/2, +L_z/2]$ and the overlap integral of electron and hole Kane function depends only on the difference $l = l_e - l_h$. The other sum runs empty and cancels the factor N in the denominator. As result, the optical density of states is

$$D(\omega) = \frac{|\mu|^2}{\varepsilon_0} \frac{1}{a} \sum_{l=-\infty}^{+\infty} \left| \int_{-\infty}^{+\infty} dz \varphi_{e1l}(z) \varphi_{h10}(z) \right|^2 \pi \delta(\hbar\omega - E_g - E_{e10} - E_{h10} - eFa_l). \quad (4.65)$$

In the Kane approximation with one miniband pair, the absorption is characterized by a single Wannier–Stark ladder of equidistant lines, in contrast to the expression (4.64), which does not suggest any regular structure of the spectrum. If several minibands were taken into account, we would have a spectrum of interleaved Wannier–Stark ladders [22, 95]. If the coupling of minibands was considered, the crossings of energy levels would turn into anticrossings. There is, however, the fundamental problem that the spectrum cannot be approximated by a finite number of Wannier–Stark ladders.

A separate calculation is necessary for the field-free case. Then the eigenfunctions are Bloch functions and the optical density of states is⁷

$$D(\omega) = \frac{|\mu|^2}{\varepsilon_0} \frac{1}{2\pi} \int_{-\frac{\pi}{a}}^{+\frac{\pi}{a}} dk \left| \frac{1}{a} \int_{-\frac{a}{2}}^{+\frac{a}{2}} dz u_{e1,+k}(z) u_{h1,-k}(z) \right|^2 \times \pi \delta \left[\hbar\omega - E_g - E_{e1}(k) - E_{h1}(k) \right]. \quad (4.66)$$

We numerically calculated the optical density of states (4.61). The eigenvalue problem for electron and hole was solved using finite differences, as described in the last subsection, with parameters $L_z = 50a$ and $\Delta z = 0.5 \text{ \AA}$. The Kane functions, which enter the approximation (4.65), were calculated as described in Sect. 4.2. The delta functions for energy conservation have been replaced by Lorentzians with a linewidth $\hbar\epsilon = 1 \text{ meV}$. As the numerical solution of one-dimensional problems is very efficient, we were able to calculate hundreds of spectra and to study the evolution of the optical transitions with the field strength. We also numerically verified the equivalence of the representations (4.61) and (4.63) by reformulation of (4.62–4.63) as initial-value problem.

The results are shown in Fig. 4.6. The derivative of the optical density of states $D'(\omega) = dD(\omega)/d\omega$ is shown as function of the photon energy $\hbar\omega$ and the electric field F . The gray scaling is nonlinear (proportional to $\text{arsinh } D'$), in order to emphasize smaller features in the spectrum. The Kane approximation (left) is compared with the full numerical calculation (right).

The Kane approximation (left of Fig. 4.6) shows one clear and distinct Wannier–Stark fan. The lines start at the middle of the miniband transition $E_g + \langle E_{e1} \rangle + \langle E_{h1} \rangle$ and are strictly linear, as expected from (4.65). Besides the main peak with $l_e = l_h$, we observe several side peaks with $l = l_e - l_h \neq 0$. In the limit of large electric field, the oscillator strengths become independent of F and are equal for $+l$ and $-l$. This is a consequence of the fact that for large field the Kane functions go over into the symmetric or antisymmetric Wannier functions. In the presence of Coulomb interaction, this symmetry of the energies and oscillator strength is destroyed, which is known as exciton asymmetry [54, 56]. For small fields $F \leq 5 \text{ kV/cm}$, we observe an interesting pattern. The Wannier–Stark levels, which originate from the middle of the band pair, interfere with Franz–Keldysh oscillations, which start at the upper and lower absorption edges, $E_g + E_{e1}(0) + E_{h1}(0)$ and $E_g + E_{e1}(\pm \frac{\pi}{a}) + E_{h1}(\pm \frac{\pi}{a})$, respectively [45].

Let us now turn to the result of the full calculation (right part of Fig. 4.6). At first glance, both spectra have not much in common. However, for small

⁷ Eq. (4.66) is indeed the limit of (4.65) for $F \rightarrow 0$. The proof, which is somewhat tedious, follows from the explicit expressions of the Kane functions (4.42–4.43) using the method of the stationary phase.

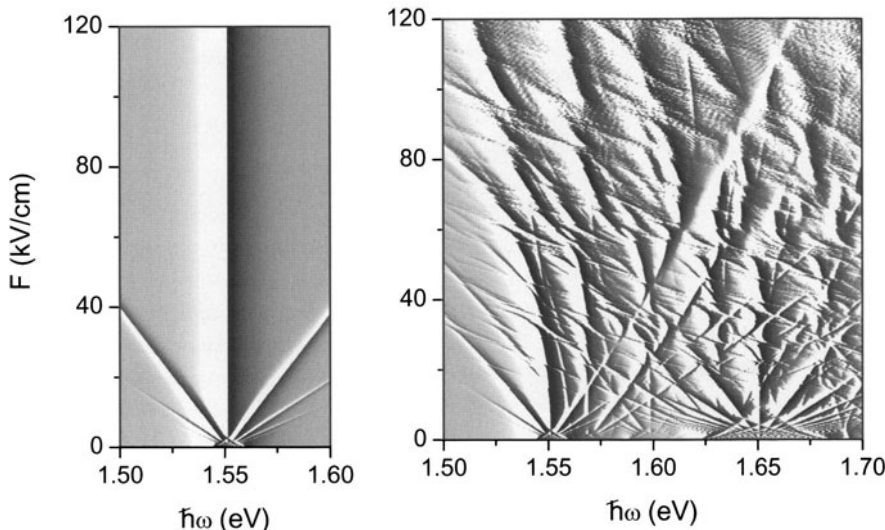


Fig. 4.6. Gray-scale plot of $D'(\omega)$ (nonlinear scale) for Sample 1 as function of the photon energy $\hbar\omega$ and the electric field F . The result of the Kane approximation (left) is compared with the exact numerical solution (right)

fields, $F \leq 20 \text{ kV/cm}$, in the region near 1.56 eV , the exact solution can be reasonably well approximated by Kane functions. Nevertheless, even for the $(j_e, j_h) = (1, 1)$ transition and small fields, there are some differences between the exact solution and the Kane approximation. In the exact solution, the Wannier–Stark transitions as function of the electric field are no longer straight lines, but show a small quadratic Stark shift towards lower energies. Furthermore, the oscillator strength does not approach a constant with increasing field, but shows a small decrease even at moderate fields, $F \leq 60 \text{ kV/cm}$. This is a precursor of the Zener breakdown, and is a result of the delocalization of the eigenfunctions (cf. Fig. 4.5).

Besides the first miniband transition, we observe many other transitions: the allowed (2,2) transition, the weakly allowed (1,3) transitions, and even the forbidden (1,2) and (1,4) transitions. The terminology “allowed,” “weakly allowed,” and “forbidden” refers to the eigenstates of a single quantum well at $F = 0$. For a field-free superlattice, the situation is already complicated, because parity rules apply only for the symmetric points $k = 0$ and $k = \pm \frac{\pi}{a}$ and the transition probability for all other k is nonzero. For superlattices in an electric field, these categories are meaningless, as can be seen in the figure. However, practically, in a type-I superlattice, the (1,1) transition is always the dominant one and the oscillator strengths of the other transitions are much smaller.

There is a large number of anticrossings in the region $0 \leq F \leq 60 \text{ kV/cm}$, where in some cases the level repulsion is vanishingly small, in other cases it

is remarkable. At about 50 kV/cm, there is a number of nearly equidistant distinct lines, which on a single spectrum look like a Wannier–Stark ladder, but they stem from the $l = 0$ transitions of various Wannier–Stark ladders. Their oscillator strength is not at all related to the parity at $F = 0$; for example, the (1,2) transition is almost as strong as the (1,1) transition. Neither does the evolution of the oscillator strength with electric field follow a simple rule. Some transitions are absent at low fields, but resurface at larger fields or after they have undergone anticrossings with other transitions.

Most features in the low- and mid-field region could be explained within the Wannier–Stark-ladder picture, taking into account a finite number of minibands. Starting at about 55 kV/cm, the spectrum becomes noisy and the lines undergo a strong broadening. At the same time, the height of the peaks decrease, which cannot be clearly seen in the gray-scale plot because of the nonlinear scaling. For $F \geq 80$ kV/cm, there are no discrete lines anymore. This is a clear signature that all electron eigenfunctions are completely delocalized. The minima and maxima are not related to Wannier–Stark ladders. The spectrum has already some resemblance with the one-dimensional semiconductor in an electric field (see left part of Fig. 1.4). Nevertheless, even at 120 kV/cm, we are not yet in this limit, because the below-barrier hole states are still completely localized.

For Sample 2 with a much smaller Al content and lower barriers, the Zener breakdown is expected to take place already at much smaller fields. To verify this assumption, we have calculated the optical density of states (4.61) for Sample 2. We used the same parameters as above and a step size $\Delta z = a/230 = 0.5$ Å.

The left part of Fig. 4.7 shows the gray-scale plot of the optical density of states as function of photon energy and electric field. This time, we plot $D(\omega)$ instead of $D'(\omega)$ and use a linear scaling. This gives a better impression of the height of the individual peaks in an optical spectrum. We show only the region of the (1,1) transition. The oscillator strengths of other Wannier–Stark ladders are much smaller, and they will be even less pronounced in the presence of Coulomb interaction. Again, for small fields, we observe interference between Wannier–Stark and Franz–Keldysh oscillations. This region is larger than for Sample 1, because the miniband width (cf. Fig. 4.2) is larger. Outside this triangle, we see clear and distinct Wannier–Stark resonances. The side peaks ($l \neq 0$) have a much smaller oscillator strength than the main peak ($l = 0$) and their oscillator strength rapidly decreases as the field increases. At about 20 kV/cm, the side peaks have practically disappeared. This is an effect of the localization of the Kane functions and could also be observed in the Kane approximation: the overlap integral of electron and hole Kane functions (4.65) becomes smaller with increasing localization. In contrast, the oscillator strength of the main peak increases as the localization of the Kane function increases. This can be observed in the spectrum: the height of the main peak, which emerges at about 8 kV/cm, steadily increases with field

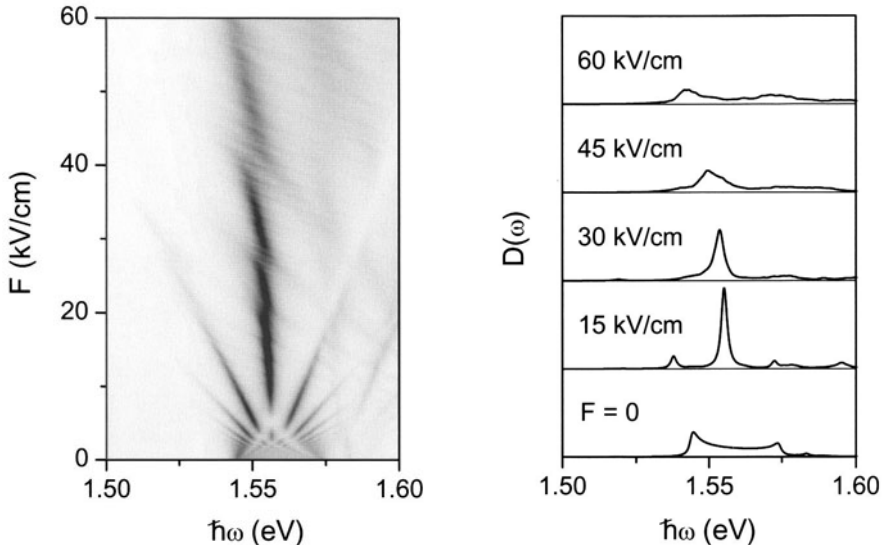


Fig. 4.7. Left: Gray-scale plot of $D(\omega)$ (linear scale) for Sample 2 as function of the photon energy $\hbar\omega$ and the electric field F . Right: $D(\omega)$ vs. ω for different values of the field $F = 0, 15, 30, 45$, and 60 kV/cm

and reaches a maximum at about 20 kV/cm. Up to this point, everything can be explained in the Kane approximation.

The situation changes for $F \geq 20$ kV/cm. In this region, we observe a decrease of the oscillator strength and a broadening of the resonance. At 60 kV/cm, one can no longer speak of a distinct line anymore; instead, the spectrum shows a weak maximum. As in the case of Sample 1, the evolution of the spectrum is interrupted by several anticrossings with higher Wannier–Stark ladders.

For more details, the right part of Fig. 4.7 shows individual spectra for different electric fields. For $F = 0$, the optical density of states is a continuum in the region of the first miniband transition $E_g + E_{e1}(0) + E_{h1}(0) < \hbar\omega < E_g + E_{e1}(\pm\frac{\pi}{a}) + E_{h1}(\pm\frac{\pi}{a})$ and vanishes outside. At the edges, the function shows $1/\sqrt{\omega}$ singularities, smeared out by convolution with a Lorentzian. At $F = 15$ kV/cm, we see a pronounced main peak ($l = 0$) at the center of the miniband and two small side peaks ($l = \pm 1$). At 30 kV/cm, the side peaks have disappeared and the height of the main peak has declined. At the same time, the peak shows some broadening beyond the homogeneous linewidth $\hbar\epsilon = 1$ meV. This is a signature that the spectrum of the electron has turned into a continuum. We shall later discuss this turning point when we study the Zener tunneling rate. For larger fields, $F \geq 45$ kV/cm one cannot speak of a single line anymore. Only a small maximum is left and the optical density of states remains nonzero in a large energy region.

The numerical results for the optical density of states are in good agreement with experimental data by Rosam and coworkers, which impressively demonstrate the Zener breakdown [70, 71]. Several features shown in the right part of Fig. 4.6 have been also found in experiments by Schneider et al. [43] and by Till et al. [65], but these authors did not yet detect the Zener breakdown.

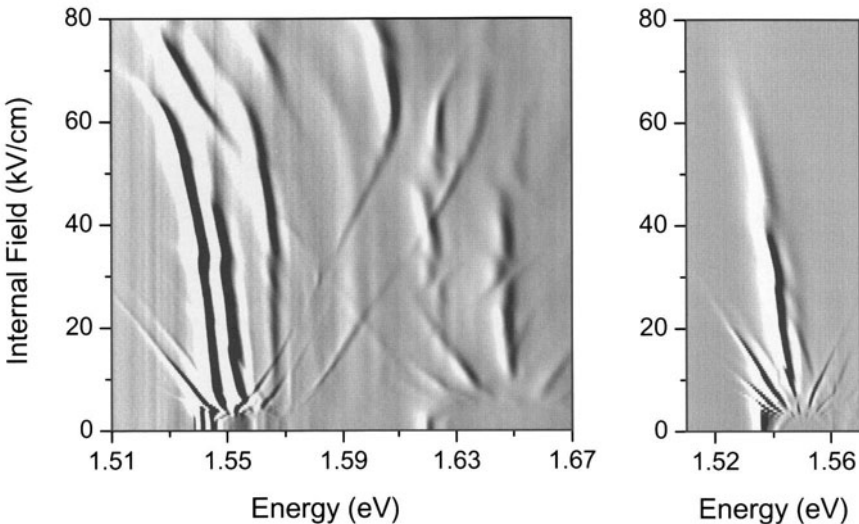


Fig. 4.8. Experimental data for Sample 1 (left) and Sample 2 (right) [70, 71]. The differentiated absorption $d\alpha/d\omega$ is shown as function of the energy $\hbar\omega$ and the electric field F (linear scale)

Figure 4.8 shows experimental data for Samples 1 and 2 [70, 71]. The derivative of the absorption coefficient is shown as function of the photon energy $\hbar\omega$ and the electric field F . The scaling of the gray-scale plot is linear. The theory (Figs. 4.6 and 4.7), even though it does not contain the Coulomb interaction, reproduces the experiment in great detail. The Coulomb interaction leads to excitonic transitions at the bottom of the miniband edges, which are seen as vertical lines in the experimental spectra around 1.54 eV. These lines dissolve at the transition to the Wannier–Stark regime, which takes place already at small fields, $F \geq 5 \text{ kV/cm}$. The influence of the Coulomb interaction will be studied in the next subsection.

Let us now concentrate on the region of intermediate and high fields. In the experimental spectra for Sample 1 (left part of Fig. 4.8), we observe many features, which are also found in the calculation (Fig. 4.6): two pronounced Wannier–Stark fans for the (1,1) and (2,2) transition, the (1,2) transition, which is visible only for nonzero field, and numerous anticrossings. The verti-

cal ($l = 0$) transitions of the (1,1) and (1,2) miniband pair show a bending to the left due to the Stark effect. At high fields, between 60 and 80 kV/cm, the vertical transitions disappear and there is a strong influence from anticrossings with other miniband transitions. The lines also show a significant broadening, compared with the low-field region. For the second miniband pair, the Wannier–Stark ladders completely disappear at about $F = 65$ kV/cm. This experiment clearly demonstrates that the Wannier–Stark picture (left part of Fig. 4.6) is valid only for small fields.

For Sample 2 (right part of Fig. 4.8), which is characterized by shallow barriers, the Zener breakdown takes place already at much lower fields, $F \approx 40$ kV/cm, in perfect agreement with the theory (Fig. 4.7). There are other features, like the modulation of the main peak by anticrossing with higher Wannier–Stark ladders, which are very well reproduced by the calculation.

4.3.2 Optical Absorption

The optical density of states, calculated in the last subsection, gives us an idea about the optical spectrum but does not include excitonic effects. For a close comparison with the experiment, we need to calculate the optical absorption. The absorption coefficient of a superlattice in an electric field can be measured by absorption or photocurrent experiments.

In Chap. 1, we have shown that the absorption coefficient $\alpha(\omega)$ is proportional to the imaginary part of the optical susceptibility $\chi(\omega)$, which can be expressed by the Elliott formula (1.96). For the geometry under consideration, we have

$$\chi(\omega) = \frac{|\mu|^2}{\varepsilon_0} \frac{1}{L_z} \sum_A \frac{\left| \int_{-L_z/2}^{+L_z/2} dz \Phi_A(\varrho=0, z, z) \right|^2}{E_g + \mathcal{E}_A - \hbar(\omega + i\epsilon)} . \quad (4.67)$$

The eigenvalues and eigenfunctions follow from the eigenvalue problem

$$\hat{H} \Phi_A(\varrho, z_e, z_h) = \mathcal{E}_A \Phi_A(\varrho, z_e, z_h)$$

$$\begin{aligned} \hat{H} = & -\frac{\hbar^2}{2m_\varrho} \Delta_\varrho - \frac{\hbar^2}{2m_e} \frac{\partial^2}{\partial z_e^2} - \frac{\hbar^2}{2m_{hz}} \frac{\partial^2}{\partial z_h^2} + U_e(z_e) + U_h(z_h) \quad (4.68) \\ & + e F(z_e - z_h) - \frac{e^2}{4\pi\varepsilon_0\varepsilon\sqrt{\varrho^2 + (z_e - z_h)^2}} , \end{aligned}$$

where Δ_ϱ denotes the radial part of the Laplacian (Table A.4) and the reduced in-plane mass is given by $1/m_\varrho = 1/m_e + 1/m_{h\varrho}$. The eigenfunctions are supposed to be normalized on a domain $[-L_z/2, +L_z/2] \times [-L_z/2, +L_z/2] \times [0, R]$ with volume element $d\varrho 2\pi\varrho dz_e dz_h$ and we consider the limit $L_z, R \rightarrow \infty$.

A direct solution of (4.67) in the variables ϱ , z_e , and z_h would be too costly because of the large domain. In the last subsection, we have seen that the problem can be reduced by taking into account the periodicity with respect to the center-of-mass coordinate. Then only eigenfunctions, which are periodic in Z have a nonzero oscillator strength and the optical susceptibility becomes

$$\chi(\omega) = \frac{|\mu|^2}{\varepsilon_0} \frac{1}{a} \sum_{\Lambda} \frac{\left| \int_{-a/2}^{+a/2} dZ \Psi_{\lambda}(\varrho=0, Z, z=0) \right|^2}{E_g + E_{\lambda} - \hbar(\omega + i\epsilon)} . \quad (4.69)$$

The periodic eigenfunctions $\Psi_{\lambda}(\varrho, Z, z)$ of the Hamiltonian (4.68) are normalized to unity on the domain $[0, R] \times [-\frac{a}{2}, +\frac{a}{2}] \times [-L_z/2, +L_z/2]$. This reduces the numerical effort by the factor $N = L_z/a$, which is of the order 100.

Besides a full numerical calculation, we shall also present an approximate solution in the single-band approximation, because this has become the standard in the numerical treatment of superlattices. The base functions used in the literature are either Kane or Wannier functions or tight-binding approximations of these functions [54, 56, 57, 60]; and there are also calculations in quasi-momentum space, which is equivalent to Wannier functions [58]. Here, we use the exact Wannier functions⁸ because of their symmetry and strong localization, which leads to a sparse matrix for the Hamiltonian.

The special Wannier functions of the first electron and hole miniband are orthonormal, i.e., $\langle w_{e1l} | w_{e1l'} \rangle = \delta_{ll'}$ and $\langle w_{h1l} | w_{h1l'} \rangle = \delta_{ll'}$, fulfill the ladder property $w_{e1l}(z) = w_{e10}(z-al)$; $w_{h1l}(z) = w_{h10}(z-al)$, and w_{e10} and w_{h10} are real and even functions. The eigenvalue problem (4.68) is solved approximately by projection onto electron and hole Wannier functions according to

$$\Phi_{\Lambda}(\varrho, z_e, z_h) = \sum_{l_e=-\infty}^{+\infty} \sum_{l_h=-\infty}^{+\infty} \Phi_{\Lambda;l_e l_h}(\varrho) w_{e1l_e}(z_e) w_{h1l_h}(z_h) . \quad (4.70)$$

The expansion coefficients $\Phi_{\Lambda;l_e l_h}(\varrho)$ are the solution of the eigenvalue problem

$$\sum_{l'_e=-\infty}^{+\infty} \sum_{l'_h=-\infty}^{+\infty} \hat{H}_{l_e l_h, l'_e l'_h} \Phi_{\Lambda;l'_e l'_h} = \mathcal{E}_{\Lambda} \Phi_{\Lambda;l_e l_h} \quad (4.71)$$

$$\hat{H}_{l_e l_h, l'_e l'_h} = \int_{-\infty}^{+\infty} dz_e \int_{-\infty}^{+\infty} dz_h w_{e1l_e}(z_e) w_{h1l_h}(z_h) \hat{H} w_{e1l'_e}(z_e) w_{h1l'_h}(z_h) ,$$

and are normalized in the usual manner.

⁸ The electron Wannier function is shown in the right part of Fig. 4.4; the hole Wannier function is much more localized and is nearly identical to the single-well eigenfunction.

Again, finite domains for z_e and z_h do not comply with the translational properties of the eigenvalue problem. However, in the limit of large L_z , the integral in the numerator of (4.67) is asymptotically equal to

$$\begin{aligned} \int_{-L_z/2}^{+L_z/2} dz \sum_{l_e, l_h = -\infty}^{+\infty} \Phi_{\Lambda; l_e l_h}(\varrho) w_{e1l_e}(z) w_{h1l_h}(z) &= \sum_{l_h = -\frac{N}{2}}^{+\frac{N}{2}} \sum_{l = -\infty}^{+\infty} \Phi_{l_h + l, l_h}(\varrho) f_l \\ f_{l_e - l_h} &= \int_{-\infty}^{+\infty} dz w_{e1l_e}(z) w_{h1l_h}(z). \end{aligned} \quad (4.72)$$

The pair of variables l_h and $l = l_e - l_h$ can be considered as the discrete analog of center and relative coordinate. The matrix elements of \hat{H} (4.71) are invariant under translation of all indices by the same amount and, therefore, depend only on the variables l , l' , and $l_h - l'_h$. Introducing periodic boundary conditions with respect to l_h , the eigenfunctions can be written as

$$\Phi_{Q\lambda; l_e l_h}(\varrho) = e^{iQl_h} \Psi_{Q\lambda; l_e - l_h}(\varrho) / \sqrt{N}, \quad (4.73)$$

where Q is a wavenumber from the discretized Brillouin zone $[-\pi, +\pi]$ and λ is a discrete quantum number if the domain of the radial motion is finite. This form of the eigenfunctions can be considered as a discrete version of the Bloch theorem.

The sum (4.72) gives the selection rule $Q = 0$ and only solutions which are invariant against lattice translation of electron and hole contribute to the optical absorption. The factor \sqrt{N}^2 cancels the prefactor $1/N$ in (4.67) and the result for the optical susceptibility is

$$\chi(\omega) = \frac{|\mu|^2}{\varepsilon_0} \frac{1}{a} \sum_{\lambda} \frac{\left| \sum_{l=-\infty}^{+\infty} \Psi_{\lambda;l}(\varrho) f_l \right|^2}{E_g + \mathcal{E}_{\lambda} - \hbar(\omega + ie)}, \quad (4.74)$$

where we wrote $\mathcal{E}_{\lambda} = \mathcal{E}_{Q=0,\lambda}$ and $\Psi_{\lambda;l} = \Psi_{Q=0,\lambda;l}$. From the normalization of the $\Phi_{\Lambda; l_e l_h}$ and the ansatz (4.73) it follows that the eigenfunctions of the relative motion are normalized as

$$\sum_{l=-\infty}^{+\infty} \int_0^R d\varrho 2\pi \varrho \Psi_{\lambda;l}^*(\varrho) \Psi_{\lambda';l}(\varrho) = \delta_{\lambda\lambda'}, \quad (4.75)$$

Inserting the two-particle Bloch function (4.73) for $Q = 0$ into the eigenvalue problem (4.71) and taking into account the translational invariance of $\hat{H}_{l_e l_h, l'_e l'_h}$, we obtain the eigenvalue problem for the relative motion:

$$\sum_{l'=-\infty}^{+\infty} \hat{H}_{ll'} \Psi_{\lambda;l'}(\varrho) = \mathcal{E}_{\lambda} \Psi_{\lambda;l}(\varrho); \quad \hat{H}_{ll'} = \sum_{l'_h=-\infty}^{+\infty} \hat{H}_{l,0; l'_h + l', l'_h}. \quad (4.76)$$

The matrix elements $\hat{H}_{ll'}$ of the reduced Hamiltonian follow from (4.71) and (4.76) and the symmetry properties of the special Wannier functions. A straightforward calculation gives:

$$\begin{aligned}\hat{H}_{ll'} = & -\frac{\hbar^2}{2m_\varrho} \Delta_\varrho \delta_{ll'} + \int_{-\infty}^{+\infty} dz w_{e1l}(z) \left[-\frac{\hbar^2}{2m_e} \frac{d^2}{dz^2} + U_e(z) \right] w_{e1l'}(z) \\ & + \int_{-\infty}^{+\infty} dz w_{h1l}(z) \left[-\frac{\hbar^2}{2m_{h_z}} \frac{d^2}{dz^2} + U_h(z) \right] w_{h1l'}(z) + e F a l \delta_{ll'} - V_{ll'}(\varrho),\end{aligned}\quad (4.77)$$

where

$$\begin{aligned}V_{ll'}(\varrho) &= \int_{-\infty}^{+\infty} dz \frac{e^2}{4\pi\epsilon_0\varepsilon\sqrt{\varrho^2+z^2}} F_{ll'}(z) \\ F_{ll'}(z) &= \int_{-\infty}^{+\infty} dZ w_{e1l}(Z+z) w_{h10}(Z) \sum_{l'_h=-\infty}^{+\infty} w_{e1,l'_h+l'}(Z+z) w_{h1,l'_h}(Z).\end{aligned}\quad (4.78)$$

We see that in the “discretized” version, the optical absorption depends only on the relative motion of the exciton. The result (4.74–4.78) can also be found using the base functions

$$W_l(Z, z) = \sum_{l_h=-\infty}^{+\infty} w_{e1,l+l_h}(z_e) w_{h1l_h}(z_h), \quad (4.79)$$

which are periodic in Z and orthonormal on $[-\frac{a}{2}, +\frac{a}{2}] \times (-\infty, +\infty)$, similar to the exciton Wannier functions used by Dignam and Sipe [53, 54] and by Whittaker [57]. Equations (4.74–4.76) take the same form if the Hamiltonian (4.68) is expanded into Kane functions instead of Wannier functions. Then the reduced Hamiltonian is $\hat{H}_{ll'} = [\hbar^2/(2m_\varrho) \Delta_\varrho + E_{e10} + E_{h10} + eF a l] \delta_{ll'} - V_{ll'}(\varrho)$, where $V_{ll'}(\varrho)$ is calculated in analogy to (4.78). This would somewhat reduce the numerical effort for the application of $\hat{H}_{ll'}$ but, at the same time, increase the effort for the calculation of the Coulomb matrix elements because of the larger extension of the Kane functions. The result should be exactly the same, because Kane and Wannier functions are related by unitary transformation.

Finally, we show numerical results for Sample 2 and make a comparison with experimental spectra. We start with a few remarks on the numerical solution. For the formulation in real space (4.69), any definition of center and relative coordinate could be used with $Z = \alpha z_e + \beta z_h$; $z = z_e - z_h$; $\alpha, \beta \in \mathbb{R}$; $\alpha + \beta = 1$ (see also [53]). The usual choice $\alpha = m_e/(m_e+m_h)$; $\beta = m_h/(m_e+m_h)$ (center-of-mass and relative coordinates) avoids mixed derivatives [see (4.62)], but leads to different meshes for z_e and z_h and to a

loss of accuracy. A better choice from the numerical standpoint is $Z = z_h ; z = z_e - z_h$ (i.e., $\alpha = 0$; $\beta = 1$), where electron and hole have the same fixed mesh. In this case, there is also no reason to transform the differential operator (4.68) to the new coordinates Z and z . Instead, the second derivatives can be calculated directly:

$$\frac{\partial^2}{\partial z_e^2} \varphi(Z, z) = \frac{\varphi(Z, z+\Delta z) - 2\varphi(Z, z) + \varphi(Z, z-\Delta z)}{2(\Delta z)^2} \quad (4.80)$$

$$\frac{\partial^2}{\partial z_h^2} \varphi(Z, z) = \frac{\varphi(Z+\Delta z, z-\Delta z) - 2\varphi(Z, z) + \varphi(Z-\Delta z, z+\Delta z)}{2(\Delta z)^2}.$$

The numerical parameters are: $L_z = 150a$, $\Delta z = a/20$, and $\Delta\varrho = 1/8$ a.u. For the z direction, we use vanishing boundary conditions. The periodicity with respect to the variable Z is enforced by setting the points $Z = \pm \frac{a}{2}$ equivalent. For the ϱ direction, we use absorbing boundary conditions with a complex mass according to (2.148) and an inner and outer radius $R_1 = 15$ a.u. and $R_2 = 20$ a.u. This further reduces the numerical effort by about a factor of five. The operator of the in-plane kinetic energy is discretized according to (2.146).

The Coulomb matrix elements were calculated by the method described in Sect. 3.3. The ground-state method (2.98) was also applied for the discretization of the regular potentials U_e and U_h , which increases the accuracy and helps to keep the step size Δz at a reasonable value. The ground-state energies and wavefunctions necessary for the calculation of the potentials were found by the numerical solution of (4.4) for $k = 0$.

In the Wannier–Stark base, for the discretization of the operator (4.77), we use the same step size as above. For this problem, the numerical effort is so low that absorbing boundary conditions are not necessary. The normalization radius was chosen to be $R = 128$ a.u. Both formulations (4.69) and (4.74) were converted into initial-value problems and solved by the methods of Sect. 2.3. As in the calculation of the optical density of states, the homogeneous broadening was chosen to be $\hbar\epsilon = 1$ meV.

The result of the calculation is shown in the left part of Fig. 4.9. The numerically exact solution (*solid line*) is compared with the expansion into Wannier functions (*dashed line*). At $F = 0$, we observe a single peak from the ground-state exciton and a flat continuum, which is associated with the $(n_e, n_h) = (1, 1)$ miniband transition. The numerically exact solution takes into account higher miniband transitions, but their transition energies are outside the range of the abscissa. For small field ($F = 10$ kV/cm), we observe a Wannier–Stark ladder. The asymmetric lineshape follows from the Fano interference between bound states of higher Wannier–Stark levels with continuum states of lower Wannier–Stark ladders [46, 57]. In principle, all excitons are Fano resonances, because the number of Wannier–Stark ladders is infinite. However, the lineshape parameter q (3.15) becomes smaller in magnitude with increasing Wannier–Stark index l , because the continuum level

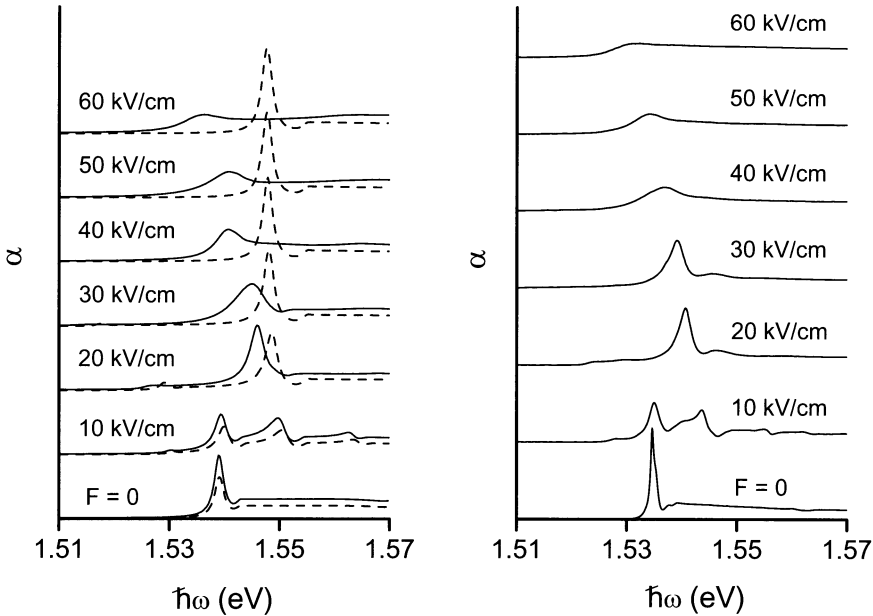


Fig. 4.9. Optical absorption of Sample 2 in a perpendicular electric field. Left: Theoretical results. The result of the full numerical calculation (4.69, *solid line*) is compared with the expansion into Wannier functions (4.74, *dashed line*). Right: Experimental results (from [72])

increases. In comparison to the optical density of states (Fig. 4.7), the peak maxima are shifted to lower energies because of the Coulomb interaction. Furthermore, we see that the peaks are not equidistant: the distance between the left ($l = -1$) and middle ($l = 0$) peak is smaller than the distance between middle ($l = 0$) and right ($l = +1$) peak. This is because the Coulomb matrix elements $V_{00}(\varrho)$ are the largest in magnitude and the exciton binding energy of the main peak ($l = 0$) is larger than the exciton binding energy of the side peaks ($l \neq 0$). This was noticed first by Dignam and Sipe, and is called absorption asymmetry [54, 56]. In the region of small fields, exact and approximate solution show the same qualitative behavior. However, there are quantitative differences. The absolute height of the absorption spectrum is smaller for the approximate solution. This is not because the single-particle eigenstates are different (they are in fact very similar at low fields; cf. Fig. 4.5), but is an effect of neglecting Coulomb interaction with nonresonant minibands, which significantly contribute to the oscillator strength (see also the discussion of Fig. 3.6). The effect is relatively large in this case because of the shallow barriers of Sample 2.

At 20 kV/cm, we see only one pronounced peak from the main transition. The side peaks are shifted far away and have a very small oscillator strength.

The height of the main peak is much larger than for 10 kV/cm , which is an effect of both the stronger localization of the Kane functions and the increase of lineshape parameter $|q|$, because the supply of continuum states from the $l = -1$ transition is drastically reduced. Furthermore, the main peak of the exact solution is shifted to the left, compared to the approximate solution. This is due to the Stark shift of the single-particle energies, mainly of the electron.

For large fields $F \geq 30\text{ kV/cm}$, the behavior of approximate and exact solution is very different. The oscillator strength of the approximate solution still increases; the absorption spectrum becomes independent of the electric field and approaches that of a two-dimensional semiconductor. In contrast, the main peak of the exact solution shows a strong red shift and the line broadening drastically increases. At 60 kV/cm , one can no longer speak of an absorption line; instead the optical spectrum has become a flat continuum.

The right part of Fig. 4.9 shows experimental spectra, measured by Rosam and Leo [72]. The homogeneous line broadening at $F = 0$ is about 0.6 meV , which is smaller than the value 1 meV used in the calculation.⁹ For nonzero electric field, the difference of the homogeneous line broadenings in theory and experiment is of minor importance, because the actual line broadening is determined by Fano interference and Zener tunneling.¹⁰ With increasing electric field, we observe exactly the same phenomena as predicted by the exact numerical solution: a quadratic Stark shift, a strong line broadening, and the transition into a flat continuum. The evolution of the line broadening slightly deviates from the theoretical result. For example, the experimental line broadening at 30 kV/cm is smaller than in theory, while it is the other way around at 40 kV/cm . This is because the linewidth shows resonances due to anticrossings of the first electron Wannier–Stark ladder with higher Wannier–Stark ladders, which are not as accurately reproduced by theory, and possibly light-hole transitions, which are not considered in theory. The evolution of the linewidth and the influence of anticrossings will be studied in more detail in the next section. Apart from these small differences, the agreement between the full numerical calculation and the experiment is excellent. Furthermore, the comparison of the experimental data with the approximate solutions, based upon Wannier functions, clearly shows the failure of the picture of Wannier–Stark ladders at high fields.

⁹ The calculations were performed prior to the analysis of the experimental data.

¹⁰ There is a never ending discussion if the line broadening due to Fano interference or Zener tunneling is homogeneous or inhomogeneous. From the theoretical standpoint, any broadening which results from the continuous nature of the spectrum of the electron–hole-pair Hamiltonian is inhomogeneous, while interaction with the “environment” (phonons, defects, impurities) in the fast modulation limit results in homogeneous broadening, subsumed in the decay constant ϵ .

4.3.3 Optical Absorption in a Perpendicular Magnetic Field

The results presented in Fig. 4.9 impressively demonstrate the Zener breakdown in the optical absorption of a superlattice and the numerical results agree very well with the experimental data. However, the experiment cannot be considered as a direct observation of Zener tunneling, because the lines are also broadened by Fano interference. In fact, the Wannier–Stark levels are never discrete, but always have a finite broadening. If this broadening is much smaller than the natural line broadening caused by Fano interference, we observe Fano resonances. In the opposite case, when the line broadening of the Wannier–Stark resonances is much larger than the line broadening due to Fano interference, we observe the Zener effect. The Zener effect could also be understood as Fano interference between confined states inside the wells and the continuum of the unrestricted motion in $-F$ direction. If the phase of the coupling is assumed to be completely random, the Fano model (Sect. 3.1) would give a Lorentzian broadening, which is nearly found true in the experimental data and the results of the numerical calculation.

The transition from Fano broadening to Zener broadening in Fig. 4.9 is unclear. The Fano interference can be switched off by applying an additional magnetic field in the growth direction of the superlattice. Then, the in-plane motion, which is asymptotically free for $B = 0$, is subjected to Landau quantization. Suppose that the picture of discrete Wannier–Stark ladders is correct, then the optical spectrum is entirely discrete, and it is a superposition of different Wannier–Stark ladders, which belong to different Landau levels. Coulomb interaction and valence-band mixing do not change the picture qualitatively. In this configuration, any increase of the line broadening with increasing electric field should be on the account of Zener tunneling.

In order to calculate the absorption spectrum in a perpendicular magnetic field, only a very small change has to be made to (4.69) and (4.74). It is shown in App. C.1.2 that center-of-mass and relative motion of the exciton perpendicular to the magnetic field can be separated and the only effect of the magnetic field is an additional parabolic potential $(eB\varrho)^2/(8m_\varrho)$. For the study of the Zener breakdown, a large magnetic field is favorable, because it increases the separation between the different Landau levels and allows to better observe the evolution of the line broadening. Therefore, we use a magnetic field of $B = 9\text{ T}$. The parameters of the numerical solution are $L_z = 150a \dots 250a$, $\Delta z = a/20 \dots a/28$, $R = 9\text{ a.u.}$, and $\Delta\varrho = 1/9\text{ a.u.}$, where vanishing boundary conditions are used for the ϱ direction.

Absorption spectra in the Faraday geometry are shown in Fig. 4.10. The results of the calculation (left) are compared with experimental spectra taken by Meinholt et al. [73] (right). Again, in the numerical results the *solid line* represents the exact solution and the one-miniband approximation is shown as a *dashed line*. The spectrum at $F = 0$ starts with a series of Landau levels, characterized by quantum numbers $n = 0, 1, 2, \dots$, which are nearly equidistant, except for the lowest peak. This is similar to the spectrum of a

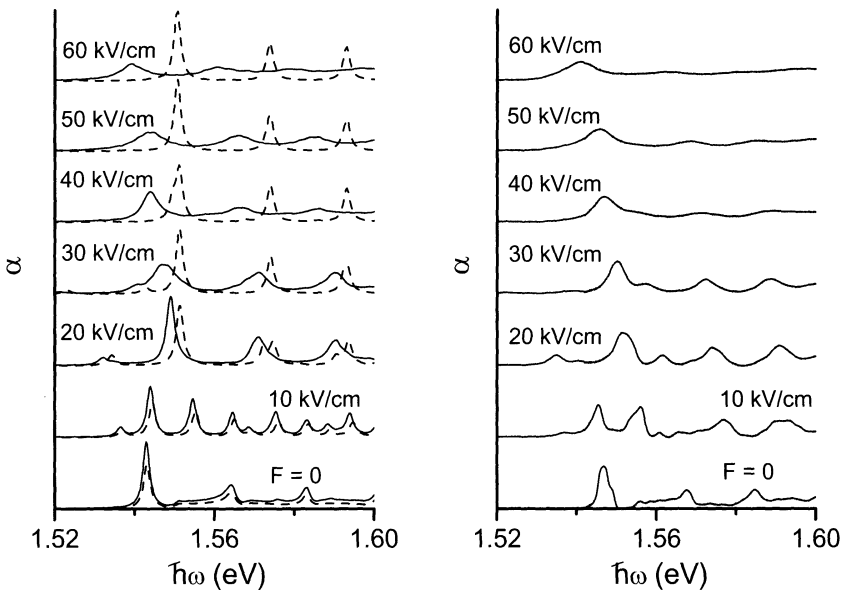


Fig. 4.10. Optical absorption of Sample 2 in Faraday geometry for fixed magnetic field $B = 9\text{ T}$ and different electric fields. Left: Numerical results. The one-band approximation is shown as a *dashed line*. Right: Experimental spectra for left-circular polarization (from [73])

bulk semiconductor in a magnetic field (Fig. 3.7). The first Landau level ($n = 1$) has a Fano lineshape, because of the interaction with the continuum of the zeroth Landau level. This feature is also clearly observed in the experiment (right) and the lineshape parameters are of the same order of magnitude. At low electric fields, $F = 10\text{ kV/cm}$, we see an ensemble of irregularly spaced lines, which stem from different Wannier–Stark states and Landau levels. The spectrum is entirely discrete and the lines have all a Lorentzian shape with a broadening $\hbar\epsilon = 1\text{ meV}$. Exact and approximate solution are in good agreement, except for the difference of oscillator strengths, which was already observed in Fig. 4.9. With increasing energy, the peak positions of exact and approximate solution become slightly different, because of the influence of excited minibands, which are neglected in the approximate solution. So far, every feature can be explained in the picture of discrete Wannier–Stark levels. The transition from a three- to a two-dimensional semiconductor when F is changed from zero to a finite value has been observed experimentally already in 1990 by Ferreira et al. [61].

First qualitative differences between exact and approximate solutions can be observed at $F = 20\text{ kV/cm}$. There is a strong peak at $\hbar\omega \approx 1.55\text{ meV}$, which belongs to the quantum numbers $l = 0; n = 0$. This peak does not show

a significant inhomogeneous broadening. However, a broadening is observed for the excited Landau levels $n \geq 1$ and increases with the Landau quantum number n . The reason is the Coulomb interaction between electron and hole, which tends to compensate the external electric field. This effect is stronger for low Landau quantum numbers. The approximate solution does not show any broadening. The lines above the main transition have a double-peak structure, because the separation of the Wannier–Stark levels is about the same as for the Landau levels. In the exact solution, the peak maxima are slightly red-shifted because of the Stark effect.

For large electric fields, $F \geq 30 \text{ kV/cm}$, only Wannier–Stark states with $l = 0$ play a role, because the overlap between electron and hole eigenfunctions from different layers is vanishingly small. This holds qualitatively true also for the exact solution. In this field range, we observe a completely different behavior of exact and approximate solution. The approximate solution becomes independent of the electric field and resembles the absorption spectrum of a quantum well in a perpendicular magnetic field (cf. Fig. 2.2). In contrast, in the exact solution, the lines show a strong Stark shift and a homogeneous broadening due to Zener tunneling. The discrete lines gradually disappear with electric field, starting from the high Landau quantum numbers. At 60 kV/cm , only the two lowest peaks survive. The broadening of the lowest peak is somewhat smaller than for $B = 0$ (cf. Fig. 4.9), which is an effect of the increased exciton binding energy: An increase of the binding energy by a factor of 2 has the same effect as a reduction of the external field by about 8 kV/cm (App. B.2). Surprisingly, for intermediate or large fields, the spectrum shows only one ladder, even in the Kane approximation. A detailed study reveals a complicated interference pattern between Wannier–Stark and Landau quantization [44, 104].

The experimental spectra (right of Fig. 4.10) qualitatively behave as predicted by the theory and demonstrate the transition from a discrete spectrum to a continuum. The agreement between theory and experiment is not as good as for $B = 0$ (Fig. 4.9) because of the complicated valence-band structure, which is ignored in theory (see also the discussion of Fig. 3.8). For low fields, $F \leq 20 \text{ kV/cm}$, some lines are actually double peaks. Starting at about 30 kV/cm , the results of the full calculation and the experimental spectra are very similar and the line shift as well as the broadening are of the same order of magnitude. The experimental spectra do no longer show any sharp resonances, as predicted in the Wannier–Stark picture. Again, apart from small details, theory and experiment are fully consistent. In the next subsection, as the last piece of the puzzle, we shall prove that the evolution of the linewidth with field follows the tunneling rate predicted by Zener theory.

4.4 The Tunneling Rate

In his pioneering work, Zener calculated the tunneling rate by means of a semiclassical approach, where the forbidden region was assigned to a complex Bloch wavenumber [6]. The idea of tunneling through complex branch points had been published already in 1932 – two years before Zener – by Landau [105]. The Landau–Zener theory of tunneling has important applications in physics and quantum chemistry [106].

Starting with the works of Houston [7], Adams [9, 10], and Kane [12, 14], the Zener theory took another direction. In the framework of the crystal-momentum representation, the tunneling rate is calculated by means of quantum-mechanical perturbation theory [7, 10–12, 16, 107]. For small fields, the result goes over into the semiclassical result [98, 99].

It is difficult to judge whether or not the perturbational result is an improvement over the semiclassical result, because both results are asymptotically equal for small F , but become inaccurate for large F . Furthermore, the quantum-mechanical approach, which appears to be more rigorous than the semiclassical one, still faces a number of conceptual difficulties and relies upon assumptions, which cannot be rigorously justified. This question has hardly been thoroughly addressed in the literature.

What are the alternatives? Of course, Bloch oscillations and Zener tunneling can be treated numerically, as done by several authors in different contexts [63, 64, 79, 80]. A problem, even more difficult than the calculation of the tunneling rate, is a rigorous definition. In the mathematical theory, the tunneling rate can be defined by the imaginary part of the ladder resonances.

This approach can also be used as the basis for numerical calculations [81], but is limited to (complex) analytic potentials $U(z)$. In our case, one could directly compare the theoretical and experimental linewidth, but this would give little physical insight.

The tunneling rate derived by Zener [6] increases monotonously with the electric field. Intuitively, one would expect an increase of the tunneling rate when two eigenstates of different Wannier–Stark ladders approach each other. This effect, which is called resonant tunneling, has been observed experimentally [66–68] and also studied analytically on the basis of the Houston–Kane theory [108].

In this chapter we rederive Zener’s result and then calculate the tunneling rate by means of perturbation theory. We correct an inconsistency in the literature and clarify the relation between the semiclassical result and the result of perturbation theory. Finally, we make a comparison between theory and experimental results, which shows that our result for the tunneling rate reproduces both nonresonant and resonant Zener tunneling. For general reading on Zener theory, we refer to a recent review article by Holthaus [80]. The mentioned paper also makes a comparison between semiclassical theory and numerical calculations. A historical review on the Landau–Zener theory is found in an article by Nikitin [106].

4.4.1 Semiclassical Approach

The semiclassical approach, developed seventy years ago by Zener, has been very powerful to explain the electric breakdown in insulators [6]. The method is very easy and intuitive; the result is physically plausible and has hardly been surpassed by later approaches. Therefore, in this subsection, we outline the basic idea and rederive Zener's result for the case of nearly free electrons. Besides of Zener's original paper [6], the derivation can also be found in the article by Holthaus [80] and in the textbook by Ziman [109].

In Sect. 1.1, we have derived an approximate solution for the Bloch electron in external fields by introduction of an envelope function. This function is assumed to obey an eigenvalue equation of the form

$$E_j(-i\frac{d}{dz})\varphi(z) + eFz\varphi(z) = \mathcal{E}\varphi(z), \quad (4.81)$$

where $E_j(k)$ is the dispersion of the j -th miniband, which is an analytic function (power series) of k . It is usually replaced by a parabolic approximation near a critical point k_0 . Here, we assume the envelope function to be valid in a larger section of the Brillouin zone.

Equation (4.81) can be solved approximately by the WKB method [37, 85, 86, 110]. Then the eigenfunction is given by¹¹

$$\varphi(z) = c \exp \left[i \int_{z_0}^z d\zeta k(\zeta) \right], \quad (4.82)$$

where the z -dependent wavenumber k fulfills

$$E_j[k(z)] = \mathcal{E} - eFz. \quad (4.83)$$

A solution for $k(z)$ exists only if the kinetic energy $\mathcal{E} - eFz$ falls into an allowed energy band. According to an idea of Zener, the forbidden regions correspond to complex values of the wavenumber k . The imaginary part causes damping of the wavefunction and a probability of reaching the next band smaller than unity.

The situation can be demonstrated in the “tilted-band picture” shown in the left part of Fig. 4.11. Here, $E_j(k) + eFz$ is plotted versus the coordinate z . The horizontal line is a line of constant energy $E_j(k) + eFz = \mathcal{E} = \text{const}$. The wavenumber k is real between the points A and B, because the electrons are located in the j -th band. In the energetically forbidden region between B and C the wavenumber is complex. The probability density $|\varphi(z)|^2$ decreases and only a portion of the carriers arrives at the $j+1$ -th band, while the others are “Bragg reflected” at the band extremum to enter the next Bloch cycle. The

¹¹ This is only the lowest order. For conventional tunneling, where k^2 is real, the additional terms lead to a z -dependent prefactor in (4.82), which is proportional to $1/\sqrt{|k(z)|}$. In the Zener literature, this effect is usually ignored. It has been shown only recently that in this case $c = \text{const}$ [111]; see also the remarks in [80].

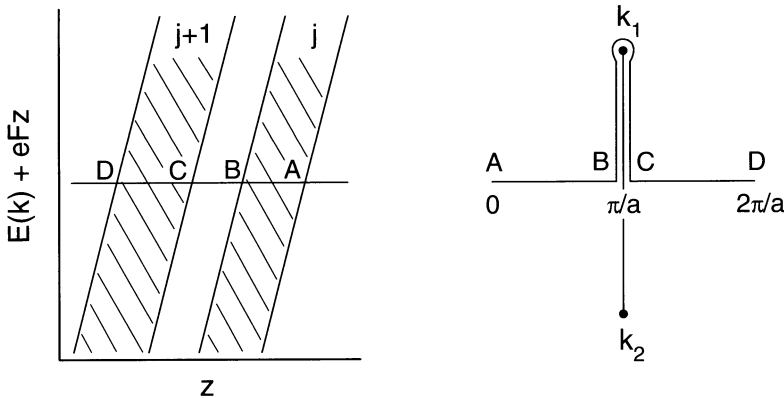


Fig. 4.11. Left: Tilted-band picture, $E(k) + eFz$ vs. z . The horizontal line is a line of constant energy \mathcal{E} . Right: Complex wavenumber k during tunneling from the first to the second band. The sign convention (4.85) is assumed

wavenumber is real again between the points C and D, when the electrons are situated in the $j+1$ -th band.

The semiclassical tunneling probability from B to C is given by

$$\begin{aligned} p &= \left| \frac{\varphi(C)}{\varphi(B)} \right|^2 = \exp \left[-2 \int_B^C dz \operatorname{Im} k(z) \right] \\ &= \exp \left[\frac{2}{eF} \int_{E_j \text{ max}}^{E_{j+1, \text{ min}}} dE \operatorname{Im} k(E) \right]. \end{aligned} \quad (4.84)$$

This quantity is equal to the proportion of carriers tunneling from the j -th to the $j+1$ -th band during one Bloch period $T_{\text{BO}} = 2\pi\hbar/|eFa|$. Thus the tunneling rate w is the ratio of the tunneling probability and the period of the Bloch oscillations

$$w = \frac{p}{T_{\text{BO}}} = \frac{|eF|a}{2\pi\hbar} \exp \left[-\frac{2}{|eF|} \int_{E_j \text{ max}}^{E_{j+1, \text{ min}}} dE \operatorname{Im} k(E) \right]; \quad \operatorname{Im} k(E) \geq 0. \quad (4.85)$$

The restriction to the upper half plane is necessary, because for each E in the gap there are two solutions k and k^* , one leading to damping and the other one to amplification.

So far, it is not clear whether there exist such connection between bands in the complex k plane. We shall now demonstrate the proposed procedure for nearly free electrons (Sect. 4.1), where the band dispersions are known analytically. The dispersion of the first and second miniband near the critical

point $k_0 = \frac{\pi}{a}$ are given by formula (4.18) with $K = 0$ and $K' = -\frac{2\pi}{a}$ and it holds that

$$E_{1,2}(k) = \frac{\hbar^2(\frac{\pi}{a})^2}{2m} + \frac{\hbar^2(k-\frac{\pi}{a})^2}{2m} \pm \sqrt{\frac{\hbar^2(k-\frac{\pi}{a})^2\hbar^2(\frac{\pi}{a})^2}{m^2} + |\tilde{U}_{2\pi/a}|^2}. \quad (4.86)$$

Here, we ignore the zeroth Fourier coefficient \tilde{U}_0 , which only shifts the energy scale and has no influence on the tunneling rate.

The extrema of the function (4.86) are at the symmetric point $k_0 = \frac{\pi}{a}$ and it holds that $E_{1\max} = \hbar^2(\frac{\pi}{a})^2/(2m) - |\tilde{U}_{2\pi/a}|$ and $E_{2\min} = \hbar^2(\frac{\pi}{a})^2/(2m) + |\tilde{U}_{2\pi/a}|$. Thus the gap is equal to $E_g^* = 2|\tilde{U}_{2\pi/a}|$. For the transition energy near the critical point we find that

$$E_2(k) - E_1(k) = E_g^* + \frac{\hbar^2(k-k_0)^2}{2m^*}; \quad m^* = \frac{|\tilde{U}_{2\pi/a}|a^2m^2}{2\hbar^2\pi^2}, \quad (4.87)$$

where m^* plays the role of a reduced effective mass (see Secs. 1.2 and 1.3).

The dispersion (4.86) as complex function of k has two branch points

$$k_{1,2} = \frac{\pi}{a} \pm i \frac{mE_g^*}{2\hbar^2\frac{\pi}{a}}, \quad (4.88)$$

for which the square root becomes zero. They are located above and below the point k_0 on the real axis. Uniqueness of the function $E(k)$ can be enforced by introducing a cut from k_1 straight through k_2 . The Riemann surface then consists of two sheets, where the left and right branch of the upper and lower sheet are mutually connected.

To determine $k(E)$ in the gap region [$E_{1\max}$, $E_{2\min}$], we note from (4.86) that E is real on the cut between the branch points. Therefore, $\text{Re } k(E) = k_0$. For the imaginary part we find that

$$\begin{aligned} \frac{\hbar^2(\text{Im } k)^2}{2m} &= - \left[E + \frac{\hbar^2(\frac{\pi}{a})^2}{2m} \right] \\ &\quad + \sqrt{\left[E + \frac{\hbar^2(\frac{\pi}{a})^2}{2m} \right]^2 + \frac{E_g^{*2}}{4} - \left[E - \frac{\hbar^2(\frac{\pi}{a})^2}{2m} \right]^2}. \end{aligned} \quad (4.89)$$

Expanding the square root in lowest order in the small quantities yields

$$\text{Im } k = \frac{m}{\hbar^2(\frac{\pi}{a})^2} \sqrt{\frac{E_g^{*2}}{4} - \left[E - \frac{\hbar^2(\frac{\pi}{a})^2}{2m} \right]^2}. \quad (4.90)$$

It is interesting to watch the evolution of $k(E)$ during the tunneling process. This is shown in the right part of Fig. 4.11. From the minimum to the maximum of the first band (A-B) the wavevector travels on the real axis from $k = 0$ to $k = k_0 = \frac{\pi}{a}$. In the gap region (B-C), k moves along the left

branch to the upper half plane, circles the branch point k_1 , and returns to the real axis on the right branch. The motion from the bottom to the top of the second band (C–D) corresponds to the interval $k_0 = \frac{\pi}{a} < k < \frac{2\pi}{a}$ on the upper sheet.

With the solution (4.90), the integral in (4.85) is elementary and for the tunneling rate we find

$$w = \frac{|eF|a}{2\pi\hbar} \exp\left(-\frac{m a E_g^{*2}}{4\hbar^2|eF|}\right), \quad (4.91)$$

which is the famous result by Zener [6]. In the limit of small fields, the tunneling rate rapidly approaches zero. The transition between the low- and high-field limits takes place at a field strength of about $|F| = maE_g^{*2}/(4\hbar^2|e|)$. For large fields, the leading term is $w \sim 1/T_{\text{BO}}$, which means physically that all carriers tunnel during one Bloch period. The accuracy of the semiclassical approach should increase for small fields, but the limit of large fields is also not unphysical and, even though there is no rigorous justification for the ansatz (4.81), (4.91) seems to be a good overall approximation.

The integration variable in (4.85) can be changed and the tunneling rate can be written in an alternative form [39, 80]

$$w = \frac{|eF|a}{2\pi\hbar} \exp\left[\frac{1}{i|eF|} \oint dk E(k)\right], \quad (4.92)$$

where $E(k)$ is the complex dispersion and the integration is carried out on a closed contour, cycling the branch points k_1 and k_2 (cf. Fig. 4.11) clockwise. This formulation directly leads to (4.91) without the approximation (4.90).

The analytical properties of the energy bands, discussed for nearly free electrons, are generally valid for one-dimensional Bloch electrons [88]. Therefore, the semiclassical approach and the result (4.92) are not limited to nearly free electrons. This raises the important question if formula (4.91) can be used beyond nearly free electrons. It is plausible that the gap region makes the main contribution to the tunneling rate, while the dispersion far away should be of minor influence. Therefore, the tunneling rate, expressed as function of the effective-mass parameters (4.87),

$$w = \frac{|eF|a}{2\pi\hbar} \exp\left(-\frac{\sqrt{m^*} \pi E_g^{*3/2}}{2\hbar|eF|}\right), \quad (4.93)$$

should not crucially depend on the assumption of nearly free electrons. The formula (4.93) was first published by McAfee et al. [112], and was derived by Franz without the assumption of nearly free electrons [113]. Eilenberger found that both the limit of nearly free electrons and the limit of tightly bound electrons leads to the same result, (4.93), except for a factor $\pi^2/9$, which frequently appears in the context of Zener theory [99]. Therefore, formula (4.93) can be considered a universal relation.

The calculations are in complete analogy for crossing of any two empty-lattice bands with $|K-K'| = 2\pi n/a$. Then, in the exponent of the tunneling rate (4.91), the parameter a has to be replaced by a/n . The same is true for the reduced effective mass (4.87) so that formula (4.93), which does not contain the variable a , is valid for all gaps.

An important assumption in the derivation of the tunneling rate was that the second band is always empty and no carriers return from the second band to the first band. Then, to avoid “traffic jam,” the tunneling through the second gap should be more efficient than tunneling through the first gap, tunneling through the third gap more efficient than tunneling through the second gap, etc., which is fulfilled if the gaps do not increase. This is in line with the criterion by Ao, where the Wannier–Stark spectrum is continuous if the gaps algebraically go to zero [29], which is always fulfilled in practice. Thus the paradox of the theory, which lead to the Wannier–Stark controversy (see the discussion at the beginning of this chapter), is resolved as follows: the restriction to a finite number of bands does not imply that the Wannier–Stark spectrum is discrete – on the contrary, this approximation can only be justified because the Wannier–Stark spectrum is continuous.

4.4.2 Perturbation Theory

In the semiclassical approximation, the tunneling rate, given by the Zener formula (4.91), monotonously increases with field. In reality, this function should exhibit $1/F$ oscillations, because the transition probability increases when two Wannier–Stark ladders become degenerate, i.e., when $E_{j'l'} - E_{jl} = E_{j'0} - E_{j0} - eFa(l'-l) = 0$. This effect, known as resonant tunneling, is observed in the optical density of states (Fig. 4.7), where the steady increase of the linewidth is interrupted by an infinite number of anticrossings with other Wannier–Stark ladders. The oscillatory behavior is also plausible in the real-space picture, where the tunneling length in the average is proportional to $1/F$ but shows oscillations because of the periodicity of $U(z)$.

Another shortcoming of the semiclassical approach is the fact that it only allows for tunneling between adjacent bands, which are connected via branch points in the complex plane. In the cases of a multiple quantum well, i.e., a superlattice with thick barriers, the below-barrier minibands are nearly dispersionless and, because m^* is huge, the tunneling rate between first and second minibands (4.93) is vanishingly small. Nevertheless, a line broadening is also observed in the context of the quantum-confined Stark effect [17], which cannot be explained by branch-point tunneling. In the picture of Wannier–Stark ladders, tunneling should be possible between all band pairs j, j' with nonzero matrix element $Z_{jj'}$ (4.40). However, for small gaps, tunneling between neighboring bands should be the dominant contribution.

In this subsection, we perform a straightforward calculation of the tunneling rate in the basis of Kane functions, solving the equation of motion for

the density matrix. Then we shall make a comparison to the result which is found in the literature.

The quantum-mechanical calculation of the tunneling rate seems to be a rigorous approach, but in fact it relies upon a number of assumptions. If the system is prepared in an initial state $|\varphi(0)\rangle$, the correlation function $|\langle\varphi(0)|\varphi(t)\rangle|^2$ is supposed to decrease like $\exp(-wt)$. Tunneling is considered during one Bloch cycle $T_{\text{BO}} = 2\pi\hbar/|eFa|$ and the tunneling rate is determined as $w = [1 - |\langle\varphi(0)|\varphi(T_{\text{BO}})\rangle|^2] / T_{\text{BO}}$, which is supposed to be correct for $w \ll 1$. If tunneling from the band j to $j' > j$ is considered, the band j' is assumed empty all the time, because the tunneling from j' to higher bands should be far more efficient than from j to j' . These assumptions are all questionable and cannot be rigorously justified within the model. For example, the linear exponential decay is in contradiction to the time-reversal symmetry. In fact, numerical calculations revealed deviations from this picture for small t [80, 114]. The limitation to one Bloch period is also a crucial assumption, as we will see later. It could be demonstrated by numerical calculations that the ablation of daughter wavepackets with the period of the Bloch oscillations is essentially correct, but these processes are not uncorrelated [80].

In a first step, we specify the matrix elements of the Wannier–Stark Hamiltonian (4.1) in the basis of Kane functions (4.43). For equal band indices $j = j'$ they are identical to the energies of the Wannier–Stark ladder:

$$H_{jl,jl'} = E_{jl} \delta_{ll'} ; \quad E_{jl} = E_{jl} + eFal . \quad (4.94)$$

The coupling of different bands $j \neq j'$ is facilitated by the functions $Z_{jj'}(k)$ (4.37) and the nondiagonal matrix elements of the Hamiltonian are

$$\begin{aligned} H_{jl,j'l'} &= \int_{-\infty}^{+\infty} dz \varphi_{jl}^*(z) e F z \varphi_{j'l'}(z) = \frac{a}{2\pi} \int_{-\frac{\pi}{a}}^{+\frac{\pi}{a}} dk \tilde{\varphi}_{jl}^*(k) e F Z_{jj'}(k) \tilde{\varphi}_{j'l'}(k) \\ &= \frac{eFa}{2\pi} \int_{-\frac{\pi}{a}}^{+\frac{\pi}{a}} dk Z_{jj'}(k) \exp \left\{ \frac{1}{ieF} \int_0^k dk' [\bar{E}_j(k') - \bar{E}_{j'}(k') - E_{jl} + E_{j'l'}] \right\} \\ &\quad (4.95) \end{aligned}$$

with $\bar{E}_j(k)$ defined in (4.60). For fixed j and j' , if both bands belong to the same case A or B (Sect. 4.1), the origin of the z axis can be chosen such that $\bar{E}_j(k) = E_j(k)$ and $\bar{E}_{j'}(k) = E_{j'}(k)$.

Now we consider the interaction between the first and second band. We calculate the tunneling rate by solving the von Neumann equation for the density matrix. This gives the same result as the solution of the time-dependent Schrödinger equation for the wavefunction, but the density matrix is a measurable quantity, in contrast to the wavefunction, and the symmetries of the

problem are more obvious. The equation of motion for the density matrix (von Neumann equation) reads:

$$\mathrm{i}\hbar \frac{d}{dt} N(t) = [H, N(t)] \quad (4.96)$$

$$H = \begin{pmatrix} H_{11} & H_{12} \\ \hline H_{21} & H_{22} \end{pmatrix}; \quad N = \begin{pmatrix} N_{11} & N_{12} \\ \hline N_{21} & N_{22} \end{pmatrix},$$

where, for convenience, we introduced the block notations $H_{jj'} = (H_{jl,j'l'})$ and $N_{jj'} = (N_{jl,j'l'})$. At $t = 0$, we assume the first Wannier–Stark ladder to be completely filled and the second Wannier–Stark ladder to be completely empty so that the initial condition for N is

$$N(t=0) = \mathrm{Diag}(1, 0). \quad (4.97)$$

This initial condition is in line with the translational symmetry of the problem, because no Wannier–Stark level stands out against the others. The diagonal part of the Hamiltonian can be treated exactly by means of Dirac's perturbation theory with $H^{(0)} = \mathrm{Diag}(H_{11}, H_{22})$ and $H^{(i)} = H - H^{(0)}$. The correspondence between Heisenberg and Dirac picture is given by

$$H_{jl,j'l'}(t) = e^{-\frac{E_{jl}t}{i\hbar}} H_{jl,j'l'}^{(i)}(t) e^{+\frac{E_{j'l'}t}{i\hbar}} \quad (4.98)$$

$$\tilde{N}_{jl,j'l'}(t) = e^{-\frac{E_{jl}t}{i\hbar}} N_{jl,j'l'}(t) e^{+\frac{E_{j'l'}t}{i\hbar}}.$$

Importantly, it holds that $[H^{(0)}, N(0)] = 0$. The quantities with the tilde obey the same equation of motion (4.96) and the initial condition is $\tilde{N}(0) = N(0)$.

The calculation of $\tilde{N}(t)$ goes alongside the same lines as in the derivation of Fermi's golden rule (App. C.3). The first nonvanishing contribution to the occupation numbers is found in second order in time and it holds that

$$\tilde{N}_{22}^{(2)}(t) = \frac{1}{\hbar^2} \int_0^t dt_1 \int_0^t dt_2 \tilde{H}_{21}(t_1) \tilde{N}_{11}(0) \tilde{H}_{12}(t_2). \quad (4.99)$$

With $\tilde{N}_{11}(0) = N_{11}(0) = 1$ and (4.98), the explicit expressions in the Heisenberg picture are

$$N_{2l,2l'}^{(2)}(t) = \frac{1}{\hbar^2} \int_0^t dt_1 \int_0^t dt_2 \sum_{l''=-\infty}^{+\infty} e^{\frac{E_{2l}(t-t_1)}{i\hbar}} H_{2l,1l''} e^{\frac{E_{1l''}(t_1-t_2)}{i\hbar}} \times H_{1l'',2l'} e^{\frac{E_{2l'}(t_2-t)}{i\hbar}}. \quad (4.100)$$

The elements of $N_{22}^{(2)}$ depend only on $l-l'$ because of the translational symmetry, which is also reflected by the initial condition. The tunneling probability in lowest order is given by $p(t) = N_{2l,2l}^{(2)}(t) = N_{20,20}^{(2)}(t) = \tilde{N}_{20,20}^{(2)}(t)$ and it follows that

$$\begin{aligned} p(t) &= \sum_{l=-\infty}^{+\infty} \left| \frac{1}{i\hbar} \int_0^t dt' e^{\frac{(E_{20}-E_{1l})t'}{i\hbar}} \right|^2 |H_{20,1l}|^2 \\ &= \sum_{l=-\infty}^{+\infty} \left(\frac{t}{\hbar} \right)^2 \operatorname{sinc}^2 \frac{(E_{20}-E_{1l})t}{2\hbar} |H_{20,1l}|^2. \end{aligned} \quad (4.101)$$

With the explicit form of the interaction matrix elements (4.95), the tunneling rate can be written as

$$w = \frac{p(T_{\text{BO}})}{T_{\text{BO}}} = \frac{|eF|a}{2\pi\hbar} \int_{-\frac{\pi}{a}}^{+\frac{\pi}{a}} dk_1 \int_{-\frac{\pi}{a}}^{+\frac{\pi}{a}} dk_2 f^*(k_1) g(k_1-k_2, b) f(k_2), \quad (4.102)$$

where

$$f(k) = Z_{12}(k) \exp \left\{ \frac{1}{ieF} \int_0^k dk' [\bar{E}_1(k') - \bar{E}_2(k')] \right\} \quad (4.103)$$

$$g(k, b) = \sum_{l=-\infty}^{+\infty} \operatorname{sinc}^2 \left[(b-al) \frac{\pi}{a} \right] e^{+i(b-al)k}; \quad b = \frac{E_{20} - E_{10}}{eF}.$$

The latter sum can be carried out explicitly (App. A.3) and it holds that

$$g(k, b) = 1 - \frac{|k|a}{2\pi} \left(1 - \cos \frac{2\pi b}{a} \right) + i \frac{ka}{2\pi} \sin \frac{2\pi b}{a}; \quad -\frac{2\pi}{a} \leq k \leq +\frac{2\pi}{a}. \quad (4.104)$$

Obviously, the lower integration limit in the definition of f (4.103) is irrelevant. Furthermore, the integration in (4.102) can be carried out over any domain of the form $[q, q+\frac{2\pi}{a}] \times [q, q+\frac{2\pi}{a}]$, which follows from the construction of the Kane functions. We also mention that for the considered case of a symmetric superlattice, the tunneling rate does not change if the sign of eF changes, which is clear from the symmetry of the original problem.

As we used second-order perturbation theory, transitions from the second to the first band are neglected and the tunneling processes of the individual Wannier–Stark levels are independent of each other. Therefore, the same result as (4.102) is obtained if the initial state is any diagonal matrix $N_{11}(0)$ and the tunneling probability is defined as $p = [N_{1l,1l}(0) - N_{1l,1l}^{(2)}(t)]/N_{1l,1l}(0)$, which is independent of l . For this choice of the initial condition, translational invariance is not fulfilled in the general case, but it still holds true that $[H^{(0)}, N(0)] = 0$.

Formula (4.102) is not limited to tunneling from the first to the second miniband but can be applied for any pair of bands j, j' . The total tunneling probability of a fixed band j follows from summation over all other bands $j' \neq j$. An important difference to the semiclassical treatment is that tunneling is possible also if $j' \neq j + 1$, i.e., for bands not directly connected via branch points.

For small values of F , the main contribution to the integral stems from a small region around the gap, located at a symmetric point k_0 . Then we have two types of transitions: allowed transitions, where $\psi_{jk_0}(z)$ and $\psi_{j'k_0}(z)$ have opposite parity and $Z_{jj'}(k_0) \neq 0$, and “forbidden” transitions, where $\psi_{jk_0}(z)$ and $\psi_{j'k_0}(z)$ have equal parity and $Z_{jj'}(k_0) = 0$. The latter transitions should have a much smaller oscillator strength.¹² We mention that there is no simple rule determining which transitions are allowed. For nearly free electrons, all transitions with $j' = j + 1$ are allowed, because the momentum matrix element (4.40) between adjacent bands is nonzero at the critical points. Therefore, for realistic superlattices, if j is sufficiently large, all transitions between j and $j + 1$ are allowed. The same is true for below-barrier minibands in simple geometries, which can be approximated as tightly bound electrons. The deviations of $g(k_1 - k_2, b)$ from unity are periodic in b , which leads to $1/F$ oscillations in the tunneling rate. This is an effect of resonant tunneling, which is related to avoided crossings of Wannier–Stark ladders, and can be partly observed in the left part of Fig. 4.7. It is worthwhile to note that resonant and nonresonant part cannot clearly be separated, because, if g is replaced by unity, the expression (4.102) strongly depends on the integration limits.

Let us now compare our result to the literature. In the context of the Houston functions and the crystal-momentum approximation, a tunneling rate of the form

$$w = \frac{|eF|a}{2\pi\hbar} \left| \int dk Z_{12}(k) \exp \left\{ \frac{1}{ieF} \int_0^k dk' [\bar{E}_1(k') - \bar{E}_2(k')] \right\} \right|^2 \quad (4.105)$$

has been derived by many authors [7, 10–12, 16, 107]. The k integration is usually carried over an interval of length $\frac{2\pi}{a}$, in some cases from $-\frac{\pi}{a}$ to $+\frac{\pi}{a}$, in other cases from 0 to $\frac{2\pi}{a}$, and some authors do not specify integral limits. Outwardly, the difference to formula (4.102) is small, but the omission of the factor g leads to a spurious dependence of the the tunneling rate (4.105) on the integration limits. This result is counter-intuitive, because in the Houston picture the particle travels the whole Brillouin zone during one Bloch period, and the tunneling rate should not depend on the starting point. Furthermore, as the function g is a major source of $1/F$ oscillations, the question arises whether (4.105) is indeed an improvement over the semiclassical result (4.91)

¹² The term “forbidden” refers to the limit $F \rightarrow 0$, in the same sense as in the discussion of Fig. 4.6.

and is able to accurately describe resonant tunneling in the limit of small fields. To study this problem in more detail, we shall rederive our result in a slightly different way, which shows the connection to the crystal-momentum representation.

We notice that, as a result of the translational symmetry, in the Dirac picture all sub-matrices of \tilde{H} and \tilde{N} are of the Toeplitz form, i.e., they depend only on the difference of the Wannier–Stark-ladder indices $l - l'$. A product of such matrices can be conveniently calculated by Fourier synthesis (App. A.1). With the Fourier-transformed Hamiltonian,

$$\begin{aligned} \tilde{H}_{12}(q, t) &= \tilde{H}_{21}^*(q, t) = \sum_{l=-\infty}^{+\infty} e^{-iaq(l-l')} \tilde{H}_{1l, 2l'}(t) \\ &= eF e^{\frac{(E_{10}-E_{20})q}{ieF}} Z_{12}(q - \frac{eFt}{\hbar}) \exp \left\{ \frac{1}{ieF} \int_0^{q - \frac{eFt}{\hbar}} dq' [\bar{E}_1(q') - \bar{E}_2(q')] \right\}, \end{aligned} \quad (4.106)$$

equation (4.99) goes over into

$$\begin{aligned} \tilde{N}_{22}(q, t) &= \frac{1}{\hbar^2} \int_0^t dt_1 \int_0^t dt_2 \tilde{H}_{21}(q, t) \tilde{N}_{11}(q, 0) \tilde{H}_{12}(q, t) \\ &= \left| \frac{eF}{\hbar} \int_0^t dt' Z_{12}(q - \frac{eFt'}{\hbar}) \exp \left\{ \frac{1}{ieF} \int_0^{q - \frac{eFt'}{\hbar}} dq' [\bar{E}_1(q') - \bar{E}_2(q')] \right\} \right|^2 \\ &\quad \times \tilde{N}_{11}(q, 0). \end{aligned} \quad (4.107)$$

The transition probability is given by

$$p(T_{\text{BO}}) = N_{20,20}^{(2)}(T_{\text{BO}}) = \tilde{N}_{20,20}^{(2)}(T_{\text{BO}}) = \frac{a}{2\pi} \int_{-\frac{\pi}{a}}^{+\frac{\pi}{a}} dq \tilde{N}_{22}(q, T_{\text{BO}}) \quad (4.108)$$

and with the initial condition $\tilde{N}_{11}(q, 0) = N_{11}(q, 0) = 1$ we find for the tunneling rate

$$w = \frac{|eF|a}{2\pi\hbar} \frac{a}{2\pi} \int_{-\frac{\pi}{a}}^{+\frac{\pi}{a}} dq \left| \int_{q-\frac{\pi}{a}}^{q+\frac{\pi}{a}} dk f(k) \right|^2 \quad (4.109)$$

with $f(k)$ defined in (4.103). It can be shown (App. A.3) that this result is equivalent to the previous formulation (4.102).

Our result (4.109) is closely related to formula (4.105), and the dependence on the integral limits is removed by taking the average. Let us now

discuss the assumption that led to the result in the literature. In order to obtain formula (4.105), the initial condition has to be chosen such that $\tilde{N}_{11}(q, t=0) = N_{11}(q, t=0) = \frac{2\pi}{a} \delta(q - q_0)$. This is actually done in the crystal-momentum representation, where the electron is initially in a Bloch state with wavenumber q_0 . Such an initial condition is compatible with the symmetry of the problem, because $\tilde{N}_{1l,1l'}(0)$ depends only on $l - l'$, but, at the same time, $[H^{(0)}, N(0)] \neq 0$ or, in other words, the initial wavefunction is not an eigenstate of the unperturbed Hamiltonian. This is also the reason why the Houston functions (4.59) are not stationary states but oscillate in time. The validity of the Houston approximation requires that the system is initially prepared in a Bloch state or, equivalently, that the electric field is switched on promptly at $t = 0$ [16, 107]. These assumptions are not realistic and lead to the paradox discussed above.

It is physical folklore that in the low-field limit the semiclassical result for the tunneling rate should become exact. In the present case, this is not clear, because the lattice-periodic part of the eigenfunction is ignored. Several authors, including Franz [98] and Eilenberger [99], found that for small F the expression (4.105) with appropriate integration limits goes over into Zener's result (4.93). It was also shown that the imaginary part of the resonances is asymptotically equal to expression (4.85) [39]. There was also some discussion over the origin of a mysterious factor $\pi^2/9$. On the other hand, the asymptotic equivalence of the result (4.105) with the semiclassical result for $F \rightarrow 0$ does not prove that the crystal-momentum representation goes beyond the semiclassical theory. We shall answer this question in the next subsection, where we compare numerical results for (4.105) and (4.109).

An important assumption of the Zener theory is that the time interval for tunneling is one Bloch period. The result (4.109) can immediately be generalized for more than one Bloch period. The function $f(k)$, defined in (4.103), fulfills $f(k + \frac{2\pi}{a}) = e^{+2\pi i b/a} f(k)$. Then, the tunneling rate for N Bloch periods is

$$w_N = \frac{p(NT_{\text{BO}})}{NT_{\text{BO}}} = \frac{1}{N} \frac{\sin^2 \frac{N\pi b}{a}}{\sin^2 \frac{\pi b}{a}} w. \quad (4.110)$$

The same prefactors would also appear in formula (4.105) if N Bloch cycles were considered [16]. In the limit $N \rightarrow \infty$, the "spectrometer function" goes over into $\underline{\delta}(\frac{b}{a})$ and the tunneling rate is given by Fermi's golden rule, which is also seen in (4.101) in the limit $t \rightarrow \infty$. We see that the restriction to one Bloch period is crucial: a tunneling rate which is nonzero in the whole field range is possible only for $N = 1$, otherwise the prefactor in (4.110) drops to zero between the band crossings.

The crucial dependence of the result on the assumption of one Bloch cycle raises further questions about the validity of the perturbational result. Therefore, even the present result, which eliminates the spurious dependence on the integration interval, should only qualitatively describe the evolution

of the tunneling rate with field. On physical grounds, as Zener tunneling is a stationary process, it seems more realistic to assume an infinite time interval but a finite dephasing (App. C.3), which leads to a series of delta functions with a finite broadening. However, the dephasing, which should increase with the field strength, cannot be determined within this model so that the broadening would be phenomenological.

4.4.3 Discussion

At the end of this section, we present numerical results for the tunneling rate. We compare the result of this section (4.109) with the result of the semiclassical theory (4.91) and the result of perturbation theory published in the literature (4.105). We also compare the linewidth measured in the absorption spectra with the prediction of the theory.

The calculations are done for the parameters of Sample 2. The tunneling rate is larger than for Sample 1 and the electronic structure is reasonably well approximated by the limit of nearly free electrons (cf. Fig. 4.2). Therefore, the difference between both formulations (4.91) and (4.93) for the semiclassical result is negligible. The eigenvalue problem for $F = 0$ (4.2) was solved as described in Sect. 4.1, using the same numerical parameters and the phase convention introduced in Sect. 4.1. The Brillouin zone was sampled by 400 points. In the parameter range of interest we observed full convergence of the results. We also numerically verified the equivalence of the formulations (4.102) and (4.109).

In Fig. 4.12, we compare the result derived in this section (4.109) with the result from the literature (4.105) and the semiclassical expression (4.91). The quantity $\hbar w$, which has the dimension of an energy, is plotted versus the field strength F . Our result for the tunneling rate (*solid line*) shows an overall increase with field strength, but reveals some modulation. These $1/F$ oscillations are the result of crossings with the second Wannier–Stark ladder (cf. Fig. 4.7). Their relative role increases as F decreases. Otherwise, the behavior of the perturbational result is similar to that of the semiclassical result (*dotted line*). For large F , the result of perturbation theory is about 50% larger than the semiclassical result. Taking into account the factor $\pi^2/9$, the difference reduces to about 40%. Because both semiclassical and perturbation theory should become less accurate for larger fields, it cannot clearly be judged if one result is systematically too large or the other is systematically too small, or both. Furthermore, there is the principal problem of defining a tunneling rate so that there is no exact solution where the approximations could be compared to. A full numerical calculation by Holthaus also gives a tunneling rate which at high fields is larger than the semiclassical result [80]. The difference between the perturbational and the semiclassical result for large fields also depends on the parameters of the superlattice.

Having discussed the relation of our result (4.109) to the semiclassical result (4.93), it is worthwhile to make a comparison to the perturbational result

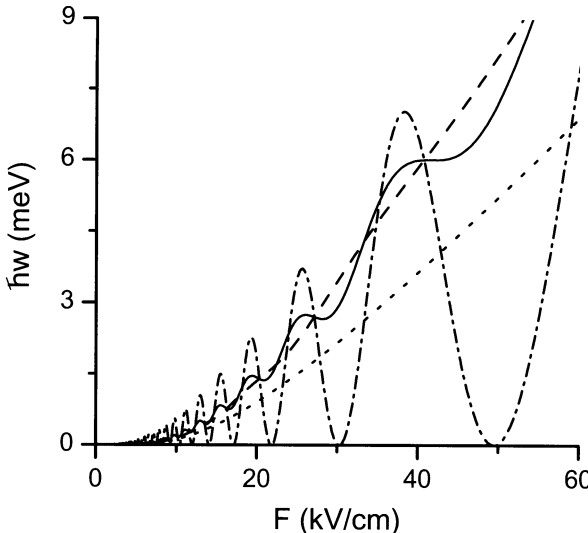


Fig. 4.12. Theoretical tunneling rate $\hbar w$ vs. electric field F .
Solid line: present result (4.109). *Dashed line:* formula (4.105) for integration limits $[0, \frac{2\pi}{a}]$. *Dash-dotted line:* formula (4.105) for integration limits $[-\frac{\pi}{2}, +\frac{\pi}{a}]$. *Dotted line:* semiclassical result (4.93)

from the literature. This tunneling rate given by formula (4.105) strongly depends on the integration limits. As the gap is located at $k_0 = \frac{\pi}{a}$, the natural choice would be $[0, +\frac{2\pi}{a}]$ (*dashed line*). In this case, the tunneling rate is very similar to the semiclassical result and does not contain the oscillations found in the *solid curve*. For $F \rightarrow 0$, this function approaches the semiclassical result (4.93), multiplied by $\pi^2/9$. However, we find that both functions are not exactly asymptotically equal. The *dashed curve* shows weak oscillations and the modulation rate increases as F decreases.

Let us see what happens for other choices of the integration limits. For the most unnatural choice $[-\frac{\pi}{a}, +\frac{\pi}{a}]$ (*dash-dotted line*), the tunneling rate shows strong oscillations and goes to zero between the crossings of Wannier–Stark ladders. For any other integration domain of length $\frac{2\pi}{a}$, the tunneling rate has no zeros. The solution from this section, (4.102), averages over all integration domains and therefore shows features of both extremes, the *dashed* and the *dash-dotted curve*. It is interesting to consider the situation when $E_{2l} = E_{1l'}$ for some l and l' or, equivalently, when b/a is an integer. Then the function g in (4.102) is equal to unity, f is periodic, and the result is the same for all integration domains of length $\frac{2\pi}{a}$. At these values of F , we observe a crossing of all three solutions (*solid line*, *dashed line*, *dash-dotted line*). The maxima of the correct tunneling rate (*solid line*) appear somewhat below these points. This is plausible, because the tunneling rate should increase if $eFa(l - l')$ is moved from the center $E_{20} - E_{10}$ to the gap $E_2(k_0) - E_1(k_0) = E_g^*$.

The solution from the literature (4.105) with integration limits symmetric around the gap, which is the state of art in analytical solutions, reproduces

the semiclassical result, but does not contain new features to be taken seriously. The quantitative difference for large F must not be overemphasized, because both approaches become less accurate with increasing field. Ao and Rammer studied the expression (4.105) with the natural integration limits to point out the important role of $1/F$ oscillations. In the light of our results, these conclusions are spurious. The difference between the result (4.105) with natural integration limits (*dashed line*) and the semiclassical result (*dotted line*) is negligible and is within the error limits of the theory. Therefore, the result from the literature with natural integration limits represents nonresonant tunneling. In contrast, for the unnatural choice of the integration limits (*dash-dotted curve*) the tunneling is purely resonant. The true solution (*solid line*) averages over all possible integration limits and, therefore, contains features of both nonresonant and resonant tunneling.

Let us now compare the theoretical predictions with the linewidth measured in the experiment. The optical absorption involves both electron and hole states, but the holes are strongly confined and their tunneling is negligible. The occupation numbers of the first Wannier–Stark ladder decrease approximately as $\exp(-wt)$. Then the amplitude of the wavefunction decreases as $\exp(-wt/2)$. A linear exponential decay of the wavefunction at a rate of $w/2$ corresponds to a Lorentzian with linewidth $w/2$. Thus the calculated tunneling rate should be compared to the full width at half maximum (FWHM) of the absorption peaks. In the experiment, various scattering mechanisms contribute to the line broadening. To correct for this influence, we simply subtract the linewidth at $F = 0$.

The experimental lineshapes were found to be closer to Gaussian than to Lorentzian, which is also observed for the calculated density of states (Fig. 4.7). This can be explained by non-exponential tunneling. In the Zener theory, the correlation function is of the form $\langle \varphi(0) | \varphi(t) \rangle = \exp(-w|t|/2)$, which gives a Lorentzian line with width $w/2$ (Table A.2). However, the kink at $t = 0$ is unphysical because of the time-reversal symmetry. The true correlation, which is a smooth function also at the origin, gives rise to a lineshape more rapidly decreasing as a Lorentzian.

In Fig. 4.13, the experimental linewidth (FWHM) for the first Wannier–Stark transition (*full circles*) is compared with our result of perturbation theory (*solid line*) and of semiclassical theory (*dotted line*). The measured linewidth is of the same order of magnitude as the prediction of the theory, which is astonishing, because the theory does not contain any adjustable parameters. Taking into account that the uncertainty of the theory is in the order of the difference between the *dashed* and the *dotted curve* in Fig. 4.12 and that the uncertainty of the experimental data (scattering mechanisms beyond Zener tunneling, measurement of the linewidth, field measurement) is in the order of 20%, one can speak of quantitative agreement. In contrast to the semiclassical result, the result of perturbation theory is also able to explain the oscillations of the linewidth. The oscillations in the experimental

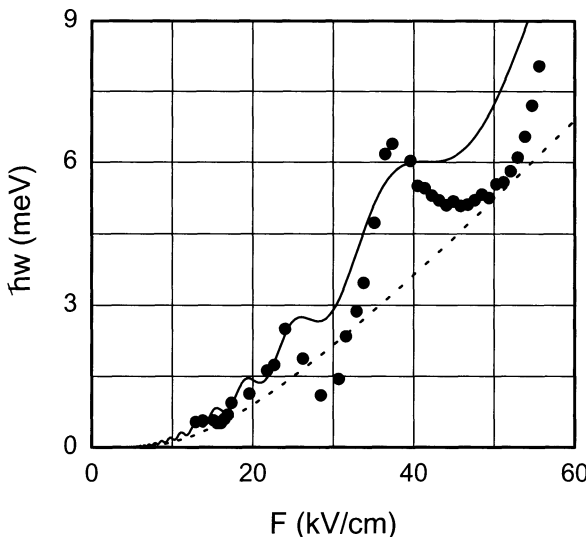


Fig. 4.13. Tunneling rate $\hbar w$ vs. electric field F . Solid line: perturbational result (4.109). Dotted line: semiclassical result (4.93). Circles: experimental line broadening (from [72])

linewidth are nearly periodic in $1/F$ and the positions of the maxima and minima are close to the theoretical values. Deviations occur for small fields, which can be addressed to the influence of Coulomb interaction. The amplitude of the oscillations in theory and experiment is of the same order of magnitude, although the theoretical values are systematically too small. This indicates that the intraband dephasing time is longer than one Bloch period and that the Bloch cycles are correlated. This is a principal limitation of the theory and a better agreement between theory and experiment would require additional assumptions and adjustable parameters which cannot be justified within the simple model. Otherwise, the experimental and theoretical results are fully consistent. We emphasize that by no means the oscillations in the experimental linewidth could be explained by the perturbational result from the literature (*dashed curve* in Fig. 4.12).

4.5 Summary and Conclusions

In this chapter we have studied the Zener breakdown in semiconductor superlattices. We have demonstrated that the nature of the Wannier–Stark spectrum, a problem of fundamental theoretical interest, has important consequences for the optical properties of superlattices.

Although a continuous spectrum seems to be common sense, a rigorous proof is very difficult and relies on higher-order smoothness of the periodic potentials. In this chapter, we provided additional evidence for the continuous nature of the spectrum, namely: (i) the divergence of the Kane expansion (4.41), (ii) an accurate numerical solution of the eigenvalue problem

(Fig. 4.5), which shows the tunneling of the wavefunction through the superlattice barriers, (iii) the evolution of the optical density of states with the electric field (Figs. 4.6 and 4.7), and (iv) the optical absorption of a shallow superlattice in a perpendicular electric field (Figs. 4.9 and 4.10).

The calculations for the optical density of states and the optical absorption show that the picture of Wannier–Stark levels is valid only for small fields. For intermediate fields the Wannier–Stark ladders are distorted by anticrossing and one observes a variety of transitions, including those forbidden for $F = 0$. For high fields the linewidths drastically increase and the individual lines disappear, showing the transition from two to three dimensions. The results for the optical density of states and the optical absorption are in good agreement with the experimental findings.

The tunneling rate was calculated by means of second-order perturbation theory, in the basis of the Kane functions. The result derived in this chapter corrects an inconsistency in a result previously published in the literature and also clarifies the origin of resonant tunneling. The tunneling rate can be directly compared to the linewidths of the optical transitions. Resonant Zener tunneling leads to $1/F$ oscillations, which are also observed in the experimental linewidth. Despite the simplicity of the model, the result of the calculation is generally in good agreement with the experiment.

The calculation of the tunneling rate by means of perturbation theory still uses a number of assumptions which cannot be rigorously justified. Furthermore, a rigorous mathematical definition of the tunneling rate for nonanalytic potentials remains an open problem.

A Mathematical Supplement

In this mathematical appendix, we introduce important notations, summarize rules for the Fourier transform and Fourier series, give the definitions of important special functions and prove mathematical relations used throughout the book.

A.1 Basic Definitions and Relations

Here we give the basic definitions, introduce notations, and summarize important facts about the Fourier transform, the delta function, and orthogonal curvilinear coordinates. These relations can be found in several mathematical textbooks [1–3].

Symbols and Notations

Table A.1 lists those mathematical symbols and notations which are either not generally used or where the use is different from the literature.

Asymptotics

The asymptotic behavior of a function can be conveniently described by Landau's order symbols O and o [2].

A function $f(x)$ is said to be $O[g(x)]$ for $x \rightarrow x_0$ if there exists two constants $c > 0$ and $\varepsilon > 0$ so that $|f(x)| \leq c|g(x)|$ for all $|x - x_0| < \varepsilon$. In particular, if $f(x) = O(1)$ for $x \rightarrow x_0$, then $f(x)$ is bounded in a neighborhood of x_0 .

Let $g(x) \neq 0$ in a neighborhood of x_0 , excluding the point x_0 . We write $f(x) = o[g(x)]$ if $\lim_{x \rightarrow x_0} |f(x)|/|g(x)| = 0$. If $f(x) = o(1)$ for $x \rightarrow x_0$, then $\lim_{x \rightarrow x_0} f(x) = 0$.

Two functions f and g are said to be asymptotically equal for $x \rightarrow x_0$, if $f(x) = g(x)[1 + o(1)]$ for $x \rightarrow x_0$. Then we write $f(x) \sim g(x)$ for $x \rightarrow x_0$, which is the same as $g(x) \sim f(x)$ for $x \rightarrow x_0$.

The generalization to $x_0 = \pm\infty$ and to arbitrary Banach spaces is straightforward. The following examples will illustrate the notations:

Table A.1. Mathematical symbols and notations

Symbol, Notation	Meaning, Remarks
\mathbb{N}, \mathbb{N}_0	natural numbers, excluding and including zero
$\llbracket a, b \rrbracket, [a, b[$	vanishing, periodic boundary conditions
a.e.	almost everywhere (i.e., up to a set of measure zero)
$\text{sinc } x$	$= \sin x / x$
$n!! = 1 \times 3 \times \dots \times (n-2) \times n$	double factorial, n odd
\propto, \sim	proportional to, asymptotically equal to
$O, o; P$	Landau's order symbols; Cauchy's principal value
$\mathbf{a} \cdot \mathbf{b} = a_1 b_1 + a_2 b_2 + a_3 b_3$	dot product
$\mathbf{a}^* \cdot \mathbf{b} = a_1^* b_1 + a_2^* b_2 + a_3^* b_3$	scalar product
$a = \mathbf{a} = \sqrt{\mathbf{a}^* \cdot \mathbf{a}}$	length of a vector
$P(\mathbf{a})$	polynomial in the components of \mathbf{a}
$\langle \varphi \psi \rangle; \ \varphi\ = \sqrt{\langle \varphi \varphi \rangle}$	scalar product, norm for Dirac vectors
$ \varphi\rangle \simeq \psi\rangle$	equivalence, $ \varphi\rangle = c \psi\rangle$, $ c = 1$
$(u v)$	scalar product for lattice-periodic functions (p. 4)
$\langle \Phi, \Psi \rangle; \ \Phi\ = \sqrt{\langle \Phi, \Psi \rangle}$	weighted scalar product; weighted norm (p. 77)
$\langle \dots \rangle, \langle\langle \dots \rangle\rangle$	statistical average (p. 31), ensemble average (p. 91)
A^T, A^*	transposed and complex conjugated matrix
$A^\dagger = A^T$	Hermitian conjugated matrix
$\ A\ $; cond $A = \ A\ \ A^{-1}\ $	matrix norm (p. 81), condition of a matrix
diag(a_1, \dots, a_n)	diagonal matrix
Diag(A_1, \dots, A_n)	block-diagonal matrix
$A \simeq B$	unitary equivalence, $A = U^\dagger B U$, U unitary
$[A, B] = AB - BA$	commutator
δ, Θ	delta function, Heavyside function
δ	weighted or periodic delta function

$$\sin z = O(z) \text{ for } z \rightarrow 0 ; \quad \ln x = o(\sqrt{x}) \text{ for } x \rightarrow +\infty \quad (\text{A.1})$$

$$n! = o(n^n) \text{ for } n \rightarrow \infty ; \quad \sinh(x) \sim \frac{1}{2} e^{-x} \text{ for } x \rightarrow -\infty .$$

Fourier Transform

The Fourier transforms with respect to the time- and n -dimensional space variable are defined as

$$F(\omega) = \int_{-\infty}^{+\infty} dt e^{+i\omega t} f(t) ; \quad f(t) = \frac{1}{2\pi} \int_{-\infty}^{+\infty} d\omega e^{-i\omega t} F(\omega) \quad (\text{A.2})$$

and

$$G(\mathbf{k}) = \int d^n \mathbf{r} e^{-i\mathbf{k} \cdot \mathbf{r}} g(\mathbf{k}) ; \quad g(\mathbf{r}) = \frac{1}{(2\pi)^n} \int d^n \mathbf{k} e^{+i\mathbf{k} \cdot \mathbf{r}} G(\mathbf{k}) . \quad (\text{A.3})$$

Table A.2. Rules for the Fourier transform and examples

Original	Fourier transform	Remarks
$\Theta(t) e^{-bt}$	$i/(\omega + ib)$	$b > 0$
$e^{-b \tau }$	$2b/(\omega^2 + b^2)$	$b > 0$
$P(\nabla) \delta(\mathbf{r})$	$P(i\mathbf{k})$	P – polynomial
$\exp(-\frac{r^2}{2\sigma^2})/(2\pi\sigma^2)^{n/2}$	$\exp(-\frac{\sigma k^2}{2})$	$\sigma > 0$
$1/r$	$4\pi/k^2$	$n = 3$

Table A.2 summarizes and Fourier transforms of selected functions and distributions. The Fourier transform of the three-dimensional Coulomb potential follows from the Fourier transform of the equation $-\Delta \frac{1}{r} = 4\pi\delta(\mathbf{r})$.

Fourier Series

Let v be a complex valued function of real variable k and $v(k + \frac{2\pi}{a})$; $a > 0$. Then the Fourier series of v is given by

$$v(k) = \sum_{l=-\infty}^{+\infty} v_l e^{-ikal}; \quad v_l = \frac{a}{2\pi} \int_{-\frac{\pi}{a}}^{+\frac{\pi}{a}} dk e^{+ikal} v(k). \quad (\text{A.4})$$

The convergence of the Fourier series is the subject of Dirichlet's theorem [1, 3, 4]. Suppose v is bounded and the interval $[-\frac{\pi}{a}, +\frac{\pi}{a}]$ can be divided in a finite number of sub-intervals such that v is continuous and monotonous in each sub-interval. Then the series (A.4) converges towards $v(k)$ for each k where v is continuous. If v is discontinuous at k , then the Fourier series converges towards the arithmetic means of left and right limit $\frac{1}{2}[v(k+0) + v(k-0)]$.

Many rules for Fourier series are in complete analogy to the rules for the Fourier transform. A selection of important Fourier series and rules is summarized in Table A.3. The symbol $\underline{\delta}$ denotes the periodic delta function, which is the neutral element of the convolution.

The functions $\{e^{ikal}\}$ are orthonormal and complete in the interval $[-\frac{\pi}{a}, +\frac{\pi}{a}]$ with weight function $\frac{a}{2\pi}$ and for the scalar product of two periodic functions it holds that

$$(v | w) = \frac{a}{2\pi} \int_{-\frac{\pi}{a}}^{+\frac{\pi}{a}} dk v^*(k) w(k) = \sum_{l=-\infty}^{+\infty} v_l^* w_l, \quad (\text{A.5})$$

which can be looked upon as Parseval's theorem for Fourier series.

Table A.3. Rules for Fourier series and important examples

Fourier coefficients	Fourier series
$\frac{a}{2\pi} e^{ik_0 al}$	$\delta(k - k_0) = \sum_{n=-\infty}^{+\infty} \delta(k - k_0 - \frac{2\pi n}{a})$
δ_{ll_0}	$e^{-ik_0 al}$
$\sum_{l=-\infty}^{+\infty} v_{l-l'} w_{l'}$	$v(k) w(k)$
$v_l w_l$	$\frac{a}{2\pi} \int_{-\frac{\pi}{a}}^{+\frac{\pi}{a}} dk' v(k - k') w(k')$

The delta Function

The delta function (Dirac function) δ and its derivatives are defined as

$$\int d^n r' P(\nabla) \delta(r - r') f(r') = P(\nabla) f(r) , \quad (\text{A.6})$$

where $P(\nabla)$ is a polynomial in $\partial/\partial x_1, \dots, \partial/\partial x_n$. The function $\delta(r)$ is completely localized at $r = 0$ and is equal to zero for $r \neq 0$. The integral over $\delta(r)$ is equal to unity.

The delta function is not a regular function, but can be approximated by regular functions. Common examples are

$$\begin{aligned} \delta(r) &= \lim_{\sigma \rightarrow +0} \frac{1}{(2\pi\sigma^2)^{n/2}} e^{-\frac{r^2}{2\sigma^2}} \\ \delta(\omega) &= \lim_{\epsilon \rightarrow +0} \frac{1}{\pi} \frac{\epsilon}{\omega^2 + \epsilon^2} = \lim_{T \rightarrow \infty} \frac{T}{\pi} \operatorname{sinc}^2(\omega T) . \end{aligned} \quad (\text{A.7})$$

The delta function in \mathbb{R}^n can be represented as a product of delta functions in \mathbb{R}^1 according to $\delta(r) = \delta(x_1) \cdots \delta(x_n)$.

Let $f(x)$ be an $\mathbb{R}^1 \rightarrow \mathbb{R}^1$ function with m isolated zeros x_1, \dots, x_m and continuous derivatives $f'(x)$ in the neighborhood of the zeros. Then it holds that

$$\delta[f(x)] = \sum_{j=1}^m \frac{\delta(x - x_j)}{|f'(x_j)|} . \quad (\text{A.8})$$

The Heavyside Function

The Heavyside function (step function, Theta function) is defined as the integral over the delta function and it holds that

$$\Theta(t) = \int_{-\infty}^t dt' \delta(t') = \begin{cases} 0 & \text{for } t < 0 \\ 1 & \text{for } t > 0. \end{cases} \quad (\text{A.9})$$

Apparently, the Fourier transform of the Heavyside function does not exist. A common trick is to introduce a damping factor $e^{-\epsilon t}$ and at the end of the calculation take the limit $\epsilon \rightarrow +0$. This is formally written as $\epsilon = +0$ and ϵ is called a positive infinitesimal. Then, according to Table A.2, the Fourier transform of the Heavyside function is

$$\tilde{\Theta}(\omega) = \frac{i}{(\omega + i\epsilon)}. \quad (\text{A.10})$$

The Heavyside function $\Theta(t)$ is the solution of the differential equation $d\Theta(t)/dt = \delta(t)$, which fulfills causality, i.e., $\Theta(t) = 0$ for $t < 0$. This can be ensured replacing d/dt by $d/dt + \epsilon$. This shifts the argument of the Fourier transform by $+i\epsilon$ and leads to the function (A.10), which is analytic on the upper half plane, as required by causality.

Consider the integral

$$\int_{-\infty}^{+\infty} d\omega \frac{1}{\omega \pm i\epsilon} \tilde{f}(\omega) = P \int_{-\infty}^{+\infty} d\omega \frac{\tilde{f}(\omega)}{\omega} \mp i\pi \tilde{f}(0), \quad (\text{A.11})$$

where P denotes the principal value. The upper relation be formally written as

$$\frac{1}{\omega \pm i\epsilon} = P\left(\frac{1}{\omega}\right) \mp i\pi \delta(\omega) \quad (\text{A.12})$$

which is known as the Dirac identity.

Consider a function g with the property $g(t) = 0$ for $t < 0$. This can be written as $g(t) = \Theta(t) g(t)$ a.e., which in Fourier space translates into

$$\tilde{g}(\omega) = \frac{1}{2\pi} \int_{-\infty}^{+\infty} d\omega' \tilde{\Theta}(\omega - \omega') \tilde{g}(\omega'). \quad (\text{A.13})$$

From the explicit form of $\tilde{\Theta}(\omega)$ (A.10) and the Dirac identity (A.12) it follows that

$$\begin{Bmatrix} \text{Re} \\ \text{Im} \end{Bmatrix} \tilde{g}(\omega) = \frac{1}{\pi} P \int_{-\infty}^{+\infty} d\omega' \frac{1}{\omega - \omega'} \begin{Bmatrix} -\text{Im} \\ +\text{Re} \end{Bmatrix} \tilde{g}(\omega'), \quad (\text{A.14})$$

which are the Kramers–Kronig relations. In many cases of physical interest, the function $g(t)$ is real. Then $\text{Re } \tilde{g}$ is even and $\text{Im } \tilde{g}$ is odd, which gives rise to alternative formulations of the Kramers–Kronig relations.

Curvilinear Coordinates

Curvilinear coordinates are a one-to-one mapping (up to a set of measure zero) between $\mathbf{r} = (x_1, \dots, x_n)^T \in G_r \subseteq \mathbb{R}^n$ and $u = (u_1, \dots, u_n) \in G_u \subseteq \mathbb{R}^n$. We consider the important case that the coordinates are orthogonal, i.e.,

$$\frac{\partial \mathbf{r}}{\partial u_j} = h_j \mathbf{e}_j ; \quad \mathbf{e}_j \cdot \mathbf{e}_{j'} = \delta_{jj'} , \quad (\text{A.15})$$

Then the transformation of the volume element and the delta function is

$$d^n \mathbf{r} = du_1 \cdots du_n g(u_1, \dots, u_n) = \underline{d}u ; \quad g(u) = h_1(u) \cdots h_n(u) > 0 \text{ a.e.}$$

$$\delta(\mathbf{r} - \mathbf{r}') = \frac{\delta(u_1 - u'_1) \cdots \delta(u_n - u'_n)}{\sqrt{g(u) g(u')}} = \frac{\delta(u - u')}{\sqrt{g(u) g(u')}} = \underline{\delta}(u, u') , \quad (\text{A.16})$$

where $g(u)$ is the weight function and $\underline{\delta}(u, u')$ is the weighted delta function. The vector differential operators grad, div, and curl can also be expressed by the coefficients h_j . For the Laplacian, we have

$$\Delta f = \frac{1}{g} \sum_i \frac{\partial}{\partial u_i} \left(\frac{g}{h_i^2} \frac{\partial f}{\partial u_i} \right) . \quad (\text{A.17})$$

Table A.4. Cylindrical and spherical coordinates

Cylindrical coordinates ϱ, φ, ζ	Spherical coordinates r, ϑ, φ
$x = \varrho \cos \varphi$	$x = r \sin \vartheta \cos \varphi$
$y = \varrho \sin \varphi$	$y = r \sin \vartheta \sin \varphi$
$z = \zeta$	$z = r \cos \vartheta$
$G_{\varrho\varphi z} = [0, \infty) \times [0, 2\pi] \times (-\infty, +\infty)$	$G_{r\vartheta\varphi} = [0, \infty) \times [0, \pi] \times [0, 2\pi]$
$h_\varrho = 1, h_\varphi = \varrho, h_\zeta = 1$	$h_r = 1, h_\vartheta = r, h_\varphi = r \sin \vartheta$
$g = \varrho$	$g = r^2 \sin \vartheta$
$\Delta = \Delta_\varrho + \frac{1}{\varrho^2} \frac{\partial}{\partial \varphi^2} + \frac{\partial^2}{\partial \zeta^2}$	$\Delta = \Delta_r + \frac{1}{r^2} \Delta_{\vartheta\varphi}$
$\Delta_\varrho = \frac{1}{\varrho} \frac{\partial}{\partial \varrho} \varrho \frac{\partial}{\partial \varrho}$	$\Delta_r = \frac{1}{r^2} \frac{\partial}{\partial r} r^2 \frac{\partial}{\partial r}$
	$\Delta_{\vartheta\varphi} = \frac{1}{\sin \vartheta} \frac{\partial}{\partial \vartheta} \sin \vartheta \frac{\partial}{\partial \vartheta} + \frac{1}{\sin^2 \vartheta} \frac{\partial^2}{\partial \varphi^2}$

We shall call curvilinear coordinates separable, if

$$g(u) = g_1(u_1) \cdots g_n(u_n) ; \quad G_u = G_{u_1} \times \cdots \times G_{u_n} . \quad (\text{A.18})$$

The g_j are usually not the same as the h_j . The second condition depends on the choice of G_r , which is usually the \mathbb{R}^n . Separable usually does not mean orthogonal and vice versa.

Important examples for curvilinear coordinates are cylindrical and spherical coordinates. They are orthogonal and separable if the domain G_r has the form of a cylinder or a sphere or, of course, if $G_r = \mathbb{R}^3$. Explicit expressions are summarized in Table A.4. The operators Δ_ϱ and Δ_r are the two- and three-dimensional radial Laplacians and $\Delta_{\vartheta\varphi}$ is the Laplacian on the unit sphere, also known as Beltrami operator.

The expressions for plane polar coordinates follow from cylindrical coordinates by ignoring the z coordinate. Often, the functions under considerations possess symmetries if represented in curvilinear coordinates. Then one or more integrals run empty. The value of these integrals has to be included in the weight function. For examples, for cylindrical symmetry we have $d^3r = d\varrho d\zeta 2\pi\varrho$ and for spherical symmetry $d^3r = dr 4\pi r^2$.

A.2 Special Functions of Mathematical Physics

Many problems of quantum mechanics lead to so-called special functions of mathematical physics. These functions are described in the mathematical literature [2–6] or in the mathematical appendices of physics textbooks [7–9]. Unfortunately, there are different definitions and conventions for the prefactors. In this appendix, we give the definitions and important properties of the special functions used in this work.

The Hermite Polynomials

The Hermite polynomials of order $n \in \mathbb{N}_0$ are defined as

$$\begin{aligned} H_n(x) &= (-1)^n e^{+x^2} \frac{d^n}{dx^n} e^{-x^2} \\ &= (2x)^n - \frac{n(n-1)}{1} (2x)^{n-2} + \frac{n(n-1)(n-2)(n-3)}{1 \cdot 2} (2x)^{n-4} \mp \dots \end{aligned} \tag{A.19}$$

They are the solutions of the differential equation

$$e^{+x^2} \frac{d}{dx} \left[e^{-x^2} \frac{d}{dx} H_n(x) \right] + 2n H_n(x) = 0 \tag{A.20}$$

and fulfill the orthogonality relation

$$\int_{-\infty}^{+\infty} dx e^{-x^2} H_n(x) H_{n'}(x) = 2^n n! \sqrt{\pi} \delta_{nn'} . \tag{A.21}$$

The Laguerre Polynomials

The generalized Laguerre polynomials of degree $n \in \mathbb{N}_0$ and order $\alpha > -1$ are defined as

$$L_n^{(\alpha)}(x) = \frac{1}{n!} e^{+x} x^{-\alpha} \frac{d^n}{dx^n} (e^{-x} x^{n+\alpha}) ; \quad L_n^{(0)}(x) = L_n(x) . \quad (\text{A.22})$$

The functions L_n are called Laguerre polynomials. The explicit expressions for the $L_n^{(\alpha)}$ are

$$L_n^{(\alpha)}(x) = \sum_{k=0}^n (-1)^k \binom{n+\alpha}{n-k} \frac{x^k}{k!} . \quad (\text{A.23})$$

The generalized Laguerre polynomials satisfy the differential equation

$$x^{-\alpha} e^{+x} \frac{d}{dx} \left[e^{-x} x^{1+\alpha} \frac{d}{dx} L_n^{(\alpha)} \right] + n L_n^{(\alpha)}(x) = 0 . \quad (\text{A.24})$$

An alternative definition, commonly used in physics [7, 9], is

$$L_n^m(x) = \frac{n!}{(n-m)!} e^{+x} \frac{d^n}{dx^n} (e^{-x} x^{n-m}) ; \quad n \in \mathbb{N}_0 ; \quad m \in \{0, \dots, n\}$$

$$L_n^0(x) = L_n(x) . \quad (\text{A.25})$$

These functions are called associated Laguerre polynomials for $m > 0$ and Laguerre polynomials for $m = 0$. The relation to the generalized Laguerre polynomials is [2]

$$L_n^m(x) = n! (-1)^m L_{n-m}^{(m)}(x) . \quad (\text{A.26})$$

The Laguerre polynomials L_n according to the definitions (A.25) and (A.22) differ by a factor of $n!$. Sometimes, the generalized Laguerre polynomials are also denoted as L_n^α , so it is recommended to always check the definition used by the authors.

Bessel Functions

The Bessel functions (of the first kind) of integer order n are defined as follows:

$$J_n(x) = \sum_{k=0}^{\infty} \frac{(-1)^k}{k! (k+n)!} \left(\frac{x}{2}\right)^{2k+n} \quad (\text{A.27})$$

$$J_{-n}(x) = (-1)^n J_n(x) ; \quad n \in \mathbb{N}_0 .$$

They are solutions of the differential equation

$$x^2 J_n''(x) + x J_n'(x) + (x^2 - n^2) J_n(x) = 0 \quad (\text{A.28})$$

and can be expressed by an integral:

$$J_n(x) = \frac{(-i)^n}{2\pi} \int_0^{2\pi} d\varphi e^{ix \cos \varphi} \cos(n\varphi). \quad (\text{A.29})$$

Their asymptotic behavior for $x \rightarrow \pm\infty$ is

$$J_n(x) \sim \sqrt{\frac{2}{\pi x}} \cos\left(x - \frac{n\pi}{2} - \frac{\pi}{4}\right). \quad (\text{A.30})$$

The Generalized Hypergeometric Series

The generalized hypergeometric series is defined as

$${}_pF_q(\alpha_1, \dots, \alpha_p; \beta_1, \dots, \beta_q; z) = F\left(\begin{matrix} \alpha_1, \dots, \alpha_p \\ \beta_1, \dots, \beta_q \end{matrix}; z\right) = \sum_{k=0}^{\infty} \frac{(\alpha_1)_k \cdots (\alpha_p)_k}{(\beta_1)_k \cdots (\beta_q)_k} \frac{z^k}{k!}$$

$$p, q \in \mathbb{N}_0; \quad z \in \mathbb{C}; \quad (\alpha)_k = \alpha(\alpha+1) \cdots (\alpha+k-1) = \frac{\Gamma(\alpha+k)}{\Gamma(\alpha)}. \quad (\text{A.31})$$

The radius of convergence depends on p , q , and the parameters $\alpha_1, \dots, \alpha_p$, β_1, \dots, β_q . For $p \leq q$, the series is convergent for every z . If any of the parameters $\alpha_1, \dots, \alpha_p$ is a negative integer, then ${}_qF_p$ is a finite sum.

The Confluent Hypergeometric Function

The confluent hypergeometric function of the first kind (Kummer's function) is defined as

$$F(\alpha, \gamma, z) = {}_1F_1(\alpha; \gamma; z) = 1 + \frac{\alpha}{\gamma} \frac{z}{1!} + \frac{\alpha(\alpha+1)}{\gamma(\gamma+1)} \frac{z^2}{2!} + \cdots = \sum_{k=0}^{\infty} \frac{(\alpha)_k}{(\gamma)_k} \frac{z^k}{k!}$$

$$z \in \mathbb{C}; \quad \gamma \notin -\mathbb{N}_0 \quad (\text{A.32})$$

and is convergent for every z . It satisfies the differential equation

$$z F''(\alpha, \gamma, z) + (\gamma - z) F'(\alpha, \gamma, z) - \alpha F(\alpha, \gamma, z) = 0. \quad (\text{A.33})$$

A.3 Miscellaneous Relations

In this appendix we summarize mathematical relations used in this book and technical proofs.

Some Lemmas on Matrices

Lemma 1 (matrix inversion by partitioning [10]). Let A be a regular matrix with the block structure

$$A = \left(\begin{array}{c|c} A_{11} & A_{12} \\ \hline A_{21} & A_{22} \end{array} \right) , \quad (\text{A.34})$$

where A_{11} is an $m \times m$ matrix, A_{12} an $m \times n$ matrix, A_{21} an $n \times m$ matrix, and A_{22} an $n \times n$ matrix. Let us further assume that A_{22} is regular. Then the inverse of A can be written in the form

$$A^{-1} = B = \left(\begin{array}{c|c} B_{11} & B_{12} \\ \hline B_{21} & B_{22} \end{array} \right) \quad (\text{A.35})$$

and the submatrices of B are given by

$$\begin{aligned} B_{11} &= [A_{11} - A_{12}A_{22}^{-1}A_{21}]^{-1}; & B_{12} &= -A_{11}A_{12}A_{22}^{-1} \\ B_{21} &= -A_{22}^{-1}A_{21}B_{11}; & B_{22} &= A_{22}^{-1} - A_{22}^{-1}A_{21}B_{12}. \end{aligned} \quad (\text{A.36})$$

The proof follows by straight insertion.

Lemma 2. Let A be a regular $n \times n$ matrix with the following structure:

$$A = \begin{pmatrix} a_{11} & a_{12} & a_{13} & a_{14} & \cdots & a_{1n} \\ a_{21} & a_{22} & 0 & 0 & \cdots & 0 \\ a_{31} & 0 & a_{33} & 0 & \cdots & 0 \\ a_{41} & 0 & 0 & a_{44} & \cdots & 0 \\ \vdots & \vdots & \vdots & \vdots & \ddots & \vdots \\ a_{n1} & 0 & 0 & 0 & \cdots & a_{nn} \end{pmatrix}. \quad (\text{A.37})$$

Furthermore, let $a_{jj} \neq 0$ for $j = 2, \dots, n$. Then the elements of the inverse matrix $B = A^{-1}$ are given by

$$\begin{aligned} b_{11} &= \left[a_{11} - \sum_{j=2}^n \frac{a_{1j}a_{j1}}{a_{jj}} \right]^{-1} \\ b_{1k} &= -\frac{b_{11}a_{1k}}{a_{kk}}; \quad b_{j1} = -\frac{a_{j1}b_{11}}{a_{jj}} \\ b_{jk} &= \frac{\delta_{jk}}{a_{jj}} + \frac{a_{j1}b_{11}a_{1k}}{a_{jj}a_{kk}}; \quad j, k = 2, \dots, n. \end{aligned} \quad (\text{A.38})$$

Proof. Lemma 2 is a special case of Lemma 1 if we identify $A_{11} = a_{11}$, $A_{12} = (a_{12}, \dots, a_{1n})$, $A_{21} = (a_{21}, \dots, a_{n1})^T$, and $A_{22} = \text{diag}(a_{22}, \dots, a_{nn})$.

Alternatively, the inversion of the matrix A can be done explicitly by means of the exchange method [11] with pivot elements a_{nn} , $a_{n-1,n-1}$, \dots , a_{11} .

A block version of Lemma 2 is obtained when a_{11} is replaced by an $m \times m$ matrix, the a_{1k} for $k > 1$ by m -dimensional row vectors, and the a_{j1} for $j > 1$ by m -dimensional column vectors. Then the formula for the inverse matrix (A.38) remains valid if the elements b_{11} , b_{1k} , and b_{j1} ($j, k > 1$) are interpreted as matrices and vectors.

Lemma 3. For any complex regular $n \times n$ matrix B and complex n -dimensional column vectors u and v it holds that

$$\det(B - uv^T) = (1 - u^T B^{-1} v) \det B. \quad (\text{A.39})$$

Proof. The left-hand side of the above equation takes the form

$$\begin{aligned} \det(B - uv^T) &= \det(b_1 - uv_1, \dots, b_n - uv_n) \\ &= \det(b_1, \dots, b_n) - \sum_{k=1}^n \det(b_1, \dots, b_{k-1}, uv_k, b_{k+1}, \dots, b_n). \end{aligned}$$

Here, b_1, \dots, b_n are the columns of the matrix B . All other $2^n - n - 1$ contributions vanish, for example, $\det(uv_1, uv_2, b_3, \dots, b_n) = 0$. Expanding each term under the sum into cofactors, we obtain

$$\sum_{k=1}^n \det(b_1, \dots, b_{k-1}, uv_k, b_{k+1}, \dots, b_n) = \sum_{j=1}^n \sum_{k=1}^n u_j \bar{B}_{jk} v_k,$$

where \bar{B}_{jk} are the minor determinants of B , including the factor $(-1)^{j-k}$. As B is regular, \bar{B} is given by $\bar{B} = B^{-1} \det B$, which proves the proposition.

Lemma 4. Let A be a real symmetric $n \times n$ matrix and x and y real column vectors. Furthermore, we suppose that $A - iyy^T$ is regular. Then it holds that

$$\operatorname{Im}[(x - iy)^T (A - iyy^T)(x - iy)] + 1 = \left| \frac{\det(A - xy^T)}{\det(A - iyy^T)} \right|^2. \quad (\text{A.40})$$

Proof. From Lemma 3 it follows that

$$\frac{\det(A - xy^T)}{\det(A - iyy^T)} = \frac{\det[A - iyy^T - (x - iy)y^T]}{\det(A - iyy^T)} = 1 - (x - iy)^T (A - iyy^T)^{-1} y.$$

Multiplication with its complex conjugate gives:

$$\begin{aligned} \left| \frac{\det(A - xy^T)}{\det(A - iyy^T)} \right|^2 &= \left[1 - (x - iy)^T (A - iyy^T)^{-1} y \right] \left[1 - y^T (A + iyy^T)^{-1} (x + iy) \right] \\ &= 1 + (x - iy)^T (A - iyy^T)^{-1} yy^T (A + iyy^T)^{-1} (x + iy) \\ &\quad - (x - iy)^T (A - iyy^T)^{-1} y - y^T (A + iyy^T)^{-1} (x + iy) \\ &= 1 + \operatorname{Im} \left[(x - iy)^T (A - iyy^T)^{-1} (A + iyy^T) (A + iyy^T)^{-1} (x + iy) \right] \end{aligned}$$

$$\begin{aligned}
& - \operatorname{Im} \left[(x - iy)^T (A - iyy^T)^{-1} 2iy \right] \\
& = 1 + \operatorname{Im} \left[(x - iy)^T (A - iyy^T)^{-1} (x - iy) \right].
\end{aligned}$$

Proof of (4.104)

We wish to calculate the function

$$g(k, b) = \sum_{l=-\infty}^{+\infty} \operatorname{sinc}^2 \left[(b - al) \frac{\pi}{a} \right] e^{i(b - al)k} = e^{+ikb} v(k).$$

For fixed b the function v is defined as

$$v(k) = \sum_{l=-\infty}^{+\infty} \operatorname{sinc}^2 \left[(b - al) \frac{\pi}{a} \right] e^{-iakl}. \quad (\text{A.41})$$

We notice that

$$\sum_{l=-\infty}^{+\infty} \operatorname{sinc} \left[(b - al) \frac{\pi}{a} \right] e^{-iakl} = w(k)$$

$$w(k) = e^{-ikb} \text{ for } k \in (-\frac{\pi}{a}, +\frac{\pi}{a}); \quad w(k + \frac{2\pi}{a}) = w(k),$$

which can be directly verified by calculating the Fourier coefficients. In order to calculate the Fourier series (A.41), we use the convolution theorem (Table A.3) and it follows that

$$\begin{aligned}
v(k) &= \frac{a}{2\pi} \int_{-\frac{\pi}{a}}^{+\frac{\pi}{a}} dk' w(k - k') w(k') \\
&= \begin{cases} (1 + \frac{ka}{2\pi}) e^{-ikb} - \frac{ka}{2\pi} e^{-i(k + \frac{2\pi}{a})b} & \text{for } -\frac{\pi}{a} \leq k \leq 0 \\ \frac{ka}{2\pi} e^{-i(k - \frac{2\pi}{a})b} + (1 - \frac{ka}{2\pi}) e^{-ikb} & \text{for } 0 \leq k \leq +\frac{\pi}{a}. \end{cases}
\end{aligned}$$

The function v is periodic with period $\frac{2\pi}{a}$ and continuous. The functional form of v is the same for $-\frac{2\pi}{a} \leq k \leq -\frac{\pi}{a}$ and $-\frac{\pi}{a} \leq k \leq 0$ and also for $0 \leq k \leq +\frac{\pi}{a}$ and $+\frac{\pi}{a} \leq k \leq +\frac{2\pi}{a}$. Multiplication with e^{+ikb} gives the result (4.104).

Equivalence of (4.102) and (4.109)

The transition probability in (4.109) is equal to

$$p = \frac{a}{2\pi} \int_{-\frac{\pi}{a}}^{+\frac{\pi}{a}} dq \left| \int_{q - \frac{\pi}{a}}^{q + \frac{\pi}{a}} dk f(k) \right|^2$$

with f defined in (4.103). The function $f(k) e^{-ikb} = u(k)$ is periodic. Therefore, f can be represented as

$$f(k) = u(k) e^{+ikb} = \sum_{l=-\infty}^{+\infty} u_l e^{+i(b-al)k}.$$

With

$$\frac{a}{2\pi} \int_{-\frac{\pi}{a}}^{+\frac{\pi}{a}} dq \int_{q-\frac{\pi}{a}}^{q+\frac{\pi}{a}} dk e^{-i(b-al)k} \int_{q-\frac{\pi}{a}}^{q+\frac{\pi}{a}} dk' e^{+i(b-al')k'} = \left(\frac{2\pi}{a}\right)^2 \operatorname{sinc}^2\left[\left(b-al\right)\frac{\pi}{a}\right] \delta_{ll'}$$

the transition probability becomes

$$p = \left(\frac{2\pi}{a}\right)^2 \sum_{l=-\infty}^{+\infty} |u_l|^2 \operatorname{sinc}^2\left[\left(b-al\right)\frac{\pi}{a}\right].$$

With the convolution theorem (Table A.3) and Parseval's theorem (A.5) it follows that

$$p = \int_{-\frac{\pi}{a}}^{+\frac{\pi}{a}} dk_1 u^*(k_1) \int_{-\frac{\pi}{a}}^{+\frac{\pi}{a}} dk_2 v(k_1 - k_2) u(k_2)$$

with v defined in (A.41). If u and v are substituted by f and g we obtain the transition probability in (4.102).

B Physical Supplement

In this appendix we introduce important physical symbols and notations, summarize material parameters for the system GaAs/Ga_{1-x}Al_xAs, explain the introduction of dimensionless units, and give an overview over basic crystallographic concepts.

B.1 Physical Constants and Material Parameters

Here we summarize symbols and notations for physical quantities, specify numerical values for physical constants and material parameters for the GaAs/(Ga,Al)As system. We shall use SI units throughout.

Table B.1. Physical symbols and notations

Symbol	Description
$g \approx 2$	g- (gyromagnetic, Landé) factor of the electron
$\mu_B = \mu_0 \hbar e / (2m_0)$	Bohr's magneton
$\epsilon(0) = \epsilon_s; \epsilon(\infty) = \epsilon_\infty$	static and background dielectric constant
ω_{LO}, ω_{TO}	LO and TO frequency
$c = c_0 / \sqrt{\epsilon}; \lambda$	speed of light in dielectric media, wavelength of light
$n = \sqrt{\epsilon}$	refractive index
$\omega_c = eB /m$	cyclotron frequency
$\lambda_{mag} = \sqrt{\hbar/ eB }$	magnetic length
$\Omega, \Omega^{(d)}$	three- and d -dimensional normalization volume
Ω_0	volume of the unit cell
G, G_0	point and space group
$\{\alpha, \mathbf{a}\}$	space-group element
$\epsilon, \bar{\epsilon}$	identity, rotation about 2π (p. 229)
O_h, T_d	octahedron group, tetrahedron group
$\{\hat{A}\hat{B}\} = \frac{1}{2}(\hat{A}\hat{B} + \hat{B}\hat{A})$	symmetrized operator product (p. 12)
\hat{L}, \hat{J}	operator of orbital and general angular momentum
$S = \frac{\hbar}{2} \sigma$	spin operator
$m_s = \uparrow, \downarrow$	same as $m_s = \pm \frac{1}{2}$
$I_\alpha, J_\alpha, \sigma_\alpha$	I, J , and Pauli matrices

Table B.1 summarizes symbols and notations for important physical quantities.

Table B.2. Fundamental physical constants

Constant	Symbol	Value	Unit
Planck's constant	$\hbar = h/(2\pi)$	$1.054\,572 \times 10^{-34}$	Js
vacuum speed of light	c_0	$2.997\,925 \times 10^8$	m/s
vacuum permeability	μ_0	$4\pi \times 10^{-7}$	Vs/Am
vacuum dielectric constant	$\epsilon_0 = 1/(\mu_0 c_0^2)$	$8.854\,188 \times 10^{-12}$	As/Vm
electron rest mass	m_0	$9.109\,382 \times 10^{-31}$	kg
electron charge	e	$1.602\,176 \times 10^{-19}$	As

Table B.2 contains numerical values of fundamental physical constants [1]. The values for c_0 , μ_0 , and ϵ_0 are exact by definition. The other numbers are rounded to six significant digits.

Table B.3. Material parameters of GaAs at 0 K

Parameter	Symbol	Value	Unit	Ref.
band gap	E_g	1.519	eV	[2]
electron effective mass	m_e	0.067	m_0	[2]
electron effective g -factor	g_e	-0.44		
Luttinger parameters	γ_1	6.85		[2]
	γ_2	2.10		
	γ_2	2.90		
	κ	1.20		
	q	0.04		
lattice constant	a_0	5.65	Å	[2]
static dielectric constant	$\epsilon_s = \epsilon(0)$	13.1		[3]

Table B.3 lists important material parameters for GaAs at $T = 0$ K. The effective hole mass depends on the direction of the wavevector \mathbf{k} (band warping). In the [100] and equivalent directions, the effective masses of heavy and light hole are

$$m_{hh} = \frac{m_0}{\gamma_1 - 2\gamma_2}; \quad m_{lh} = \frac{m_0}{\gamma_1 + 2\gamma_2}. \quad (\text{B.1})$$

For some applications it is desirable to work with averaged effective masses. There is no unique definition of an averaged effective mass, instead, the averaging procedure depends on the physical problem. The cyclotron mass for a magnetic field in the [100] direction in the limit of large Landau quantum number is equal to [4, 5]

$$m_{hh} = \frac{m_0}{\gamma_1 - \sqrt{\gamma_2^2 + \frac{3}{4}(\gamma_2 + \gamma_3)^2}}; \quad m_{lh} = \frac{m_0}{\gamma_1 + \sqrt{\gamma_2^2 + \frac{3}{4}(\gamma_2 + \gamma_3)^2}}, \quad (\text{B.2})$$

which plays the role of an averaged mass for the motion in the (100) plane. There are several definitions of a spherically averaged mass. Table B.4 gives the theoretical and experimental values for the different effective masses in GaAs.

Table B.4. Effective hole masses for GaAs at 0 K in units of m_0 .

Mass	Theory		Experiment		Ref.
	m_{hh}	m_{lh}	m_{hh}	m_{lh}	
effective mass, $\mathbf{k} \parallel [100]$	0.377	0.0905			
cyclotron mass, $\mathbf{B} \parallel [100]$	0.491	0.0857	0.475	0.087	[2]
density-of-states mass			0.50	0.087	[6]

Material parameters for $\text{Ga}_{1-x}\text{Al}_x\text{As}$ are usually determined from interpolation between the values for GaAs and AlAs [2, 3, 6]. In the calculations we use a linear interpolation formula for the band offsets at the Γ point [3]

$$\begin{aligned} E_c(\text{Ga}_{1-x}\text{Al}_x\text{As}) - E_c(\text{GaAs}) &= +790x \text{ meV} \\ &\quad ; \quad x \leq 0.4 . \quad (\text{B.3}) \\ E_v(\text{Ga}_{1-x}\text{Al}_x\text{As}) - E_v(\text{GaAs}) &= -460x \text{ meV} \end{aligned}$$

For GaAs/(Ga,Al)As heterostructures, for simplicity, we use the GaAs effective masses and dielectric constant.

B.2 Dimensionless Quantities

A physical quantity A is expressed as $A = \{A\} [A]$, where $\{A\}$ is the numerical value and $[A]$ is the unit of A . In the SI, any mechanical or electrical unit is expressed by the basis units kg, m, s, and A as $[A] = \text{kg}^a \text{m}^b \text{s}^c \text{A}^d$ with integer exponents a, b, c , and d . The Gaussian (cgs) system uses only the basis units cm, g, and s. Electromagnetic quantities are expressed through mechanical quantities by the cgs form of Coulomb's law $F = Q_1 Q_2 / r^2$, which leads to half-integer exponents.

Natural units are often employed in order to perform numerical calculations or to get a feeling whether a quantity is small, medium, or large. Consider the eigenvalue problem for the relative motion of the exciton

$$\left(-\frac{\hbar^2}{2m} \Delta - \frac{e^2}{4\pi\varepsilon_0\varepsilon r} \right) \varphi(\mathbf{r}) = E \varphi(\mathbf{r}) , \quad (\text{B.4})$$

where $m = m_e m_h / (m_e + m_h)$ is the reduced effective mass and ε is the dielectric constant. To go over to dimensionless quantities, we use the mechanical basis units \hbar, m , and $e^2 / (4\pi\varepsilon_0\varepsilon)$, known as excitonic Hartree units. Formally, this can be written as $\hbar = m = e^2 / (4\pi\varepsilon_0\varepsilon) = 1$.

Then the unit of any mechanical quantity A is

$$[A] = \hbar^\alpha m^\beta \left(\frac{e^2}{4\pi\varepsilon_0\varepsilon} \right)^\gamma ; \quad \alpha, \beta, \gamma \in \mathbb{Z}. \quad (\text{B.5})$$

The units for energy, length, and time are

$$\begin{aligned} [E] &= 2 \text{Ry}^* = \frac{m}{\hbar^2} \left(\frac{e^2}{4\pi\varepsilon_0\varepsilon} \right)^2 = 27.21 \text{ eV} \times \frac{m}{m_0} \varepsilon^{-2} \\ [a] &= a_B^* = \frac{\hbar^2}{m} \frac{4\pi\varepsilon_0\varepsilon}{e^2} = 0.5292 \text{ \AA} \times \left(\frac{m}{m_0} \right)^{-1} \varepsilon \\ [t] &= \frac{\hbar}{2 \text{Ry}^*}. \end{aligned} \quad (\text{B.6})$$

The quantities 1Ry^* and a_B^* are the excitonic Rydberg and the Bohr radius of the exciton. For GaAs parameters $m_e = 0.076 m_0$, $m_h = 0.50 m_0$, and $\varepsilon = 13.1$, we have $[E] = 9.37 \text{ meV}$ and $[a] = 11.7 \text{ nm}$. The unit $[t]$ is the characteristic time for quantum beats between exciton states. The value for GaAs parameters is $[t] = 70.3 \text{ fs}$.

An alternative to excitonic Hartree units are excitonic Rydberg units, defined by $\hbar = 2m = e^2/(8\pi\varepsilon_0\varepsilon) = 1$. The excitonic Rydberg units for energy, length, and time are 1Ry^* , a_B^* , and \hbar/Ry^* .

In excitonic Hartree units, the eigenvalue problem (B.4) writes as

$$\left(-\frac{1}{2} \Delta - \frac{1}{r} \right) \varphi(\mathbf{r}) = E \varphi(\mathbf{r}), \quad (\text{B.7})$$

where \mathbf{r} , E , and φ are dimensionless quantities. The ground-state energy and eigenfunction of the equation (B.7) are $E_{1s} = -\frac{1}{2}$ and $\varphi_{1s}(\mathbf{r}) = e^{-r}/\sqrt{\pi}$. In physical units, E_{1s} and φ_{1s} have the dimensions energy and length $^{-3/2}$. Therefore, the solution of (B.4) for the ground state is

$$E_{1s} = -1 \text{ Ry}^* ; \quad \varphi_{1s}(\mathbf{r}) = \frac{1}{\sqrt{\pi a_B^{*3}}} e^{-r/a_B^*}. \quad (\text{B.8})$$

Finally, we extend the excitonic Hartree units to include electromagnetic quantities. In the presence of electric and magnetic field in z direction, the Hamiltonian (B.4) contains the additional potentials $e F z$ and $e^2 B^2 \rho^2/(8m)$, which have the dimension of an energy. In addition to the units (B.5), we use the elementary charge e as the unit for the charge. Then the units for the electric and magnetic field are

$$[F] = \frac{[E]}{e[a]} = \left(\frac{m}{\hbar^2} \right)^2 \left(\frac{e^2}{4\pi\varepsilon_0\varepsilon} \right)^3 \frac{1}{e} = 5.142 \times 10^{11} \frac{\text{V}}{\text{m}} \times \left(\frac{m}{m_0} \right)^2 \varepsilon^{-3} \quad (\text{B.9})$$

$$[B] = \frac{\sqrt{m[E]}}{e[a]} = \frac{m^2}{\hbar^3} \left(\frac{e^2}{4\pi\varepsilon_0\varepsilon} \right)^2 \frac{1}{e} = 2.351 \times 10^5 \text{ T} \times \left(\frac{m}{m_0} \right)^2 \varepsilon^{-2}.$$

For GaAs parameters, we have $[F] = 7.98 \text{ kV/cm}$ and $[B] = 4.78 \text{ T}$.

B.3 Crystal Symmetry

In this appendix we summarize important facts about crystal symmetry and give an introduction to crystallographic groups. This topic is dealt with in many textbooks on theoretical physics, e.g., in the work of Landau and Lifshitz [7]. There are also several books on the application of group theory in physics, which have a chapter on crystal symmetry [8, 9]. The work by Streitwolf specializes in the application of group theory in solid-state physics [10]. Yu and Cardona give an easy-to-read introduction to crystallographic groups [11].

A three-dimensional crystal lattice (or direct lattice) is defined as the set of points

$$\mathbf{R} = \sum_{i=1}^3 m_i \mathbf{a}_i ; \quad m_i \in \mathbb{Z} . \quad (\text{B.10})$$

the linearly independent vectors $\mathbf{a}_1, \mathbf{a}_2, \mathbf{a}_3$ are called primitive lattice vectors. Without loss of generality, we assume that

$$[\mathbf{a}_1, \mathbf{a}_2, \mathbf{a}_3] = \mathbf{a}_1 \cdot (\mathbf{a}_2 \times \mathbf{a}_3) = \det(\mathbf{a}_1, \mathbf{a}_2, \mathbf{a}_3) = \Omega_0 > 0 . \quad (\text{B.11})$$

The primitive unit cell is the set of points

$$\mathbf{r} = \sum_i \mu_i \mathbf{a}_i ; \quad \mu_i \in [0, 1) . \quad (\text{B.12})$$

It is a parallelepiped with volume Ω_0 . The choice of the primitive lattice vectors is not unique and any three lattice vectors $\mathbf{R}_1, \mathbf{R}_2, \mathbf{R}_3$ with $[\mathbf{R}_1, \mathbf{R}_2, \mathbf{R}_3] = \Omega_0$ can serve as primitive lattice vectors. A unique construction of a primitive cell is the Wigner–Seitz cell, which is the set of points \mathbf{r} with the property

$$|\mathbf{r}| < |\mathbf{r} - \mathbf{R}| \quad \text{for all } \mathbf{R} \neq \mathbf{0} . \quad (\text{B.13})$$

The volume of the Wigner–Seitz cell is the same as for the primitive unit cell, Ω_0 .

Besides translations about lattice vectors \mathbf{R} , a lattice is invariant under orthogonal transforms. For a given lattice, the group of these matrices is called the holohedric point group. There may different types of lattices belonging to the same holohedric point group. It is clear that the Wigner–Seitz cell (B.13) is invariant under the holohedric point group.

The reciprocal lattice is the set of points \mathbf{K} with the property

$$\mathbf{K} \cdot \mathbf{R} \in 2\pi\mathbb{Z} . \quad (\text{B.14})$$

It is easy to show that the reciprocal lattice is equal to the set

$$\mathbf{K} = \sum_{j=1}^3 n_j \mathbf{b}_j ; \quad n_j \in \mathbb{Z} ; \quad \mathbf{a}_i \cdot \mathbf{b}_j = 2\pi\delta_{ij} , \quad (\text{B.15})$$

where the vectors $\mathbf{b}_1, \mathbf{b}_2, \mathbf{b}_3$ are the reciprocal vectors of $\mathbf{a}_1, \mathbf{a}_2, \mathbf{a}_3$.¹ They can be calculated from

$$\begin{pmatrix} \mathbf{b}_1^T \\ \mathbf{b}_2^T \\ \mathbf{b}_3^T \end{pmatrix} = 2\pi (\mathbf{a}_1, \mathbf{a}_2, \mathbf{a}_3)^{-1}; \quad \mathbf{b}_i = 2\pi \frac{\mathbf{a}_{i+1} \times \mathbf{a}_{i+2}}{\Omega_0}. \quad (\text{B.16})$$

Again, the choice of the primitive vectors of the reciprocal lattice is not unique, except that a particular set of primitive vectors of the direct lattice corresponds to a particular set of primitive vectors of the reciprocal lattice and vice versa. The Wigner–Seitz cell of the reciprocal lattice is called the (first) Brillouin zone. According to (B.16), the volume of the Brillouin zone is $(2\pi)^3/\Omega_0$. From the definition (B.14) it follows that the reciprocal lattice has the same holohedric point group as the direct lattice.

Crystallographic directions are characterized by a lattice vector $\mathbf{R} = h\mathbf{a}_1 + k\mathbf{a}_2 + l\mathbf{a}_3$, where the Miller indices h, k, l are integers with no common divisor. The symbol for a crystallographic direction is $[hkl]$. An overbar denotes a minus sign, i.e., \bar{h} stands for $-h$. A plane of the direct lattice is perpendicular to a crystallographic direction of the reciprocal lattice and vice versa. The symbol for a lattice plane is (hkl) , with h, k, l being the Miller indices of the normal direction in the reciprocal lattice. An ensemble of parallel planes with the same Miller indices (hkl) is denoted as $\{hkl\}$. The distance between neighboring planes is equal to $d_{hkl} = 2\pi / |h\mathbf{b}_1 + k\mathbf{b}_2 + l\mathbf{b}_3|$. The above relations are valid only for the primitive unit cell. On the other hand, Miller indices are often derived from the conventional (nonprimitive) unit cell. Then, in cubic semiconductors, the (hkl) plane is perpendicular to the $[hkl]$ direction. There are four Miller indices for hexagonal lattices in the description of the conventional unit cell.

An ideal crystal is a periodic array of atoms. An S -atomic crystal is described by the crystal lattice $\{ \mathbf{R} \}$, the atomic positions, relative to the lattice vectors, $\{ \boldsymbol{\tau}_1, \dots, \boldsymbol{\tau}_S \}$, and the atom species $\{ A_1, \dots, A_S \}$. We assume a primitive unit cell so that the number of atoms per unit cell S is the smallest possible value.

The symmetry of a crystal is somewhat more complicated than the symmetry of a lattice. The space group G of the crystal is the group of all transformations

$$\mathbf{r}' = \alpha \mathbf{r} + \mathbf{a} = \{ \alpha, \mathbf{a} \} \mathbf{a}; \quad \alpha \in O(3); \quad \mathbf{a} \in \mathbb{R}^3 \quad (\text{B.17})$$

which leaves the crystal invariant. In contrast to the three-dimensional empty space, this group is discrete. The product of two group elements, the neutral, and the inverse element are given by

¹ In mathematics or classical crystallography, reciprocal vectors are defined without the factor 2π .

$$\begin{aligned} \{\alpha, \mathbf{a}\} \{\beta, \mathbf{b}\} &= \{\alpha\beta, \alpha\mathbf{b} + \mathbf{a}\} \\ \{\varepsilon, \mathbf{0}\} \mathbf{r} &= \mathbf{r} \\ \{\alpha, \mathbf{a}\}^{-1} &= \{\alpha^{-1}, -\alpha^{-1}\mathbf{a}\}, \end{aligned} \quad (\text{B.18})$$

where in this context ε denotes the three-dimensional unity matrix. An important subgroup of G is the Abelian translation group with elements $\{\varepsilon, \mathbf{R}\}$, where \mathbf{R} is a lattice vector. From (B.18) we see that the orthogonal matrices from the space group fulfill the group properties with respect to the matrix multiplication. This finite group of orthogonal transformations is called the point group of the crystal. However, the crystal is not necessarily invariant under the point group. If the origin of the atomic positions can be chosen such that the point group leaves the crystal invariant, then the crystal is called *symmorphic*, otherwise, the crystal is called *nonsymmorphic*. Now, we deduce an important property of the point group. Consider the space-group operation

$$\{\alpha, \mathbf{a}\} \{\varepsilon, \mathbf{R}\} \{\alpha, \mathbf{a}\}^{-1} = \{\varepsilon, \alpha\mathbf{R}\}. \quad (\text{B.19})$$

Because the r.h.s. is a pure translation, the vector $\mathbf{R}' = \alpha\mathbf{R}$ must be a lattice vector. As a consequence, the crystal lattice is invariant under the operations of the point group, which means that the point group must be a subgroup of the holohedric point group of the lattice. Obviously, for a one-atomic crystal the point group is identical to the holohedric point group.

In three dimensions, there are 7 holohedries, leading to 7 crystal systems: triclinic, monoclinic, orthorhombic, tetragonal, rhombohedral, hexagonal, and cubic. There are 14 different lattices, called Bravais lattices, which belong to the 7 crystal systems. The 32 crystallographic point groups, which are the subgroups of the holohedric point groups give rise to 32 crystal classes. If the point groups are combined with the translations, they give rise to 230 space groups, or 230 crystal structures, 73 of them being *symmorphic* and 157 being *nonsymmorphic*.

If the spin of the electron is taken into account, a rotation or rotation-reflection $\alpha \in O(3)$ also effects the spinor components so that the space group and the point group become double-valued (App. C.2). This problem can be resolved using a trick by Bethe [12], who treated the rotation by 2π as an extra operation $\bar{\varepsilon}$. Then, formally, the groups $G \times \{\{\varepsilon, \mathbf{0}\}, \{\bar{\varepsilon}, \mathbf{0}\}\}$ and $G_0 \times \{\varepsilon, \bar{\varepsilon}\}$, known as double space group and double point group, are single-valued.

An important crystal system are cubic crystals. There are three cubic Bravais lattices: the simple cubic (sc), the body-centered cubic (bcc), and the face-centered cubic (fcc) lattice. The holohedric group of the cubic lattices is the octahedral group O_h and its elements are matrices with exactly one nonzero element, +1 or -1 in every row and every column, which gives 48 group elements in total. The crystallographic (or conventional) unit cell for cubic crystals is a cube with the length of the edge a_0 , called lattice constant.

For the sc lattice, the primitive unit cell is equal to the crystallographic unit cell and its volume is $\Omega_0 = a_0^3$. For the bcc lattice, we have 2 lattice points per conventional unit cell and thus $\Omega_0 = a_0^3/2$. A common choice of the primitive lattice vectors is $\mathbf{a}_1 = \frac{a_0}{2}(-1, 1, 1)^T$, $\mathbf{a}_2 = \frac{a_0}{2}(1, -1, 1)^T$, and $\mathbf{a}_3 = \frac{a_0}{2}(1, 1, -1)^T$. For the fcc lattice, we have 4 lattice points per crystallographic unit cell and the volume of the primitive unit cell is $\Omega_0 = a_0^3/4$. The primitive lattice vectors are typically chosen as $\mathbf{a}_1 = \frac{a_0}{2}(0, 1, 1)^T$, $\mathbf{a}_2 = \frac{a_0}{2}(1, 0, 1)^T$, and $\mathbf{a}_3 = \frac{a_0}{2}(1, 1, 0)^T$. The reciprocal lattice of an sc lattice is again an sc lattice. The reciprocal lattice of a bcc lattice is an fcc lattice and vice versa.

Examples for cubic crystals are the diamond and the zincblende structure, which are both fcc crystals with two atoms per primitive unit cell. For the diamond structure, the two atoms are equal, i.e., $A_1 = A_2$ (e.g., $A_1 = A_2 = \text{Si}$), and the atomic positions are $\tau_1 = 0$ and $\tau_2 = \frac{a_0}{4}(1, 1, 1)$. An alternative choice is $\tau_{1,2} = \pm \frac{a_0}{8}(1, 1, 1)$. The diamond crystal is non-symmorphic and the point group is equal to the holohedric point group O_h . For the zincblende structure, the two atoms are different, i.e., $A_1 \neq A_2$ (e.g., $A_1 = \text{Ga}$, $A_2 = \text{As}$), and the atomic positions are commonly chosen to be $\tau_1 = 0$ and $\tau_2 = \frac{a_0}{4}(1, 1, 1)$. The zincblende structure is symmorphic and the point group T_d , known as the tetrahedron group, is a subgroup of O_h , which does not contain the inversion $-\varepsilon$.

The Fourier series of a lattice-periodic function $u(\mathbf{r}) = u(\mathbf{r} + \mathbf{R})$ can be written as

$$u(\mathbf{r}) = \sum_{\mathbf{K}} c_{\mathbf{K}} e^{+i\mathbf{K}\cdot\mathbf{r}} ; \quad c_{\mathbf{K}} = \frac{1}{\Omega_0} \int_{\Omega_0} d^3\mathbf{r} e^{-i\mathbf{K}\cdot\mathbf{r}} u(\mathbf{r}) , \quad (\text{B.20})$$

where the sum runs over all points of the reciprocal lattice.

C Essentials of Quantum Mechanics

In this appendix we summarize important facts from quantum mechanics. We first review the quantum mechanical eigenvalue problem: after a discussion of the general properties we give explicit solutions for a number of selected eigenvalue problems. Then we outline the quantum theory of angular momenta. Finally, we derive important formulas from time-independent and time-dependent perturbation theory.

C.1 The Quantum-Mechanical Eigenvalue Problem

In the following we summarize important facts about the quantum mechanical eigenvalue problem. We discuss the general properties of the spectrum of Schrödinger operators, write the eigenvalue problem as variational problem, and outline the method of artificial boundary conditions. These topics are discussed in almost every textbook on quantum mechanics. We recommend the works by Landau and Lifshitz [1] and by Merzbacher [2]. A large number of quantum-mechanical eigenvalue problems is discussed by Flügge and Marschall [3] and, with particular emphasis on low-dimensional semiconductors, by Davies [4].

C.1.1 The Spectrum of Schrödinger Operators

We consider an l -dimensional domain $G \subset \mathbb{R}^l$ and a Hermitian differential operator \hat{H} with an entirely discrete spectrum. The eigenvalue problem of \hat{H} is

$$\hat{H} \varphi_\lambda(u) = E_\lambda \varphi_\lambda(u) ; \quad \lambda \in \mathbb{N} . \quad (\text{C.1})$$

Because of the Hermiticity of \hat{H} , eigenfunctions of different eigenvalues are orthogonal. Furthermore, eigenfunctions which belong to degenerate eigenvalues can be orthonormalized. Therefore, we can always assume a normalization of the eigenfunctions of the form

$$\int \underline{du} \varphi_\lambda^*(u) \varphi_{\lambda'}(u) = \delta_{\lambda\lambda'} . \quad (\text{C.2})$$

The set of eigenfunctions is complete, which means that any square-integrable function is a linear combination of the eigenfunctions. Formally, this can be written as

$$\sum_{\lambda} \varphi_{\lambda}(u) \varphi_{\lambda}^*(u') = \delta(u, u') , \quad (\text{C.3})$$

known as closure relation. In Dirac notation, orthonormality and closure relation write as

$$\langle \varphi_{\lambda} | \varphi_{\lambda'} \rangle = \delta_{\lambda\lambda'} ; \quad \sum_{\lambda} |\varphi_{\lambda}\rangle \langle \varphi_{\lambda}| = 1 . \quad (\text{C.4})$$

The quantum-mechanical eigenvalue problem can be deduced from a variational principle. We consider a separable Hilbert space and a Hermitian operator \hat{H} with discrete spectrum. The function $\varphi \neq 0$ is an eigenfunction of \hat{H} if and only if

$$\delta E[\varphi] = 0 ; \quad E[\varphi] = \frac{\langle \varphi | \hat{H} | \varphi \rangle}{\langle \varphi | \varphi \rangle} . \quad (\text{C.5})$$

In this case, the eigenvalue is equal to $E[\varphi]$. Equation (C.5) can also be written as a variational problem with constraint:

$$\delta E[\varphi] = 0 ; \quad E[\varphi] = \langle \varphi | \hat{H} | \varphi \rangle ; \quad I[\varphi] = \langle \varphi | \varphi \rangle = \text{const} = 1 . \quad (\text{C.6})$$

A necessary condition for (C.6) is the existence of a Lagrange multiplier λ such that

$$\delta E[\varphi] - \lambda \delta I[\varphi] = 0 . \quad (\text{C.7})$$

For the solution φ of (C.6), the Lagrange multiplier is equal to the eigenvalue $E[\varphi]$. Because the functionals E and I are real, it is sufficient to carry out the variation with respect to φ^* , which leads to the eigenvalue problem $\hat{H}\varphi = E\varphi$. Variation with respect to φ would give the conjugate complex equation $(\hat{H}\varphi)^* = E\varphi^*$.

Now we turn to the case that \hat{H} has bound and scattering states. In the mathematical literature, only the points of the discrete spectrum are called eigenvalues. In physics, it is common also to speak of continuous eigenvalues and eigenfunctions. Without loss of generality, we assume an infinite number of discrete states at negative energies and a continuum which is identical with the nonnegative real axis $[0, +\infty)$. The eigenvalue problem of \hat{H} is

$$\hat{H} \varphi_{\lambda}(u) = E_{\lambda} \varphi_{\lambda}(u) ; \quad E_{\lambda} < 0 ; \quad \lambda \in \mathbb{N} ; \quad \lim_{\lambda \rightarrow \infty} E_{\lambda} = 0 \quad (\text{C.8})$$

$$\hat{H} \varphi_q(u) = E(q) \varphi_q(u) ; \quad 0 \leq E(q) < \infty ; \quad q = (q_1, \dots, q_m) .$$

Typical examples are the Hydrogen atom in two ($m = 2$) or three ($m = 3$) dimensions (App. C.1.2).

As many quantum-mechanical calculations are purely symbolic, a common methodical trick is to introduce a normalization domain $G' \subset G$ with artificial boundary conditions like vanishing or periodic (Born–von Kármán) boundary conditions. Thus we ensure that the spectrum is entirely discrete, the Hilbert space is separable, and the eigenfunctions are square integrable. At the end of the calculation, in order to obtain explicit results, we perform the limit $G' \rightarrow G$.

Let \mathcal{E}_Λ and Φ_Λ be eigenvalues and eigenfunctions of \hat{H} on the normalization domain G' , normalized according to (C.2). In the limit $G' \rightarrow G$, the eigenvalues and eigenfunctions will approach the exact solutions (C.8). For the discrete eigenstates it holds that

$$\mathcal{E}_\lambda \longrightarrow E_\lambda ; \quad \Phi_\lambda(u) \longrightarrow \varphi_\lambda(u) \text{ for } u \in G' . \quad (\text{C.9})$$

For the continuum states, one cannot strictly speak of convergence for eigenvalues and eigenfunctions, as a continuous set is approximated by a quasi-continuum of discrete states. Each quantum number Λ with $\mathcal{E}_\Lambda > 0$ is associated with a cell in q -space. In the limit $G' \rightarrow G$, the q -cells become increasingly small and the density of states $D(q)$, which is the reciprocal volume of the q -cells, goes to infinity. The transition to the continuum is given by the following relations:

$$\sum_{\Lambda}' \cdots = \int \underline{dq} D(q) \cdots \quad (\text{C.10})$$

$$\delta_{\Lambda\Lambda'} = \frac{\delta(q, q')}{\sqrt{D(q)D(q')}} ; \quad \Phi_\Lambda(u) = \frac{\varphi_q(u)}{\sqrt{D(q)}} ,$$

where the prime stands for “summation over the continuum states.” With (C.9) and (C.10), we obtain the general rule:¹

$$\sum_{\Lambda} \Phi_{\Lambda}(u) \Phi_{\Lambda}^*(u') \cdots = \sum_{\lambda} \varphi_{\lambda}(u) \varphi_{\lambda}^*(u') \cdots + \int \underline{dq} \varphi_q(u) \varphi_q^*(u') \cdots \quad (\text{C.11})$$

In the continuum limit, the orthonormality and closure of the eigenfunctions reads

$$\int \underline{du} \begin{Bmatrix} \varphi_{\lambda}^*(u) \varphi_{\lambda'}(u) \\ \varphi_{\lambda}^*(u) \varphi_{q'}(u) \\ \varphi_q^*(u) \varphi_{q'}(u) \end{Bmatrix} = \begin{Bmatrix} \delta_{\lambda\lambda'} \\ 0 \\ \underline{\delta}(q, q') \end{Bmatrix} \quad (\text{C.12})$$

and

$$\sum_{\lambda} \varphi_{\lambda}(u) \varphi_{\lambda}^*(u') + \int \underline{dq} \varphi_q(u) \varphi_q^*(u') = \underline{\delta}(u, u') . \quad (\text{C.13})$$

¹ The sum over the discrete states plus the integral over the continuum states is often written as a “sum-integral” \sum_{Λ} .

Unless otherwise noted, (C.12) will be the standard normalization in the presence of a discrete and a continuous spectrum.

Sometimes, in the evaluation of integrals of the form (C.11) it is desirable to use the energy as integration variable. For $m = 1$, it is common to use the energy itself as parameter (energy normalization). For $m > 1$, we change over to the variables ε, s , where $s = (s_1, \dots, s_{m-1})$ is the parameterization of the surface $E(q) = \varepsilon$. The volume element in q -space is $\underline{dq} = dr \underline{ds}$, where dr is the distance between the surfaces ε and $\varepsilon + d\varepsilon$, and \underline{ds} is the surface element. Since $d\varepsilon = |\nabla E| dr$, the integral in the new variables is

$$\int \underline{dq} \cdots = \int d\varepsilon \int_{E(q)=\varepsilon} \frac{\underline{ds}}{|\nabla E(q)|} \cdots \quad (\text{C.14})$$

C.1.2 Selected Eigenvalue Problems

In the following, we specify the eigenvalues and eigenfunctions for a number of Schrödinger operators.

A. Free electron

The Hamiltonian of a nonrelativistic free electron with mass m in real space is

$$\hat{H} = -\frac{1}{2m} \Delta \quad (\text{C.15})$$

and the domain is the real space \mathbb{R}^3 . The eigenvalues and eigenfunctions are

$$E(\mathbf{k}) = \frac{\hbar^2 k^2}{2m} ; \quad \varphi_{\mathbf{k}}(\mathbf{r}) = \frac{1}{(2\pi)^{3/2}} e^{i\mathbf{k}\cdot\mathbf{r}} ; \quad \mathbf{k} \in \mathbb{R}^3 . \quad (\text{C.16})$$

These functions are the simultaneous eigenfunctions of the momentum operator $\hat{\mathbf{p}} = \frac{\hbar}{i} \nabla$ with eigenvalues $\hbar\mathbf{k}$. Orthonormality and closure of the eigenfunctions (C.16) read as:

$$\int d^3\mathbf{r} \varphi_{\mathbf{k}}^*(\mathbf{r}) \varphi_{\mathbf{k}'}(\mathbf{r}) = \delta(\mathbf{k}-\mathbf{k}') ; \quad \int d^3\mathbf{k} \varphi_{\mathbf{k}}(\mathbf{r}) \varphi_{\mathbf{k}}^*(\mathbf{r}') = \delta(\mathbf{r}-\mathbf{r}') . \quad (\text{C.17})$$

For many applications, it is useful to introduce a finite normalization domain $\Omega = [-L_x/2, +L_x/2] \times [-L_y/2, +L_y/2] \times [-L_z/2, +L_z/2]$ and, in the finite result, take the limit $L_x, L_y, L_z \rightarrow \infty$. For hard walls, the eigenfunctions are products of cosine and sine functions for the different coordinates, which are difficult to handle. Much more convenient are periodic (or Born-von Kármán) boundary conditions with $\varphi(\mathbf{r}) = \varphi(\mathbf{r} + L_{\alpha} \mathbf{e}_{\alpha})$ for $\alpha = 1, 2, 3$. Then the eigenfunctions remain plane waves, but the wavevectors are restricted to discrete values. The explicit form of the solutions is

$$E(\mathbf{k}) = \frac{\hbar^2 k^2}{2m} ; \quad \varphi_{\mathbf{k}}(\mathbf{r}) = \frac{1}{\sqrt{\Omega}} e^{i\mathbf{k}\cdot\mathbf{r}} \quad (\text{C.18})$$

$$\mathbf{k} = 2\pi \left(\frac{n_x}{L_x}, \frac{n_y}{L_y}, \frac{n_z}{L_z} \right)^T ; \quad n_x, n_y, n_z \in \mathbb{Z}$$

and the orthogonality and closure relations are²

$$\int_{\Omega} d^3 r \varphi_{\mathbf{k}}^*(\mathbf{r}) \varphi_{\mathbf{k}'}(\mathbf{r}) = \delta_{n_x n'_x} \delta_{n_y n'_y} \delta_{n_z n'_z} = \delta_{\mathbf{k}\mathbf{k}'} \quad (\text{C.19})$$

$$\sum_{n_x n_y n_z} \varphi_{\mathbf{k}}(\mathbf{r}) \varphi_{\mathbf{k}}^*(\mathbf{r}') = \sum_{\mathbf{k}} \varphi_{\mathbf{k}}(\mathbf{r}) \varphi_{\mathbf{k}}^*(\mathbf{r}') = \delta(\mathbf{r}-\mathbf{r}') \quad \text{for } \mathbf{r}, \mathbf{r}' \in \Omega .$$

One wavevector \mathbf{k} occupies a cell in reciprocal space with volume $(2\pi)^3/\Omega$. Therefore, the density of states of the \mathbf{k} points is $\Omega/(2\pi)^3$. In the limit $L_x, L_y, L_z \rightarrow \infty$, the sum over the \mathbf{k} -points goes over into

$$\frac{1}{\Omega} \sum_{\mathbf{k}} \dots = \frac{1}{(2\pi)^3} \int d^3 \mathbf{k} \dots \quad (\text{C.20})$$

B. Bloch electron

The eigenvalue problem of an electron in a periodic lattice, known as Bloch electron, is treated in a number of original papers (for references, see Chap. 4) and in textbooks on quantum mechanics and solid-state physics [5–8].

The Hamiltonian of a Bloch electron is of the form

$$\hat{H} = -\frac{\hbar^2}{2m} \Delta + W(\mathbf{r}) ; \quad W(\mathbf{r}) = W(\mathbf{r} + \mathbf{R}) , \quad (\text{C.21})$$

where \mathbf{R} is an arbitrary vector of the direct lattice. Formally, lattice translations can be described by a lattice translation operator

$$\hat{T}_{\mathbf{R}} \varphi(\mathbf{r}) = \varphi(\mathbf{r} + \mathbf{R}) ; \quad \hat{T}_{\mathbf{R}} = \exp(\mathbf{R} \cdot \boldsymbol{\nabla}) = \exp\left(\frac{i}{\hbar} \mathbf{R} \cdot \hat{\mathbf{p}}\right) . \quad (\text{C.22})$$

The orthonormal and complete eigenfunctions are the same as for the momentum operator, (C.16), and the eigenvalues are $e^{i\mathbf{k}\cdot\mathbf{R}}$. However, because wavevectors, which differ by a reciprocal lattice vector, lead to the same eigenvalue, we can restrict the wavevector to the first Brillouin zone and the general expression for the orthonormal and complete eigenfunctions is

$$\varphi_{j\mathbf{k}}(\mathbf{r}) = \frac{1}{(2\pi)^3/2} e^{i\mathbf{k}\cdot\mathbf{r}} \sum_{\mathbf{K}} c_{j\mathbf{k}}(\mathbf{K}) e^{i\mathbf{K}\cdot\mathbf{r}} \quad (\text{C.23})$$

$$\sum_{\mathbf{K}} c_{j\mathbf{k}}^*(\mathbf{K}) c_{j'\mathbf{k}}(\mathbf{K}) = \delta_{jj'} ; \quad \mathbf{k} \in \text{BZ} .$$

² Usually, the normalization domain Ω is not explicitly written at the integral sign.

On the other hand, the sum over the $e^{i\mathbf{K}\cdot\mathbf{r}}$ is the general expression for a lattice-periodic function (B.20). Therefore, the eigenfunctions of $\hat{T}_{\mathbf{R}}$ can be written as:

$$\begin{aligned} \varphi_{j\mathbf{k}}(\mathbf{r}) &= \frac{1}{(2\pi)^{3/2}} e^{i\mathbf{k}\cdot\mathbf{r}} u_{j\mathbf{k}}(\mathbf{r}) ; \quad u_{j\mathbf{k}}(\mathbf{r}) = u_{j\mathbf{k}}(\mathbf{r} + \mathbf{R}) \\ (\langle u_{j\mathbf{k}} | u_{j'\mathbf{k}} \rangle) &= \frac{1}{\Omega_0} \int_{\Omega_0} d^3\mathbf{r} u_{j\mathbf{k}}^*(\mathbf{r}) u_{j'\mathbf{k}}(\mathbf{r}) = \delta_{jj'} . \end{aligned} \quad (C.24)$$

The wavevector $\mathbf{k} \in \text{BZ}$ is called reduced or Bloch wavevector and the eigenfunctions of the translation operator (C.24) are called Bloch functions. The orthonormality and closure relations for the Bloch functions are

$$\begin{aligned} \int d^3\mathbf{r} \varphi_{j\mathbf{k}}^*(\mathbf{r}) \varphi_{k'\mathbf{j}'}(\mathbf{r}) &= \delta(\mathbf{k}-\mathbf{k}') \delta_{jj'} ; \quad \mathbf{k}, \mathbf{k}' \in \text{BZ} \\ \sum_j \int_{\text{BZ}} d^3\mathbf{k} \varphi_{j\mathbf{k}}(\mathbf{r}) \varphi_{j\mathbf{k}}^*(\mathbf{r}') &= \delta(\mathbf{r}-\mathbf{r}') . \end{aligned} \quad (C.25)$$

Because of the periodicity of the potential W (C.21), the Hamiltonian \hat{H} commutes with the translation operator $\hat{T}_{\mathbf{R}}$. Therefore, the eigenfunctions of \hat{H} can be written as Bloch functions, which is the essence of the Bloch theorem. Inserting the Bloch functions (C.24) into the eigenvalue problem of the Hamiltonian (C.21) and applying the product rule, we obtain the eigenvalue problem for the lattice-periodic functions:

$$\left[\frac{1}{2m} \left(\frac{\hbar}{i} \nabla + \hbar \mathbf{k} \right)^2 + W(\mathbf{r}) \right] u_{j\mathbf{k}}(\mathbf{r}) = E_j(\mathbf{k}) u_{j\mathbf{k}}(\mathbf{r}) . \quad (C.26)$$

The discrete variable j is the band index and the eigenvalues $E_j(\mathbf{k})$ as functions of \mathbf{k} for fixed j are called energy bands. The ensemble of the functions $E_j(\mathbf{k})$ is called the band structure of the crystal. It can be shown that, for fixed j , the functions $E_j(\mathbf{k})$ are continuous and, in the absence of band degeneracies, analytic functions [6]. Thus the spectrum of a Bloch electron is entirely continuous. The intervals between bands, for which $E = E_j(\mathbf{k})$ has no solutions, are called gaps. We distinguish between three types of degeneracies: band degeneracy, where $E_j(\mathbf{k}) = E_{j'}(\mathbf{k})$ for $j \neq j'$; star degeneracy, where $E_j(\mathbf{k}) = E_{j'}(\alpha\mathbf{k} + \mathbf{K})$ for $\alpha \in G_0$, $\alpha \neq \varepsilon$; and band overlap, where $E_j(\mathbf{k}) = E_{j'}(\mathbf{k}')$ with general \mathbf{k}, \mathbf{k}' .

It is often desirable to work with a finite normalization volume. Vanishing boundary conditions cannot be applied for Bloch electrons, because they would violate the translation symmetry. Born–von Kármán boundary conditions can be introduced similarly to the case of free electrons (last example). We consider a finite domain Ω of $N_1 \times N_2 \times N_3$ unit cells in the directions of the primitive lattice vectors $\mathbf{a}_1, \mathbf{a}_2, \mathbf{a}_3$. Then we request periodicity of the

Bloch functions with respect to the translations $N_i \mathbf{a}_i$. This limits the Bloch wavevectors to the discrete values

$$\mathbf{k} = \sum_{j=1}^3 \frac{n_j}{N_j} \mathbf{b}_j ; \quad n_1, n_2, n_3 \in \mathbb{Z} ; \quad \mathbf{k} \in \text{BZ} , \quad (\text{C.27})$$

where $\mathbf{a}_i \cdot \mathbf{b}_j = 2\pi \delta_{ij}$. The number of \mathbf{k} -points in the Brillouin zone is equal to the number of lattice points, namely $N_1 N_2 N_3$. Therefore, the volume, occupied by one \mathbf{k} -point, is the volume of the Brillouin zone, divided by $N_1 N_2 N_3$, that is $(2\pi)^3 / \Omega$. The sum-integral correspondence is the same as for the free electron (C.20), except that \mathbf{k} is restricted to the first Brillouin zone. The Bloch functions, normalized to $\delta_{\mathbf{kk}'} \delta_{jj'}$, are

$$\varphi_{jk}(\mathbf{r}) = \frac{1}{\sqrt{\Omega}} e^{i\mathbf{k}\cdot\mathbf{r}} u_{jk}(\mathbf{r}) \quad (\text{C.28})$$

with the lattice-periodic parts normalized according to (C.24).

C. Particle in a circle

We consider a particle in a circle of radius R with hard walls. The eigenvalue problem for the radially symmetric eigenfunction

$$-\frac{1}{2} \left\{ \varphi_n''(\varrho) - \frac{1}{\varrho} [\varrho \varphi_n'(\varrho)]' \right\} = E_n \varphi_n(\varrho) ; \quad \varphi_n(R) = 0 . \quad (\text{C.29})$$

has the solutions

$$\varphi_n(\varrho) = \frac{1}{\sqrt{\pi} R |J'_0(x_n)|} J_0\left(\frac{x_n \varrho}{R}\right) ; \quad E_n = \frac{1}{2} \left(\frac{x_n}{R}\right)^2 ; \quad n \in \mathbb{N} , \quad (\text{C.30})$$

where J_0 is the Bessel function of zero order, J'_0 is the first derivative, and x_n is the n -th zero (App. A.2). The eigenfunctions (C.30) are orthonormal and complete in $L_{2,2\pi\varrho}(0, R)$.

Now we perform the transition $R \rightarrow \infty$, where the spectrum becomes continuous. For this purpose, we replace the index n by the continuous variable k , defined as

$$k = \frac{x_n}{R} ; \quad dk = 2\pi k dk . \quad (\text{C.31})$$

From the asymptotic behavior of the Bessel function (A.30) we find

$$|J'_0(x_n)| \sim \sqrt{\frac{2}{\pi x_n}} ; \quad D(k) \sim \left(\frac{dk}{dn}\right)^{-1} \sim \frac{R^2}{2\pi^2 x_n} . \quad (\text{C.32})$$

Then the continuous eigenvalues and eigenfunctions of $-\frac{1}{2} \Delta_\varrho$ on the interval $[0, \infty)$ are

$$E(k) = \frac{k^2}{2} ; \quad \varphi_k(\varrho) = \sqrt{D(k)} \varphi_n(\varrho) = \frac{1}{2\pi} J_0(k\varrho) ; \quad k \in [0, \infty) . \quad (\text{C.33})$$

These eigenfunctions fulfill the orthonormality and closure relations

$$\begin{aligned} 2\pi \int_0^\infty d\varrho \varrho \varphi_k^*(\varrho) \varphi_{k'}(\varrho) &= \frac{\delta(k-k')}{2\pi k} \\ 2\pi \int_0^\infty dk k \varphi_k(\varrho) \varphi_k^*(\varrho') &= \frac{\delta(\varrho-\varrho')}{2\pi \varrho}. \end{aligned} \quad (\text{C.34})$$

To change from k normalization to energy normalization, we need to multiply the functions φ_k with the factor $\sqrt{D(E)/D(k)} = \sqrt{dE/dk} = \sqrt{2\pi}$.

D. Harmonic oscillator in one dimension

The eigenvalue problem for the one-dimensional harmonic oscillator is

$$\left(-\frac{\hbar^2}{2m} \frac{d^2}{dx^2} + \frac{k^2}{2} x^2 \right) \varphi_n(x) = E_n(x), \quad (\text{C.35})$$

where k is the spring constant ($[k] = \text{N/m}$). The domain and the volume element are $G = (-\infty, +\infty)$ and $dx = dx$. In dimensionless units, $\hbar = m = k = 1$, the above equation reads

$$\left(-\frac{1}{2} \frac{d^2}{dx^2} + \frac{1}{2} x^2 \right) \varphi_n(x) = E_n \varphi_n(x). \quad (\text{C.36})$$

The solutions for the eigenvalues and eigenfunctions are

$$E_n = n + \frac{1}{2}; \quad \varphi_n(x) = \frac{1}{\sqrt{2^n n! \sqrt{\pi}}} e^{-\frac{x^2}{2}} H_n(x); \quad n \in \mathbb{N}_0, \quad (\text{C.37})$$

where H_n are the Hermite polynomials (App. A.2). The spectrum is entirely discrete. The n -th eigenfunction has n zeros on the real axis.

In order to return to physical dimensions, energies are expressed in units of $\hbar\omega$, where $\omega = \sqrt{k/m}$ is the classical frequency of the harmonic oscillator. The length scale is $\sqrt{\hbar/(2m\omega)}$.

E. Harmonic oscillator in two dimensions

We consider an harmonic oscillator in two dimensions with isotropic mass m and spring constant k . This problem can be separated in polar coordinates. This time, we assume $\hbar = m = 2k = 1$ so that the radially symmetric eigenfunctions obey the eigenvalue problem

$$\begin{aligned} \left(-\frac{1}{2} \frac{1}{\varrho} \frac{d}{d\varrho} \varrho \frac{d}{d\varrho} + \frac{1}{8} \varrho^2 \right) \varphi_n(\varrho) &= E_n \varphi_n(\varrho) \\ G = [0, \infty) ; \quad d\varrho &= 2\pi \varrho d\varrho. \end{aligned} \quad (\text{C.38})$$

The solutions are given by the Laguerre functions (App. A.2):

$$E_n = n + \frac{1}{2}; \quad \varphi_n(\varrho) = \frac{1}{\sqrt{2\pi}} e^{-\frac{\varrho^2}{4}} L_n\left(\frac{\varrho^2}{2}\right); \quad n \in \mathbb{N}_0. \quad (\text{C.39})$$

They are orthonormal and complete in $L_{2,2\pi\rho}(0, \infty)$. Beyond the classical point of return, $\sqrt{8E_n}$, the eigenfunction φ_n rapidly decreases. This is important for numerical calculations on a finite domain. For example, the probability of finding the particle in the state n outside the circle $0 \leq \varrho \leq \sqrt{8E_n} + 3$ is smaller than 10^{-5} .

F. Particle in an electric field

We consider a particle with charge $-e$ in an electric field of strength F . Without loss of generality, we assume that $eF > 0$. In dimensionless units $\hbar = 2m = eF$ we have

$$\left(-\frac{d^2}{dz^2} + z\right) \varphi_E(z) = E \varphi_E(z). \quad (\text{C.40})$$

This equation can be solved conveniently by Fourier transform. From

$$\left(k^2 + i\frac{d}{dk}\right) \tilde{\varphi}_E(k) = E \tilde{\varphi}_E(k) \quad (\text{C.41})$$

it follows that

$$\tilde{\varphi}_E(k) = c \exp\left(-iEk + \frac{1}{3}ik^3\right) \quad (\text{C.42})$$

and the solution in real space is

$$\varphi_E(z) = c \frac{1}{2\pi} \int_{-\infty}^{+\infty} dk e^{ik(z-E)} e^{+\frac{1}{3}ik^3} = c \text{Ai}(z-E). \quad (\text{C.43})$$

Here, Ai is the Airy function of first kind [9]. The normalization of the eigenfunctions is

$$\int_{-\infty}^{+\infty} dz \varphi_E^*(z) \varphi_{E'}(z) = \frac{1}{2\pi} \int_{-\infty}^{+\infty} dk \tilde{\varphi}_E^*(k) \tilde{\varphi}_{E'}(k) = |c|^2 \delta(E - E'); \quad (\text{C.44})$$

so we set $c = 1$. Changing the integration variable from z to E gives us immediately the closure relation. The spectrum is identical to the real axis.

As an alternative to the solution in Fourier space, we can start with the general solution of (C.40), which is $\varphi_E(z) = c \text{Ai}(z-E) + d \text{Bi}(z-E)$. As the Airy function of the second kind $\text{Bi}(z)$ is divergent for $z \rightarrow \infty$ [9], the second contribution is not normalizable and d must be zero.

The Airy function of the first kind, Ai , is shown in Fig. C.1. The probability density $|\text{Ai}(z-E)|^2$ has a maximum near the classical point of return

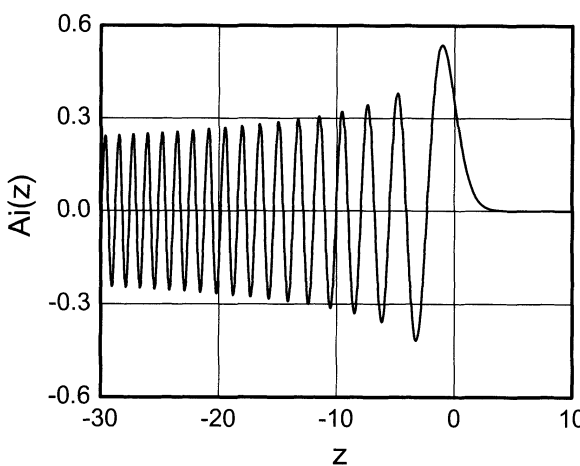


Fig. C.1. Airy function of the first kind
Ai

$z = E$. The asymptotic form of the eigenfunctions (C.43) follows from the asymptotics of the Airy function [9]

$$\text{Ai}(z) \sim \frac{1}{2\sqrt{\pi}z^{1/4}} e^{-\frac{2}{3}z^{3/2}} ; \quad \text{Ai}(-z) \sim \frac{1}{\sqrt{\pi}z^{1/4}} \sin\left(\frac{2}{3}z^{3/2} + \frac{\pi}{4}\right) \text{ for } z \rightarrow +\infty , \quad (\text{C.45})$$

which is identical to the semiclassical result [1].

To return to physical units, we note that lengths and energies are measured in $a^* = \hbar^{2/3}(2meF)^{-1/3}$ and $E^* = eFa^* = \hbar^{2/3}(eF)^{2/3}(2m)^{-1/3}$. Then the eigenfunctions become:

$$\varphi_E(z) = \frac{(2m)^{1/3}}{(eF)^{1/6}\hbar^{2/3}} \text{Ai}\left[\left(\frac{2meF}{\hbar^2}\right)^{1/3}\left(z - \frac{E}{eF}\right)\right] . \quad (\text{C.46})$$

G. Three-dimensional Hydrogen atom

The eigenvalue problem for the Hydrogen atom without spin in dimensionless units is

$$\left(-\frac{1}{2}\Delta - \frac{1}{r}\right)\Phi_A(\mathbf{r}) = E_A\Phi_A(\mathbf{r}) \quad (\text{C.47})$$

$$G = \mathbb{R}^3 ; \quad d\mathbf{r} = d^3\mathbf{r} = dx dy dz .$$

The problem can be separated in spherical coordinates r, ϑ, φ .

The discrete spectrum is characterized by eigenvalues and eigenfunctions

$$E_n = -\frac{1}{2n^2} ; \quad \Phi_{nlm}(r, \vartheta, \varphi) = Y_{lm}(\vartheta, \varphi) R_{nl}(r) \quad (\text{C.48})$$

$n \in \mathbb{N} ; \quad l \in \{0, \dots, n-1\} ; \quad m \in \{-l, \dots, +l\} ,$

where Y_{lm} are the spherical harmonics (App. A.2). The energy depends only on the principal quantum number n . Eigenstates with the angular quantum number $l = 1, 2, 3, 4, \dots$ are called s, p, d, f, ... states. The quantum number m is called the magnetic quantum number, because the linear Zeeman splitting is proportional to m . The multiplicity of an eigenvalue E_n is n^2 . The radial parts of the eigenfunctions R_{nl} have $n_r = n - l - 1$ nodes, where n_r is called radial quantum number.

The eigenfunctions of the continuous spectrum are of the form

$$\Phi_{Elm}(r, \vartheta, \varphi) = Y_{lm}(\vartheta, \varphi) R_{El}(r) \quad (\text{C.49})$$

$$E \in [0, \infty) ; \quad l \in \{0, \dots, n-1\} ; \quad m \in \{-l, \dots, +l\} .$$

For each continuous eigenvalue $E \geq 0$, the multiplicity is infinite. This is because the continuum is three-parametric.

The normalization of the eigenfunctions according to the prescription (C.12) is

$$\int_0^{2\pi} d\varphi \int_0^\pi d\vartheta \int_0^\infty dr r^2 \left\{ \begin{array}{l} \Phi_{nlm}^*(r, \vartheta, \varphi) \Phi_{n'l'm'}(r, \vartheta, \varphi) \\ \Phi_{nlm}^*(r, \vartheta, \varphi) \Phi_{E'l'm'}(r, \vartheta, \varphi) \\ \Phi_{Elm}^*(r, \vartheta, \varphi) \Phi_{E'l'm'}(r, \vartheta, \varphi) \end{array} \right\} = \begin{cases} \delta_{nn'} \delta_{ll'} \delta_{mm'} & \\ 0 & \\ \delta(E-E') \delta_{ll'} \delta_{mm'} & \end{cases} . \quad (\text{C.50})$$

The eigenfunctions fulfill the closure relation

$$\sum_{l=0}^{\infty} \sum_{m=-l}^{+l} \left[\sum_{n=l+1}^{\infty} \Phi_{nlm}(\mathbf{r}) \Phi_{nlm}^*(\mathbf{r}') + \int_0^{\infty} dE \Phi_{Elm}(\mathbf{r}) \Phi_{Elm}^*(\mathbf{r}') \right] = \delta(\mathbf{r}-\mathbf{r}') . \quad (\text{C.51})$$

For $r \rightarrow 0$, the eigenfunctions behave like $\Phi_{nlm}(\mathbf{r}) \propto r^l$ and $\Phi_{Elm}(\mathbf{r}) \propto r^l$. The explicit eigenfunctions of the s orbitals ($l = m = 0$) are

$$\Phi_{ns}(\mathbf{r}) = \frac{1}{\sqrt{\pi}} \frac{1}{n^{5/2}} e^{-\frac{r}{n}} L_{n-1}^{(1)}\left(\frac{2r}{n}\right) \quad (\text{C.52})$$

$$\Phi_{Es}(\mathbf{r}) = \frac{1}{\sqrt{\pi}} \frac{1}{\sqrt{1 - e^{-2\pi/k}}} e^{-ikr} F\left(1 + \frac{i}{k}, 2; 2ikr\right) ; \quad k = \sqrt{2E} ,$$

where $L_{n-1}^{(1)}$ are the generalized Laguerre polynomials³ and F is the confluent hypergeometric function (App. A.2). The ground state $n=1, l=m=0$ has the energy $E_1 = -\frac{1}{2}$ and the eigenfunction

³ Not to be confused with the associated Laguerre polynomials, see App. A.2.

$$\Phi_{1s}(\mathbf{r}) = \frac{1}{\sqrt{\pi}} e^{-r}. \quad (\text{C.53})$$

The amplitudes of the s eigenfunctions at $\mathbf{r} = 0$ are

$$\Phi_{ns}(0) = \frac{1}{\sqrt{\pi} n^{3/2}}; \quad \Phi_{Es}(0) = \frac{1}{\sqrt{\pi} \sqrt{1 - e^{-2\pi/k}}}. \quad (\text{C.54})$$

H. Two-dimensional Hydrogen atom

The eigenvalue problem for the two-dimensional Hydrogen atom in dimensionless units is

$$\left(-\frac{1}{2} \Delta - \frac{1}{\varrho} \right) \Phi_A(\varrho) = E_A \Phi_A(\varrho); \quad G = \mathbb{R}^2; \quad d\varrho = d^2\varrho = dx dy. \quad (\text{C.55})$$

The explicit calculations are carried out in the textbook by Chuang [10]. Here, we summarize the main results.

Equation (C.55) can be separated in polar coordinates ϱ, φ . The eigenfunctions and eigenvalues of the discrete spectrum are

$$E_n = -\frac{1}{2(n-\frac{1}{2})^2}; \quad \Phi_{nm}(\varrho, \varphi) = \frac{1}{\sqrt{2\pi}} e^{im\varphi} R_{nm}(\varrho) \quad (\text{C.56})$$

$$n \in \mathbb{N}; \quad m \in \{-n+1, \dots, +n-1\},$$

where n and m are the principal and the magnetic quantum number, respectively. The function R_{nm} possesses $n_\varrho = n - |m| - 1$ nodes on the real axis, where n_ϱ is called the radial quantum number. The multiplicity of an eigenvalue E_n is $2n - 1$.

The continuous spectrum is two-parametric and, therefore, has an infinite multiplicity. The quantum numbers are $A = E, m$, with the energy $E \in [0, \infty)$ and the magnetic quantum number $m \in \mathbb{Z}$, independent of E . The continuous eigenfunctions are of the form

$$\Phi_{Em}(\varrho, \varphi) = \frac{1}{\sqrt{2\pi}} e^{im\varphi} R_{Em}(\varrho). \quad (\text{C.57})$$

Discrete and continuous eigenfunctions fulfill the orthonormality and closure relations

$$\int_0^{2\pi} d\varphi \int_0^\infty d\varrho \varrho \begin{Bmatrix} \Phi_{nm}^*(\varrho, \varphi) \Phi_{n'm'}(\varrho, \varphi) \\ \Phi_{nm}^*(\varrho, \varphi) \Phi_{E'm'}(\varrho, \varphi) \\ \Phi_{Em}^*(\varrho, \varphi) \Phi_{E'm'}(\varrho, \varphi) \end{Bmatrix} = \begin{Bmatrix} \delta_{nn'} \delta_{mm'} \\ 0 \\ \delta(E-E') \delta_{mm'} \end{Bmatrix} \quad (\text{C.58})$$

and

$$\sum_{m=-\infty}^{+\infty} \left[\sum_{n=|m|+1}^{\infty} \Phi_{nm}(\varrho) \Phi_{nm}^*(\varrho') + \int_0^{\infty} dE \Phi_{Em}(\varrho) \Phi_{Em}^*(\varrho') \right] = \delta(\varrho - \varrho') . \quad (\text{C.59})$$

The behavior of the radial functions for $\varrho \rightarrow 0$ is $R_{nm}(\varrho) \propto \varrho^{|m|}$ and $R_{Em}(\varrho) \propto \varrho^{|m|}$. The explicit expressions for the radially symmetric eigenfunctions ($m = 0$) are

$$\Phi_{n,m=0}(\varrho) = \frac{1}{\sqrt{\pi}} \frac{1}{(n - \frac{1}{2})^{3/2}} e^{-r/(n - \frac{1}{2})} L_{n-1}\left(\frac{2\varrho}{n - \frac{1}{2}}\right) \quad (\text{C.60})$$

$$\Phi_{E,m=0}(\varrho) = \frac{1}{\sqrt{\pi}} \frac{1}{\sqrt{1 + e^{-2\pi/\kappa}}} e^{-i\kappa\varrho} F\left(\frac{1}{2} + \frac{1}{\kappa}, 1; 2i\kappa\varrho\right); \quad \kappa = \sqrt{2E} .$$

Here, the L_{n-1} are the Laguerre polynomials according to the definition (A.22). For the ground state, $n = 1$, $m = 0$ we have $E_1 = -2$ and

$$\Phi_{1,m=0}(\varrho) = \sqrt{\frac{8}{\pi}} e^{-2\varrho} . \quad (\text{C.61})$$

The amplitudes of the normalized s eigenfunctions (C.60) at the origin are

$$\Phi_{n,m=0}(0) = \frac{1}{\sqrt{\pi}} \frac{1}{(n - \frac{1}{2})^{3/2}}; \quad \Phi_{E,m=0}(0) = \frac{1}{\sqrt{\pi}} \frac{1}{\sqrt{1 + e^{-2\pi/\kappa}}} . \quad (\text{C.62})$$

I. Exciton in a magnetic field

The Hamiltonian of an exciton in a constant magnetic field \mathbf{B} is

$$\begin{aligned} \hat{H} = & \frac{1}{2m_e} \left(\frac{i}{\hbar} \nabla_e + \frac{1}{2} e \mathbf{B} \times \mathbf{r}_e \right)^2 + \frac{1}{2m_h} \left(\frac{i}{\hbar} \nabla_h - \frac{1}{2} e \mathbf{B} \times \mathbf{r}_h \right)^2 \\ & - \frac{e^2}{4\pi\epsilon_0\varepsilon |\mathbf{r}_e - \mathbf{r}_h|} , \end{aligned} \quad (\text{C.63})$$

where we used the symmetric gauge for the vector potential. For the eigenfunctions Ψ_A of \hat{H} we make the ansatz [11]:

$$\begin{aligned} \Psi_A(\mathbf{r}_e, \mathbf{r}_h) &= \Psi_{P\lambda}(\mathbf{r}_e, \mathbf{r}_h) \\ &= \frac{1}{(2\pi)^{3/2}} \exp\left[\frac{i}{\hbar} (\mathbf{P} + \frac{1}{2} e \mathbf{B} \times \mathbf{r}) \cdot \mathbf{R}\right] \psi_{P\lambda}(\mathbf{r}) , \end{aligned} \quad (\text{C.64})$$

where $\mathbf{R} = (m_e \mathbf{r}_e + m_h \mathbf{r}_h)/(m_e + m_h)$ and $\mathbf{r} = \mathbf{r}_e - \mathbf{r}_h$ are the center-of-mass and relative coordinates, respectively. Using $(\mathbf{B} \times \mathbf{r}) \cdot \mathbf{R} = (\mathbf{B} \times \mathbf{r}_e) \cdot \mathbf{r}_h$ we obtain

$$\begin{aligned}
\hat{H} \Psi_{\mathbf{P}\lambda}(\mathbf{r}_e, \mathbf{r}_h) &= \exp\left[\frac{i}{\hbar}(\mathbf{P} + \frac{1}{2}e\mathbf{B} \times \mathbf{r}) \cdot \mathbf{R}\right] \hat{H}_{\mathbf{P}} \psi_{\mathbf{P}\lambda}(\mathbf{r}) \\
\hat{H}_{\mathbf{P}} &= -\frac{\hbar^2}{2m} \Delta + \frac{\hbar^2}{2m} \gamma e \mathbf{B} \cdot \hat{\mathbf{L}} + \frac{1}{8m} |e\mathbf{B} \times \mathbf{r}|^2 \\
&\quad + \frac{1}{M} (e\mathbf{B} \times \mathbf{r}) \cdot \mathbf{P} + \frac{P^2}{2m} - \frac{e^2}{4\pi\epsilon_0\varepsilon r} \\
M &= m_e + m_h ; \quad m = \frac{m_e m_h}{m_e + m_h} ; \quad \gamma = \frac{m_e - m_h}{m_e + m_h} .
\end{aligned} \tag{C.65}$$

The eigenstates $\psi_{\mathbf{P}\lambda}$ (discrete or continuous) of the reduced Hamiltonian $\hat{H}_{\mathbf{P}}$ can be assumed to be orthonormal and complete. Then, the functions $\Psi_{\mathbf{P}\lambda}$ (C.64) of \hat{H} fulfill

$$\begin{aligned}
\iint d^3\mathbf{r}_e d^3\mathbf{r}_h \Phi_{\mathbf{P}\lambda}^*(\mathbf{r}_e, \mathbf{r}_h) \Phi_{\mathbf{P}'\lambda'}(\mathbf{r}_e, \mathbf{r}_h) &= \delta(\mathbf{P} - \mathbf{P}') \delta_{\lambda\lambda'} \\
\int d^3\mathbf{P} \sum_{\lambda} \Phi_{\mathbf{P}\lambda}(\mathbf{r}_e, \mathbf{r}_h) \Phi_{\mathbf{P}\lambda}^*(\mathbf{r}'_e, \mathbf{r}'_h) &= \delta(\mathbf{r}_e - \mathbf{r}'_e) \delta(\mathbf{r}_h - \mathbf{r}'_h) .
\end{aligned} \tag{C.66}$$

For $\mathbf{B} \neq 0$, the spectrum is fairly complicated and no exact solution is known. For $\mathbf{P} = 0$, the reduced Hamiltonian commutes with the projection of $\hat{\mathbf{L}}$ on the direction of \mathbf{B} and the problem can be separated in cylindrical coordinates. Choosing $e_z \parallel \mathbf{B}$, the eigenfunctions take the form $\psi_{\mathbf{P}=0,n,m}(\mathbf{r}) = R_{\mathbf{P}=0,n,m}(\varrho, z) e^{im\varphi} / \sqrt{(2\pi)}$, where $R_{\mathbf{P}=0,n,m}(0, z) = 0$ for $m \neq 0$. The Hamiltonian for the radially symmetric eigenfunctions ($m = 0$) is

$$\hat{H}_{\mathbf{P}=0,m=0} = -\frac{\hbar^2}{2m} \left(\frac{1}{\varrho} \frac{\partial}{\partial \varrho} \varrho \frac{\partial}{\partial \varrho} + \frac{\partial^2}{\partial z^2} \right) + \frac{e^2 B^2}{8m} \varrho^2 - \frac{e^2}{4\pi\epsilon_0\varepsilon\sqrt{\varrho^2+z^2}} . \tag{C.67}$$

C.2 Angular Momentum in Quantum Mechanics

The properties of angular-momentum matrices and the three-dimensional orthogonal group are extensively discussed in a booklet by Edmonds, entitled “Angular Momentum in Quantum Mechanics” [12]. Also, most quantum-mechanics textbooks have a separate chapter or a mathematical appendix dealing with this subject [1, 2, 13]. We especially recommend the appendix of Weissbluth’s book [14]. The group-theoretical aspects are emphasized in the book by Inui et al. [15].

In the following we set $\hbar = 1$. There are different conventions for the phase normalizations of the eigenfunctions of the angular-momentum operator. Although these phase factors have no direct physical impact, it is important

to be consistent in the definition of the spherical harmonics, the angular-momentum matrices, the Clebsch–Gordan coefficients, and the time-reversal. Here we shall adopt the widely accepted Condon–Shortley convention [16].

C.2.1 The Eigenvalue Problem

An angular-momentum operator is a Hermitian operator $\hat{\mathbf{J}}$, where the components fulfill the relations

$$[\hat{J}_\alpha, \hat{J}_{\alpha+1}] = i \hat{J}_{\alpha+2}; \quad [\hat{J}_\alpha, \hat{J}^2] = 0. \quad (\text{C.68})$$

It can be shown by algebraic methods that the eigenvalue problem of $\hat{\mathbf{J}}$ has the solutions

$$\begin{aligned} \hat{J}^2 |j, m\rangle &= j(j+1) |j, m\rangle; \quad \hat{J}_z |j, m\rangle = m |j, m\rangle \\ j \in \frac{\mathbb{N}_0}{2}; \quad m \in \{+j, +j-1, \dots, -j+1, -j\}. \end{aligned} \quad (\text{C.69})$$

If the quantum number of the total angular momentum j is fixed, the components of $\hat{\mathbf{J}}$ are represented by $n=2j+1$ -dimensional matrices, so-called angular-momentum matrices, which are characterized by

$$[J_\alpha, J_{\alpha+1}] = i J_{\alpha+2}; \quad J^2 = J_x^2 + J_y^2 + J_z^2 = j(j+1) = \frac{n^2-1}{4}. \quad (\text{C.70})$$

In compact notation, they are written as $\mathbf{J} = (J_x, J_y, J_z)^T$. For $n = 1$, the only solution is $\mathbf{J} = 0$. For any $n \in \mathbb{N}$, the matrices J_x, J_y, J_z are uniquely determined up to equivalence. In the Condon–Shortley convention, $J_z = \text{diag}(+j, \dots, -j)$, $J_{xmm'}$ and $J_{ymm'}$ are nonzero only for $m' = m \pm 1$, the elements of J_x are real and positive, and the elements of J_y are imaginary. Formulas for the matrix elements for general n can be found, e.g., in [1, 12, 14, 16].

The angular-momentum matrices for $j = \frac{1}{2}, 1$, and $\frac{3}{2}$, corresponding to $n = 2, 3$, and 4 , are

$$\begin{aligned} \mathbf{J}^{(1/2)} &= \mathbf{S} = \frac{1}{2} \boldsymbol{\sigma} \\ \sigma_x &= \begin{pmatrix} 0 & 1 \\ 1 & 0 \end{pmatrix}; \quad \sigma_y = \begin{pmatrix} 0 & -i \\ +i & 0 \end{pmatrix}; \quad \sigma_z = \begin{pmatrix} +1 & 0 \\ 0 & -1 \end{pmatrix}, \end{aligned} \quad (\text{C.71})$$

where σ_x, σ_y , and σ_z are the Pauli matrices and \mathbf{S} is the spin operator;

$$J_x^{(1)} = \begin{pmatrix} 0 & \frac{\sqrt{2}}{2} \\ \frac{\sqrt{2}}{2} & 0 \\ \frac{\sqrt{2}}{2} & 0 \end{pmatrix}; \quad J_y^{(1)} = \begin{pmatrix} 0 & -\frac{\sqrt{2}}{2}i \\ +\frac{\sqrt{2}}{2}i & 0 \\ +\frac{\sqrt{2}}{2}i & 0 \end{pmatrix}$$

$$J_z^{(1)} = \text{diag}(+1, 0, -1); \quad (\text{C.72})$$

and

$$\mathbf{J}^{(3/2)} = \mathbf{J}; \quad J_x = \begin{pmatrix} 0 & \frac{\sqrt{3}}{2} & & \\ \frac{\sqrt{3}}{2} & 0 & 1 & \\ & 1 & 0 & \frac{\sqrt{3}}{2} \\ & & \frac{\sqrt{3}}{2} & 0 \end{pmatrix}; \quad J_y = \begin{pmatrix} 0 & -\frac{\sqrt{3}}{2} i & & \\ +\frac{\sqrt{3}}{2} i & 0 & -i & \\ & +i & 0 & -\frac{\sqrt{3}}{2} i \\ & & +\frac{\sqrt{3}}{2} i & 0 \end{pmatrix}$$

$$J_z = \text{diag} (+\frac{3}{2}, +\frac{1}{2}, -\frac{1}{2}, -\frac{3}{2}), \quad (\text{C.73})$$

known as the J matrices.

A special case of an angular-momentum operator is the operator of the orbital angular momentum $\hat{\mathbf{L}} = \hat{\mathbf{r}} \times \hat{\mathbf{p}} = \hat{\mathbf{r}} \times \frac{1}{i} \nabla$. In spherical coordinates (App. A.1), the simultaneous eigenfunctions of $\hat{L}^2 = -\Delta_{\vartheta\varphi}$ and $\hat{L}_z = -i\partial/\partial\varphi$ are the spherical harmonics

$$\hat{L}^2 Y_{lm}(\vartheta, \varphi) = l(l+1) Y_{lm}(\vartheta, \varphi); \quad \hat{L}_z Y_{lm}(\vartheta, \varphi) = m Y_{lm}(\vartheta, \varphi)$$

$$l \in \mathbb{N}_0; \quad m \in \{+l, \dots, -l\}. \quad (\text{C.74})$$

They are defined as⁴

$$\begin{aligned} Y_{lm}(\vartheta, \varphi) &= \sqrt{\frac{2l+1}{2} \frac{(l-m)!}{(l+m)!}} P_l^m(\cos \vartheta) \frac{1}{\sqrt{2\pi}} e^{im\varphi} \\ &= \sqrt{\frac{2l+1}{2} \frac{(l-|m|)!}{(l+|m|)!}} (-1)^{\frac{|m|-m}{2}} P_l^{|m|}(\cos \vartheta) \frac{1}{\sqrt{2\pi}} e^{im\varphi} \\ &= \frac{(-1)^l}{2^l l!} \sqrt{\frac{2l+1}{2} \frac{(l+m)!}{(l-m)!}} \frac{1}{\sin^m \vartheta} \frac{d^{l-m}}{d(\cos \vartheta)^{l-m}} (\sin \vartheta)^{2l} \frac{1}{\sqrt{2\pi}} e^{im\varphi} \end{aligned} \quad (\text{C.75})$$

and are orthonormal and complete on the surface of the unit sphere. In spectroscopy, eigenstates of \hat{L}^2 with $l = 0, 1, 2, 3, 4$ etc. are denoted as s, p, d, f, g, etc. orbitals. The explicit expressions for the Y_{lm} for $l = 0$ and $l = 1$ are

$$Y_{00} = \sqrt{\frac{1}{4\pi}} \quad (\text{C.76})$$

$$Y_{10} = \sqrt{\frac{3}{4\pi}} \cos \vartheta = \sqrt{\frac{3}{4\pi}} \frac{z}{r}; \quad Y_{1,\pm 1} = \mp \sqrt{\frac{3}{8\pi}} \sin \vartheta e^{\pm i\varphi} = \mp \sqrt{\frac{3}{8\pi}} \frac{x \pm iy}{r}.$$

The spherical harmonics Y_{lm} are polynomials of degree l in the variables $X = x/r$, $Y = Y/r$, and $Z = Z/r$. For $l = 1$, the Cartesian p orbitals

⁴ The definition of the spherical harmonics is widely consistent in the literature with the exception of Landau–Lifshitz [1]. The associated Legendre functions P_l^m in the mathematical and physical literature differ by a factor $(-1)^l$. For the P_l^m we use the definition from the mathematical literature.

$$|X\rangle = \frac{-|1,+1\rangle + |1,-1\rangle}{\sqrt{2}}; \quad |Y\rangle = \frac{-|1,+1\rangle - |1,-1\rangle}{\sqrt{2}i}$$

$$|Z\rangle = |1,0\rangle \quad (\text{C.77})$$

are often used as base functions, because they transform like the Cartesian axes. The behavior of the functions (C.75) upon space and time inversion is

$$Y_{lm}(\pi-\vartheta, \pi+\varphi) = (-1)^l Y_{lm}(\vartheta, \varphi); \quad Y_l^{m*}(\vartheta, \varphi) = (-1)^m Y_{lm}(\vartheta, \varphi) \quad (\text{C.78})$$

The matrices $J_x^{(1)}, J_y^{(1)}, J_z^{(1)}$ are the matrix representation of the components of the orbital angular-momentum operator in the basis $\{Y_{1,+1}, Y_{1,\pm 0}, Y_{1,-1}\}$. In the basis of the Cartesian p orbitals $|X\rangle, |Y\rangle, |Z\rangle$, the three-dimensional angular-momentum matrices are the I matrices

$$I_x = \begin{pmatrix} 0 & 0 & 0 \\ 0 & 0 & -i \\ 0 & i & 0 \end{pmatrix}; \quad I_y = \begin{pmatrix} 0 & 0 & +i \\ 0 & 0 & 0 \\ -i & 0 & 0 \end{pmatrix}; \quad I_z = \begin{pmatrix} 0 & -i & 0 \\ +i & 0 & 0 \\ 0 & 0 & 0 \end{pmatrix}. \quad (\text{C.79})$$

C.2.2 Orthogonal Transformations

The full three-dimensional orthogonal group $O(3)$ consists of all real matrices α with the property $\alpha^T = \alpha^{-1}$, called orthogonal matrices. The neutral element is the identity matrix $\varepsilon = \text{diag}(1, 1, 1)$. The determinant of an orthogonal matrix is $\det \alpha = \pm 1$. If $\det \alpha = 1$, then α is a (proper) rotation by an angle φ around a rotation axis e_φ , often expressed as a vector-valued angle $\varphi = \varphi e_\varphi$. The proper rotations are a subgroup $SO(3)$ of $O(3)$. An improper rotation (rotation-reflection) with $\det \alpha = -1$ corresponds to a rotation and subsequent reflection on a plane perpendicular to the rotation axis. Every rotation-reflection can be obtained by multiplying a proper rotation with the inversion $-\varepsilon = \text{diag}(-1, -1, -1)$.

According to their behavior with respect to orthogonal transformations, we distinguish between vectors (or polar vectors) with $\mathbf{a}' = \alpha \mathbf{a}$ and pseudovectors (axial vectors) with $\mathbf{a}' = \det(\alpha) \alpha \mathbf{a}$. The operator of the orbital angular momentum is an axial vector, which can be verified explicitly. The general angular-momentum operator $\hat{\mathbf{J}}$ is by definition an axial vector and transforms like

$$\hat{\mathbf{J}}' = \det(\alpha) \alpha \hat{\mathbf{J}}. \quad (\text{C.80})$$

The same is true for any matrix representation \mathbf{J} of $\hat{\mathbf{J}}$.

Consider a scalar function $f(\mathbf{r})$. A proper rotation α of the coordinates by the angle φ can be expressed as

$$f'(\mathbf{r}) = f(\alpha \mathbf{r}) = e^{i\alpha \cdot \hat{\mathbf{L}}} f(\mathbf{r}). \quad (\text{C.81})$$

Let f be a linear combination of spherical harmonics $\{Y_{lm}\}$ for fixed $l \in \mathbb{N}_0$ with coefficients $\mathbf{f} = (f_{+l}, \dots, f_{-l})^T$. Then the coefficients $\mathbf{f}' = (f'_{+j}, \dots, f'_{-j})^T$ of $f'(\mathbf{r}) = f(\alpha\mathbf{r})$ are given by

$$\mathbf{f}' = D(\alpha) \mathbf{f}; \quad D(\alpha) = (\det \alpha)^l e^{i\alpha \cdot \mathbf{L}}. \quad (\text{C.82})$$

If α is a proper rotation, (C.82) is simply the matrix representation of (C.81). The factor $(\det \alpha)^l$ for improper rotations follows from the behavior of the spherical harmonics upon space inversion (C.78). The $2l+1$ -dimensional representation of the full orthogonal group is called a vector representation.

For general $j \in \mathbb{N}_0/2$, the transformation law for spinors (C.82) is used as a definition. A peculiarity is observed if j is a half-integer, which corresponds to even dimensions $n = 2l+1$. First, the function $(\det \alpha)^j$ is two-valued. Second, if α is a rotation by 2π (e.g., around the z axis), then $D(\alpha) = \exp(2\pi i J_z) = -1$. Therefore, each orthogonal matrix is represented by two unitary matrices $\pm D(\alpha)$ and it holds that $D(\alpha) D(\beta) = \pm D(\alpha\beta)$. Such representations are called double-valued or spinor representations.

The transformation of the spinors entails a transformation law for the angular-momentum matrices:

$$\mathbf{J}' = D(\alpha) \mathbf{J} D^{-1}(\alpha). \quad (\text{C.83})$$

The equivalence of (C.80) and (C.83) follows directly from the commutator relations (C.68).

C.2.3 Addition of Angular Momenta

Consider the operator⁵

$$\hat{\mathbf{J}} = \hat{\mathbf{J}}_1 + \hat{\mathbf{J}}_2, \quad (\text{C.84})$$

where $\hat{\mathbf{J}}_1$ and $\hat{\mathbf{J}}_2$ are angular-momentum operators and $[\hat{J}_{1\alpha}, \hat{J}_{2\beta}] = 0$. The simultaneous eigenstates of $\{\hat{J}_1^2, \hat{J}_{1z}, \hat{J}_2^2, \hat{J}_{2z}\}$ are the products of the eigenstates of $\{\hat{J}_1^2, \hat{J}_{1z}\}$ and $\{\hat{J}_2^2, \hat{J}_{2z}\}$, namely:

$$|j_1, m_1; j_2, m_2\rangle = |j_1, m_1\rangle \otimes |j_2, m_2\rangle. \quad (\text{C.85})$$

The sum $\hat{\mathbf{J}}$ is also an angular-momentum operator, because it fulfills the commutation relations (C.68), and its eigenstates are

$$\left\{ \begin{array}{c} \hat{J}_1^2 \\ \hat{J}_2^2 \\ \hat{J}^2 \\ \hat{J}_z \end{array} \right\} |j_1, j_2, j, m\rangle = \left\{ \begin{array}{c} j_1(j_1+1) \\ j_2(j_2+1) \\ j(j+1) \\ m \end{array} \right\} |j_1, j_2, j, m\rangle \quad (\text{C.86})$$

$$j_1, j_2 \in \mathbb{N}_0/2; \quad j \in \{|j_1-j_2|, \dots, j_1+j_2\}; \quad m \in \{-j, \dots, +j\}.$$

⁵ Here, $\hat{\mathbf{J}}_1$ and $\hat{\mathbf{J}}_2$ are to be interpreted as $\hat{\mathbf{J}}_1 \otimes \mathbf{1}_2 = (\hat{J}_{1x} \otimes 1_2) \mathbf{e}_x + (\hat{J}_{1y} \otimes 1_2) \mathbf{e}_y + (\hat{J}_{1z} \otimes 1_2) \mathbf{e}_z$ and $\mathbf{1}_1 \otimes \hat{\mathbf{J}}_2 = (1_1 \otimes \hat{J}_{2x}) \mathbf{e}_x + (1_1 \otimes \hat{J}_{2y}) \mathbf{e}_y + (1_1 \otimes \hat{J}_{2z}) \mathbf{e}_z$, respectively.

Equation (C.86) is known as the vector-addition or Clebsch–Gordan theorem. For fixed j_1, j_2 , the $(2j_1 + 1)(2j_2 + 1)$ eigenfunctions (C.86) are linear combinations of the $(2j_1 + 1)(2j_2 + 1)$ eigenfunctions (C.85) and the elements $\langle j_1, m_1; j_2, m_2 | j_1, j_2, j, m \rangle$ of the unitary transformation matrix are called Clebsch–Gordan or Wigner coefficients. They can be determined by algebraic methods and given in closed form.

The group-theoretical formulation of the Clebsch–Gordan theorem is

$$D^{(j_1)}(\alpha) \otimes D^{(j_2)}(\alpha) \simeq \bigoplus_{j=|j_1-j_2|}^{j_1+j_2} D^{(j)}(\alpha), \quad (\text{C.87})$$

where $D^{(j)}$ is the $2j+1$ -dimensional vector or spinor representation of the full orthogonal group. The group-reduction coefficients are equal to the Clebsch–Gordan coefficients.

An important application is the spin–orbit coupling of the Hydrogen atom. Here, the perturbation is proportional to $\hat{\mathbf{L}} \cdot \hat{\mathbf{S}} = \frac{1}{2}(\hat{j}^2 - \hat{L}^2 - \hat{S}^2)$. Hence the new eigenstates have the quantum numbers $l, s=\frac{1}{2}, j, m_j$. The shift of the eigenvalues induced by the perturbation is proportional to $j(j+1) - l(l+1) - s(s+1)$. The nonzero Clebsch–Gordan coefficients for $l = 1$ (p electrons) are given in Table C.1 [14].

Table C.1. Clebsch–Gordan coefficients for p electrons with spin. We use the abbreviations $|1, m_1; \uparrow\downarrow\rangle = |1, m_1; s=\frac{1}{2}, \pm\frac{1}{2}\rangle$ and $|j, m_j\rangle = |1, s=\frac{1}{2}, j, m_j\rangle$

	$ \frac{1}{2}, +\frac{1}{2}\rangle$	$ \frac{1}{2}, -\frac{1}{2}\rangle$	$ \frac{3}{2}, +\frac{3}{2}\rangle$	$ \frac{3}{2}, +\frac{1}{2}\rangle$	$ \frac{3}{2}, -\frac{1}{2}\rangle$	$ \frac{3}{2}, -\frac{3}{2}\rangle$
$\langle 1, +1; \uparrow $				1		
$\langle 1, +1; \downarrow $	$\sqrt{\frac{2}{3}}$			$\sqrt{\frac{1}{3}}$		
$\langle 1, \pm 0; \uparrow $	$-\sqrt{\frac{1}{3}}$			$\sqrt{\frac{2}{3}}$		
$\langle 1, \pm 0; \downarrow $		$\sqrt{\frac{1}{3}}$			$\sqrt{\frac{2}{3}}$	
$\langle 1, -1; \uparrow $		$-\sqrt{\frac{2}{3}}$			$\sqrt{\frac{1}{3}}$	
$\langle 1, -1; \downarrow $						1

C.2.4 Time Reversal

For spinless particles, if the Hamiltonian \hat{H} is a real differential operator, the complex conjugate of the wavefunction describes a particle propagating backwards in time. In real-space representation, the complex conjugate of an operator is called the time-reversed operator. For the orbital angular momentum we find $\hat{\mathbf{L}}^* = \mathbf{r} \times (-\frac{1}{i})\nabla = -\hat{\mathbf{L}}$.

The situation is somewhat more complicated if the wavefunction is a spinor with many components. Suppose that the wavefunction is a linear combination of spherical harmonics of order l with coefficients $\mathbf{f} = (f_{+l}, \dots, f_{-l})^T$. From (C.78) it follows that the m -th components of the complex conjugate wavefunction is equal to $(-1)^m f_{-m}^*$. The generalization for particles with arbitrary spin, in conformity with the Condon–Shortley convention, is

$$(K\mathbf{f})_m = (-i)^{(2m)} f_{-m}^*; \quad K\mathbf{f} = T\mathbf{f}^*, \quad (\text{C.88})$$

where the antilinear operator K is called the time-reversal operator. For operators, time reversal is defined as $K \hat{A} K^{-1} = T \hat{A}^* T^{-1}$. The time-reversed angular-momentum matrices are $K\mathbf{J}K^{-1} = T\mathbf{J}^*T^{-1} = -\mathbf{J}$. Furthermore, the time-reversal operator fulfills $K^2 = (-1)^{2j}$.

The explicit expressions of the Hermitian matrices T in the basis $|j, m\rangle$ for $j = \frac{1}{2}, 1, \frac{3}{2}$ are

$$T^{(1/2)} = \begin{pmatrix} & -i \\ +i & \end{pmatrix}; \quad T^{(1)} = \begin{pmatrix} & -1 \\ +1 & \\ -1 & \end{pmatrix}; \quad T^{(3/2)} = \begin{pmatrix} & & +i \\ & -i & \\ +i & & \\ -i & & \end{pmatrix}. \quad (\text{C.89})$$

C.3 Perturbation Theory

In this section we summarize important formulas for time-independent and time-dependent perturbation theory.

C.3.1 Degenerate Time-Independent Perturbation Theory

We consider a Hamiltonian of the form $H = H^{(0)} + H^{(i)}$, where the eigenvalues E_1, \dots, E_n and eigenstates $|\varphi_1\rangle, \dots, |\varphi_n\rangle$ of $H^{(0)}$ are known. Without loss of generality, we assume that the $|\varphi_1\rangle, \dots, |\varphi_n\rangle$ are orthonormal.

We wish to determine the second-order eigenvalues $\mathcal{E}^{(1)}, \dots, \mathcal{E}^{(m)}$ and first-order eigenstates $|\psi^{(1)}\rangle, \dots, |\psi^{(m)}\rangle$ of H in case that the unperturbed eigenstates $|\varphi_1\rangle, \dots, |\varphi_m\rangle$ are degenerate. Using the matrix notation, $H_{ij} = \langle \varphi_i | H | \varphi_j \rangle$; $|\psi^{(\lambda)}\rangle = \sum_i c_i^{(\lambda)} |\varphi_i\rangle$, the eigenvalue problem writes

$$H \mathbf{c}^{(\lambda)} = \mathcal{E}^{(\lambda)} \mathbf{c}^{(\lambda)}. \quad (\text{C.90})$$

The matrix H has the form $H = D + F$, where $D = \text{diag}(E_1, \dots, E_n)$ is diagonal and contains the unperturbed eigenvalues, whereas F is in general nondiagonal and contains the matrix elements of $H^{(i)}$.

According to Löwdin [17], the eigenstates are divided into two classes A and B , which correspond to subspaces of strongly and weakly interacting eigenstates, respectively. $A = \{1, \dots, m\}$ contains the degenerate

or quasi-degenerate eigenstates. The other eigenstates are summarized in $B = \{m+1, \dots, n\}$. Introducing the block notation

$$H = \begin{pmatrix} D_{AA} + F_{AA} & F_{AB} \\ F_{BA} & D_{BB} + F_{BB} \end{pmatrix}; \quad \mathbf{c}^{(\lambda)} = \begin{pmatrix} \mathbf{c}_A^{(\lambda)} \\ \mathbf{c}_B^{(\lambda)} \end{pmatrix} \quad (\text{C.91})$$

the eigenvalue problem can be decomposed into two coupled equations:

$$\begin{aligned} (D_{AA} + F_{AA}) \mathbf{c}_A^{(\lambda)} + F_{AB} \mathbf{c}_B^{(\lambda)} &= \mathcal{E}^{(\lambda)} \mathbf{c}_A^{(\lambda)} \\ F_{BA} \mathbf{c}_A^{(\lambda)} + (D_{BB} + F_{BB}) \mathbf{c}_B^{(\lambda)} &= \mathcal{E}^{(\lambda)} \mathbf{c}_B^{(\lambda)}. \end{aligned} \quad (\text{C.92})$$

We use the second equation to express $\mathbf{c}_B^{(\lambda)}$ by $\mathbf{c}_A^{(\lambda)}$,

$$\mathbf{c}_B^{(\lambda)} = (\mathcal{E}^{(\lambda)} - D_{BB} - F_{BB})^{-1} F_{BA} \mathbf{c}_A^{(\lambda)}, \quad (\text{C.93})$$

and insert this expression into (C.92):

$$\left[D_{AA} + F_{AA} + F_{AB} (\mathcal{E}^{(\lambda)} - D_{BB} - F_{BB})^{-1} F_{BA} \right] \mathbf{c}_A^{(\lambda)} = \mathcal{E}^{(\lambda)} \mathbf{c}_A^{(\lambda)}. \quad (\text{C.94})$$

If the eigenvalues of class A are to be determined second order in the perturbation, we can neglect F_{BB} and approximate $\mathcal{E}^{(\lambda)}$ as $E_A = E_1 = \dots = E_m$.⁶ This results in an eigenvalue problem (secular equation) for the class-A components:

$$\begin{aligned} H_{\text{eff}} \mathbf{c}_A^{(\lambda)} &= \mathcal{E}^{(\lambda)} \mathbf{c}_A^{(\lambda)} \\ H_{\text{eff}}{}_{ij} &= E_i \delta_{ij} + F_{ij} + \sum_{k \in B} \frac{F_{ik} F_{kj}}{E_A - E_k}; \quad i, j \in A. \end{aligned} \quad (\text{C.95})$$

Using the relation between the class-B and the class-A components, the first-order eigenstates (not orthonormalized) become

$$|\psi^{(\lambda)}\rangle = \sum_{i \in A} c_i^{(\lambda)} |\varphi_{\text{eff}\,i}\rangle; \quad |\varphi_{\text{eff}\,i}\rangle = |\varphi_i\rangle + \sum_{j \in B} \frac{F_{ji}}{E_A - E_j} |\varphi_j\rangle. \quad (\text{C.96})$$

C.3.2 Time-Dependent Perturbation Theory

The transition rate between quantum states due to a time-periodic perturbation can be described by Fermi's golden rule. This formula is derived in most textbooks of quantum mechanics, e.g., in [1, 2, 13] and is known to most

⁶ For quasi-degeneracy, we can use $E_A = (E_1 + \dots + E_m)/m$.

readers at least in qualitative form. Here we specify the major assumptions, outline the derivation, and give the final result.

We consider a two-level system with initial state $|a\rangle$ and final state $|b\rangle$. The unperturbed Hamiltonian has the form

$$H^{(0)} = \text{diag}(E_a, E_b); \quad E_a < E_b. \quad (\text{C.97})$$

We assume a time-dependent perturbation of the form

$$H^{(\text{i})}(t) = \underline{H}^{(\text{i})} e^{-i\omega t} + \underline{H}^{(\text{i})\dagger} e^{+i\omega t}; \quad \omega > 0, \quad (\text{C.98})$$

which has no diagonal matrix elements. The total Hamiltonian is given by $H(t) = H^{(0)} + H^{(\text{i})}(t)$.

Suppose that at $t = 0$ the occupation numbers of the states $|a\rangle$ and $|b\rangle$ are f_a and f_b , respectively, both in the range $[0, 1]$. To calculate the occupation numbers at time $t > 0$, we have to solve the von Neumann equation for the density matrix

$$i\hbar \frac{d}{dt} N(t) = [H(t), N(t)]; \quad N(0) = \text{diag}(f_a, f_b). \quad (\text{C.99})$$

The contribution of $H^{(0)}$ is taken into account exactly by going over to the Dirac picture:

$$i\hbar \frac{d}{dt} \tilde{N}(t) = [\tilde{H}^{(\text{i})}(t), \tilde{N}(t)], \quad (\text{C.100})$$

where

$$\tilde{N}(t) = e^{-\frac{H^{(0)}t}{i\hbar}} N(t) e^{+\frac{H^{(0)}t}{i\hbar}}; \quad \tilde{H}^{(\text{i})}(t) = e^{-\frac{H^{(0)}t}{i\hbar}} H^{(\text{i})}(t) e^{+\frac{H^{(0)}t}{i\hbar}} \quad (\text{C.101})$$

and, in particular, $\tilde{N}(0) = N(0)$. The calculation of the exponential is very easy, because $H^{(0)}$ is a diagonal matrix. Equation (C.100) can be solved iteratively and the contributions up to second order are

$$\begin{aligned} \tilde{N}(t) &= \tilde{N}(0) + \frac{1}{i\hbar} \int_0^t dt_1 [\tilde{H}^{(\text{i})}(t_1), \tilde{N}(0)] \\ &\quad + \frac{1}{(i\hbar)^2} \int_0^t dt_1 \int_0^{t_1} dt_2 [\tilde{H}^{(\text{i})}(t_1), [\tilde{H}^{(\text{i})}(t_2), \tilde{N}(0)]]. \end{aligned} \quad (\text{C.102})$$

The first-order contribution does not change the occupation numbers, i.e., the diagonal elements, but only the polarization, which is given by the non-diagonal elements. Writing the above equation explicitly and returning to the Heisenberg picture, the occupation number of the state $|b\rangle$ becomes

$$N_{bb}(t) = f_b + (f_a - f_b) \frac{1}{\hbar^2} \int_0^t dt_1 \int_0^t dt_2 \times e^{\frac{E_b(t-t_1)}{i\hbar}} H_{ba}^{(i)}(t_1) e^{\frac{E_a(t_1-t_2)}{i\hbar}} H_{ab}^{(i)}(t_2) e^{\frac{E_b(t_2-t)}{i\hbar}}. \quad (\text{C.103})$$

These integrals can be calculated explicitly, which leads to four contributions, corresponding to the four sign combinations $\pm i\omega$ (C.98). We keep only the one resonant contribution with $\hbar\omega \approx E_b - E_a$ and the result is

$$N_{bb}(t) = f_b + (f_a - f_b) \underline{H}_{ba}^{(i)\dagger} \underline{H}_{ab}^{(i)} \left(\frac{t}{\hbar}\right)^2 \text{sinc}^2 \frac{(E_b - E_a - \hbar\omega)t}{2\hbar}. \quad (\text{C.104})$$

The transition rate,

$$w = \lim_{t \rightarrow \infty} \frac{N_{bb}(t) - N_{bb}(0)}{t}, \quad (\text{C.105})$$

is the number of particles passing from $|a\rangle$ to $|b\rangle$ per unit time, in the long-time limit. Then the sinc function in (C.104) goes over into a delta function (A.7), the non-resonant terms neglected in (C.104) exactly vanish, and the final result is

$$w = \frac{2\pi}{\hbar} |\underline{H}_{ab}^{(i)}|^2 (f_a - f_b) \delta(E_b - E_a - \hbar\omega). \quad (\text{C.106})$$

This is Fermi's golden rule in its simplest form. In the case of many states, one has to perform a sum or integral over the quantum numbers and the density of states comes into play. The neglect of the non-resonant terms is equivalent to replacing the interaction Hamiltonian (C.98) by the non-Hermitian operator

$$\underline{H}^{(i)}(t) = \underline{H}_{ab}^{(i)} e^{-i\omega t}, \quad (\text{C.107})$$

known as rotating-wave approximation. The delta function stands for energy conservation: to absorb a photon, its energy $\hbar\omega$ has to be equal to the energy of the transition $E_b - E_a$. The absorption is furthermore governed by the factor $f_a - f_b$ ("Pauli blocking factor"). If this factor becomes negative, absorption changes into stimulated emission.

Let us briefly derive the the result (C.106) in a slightly different way. The equation of motion (C.100) can be solved iteratively. We replace the diagonal elements N_{aa} and N_{bb} by f_a and f_b , respectively, and the first-order correction for the nondiagonal elements, neglecting the nonresonant contributions, follows from

$$i\hbar \frac{d}{dt} \tilde{N}_{ab}(t) = \underline{H}_{ab}^{(i)} e^{-i(\omega_a - \omega_b + \omega_a)} (f_b - f_a), \quad (\text{C.108})$$

where $\omega_a = E_a/\hbar$ and $\omega_b = E_b/\hbar$. We introduce a phase relaxation (dephasing) by replacing the time derivative in (C.108) by $d/dt + \epsilon$; $\epsilon > 0$ and assume

that the interaction $\underline{H}^{(i)}(t)$ has been switched on a long time ago. Then the solution of (C.108) is given by the stationary solution

$$\tilde{N}_{ab}(t) = \frac{\underline{H}_{ab}^{(i)} e^{-i(\omega - \omega_b + \omega_a)}}{\hbar(\omega + i\epsilon) - E_b + E_a} (f_b - f_a). \quad (\text{C.109})$$

The next order affects the diagonal elements and from (C.100) it follows that

$$i\hbar \frac{d}{dt} \tilde{N}_{bb}(t) = \tilde{H}_{ba}(t) \tilde{N}_{ab}(t) - \text{c.c.} \quad (\text{C.110})$$

with the solution (C.109), the transition rate is equal to

$$w = \frac{d}{dt} \tilde{N}_{bb}(t) = \frac{2}{\hbar} |\underline{H}_{ab}^{(i)}|^2 (f_b - f_a) \frac{\hbar\epsilon}{(E_b - E_a - \hbar\omega)^2 + (\hbar\epsilon)^2}. \quad (\text{C.111})$$

The linear exponential decay of the polarization leads to a Lorentzian resonance with linewidth $\hbar\epsilon$, which is often observed in spectroscopy. In the limit $\epsilon \rightarrow +0$ we again obtain the result (C.106).

D Computer Programs

In this appendix, we list Fortran programs to demonstrate the calculation of the optical absorption $\alpha(\omega) = \text{Im } \chi(\omega)$ by reformulation as initial-value problem, using finite differences for the discretization in real space. The optical susceptibility is calculated according to (2.76); the Fourier integral is evaluated numerically by fast Fourier transform (FFT) and the time-dependent Schrödinger equation is solved by the leapfrog method (2.111).

D.1 Cartesian Coordinates

The following program `i2d2.for` calculates the absorption spectrum of an ideal two-dimensional semiconductor in Cartesian coordinates (Example C in Chap. 2), using second-order finite differences (2.80). The calculation gives the *dashed curve* in Fig. 2.7.

```
program i2d2
  character*12 name
  parameter(name='abs.dat')
  integer n,nn,l,p,k
  c      n odd; p in 2^N for FFT
  parameter(n=999,l=15,p=2**l)
  c      Psi(x,y,t-Delta t), Psi(x,y,t), Psi(x,y,t+Delta t), -V(x,y)
  complex psio(n,n),psi(n,n),psin(n,n),v(n,n)
  c      P(t)
  complex pol(p),pl
  complex a,b
  real lenx,dx,lent,dt,t,lenw,dw,w
  real tmax,ep,pi
  common /nn/ nn
  common /len/ len
  common /dx/ dx
  common /dt/ dt
  common /ab/ a,b
  common /pi/ pi
  nn=n
  pi=4*atan(1.e0)
```

```

c      length of the side  $L_x = L_y$ , mesh size  $h_x = h_y$ 
len=150.e0
dx=len/(n+1)

c      homogeneous broadening, upper integration limit
ep=0.1e0
tmax=5/ep

c      time step and time interval
call setdt(dt)
lent=p*dt
if (lent/2.lt.tmax) pause ' p too small '

c      frequency step and frequency interval by sampling theorem
dw=2*pi/lent
lenw=p*dw

c      discretization of kinetic energy and Coulomb potential
call setab(a,b)
call setv(v,psio)

call null(pol,p)

c      set  $\Psi(0)$ ,  $P(0)$ ; factor  $\frac{1}{2}$  because of the discretization of integral (2.76)
call init(psio)
pol(p/2)=pl(psio)/2
write(*,100) 0.e0,pol(p/2)

c      first step to calculate  $\Psi(\Delta t)$ 
call dstep(psi,psio,psin,v)

do k=1,p/2
  t=k*dt
  if (t.lt.tmax) then
    pol(p/2+k)=pl(psi)*cmplx(exp(-ep*t))
    if(mod(k,10).eq.0) write(*,100) t,pol(p/2+k)

c      leapfrog step
    call lstep(psin,psi,psio,v)
    call vcpy(psio,psi,n*n)
    call vcpy(psi,psin,n*n)
  endif
enddo

c      FFT for array in normal order (most FFTs require bit-reverse order)
call fft(pol,p,dt,+1)

c      write  $\alpha(\omega)$  for  $\omega \in [-5, +20]$ 
open(1,file=name)
do k=1,p
  w=-lenw/2+k*dw
  if (w.ge.-5.e0.and.w.le.+20.e0) write(1,100) w,aimag(pol(k))
enddo
close(1)

100 format(1x,6(e13.6e2,1x))

end

```

```

c      upper bound for  $-\frac{1}{2}\Delta$  according to (2.93)
      subroutine setdt(dt)
      real dt,dx,ub
      common /dx/ dx
      ub=8/(2*dx**2)
      dt=0.95e0/ub
      end

c       $\Psi(x,y,t=0) = i\mu(x,y) = i\delta(x)\delta(y)$ 
      subroutine init(psi)
      integer n
      complex psi(n,n)
      real dx
      common /nn/ n
      common /dx/ dx
      call null(psi,n*n)
      psi((n+1)/2,(n+1)/2)=cmplx(0.e0,1/dx**2)
      end

c       $P(t) = \Psi(x=0,y=0,t)$ 
      function pl(psi)
      integer n
      complex pl,psi(n,n)
      common /nn/ n
      pl=psi((n+1)/2,(n+1)/2)
      end

c      coefficients for the discretization of  $-\frac{1}{2}\Delta$  (2.80)
      subroutine setab(a,b)
      complex a,b
      real dx
      common /dx/ dx
      a=cmplx(+1/dx**2)
      b=cmplx(-1/(2*dx**2))
      end

c      ground-state method (2.98)
      subroutine setv(v,hlp)
      integer n,i,j
      complex v(n,n),hlp(n,n)
      real len,dx,x,y
      common /nn/ n
      common /len/ len
      common /dx/ dx
      do j=1,n
          do i=1,n
              x=-len/2+i*dx
              y=-len/2+j*dx
              r=sqrt(x*x+y*y)
              hlp(i,j)=cmplx(exp(-2*r))
          enddo
      enddo
      call mult(v,hlp,v,0)
      do j=1,n
          do i=1,n
              x=-len/2+i*dx
              y=-len/2+j*dx
              r=sqrt(x*x+y*y)
              if (r.ge.5.e0) v(i,j)=-1/r
          enddo
      enddo
  
```

```

        if (r.le.5.e0) v(i,j)=-v(i,j)/hlp(i,j)-2.e0
    enddo
enddo
end

c calculate  $\Psi(\Delta t)$  from  $\Psi(0)$  by second-order Taylor expansion (2.115)
subroutine dstep(psi,psio,hlp,v)
integer n
complex psi(n,n),psio(n,n),hlp(n,n),v(n,n)
real dt
common /nn/ n
common /dt/ dt
call mult(psi,psio,v,1)
call mult(hlp,psi,v,1)
call vadd(psi,psio,hlp,cmplx(-dt**2/2),n*n)
call mult(hlp,psio,v,1)
call vadd(psi,psi,hlp,cmplx(0.e0,-dt),n*n)
end

c three-level recursion (2.112)
subroutine lstep(psin,psi,psio,v)
integer n
complex psin(n,n),psi(n,n),psio(n,n),v(n,n)
real dt
common /nn/ n
common /dt/ dt
call mult(psin,psi,v,1)
call vadd(psin,psio,psin,cmplx(0.e0,-2*dt),n*n)
end

c  $\Psi_1 = H \Psi_2$ 
subroutine mult(psi1,psi2,v,switch)
integer n,switch,j
complex psi1(n,n),psi2(n,n),v(n,n),a,b
common /nn/ n
common /ab/ a,b
if (switch.ne.1) call null(psi1,n*n)
if (switch.eq.1) call vmlt(psi1,v,psi2,n*n)
call vadd(psi1,psi1,psi2,2*a,n*n)
do j=1,n
    call vadd(psi1(1,j),psi1(1,j),psi2(2,j),b,n-1)
    call vadd(psi1(2,j),psi1(2,j),psi2(1,j),b,n-1)
enddo
do j=1,n
    if (j.lt.n) call vadd(psi1(1,j),psi1(1,j),psi2(1,j+1),b,n)
    if (j.gt.1) call vadd(psi1(1,j),psi1(1,j),psi2(1,j-1),b,n)
enddo
end

c The following vector operations consume about 99% of the CPU time
c and should be optimized for the computer architecture. The version
c below works best on vector machines.
subroutine vcpy(a,b,n)           subroutine vadd(a,b,c,d,n)
integer n,i
complex a(n),b(n)
do i=1,n
    a(i)=b(i)
enddo
end                                integer i,n
complex a(n),b(n),c(n),d
do i=1,n
    a(i)=b(i)+c(i)*d
enddo
end

```

```

subroutine vmlt(a,b,c,n)
integer n,i
complex a(n),b(n),ca(n)
do i=1,n
  a(i)=b(i)*c(i)
enddo
end

subroutine null(a,n)
integer n,i
complex a(n)
do i=1,n
  a(i)=cmplx(0.e0)
enddo
end

```

For the discretization by fourth-order finite differences (2.81), a few changes have to be made to the previous program. The calculation leads to the *dotted curve* in Fig. 2.7.

```

program i2d4

c   upper bound for  $-\frac{1}{2}\Delta$  (2.94)
subroutine setdt(dt)
real dt,dx,ub
common /dx/ dx
ub=(32.e0/3)/(2*dx**2)
dt=0.95e0/ub
end

c   discretization of  $-\frac{1}{2}\Delta$  (2.81)
subroutine setabc(a,b,c)
complex a,b,c
real dx
common /dx/ dx
a=cmplx(+30/(24*dx**2))
b=cmplx(-16/(24*dx**2))
c=cmplx(+01/(24*dx**2))
end

c    $\Psi_1 = H \Psi_2$ ; treatment of boundary effects according to (2.122)
subroutine mult(psi1,psi2,v,switch)
integer n,switch,j
complex psi1(n,n),psi2(n,n),v(n,n),a,b,c
common /nn/ n
common /abc/ a,b,c
if (switch.ne.1) call null(psi1,n*n)
if (switch.eq.1) call vmlt(psi1,v,psi2,n*n)
call vadd(psi1,psi1,psi2,2*a,n*n)
do j=1,n
  call vadd(psi1(1,j),psi1(1,j),psi2(2,j),b,n-1)
  call vadd(psi1(2,j),psi1(2,j),psi2(1,j),b,n-1)
  call vadd(psi1(1,j),psi1(1,j),psi2(3,j),c,n-2)
  call vadd(psi1(3,j),psi1(3,j),psi2(1,j),c,n-2)
  call vadd(psi1(1,j),psi1(1,j),psi2(1,j),-c,1)
  call vadd(psi1(n,j),psi1(n,j),psi2(n,j),-c,1)
enddo
do j=1,n
  if (j.lt.n) call vadd(psi1(1,j),psi1(1,j),psi2(1,j+1),b,n)
  if (j.gt.1) call vadd(psi1(1,j),psi1(1,j),psi2(1,j-1),b,n)
  if (j.lt.n-1) call vadd(psi1(1,j),psi1(1,j),psi2(1,j+2),c,n)
  if (j.gt.2)   call vadd(psi1(1,j),psi1(1,j),psi2(1,j-2),c,n)
  if (j.eq.1)   call vadd(psi1(1,j),psi1(1,j),psi2(1,j),-c,n)
  if (j.eq.n)   call vadd(psi1(1,j),psi1(1,j),psi2(1,j),-c,n)
enddo
end

```

D.2 Polar Coordinates

The following program `i2dr.for` calculates the absorption of the ideal two-dimensional semiconductor using polar coordinates (Example A for $B = 0$).

```

program i2dr

character*12 name
parameter(name='abs.dat')
integer n,nn,l,p,k
parameter(n=2000,l=15,p=2**l)
complex psio(n),psi(n),psin(n),v(n)

c      tridiagonal matrix, contains the discretization of  $-\frac{1}{2} \Delta_\rho$ 
complex kr(n,3)
complex pol(p),pl
real lenr,dr,lent,dt,t,lenw,dw,w
real tmax,ep,pi

common /nn/ nn
common /len/ len
common /dr/ dr
common /dt/ dt
common /pi/ pi

nn=n
pi=4*atan(1.e0)

len=200.e0
dr=len/n
ep=0.1e0
tmax=5/ep

call setdt(dt)
lent=p*dt
if (lent/2.lt.tmax) pause ' p too small '
dw=2*pi/lent
lenw=p*dw

call setkr(kr)
call setv(v,kr,psio)

call null(pol,p)
call init(psio)
pol(p/2)=pl(psio)/2
write(*,100) 0.e0,pol(p/2)

call dstep(psi,psio,psin,kr,v)

do k=1,p/2
  t=k*dt
  if (t.lt.tmax) then
    pol(p/2+k)=pl(psi)*cmplx(exp(-ep*t))
    if(mod(k,10).eq.0) write(*,100) t,pol(p/2+k)
    call lstep(psin,psi,psio,kr,v)
    call vcpy(psio,psi,n)
    call vcpy(psi,psin,n)
  endif
enddo

```

```

call fft(pol,p,dt,+1)

open(1,file=name)
do k=1,p
  w=-lenw/2+k*dt
  if (w.ge.-5.e0.and.w.le.+20.e0) write(1,100) w,aimag(pol(k))
enddo
close(1)

100 format(1x,6(e13.6e2,1x))

end

c      upper bound of  $-\frac{1}{2} \Delta_\rho$  (2.95)
subroutine setdt(dt)
real dt,dr,bnd
common /dr/ dr
bnd=4.84194e0/(2*dr**2)
dt=0.95e0/bnd
end

c       $\Psi(\rho, t=0) = i \delta(\rho)/(2\pi\rho)$  (2.85)
subroutine init(psi)
integer n
complex psi(n)
real dr,pi
common /nn/ n
common /dr/ dr
common /pi/ pi
call null(psi,n)
psi(1)=cmplx(0.e0,4/(pi*dr**2))
end

c       $P(t) = \Psi(\rho=0, t)$ 
function pl(psi)
integer n
common /nn/ n
complex pl,psi(n)
pl=psi(1)
end

c      discretization of  $-\frac{1}{2} \Delta_\rho$  (2.87, 2.90)
subroutine setkr(kr)
integer n,i
real dr,r
complex kr(n,3)
common /nn/ n
common /dr/ dr
kr(1,2)=cmplx(+4/dr**2)/2
kr(1,3)=cmplx(-4/dr**2)/2
do i=2,n
  r=(i-1)*dr
  kr(i,1)=cmplx(-(r-dr/2)/(r*dr**2))/2
  kr(i,3)=cmplx(-(r+dr/2)/(r*dr**2))/2
  kr(i,2)=-kr(i,1)-kr(i,3)
enddo
end

```

```

subroutine setv(v,kr,hlp)
integer n,i
complex v(n),kr(n,3),hlp(n)
real dr,r
common /nn/ n
common /dr/ dr
do i=1,n
    r=(i-1)*dr
    hlp(i)=cmplx(exp(-2*r))
enddo
call mult(v,hlp,kr,v,0)
do i=1,n
    r=(i-1)*dr
    if (r.gt.5.e0) v(i)=-1/r
    if (r.le.5.e0) v(i)=-v(i)/hlp(i)-2.e0
enddo
end

subroutine dstep(psi,psio,hlp,kr,v)
integer n
complex psi(n),psio(n),hlp(n),kr(n,3),v(n)
real dt
common /nn/ n
common /dt/ dt
call mult(psi,psio,kr,v,1)
call mult(hlp,psi,kr,v,1)
call vadd(psi,psio,hlp,cmplx(-dt**2/2),n)
call mult(hlp,psio,kr,v,1)
call vadd(psi,psi,hlp,cmplx(0.e0,-dt),n)
end

subroutine lstep(psin,psi,psio,kr,v)
integer n
complex psin(n),psi(n),psio(n),v(n)
complex kr(n,3)
real dt
common /nn/ n
common /dt/ dt
call mult(psin,psi,kr,v,1)
call vadd(psin,psio,psin,cmplx(0.e0,-2*dt),n)
end

subroutine mult(psi1,psi2,kr,v,switch)
integer n,switch
complex psi1(n),psi2(n),v(n)
complex kr(n,3)
common /nn/ n
call vmlt(psi1(1),psi2(1),kr(1,2),n)
call vadl(psi1(2),psi2(1),kr(2,1),n-1)
call vadl(psi1(1),psi2(2),kr(1,3),n-1)
if (switch.eq.1) call vadl(psi1,v,psi2,n)
end

c
The vector operations vcpy, vmlt, vadd, and null are the same as above
subroutine vadl(a,b,c,n)
integer n,i
complex a(n),b(n),c(n)
do i=1,n
    a(i)=a(i)+b(i)*c(i)
enddo
end

```

It takes only very few changes to treat Example A for $B \neq 0$. The domain radius is determined by the classical point of return, $R = \sqrt{8\omega_{\max}}/B + 5/\sqrt{B}$ with $\omega_{\max} = 20$. As the extension of the eigenfunctions is proportional $1/\sqrt{B}$, the step size is chosen to be $h_\rho = 0.1/\sqrt{B}$. The result should be identical to that of Fig. 2.2.

```

program i2drb
parameter(n=141,l=16,p=2**l)
common /b/ b
b=2.e0
len=10.e0

subroutine setdt(dt)
real dt,len,dr,b,bnd
common /len/ len
common /dr/ dr
common /b/ b
bnd=4.84194e0/(2*dr**2)+(b*len)**2/8
dt=0.95e0/bnd
end

subroutine setv(v,kr,hlp)
integer n,i
complex v(n),kr(n,3),hlp(n)
real dr,r,b
common /nn/ n
common /dr/ dr
common /b/ b
do i=1,n
    r=(i-1)*dr
    hlp(i)=cmplx(exp(-2*r))
enddo
call mult(v,hlp,kr,v,0)
do i=1,n
    r=(i-1)*dr
    if (r.gt.5.e0) v(i)=-1/r
    if (r.le.5.e0) v(i)=-v(i)/hlp(i)-2.e0
    v(i)=v(i)+cmplx((b*r)**2/8)
enddo
end

```

It is also straightforward to include a parabolic potential $B^2(x^2+y^2)/8$ in `i2d2.for` or `i2d4.for`.

D.3 Time-Reversal Symmetry

If the the Hamiltonian is real, the efficiency can be increased by about a factor of two using the relation (2.119). For example, the following changes have to be made to the programs `i2d2.for` and `i2d4.for`.

```

c      p and time interval reduced by a factor of 2
      if (lent/2.lt.tmax/2) pause ' p too small '
      pol(p/2)=pl2(psi)/2

      do k=1,p/2
          t=k*dt
          if (t.lt.tmax/2) then
              pol(p/2+k)=pl2(psi)*cmplx(exp(-2*ep*t))
              if(mod(k,10).eq.0) write(*,100) 2*t,pol(p/2+k)
              call lstep(psin,psi,psio,v)
              call vcpy(psio,psi,n*n)
              call vcpy(psi,psin,n*n)
          endif
      enddo

c      time step doubled
      call fft(pol,p,2*dt,+1)
      open(1,file=name)
      do k=1,p

c      frequency halved
      w=-lenw/4+k*dw/2
      if (w.ge.-5.e0.and.w.le.+20.e0) write(1,100) w,aimag(pol(k))
      enddo
      close(1)

100 format(1x,6(e13.6e2,1x))

      end

c       $P(2t) = -i \langle \Psi^*(t), \Psi(t) \rangle$ 
      function pl2(psi)
      integer n,i,j
      complex pl2,psi(n,n)
      real dx
      common /nn/ n
      common /dx/ dx
      pl2=cmplx(0.e0)
      do j=1,n
          do i=1,n
              pl2=pl2+psi(i,j)**2
          enddo
      enddo
      pl2=pl2*cmplx(0.e0,-dx**2)
      end

```

D.4 Absorbing Boundary Conditions

The following program demonstrates the use of absorbing boundary conditions. The subroutines not specified are the same as in `i2dr.for`. The number of mesh points is reduced by a factor of 10. The result is the *dashed line* in Fig. 2.10.

```

program i2drabc

character*12 name
parameter(name='abs.dat')
integer n,nn,l,p,k
parameter(n=200,l=15,p=2**l)
complex psio(n),psi(n),psin(n),v(n),kr1(n,3),kr2(n,3)
complex pol(p),pl
real len1,len2,dr,lent,dt,t,lenw,dw,w
real tmax,ep,pi

common /nn/ nn
common /len/ len1,len2
common /dr/ dr
common /dt/ dt
common /pi/ pi

nn=n
pi=4*atan(1.e0)

c      set inner and outer radius
len1=15.e0
len2=20.e0
dr=len2/n
ep=0.1e0
tmax=5.e0/ep

call setdt(dt)
lent=p*dt
if (lent/2.lt.tmax) pause ' p too small '
dw=2*pi/lent
lenw=p*dw

call setkr(kr1,kr2)
call setv(v,kr1,psio)

call null(pol,p)
call init(psio)
pol(p/2)=pl(psio)/2
write(*,100) 0.e0,pol(p/2)
call dstep(psi,psio,psin,kr1,v)

do k=1,p/2
  t=k*dt
  if (t.lt.tmax) then
    pol(p/2+k)=pl(psi)*cmplx(exp(-ep*t))
    if(mod(k,10).eq.0) write(*,100) t,pol(p/2+k)
    call step(psin,psi,psio,kr1,kr2,v)
    call vcpy(psio,psi,n)
    call vcpy(psi,psin,n)
  endif
enddo

```

```

call fft(pol,p,dt,+1)

open(1,file=name)
do k=1,p
  w=k*dt-lenw/2
  if (w.gt.-5.e0.and.w.lt.+20.e0) write(1,100) w,aimag(pol(k))
enddo
close(1)

100 format(1x,6(e13.6e2,1x))

end

c      complex mass (2.148)
function m(r)
complex m
real r,len1,len2,pi
common /len/ len1,len2
common /pi/ pi
m=cmplx(1.e0)
if (r.gt.len1) then
  m=cmplx(1.e0,1/cos(0.5e0*pi*(r-len1)/(len2-len1))-1.e0)
endif
end

c      set Hermitian and anti-Hermitian part of kinetic-energy operator (2.146)
subroutine setkr(kr1,kr2,n,dr)
integer n,i
real dr,r
complex kr1(n,3),kr2(n,3),m
kr1(1,1)=cmplx(+777.7777e0)
kr1(1,2)=cmplx(+4/dr**2)/2
kr1(1,3)=cmplx(-4/dr**2)/2
do i=2,n
  r=(i-1)*dr
  kr1(i,1)=cmplx(-(r-dr/2)/(2*r*dr**2))/m(r-dr/2)
  kr1(i,3)=cmplx(-(r+dr/2)/(2*r*dr**2))/m(r+dr/2)
  kr1(i,2)=-kr1(i,1)-kr1(i,3)
enddo
call vimag(kr2,kr1,3*n)
call vreal(kr1,kr1,3*n)
end

c      combination of leapfrog and Euler step (2.147)
subroutine step(psin,psi,psio,kr1,kr2,v)
integer n
complex psin(n),psi(n),psio(n),v(n)
complex kr1(n,3),kr2(n,3)
real dt
common /nn/ n
common /dt/ dt
call mult(psin,psi,kr1,v,1)
call vadd(psin,psio,psin,cmplx(0.e0,-2*dt),n)
call mult(psio,psin,kr2,v,0)
call vadd(psin,psin,psio,cmplx(0.e0,-2*dt),n)
end

```

```
subroutine vreal(a,b,n)
integer n,i
complex a(n),b(n)
do i=1,n
    a(i)=cmplx(real(b(i)))
enddo
end

subroutine vimag(a,b,n)
integer n,i
complex a(n),b(n)
do i=1,n
    a(i)=cmplx(0.e0,aimag(b(i)))
enddo
end
```

D.5 Cylindrical Coordinates

The Cartesian and plane polar coordinates from the previous examples can be combined to cylindrical coordinates. The following program calculates the absorption spectrum for the problem (3.69). The result is the curve for $B = 2$ in Fig. 3.7. We took advantage of the symmetry $\Psi(\rho, +z, t) = \Psi(\rho, -z, t)$ and introduced absorbing boundary conditions for the z direction. Thus the z interval is reduced to $[0, 30]$ from $[-200, +200]$ in the original version. The vector operations are the same as used in the previous programs.

```

program bmabc

character*12 name
parameter(name='abs.dat')
integer nr,nnr,nz,nnz,l,p,k
parameter(nr=113,nz=300,l=18,p=2**l)
complex psio(nr,nz),psi(nr,nz),psin(nr,nz)
complex kr(nr,3),kz1(nz,3),kz2(nz,3),v(nr,nz)
complex pol(p),pl
real lenr,lenz1,lenz2,dr,dz,lent,dt,t,lenw,dw,w
real tmax,ep,pi,b

common /nn/ nnr,nnz
common /lenr/ lenr
common /lenz/ lenz1,lenz2
common /d/ dr,dz
common /dt/ dt
common /pi/ pi
common /b/ b

nnr=nr
nnz=nz
pi=4*atan(1.e0)

b=2.e0

lenr=8.e0
lenz1=20.e0
lenz2=30.e0
dr=lenr/nr
dz=lenz2/nz

ep=0.05e0
tmax=5/ep
call setdt(dt)
lent=p*dt
if (lent/2.lt.tmax) pause ' p too small '
dw=2*pi/lent
lenw=p*dw

call setkr(kr)
call setkz(kz1,kz2)
call setv(v,kr,kz1,psio)

call null(pol,p)

call init(psio)
pol(p/2)=pl(psio)/2

```

```

write(*,100) 0.e0,pol(p/2)
call dstep(psi,psio,psin,kr,kz1,v)

do k=1,p/2
  t=k*dt
  if (t.lt.tmax) then
    pol(p/2+k)=pl(psi)*cmplx(exp(-ep*t))
    if (mod(k,10).eq.0) write(*,100) t,pol(p/2+k)
    call step(psin,psi,psio,kr,kz1,kz2,v)
    call vcpy(psio,psi,nr*nz)
    call vcpy(psi,psin,nr*nz)
  endif
enddo

call fft(pol,p,dt,+1)

open(1,file=name)
do k=1,p
  w=-lenw/2+k*dt
  if (w.ge.-5.e0.and.w.le.+15.e0) write(1,100) w,aimag(pol(k))
enddo
close(1)

100 format(1x,6(e15.6e4,1x))

end

subroutine setdt(dt)
implicit none
real dt,lenr,dr,dz,b,ub
common /lenr/ lenr
common /d/ dr,dz
common /b/ b
ub=4.84194e0/(2*dr**2)+4/(2*dz**2)+(b*lenr)**2/8
dt=0.95e0/ub
end

subroutine init(psi)
implicit none
integer nr,nz
complex psi(nr,nz)
real dr,dz,pi
common /nn/ nr,nz
common /d/ dr,dz
common /pi/ pi
call null(psi,nr*nz)
psi(1,1)=cmplx(0.e0,4/(pi*dr**2*dz))
end

function pl(psi)
implicit none
integer nr,nz
complex pl,psi(nr,nz)
common /nn/ nr,nz
pl=psi(1,1)
end

```

```

subroutine setkr(kr)
implicit none
integer nr,nz,i
real dr,dz,r
complex kr(nr,3)
common /nn/ nr,nz
common /d/ dr,dz
kr(1,2)=cmplx(+4/dr**2)/2
kr(1,3)=cmplx(-4/dr**2)/2
do i=2,nr
    r=(i-1)*dr
    kr(i,1)=cmplx(-(r-dr/2)/(r*dr**2))/2
    kr(i,3)=cmplx(-(r+dr/2)/(r*dr**2))/2
    kr(i,2)=-kr(i,1)-kr(i,3)
enddo
end

function m(z)
complex m
real z,lenz1,lenz2,pi
common /lenz/ lenz1,lenz2
common /pi/ pi
m=cmplx(1.e0)
if (z.gt.lenz1) then
    m=cmplx(1.e0,1/cos(0.5e0*pi*(z-lenz1)/(lenz2-lenz1))-1.e0)
endif
end

subroutine setkz(kz1,kz2)
implicit none
integer nr,nz,j
complex kz1(nz,3),kz2(nz,3),m
real dr,dz,z
common /nn/ nr,nz
common /d/ dr,dz
kz1(1,1)=cmplx(+7777.777e0)
kz1(1,2)=cmplx(+2/(2*dz**2))
kz1(1,3)=cmplx(-2/(2*dz**2))
do j=2,nz
    z=(j-1)*dz
    kz1(j,1)=cmplx(-1/(2*dz**2))/m(z-dz/2)
    kz1(j,3)=cmplx(-1/(2*dz**2))/m(z+dz/2)
    kz1(j,2)=-kz1(j,1)-kz1(j,3)
enddo
call vimag(kz2,kz1,3*nz)
call vreal(kz1,kz1,3*nz)
end

subroutine setv(v,kr,kz,hlp)
implicit none
integer nr,nz,i,j
complex v(nr,nz),kr(nr,3),kz(nz,3),hlp(nr,nz)
real dr,dz,b,r,z,rr
common /nn/ nr,nz
common /d/ dr,dz
common /b/ b
do j=1,nz
    do i=1,nr
        r=(i-1)*dr
        z=(j-1)*dz

```

```

rr=sqrt(r**2+z**2)
    hlp(i,j)=cmplx(exp(-rr))
  enddo
enddo
call mult(v,hlp,kr,kz,v,0)
do j=1,nz
  do i=1,nr
    r=(i-1)*dr
    z=(j-1)*dz
    rr=sqrt(r**2+z**2)
    if (rr.gt.5.e0) v(i,j)=-1/rr
    if (rr.le.5.e0) v(i,j)=-v(i,j)/hlp(i,j)-0.5e0
    v(i,j)=v(i,j)+cmplx((b*r)**2/8)
  enddo
enddo
end

subroutine dstep(psi,psio,hlp,kr,kz,v)
implicit none
integer nr,nz
complex psi(nr,nz),psio(nr,nz),hlp(nr,nz)
complex kr(nr,3),kz(nz,3),v(nr,nz)
real dt
common /nn/ nr,nz
common /dt/ dt
call mult(psi,psio,kr,kz,v,2)
call mult(hlp,psi,kr,kz,v,2)
call vadd(psi,psio,hlp,cmplx(-dt**2/2),nr*nz)
call mult(hlp,psio,kr,kz,v,2)
call vadd(psi,psi,hlp,cmplx(0.e0,-dt),nr*nz)
end

subroutine step(psin,psi,psio,kr,kz1,kz2,v)
implicit none
integer nr,nz
complex psin(nr,nz),psi(nr,nz),psio(nr,nz)
complex kr(nr,3),kz1(nz,3),kz2(nz,3),v(nr,nz)
real dt
common /nn/ nr,nz
common /dt/ dt
call mult(psin,psi,kr,kz1,v,2)
call vadd(psin,psio,psin,cmplx(0.e0,-2*dt),nr*nz)
call mult(psio,psin,kr,kz2,v,1)
call vadd(psin,psin,psio,cmplx(0.e0,-2*dt),nr*nz)
end

subroutine mult(psi1,psi2,kr,kz,v,switch)
implicit none
integer nr,nz,switch,j
complex psi1(nr,nz),psi2(nr,nz),kr(nr,3),kz(nz,3),v(nr,nz)
common /nn/ nr,nz
if (switch.eq.0.or.switch.eq.1) call null(psi1,nr*nz)
if (switch.eq.2) call vmlt(psi1,v,psi2,nr*nz)
if (switch.eq.0.or.switch.eq.2) then
  do j=1,nz
    call vadl(psi1(1,j),psi2(1,j),kr(1,2),nr)
    call vadl(psi1(2,j),psi2(1,j),kr(2,1),nr-1)
    call vadl(psi1(1,j),psi2(2,j),kr(1,3),nr-1)
  enddo
endif

```

```
do j=1,nz
  if (j.gt.1)
&    call vadd(psi1(1,j),psi1(1,j),psi2(1,j-1),kz(j,1),nr)
    call vadd(psi1(1,j),psi1(1,j),psi2(1,j),kz(j,2),nr)
    if (j.lt.nz)
&    call vadd(psi1(1,j),psi1(1,j),psi2(1,j+1),kz(j,3),nr)
  enddo
end
```

References

Chapter 1

1. L.D. Landau, E.M. Lifshitz: *Course of Theoretical Physics*, vol 3, 3rd edn (Pergamon, Oxford 1999)
2. E. Merzbacher: *Quantum Mechanics*, 3rd edn (Wiley, New York 1998)
3. H. Friedrich: *Theoretical Atomic Physics* (Springer, New York 1991)
4. J.M. Ziman: *Principles of the Theory of Solids* (Cambridge University Press, London 1979)
5. F. Bassani, G. Pastori Parravicini, *Electronic States and Optical Transitions in Solids*, ed by R.A. Ballinger (Pergamon, Oxford 1975)
6. P.Y. Yu, M. Cardona: *Fundamentals of Semiconductors*, 2nd edn (Springer, Berlin 1999)
7. C.F. Klingshirn: *Semiconductor Optics* (Springer, Berlin 1997)
8. S.L. Chuang: *Physics of Optoelectronic Devices* (Wiley, New York 1995)
9. C. Weisbuch, B. Vinter: *Quantum Semiconductor Structures: Fundamentals and Applications* (Academic, Boston 1991)
10. M.J. Kelly: *Low-Dimensional Semiconductors: Materials, Physics, Technology, Devices* (Clarendon, Oxford 1995)
11. J.H. Davies: *The Physics of Low-Dimensional Semiconductors: An Introduction* (Cambridge University Press 1998)
12. A.Y. Shik: *Quantum Wells: Physics and Electronics of Two-Dimensional Systems* (World Scientific, Singapore 1998)
13. F. Bloch: Z. Physik **52**, 555 (1928)
14. H. Bethe: Annalen der Physik (Leipzig), 5. Folge, Bd. **3**, 133 (1929)
15. G. Dresselhaus, A.F. Kip, C. Kittel: Phys. Rev. **98**, 368 (1955)
16. J.M. Luttinger: Phys. Rev. **102**, 1030 (1956)
17. M. Altarelli. In: *Heterojunctions and Semiconductor Superlattices*, ed by G. Allan, G. Bastard, N. Boccara, M. Lannoo, M. Voos (Springer, Berlin 1986) pp 12–37
18. T. Inui, Y. Tanabe, Y. Onodera: *Group Theory and Its Application in Physics* (Springer, Berlin 1990)
19. H.-W. Streitwolf: *Gruppentheorie in der Festkörperphysik* (Geest & Portig, Leipzig 1967)
20. E.O. Kane. In: *Semiconductors and Semimetals*, ed by R.K. Willardson, A.C. Beer, vol 1 (Academic, New York 1966) pp 75–100.
21. I.M. Tsidilkovski: *Band Structure of Semiconductors* (Pergamon, Oxford 1982)

22. H. J. Zeiger, G. W. Pratt: *Magnetic Interactions in Solids* (Clarendon, Oxford 1973)
23. G. L. Bir, G. E. Pikus: *Symmetry and Strain-Induced Effects in Semiconductors* (Wiley, New York 1974)
24. G. Bastard: *Wave Mechanics Applied to Semiconductor Heterostructures* (Les Editions de Physique, Les Ulis 1992)
25. E. I. Ivchenko, G. Pikus: *Superlattices and Other Heterostructures* (Springer, Berlin 1995)
26. R. Enderlein, N. J. M. Horing, *Fundamentals of Semiconductor Physics and Devices* (World Scientific, Singapore 1997)
27. J. M. Luttinger, W. Kohn: Phys. Rev. **97**, 869 (1955)
28. A. Baldereschi, N. O. Lipari: Phys. Rev. B **8**, 2697 (1973)
29. R. E. Peierls: Z. Physik **80**, 763 (1933)
30. L. Onsager, Phil. Mag. **43**, 1006 (1952)
31. E. O. Kane: J. Phys. Chem. Solids. **1**, 249 (1957)
32. U. Rössler: Solid State Commun. **49**, 943 (1984)
33. L. Esaki, R. Tsu, IBM J. Res. Dev. **14**, 61 (1970)
34. R. Dingle. In: *Festkörperprobleme/Advances in Solid-State Physics*, vol 15 (Vieweg, Braunschweig 1975) pp 21–48
35. L. J. Sham. In: *Physics of Low-dimensional Structures*, ed by P. Butcher, N. H. March, M. P. Tosi (Plenum, New York London 1993) pp 1–56
36. J. O. Dimmock. In: *Semiconductors and Semimetals*, ed by R. K. Willardson, A. C. Beer, vol 3 (Academic, New York 1967) pp 259–319
37. U. Ekenberg: Phys. Rev. B **36**, 6152 (1987); Phys. Rev. B **40**, 7714 (1989)
38. L. C. Andreani, A. Pasquarello: Phys. Rev. B **42**, 8928 (1990)
39. G. F. Bassani. In: *The Optical Properties of Solids*, ed by J. Tauc (Academic, New York London 1966) pp 33–61
40. H. Puff: Einführung in die allgemeine Theorie der optischen Eigenschaften von Festkörpern. Preprint, Zentralinstitut für Elektronenphysik, Berlin (1969)
41. W. Tan, J. C. Inkson, G. P. Srivastava: Semicond. Sci. Technol. **9**, 1305 (1994)
42. W. Franz: Z. Naturforschg. **13 a**, 484 (1958)
43. L. V. Keldysh: ZETP **34**, 1138 (1958) [Sov. Phys. JETP **34**, 788 (1958)]
44. K. Tharmalingam: Phys. Rev. **130**, 2204 (1963)
45. G. H. Wannier: Phys. Rev. **52**, 191 (1937)
46. R. J. Elliott: Phys. Rev. **108**, 1384 (1957)
47. M. Shinada, S. Sugano: J. Phys. Soc. Jpn. **21**, 1936 (1966)
48. U. Rössler, H.-R. Trebin: Phys. Rev. B **23**, 1961 (1981)
49. J. J. Hopfield: Phys. Rev. **112**, 1555 (1958)
50. D. L. Dexter, R. S. Knox: *Excitons* (Wiley, New York 1965)
51. A. Stahl, I. Balslev: phys. stat. sol. (b) **113**, 583 (1982)
52. R. S. Knox: *Theory of Excitons* (Academic, New York London 1963)
53. *Polarons and Excitons*, ed by C. G. Kuper and G. D. Whitfield (Oliver and Boyd, Edinburgh London 1963)
54. A. Stahl, I. Balslev: *Electrodynamics of the Semiconductor Band Edge* (Springer, Berlin 1987)
55. R. Zimmermann: *Many-Particle Theory of Highly Excited Semiconductors* (Teubner, Leipzig 1988)
56. H. Haug, S. W. Koch: *Quantum Theory of the Optical and Electronic Properties of Semiconductors*, 3rd edn (World Scientific, Singapore 1994)

57. D. E. Aspnes, N. Bottka. In: *Semiconductors and Semimetals*, ed by R. K. Willardson, A. C. Beer, vol 9 (Academic, New York 1972) pp 457–543
58. H. Stoltz: phys. stat. sol. **32**, 631 (1969)
59. H. Haug, S. Schmitt-Rink: Prog. Quant. Electr. **9**, 3 (1984)
60. L. Allen, J. H. Eberly: *Optical Resonance and Two-Level Atoms* (Dover, New York 1987)
61. S. Schmitt-Rink, D. S. Chemla: Phys. Rev. Lett. **57**, 2752 (1986)
62. M. Lindberg, S. W. Koch: Phys. Rev. B **38**, 3342 (1988)
63. L. Bányai, E. Reitsamer, D. B. Tran Thoai, H. Haug: J. Opt. Soc. Am. B **13**, 1278 (1996)
64. L. Bányai, Q. T. Vu, B. Mieck, H. Haug: Phys. Rev. Lett. **81**, 882 (1998)
65. V. M. Axt, A. Stahl, Z. Phys. B **93**, 195 (1994)
66. W. Schäfer. In: *Optics of Semiconductor Nanostructures*, ed by F. Henneberger, S. Schmitt-Rink, E. O. Göbel (Akademie-Verlag, Berlin 1992) pp 21–50
67. I. Balslev, R. Zimmermann, A. Stahl: Phys. Rev. B **40**, 4095 (1989)
68. L. V. Keldysh, Pisma ZETF **29**, 716 (1979) [Sov. Phys. Lett. **29**, 658 (1979)]
69. M. Kumagai, T. Takagahara: Phys. Rev. B **40**, 12359 (1989)
70. S. Glutsch, Nguyen Trung Dan, F. Bechstedt: Phys. Rev. B **52**, 13776 (1995)
71. P. W. Anderson: J. Phys. Soc. Jpn. **9**, 316 (1954)
72. R. Kubo: J. Phys. Soc. Jpn. **17**, 1100 (1962)
73. R. Zimmermann: phys. stat. sol. (b) **159**, 317 (1990)
74. R. L. Greene, K. K. Bajaj, D. E. Phelps: Phys. Rev. B **29**, 1807 (1984)
75. S. Glutsch, D. S. Chemla: Phys. Rev. B **53**, 15902 (1996)
76. P. Lefebvre, P. Christol, H. Mathieu: Phys. Rev. B **48**, 17308 (1993)
77. P. Lefebvre, P. Christol, H. Mathieu, S. Glutsch: Phys. Rev. B **52**, 5756 (1995)
78. R. Zimmermann: phys. stat. sol. (b) **135**, 681 (1986)
79. T. Ogawa, T. Takagahara: Phys. Rev. B **44**, 8138 (1991)

Chapter 2

1. R. J. Elliott: Phys. Rev. **108**, 1384 (1957)
2. M. Shinada, S. Sugano: J. Phys. Soc. Jpn. **21**, 1936 (1966)
3. T. Ogawa, T. Takagahara: Phys. Rev. B **44**, 8138 (1991)
4. P. Lefebvre, P. Cristol, H. Mathieu: Phys. Rev. B **48**, 17308 (1993)
5. G. D. Maan: Phys. Rev. **153**, 882 (1967)
6. D. F. Blossey: Phys. Rev. B **2**, 3976 (1970); Phys. Rev. B **3**, 1382 (1971)
7. D. F. Blossey, P. Handler, In: *Semiconductors and Semimetals*, ed by R. K. Willardson, A. C. Beer, vol 9 (Academic, New York 1972) pp 257–314
8. L. Esaki, R. Tsu, IBM J. Res. Dev. **14**, 61 (1970)
9. H. R. Schwarz: *Numerische Mathematik* (Teubner, Stuttgart 1997)
10. W. H. Press, S. A. Teukolsky, W. T. Vetterling, B. P. Flannery: *Numerical Recipes in FORTRAN: The Art of Scientific Programming*, 2nd edn (Cambridge University Press, Cambridge 1992); *Numerical Recipes in C: The Art of Scientific Programming*, 2nd edn (Cambridge University Press, Cambridge 1992)
11. A. Jennings, J. J. McKeown: *Matrix Computation*, 2nd edn (Wiley, Chichester 1992)
12. B. N. Parlett: *The Symmetric Eigenvalue Problem* (SIAM, Philadelphia 1998)

13. G. H. Golub, C. F. Van Loan: *Matrix Computations*, 4th printing (Hopkins University Press, Baltimore London 1993)
14. R. Barrett, M. Berry, T. F. Chan, J. Demmel, J. Donato, J. Dongarra, V. Eijkhout, R. Pozo, C. Romine, H. van der Vorst: *Templates for the Solution of Linear Systems: Building Blocks for Iterative Methods* (SIAM, Philadelphia 1994)
15. C. Stafford, S. Schmitt-Rink, W. Schäfer: Phys. Rev. B **41**, 10000 (1990); S. Schmitt-Rink, J. B. Stark, W. H. Knox, D. S. Chemla, W. Schäfer: Appl. Phys. A **91** (1991)
16. R. Zimmerman: phys. stat. sol. (b) **135**, 681 (1986)
17. S. Glutsch, F. Bechstedt: Phys. Rev. B **50**, 7733 (1994); Superlatt. Microstr. **15**, 5 (1994)
18. O. Di Stefano, S. Savasta, G. Martino, R. Girlanda: Phys. Rev. B **62**, 11071 (2000)
19. S. Glutsch, U. Siegner, M.-A. Mycek, D. S. Chemla: Phys. Rev. B **50**, 17009 (1994)
20. H. Chu, Y.-C. Chang: Phys. Rev. B **40**, 5497 (1989)
21. D. M. Whittaker, In: *22nd International Conference on the Physics of Semiconductors*, ed by D. J. Lookwood (World Scientific, Singapore 1995) vol 2, p 1420
22. S. Glutsch, P. Lefebvre, D. S. Chemla: Phys. Rev. B **55**, 15786 (1997)
23. D. M. Whittaker: Journal de Physique IV, Colloque C5, vol 3, p 199 (1993)
24. D. M. Whittaker: Europhys. Lett. **31**, 55 (1995)
25. N. Linder: Phys. Rev. B **55**, 13664 (1997)
26. A. Thränhardt, H.-J. Kolbe, J. Hader, T. Meier, G. Weiser, S. W. Koch: Appl. Phys. Lett. **73**, 2612 (1998)
27. S. Glutsch, F. Bechstedt, B. Rosam, K. Leo: Phys. Rev. B **63**, 085307 (2001)
28. G. D. Sanders, Y.-C. Chang: Phys. Rev. B **35**, 1300 (1987)
29. G. D. Sanders, K. K. Bajaj: Phys. Rev. B **35**, 2308 (1987)
30. A. R. K. Willcox, D. M. Whittaker: Superlatt. Microstr. **16**, 59 (1994)
31. R. Winkler: Phys. Rev. B **51**, 14395 (1995)
32. S. Bischoff, A. Knorr, S. W. Koch: Phys. Rev. B **55**, 7715 (1997)
33. G. Rau, A. R. Glanfield, P. C. Klipstein, N. F. Johnson, G. W. Smith: Phys. Rev. B **60**, 1900 (1999)
34. K. Hino: Phys. Rev. B **62**, 10626 (2000)
35. S.-L. Chuang, S. Schmitt-Rink, D. A. B. Miller, D. S. Chemla: Phys. Rev. B **43**, 1500 (1991)
36. G. Wen, Y.-C. Chang: Phys. Rev. B **45**, 6101 (1992)
37. C. Y.-P. Chao, S.-L. Chuang: Phys. Rev. B **48**, 8210 (1993)
38. S. Glutsch, D. S. Chemla: Phys. Rev. B **53**, 15902 (1996)
39. A. N. Forshaw, D. M. Whittaker: Phys. Rev. B **54**, 8794 (1996)
40. M. Graf, P. Vogl, A. B. Dzyubenko: Phys. Rev. B **54**, 17003 (1996)
41. S. Glutsch, D. S. Chemla, F. Bechstedt: Phys. Rev. B **54**, 11592 (1996)
42. E. Runge, R. Zimmerman: phys. stat. sol. (b) **206**, 167 (1998)
43. O. Di Stefano, S. Savasta, G. Martino, R. Girlanda: Appl. Phys. Lett. **77**, 2804 (2000)
44. A. Ahland, M. Wiedenhaus, D. Schulz, E. Voges: IEEE J. Quant. Electron. **36**, 842 (2000)
45. H. Chu, Y.-C. Chang: Phys. Rev. B **39**, 10861 (1989)

46. G. Wen, Y.-C. Chang: Phys. Rev. B **49**, 16585 (1994)
47. K. Bott, J. Hader, S. W. Koch, P. Thomas: Phys. Rev. B **56**, 12784 (1997)
48. M. L. Zambrano, J. C. Arce: Phys. Rev. B **66**, 155340 (2002)
49. S. M. Stepanow: Optische Absorption von Supergittern in gekreuzten äußeren elektrischen und magnetischen Feldern. Diplomarbeit, Friedrich-Schiller-Universität Jena (2002)
50. O. Stier, D. Bimberg: Phys. Rev. B **55**, 7726 (1997)
51. S. Glutsch, F. Bechstedt, W. Wegscheider, G. Schedelbeck: Phys. Rev. B **56**, 4108 (1997)
52. S. Schmitt-Rink, C. Ell, H. Haug: Phys. Rev. B **33**, 1183 (1986)
53. H. Haug, S. W. Koch: *Quantum Theory of the Optical and Electronic Properties of Semiconductors*, 3rd edn (World Scientific, Singapore 1994)
54. K. Hannewald, S. Glutsch, F. Bechstedt: Phys. Rev. B **62**, 4519 (2000)
55. S. Glutsch, D. S. Chemla, F. Bechstedt: Phys. Rev. B **51**, 16885 (1995)
56. R. Haydock: Computer Phys. Commun. **20**, 11 (1980)
57. *The Recursion Method and Its Applications*, ed by D. G. Pettifor, D. L. Weaire (Springer, Berlin 1985)
58. Th. Östreich: phys. stat. sol. (b) **164**, 313 (1997)
59. A. MacKinnon, In: Ref. 57, pp 84–90
60. R. Kosloff: J. Phys. Chem. **92**, 2087 (1988)
61. D. Weaire, D. Hobbs, G. J. Morgan, J. M. Holender, F. Wooten: J. Non-Crystalline Solids **164–166**, 877 (1993); D. Hobbs, D. Weaire, S. McMurry, O. Zuchuat: J. Phys.: Condens. Matt. **8**, 4691 (1996)
62. N. A. Hill, K. B. Whaley: J. Chem. Phys. **99**, 3707 (1993)
63. T. Iitaka, S. Nomura, H. Hirayama, X. Zhao, Y. Aoyagi, T. Sugano: Phys. Rev. B **56**, 1222 (1997)
64. S. Nomura, T. Iitaka, X. Zhao, T. Sugano, Y. Aoyagi: Phys. Rev. B **56**, 4348 (1997)
65. D. F. Montaño, J. C. Arce, N. Porras-Montenegro: J. Phys.: Condens. Matt. **12**, 9917 (2000)
66. D. M. Sullivan, D. S. Citrin: J. Appl. Phys. **89**, 3841 (2001); J. Appl. Phys. **91**, 3219 (2002)
67. A. Ahland, D. Schulz, E. Voges: Phys. Rev. B **60**, 5109 (1999)
68. D. B. Tran Thoai, H. Haug: Phys. Rev. B **47**, 3574 (1993)
69. K. Hannewald, S. Glutsch, F. Bechstedt: Phys. Rev. B **61**, 10792 (2000)
70. P. H. Hahn, W. G. Schmidt, F. Bechstedt: Phys. Rev. Lett. **88**, 016402 (2002); W. G. Schmidt, S. Glutsch, P. H. Hahn, F. Bechstedt: Phys. Rev. B **67**, 085307 (2003)
71. R. D. Richtmyer, K. W. Morton: *Difference Methods for Initial-Value Problems* (Academic, New York 1967)
72. J. C. Strikwerda: *Finite Difference Schemes and Partial Differential Equations* (Chapman & Hall, New York 1989)
73. W. F. Ames: *Numerical Methods for Partial Differential Equations*, 3rd edn (Academic, Boston 1992)
74. M. A. Celia, W. G. Gray: *Numerical Methods for Differential Equations: Fundamental Concepts for Scientific and Engineering applications* (Prentice Hall, Englewood Cliffs 1992)
75. P. Lancaster, K. Šalkauskas: *Curve and Surface Fitting* (Academic, London 1986)

76. P. O. Löwdin: J. Chem. Phys. **18**, 365 (1950)
77. J. C. Slater, G. F. Koster: Phys. Rev. **94**, 1498 (1954)
78. A. P. Prudnikov, Yu. A. Brychkov, O. I. Marichev: *Integrals and Series*, Vol. 2: Special Functions (Gordon and Breach, New York 1992)
79. M. Abramowitz, I. A. Stegun: *Pocketbook of Mathematical Functions*, abridged edn of *Handbook of Mathematical Functions*, Material selected by M. Danos, J. Rafelski (Verlag Harry Deutsch, Thun Frankfurt/Main 1984)
80. M. D. Feit, J. A. Fleck, Jr., A. Steiger: J. Comp. Phys. **47**, 412 (1982)
81. D. Kosloff, R. Kosloff: J. Comp. Phys. **52**, 35 (1983)
82. K. Hannewald, S. Glutsch, F. Bechstedt: J. Phys.: Condens. Matt. **13**, 275 (2001)
83. R. Guardiola, J. Ros: J. Comp. Phys. **45**, 374 (1982)
84. A. Siarkos, E. Runge, R. Zimmermann: Phys. Rev. B **61**, 10854 (2000)
85. T. R. Taha, M. J. Ablowitz: J. Comp. Phys. **55**, 192 (1984); J. Comp. Phys. **55**, 203 (1984)
86. A. Askar, A. A. Cakmak: J. Chem. Phys. **68**, 2794 (1978)
87. M. D. Feit, J. A. Fleck, Jr.: J. Chem. Phys. **80**, 2578 (1984)
88. T. Iitaka: Phys. Rev. B **49**, 4684 (1994)
89. P. H. Hahn: private communication
90. V. Savona, C. Piermarocchi, A. Quattropani, F. Tassone, P. Schwendimann: Phys. Rev. Lett. **78**, 4470 (1997)
91. D. M. Whittaker: Phys. Rev. Lett. **80**, 4791 (1998)
92. J. P. Prineas, J. Shah, B. Grote, C. Ell, G. Khitova, H. M. Gibbs, S. W. Koch: Phys. Rev. Lett. **85**, 3041 (2000)
93. B. I. Halperin: Phys. Rev. **139**, A 104 (1965)
94. D. Neuhasuer, M. Baer: J. Chem. Phys. **90**, 4351 (1989)
95. C. S. Lent, D. J. Kirkner: J. Appl. Phys. **67**, 3653 (1990)
96. G. R. Hadley: IEEE J. Quant. Electron. **28**, 363 (1992)
97. J.-P. Berenger: J. Comp. Phys. **114**, 185 (1994)

Chapter 3

1. U. Fano: Phys. Rev. **124**, 1866 (1961)
2. H. Beutler: Z. Physik **93**, 177 (1935)
3. U. Fano, J. W. Cooper: Phys. Rev. **137**, A 1364 (1965); Rev. Mod. Phys. **40**, 441 (1968)
4. H. Friedrich: *Theoretical Atomic Physics* (Springer, New York 1991)
5. G. Breit, E. Wigner: Phys. Rev. B **49**, 519 (1936)
6. J. M. Blatt, V. F. Weisskopf: *Theoretical Nuclear Physics* (Wiley, New York 1952), see Chap. VIII, Fig. 8.2 and Chap. IX, Fig. 2.2
7. H. Feshbach: Ann. Phys. (N.Y.) **5**, 357 (1958); **19**, 287 (1962); **43**, 410 (1967)
8. A. K. Bhatia, A. Temkin: Phys. Rev. A **29**, 1895 (1984)
9. J. J. Hopfield: J. Chem. Phys. **22**, 63 (1961)
10. T. Ueno: J. Phys. Soc. Jpn. **26**, 438 (1969)
11. J. C. Phillips: Phys. Rev. **136**, A 1705 (1964)
12. K. P. Jain: Phys. Rev. B **139**, A 544 (1965)
13. J. J. Hopfield, P. J. Dean, D. G. Thomas: Phys. Rev. **158**, 748 (1967)
14. M. D. Sturge: J. Chem. Phys. **51**, 1254 (1969)

15. D. L. Rousseau, S. P. S. Porto: Phys. Rev. Lett. **20**, 1354 (1968)
16. F. Cerdeira, T. A. Fjeldly, M. Cardona: Phys. Rev. B **8**, 4734 (1973)
17. G. Abstreiter, M. Cardona, A. Pinczuk. In: *Light Scattering in Solids*, vol 4, ed by M. Cardona, G. Güntherodt (Springer, Berlin 1984) pp 5–150
18. A. Maruani, D. S. Chemla: Phys. Rev. B **23**, 841 (1981)
19. W. T. Masselink, P. J. Pearah, J. Klem, C. K. Peng, H. Morkoç, G. D. Sanders, Y.-C. Chang: Phys. Rev. B **32**, 8027 (1985)
20. F. Agulló-Rueda, E. E. Mendez, J. M. Hong: Phys. Rev. B **40**, 1357 (1989)
21. A. Alexandrou, E. E. Mendez, J. M. Hong: Phys. Rev. B **44**, 1934 (1991)
22. D. M. Whittaker: Journal de Physique IV, Colloque C5, vol 3, p 199 (1993)
23. D. M. Whittaker. In: *22nd International Conference on the Physics of Semiconductors*, ed by D. J. Lockwood (World Scientific, Singapore 1995) vol 2, p 1420
24. D. M. Whittaker: Europhys. Lett. **31**, 55 (1995)
25. N. Linder: Phys. Rev. B **55**, 13664 (1997)
26. S. Glutsch, P. Lefebvre, D. S. Chemla: Phys. Rev. B **55**, 15786 (1997)
27. M. Dinu, D. D. Nolte, M. R. Melloch: Phys. Rev. B **56**, 1987 (1997)
28. K. Bott, J. Hader, S. W. Koch, P. Thomas: Phys. Rev. B **56**, 12784 (1997)
29. C.P. Hofeld, F. Löser, M. Sudzius, K. Leo, D. M. Whittaker, K. Köhler: Phys. Rev. Lett. **81**, 874 (1998)
30. S. Glutsch, F. Bechstedt: Phys. Rev. B **57**, 11887 (1998)
31. S. Glutsch: Phys. Rev. B **58**, 15909 (1998)
32. S. Glutsch, F. Bechstedt: Phys. Rev. B **60**, 16584 (1999)
33. B. Rosam, D. Meinholt, F. Löser, V. G. Lyssenko, S. Glutsch, F. Bechstedt, F. Rossi, K. Köhler, K. Leo: Phys. Rev. Lett. **86**, 1307 (2001)
34. S. Glutsch, F. Bechstedt, B. Rosam, K. Leo: Phys. Rev. B **63**, 085307 (2001)
35. R. C. Miller, D. A. Kleinman, W. A. Nordland, Jr., A. C. Gossard: Phys. Rev. B **22**, 863 (1980); R. C. Miller, A. C. Gossard, W. T. Tsang, O. Munteanu: Phys. Rev. B **25**, 3871 (1982); R. C. Miller, A. C. Gossard: Phys. Rev. B **28**, 3645 (1983); R. C. Miller, A. C. Gossard, D. A. Kleinman: Phys. Rev. B **32**, 5443 (1985); Phys. Rev. B **33**, 7309 (1986); R. C. Miller, A. C. Gossard, G. D. Sanders, Y.-C. Chang, J. N. Schulman: Phys. Rev. B **32**, 8452 (1985)
36. K. Yamanaka, T. Fukunaga, N. Tsukada, K. L. I. Kobayashi, M. Ishii: Appl. Phys. Lett. **48**, 840 (1986)
37. L. Viña, G. E. W. Bauer, E. E. Mendez, W. I. Yang: Phys. Rev. B **41**, 10767 (1990)
38. H. Chu, Y.-C. Chang: Phys. Rev. B **39**, 10861 (1989)
39. G. Wen, Y.-C. Chang: Phys. Rev. B **45**, 6101 (1992)
40. J. A. Brum, D. Oberli: Journal de Physique IV, Colloque C5, vol 3, p 191 (1993)
41. D. Y. Oberli, B. Böhm, G. Weimann, J. A. Brum: Phys. Rev. B **49**, 5757 (1994)
42. P. E. Simmonds, M. J. Birkett, M. S. Skolnick, W. I. E. Tagg, P. Sobkowicz, G. W. Smith, D. M. Whittaker: Phys. Rev. B **50**, 11251 (1994); P. E. Simmonds: private communication
43. A. R. K. Willcox, D. M. Whittaker: Superlatt. Microstr. **16**, 59 (1994)
44. R. Winkler: Phys. Rev. B **51**, 14359 (1995)
45. S. Glutsch, F. Bechstedt, D. S. Chemla: Phys. Rev. B **51**, 16885 (1995)

46. S. Glutsch, D. S. Chemla, F. Bechstedt. In: *23rd International Conference on the Physics of Semiconductors*, ed by M. Scheffler, R. Zimmermann (World Scientific, Singapore 1996) vol 3, p 1987
47. V. Bellani, E. Pérez, S. Zimmermann, L. Viña, R. Hey, and K. Ploog: Solid State Electron. **40**, 85 (1996)
48. V. Bellani, E. Pérez, S. Zimmermann, L. Viña, R. Hey, and K. Ploog: Solid State Commun. **97**, 459 (1996)
49. S. Bischoff, A. Knorr, S. W. Koch: Phys. Rev. B **55**, 7715 (1997)
50. A. Thränhardt, J. Hader, S. W. Koch: Phys. Rev. B **58**, 1512 (1998)
51. S. Arlt, U. Siegner, F. Morier-Genoud, U. Keller, Phys. Rev. B **58**, 13073 (1998); S. Arlt, F. Morier-Genoud, U. Keller, U. Siegner: Phys. Rev. B **62**, 1588 (2001)
52. A. Melitti, M. A. Maaref, R. Planel, J. M. Gerard: Solid State Commun. **105**, 747 (1998)
53. K. Hino: Phys. Rev. B **62**, 10626 (2000); Phys. Rev. B **63**, 119901 (2001); Phys. Rev. B **64**, 075318 (2001)
54. R. P. Sešyan, M. A. Abdullaev, B. P. Zakharchenya: Fiz. Tekh. Poluprovodn. **7**, 958 (1973) [Sov. Phys. Semicond. **7**, 649 (1973)]
55. W. Becker, B. Gerlach, T. Hornung, R. G. Ulbrich. In: *18th International Conference on the Physics of Semiconductors*, ed by O. Engström (World Scientific, Singapore 1987) vol 2, p 1713
56. H. Lage: Magnetooptische Untersuchungen an Galliumarsenid. Diplomarbeit, Universität Dortmund (1989)
57. U. Siegner, M.-A. Mycek, D. S. Chemla. In: *Int. Quant. Electronics Conf.*, vol 9, 1994 OSA Technical Digest Series (Opt. Soc. Am., Washington, D.C., 1994) p 75; M.-A. Mycek, U. Siegner, D. S. Chemla: ibid., p 78; U. Siegner, M.-A. Mycek, D. S. Chemla: ibid., p 79
58. S. Glutsch, U. Siegner, M.-A. Mycek, D. S. Chemla: Phys. Rev. B **49**, 17009 (1994)
59. S. Glutsch, Chemical Phys. **210**, 109 (1996)
60. S. Glutsch, D. S. Chemla, F. Bechstedt: Phys. Rev. B **54**, 11592 (1996)
61. V. Bellani, L. Viña, R. Hey, K. Ploog: Semicond. Sci. Technol. **11**, 1411 (1996)
62. S. Bar-Ad, P. Kner, M. V. Marquezini, S. Mukamel, D. S. Chemla: Phys. Rev. Lett. **78**, 1363 (1997)
63. D. V. Vasilenko, N. V. Luk'yanova, R. P. Sešyan: Fiz. Tekh. Poluprovodn. **33**, 19 (1999) [Semiconductors **33**, 15 (1999)]
64. D. Meinholt, K. Leo, N. A. Fromer, D. S. Chemla, S. Glutsch, F. Bechstedt, K. Köhler: Phys. Rev. B **65**, 161307 (2002)
65. S. Glutsch, D. S. Chemla: Phys. Rev. B **53**, 15902 (1996)
66. A. N. Forshaw, D. M. Whittaker: Phys. Rev. B **54**, 8794 (1996)
67. M. Graf, P. Vogl, A. B. Dzyubenko: Phys. Rev. B **54**, 17003 (1996)
68. S. Glutsch, F. Bechstedt, D. S. Chemla: Superlatt. Microstr. **22**, 31 (1997)
69. S. Glutsch. In: *Festkörperprobleme/Advances in Solid State Physics* **37**, ed by R. Helbig (Vieweg, Braunschweig 1998) pp 151–167
70. D. A. Broido, E. S. Koteles, C. Jagannath, J. Y. Chi: Phys. Rev. B **37**, 2725 (1988)
71. L. Reining, I. Egri: Solid State Commun. **68**, 981 (1988)
72. G. Rau, P. C. Klipstein, N. F. Johnson: Phys. Rev. B **58**, 7210 (1998)
73. A. V. Gopal, A. S. Vengurlekar: Phys. Rev. B **62**, 4624 (2000)

74. Th. Östreich: Phys. Rev. B **164**, 313 (1997)
75. T. dell'Orto, M. Di Ventra, J. Almeida, C. Coluzza, G. Margaritondo: Phys. Rev. B **52**, 2265 (1995)
76. J. Faist, F. Capasso, C. Sirtori, A. L. Hutchinson, K. W. West, L. N. Pfeiffer: Appl. Phys. Lett. **71**, 3477 (1997)
77. Ph. Lelong, S.-W. Lee, K. Hirakawa, H. Sakaki: Physica E **7**, 174 (2000)
78. E. Tekman, P. F. Bagwell: Phys. Rev. B **48**, 2553 (1993)
79. J. U. Nöckel, A. D. Stone: Phys. Rev. B **50**, 17415 (1994); Phys. Rev. B **51**, 17219 (1994)
80. J. Göres, D. Goldhaber-Gordon, S. Heemeyer, M. A. Kastner, H. Shtrikman, D. Mahalu, U. Meirav: Phys. Rev. B **62**, 2188 (2000)
81. A. A. Clerk, X. Waintal, P. W. Brouwer: Phys. Rev. Lett. **86**, 4636 (2001)
82. W. Li, L. E. Reichl: Phys. Rev. B **60**, 15732 (1999)
83. R.-B. Liu, B.-F. Zhu: J. Phys.: Condens. Matt. **12**, L741 (2000)
84. C. Cohen-Tannoudji, J. Dupont-Roc, G. Grynberg: *Atom-Photon Interactions* (Wiley, New York 1992)
85. F. H. Mies: Phys. Rev. **175**, 164 (1968)
86. A. F. Starace: Phys. Rev. B **5**, 1773 (1972)
87. F. Combet Farnoux: Phys. Rev. A **25**, 287 (1982)
88. K. Ueda: Phys. Rev. A **35**, 2484 (1987)
89. J.-P. Connerade, A. M. Lane, Rep. Prog. Phys. **51**, 1439 (1988)
90. L. C. Davis, L. A. Feldkamp: Phys. Rev. B **15**, 2961 (1977)
91. A. Shibatani, Y. Toyozawa: J. Phys. Soc. Jpn. **25**, 335 (1968)
92. K. Cho: phys. stat. sol. (b) **54**, 583 (1972)
93. M. Wagner, J. Vázquez-Màrquez: J. Phys. A **21**, 4347 (1988)
94. S. Glutsch: Phys. Rev. B **66**, 075310 (2002)
95. H. Friedrich, D. Wintgen: Phys. Rev. A **32**, 3231 (1985)
96. J. H. Davies: *The Physics of Low-Dimensional Semiconductors: An Introduction* (Cambridge University Press 1998)
97. K. Maschke, P. Thomas, E. O. Göbel: Phys. Rev. Lett. **67**, 2646 (1991)
98. W. Tan, J. C. Inkson, G. P. Srivastava, Semicond. Sci. Technol. **9**, 1305 (1994)
99. S. M. Stepanow: Optische Absorption von Supergittern in gekreuzten äußeren elektrischen und magnetischen Feldern. Diplomarbeit, Friedrich-Schiller-Universität Jena (2002)
100. F. Rossi, E. Molinari: Phys. Rev. Lett. **76**, 3642 (1996); Phys. Rev. B **53**, 16462 (1996)
101. K. Brunner, G. Abstreiter, M. Walther, G. Böhm, G. Tränkle: Surface Sci. **267**, 218 (1992)
102. F. Vouilloz, D. Y. Oberli, M.-A. Dupertuis, A. Gustafsson, F. Reinhardt, E. Kapon: Phys. Rev. B **57**, 12378 (1998)
103. E. Martinet, M.-A. Dupertuis, F. Reinhardt, G. Biasiol, E. Kapon, O. Stier, M. Grundmann, D. Bimberg: Phys. Rev. B **61**, 4488 (2000)
104. R. P. Seisyan, B. P. Zakharchenya. In: *Landau Level Spectroscopy*, ed by G. Landwehr, E. I. Rashba (Elsevier, Amsterdam 1991) pp 347–443
105. T. Ogawa, T. Takagahara: Phys. Rev. B **44**, 8138 (1991)
106. P. Lefebvre, P. Cristol, H. Mathieu: Phys. Rev. B **48**, 17308 (1993)
107. H. Chu, Y. C. Chang: Phys. Rev. B **40**, 5479 (1989)
108. U. Siegner, M.-A. Mycek, S. Glutsch, D. S. Chemla: Phys. Rev. Lett. **74**, 470 (1995); Phys. Rev. B **51**, 4953 (1995)
109. G. Cohen, H. Shtrikman, I. Bar-Joseph: Phys. Rev. B **52**, 11642 (1995)

Chapter 4

1. F. Bloch: Z. Physik **52**, 555 (1928)
2. A. Sommerfeld, H. Bethe. In: *Handbuch der Physik*, ed by H. Geiger, K. Scheel, Band 24, Teil 2 (Springer, Berlin 1933) pp 333–413
3. W. Franz: Z. Naturforschg. **13a**, 484 (1958)
4. L. V. Keldysh: ZETP **34**, 1138 (1958) [Sov. Phys. JETP **34**, 788 (1958)]
5. L. Fritzsche: phys. stat. sol. **13**, 487 (1966)
6. C. Zener, Proc. Roy. Soc. A **145**, 523 (1934)
7. W. V. Houston: Phys. Rev. **57**, 184 (1940)
8. P. Feuer: Phys. Rev. **88**, 92 (1952)
9. E.N. Adams: J. Chem. Phys. **21**, 2013 (1953)
10. E.N. Adams: Phys. Rev. **107**, 698 (1957)
11. L. V. Keldysh: ZETP **33**, 994 (1957) [Sov. Phys. JETP **6**, 763 (1958)]
12. E.O. Kane: J. Phys. Chem. Solids. **12**, 181 (1959)
13. G.H. Wannier: Phys. Rev. **117**, 432 (1960)
14. E.O. Kane: J. Appl. Phys. **32**, 83 (1961)
15. D.E. Aspnes, N. Bottka. In: *Semiconductors and Semimetals*, ed by R. K. Willardson, A. C. Beer, vol 9 (Academic, New York 1972) pp 457–543
16. J.B. Krieger, G.J. Iafrate: Phys. Rev. B **33**, 5494 (1986)
17. D.A.B. Miller, D.S. Chemla, T.C. Damen, A.C. Gossard, W. Wiegmann, T.H. Wood, C.A. Burrus: Phys. Rev. B **32**, 1043 (1985)
18. S. Katsura, T. Hatta, A. Morita, Sci. Rep. Tōhoku Imp. Univ. (Ser. I) **34**, 19 (1950)
19. K. Hacker, G. Obermair: Z. Physik **234**, 1 (1970)
20. S.G. Davison, K.P. Tan: Z. Physik **251**, 6 (1972)
21. G.C. Stay, G. Gusman: J. Phys. C **6**, 650 (1973)
22. H. Fukuyama, R.A. Bari, H.C. Fogedby: Phys. Rev. B **8**, 5579 (1973)
23. J.E. Avron: Phys. Rev. Lett. **37**, 1568 (1976)
24. J. Zak: Phys. Rev. Lett. **20**, 1477 (1968); G.H. Wannier: Phys. Rev. **181**, 1364 (1969); J. Zak: ibid., 1366 (1969)
25. A. Rabinovitch, J. Zak: Phys. Rev. B **4**, 2358 (1971); W. Shockley: Phys. Rev. Lett. **28**, 349 (1972)
26. A. Rabinovitch, J. Zak: Phys. Lett. **40A**, 189 (1972)
27. J.E. Avron, J. Zak, A. Grossmann, L. Gunther: J. Math. Phys. **18**, 918 (1977)
28. F. Bentosela, R. Carmona, P. Duclos, B. Simon, B. Souillard, R. Weder: Comm. Math. Phys. **88**, 387 (1983)
29. P. Ao: Phys. Rev. B **41**, 3998 (1990)
30. D. Emin, C.F. Hart: Phys. Rev. B **36**, 7353 (1987); C.F. Hart and D. Emin: Phys. Rev. B **37**, 6100 (1988); C.F. Hart: Phys. Rev. B **38**, 2158 (1988); L. Kleinman, Phys. Rev. B **41**, 3857 (1990); D. Emin, C.F. Hart: ibid., 3859 (1990); D.A. Page, E. Brown: Phys. Rev. B **43**, 2423 (1991); D. Emin, C.F. Hart: ibid., 2426 (1991); J. Zak: Phys. Rev. B **43**, 4519 (1991); C.F. Hart, D. Emin: ibid., 4521 (1991); J. Leo, A. MacKinnon: Phys. Rev. B **43**, 5166 (1991); D. Emin, C.F. Hart: ibid., 5169 (1991); C.F. Hart: Phys. Lett. A **132**, 453 (1988); P.N. Argyres, S. Sfiat: Phys. Lett. A **146**, 231 (1990)
31. J.J. Sakurai: *Modern Quantum Mechanics*, revised edn, ed by S.F. Tuan (Addison-Wesley, Reading 1994)

32. M. Reed, B. Simon: *Methods of Mathematical Physics*, vol IV: *Analysis of Operators* (Academic, San Diego 1978)
33. I. W. Herbst, J. S. Howland: Comm. Math. Phys. **80**, 23 (1981)
34. J.-M. Combes, P. D. Hislop: Comm. Math. Phys. **140**, 291 (1991)
35. F. Bentosela, V. Grecchi: Comm. Math. Phys. **142**, 169 (1991)
36. P. D. Hislop, I. M. Sigal: *Introduction to Spectral Theory With Application to Schrödinger Operators* (Springer, New York 1996)
37. E. Merzbacher: *Quantum Mechanics*, 3rd edn (Wiley, New York 1998)
38. I. W. Herbst: Comm. Math. Phys. **75**, 197 (1980)
39. V. Grecchi, M. Maioli, A. Sacchetti: J. Phys. A **26**, L379 (1993); Comm. Math. Phys. **159**, 605 (1994)
40. L. Esaki, R. Tsu, IBM J. Res. Dev. **14**, 61 (1970)
41. E. E. Mendez, F. Agulló-Rueda, J. M. Hong: Phys. Rev. Lett. **60**, 2426 (1988); F. Agulló-Rueda, E. E. Mendez, J. M. Hong: Phys. Rev. B **40**, 1357 (1989)
42. P. Voisin, J. Bleuse, C. Bouche, S. Gaillard, C. Alibert, and A. Regreny: Phys. Rev. Lett. **61**, 1639 (1988)
43. H. Schneider, H. T. Grahn, K. v. Klitzing, K. Ploog: Phys. Rev. Lett. **65**, 2720 (1990)
44. A. Alexandrou, E. E. Mendez, J. M. Hong: Phys. Rev. B **44**, 1934 (1991)
45. K. H. Schmidt, N. Linder, G. H. Döhler, H. T. Grahn, K. Ploog, H. Schneider: Phys. Rev. Lett. **72**, 2769 (1994); N. Linder, K. H. Schmidt, W. Geisselbracht, G. H. Döhler, H. T. Grahn, K. Ploog, H. Schneider: Phys. Rev. B **52**, 17352 (1995)
46. C. P. Hofeld, F. Löser, M. Sudzius, K. Leo, D. M. Whittaker, K. Köhler: Phys. Rev. Lett. **81**, 874 (1998)
47. J. Feldmann, K. Leo, J. Shah, D. A. B. Miller, J. E. Cunningham, T. Meier, G. von Plessen, A. Schulze, P. Thomas, S. Schmitt-Rink: Phys. Rev. B **46**, 7252 (1992)
48. K. Leo, P. Haring Bolivar, F. Brüggemann, R. Schwedler, K. Köhler: Solid State Commun. **84**, 943 (1992)
49. C. Waschke, H. G. Roskos, R. Schwedler, K. Leo, H. Kurz, and K. Köhler: Phys. Rev. Lett. **70**, 3319 (1993)
50. T. Dekorsy, R. Ott, H. Kurz, K. Köhler: Phys. Rev. B **51**, 17275 (1995); P. Leisching, T. Dekorsy, H. J. Bakker, H. Kurz, K. Köhler: Phys. Rev. B **51**, 18015 (1995)
51. K. Unterrainer, B. J. Keay, M. C. Wanke, S. J. Allen, D. Leonard, G. Medeiros-Ribeiro, U. Bhattacharya, M. J. W. Rodwell: Phys. Rev. Lett. **76**, 2973 (1996)
52. V. G. Lyssenko, G. Valušis, F. Löser, T. Hasche, K. Leo, M. M. Dignam, K. Köhler: Phys. Rev. Lett. **79**, 301 (1997)
53. M. M. Dignam, J. E. Sipe: Phys. Rev. B **41**, 2865 (1990)
54. M. M. Dignam, J. E. Sipe: Phys. Rev. Lett. **64**, 1797 (1990); Phys. Rev. B **43**, 4097 (1991)
55. A. M. Fox, D. A. B. Miller, J. E. Cunningham, W. Y. Jan, C. Y. P. Chao, S. L. Chuang: Phys. Rev. B **46**, 15365 (1992)
56. N. Linder, W. Geisselbrecht, G. Philipp, K. H. Schmidt, and G. H. Döhler: Journal de Physique IV, Colloque C5, vol 3, p 195 (1993); N. Linder: Phys. Rev. B **55**, 13664 (1997)
57. D. M. Whittaker: Journal de Physique IV, Colloque C5, vol 3, p 199 (1993); D. M. Whittaker. In: 22nd International Conference on the Physics of Semiconductors, ed by D. J. Lockwood (World Scientific, Singapore 1995) vol 2, p 1420; D. M. Whittaker: Europhys. Lett. **31**, 55 (1995)

58. T. Meier, G. von Plessen, P. Thomas, S. W. Koch: Phys. Rev. Lett. **73**, 902 (1994); Phys. Rev. B **51**, 14490 (1995); T. Meier, H. J. Kolbe, A. Thränhardt, G. Weiser, P. Thomas, S. W. Koch: Physica E **7**, 267 (2000)
59. M. Dignam, J. E. Sipe, J. Shah: Phys. Rev. B **49**, 10502 (1994)
60. Z. Barticevic, M. Pachecho, F. Claro: Phys. Rev. B **51**, 14414 (1995)
61. R. Ferreira, B. Soucail, P. Voisin, G. Bastard: Phys. Rev. B **42**, 11404 (1990)
62. J. Leo, A. MacKinnon: J. Phys.: Condens. Matt. **1**, 1449 (1989)
63. A. M. Bouchard, M. Luban: Phys. Rev. B **47**, 6815 (1993)
64. A. M. Bouchard, M. Luban: Phys. Rev. B **52**, 5105 (1995)
65. R. Till, H. Kümmel, A. Philipp, G. Böhm, G. Weimann: Superlatt. Microstr. **24**, 227 (1998)
66. K. Murayama, H. Nagasawa, S. Ozaki, M. Morifuji, C. Hamaguchi, A. Di Carlo, P. Vogl, G. Böhm, G. Weimann: Superlatt. Microstr. **20**, 493 (1996); M. Morifuji, K. Murayama, C. Hamaguchi, A. Di Carlo, P. Vogl, G. Böhm, M. Sexl: phys. stat. sol. (b) **204**, 368 (1997)
67. A. Sibille, J. F. Palmier, F. Laruelle: Phys. Rev. Lett. **80**, 4506 (1998)
68. M. Helm, W. Hilber, G. Strasser, R. De Meester, F. M. Peeters, A. Wacker: Phys. Rev. Lett. **82**, 3120 (1999)
69. S. Glutsch, F. Bechstedt: Phys. Rev. B **60**, 16584 (1999)
70. B. Rosam, D. Meinholt, F. Löser, V. G. Lyssenko, K. Leo, S. Glutsch, F. Bechstedt, K. Köhler: phys. stat. sol. **221**, 463 (2000)
71. B. Rosam, D. Meinholt, F. Löser, V. G. Lyssenko, S. Glutsch, F. Bechstedt, F. Rossi, K. Köhler, K. Leo: Phys. Rev. Lett. **86**, 1307 (2001); F. Löser, B. Rosam, D. Meinholt, V. G. Lyssenko, M. Sudzius, M. M. Dignam, S. Glutsch, F. Bechstedt, F. Rossi, K. Köhler, K. Leo: Physica E **11**, 268 (2001)
72. S. Glutsch, F. Bechstedt, B. Rosam, K. Leo: Phys. Rev. B **63**, 085307 (2001)
73. D. Meinholt, K. Leo, N. A. Fromer, D. S. Chemla, S. Glutsch, F. Bechstedt, K. Köhler: Phys. Rev. B **65**, 161307 (2002)
74. M. Ben Dahan, E. Peik, J. Reichel, Y. Castin, C. Salomon: Phys. Rev. Lett. **76**, 4508 (1996)
75. S. R. Wilkinson, C. F. Bharucha, K. W. Madison, Q. Niu, M. G. Raizen: Phys. Rev. B **76**, 4512 (1996); C. F. Bharucha, K. W. Madison, P. R. Morrow, S. R. Wilkinson, B. Sundaram, M. G. Raizen: Phys. Rev. A **55**, 857 (1997)
76. U. Peschel, T. Pertsch, F. Lederer, Optics Letters **23**, 1701 (1998)
77. T. Pertsch, P. Dannberg, W. Elflein, A. Bräuer, F. Lederer: Phys. Rev. Lett. **83**, 4752 (1999)
78. R. Morandotti, U. Peschel, J. S. Aitchison, H. S. Eisenberg, Y. Silberberg: Phys. Rev. Lett. **83**, 4756 (1999)
79. A. Di Carlo, P. Vogl, W. Pötz: Phys. Rev. B **50**, 8358 (1994)
80. M. Holthaus, J. Opt. B **2**, 589 (2000)
81. M. Glück, A. R. Kolovsky, H. J. Korsch, N. Moiseyev, Eur. Phys. J. D **4**, 239 (1998); M. Glück, A. Kolovsky, H. J. Korsch: J. Phys. A **32**, L49 (1999); M. Glück, A. R. Kolovsky, H. J. Korsch, F. Zimmer: Phys. Rev. B **65**, 115302 (2002)
82. G. Nenciu: Rev. Mod. Phys. **63**, 91 (1991)
83. G. H. Döhler. In: *Physics of Low-dimensional Structures*, ed by P. Butcher, N. H. March, M. P. Tosi (Plenum, New York London 1993) pp 375–406
84. R. de L. Kronig, W. G. Penney: Proc. Roy. Soc. A **130**, 499 (1931)

85. S. Flügge, H. Marschall: *Rechenmethoden der Quantentheorie*, Teil 1 (Springer, Berlin 1952)
86. J. H. Davies: *The Physics of Low-Dimensional Semiconductors: An Introduction* (Cambridge University Press 1998)
87. H. M. James: Phys. Rev. **76**, 1602 (1949)
88. W. Kohn: Phys. Rev. **115**, 809 (1959)
89. E. H. Lieb, D. C. Mattis: *Mathematical Physics in One Dimension* (Academic, New York 1966)
90. J. Yellin: Phys. Rev. B **52**, 2208 (1995)
91. J. Callaway: *Quantum Theory of the Solid State*, 2nd edn (Academic, San Diego 1991)
92. W. Magnus, F. Oberhettinger, R. P. Sony, *Formulas and Theorems for the Special Functions of Mathematical Physics* (Springer, Berlin 1966)
93. M. Abramowitz, I. A. Stegun: *Pocketbook of Mathematical Functions*, abridged edn of *Handbook of Mathematical Functions*, Material selected by M. Danos, J. Rafelski (Verlag Harry Deutsch, Thun Frankfurt/Main 1984)
94. T. Pertsch, U. Peschel, F. Lederer (unpublished)
95. D. W. Hone, X.-G. Zhao: Phys. Rev. B **53**, 4834 (1996)
96. J. Hader, P. Thomas, S. W. Koch: Prog. Quant. Electr. **22**, 123 (1998)
97. S. Glutsch: J. Phys.: Condens. Matt. **11**, 5533 (1999)
98. W. Franz, Z. Naturforschg. **14a**, 415 (1959)
99. G. Eilenberger: Z. Physik **164**, 59 (1961)
100. M. Ritze, N. J. M. Horing, R. Enderlein: Phys. Rev. B **47**, 10437 (1993)
101. S. Glutsch, F. Bechstedt: Phys. Rev. B **57**, 11887 (1998)
102. A. Ahland, D. Schulz, E. Voges: Phys. Rev. B **60**, 5109 (1999)
103. M. L. Zambrano, J. C. Arce: Phys. Rev. B **66**, 155340 (2002)
104. A. B. Hummel, T. Bauer, H. G. Roskos, S. Glutsch, K. Köhler Phys. Rev. B **67**, 045319 (2003)
105. L. Landau: Phys. Z. Sowjetunion **1**, 88 (1932); **2**, 46 (1932)
106. E. E. Nikitin, Annual Rev. Chem. **50**, 1 (1999)
107. J. B. Krieger, G. J. Iafrate: Phys. Rev. B **35**, 9644 (1987)
108. P. Ao, J. Rammer: Phys. Rev. B **44**, 11494 (1991)
109. J. M. Ziman: *Principles of the Theory of Solids* (Cambridge University Press, London 1979)
110. L. D. Landau, E. M. Lifshitz: *Course of Theoretical Physics*, vol 3, 3rd edn (Pergamon, Oxford 1999)
111. M. V. Berry, R. Lim: J. Phys. A **26**, 4737 (1993)
112. K. B. McAfee, E. J. Ryder, W. Shockley, M. Sparks: Phys. Rev. **83**, 650 (1951)
113. W. Franz. In: *Encyclopedia of Physics*, ed by S. Flügge, vol 17 (Springer, Berlin 1956) pp 155–263
114. Q. Niu, M. G. Raizen: Phys. Rev. Lett. **80**, 3491 (1998)

Appendix A

1. W. I. Smirnow: *Lehrgang der höheren Mathematik* (Deutscher Verlag der Wissenschaften, Berlin 1971)
2. H.-J. Glaeske, J. Reinhold, P. Volkmer: *Quantenchemie*, Bd. 5 (Deutscher Verlag der Wissenschaften, Berlin 1987)

3. I. N. Bronstein, K. A. Semendjajew, G. Musiol, H. Mühlig: *Taschenbuch der Mathematik*, 5. erweiterte und überarbeitete Auflage (Verlag Harry Deutsch, Thun Frankfurt/Main 2000)
4. I. S. Gradstein, I. M. Ryshik: *Summen-, Produkt- und Integraltafeln/Tables of Series, Products, and Integrals* (Verlag Harry Deutsch, Thun Frankfurt/Main 1981)
5. W. Magnus, F. Oberhettinger, R. P. Sony: *Formulas and Theorems for the Special Functions of Mathematical Physics* (Springer, Berlin 1966)
6. M. Abramowitz, I. A. Stegun: *Pocketbook of Mathematical Functions*, abridged edn of *Handbook of Mathematical Functions*, Material selected by M. Danos, J. Rafelski (Verlag Harry Deutsch, Thun Frankfurt/Main 1984)
7. L. D. Landau, E. M. Lifshitz: *Course of Theoretical Physics*, vol 3, 3rd edn (Pergamon, Oxford 1999)
8. H. Friedrich: *Theoretical Atomic Physics* (Springer, New York 1991)
9. S. L. Chuang: *Physics of Optoelectronic Devices* (Wiley, New York 1995)
10. G. Hadley: *Linear Algebra* (Addison-Wesley, Reading, MA 1980)
11. H. Rutishauser: *Lectures on Numerical Mathematics*, ed by M. Gutknecht (Birkhäuser, Boston 1990)

Appendix B

1. P. J. Mohr, B. N. Taylor: Rev. Mod. Phys. **72**, 351 (2000).
2. Landolt-Börnstein: *Numerical Data and Functional Relationships in Science and Technology*, New Series, vol 17a, ed by O. Madelung (Springer, Berlin 1982)
3. S. Adachi: *GaAs and Related Materials: Bulk Semiconducting and Superlattice properties* (World Scientific, Singapore 1994)
4. J. M. Luttinger: Phys. Rev. **102**, 1030 (1956).
5. U. Rössler: Solid State Commun. **65**, 1279 (1988).
6. S. L. Chuang: *Physics of Optoelectronic Devices* (Wiley, New York 1995)
7. L. D. Landau, E. M. Lifshitz: *Course of Theoretical Physics*, vol 5, 3rd edn (Pergamon, Oxford 1999)
8. W. Ludwig and C. Falter: *Symmetries in Physics* (Springer, Berlin 1988)
9. T. Inui, Y. Tanabe, and Y. Onodera: *Group Theory and Its Application in Physics* (Springer, Berlin 1990)
10. H.-W. Streitwolf: *Gruppentheorie in der Festkörperphysik* (Geest & Portig, Leipzig 1967)
11. P. Y. Yu and M. Cardona: *Fundamentals of Semiconductors*, 2nd ed. (Springer, Berlin 1999)
12. H. Bethe, Annalen der Physik (Leipzig), 5. Folge, Bd. **3**, 133 (1929)

Appendix C

1. L. D. Landau, E. M. Lifshitz: *Course of Theoretical Physics*, vol 3, 3rd edn (Pergamon, Oxford 1999)
2. E. Merzbacher: *Quantum Mechanics*, 3rd edn, (Wiley, New York 1998)

3. S. Flügge, H. Marschall: *Rechenmethoden der Quantentheorie*, Teil 1 (Springer, Berlin 1952)
4. J. H. Davies: *The Physics of Low-Dimensional Semiconductors: An Introduction* (Cambridge University Press, 1998)
5. L. D. Landau, E. M. Lifshitz: *Course of Theoretical Physics*, vol 9, 3rd edn (Pergamon, Oxford 1998)
6. W. Brauer: *Einführung in die Elektronentheorie der Metalle*, 2. Auflage (Geest & Portig, Leipzig 1972)
7. F. Bassani, G. Pastori Parravicini: *Electronic States and Optical Transitions in Solids*, ed by R. A. Ballinger (Pergamon, Oxford 1975)
8. J. M. Ziman: *Principles of the Theory of Solids* (Cambridge University Press, London 1979)
9. M. Abramowitz, I. A. Stegun: *Pocketbook of Mathematical Functions*, abridged edn of *Handbook of Mathematical Functions*, Material selected by M. Danos, J. Rafelski (Verlag Harry Deutsch, Thun Frankfurt/Main 1984)
10. S. L. Chuang: *Physics of Optoelectronic Devices* (Wiley, New York 1995)
11. L. P. Gor'kov, I. E. Dzyaloshinskii: Soviet Physics JETP **26**, 449 (1968) [Zh. Exp. Teor. Fiz. **53**, 717 (1967)]
12. A. R. Edmonds: *Angular Momentum in Quantum Mechanics* (Princeton University Press, 1957)
13. J. J. Sakurai: *Modern Quantum Mechanics*, revised edition, ed by S. F. Tuan (Addison-Wesley, Reading 1994)
14. M. Weissbluth: *Atoms and Molecules* (Academic Press, New York 1978)
15. T. Inui, Y. Tanabe, Y. Onodera: *Group Theory and Its Application in Physics* (Springer, Berlin 1990)
16. E. U. Condon, G. H. Shortley: *The Theory of Atomic Spectra*, Reprint (Cambridge University Press, 1970)
17. P. O. Löwdin: J. Chem. Phys. **19**, 1396 (1951)

Index

- absorption
asymmetry 176, 186
coefficient 21–23, 35–43, 49
edge *see* band gap
free-particle *see* optical density of states
spectrum 102–121, 129–136, 138–142, 172–190
discrete and continuous 38, 41–43, 55, 59, 123, 129–131
ADI *see* method, alternating direction implicit
alloy 13
angular momentum matrices 10–12, **245–246**, 248
approximation
crystal-momentum 145, 191, 200, 202
effective-mass **2–17**, 21, 38, 43, 62
Hartree–Fock 3, 30–32
Kane *see* functions, Kane
of nearly free electrons **153–154**, 156–158
rotating-wave (RWA) 18–21, 32, 38, **253**
semiclassical 192–196, 202–206
tight-binding **151–153**, 156–158, 161, 164, 166–169
virtual-crystal (VCA) 13
- band 236
alignment 13
conduction (c) 5–7, 12–13, 21
nonparabolicity 13, 17
degeneracy 4–7, 11, 236
dispersion
in-plane 16–17
isotropic 11, 23, 123
- edges
modulation of 13, 14, 147
empty-lattice 153
gap(s) 18, 21, 24, 41, 42, 150–151, 224, 236
one-dimensional 25
two-dimensional 25, 42, 53
offset 15, 225
renormalization 34–35
split-off (so) 6, 19
valence (v) 5–9, 21
heavy-hole (hh) and light-hole (lh) 6, 13, 16–17
mixing 11, 15–17, 133–134, 140
base functions 57
general-purpose 64
non-orthonormal 69–76
orthonormal **50**, 57, 61–69, 88
piecewise linear *see* finite elements
Bloch
electron **3–7, 235–237**
 $+F$ 145–148, **158–172**, 191–203
one-dimensional 149–158
functions **3–5**, 21, 150, 156–158, 162, 174, 176, **235–237**
special **151**, 166, 167
zone-center *see* functions,
lattice-periodic
oscillations 145–148, 168
theorem 183, **236**
wavenumber, complex 192–195
bound and scattering state(s) *see*
eigenstate(s), discrete and
continuous
boundary conditions
absorbing 60, **93–99**, 185, 265–267
artificial 63, 73–74, **233–234**

- periodic 20, 54, 72, 86, 90, 151, 174, **234–237**
vanishing 64, 94, 97, 115
Brillouin zone 18, 151, 183, 200, **228**, 235
- characteristic
field(s) 44, 45, 127, **226**
length 10, 25, 44, 45, **226**
units *see* dimensionless units
class of complexity 48, **55**, 69, 122, 124, 126
classical point of return 67, 239, 240
Clebsch–Gordan coefficients 9, 19, **248–249**
computational effort **57–58**, 60, 88
confinement **13–16**, 114
geometric vs. field-induced 14, 20–21, 122–124
perfect 24, 74, 115
potential 14–15
strong 24, 69, 83, 124, 138, 141, 155
weak 118, 169
- constant
dielectric 18, 30, 33–35, 224–225
lattice 10, 13, 18, 224, **230**
continuum edge *see* band gap
coordinates
Cartesian 73, 78–79, 86, 255–259
center-of-mass and relative 40, 119, 174, 182, 184, 243
curvilinear 50–51, **214–215**
cylindrical **214–215**, 268–272
polar 73–74, 80–81, **215**, 260–263
- Coulomb enhancement 42, 99, 121
Coulomb integrals *see* matrix elements, Coulomb
- crystal
artificial 147, 148
cubic 21, 36, **229–230**
diamond 7, **230**
zincblende 5–6, 13, 19, **230**
- cyclotron frequency 25, 52, 82, 83, 131, 133
- density matrix 31–33, 36, 197–199
density of states 20, 24, 104, 233
dephasing 107, 203, 254
differential equation(s) 56, 57, 60
vs. difference equation 33, 37
vs. integral equation 51, 58, 121, 146
ordinary vs. partial 48, 51, 55, 59, 60, 122, 149
set of 55, 59, 63, 70
diffusion equation 85, 96, 97
- dimension
confinement $l-m$ 63, 114, 115
density-of-states q 20, **122–124**, 125–126, 133, 137
geometric d 20, 27, **122–124**, 126, 137
mathematical l 48, 52, **55**, 114, **122–124**, 126, 137
non-integer 43, 47
physical p 27, **122–124**, 125
scattering m 48, 52, **55**, 114, **122–124**, 126, 137
- dimensionless units 41, 44, 45, 49, 75, 126, **225–226**
mesoscopic vs. microscopic 44, 45
- Dirac identity 38, 105, **213**
- discretization
ground-state-adapted **82**, 89, 97, 127–128, 138
of Laplacians 79–81
of the scalar product 78, 80
in time *see* propagation scheme
- eigenstate(s)
below-barrier 16, 138, 157, 164, 178, 196
vs. above-barrier 118, 153, 170
discrete and continuous 16, 38, 40, 42, 49, 104, 106, 107, 117, 118, 120, 121, 123, 160, 232
electron–hole-pair 22, 28, 30, 174
hole 16
initial and final 20, 252
- eigenvalue(s) 38, 84, 114–121
complex 146, 191, 202
discrete and continuous 26, 28, 34, 64, 150, 162, 196, 236
- electron gas 20, 24, 25
- electron–hole pair(s) 14, 22
amplitude 31, 36–37, 50
density 30, 31, 34
- Elliott formula 30, **35–39**, 41, 42, 49

- energy normalization 28, 40, 175, **234**
 equation(s)
 Bethe-Salpeter 30
 coupled vs. single channel 116–117, 128, 138
 secular 154, 251
 semiconductor Bloch **31–35**, 36
 von Neumann 32, 197, 198, 252
 exciton 29–43, 118
 $+B$ 243–244
 binding energy 34, 41–43
 Bohr radius 43, **226**
 d-dimensional 43
 ground state 42, 43, **226**
 Rydberg 41, **226**
 saddle-point 118, 121
 two-dimensional 42, 76
 Wannier–Mott vs. Frenkel 29, 43
 excitonic units *see* dimensionless units
 external field(s) 3, 9–10, 21, 26
- $1/F$ oscillations 196, 200
 Fano
 decay 107
 interference 117, 173, 187–188
 model 102–113
 profile **106–107**, 130–131
 resonances 101–113, 118, 122–142, 147, 185
 Fermi’s golden rule 21, 107, 146, 202, **253**
 FFT *see* Fourier transform, fast
 finite differences 55–57, **76–83**, 88–90, 96, 161–162, 255–272
 finite elements 55–57, **71–73**, 74–76, 88
 finite vs. infinite barriers 24, 43, 53, 137, 139–140
 Fourier
 method 79, 86, 88
 series 154, 159, 167, 201, **211–212**, 230
 transform 37, 50, 51, **210–211**, 239
 fast (FFT) 63, 79, 86, 256
 Franz–Keldysh effect 28–29, 98, 145, 147, 162, 176, 178
 function(s)
 Airy 28, 29, 99, 162, 172, **239–240**
- autocorrelation 54, 90
 Bessel 64, 67–69, 159–160, **216–217**, 237
 delta 21, 26, 27, 38, 106, 211, **212**
 discretization of 77, 79, 80
 periodic 151, 211, 212
 weighted 50, 77, 214
 envelope 9–10, 14, 22, 33, 192
 Green’s 32, 103, 104
 Houston **167–168**, 200
 Kane 55, 64, 158, **162–169**, 175–177, 184
 Laguerre 63, 66, 68–69, **239**
 lattice-periodic 4, 7, 9, 14, 22, 150, 153, **230**, **236**
 slowly varying *see* function(s), envelope
 Wannier 37, 64, **166–167**, 176, 182–187
 weight 50, 63, 70, 214, 215
 fundamental gap *see* band gap
- g -factor 12, 224
 $\text{Ga}_{1-x}\text{Al}_x\text{As}$ 225
 GaAs 10, 18, 24, 34, 43–45, 131, 133–136, **224–225**, 226
 $\text{GaAs}/\text{Ga}_{1-x}\text{Al}_x\text{As}$ heterostructures 14–16, 138, 139, 142, 155, 225
- Hamiltonian
 effective **7–13**, 14–15, 32
 electron and hole 14–15, 23, 36
 electron–hole-pair 30, 37–40, 119
 Luttinger **11–12**, 17
 non-Hermitian 19, 58, 95–97, 253
 Peierls–Onsager 12
 reduced 39, 40, 114, 119, 183–184, 243–244
 hole 11, **14–15**, 15–17, 22, 23
 HOMO and LUMO 6
 Hydrogen atom 29, 40, 45, **240–242**, 249
 $+B$ 126
 two-dimensional 42, **242–243**
- integral equation *see* differential vs. integral equation
 interaction

- Coulomb 37, 39–43, 114–117, 120–121, 123, 140, 176, 186, 190
 dipole vs. vector-potential **19–20**, 21, 163
 electron-light 17–29, 31
 nonresonant 106, 118, 131, 140, 186
 spin-orbit **5–6**, 9, 12, 13, 18–19, 249
- Kohn's cases A and B **151**, 157, 167
 Koster vs. BSW notation 5, 7
- ladder property 160, 164–166, 175, 182
 Lanczos recursion 59, 122
 Landau levels 26, 66–67, 124–125, 127–136, 188–190
 line broadening 93, 178–179, 187–190, 205–206, 254
 homogeneous 38–39, 42, 49
 vs. inhomogeneous 187
 natural 106–107, 131
 linear response 35–38
- mass
 complex 95–97
 effective 15, 25, 75
 electron 24, 224
 energy-dependent 17
 hole **11**, 15–17, 24, 134, 136, **224–225**
 in-plane 17
 reduced 24, 26, 52, 225
 reversal 17, 134
- matrix
 band 55–59, 65, 70–72, 75, 76
 condition 66, 71
 dimension 55–58, 75, 76
 full 55–59
 Gram's **64**, 66, 69–72, 84, 88
 norm **81–82**, 84
 pattern 57–58
 sparse 55–59
 Toeplitz 201
 tridiagonal 55–59, 72
- matrix element(s)
 Coulomb 76, 83, 116, 117, 127, 128, 137
 dipole **19–20**, 21–22, 127, 163
 momentum 7, **19–20**, 163
 transition 18–21
- memory **57**, 60
 method
 alternating direction implicit (ADI) 72, 86, 88
 Bubnov–Galerkin 63, 70
 equation-of-motion 60, 122, 126, 173, 255
 ground-state *see* discretization, ground-state-adapted
 Haydock *see* Lanczos recursion of invariants 10–13
 iterative 59–60
 leapfrog *see* propagation scheme, leapfrog
 of lines 63
 real-space–real-time *see* method, equation-of-motion
 miniband(s) 123, 125, 156–157
 dispersionless 124, 155, 196
 model
 discrete 146, **158–162**
 Kronig–Penney 149
 two-band **23**, 31, 123
- motion
 asymptotically free 94, 98, 188
 bound and unbound 98, 115, 119, 126
 center-of-mass and relative 28, 40, 125, 126, 184, 188
 motional narrowing 93
 multiple quantum well (MQW) 124
- natural units *see* dimensionless units
 normalization domain (volume, area, length) 3, 21, **22**, 26, 52, **73–74**, 122, **233–234**, 234–237
 numerical effort *see* computational effort
- occupation numbers 31, 198, 205, 252
 open systems 93
 operator
 dipole vs. momentum 18–19, **19–20**
 inverse 37, 49, 103
- optical
 absorption *see* absorption
 density of states **20–23**, 23–29, 41–43, 115, 120, 122–123, 129–130, 138–139, 173–181

- limit 18, 40
- susceptibility 35–38, 49, 104–106, 108–109
- orthonormalization 64–66
- oscillator strength 22, 38, 40, 42–43, 51
- overlap integrals 22, 138, 161, 169, 175, 178, 190
- parameter(s)
 - lineshape q, Γ 103, 106–107, 130–131, 140
 - Luttinger 11–12, 14, 224–225
- perturbation theory 196–206, 250–254
 - $\mathbf{k} \cdot \mathbf{p}$ 7–13
- photoluminescence excitation (PLE) 22, 136, 142
- photon 22
 - energy 21, 24, 38
 - wavelength, wavenumber 18, 21
- picture
 - channel 114–119, 123
 - electron-hole 22, 31, 36
 - subband 119–121
 - tilted-band 145, 192–193
- point group 4–7, 11, 228–229
 - diamond O_h 7, 11, 230
 - zincblende T_d 5, 230
- polariton 30
- polarization
 - of light 18–19, 21, 36
 - microscopic 31, 252, 254
 - optical 31, 32, 37, 51
- potential(s)
 - Coulomb 43, 82, 86, 89, 118
 - Fourier transform of 211
 - one-dimensional 43, 119
 - statically screened 32, 34
- long vs. short 34
- long vs. short ranged 116, 129
- periodic 119, 151
 - delta 149, 154
- singular 43, 138
 - discretization of *see* discretization, ground-state-adapted
- stochastic 54, 56, 90–93
- Thomas–Fermi (Debye, Yukawa) 34, 47
- vector 3, 18, 25, 243
- Poynting vector 21
- problem
 - boundary-value 51, 57–59, 70, 78, 126
 - as variational problem 62–63
 - eigenvalue 49, 51, 58, 70, 77–78, 102–103, 150, 231–234, 234–247
 - algebraic (ordinary or generalized) 57–59, 62, 70, 78
 - as variational problem 61–62, 232
 - initial-value 50, 51, 63, 70–71, 78, 83–99, 138
- propagation scheme 84–88
 - Euler 85, 87, 97, 266
 - leapfrog 86, 88, 97, 255, 266
- quantum
 - dot 22, 27, 55, 123
 - structures 123
 - well (QW) 15–17, 22, 24–25, 27, 42, 56, 58, 124, 136–142
 - asymmetric double 141
 - $+B_\perp$ 26, 123
 - $+F_\perp$ 124
 - ideal 53, 74–76, 140
 - wire 22, 25, 26–27, 56, 122, 124–126, 140
 - $+B_\perp$ 124, 125
- quasi-continuum 42, 129, 233
- refractive index 36, 38
- relation(s)
 - Kramers–Kronig 35, 38, 62, 213
 - Lyddane–Sachs–Teller 34
 - orthonormality and closure 14, 37, 50, 150, 159, 164, 231–232, 236
- representation(s)
 - Bloch 31–33
 - crystal-momentum *see* approximation, crystal-momentum
 - (quasi-)momentum 51, 79, 86
 - real-space (Wannier) 33, 52, 86
 - vector and spinor 5–7, 10, 11, 248, 249
- resolvent 104, 146
- resonances 38, 118, 146–147, 170, 191, 202

- Rydberg series 41, 98, 117, 129–133, 140
- scattering approach 59, 122
- Schrödinger equation
- inhomogeneous vs. homogeneous 37, 50
 - time-dependent 60, 84, 97, 197, 255
- screening 32–35, 47
- semiconductor
- bulk *see* semiconductor, three-dimensional
 - d -dimensional 43, 47, 56
 - heterostructure 13–14
 - highly excited 30
 - low-dimensional **13–17**, 24–29, 33, 35, 122–124
 - one-dimensional 25–27, 43, 47, 122–124
 - + F 28–29, 175
 - three-dimensional 23–24, 27, 31–33, 35, **39–43**, 47, 122–124
 - + B 25–27, 56, 124–125, **126–136**
 - + F 27–29, 54, 56, **98–99**
 - two-dimensional 24–25, 122–124
 - + B_{\perp} 26, 52–53, 56, **66–67**, 125
 - ideal 24–27, 39, **42–43**, 47, 52–53, **89–90**, 122, 123
 - zero-dimensional 26, 122–123
- zincblende *see* crystal, zincblende
- shift
- diamagnetic 67, 127, 133
 - Dirac 106, 118
 - Stark 177, 186–187, 190
- Sommerfeld factor 41–43, 129
- spectral gap *see* band gap
- spectrum
- of operators *see* eigenvalues
 - optical *see* absorption
- splines
- B- 73, 83, 156
 - cubic 57, **64**, 65, 68–69
- stability criterion 85, 87, 97
- state *see* eigenstate
- storage *see* memory
- strain 13
- subband 16–17, 115, 120
- superlattice 56, 58, 119, 121, 123–124, 147–148, 154
 - + B_{\perp} 56, 119, 124, 125
 - + F_{\perp} 56, 121, 124, 162, **172–187**, 203–206
- in Faraday geometry 188–190
- shallow 155, 181, 186
- in Voigt geometry 56, 125
- symmetry 33, 39, 50, 65
 - cubic 8, 13
 - translational 15, 26, 28, 199
- time reversal 4, 15, 88, 197, 205, **249–250**, 264
- transition rate 21, 24, 140, 253–254
- transition(s)
- allowed, weakly allowed, and forbidden 24, 76, 137, **138–140**, 142, 177
 - even vs. odd parity 137–138, 200
 - heavy vs. light hole 16–17
 - vertical 21
- Wannier–Stark
- controversy 146, 158, 196
 - ladders 121, 145–148, 160, 173–181, 188–190, 200
 - problem 145, 149, 162
 - resonances 119, 146
- Wigner–Seitz cell 4, 9, 18, **227**, 228
- window resonance 107, 140
- Zeeman effect 10, 12
- Zener
- breakdown 177, 180–181
 - tunneling 145–148, 187–188, 191–206
 - exponential vs. non-exponential 197, 205
 - nonresonant vs. resonant 204–205

Springer Series in Solid-State Sciences

Editors: M. Cardona P. Fulde K.von Klitzing H.-J. Queisser

-
- 1 **Principles of Magnetic Resonance**
3rd Edition By C. P. Slichter
- 2 **Introduction to Solid-State Theory**
By O. Madelung
- 3 **Dynamical Scattering of X-Rays in Crystals** By Z. G. Pinsker
- 4 **Inelastic Electron Tunneling Spectroscopy**
Editor: T. Wolfram
- 5 **Fundamentals of Crystal Growth I**
Macroscopic Equilibrium and Transport Concepts
By F. E. Rosenberger
- 6 **Magnetic Flux Structures in Superconductors**
2nd Edition By R. P. Huebener
- 7 **Green's Functions in Quantum Physics**
2nd Edition By E. N. Economou
- 8 **Solitons and Condensed Matter Physics**
Editors: A. R. Bishop and T. Schneider
- 9 **Photoferroelectrics** By V. M. Fridkin
- 10 **Phonon Dispersion Relations in Insulators** By H. Bilz and W. Kress
- 11 **Electron Transport in Compound Semiconductors** By B. R. Nag
- 12 **The Physics of Elementary Excitations**
By S. Nakajima, Y. Toyozawa, and R. Abe
- 13 **The Physics of Selenium and Tellurium**
Editors: E. Gerlach and P. Grosse
- 14 **Magnetic Bubble Technology** 2nd Edition
By A. H. Eschenfelder
- 15 **Modern Crystallography I**
Fundamentals of Crystals
Symmetry, and Methods of Structural Crystallography
2nd Edition
By B. K. Vainshtein
- 16 **Organic Molecular Crystals**
Their Electronic States By E. A. Silinsh
- 17 **The Theory of Magnetism I**
Statics and Dynamics
By D. C. Mattis
- 18 **Relaxation of Elementary Excitations**
Editors: R. Kubo and E. Hanamura
- 19 **Solitons** Mathematical Methods for Physicists
By G. Eilenberger
- 20 **Theory of Nonlinear Lattices**
2nd Edition By M. Toda
- 21 **Modern Crystallography II**
Structure of Crystals 2nd Edition
By B. K. Vainshtein, V. L. Indenbom, and V. M. Fridkin
- 22 **Point Defects in Semiconductors I**
Theoretical Aspects
By M. Lannoo and J. Bourgoin
- 23 **Physics in One Dimension**
Editors: J. Bernasconi and T. Schneider
- 24 **Physics in High Magnetism Fields**
Editors: S. Chikazumi and N. Miura
- 25 **Fundamental Physics of Amorphous Semiconductors** Editor: F. Yonezawa
- 26 **Elastic Media with Microstructure I**
One-Dimensional Models By I. A. Kunin
- 27 **Superconductivity of Transition Metals**
Their Alloys and Compounds
By S. V. Vonsovsky, Yu. A. Izumov, and E. Z. Kurmaev
- 28 **The Structure and Properties of Matter**
Editor: T. Matsubara
- 29 **Electron Correlation and Magnetism in Narrow-Band Systems** Editor: T. Moriya
- 30 **Statistical Physics I** Equilibrium Statistical Mechanics 2nd Edition
By M. Toda, R. Kubo, N. Saito
- 31 **Statistical Physics II** Nonequilibrium Statistical Mechanics 2nd Edition
By R. Kubo, M. Toda, N. Hashitsume
- 32 **Quantum Theory of Magnetism**
2nd Edition By R. M. White
- 33 **Mixed Crystals** By A. I. Kitaigorodsky
- 34 **Phonons: Theory and Experiments I**
Lattice Dynamics and Models of Interatomic Forces By P. Brüesch
- 35 **Point Defects in Semiconductors II**
Experimental Aspects
By J. Bourgoin and M. Lannoo
- 36 **Modern Crystallography III**
Crystal Growth
By A. A. Chernov
- 37 **Modern Chrystallography IV**
Physical Properties of Crystals
Editor: L. A. Shuvalov
- 38 **Physics of Intercalation Compounds**
Editors: L. Pietronero and E. Tosatti
- 39 **Anderson Localization**
Editors: Y. Nagaoka and H. Fukuyama
- 40 **Semiconductor Physics** An Introduction 6th Edition By K. Seeger
- 41 **The LMTO Method**
Muffin-Tin Orbitals and Electronic Structure
By H. L. Skriver
- 42 **Crystal Optics with Spatial Dispersion, and Excitons** 2nd Edition
By V. M. Agranovich and V. L. Ginzburg
- 43 **Structure Analysis of Point Defects in Solids**
An Introduction to Multiple Magnetic Resonance Spectroscopy
By J.-M. Spaeth, J. R. Niklas, and R. H. Bartram
- 44 **Elastic Media with Microstructure II**
Three-Dimensional Models By I. A. Kunin
- 45 **Electronic Properties of Doped Semiconductors**
By B. I. Shklovskii and A. L. Efros
- 46 **Topological Disorder in Condensed Matter**
Editors: F. Yonezawa and T. Ninomiya
-

Springer Series in Solid-State Sciences

Editors: M. Cardona P. Fulde K.von Klitzing H.-J. Queisser

-
- 47 **Statics and Dynamics of Nonlinear Systems**
Editors: G. Benedek, H. Bilz, and R. Zeyher
- 48 **Magnetic Phase Transitions**
Editors: M. Ausloos and R. J. Elliott
- 49 **Organic Molecular Aggregates**
Electronic Excitation and Interaction Processes
Editors: P. Reineker, H. Haken, and H. C. Wolf
- 50 **Multiple Diffraction of X-Rays in Crystals**
By Shih-Lin Chang
- 51 **Phonon Scattering in Condensed Matter**
Editors: W. Eisenmenger, K. Laßmann, and S. Dötzinger
- 52 **Superconductivity in Magnetic and Exotic Materials** Editors: T. Matsubara and A. Kotani
- 53 **Two-Dimensional Systems, Heterostructures, and Superlattices**
Editors: G. Bauer, F. Kuchar, and H. Heinrich
- 54 **Magnetic Excitations and Fluctuations**
Editors: S. W. Lovesey, U. Balucani, F. Borsa, and V. Tognetti
- 55 **The Theory of Magnetism II** Thermodynamics and Statistical Mechanics By D. C. Mattis
- 56 **Spin Fluctuations in Itinerant Electron Magnetism** By T. Moriya
- 57 **Polycrystalline Semiconductors**
Physical Properties and Applications
Editor: G. Harbecke
- 58 **The Recursion Method and Its Applications**
Editors: D. G. Pettifor and D. L. Weaire
- 59 **Dynamical Processes and Ordering on Solid Surfaces** Editors: A. Yoshimori and M. Tsukada
- 60 **Excitonic Processes in Solids**
By M. Ueta, H. Kanzaki, K. Kobayashi, Y. Toyozawa, and E. Hanamura
- 61 **Localization, Interaction, and Transport Phenomena** Editors: B. Kramer, G. Bergmann, and Y. Bruynseraede
- 62 **Theory of Heavy Fermions and Valence Fluctuations** Editors: T. Kasuya and T. Sasó
- 63 **Electronic Properties of Polymers and Related Compounds**
Editors: H. Kuzmany, M. Mehring, and S. Roth
- 64 **Symmetries in Physics** Group Theory Applied to Physical Problems 2nd Edition By W. Ludwig and C. Falter
- 65 **Phonons: Theory and Experiments II**
Experiments and Interpretation of Experimental Results By P. Brüesch
- 66 **Phonons: Theory and Experiments III**
Phenomena Related to Phonons By P. Brüesch
- 67 **Two-Dimensional Systems: Physics and New Devices**
Editors: G. Bauer, F. Kuchar, and H. Heinrich
- 68 **Phonon Scattering in Condensed Matter V**
Editors: A. C. Anderson and J. P. Wolfe
- 69 **Nonlinearity in Condensed Matter**
Editors: A. R. Bishop, D. K. Campbell, P. Kumar, and S. E. Trullinger
- 70 **From Hamiltonians to Phase Diagrams**
The Electronic and Statistical-Mechanical Theory of sp-Bonded Metals and Alloys By J. Hafner
- 71 **High Magnetic Fields in Semiconductor Physics**
Editor: G. Landwehr
- 72 **One-Dimensional Conductors**
By S. Kagoshima, H. Nagasawa, and T. Sambongi
- 73 **Quantum Solid-State Physics**
Editors: S. V. Vonsovsky and M. I. Katsonel
- 74 **Quantum Monte Carlo Methods in Equilibrium and Nonequilibrium Systems** Editor: M. Suzuki
- 75 **Electronic Structure and Optical Properties of Semiconductors** 2nd Edition
By M. L. Cohen and J. R. Chelikowsky
- 76 **Electronic Properties of Conjugated Polymers**
Editors: H. Kuzmany, M. Mehring, and S. Roth
- 77 **Fermi Surface Effects**
Editors: J. Kondo and A. Yoshimori
- 78 **Group Theory and Its Applications in Physics**
2nd Edition
By T. Inui, Y. Tanabe, and Y. Onodera
- 79 **Elementary Excitations in Quantum Fluids**
Editors: K. Ohbayashi and M. Watabe
- 80 **Monte Carlo Simulation in Statistical Physics**
An Introduction 4th Edition
By K. Binder and D. W. Heermann
- 81 **Core-Level Spectroscopy in Condensed Systems**
Editors: J. Kanamori and A. Kotani
- 82 **Photoelectron Spectroscopy**
Principle and Applications 2nd Edition
By S. Hüfner
- 83 **Physics and Technology of Submicron Structures**
Editors: H. Heinrich, G. Bauer, and F. Kuchar
- 84 **Beyond the Crystalline State** An Emerging Perspective By G. Venkataraman, D. Sahoo, and V. Balakrishnan
- 85 **The Quantum Hall Effects**
Fractional and Integral 2nd Edition
By T. Chakraborty and P. Pietiläinen
- 86 **The Quantum Statistics of Dynamic Processes**
By E. Fick and G. Sauermann
- 87 **High Magnetic Fields in Semiconductor Physics II**
Transport and Optics Editor: G. Landwehr
- 88 **Organic Superconductors** 2nd Edition
By T. Ishiguro, K. Yamaji, and G. Saito
- 89 **Strong Correlation and Superconductivity**
Editors: H. Fukuyama, S. Maekawa, and A. P. Malozemoff

Springer Series in Solid-State Sciences

Editors: M. Cardona P. Fulde K. von Klitzing H.-J. Queisser

- 90 **Earlier and Recent Aspects of Superconductivity**
Editors: J. G. Bednorz and K. A. Müller
- 91 **Electronic Properties of Conjugated Polymers III** Basic Models and Applications
Editors: H. Kuzmany, M. Mehring, and S. Roth
- 92 **Physics and Engineering Applications of Magnetism** Editors: Y. Ishikawa and N. Miura
- 93 **Quasicrystals** Editors: T. Fujiwara and T. Ogawa
- 94 **Electronic Conduction in Oxides** 2nd Edition
By N. Tsuda, K. Nasu, F. Atsushi, and K. Siratori
- 95 **Electronic Materials**
A New Era in Materials Science
Editors: J. R. Chelikowsky and A. Franciosi
- 96 **Electron Liquids** 2nd Edition By A. Isihara
- 97 **Localization and Confinement of Electrons in Semiconductors**
Editors: F. Kuchar, H. Heinrich, and G. Bauer
- 98 **Magnetism and the Electronic Structure of Crystals** By V.A.Gubanov, A.I. Liechtenstein, and A.V. Postnikov
- 99 **Electronic Properties of High-T_c Superconductors and Related Compounds**
Editors: H. Kuzmany, M. Mehring, and J. Fink
- 100 **Electron Correlations in Molecules and Solids** 3rd Edition By P. Fulde
- 101 **High Magnetic Fields in Semiconductor Physics III** Quantum Hall Effect, Transport and Optics By G. Landwehr
- 102 **Conjugated Conducting Polymers**
Editor: H. Kiess
- 103 **Molecular Dynamics Simulations**
Editor: F. Yonezawa
- 104 **Products of Random Matrices**
in Statistical Physics By A. Crisanti, G. Paladin, and A. Vulpiani
- 105 **Self-Trapped Excitons**
2nd Edition By K. S. Song and R. T. Williams
- 106 **Physics of High-Temperature Superconductors**
Editors: S. Maekawa and M. Sato
- 107 **Electronic Properties of Polymers**
Orientation and Dimensionality of Conjugated Systems Editors: H. Kuzmany, M. Mehring, and S. Roth
- 108 **Site Symmetry in Crystals**
Theory and Applications 2nd Edition
By R. A. Evarestov and V. P. Smirnov
- 109 **Transport Phenomena in Mesoscopic Systems** Editors: H. Fukuyama and T. Ando
- 110 **Superlattices and Other Heterostructures**
Symmetry and Optical Phenomena 2nd Edition
By E. L. Ivchenko and G. E. Pikus
- 111 **Low-Dimensional Electronic Systems**
New Concepts
Editors: G. Bauer, F. Kuchar, and H. Heinrich
- 112 **Phonon Scattering in Condensed Matter VII**
Editors: M. Meissner and R. O. Pohl
- 113 **Electronic Properties of High-T_c Superconductors**
Editors: H. Kuzmany, M. Mehring, and J. Fink
- 114 **Interatomic Potential and Structural Stability**
Editors: K. Terakura and H. Akai
- 115 **Ultrafast Spectroscopy of Semiconductors and Semiconductor Nanostructures**
2nd Edition By J. Shah
- 116 **Electron Spectrum of Gapless Semiconductors**
By J. M. Tsidilkovski
- 117 **Electronic Properties of Fullerenes**
Editors: H. Kuzmany, J. Fink, M. Mehring, and S. Roth
- 118 **Correlation Effects in Low-Dimensional Electron Systems**
Editors: A. Okiji and N. Kawakami
- 119 **Spectroscopy of Mott Insulators and Correlated Metals**
Editors: A. Fujimori and Y. Tokura
- 120 **Optical Properties of III-V Semiconductors**
The Influence of Multi-Valley Band Structures By H. Kalt
- 121 **Elementary Processes in Excitations and Reactions on Solid Surfaces**
Editors: A. Okiji, H. Kasai, and K. Makoshi
- 122 **Theory of Magnetism**
By K. Yosida
- 123 **Quantum Kinetics in Transport and Optics of Semiconductors**
By H. Haug and A.-P. Jauho
- 124 **Relaxations of Excited States and Photo-Induced Structural Phase Transitions**
Editor: K. Nasu
- 125 **Physics and Chemistry of Transition-Metal Oxides**
Editors: H. Fukuyama and N. Nagaosa
-